Gluing and Creasing Paper along Curves: Computational Methods for Analysis and Design

By

Klara Mundilova

B.S., TU Wien (2015)
S.M., TU Wien (2017)

Submitted to the Department of Electrical Engineering and Computer Science
in partial fulfillment of the requirements for the degree of

Doctor of Philosophy

at the

MASSACHUSETTS INSTITUTE OF TECHNOLOGY

February 2024

Authored by: Klara Mundilova
Department of Electrical Engineering and Computer Science
October 23, 2023

Certified by: Erik D. Demaine
Professor of Electrical Engineering and Computer Science
Thesis Supervisor

Accepted by: Leslie A. Kolodziejski
Professor of Electrical Engineering and Computer Science
Chair, Department Committee on Graduate Students

Gluing and Creasing Paper along Curves:
Computational Methods for Analysis and Design

by

Klara Mundilova

Submitted to the Department of Electrical Engineering and Computer Science
on October 23, 2023 in partial fulfillment of the requirements for the degree of

Doctor of Philosophy

Abstract

Curved geometries that can be obtained from flat sheets of material have many potential applications in design and engineering. In this thesis, we consider shapes achievable by joining planar patches of material along their curved boundaries, focusing specifically on curved-crease origami as a special case. Our research makes a threefold contribution.

First, we extend the theory behind the computation of shapes consisting of developable patches. Based on classical differential geometry using curvature-based analysis, we consider the gluing of two patches with specified rulings and the pairwise joining of three patches with partial ruling information. We highlight a simplified computational approach for the case when the joined two patches are cylinders or cones that is also applicable in the discrete case. Additionally, we show how to compute a crease that connects a patch with a patch that is composed of tangent-continuous cylinders and cones.

Using this theory, we are able to extend the family of shapes that allow a parametric reconstruction. We provide examples of shapes that allow explicit parametrizations, parametrizations using elliptic integrals, and parametrizations that require numerical integration.

Finally, we employ the developed theory to devise algorithmic design strategies for shapes with curved creases. Inspired by artistic origami, we offer a parametric design tool for the construction of origami spirals. Additionally, we consider two strategies that approximate a polyhedral shape with a modular curved-crease design. Finally, we provide a constructive linear subdivision scheme for regular developable planar quad meshes that correspond to a discretized curved-crease shape.

With this thesis, we aim to make curved-crease origami more accessible for interdisciplinary research in various design and engineering contexts.

Thesis supervisor: Erik D. Demaine
Title: Professor of Electrical Engineering and Computer Science

Acknowledgments

This thesis was shaped by the insights and support of many, and I am deeply grateful to everyone who played a part in its creation.

First, I would like to thank my thesis committee. I'm deeply grateful to Erik Demaine for his mentorship, technical guidance, and support. I'm very thankful to Tomohiro Tachi for many discussions and insights, which helped shape the thesis. I would also like to thank Justin Solomon for his valuable comments on the thesis and for encouraging me to see the bigger picture.

My fascination with curved-crease origami began during my time at TU Wien. A significant portion of this thesis was inspired by a sculpture by Susan Latham, brought to my attention by Tony Wills. I extend my thanks to Helmut Pottmann, Christian Müller, and Simon Flöry for sharing their knowledge and support. The knowledgeable atmosphere at the Institut für Diskrete Mathematik und Geometrie at TU Wien, especially the insights from Martin Peternell and Georg Nawratil, were a great resource of information on developable surfaces and kinematic mechanisms. A special thank you goes to Hannes Wallner from TU Graz for discussions on the fundamentals of developable surfaces.

With the support of the research group at TU Wien, I had the opportunity to participate in the Structural Origami Workshop, an international interdisciplinary forum on origami research. It was here that I met my future research supervisors, Erik Demaine and Tomohiro Tachi, as well as future collaborators like Rupert Maleczek, a fountain of innovative folding ideas, and Duks Koschitz, an expert on David Huffman's work. I'd also like to acknowledge the many insightful discussions I had with other participants of the Structural Origami Workshop, especially Marcus Bernhard, Kenny Chung, Riccardo Foschi, Yves Klett, Robby Kraft, and Simon Thiessen. Additionally, I would like to thank Martin Demaine and Robert Lang for many inspiring conversations.

Over the past year, it has been fun to collaborate with Alfonso Parra Rubio on origami applications and experimenting with fabrication of small and large scale structures, in particular in collaboration with others from the RnKOLEKTIVE.

My academic journey wouldn't have been built on such solid ground without the support of my friends, Moana Glade and Elisabeth Krassnigg, as well as the connections I forged while studying at TU Wien and MIT. This includes Natalia Bialowas, Tobias Fellinger, Andreas Fuchs, Jane Gleizer, Alexander Palmrich, and many others. I would also like to acknowledge the thoughtful feedback I received from Jakub Černý in the final moments of completing this thesis.

Last but not least, heartfelt thanks go to my family: my parents Lucie and David, my sister Tereza, and grandparents Marie, Richard, Hana, and Jan. Their steady support and belief in me have consistently been my anchor. I'm also profoundly grateful to my partner, Kurt Wettstein, for being a reliable belay both in life and on the mountain, always supporting my wildest ideas.

Contents

List of Figures **15**

List of Tables **25**

Prologue **29**

1 Introduction **29**
1.1 Motivation . . . 29
1.2 Basic Definitions . . . 30
1.3 Contributions and Related Work . . . 32
1.3.1 Theory of Gluing and Creasing Developable Patches . . . 32
1.3.2 Parametric Construction of Shapes Obtained by Gluing or Creasing Patches . 33
1.3.3 Computational Design Tools for Shapes Obtained by Gluing or Creasing Patches . . . 34
1.4 Thesis Overview . . . 35
1.4.1 Part I: Curvature-Based Computation of Configurations . . . 35
1.4.2 Part II: Ruling-Length-Based Computation of Configurations of Joined Cylinders and Cones . . . 37
1.4.3 Part III: Ruling-Length-Based Computation of Creases . . . 38

2 Preliminaries on Smooth and Discrete Developable Surfaces **41**
2.1 Ruled Surfaces . . . 41
2.1.1 Smooth Ruled Surfaces . . . 41
2.1.2 Discrete Ruled Surfaces . . . 41
2.2 Developability Condition and Development . . . 42
2.2.1 Smooth Developability Condition and Development . . . 43
2.2.2 Discrete Developability Condition and Development . . . 46
2.3 Singularities . . . 46
2.3.1 Singularities on Smooth Patches . . . 46
2.3.2 Singularities on Discrete Patches . . . 47
2.4 Tangent-Parallel Curves . . . 49
2.4.1 Tangent-Parallel Curves on Smooth Patches . . . 49
2.4.2 Tangent-Parallel Polylines on Discrete Patches . . . 50

I Curvature-Based Computation of Configurations **51**

3 Gluing and Creasing Using Patch Characteristics **53**
3.1 Introduction . . . 53
3.2 Patch Characteristics . . . 54
3.2.1 Parametrization of Ruled Patches . . . 54
3.2.2 Developability Condition and Development . . . 56
3.2.3 Developed Curvature of the Directrix . . . 56
3.2.4 Singularities . . . 58
3.2.5 Tangent-Parallel Curves . . . 58
3.2.6 Ruling Curvature . . . 60
3.2.7 Bending a Developed Patch with Specified Rulings . . . 64
3.2.8 Gluing a Patch to a Specified Curve . . . 65
3.3 Joining Two Patches Patches with Specified Rulings . . . 66
3.3.1 Notation . . . 66
3.3.2 Constraints . . . 67
3.3.3 Gluing: Joining Along Two Curves . . . 68
3.3.4 Creasing: Joining Along Two Matching Curves . . . 74
3.3.5 Practical Considerations . . . 76
3.4 Joining Three Patches with Partial Ruling Information . . . 76
3.4.1 Notation . . . 76
3.4.2 Constraints . . . 77
3.4.3 Gluing: Joining Two Pairs of Curves . . . 78
3.4.4 Creasing: Joining two Pairs of Matching Curves . . . 80
3.4.5 Towards Joining More Surfaces . . . 82
3.5 Gluing Patches along Curves on Patches . . . 83
3.5.1 Gluing a Patch with Unspecified Rulings to a Curve on a Patch . . . 83
3.5.2 Gluing Along a Tangent-Parallel Curve on a Patch . . . 84
3.5.3 Practical Considerations . . . 86

Applications **87**

4 Gluing and Creasing Ellipses **87**
4.1 Introduction . . . 87
4.2 Joining two Ellipses to an Anti D-Form . . . 88
4.2.1 Computation . . . 88
4.2.2 Remarks on the Closure of the Gluing Curve . . . 89
4.2.3 Further Variations . . . 92
4.3 Elliptic Creases . . . 92
4.3.1 Computation of the First Curve . . . 93
4.3.2 Remarks on the Closure of the Crease Curve . . . 93
4.3.3 Adding Pleats . . . 94
4.3.4 Further Variations . . . 96
4.4 Final Remarks . . . 98

5 Connecting Two Patches with Specified Rulings to a Central Patch with Unspecified Rulings **99**
5.1 Introduction . . . 99
5.2 Variations of the Squaricle . . . 100
5.2.1 Ruling Analysis . . . 100
5.2.2 Computation . . . 101
5.2.3 Conclusion . . . 105
5.3 Huffman's Hexagonal Tower . . . 108
5.3.1 Ruling Analysis . . . 108
5.3.2 Computation . . . 109
5.3.3 Conclusion . . . 113

6 Connecting Two Planar or Constant Fold Angle Creases **115**
6.1 Introduction . . . 115
6.2 Kinetic Sculpture from Annuli . . . 116
6.2.1 Computation . . . 116
6.2.2 Kinetic Motion . . . 121
6.3 Constant Angle Creases Along Logarithmic Spirals . . . 122
6.3.1 Computation . . . 122
6.3.2 Conclusion . . . 123

7 Parametrization of Ruling Polylines **125**
7.1 Introduction . . . 125
7.2 Pleated Annulus . . . 126
7.2.1 Computation . . . 126
7.2.2 Remarks on the Closure of the Shape . . . 128
7.2.3 Limitations . . . 130
7.3 Circular Spiral . . . 130
7.3.1 Ruling Analysis . . . 130
7.3.2 Computation . . . 131
7.3.3 Conclusion . . . 132

II Ruling-Length-Based Computation of Configurations of Cylinders and Cones **133**

8 Join-and-Fan Method **135**
8.1 Introduction . . . 135
8.2 Smooth Join-and-Fan Method . . . 136
8.2.1 Input . . . 136
8.2.2 Unknowns . . . 136
8.2.3 Constraints . . . 136
8.2.4 Computation Details . . . 137
8.2.5 Limitations . . . 139
8.3 Discrete Join-and-Fan Method . . . 139
8.3.1 Input . . . 139
8.3.2 Unknowns . . . 139
8.3.3 Constraints . . . 140

8.4 Rigid-Ruling Folding Motions . . . 140
8.5 Rigid Foldability of Discrete Creases between Cylinders and Cones . . . 141
8.5.1 Diagonal Property of Four-bar Linkages . . . 142
8.5.2 Extracting Linkages from Crease Pattern . . . 144
8.5.3 Collinear Linkage Configurations . . . 145
8.5.4 Linkage Motions and the Joining Step . . . 150
8.5.5 Linkage Motions and the Fanning Step . . . 153
8.6 Selected Proofs from Section 8.5 . . . 154

Applications **158**

9 Rotationally Symmetric Polygircles **159**
9.1 Introduction . . . 159
9.2 Notation . . . 162
9.3 Convex Gluing of a Cylindrically-ruled Circle and Polygon . . . 163
9.4 Gluing of a Conically-ruled Circle and a Cylindrically-ruled Polygon . . . 165
9.5 Gluing of a Cylindrically-ruled Circle and a Conically-ruled Polygon . . . 167
9.6 Gluing of a Conically-ruled Circle and Polygon . . . 168

10 Conic Creases with Reflecting Rule Lines **171**
10.1 Introduction . . . 171
10.2 Review of Properties of Conic Sections . . . 172
10.2.1 Conics as Loci of Points . . . 173
10.2.2 Parametrization of Conics with Polar Coordinates . . . 173
10.2.3 Intersections of Tangents of Conics . . . 174
10.2.4 Reflection Properties of Conics . . . 174
10.3 Smooth Conic Crease Patterns with Reflecting Rule Lines . . . 175
10.4 Discretized Conic Crease Patterns with Reflecting Rule Lines . . . 176
10.5 Local Flat Foldability of Discretized Conic Crease Patterns . . . 176
10.5.1 Circumscribed Discretizations . . . 177
10.5.2 Inscribed Discretizations . . . 177
10.6 Conic Creases and the Join-and-Fan Method . . . 178
10.6.1 Input . . . 178
10.6.2 Joining Step . . . 180
10.6.3 Smooth Fanning Step: Parametrization of Conic Creases . . . 182
10.6.4 Discrete Fanning Step: Rigidly Foldable Discretizations . . . 183
10.7 Compatibility of Conic Creases . . . 187
10.7.1 Conic Creases Connected by a Cylinder . . . 187
10.7.2 Conic Creases Connected by a Cone . . . 187
10.8 Implementation . . . 189
10.9 Selected Proofs from Chapter 10 . . . 189

11 Sliding Developables and Planar Creases **193**
11.1 Introduction . . . 193
11.2 Sliding Cylinders and Cones and the Join-and-Fan Method . . . 194
11.2.1 Input . . . 194
11.2.2 Joining Step . . . 194
11.2.3 Discrete Fanning Step: Existence of a Motion . . . 195

11.2.4 Smooth Fanning Step: Existence of a Motion . . . 196
11.3 From Sliding Cones to Sliding Tangent Developables . . . 197
11.3.1 Discrete Case . . . 198
11.3.2 Smooth Case . . . 198
11.4 Folding Motion of Planar Creases . . . 199

III Ruling-Length-Based Computation of Creases 201

12 Patch-to-Patch Construction 203
12.1 Introduction . . . 203
12.2 Notation . . . 204
12.3 Patch-to-Cylinder and Patch-to-Cone Constructions . . . 205
12.3.1 Locating the Crease . . . 205
12.3.2 Planar Creases . . . 206
12.3.3 Valid Patch Combinations . . . 207
12.3.4 Alternative User Input . . . 208
12.3.5 Lotus 1.0 . . . 210
12.4 Patch-to-Projective-Cone . . . 211
12.4.1 Scaling Transformations . . . 211
12.4.2 Locating the Crease . . . 212
12.4.3 Valid Patch Combination . . . 213
12.4.4 Alternative User-Input . . . 215
12.5 Preventing Local Surface Intersections . . . 215
12.6 Tangent Continuity . . . 216
12.6.1 Computing Tangents . . . 216
12.6.2 Combinations of Patch-to-Projective-Cone Constructions . . . 217
12.6.3 Closed Developable Rings and Tangent-continuous Creases . . . 218
12.7 Patch-to-Piecewise-Projective-Cone Construction . . . 220
12.7.1 Input . . . 220
12.7.2 Patch-to-Piecewise-Projective-Cone Construction using Ruling Planes . . . 221
12.7.3 Patch-to-Piecewise-Projective-Cone Construction using Crease Points . . . 222
12.7.4 Lotus 2.0 . . . 223
12.8 Selected Proofs from Chapter 12 . . . 223

Applications 225

13 Analytic Parametrization of Geometric Shapes 225
13.1 Introduction . . . 225
13.2 Parametrization of the Folded Vesica Piscis . . . 226
13.2.1 Vesica Piscis . . . 226
13.2.2 Notation . . . 227
13.2.3 Parametrization of the Seam Curve . . . 227
13.2.4 Parametrization of the Crease Curve . . . 229
13.2.5 Circular Crease Curves . . . 229
13.3 Curved-Crease Designs from Spherical Polyhedra with Regular Faces . . . 230
13.3.1 Spherical Polyhedra with Regular Faces . . . 230
13.3.2 Construction Overview . . . 230

13.3.3 Construction Details . . . 231
13.3.4 Fabrication . . . 234

14 Design of Conic Spirals with Planar Creases **237**
14.1 Introduction . . . 237
14.2 Triangle Wreaths . . . 238
14.3 Curved Spiral Construction . . . 239
14.4 Software Implementation . . . 241

15 Rounded Corner Polyhedra **243**
15.1 Introduction . . . 243
15.2 Notation . . . 245
15.3 Constraints on the Location of the Cone Apices . . . 246
15.3.1 Valid Surface Patch Combinations and Valid Range . . . 246
15.3.2 Preventing Self-intersection . . . 248
15.3.3 Tangent Continuity . . . 249
15.3.4 Feasible Apex Directions . . . 249
15.4 Locating Cone Apices Through Optimization . . . 250
15.4.1 Vertex Normals . . . 250
15.4.2 Optimization Setup . . . 251
15.5 Consistent Material Loss . . . 253
15.5.1 Material Loss . . . 253
15.5.2 Consistency Condition . . . 254
15.5.3 Optimization Setup . . . 255
15.6 Conical Convex Mesh . . . 256
15.7 Design Examples, Limitations, and Future Work . . . 257

16 Wrinkling Paper **259**
16.1 Introduction . . . 259
16.2 Quad Filling . . . 260
16.2.1 Construction of the First Surface . . . 260
16.2.2 Non-Self-Intersecting Cones and Central Functions . . . 261
16.2.3 Surface Fitting . . . 262
16.2.4 Construction of the Remaining Surface(s) . . . 263
16.3 Modular Curved-Crease Designs . . . 264
16.4 Towards Global Origami Development . . . 265
16.4.1 Constraints . . . 266
16.4.2 Filling a 3D Quad with a Prescribed Development . . . 267
16.5 Fabrication . . . 267

17 Developable Regular Planar Quad Mesh Subdivision **271**
17.1 Introduction . . . 271
17.2 PQ Strip Subdivision . . . 272
17.2.1 Limitations . . . 274
17.3 Regular PQ Mesh Subdivision . . . 274
17.3.1 Limitations . . . 275
17.4 Developable PQ Mesh Subdivision . . . 275
17.4.1 Results . . . 277

17.4.2 Limitations and Future Work 277

Epilogue **283**

18 Conclusion **283**
18.1 Summary and Limitations 283
18.1.1 Theory of Gluing and Creasing Developable Patches 283
18.1.2 Parametric Construction of Shapes Obtained by Gluing or Creasing Patches . 284
18.1.3 Computational Design Tools for Shapes Obtained by Gluing or Creasing Patches 285
18.2 Open Problems and Future Work 285
18.2.1 Theoretical Background 286
18.2.2 Part I: Curvature-Based Computation of Configurations 286
18.2.3 Part II: Ruling-Length-Based Computation of Configurations of Joined Cylinders and Cones 287
18.2.4 Part III: Ruling-Length-Based Computation of Creases 287

Bibliography **288**

List of Figures

1.1 Selection of shapes that inspired the research presented in this thesis. Not for reproduction. . . . 30
a Bauhaus model (Albers, 1927–1928). Figure from page 434 of Wingler [109]. 30
b Hexagonal tower with cusps (David Huffman, 1978). Photo by Tony Grant. Figure 4.4.48 in Koschitz [43]. . . . 30
c Squaricle (Tony Wills, 2006). Figure 4 in Wills [108]. . . . 30
d Four columns (David Huffman, 1978). Photo by Tony Grant. Figure 4.4.70 in Koschitz [43]. . . . 30
e Folded Vesica Piscis (Susan Latham, 2008). Figure from author's homepage [49]. . . . 30
f Exploded vertex spiral (David Huffman, undated). Figure 4.11.27 in Koschitz [43]. . . . 30
1.2 Illustration of the terminology used in this thesis. . . . 31
a Smooth boundary-rule and crease-rule pattern. . . . 31
b Folded configuration. . . . 31
c Discrete boundary-rule and crease-rule pattern. . . . 31
d Folded discrete configuration. . . . 31
1.3 Selection of shapes discussed in Part I. . . . 37
a Elliptic pleats (Section 4.3). . . . 37
b Huffman's tower (Section 5.3). . . . 37
c Kinetic sculpture (Section 6.2). . . . 37
d Circular pleats (Section 7.2). . . . 37
1.4 Selection of shapes discussed in Part II. . . . 38
a Two gluings of a square and a circle and their developments with specified rulings (Chapter 9). . . . 38
b Rigid-ruling folding motion of conic crease patterns with reflecting rule lines and their flat and rigidly foldable discretization (Chapter 10). . . . 38
1.5 Selection of shapes discussed in Part III. . . . 39
a Folded Vesica Piscis (Section 13.2). . . . 39
b Origami spirals from cones with planar creases (Chapter 14). . . . 39
c Rounded corner design approach (Chapter 15). . . . 39
d Wrinkling paper design approach (Chapter 16). . . . 39
e Developable subdivision scheme for regular PQ meshes (Chapter 17). . . . 39

2.1 Illustration of smooth ruled patches. . . . 42
a A smooth ruled surface patch that is not developable. . . . 42
b A smooth ruled developable patch and its development. . . . 42

2.2 Illustration of discrete ruled patches. . . . 42
a A discrete ruled surface patch that is not developable. . . . 42
b A discrete ruled developable patch and its development. . . . 42
2.3 Three basic types of a smooth developable patch. . . . 47
a Cylinder. . . . 47
b Cone. . . . 47
c Tangent developable. . . . 47
2.4 Illustration of the edge of regression and tangent-parallel curves of a developable patch. 48

3.1 Illustration of the notation of a patch and its development involving patch characteristics. . . . 55
3.2 Illustration of the relationship between curvatures $K(t)$ and $k(t)$. . . . 57
3.3 Illustration of the Darboux-frame of a principal curvature line of a patch. . . . 61
3.4 Various configurations of a developed patch with specified rulings. . . . 63
a Developed patch with specified rulings. . . . 63
b Bending with prescribed torsion. . . . 63
c Bending with prescribed inclination angle. . . . 63
d Bending with prescribed curvature. . . . 63
3.5 Parametrization of a Möbius-strip in equilibrium. . . . 65
3.6 Two developed patches with specified rulings and their configuration when glued along their directrices. . . . 66
3.7 Illustration of the notation used for gluing two patches with specified rulings in Section 3.3. . . . 67
a Development. . . . 67
b Glued configuration. . . . 67
3.8 Four congruent solutions corresponding to the same development and same initial frame. . . . 69
a Development. . . . 69
b Glued configurations corresponding to S_0, S_1, S_2, and S_3. . . . 69
3.9 Illustration of the relationship between the fold angle ρ and the angles between the left and right surface patches. . . . 71
3.10 Gluing of the two patches depicted in Figure 3.8a for varying opening angles. . . . 73
3.11 Illustration of the two special families of curved creases. . . . 76
a Planar crease. . . . 76
b Crease of constant fold angle. . . . 76
3.12 Illustration of the notation used for gluing three patches with partial ruling information in Section 3.4. . . . 77
a Development. . . . 77
b Glued configuration. . . . 77
3.13 Illustration of two rigidly-foldable crease-rule patterns with tangent-parallel crease curves. . . . 86
a Two tangent-parallel planar creases. . . . 86
b Two tangent-parallel creases of constant fold angle. . . . 86

4.1 Shapes that inspired the content of Chapter 4. . . . 88
a Anti D-form (Tony Wills, 2006). Figure 6 in Wills [108]. . . . 88
b Variations of Bauhaus model with ellipses and circles (Duks Koschitz, 2015). Parts of Figure 3 in Demaine et al. [15] 88

4.2 Two elliptic holes with specified rulings and their gluing. 89
4.3 Illustration of the rigid-ruling folding motion of two glued elliptic holes. 90
4.4 Numerically closed shapes from two elliptic glue curves. 91
4.5 Numerically closed shapes from two elliptic glue curves with modified ruling directions. 91
4.6 Numerically closed folding along a single elliptic crease. 92
4.7 Illustration of the rigid-ruling folding motion of a single elliptic crease. 93
4.8 Numerically closed folded states of a pleated ellipse. 95
4.9 Elliptic crease depicted in Figure 4.6 with tangent-parallel pleats. 96
4.10 Numerically closed folded states of the pleated ellipse with tangent parallel pleats. . 97
4.11 Illustration of the rigid-ruling folding motion in Figure 4.7 with tangent-parallel pleats. 97

5.1 The squaricle and its variations as considered in Section 5.2. 100
a Squaricle (Figure 4 in Wills [108]). 100
b Variation of the squaricle with a central square. 100
5.2 Crease pattern and notation. 101
5.3 Notation of the quantities used in the analysis of the variation of a squaricle. 102
5.4 Illustration of the notation of the development. 103
5.5 Squaricle variations for $r = 0.05$. 106
5.6 Squaricle variations for $r = 0.1$. 107
5.7 Left: Hexagonal tower with cusps (David Huffman, 1978). Photo by Tony Grant. Figure 4.4.48 in Koschitz [43]. Right: Reconstructed crease pattern with guessed rulings. 108
5.8 Folding of the first module. 109
5.9 Composition of two modules of Huffman's tower. 111
a Not aligned boundaries. 111
b Aligned boundaries. 111
5.10 Notation and folding of the modified module. 112
5.11 Final assembled Huffman's hexagonal tower. 113
5.12 Variations of David Huffman's hexagonal tower with circular creases. 114
a Circular creases with radius $r = 4$. 114
b Circular creases with radius $r = 5$. 114

6.1 Kinetic sculpture "Polyannular Cyclide" from annuli designed by Maximilian Klammer (Courtesy Maximilian Klammer). 116
6.2 Illustration of the computational approach for the analysis of the kinetic sculpture. . 117
6.3 Illustration of the construction of the initial values in Section 6.2.1. 118
6.4 Illustration of solutions for $r = \frac{1}{2}$ corresponding to different initial values. 119
a Constant opening angle α and varying distance d. 119
b Varying opening angle α and constant distance d. 119
6.5 Illustration of a motion of a circular patch. 120
6.6 Shape from periodic developable patches that contains the configurations of a variation of the sculpture. 121
6.7 Illustration of the kinetic motion of two variations of the the sculpture. 121
6.8 Illustration of the computations in Section 6.3. 122
a Notation. 122
b Computed developed rulings and folded state. 122
6.9 Illustration of a rigid-ruling folding motion of the spiral. 123

7.1 Two concentric circles with constant fold angle computed with the method discussed in Section 6.3. . . . 126
7.2 Illustration of shapes obtained from the computations in Section 7.2. . . . 127
a Folded shapes with $s = 0.9$. . . . 127
b Folded shapes with $s = 0.8$. . . . 127
7.3 Numerically closed circular creases with added circular pleats towards the center of the shape. . . . 129
7.4 Possible ruling layouts for origami spirals. . . . 130
a Spiral with "spiraling" rulings. . . . 130
b Spiral with "closed" rulings. . . . 130
c Spiral with "conical" rulings. . . . 130
7.5 Illustration of the computations in Section 7.3. . . . 131
a Notation. . . . 131
b Computed developed rulings and folded state. . . . 131

8.1 Illustration of the smooth join-and-fan method for two cones. . . . 137
a Input: Two developed cones. . . . 137
b Joining step. . . . 137
c Fanning step. . . . 137
8.2 Rigid-ruling folding motion of the two cones from Figure 8.1. . . . 141
8.3 Illustration of a linkage derived from a crease between two cones. . . . 142
8.4 Illustration of the three types of a four-bar linkage. . . . 142
8.5 Illustration of the three types of a four-bar linkage with a pair of parallel bars. . . . 143
8.6 Illustration of the three types of a four-bar linkage with two pairs of parallel bars. . . . 144
8.7 Illustration of two collinear configurations of extracted linkages corresponding to cone-cone combinations. . . . 146
8.8 Illustration of two collinear configurations of extracted linkages corresponding to cylinder-cone combinations. . . . 148
8.9 Motions of an extracted four-bar linkage corresponding to a cone-cone combination in standard position. . . . 150
8.10 Motions of an extracted four-bar linkage corresponding to a cylinder-cone combination in standard position. . . . 151
8.11 Motion of a four-bar linkage corresponding to a cylinder-cylinder combination. . . . 152
8.12 Illustration of linkages obtained from the joining step and their corresponding configurations after the fanning step. . . . 153
a Case 1: Cable length increases beyond the configuration corresponding to the flat-folded state. . . . 153
b Case 2: Cable length decreases beyond the configuration corresponding to the flat-folded state. . . . 153
8.13 Illustration of the case analysis from the proof of Theorem 8.2. . . . 154

9.1 Considered ruling variations of circles and polygons. . . . 160
a Circles with conical rulings. . . . 160
b Polygons with conical rulings. . . . 160
c Circles with cylindrical rulings. . . . 160
d Polygons with cylindrical rulings. . . . 160
9.2 Considered gluings of a polygon and a circle. . . . 161
a Convex gluing of a cylindrically-ruled circle and n-gon. . . . 161

b Gluing of a conically-ruled circle and cylindrically-ruled n-gon. 161
c Gluing of a cylindrically-ruled circle and conically-ruled n-gon. 161
d Gluing of a conically-ruled circle and n-gon. 161
9.3 Convex shapes used in the proof of Lemma 9.2. 164
9.4 Illustration of the notation in the proof of Lemma 9.2. 165
9.5 Notation describing the parametrization of the glue curve between a cylindrically-ruled n-gon and a conically-ruled circle. 166
9.6 Notation describing the parametrization of the glue curve between a cylindrically-ruled n-gon and a conically-ruled circle. 168

10.1 Two designs by David Huffman using conic creases with crease-rule pattern sketches. Not for reproduction. 172
a 4-lobed cloverleaf design (1977). Figure 5.3.3. in Koschitz [43]. 172
b Starburst design (undated). Figure 5.8.23 in Koschitz [43]. 172
10.2 A locally flat and rigidly foldable discretization of one of David Huffman's designs with scaled and reflected parabolas. 173
10.3 Illustration of Lemma 10.4. 174
10.4 The nine distinct cases of compatible conic creases with reflecting rule lines sharing a focal point. 175
10.5 Illustration of the considered crease patterns, exemplified by two scaled ellipses with reflecting rule lines. 176
a Smooth crease pattern. 176
b Inscribed discretization. 176
c Circumscribed discretization. 176
10.6 Illustration of the angles around a locally flat-foldable inscribed vertex. 177
10.7 Illustration of Lemma 10.6. 178
10.8 Illustration of the join-and-fan method for conic crease curves. 179
a Elliptic crease. 179
b Hyperbolic crease. 179
c Parabolic crease. 179
10.9 Illustration of the argument for the existence of a contracted configuration of the circumscribed discretization. 184
10.10 Illustration of the argument on the existence of a contracted configuration of the inscribed discretization. 186
10.11 Illustration of the folding motion of compatible elliptic creases. 187
a Smooth creases with a rigid-ruling folding motions. 187
b Locally flat and rigidly-foldable circumscribed discretization. 187
c Rigidly-foldable inscribed discretization. 187
10.12 Illustration of folding motion computed using our implementation. 188
a David Huffman's "4-lobed cloverleaf design" (see Figure 10.1a) and a variation featuring five leaves. 188
b Rigidly-foldable spiral with parabolic creases. 188
c Rigidly-foldable modification of David Huffman's "starburst design" (see Figure 10.1b). 188
10.13 Rigidly foldable design with parabolic creases. 189
10.14 Notation used in the proof of Lemma 10.7 (case (EH1)). 190

11.1 Illustration of the extremal angle $\varphi_{\max}$ used in the sliding cylinder computation. . . 195

11.2 Illustration of the extremal height h used in the sliding cone computation. 196
11.3 Illustration of the connection between sliding cylinders and sliding tangent developables. 197
a Tangent developable $\mathbf{s}(t,u)$. 197
b Cone $\mathbf{s}_\triangle(t,u)$. 197
c Slided configurations $\mathbf{S}_\triangle(t,u)$ of the cone $\mathbf{s}_\triangle(t,u)$. 197
d Slided configurations $\mathbf{S}(t,u)$ of the tangent developable $\mathbf{s}(t,u)$. 197
11.4 Illustration of a rigid-ruling folding motion with planar parallel pleats. 199

12.1 Illustration of the notation for the patch-to-cone and patch-to-cylinder constructions. 204
a Input and result of the patch-to-cone construction. 204
b Input and result of the patch-to-cylinder construction. 204
12.2 Illustration of how the patch-to-cone construction can be used to locate a planar crease. 206
12.3 Four possible combinations of subpatches obtained by intersecting two patches along a curved crease. 207
12.4 Illustration of the notation for user-input 3pt and user-input Tan in the patch-to-cone and patch-to-cylinder constructions. 209
a User-input 3pt. 209
b User-input Tan. 209
12.5 Example of a design process with Lotus 1.0. 210
12.6 Example of a bus stop designed with Lotus 1.0 (Figure 1 in [65]). 210
12.7 Illustration of a scaling transformation. 211
12.8 Notation of the patch-to-projective-cone construction. 212
a Input and result of the patch-to-projective-cone construction with $s = \frac{1}{2}$. . . 212
b Input and result of the patch-to-projective-cone construction with $s = 1$. . . . 212
12.9 Illustration of the notation used in Lemma 12.5. 213
12.10Illustration of non-intersecting surfaces. 215
12.11Closed tangent-continuous curves on closed patches that can be unrolled without a cut. 218
12.12Closed curves on closed patches that require a cut when being unrolled. 219
12.13Illustration of the patch-to-piecewise-projective-cone construction using ruling planes. 221
12.14Illustration of the patch-to-piecewise-projective-cone construction using crease points. 222

13.1 Two shapes with curved creases discussed in Chapter 13. 226
a Reconstruction of Susan Latham's sculpture "Attraction". 226
b Curved-crease design of an icosahedron. 226
13.2 Vesica Piscis in Euclid's Elements. 226
13.3 Susan Latham's "Attraction", Santa Fe (2008). Figure from author's homepage [49]. Not for reproduction. 227
13.4 Parametric setup for the folded configuration and development of one half of the Vesica Piscis. 228
13.5 Diagram representing the crease curves of the two-parameter family of closed shapes. 229
13.6 Examples of folded closed shapes with circular creases. 230
13.7 Curved crease design from a icosidodecahedron. 231
13.8 Part of the curved-folded Icosidodecahedron's development. 231

13.9 Illustration of the proposed three steps in the construction of a folded spherical regular polygon. . . . 232
13.10 Spherical Platonic solids with curved creases and their developments. . . . 233
a Spherical tetrahedron with curved creases. . . . 233
b Spherical hexahedron with curved creases. . . . 233
c Spherical octahedron with curved creases. . . . 233
d Spherical dodecahedron with curved creases. . . . 233
e Spherical icosahedron with curved creases. . . . 233
13.11 Fabricated spherical icosahedron in collaboration with RnKOLEKTIVE. . . . 234

14.1 David Huffman's variations with (un)exploded vertices reconstructed by Duks Koschitz. Figures 5, 7, and 8 in [19]. . . . 238
14.2 Triangle wreath. . . . 238
14.3 Construction steps for the conical spiral (top) and the exploded-vertex spiral (bottom). 239
14.4 Examples of spirals designed using our plug-in and folded from paper. . . . 240
14.5 Examples of more complex spirals designed using our plug-in. . . . 241

15.1 Illustration of an edge-rounded icosahedron. . . . 244
15.2 Overview of the proposed method for edge-rounding a polyhedron. . . . 245
a Step 1: Replace edges with right circular cylinders. . . . 245
b Step 2: Determine the cone that is connected to incident cylinders with curved creases. The crease's shape can be influenced by the user. . . . 245
15.3 Illustration of the notation of the edge-rounded area around a vertex. . . . 246
15.4 Illustration of the desirable region of the spatial cone apex. . . . 247
15.5 Illustration of the considerations to prevent intersecting surfaces. . . . 248
a Curved crease with self-intersections and top view of admissible and forbidden regions for the location of the 3D apex (blue and red, respectively) for a given cylindrical patch. . . . 248
b Illustration of the intersection of all admissible regions. . . . 248
15.6 Illustration of the constraint for valid patch combinations. . . . 251
a Non-saddle vertex. . . . 251
b Saddle vertex. . . . 251
15.7 Edge-rounded low-poly Stanford bunny computed with our Grasshopper component. Notice that only non-saddle shaped vertices can connected to cones with curved creases. 253
15.8 Illustrations highlighting considerations to achieve consistent material loss during the edge-rounding step. . . . 254
a Illustration of the material loss induced by rounding an edge. . . . 254
b Developable tessellation with contracting cycles and regions before and after contraction. . . . 254
15.9 Illustration showcasing the notation used for constraints at a vertex. . . . 254
15.10 Developable edge-rounded chicken wire tesselation. . . . 255
a Computed material loss. . . . 255
b Computed developable edge-rounded shape. . . . 255
c Development. . . . 255
15.11 Developable edge-rounded Miura-ori tessellation. . . . 256
a Computed material loss. . . . 256
b Computed developable edge-rounded shape. . . . 256
c Development. . . . 256

15.12Illustration of the construction of consistent material loss and apex location. 256
15.13Variation of the edge-rounded icosahedron in Figure 15.1, crafted from oak veneer, in collaboration with Alfonso Parra Rubio and other participants of Haystack Labs 2023. 257
15.14Curved origami based shell structure and folded model. 258

16.1 Illustration of the two molecule types suitable for filling a non-planar quad. 260
a Smooth and discrete cone-cone molecule. 260
b Smooth and discrete lens molecule. 260
16.2 Two steps of the quad filling method for the cone-cone molecule and the lens molecule. 261
16.3 Illustration highlighting considerations to avoid creating intersecting surfaces. 261
a Intersecting surfaces. 261
b Projective mapping used for the construction of the base curve of the first surface. 261
16.4 Illustration of the pencil of ruling planes used in the argumentation in Section 16.2.2 for the cone-cone molecule and lens molecule. 262
16.5 Surface fitting. Illustration of the construction steps 1(a) – 1(d). 263
16.6 Pavilion structure designed with modular quads with lenses. 264
16.7 Illustration of the modular curved-crease design workflow. 265
16.8 Illustration of the six possible designs for a non-planar quad. 265
16.9 Patters generated by subdivision and quad filling. 266
16.10Three globally developable curved-crease designs that are based on the same mesh and their crease patterns. 267
16.11A tower with discretized lens molecules, displayed at the MIT MediaLab during summer 2023. 268
16.12Two shapes made from paper-backed veneer. 269
a A curved-crease icosahedron made from oak veneer consisting of 30 trimmed lenses. 269
b An ornament fabricated from four types of paper-backed veneer. 269

17.1 Illustration of the robust behavior of our method for significantly changing rulings. . 272
17.2 Illustration of the proposed subdivision scheme on a PQ strip in the shape of a trefoil knot. 272
17.3 Illustration of the PQ strip subdivision notation. 273
17.4 Illustration of a problematic input for the PQ strip subdivision scheme. 274
17.5 Illustration of the proposed regular PQ mesh subdivision construction. 275
17.6 Examples of the proposed regular PQ mesh subdivision. 276
a First row: Input mesh and the proposed one-directional subdivisions. Second row: Two-directional subdivision with $m \in \{2, 4, 8\}$. 276
b Bidirectional subdivision with $m \in \{2, 4, 8\}$ of the freeform eggbox origami variation. 276
17.7 Illustration of the proposed developable regular PQ mesh subdivision construction. 277
17.8 Illustration of the proposed developable subdivision scheme on a freeform variation of the Miura-ori tessellation. 278
17.9 Illustration of the proposed developable subdivision scheme on a freeform variation of the eggbox tessellation. 278
17.10Application of the developable PQ mesh subdivision to a mesh approximating an open curve in shape of a trefoil knot with pleats. 279

17.11Application of the developable PQ mesh subdivision to a mesh approximating an open curve with pleats. 279
17.12The motion of a subdivided tripod demonstrates a limitation of our method on a non-regular PQ mesh. 279

List of Tables

9.1 Numerically found solutions of $\eta(t_{\max}) = \frac{\pi}{n}$ for h and different n. 169

Prologue

Chapter 1

Introduction

1.1 Motivation

The process of joining planar sheets of non-stretchable material, such as paper or sheet metal, along curved boundaries yields intricate geometries that offer cost-efficient fabrication and space-efficient transportation, while having beneficial structural properties [110, 112]. Consequently, such shapes have multiple applications across various disciplines.

One of the primary engineering applications of joined bent metal or wood sheets is in the design of ship hulls [70, 13]. Another notable domain is in architectural applications, where single curved panels are employed to create semi-discrete surfaces [74]. Traditional examples include onion domes, often seen atop churches in Central Europe. Examples in contemporary architectural designs can be observed in the works of Frank Gehry [30], Carlos Martinez Architekten [5], Zaha Hadid [32], Rupert Maleczek [54], and Duks Koschitz [44].

In the special case where the boundary curves are identical, the joined bent shape can be obtained by creasing a planar sheet along the shared curve, resulting in a so-called curved crease. Shapes composed of bent sheets with curved creases can be found in product design and packaging, such as the furniture designs of Flux [27] and McDonald's packaging of fries. Recent engineering developments have introduced aluminum curved-crease fold cores [28, 62] and functional metamaterials [50].

However, artistic explorations often yield the most intricate and diverse shapes. One of the first references of a sculpture with curved creases dates back to a course in paper study at Bauhaus by Josef Albers, circa 1927—1928 [2]. In the early 1970s, pioneers such as David Huffman [19] and Ron Resch [80] were among the first to systematically explore the potential of shapes created by creasing paper along curves. Contemporary artists continue to expand upon this foundation. For example, Erik and Marty Demaine use swirling surfaces, primarily crafted from circular pleats, to compose captivating sculptures. Richard Sweeney [97] uses pleated creases to sculpt freeform designs. Saadya Sternberg [95] is recognized for his origami faces and animals. Besides sculptural faces, Polly Verity is known for her Bauhaus-inspired tessellations that feature curved creases. Meanwhile, Ekaterina Lukascheva's work [53] is a large collection of mesmerizing patterns and kusudama artworks.

While many technical applications of these shapes face constraints related to practicality and fabrication, the complexity of digital design involving bent planar sheets is another significant limiting factor. As innovative technologies look to harness the potential of these forms, the need for analysis and digital design of these designs grows.

Much of the theory outlined in this thesis stems from the analysis of artistic designs; see

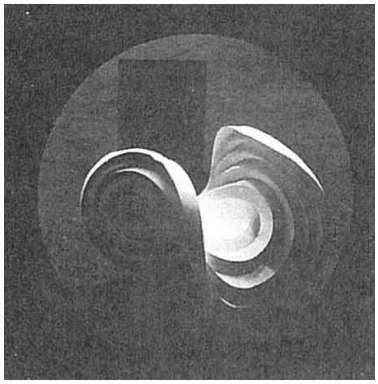

(a) Bauhaus model
(Albers, 1927–1928).
Figure from Wingler [109].

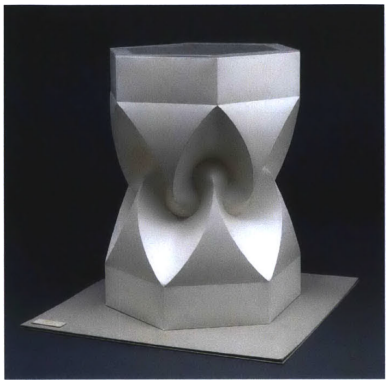

(b) Hexagonal tower with cusps
(David Huffman, 1978).
Figure 4.4.48 in Koschitz [43].

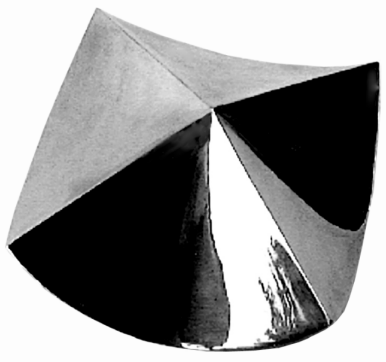

(c) Squaricle
(Tony Wills, 2006).
Figure 4 in Wills [108].

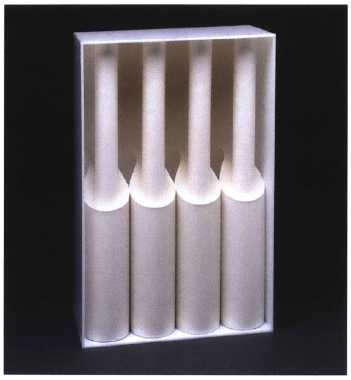

(d) Four columns
(David Huffman, 1978).
Figure 4.4.70 in Koschitz [43].

(e) Folded Vesica Piscis
(Susan Latham, 2008).
Figure from author's
homepage [49].

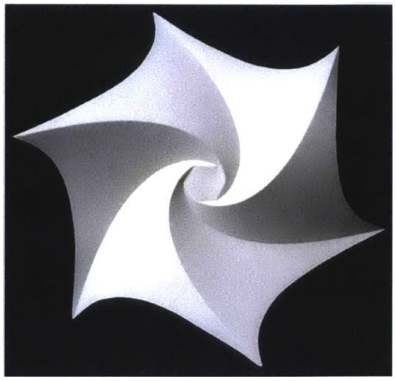

(f) Exploded vertex spiral
(David Huffman, undated).
Figure 4.11.27 in Koschitz [43].

Figure 1.1: Selection of shapes that inspired the research presented in this thesis. Not for reproduction.

Figure 1.1. The first part of this thesis builds on the Bauhaus model, artwork of David Huffman (particularly his hexagonal tower), and (Anti) D-forms designed by Tony Wills. The second part is inspired by Tony Wills' squaricle and David Huffman's conic crease patterns with reflecting rule lines. The final part builds upon the theory developed from analyzing Susan Latham's folded Vesica Piscis and David Huffman's exploded vertex spirals.

1.2 Basic Definitions

Mathematical surfaces resembling a piece of bent paper or another sheet of material, that is, smooth (tangent-continuous) surfaces that can be flattened onto a plane without stretching or tearing, are known as developable surfaces. Developable surfaces are spanned by a family of lines known as rule lines or rulings, and are characterized by a constant tangent plane along these lines. Although developable surfaces can theoretically be infinitely long, we typically consider only a finite part for practical reasons. We refer to such finite parts of developable surfaces as smooth patches. We refer

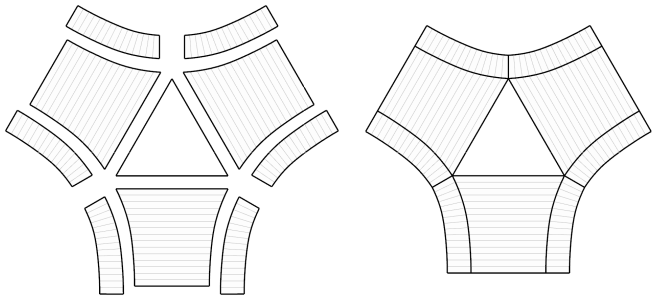

(a) Smooth boundary-rule (left) and crease-rule (right) pattern.

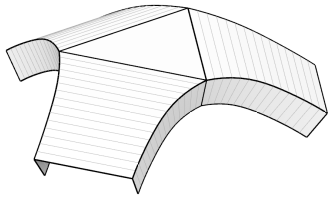

(b) Folded configuration.

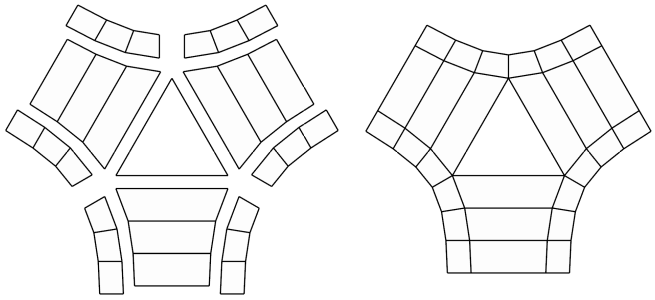

(c) Discrete boundary-rule (left) and crease-rule (right) pattern.

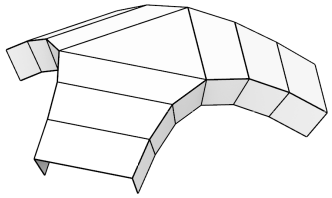

(d) Folded discrete configuration.

Figure 1.2: Illustration of the terminology used in this thesis.

to the flattened counterpart of a developable patch as its development.

The discrete counterparts of smooth patches are strips of triangles and planar quadrangles (quads), as they can also be laid out on the plane without distortion. We will refer to such strips as discrete patches, and to their interior edges as rule lines or rulings.

This thesis studies compositions of patches obtained by gluing their curved or polygonal boundaries and examines their kinematic properties. In the special case where the common curves or polylines match in the development (and the developed patches belong to opposite sides of the common curve), the shape can be made from one sheet by creasing the common curve.

For both smooth and discrete patches with specified rulings, each ruling represents a degree of freedom in the patch's configuration. A smooth patch offers an infinite number of degrees of freedom, while a discrete patch has a finite number. Yet, when joining two patches with specified rulings, there is typically only a one-parameter family of configurations. Joining three patches with specified rulings, a configuration only exists in special cases, as specifying rulings for all three patches becomes over-constraining.

Moving forward, we will refer to a set of developed patches with specified rulings as a boundary-rule pattern; see Figure 1.2. In cases where patches are joined by creases, a crease pattern with ruling assignment will be termed a crease-rule pattern. Motions that preserve the same boundary-rule or crease-rule pattern will be referred to as rigid-ruling folding (for smooth patterns) or rigid folding (for discrete patterns).

1.3 Contributions and Related Work

This thesis contributes to three research areas. The following subsections provide an overview of related work and summarize the findings for each domain.

1.3.1 Theory of Gluing and Creasing Developable Patches

Developable surfaces are extensively studied in differential geometry literature [8, 75]. For many years, the emphasis was on understanding the behavior of individual developable patches. However, recently, there has been an increasing interest in combining these surfaces. Two key questions are:

- How can we compute shapes that are combinations of smooth or discrete patches?
- Which families of shapes possess kinematic properties such as rigid-ruling folding motions?

Related work

Gluing developable patches has in particular been studied in the context of generating convex shapes. Tony Wills [108] introduced D-forms as the shapes obtained by gluing two planar regions of equal perimeter along their boundaries [86]. This concept was further formalized by Pottmann and Wallner [75]. Demaine and Price [21] demonstrate that the unique convex gluing of two smooth convex regions results in the convex hull of its seam curve and is free of creases. However, the parametrization of D-forms from even simple boundary curves are known only in a limited number of cases. Another family of shapes consisting of multiple developable surfaces are T-surfaces, the smooth analogue of T-hedra. Here, the curve shared by two neighboring patches is planar. Izmestiev et al. [37] provide analytic descriptions and discuss their isometric deformations.

David Huffman [34] was one of the first to systematically explore the behavior of curved-creased paper [19, 15]. Notably, he designed many intriguing shapes by creasing paper along conics [43]. Fuchs and Tabachnikov [26] formalized joining two patches along a curved crease using differential geometric terms. Tachi [100] shows how to generate rigidly foldable vault structures from a single curved crease. In collaboration with Demaine et al., the authors describe geometric characteristics of creases and rulings [16, 17]. Additionally, the authors introduce a crease-to-crease compatibility condition [18], and identify families of crease-rule patterns that allow a rigid-ruling folding motion.

Contributions

We provide a set of tools for the computation of glued and creased shapes, accompanied by numerous examples for computation. Specifically, we extend existing methods for curved-crease folding to include the gluing of two patches with specified rulings (Section 3.3). In addition, we devise a framework for reconstructing shapes from three patches when only partial ruling information is available (Section 3.4). We also highlight kinematic properties of shapes consisting of tangent parallel curves (Section 3.5.2).

In addition, we consider the joining of two smooth or discrete patches that are either cylinders or cones. We demonstrate that these computations can be significantly simplified. Specifically, we introduce the "join-and-fan" method, which allows for the computation of the glued or creased configurations of a cylinder or a cone in two steps (Chapter 8). In the special case of developable discrete crease patterns between cylinders and cones, we discuss sufficient constraints for the existence of a rigid-ruling folding motion which is also applicable to non-flat-foldable patterns (Section 8.5). We apply this method to establish the rigid-foldability of two discretizations of conic crease patterns with reflecting rulings (Section 10.6.4).

We also demonstrate how to determine the crease curve on a patch that connects a given developable surface with either a cylinder or a cone (Section 12.3). Finally, we formalize two approaches to compute the crease between a patch and another patch composed of piece-wise cylinders and cones (Section 12.7).

1.3.2 Parametric Construction of Shapes Obtained by Gluing or Creasing Patches

The complexity of the mathematical expressions involved often restricts the practical application of the theory to shapes that can be readily created by gluing or creasing paper. Moreover, determining the correct ruling layout based solely on observations is challenging [25]. Paper's potential to allow small imperfections, like minor buckling, add to the complications. For instance, the hyperbolic paraboloid [16] has been demonstrated to not exist mathematically without incorporating additional creases. As a result, there are only a few known parametrizations that describe naturally occurring non-trivial shapes. Key questions related to this exploration include:

- Given a shape, does it mathematically "exist"? In other words, can it be parametrized using developable patches with the specified glue or crease curves?
- What properties can be derived from this parametrization? Does it allow a rigid-ruling folding motion?

Related Work

Wunderlich [111] introduces a family of closed-form parametrizations of a Möbius strip in equilibrium. For an English translation, see Todres [104]. Dirnböck and Stachel [23] analytically examine the properties of the oloid, which is the convex hull of two congruent circles in perpendicular planes, with each circle containing the center of the other. However, other shapes from a single sheet, as discussed by Stachel [91], are not straightforward to describe parametrically. Mayrhofer [56] offers a discussion on the analytic reconstruction of D-forms from ellipses. Yet, determining a parametrization of a D-form originating from two congruent ellipses joined with an arbitrary offset remains an open problem.

Mosley [61] details a parametrization of her design, the "Orb", using elliptic integrals. With a similar approach, Demaine et al. [17] show the existence of lens tessellations with convex curves. Drawing inspiration from Huffman's research on conic crease patterns, Demaine et al. [18] characterize valid conic crease combinations with reflecting rule lines. They demonstrate that valid combinations support a rigid-ruling folding motion.

Lastly, Alese [3] explores concentric circular pleats by attaching circular patches to appropriately chosen space curves and introducing additional circular creases. The author shows that for sufficiently small radii, circular creases can be propagated finitely many times.

Contributions

In this thesis, we provide analytic descriptions of multiple families of shapes that serve as examples of the developed theory.

We use the smooth join-and-fan method to find explicit parametrizations of the convex polygircle, that is, the unique gluing between a polygon and a circle (Section 9.3). Additionally, we determine explicit parametrizations of a family of modular curved crease designs in the shape of spherical polyhedra (Section 13.3).

Up to elliptic integrals, we find parametrizations of shapes with conic creases and (Section 10.6.3) and variations of the Vesica Piscis (Section 13.2).

In addition, we apply the developed theory to obtain examples visualized through numerical integration. These examples include Anti D-forms from elliptical holes (Section 4.2) and pleated closed shapes exemplified by elliptic creases (Section 4.3), which we determined by estimating suitable ruling angles. Furthermore, we analyze Huffman's hexagonal tower (Section 5.3) and variations of the gluing of a square and a circle (Section 5.2), which we compute using partial ruling information. Inspired by Maximilian Klammer's kinetic sculpture "Polyannular Cyclide", we determine the rulings of patches subject to their curved boundaries being planar (Section 6.2). Lastly, we identify a computational approach for periodic shapes corresponding to circular pleats with at least two creases (Section 7.2). While we do not answer the open problem of whether the pleats can be propagated infinitely many times, our computations provide a three-parameter family of (numerically) closed folded shapes (with a finite number of creases), reflecting the flexibility of a folded shape with periodic symmetry.

1.3.3 Computational Design Tools for Shapes Obtained by Gluing or Creasing Patches

Developable surfaces are popular in industrial applications due to their cost-efficient fabrication properties as they can be derived from a one-directional bending of a planar sheet. Consequently, recent work has introduced many strategies to approximate geometric data with developable patches or to devise strategies for their designs. However, some of these methods rely on a favorable initial configuration and face a trade-off between computational stability and the resolution of the result. While many of these efforts have produced impressive results, there remains room for new algorithmic strategies for the design of complex shapes from glued or creased patches.

Related Work

Various strategies have been developed from different perspectives to approximate geometric data using developable surfaces. Peternell [71] studies developable surface fitting to point clouds. Kilian et al. [41] propose an optimization-based framework for digital reconstruction of shapes consisting of developable surfaces as planar quad-dominant meshes. Stein et al. [92] propose a variational approach to modify a given mesh toward developable pieces separated by regular seam curves. Sellán et al. [83] obtain piecewise developable meshes by phrasing a rank minimization problem which results in a convex semidefinite optimization. Ion et al. [36] wrap a shape into piecewise developables by projecting developable patches, each modeled as a discrete orthogonal geodesic net, onto the shape. Binninger et al. [9] use the approach of Gauss image thinning to obtain a piecewise developable mesh. Verhooven et al. [107] propose an algorithm to remesh triangle meshes representing developable surfaces to planar quad dominant meshes.

Approaches for interactive modeling of surfaces consisting of developable patches have also been subject to investigations. Mitani et al. [60, 58] develop an interactive design tool for shapes consisting of planar creases. Solomon et al. [88] represent curved-crease designs by quad-dominant meshes optimized with discrete bending energies. Tang et al. [103] optimize the control points of B-spline surfaces for developability for interactive design. Another line of work by [77, 76, 78] uses discrete orthogonal geodesic nets to allow manipulating developable surfaces with curved creases. This method has the benefit that the edges of the underlying mesh do not need to be aligned with the rule lines of the surface which benefits robustness. Recently, developable quad meshes and discrete-isometric mappings have been studied in the context of canonical checkerboard patterns [39, 35], where developability is imposed by constraining the rank of the second fundamental form.

Contributions

Based on the developed theory, we devise multiple design tools for shapes with curved creases, which we implemented in Grasshopper/Rhino [81, 57].

Our implementation of the patch-to-patch method (Section 12.3) provides an interactive software tool for designing complex shapes using the additive construction of creases.

Inspired by curved-crease origami spirals, we develop a constructive approach to generate origami spirals using cones and planar creases (Chapter 14).

In our goal to approximate a polyhedral mesh with modular curved-crease shapes, we devise two design strategies. The first replaces each edge of the shape with a cylinder and connects all cylinders incident with a vertex using a tangent-continuous cone (Chapter 15). The second family of shapes approximates an input polyhedron using modular curved-crease origami molecules that are inspired by Huffman's tessellations (Chapter 16).

Finally, we introduce a linear-time subdivision scheme for regular developable planar quad meshes (Chapter 17). In combination with a solver that optimizes the coarse mesh for developability and planar faces, this tool allows for interactive exploration of fine and precise developable regular planar quad meshes.

1.4 Thesis Overview

In this thesis, we examine gluing and creasing of developable patches using two techniques. The first technique employs a curvature-based analysis, using tools from classical differential geometry. The second technique uses a ruling-length-based approach, applicable only to cases involving cylinders and cones.

The thesis is structured into three parts, with each focusing on a unique combination of methods or objectives. In Part I, we compute configurations of combinations of smooth patches using the curvature-based approach. In Part II, we adopt a ruling-length-based approach to determine configurations of either smooth or discrete combinations of cylinders and cones. Finally, Part III uses a ruling-length-based approach to compute the crease between a developable patch and a patch consisting of tangent-continuous cylinders and cones.

When applied successfully, the presented computational methods yield precise glued or creased shapes that comprise a sequential combination of developable patches. However, in many instances, closing a loop of patches remains limited to special cases.

Each part begins with a chapter introducing the theory, followed by chapters showcasing its practical applications.

1.4.1 Part I: Curvature-Based Computation of Configurations

In Chapter 3, we introduce a toolbox that can be used to analyze and reconstruct glued or creased shapes through classical differential-geometric methods. Specifically, we build upon existing work of Fuchs and Tabachnikov [26], as well as that of Demaine et al. [18], and express the ruling directions of a smooth developable patch using quantities associated with the Frenet-Serret equations specifying a space curve incident to the considered developable patch. This toolbox includes:

- We show how to glue two patches with complete ruling information. For computational purposes, we propose a simplification of the corresponding differential-algebraic system to a single differential equation and algebraic equalities. In addition, we connect the opening angle of the surfaces to the initial values of the differential equation.

- We show how to join three patches with only partial ruling information. Specifically, we discuss three cases how to encode the partial ruling information:
  - The rulings of the left and right patch are given, and our goal is to determine the rulings of the central patch.
  - In case of creasing, the type of connection is specified (planar or constant angle).
  - The shape of polylines consisting of three consecutive rulings is encoded by an unknown function.
- Lastly, we discuss methods to append additional surfaces to the existing shape. In general, the ruling directions of an attached surface depend on the shape of the patch they are attached to. Even if a bending of the to-be-appended-to patch preserves the developed ruling directions, in general it results in a change of the rulings of the appended patch. We highlight a special case where the composition of surfaces still allows a rigid ruling motion, that is, when the surfaces are joined along tangent parallel curves.

Our proposed toolkit allows for computational analysis or design of shapes by joining either two patches with specified rulings or three patches with only partially specified rulings. Additionally, one can append further patches to the 3D configuration.

Advantages. The proposed approach of joining two developable patches is suitable for application to any composition of parametrized patches with specified rulings. However, not every combination of patches with specified rulings and opening angles results in a valid glued or creased state. Since deducing the correct rulings of a shape is non-trivial, allowing for partial ruling specification broadens the range of shapes that can be analyzed and reconstructed. Joining patches along tangent parallel curves enables the creation of complex structures with glue or crease curves that fold with rigid rulings.

Generally, the proposed methods yield precise glued or creased shapes applicable to a wide variety of developable patches, and their accuracy is limited only by the numerical precision of the computational mathematical tool used.

Disadvantages. One of the primary limitations of the proposed methods is that it is often non-trivial to determine or even estimate ruling directions that would achieve the desired shape. Furthermore, we lack control over the ruling directions of the appended surfaces.

Additionally, the setup and computation often requires mathematical background and careful preparation, making it unsuitable for users without a foundation in differential geometry and differential equations. Except for very basic shapes, integration of the Frenet-Serret equations typically does not yield explicit parametrizations, limiting the computation to numerical integrals. As the number of attached patches grows, the resulting expressions become more complicated, potentially leading to the accumulation of numerical errors.

In its current formulation, the proposed method to join three patches with only partial ruling information is constrained to cases with an explicit relationship between the curve's parametrization and its curvature (at arc-length parameter) of both curves corresponding to a joined pair.

Applications. To illustrate the versatility of the proposed methods, we consider multiple examples and applications:

- In Chapter 4, we consider the gluing and creasing of ellipses. The discussed examples are inspired by Anti D-form and the Bauhaus model; see Figure 1.3a.

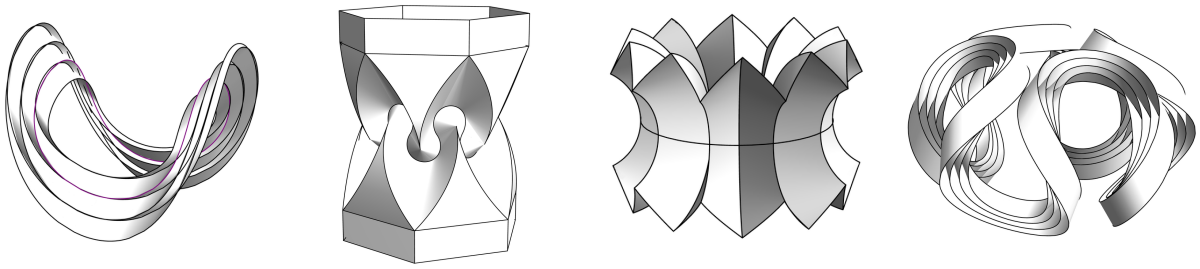

(a) Elliptic pleats (Section 4.3).

(b) Huffman's tower (Section 5.3).

(c) Kinetic sculpture (Section 6.2).

(d) Circular pleats (Section 7.2).

Figure 1.3: Selection of shapes discussed in Part I.

- In Chapter 5, we consider how to connect two patches with specified rulings with a central patch with unspecified rulings. The discussed examples include variations of the squaricle and the analysis of Huffman's hexagonal tower; see Figure 1.3b.
- In Chapter 6, we consider how to connect two planar and two constant angle creases. The discussed examples include a kinetic sculpture (see Figure 1.3c) and a rigid-ruling folding of two logarithmic spiral curves.
- In Chapter 7, we consider approaches that encode the rulings of the shape using an initially unknown function. The computed examples include circular pleats (see Figure 1.3d) and an unsuccessful attempt to analyze a spiral with circular creases.

1.4.2 Part II: Ruling-Length-Based Computation of Configurations of Joined Cylinders and Cones

In Chapter 8, we consider the special case of computing the configuration that corresponds to the gluing of two smooth or discrete patches that are either cylinders or cones. Since the developability condition is trivially satisfied when the 3D rulings are kept parallel or converge at a point, the problem simplifies to ensuring that intrinsic distances are the same in 2D and 3D.

We formalize the join-and-fan method that allows for the computation of the configuration of two glued or creased cylinders or cones in two steps. In the joining step, we combine the rulings of the two involved cylinders to a planar linkage, using explicit algebraic expressions. In the second step, we fan out the bars of the planar linkage, resulting in at most one differential or difference equation to compute the gluing curve.

In the special case of joining two discrete cylinders or cones along a crease, we use a linkage-based argument to show sufficient conditions for a rigid folding motion between the developed and the folded configuration.

Advantages. The simplified computations give further insight into the existence of folded states and motions of shapes obtained by gluing or creasing two cylinders or cones, and are applicable to both the smooth and discrete case.

Additionally, the presented computations have the benefit of requiring at most one (smooth or discrete) integration step, which in some cases allows us to find a closed form parametrization.

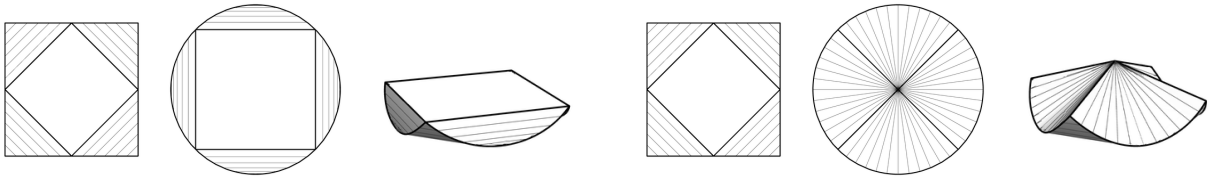

(a) Two gluings of a square and a circle and their developments with specified rulings. Left: Convex gluing. Right: Tony Wills' squaricle (Chapter 9).

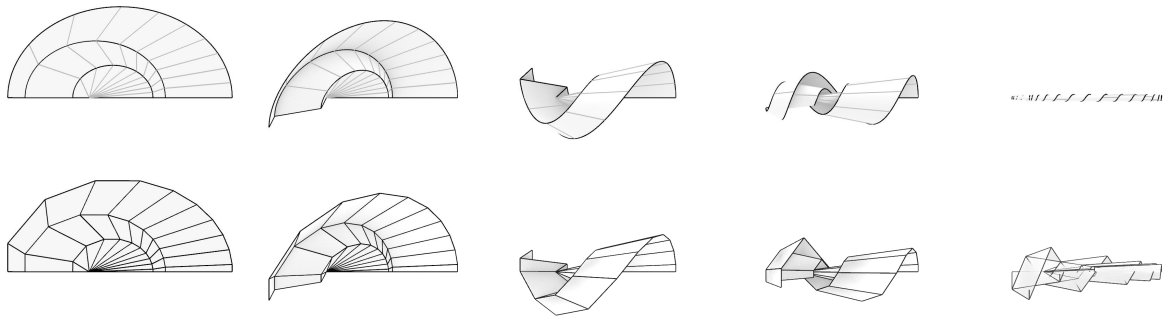

(b) Rigid-ruling folding motion of conic crease patterns with reflecting rule lines and their flat and rigidly foldable discretization (Chapter 10).

Figure 1.4: Selection of shapes discussed in Part II.

Disadvantages. The proposed method is limited to only combinations of two surfaces that are either cylinders or cones.

Applications. To illustrate the simplified computations, we consider multiple examples and applications:

- In Chapter 9, we consider rotationally symmetric gluings of a polygon and a circle; see Figure 1.4a. We state an explicit arc-length parametrization of the convex realization of such a gluing, and provide computational insights into shapes with other ruling combinations.
- In Chapter 10, we apply the join-and-fan method to find parametrizations of conic creases with reflecting rule lines. In addition, we introduce two discretizations of conic crease patterns with reflecting rule lines, and use the join-and-fan method to provide a constructive proof for their rigid foldability; see Figure 1.4b.
- In Chapter 11, we explore a type of rigid-ruling folding that maintains the planarity of a fixed curve on the patch. Because the folding motion resembles a gliding motion, we have termed the resulting patches sliding developables. These sliding developables offer practical advantages, providing an intuitive design framework for developable patches.

1.4.3 Part III: Ruling-Length-Based Computation of Creases

In Chapter 12, we introduce a ruling-based design approach which begins with either a smooth or discrete bent developable patch and sequentially computes creases (whether smooth or discrete) that connect the patch with a sequence of cylinders or cones.

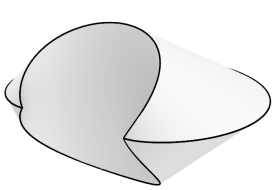

(a) Folded Vesica Piscis (Section 13.2).

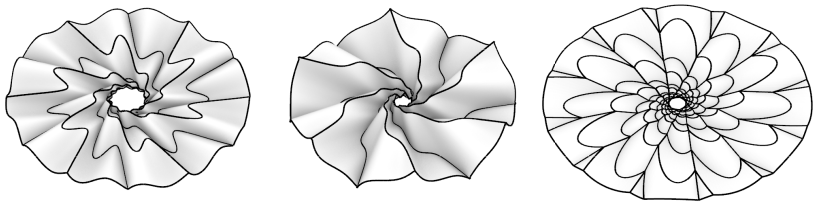

(b) Origami spirals from cones with planar creases (Chapter 14).

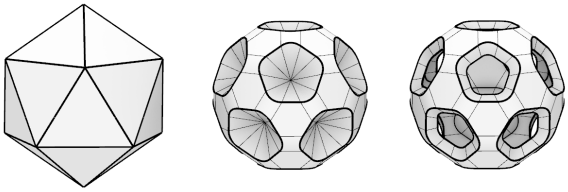

(c) Rounded corner design approach (Chapter 15).

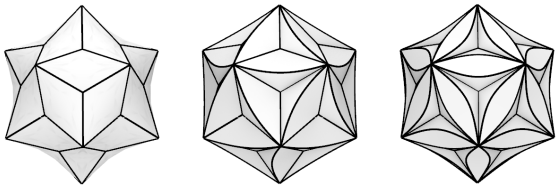

(d) Wrinkling paper design approach (Chapter 16).

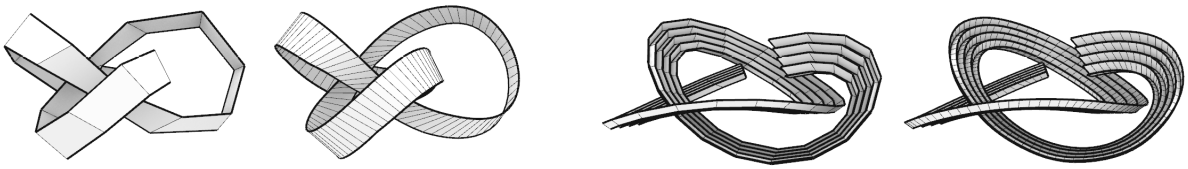

(e) Developable subdivision scheme for regular PQ meshes (Chapter 17).

Figure 1.5: Selection of shapes discussed in Part III.

Initially, we outline the patch-to-cylinder and patch-to-cone construction methods. These techniques determine a crease connecting a given developable patch with a cylinder, defined by its ruling direction, or a cone, defined by its apex.

To avoid the need for a case-by-case analysis between cylinders and cones, and to enhance the computational robustness, we combine both methods into the patch-to-projective-cone construction. Finally, we show a method for constructing a crease between a patch and a tangent-continuous sequence of projective cones.

Advantages. The presented construction methods offer the advantage that if a patch's development is known, the crease can be determined using an explicit algebraic expression. As a result, they are well-suited for implementation in CAD environments. Furthermore, these methods provide an intuitive input based solely on 3D information, making them suitable for interactive design by users without an in-depth understanding of the underlying computation.

Disadvantages. Unlike optimization-based approaches, the design of shapes with this method is additive, supporting only a tree-like connectivity of connected patches. Consequently, closure of the designed shapes mostly relies on symmetry. Additionally, the control over the location of the crease curve is limited.

Applications. We show the versatility of the proposed method in multiple examples:

- In Chapter 13, we show two applications of the patch-to-cylinder and patch-to-cone methods and find (up to elliptic integrals) closed-form parametrizations of two families of shapes, generalizations of the folded Vesica Piscis, see Figure 1.5a, and curved-crease designs of rounded regular spherical polyhedra.
- In Chapter 14, we show how to construct smooth and discrete origami spirals composed of cones and planar creases; see Figure 1.5b.
- In Chapter 15, we design curved-crease shapes by rounding the edges of a polyhedron with right circular cylinders and replacing its vertices with a cone that is connected to adjacent cylinders by a curved crease; see Figure 1.5c.
- In Chapter 16, we design curved-crease shapes by filling each non-planar face of a mesh with modular tessellation-inspired molecules; see Figure 1.5d.
- In Chapter 17, we show how to use the patch-to-projective-cone construction to subdivide an almost developable planar quad mesh into a developable planar quad mesh; see Figure 1.5e. This construction is linear in the number of constructed rulings and therefore suited for interactive design.

Chapter 2

Preliminaries on Smooth and Discrete Developable Surfaces

In the following, we introduce smooth (developable) patches and their discrete analogues as (finite parts of) either smooth or discrete ruled surfaces[1]. To ensure developability, we will impose a condition that these surfaces must satisfy.

2.1 Ruled Surfaces

A smooth ruled surface is a surface that consists of a continuous one-parameter family of lines; see Figure 2.1. Its discrete counterpart, a discrete ruled surface, consists of a discrete set of lines; see Figure 2.2. In both contexts, these lines are called *rulings* or *rule lines*. For finite parts of surfaces, we may also refer to them as *rule segments*.

2.1.1 Smooth Ruled Surfaces

In this thesis, we describe a *smooth*[2] *ruled surface* by

$$\mathbf{S}(t,u) = \mathbf{X}(t) + u\mathbf{R}(t), \tag{2.1}$$

for $t \in T = [0, t_{\max}]$ and $u \in \mathbb{R}$. Here, $\mathbf{X}(t) : T \to \mathbb{R}^3$ is a regular[3] C^1 space curve, the *directrix*, and $\mathbf{R}(t) : T \to S^2$ a C^1 space curve on the unit sphere, the *ruling directions*. Unless specified otherwise, we assume that the ruling directions are not aligned with the incident tangent direction of $\mathbf{X}(t)$, meaning $|\mathbf{X}'(t) \times \mathbf{R}(t)| \neq 0$.

2.1.2 Discrete Ruled Surfaces

In the discrete case, let $T = (t_0, t_1, \ldots, t_n)$ be an array of parameter values. We describe a *discrete ruled surface* by

$$\mathbf{S}(t,u) = \mathbf{X}(t) + u\mathbf{R}(t), \tag{2.2}$$

[1] In this thesis, we use the term *smooth or discrete surface* to refer to a map from a subset of $\mathbb{R}^2$, the *domain*, to $\mathbb{R}^3$. Typically, the domains used in this thesis can be represented as $T \times \mathbb{R}$, where T is a continuous subset of $\mathbb{R}$ for smooth surfaces, or a discrete subset of $\mathbb{R}$ for discrete surfaces.

[2] Note that in our context, we employ the term "smooth" to distinguish between smooth and discrete surfaces. Unlike other literature on differential geometry, when we refer to "smooth," it indicates that both the directrix and ruling vectors possess C^1 continuity (unless specified otherwise).

[3] We refer to a space curve $\mathbf{X}(t)$ as *regular* if $|\mathbf{X}'(t)| \neq 0$ for all parameter values t.

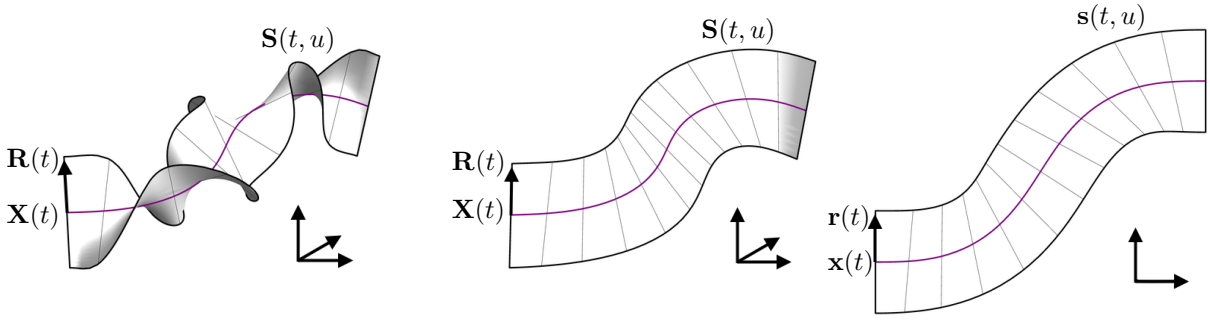

(a) A smooth ruled surface patch that is not developable.

(b) A smooth ruled developable patch (left) and its development (right).

Figure 2.1: Illustration of smooth ruled patches.

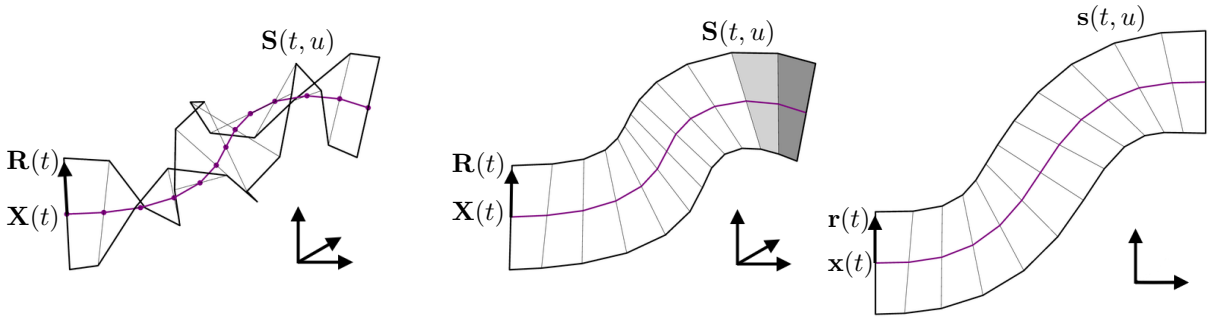

(a) A discrete ruled surface patch that is not developable.

(b) A discrete ruled developable patch (left) and its development (right).

Figure 2.2: Illustration of discrete ruled patches.

for $t \in T$ and $u \in \mathbb{R}$. Here, $\mathbf{X}(t) : T \to \mathbb{R}^3$ is a regular[4] polyline, and $\mathbf{R}(t) : T \to S^2$ is a polyline on the unit sphere. Similar to the smooth case, we refer to $\mathbf{X}(t)$ as the *directrix* and to $\mathbf{R}(t)$ as *rulings directions*. Unless specified otherwise, we assume that the ruling directions are not aligned with the edges of the incident polyline, that is, $|\mathbf{R}(t_i) \times (\mathbf{X}(t_{i+1}) - \mathbf{X}(t_i))| \neq 0$ and $|\mathbf{R}(t_{i+1}) \times (\mathbf{X}(t_{i+1}) - \mathbf{X}(t_i))| \neq 0$.

2.2 Developability Condition and Development

Smooth and discrete surfaces that can be flattened into the plane without distortion are called developable surfaces. We will refer to an isometric planar counterpart (typically in the xy-plane) as the *development*.

Both smooth and discrete developable surfaces come in many forms. However, for our practical applications, we are primarily interested in smooth surfaces and their corresponding discrete versions, rather than in shapes that resemble crumpled paper.

In the following, we adopt the notation of Demaine et al. [17, 18]. Specifically, we use uppercase letters to denote 3D quantities and lowercase letters for the corresponding quantities in the development.

[4]We refer to a polyline $\mathbf{X}(t)$ as *regular* if $|\mathbf{X}(t_i) - \mathbf{X}(t_{i+1})| \neq 0$ for all $i < n$.

2.2.1 Smooth Developability Condition and Development

Smooth developable surfaces are well-studied in classical differential geometric literature [90, 75], and in the context of curved-crease origami [16, 17, 18].

According to Gauss's Theorema Egregium [29], a C^2 surface that can be flattened into a plane without stretching or tearing is characterized by vanishing Gaussian curvature. Moreover, points on a C^2 surface with zero Gaussian curvature are essentially either parabolic or flat [75, 33]. This allows for parametrizations using ruled surfaces that maintain constant tangent planes along their rulings.

However, the situation differs for surfaces that are only C^1 [75]. According to Nash's embedding theorem [68], a developable C^1 surface can take the shape of a torus in Euclidean space. Recently, Borrelli et al. [11] published an algorithm that enables the visualization of such a flat torus. The resulting "wrinkled" surface has tangent planes defined at every point, but the normals exhibit fractal behavior.

For computational convenience, we focus on ruled surfaces that possess an isometric counterpart in the xy-plane. We show that a tangent-continuous ruled surface is developable if and only if all its rulings are torsal; meaning, the tangent planes (if defined) corresponding to the same rulings coincide.

Lemma 2.1. *A smooth ruled surface* $\mathbf{S}(t,u) = \mathbf{X}(t) + u\mathbf{R}(t)$ *(as defined in Section 2.1.1) is developable if it satisfies the* developability condition *for all* $t \in T$*,*

$$\det(\mathbf{R}(t), \mathbf{R}'(t), \mathbf{X}'(t)) = 0. \tag{2.3}$$

The development $\mathbf{s}(t,u) = \mathbf{x}(t) + u\mathbf{r}(t)$ *of a developable patch* $\mathbf{S}(t,u)$ *can be obtained as* $\mathbf{r}(t) = (\cos\alpha(t), \sin\alpha(t), 0)$ *where*

$$\alpha'(t) = \frac{\mathbf{R}'(t)\cdot\mathbf{X}'(t)}{\sqrt{|\mathbf{X}'(t)|^2 - |\mathbf{R}(t)\cdot\mathbf{X}'(t)|^2}}, \tag{2.4}$$

and $\mathbf{x}(t) = (\mathbf{x}_x(t), \mathbf{x}_y(t), 0)$ *where*

$$\begin{pmatrix}\mathbf{x}_x'(t)\\ \mathbf{x}_y'(t)\end{pmatrix} = \begin{pmatrix}(\mathbf{R}(t)\cdot\mathbf{X}'(t))\cos\alpha(t) + \sqrt{|\mathbf{X}'(t)|^2 - |\mathbf{R}(t)\cdot\mathbf{X}'(t)|^2}\sin\alpha(t)\\ (\mathbf{R}(t)\cdot\mathbf{X}'(t))\sin\alpha(t) - \sqrt{|\mathbf{X}'(t)|^2 - |\mathbf{R}(t)\cdot\mathbf{X}'(t)|^2}\cos\alpha(t)\end{pmatrix}. \tag{2.5}$$

Since $|\mathbf{X}'(t)| > |\mathbf{R}(t)\cdot\mathbf{X}'(t)|$*, the solution to the differential equations are real-valued, and* $\mathbf{x}(t)$ *and* $\mathbf{r}(t)$ *are tangent-continuous.*

Proof. We prove the claim in three steps:

- *Step 1:* First, we gather five constraints necessary for the developed quantities. This results in a system of differential-algebraic equations for the coordinate functions of $\mathbf{r}(t)$ and $\mathbf{x}(t)$.
- *Step 2:* We show that a solution that satisfies the differential-algebraic system corresponds to the directrix and ruling direction of the development of $\mathbf{s}(t,u)$.
- *Step 3:* We then confirm that the integrals in Equation (2.4) and Equation (2.5) provide solutions to the stated differential-algebraic system.

Step 1. We start by identifying five constraints necessary for specifying the development. Since isometry preserves both distances and angles, the involved quantities must meet the following constraints:

(1) The developed rulings are of unit length, that is, $|\mathbf{r}(t)| = |\mathbf{R}(t)| = 1$.

(2) The parametrization speed of the 3D and 2D directrices need to be the same, that is, $|\mathbf{x}'(t)| = |\mathbf{X}'(t)|$.

(3) The angle between the ruling and tangent needs to be the same. With constraints (1) and (2), this requirement simplifies to $\mathbf{r}(t) \cdot \mathbf{x}'(t) = \mathbf{R}(t) \cdot \mathbf{X}'(t)$.

(4) As the developability condition implies that $\mathbf{R}'(t)$ lies in the tangent plane, the scalar product between the derivative of the ruling direction and tangent must be the same in both 2D and 3D. This results in $\mathbf{r}'(t) \cdot \mathbf{x}'(t) = \mathbf{R}'(t) \cdot \mathbf{X}'(t)$.

We will make note that a solution to constraints (1)–(4) also satisfies $|\mathbf{r}'(t)| = |\mathbf{R}'(t)|$. This is because it follows from constraint (1) that $\mathbf{R}'(t)$ and $\mathbf{r}'(t)$ are perpendicular to $\mathbf{R}(t)$ or $\mathbf{r}(t)$, respectively. With constraint (3), it follows that the direction of $\mathbf{r}'(t)$ is specified up to sign. With constraint (4), a solution satisfies $|\mathbf{r}'(t)| = |\mathbf{R}'(t)|$. We will see in Section 3.2.6 that this constraint ensures that the absolute value of the intrinsic curvature of the non-straight principal curvature lines on $\mathbf{S}(t,u)$ and $\mathbf{s}(t,u)$ are the same.

Step 2. We now show that a solution to the above system of differential-algebraic equations corresponds to the development $\mathbf{s}(t,u)$ of $\mathbf{S}(t,u)$.

This claim can be verified by confirming that the coefficients of the respective first fundamental forms[5] of $\mathbf{s}(t,u)$ and $\mathbf{S}(t,u)$ are the same [12]:

$$\begin{aligned} E_{\mathbf{S}} - E_{\mathbf{s}} &= |\mathbf{X}'(t) + u\mathbf{R}'(t)|^2 - |\mathbf{x}'(t) + u\mathbf{r}'(t)|^2 = 0, \\ F_{\mathbf{S}} - F_{\mathbf{s}} &= (\mathbf{X}'(t) + u\mathbf{R}'(t)) \cdot \mathbf{R}(t) - (\mathbf{x}'(t) + u\mathbf{r}'(t)) \cdot \mathbf{r}(t) = 0, \\ G_{\mathbf{S}} - G_{\mathbf{s}} &= |\mathbf{R}(t)|^2 - |\mathbf{r}(t)|^2 = 0. \end{aligned}$$

Step 3. The stated solution assumes that the ruling vector is parametrized in terms of an angular function $\alpha(t)$ as $\mathbf{r}(t) = (\cos\alpha(t), \sin\alpha(t))$, and that the unknown functions $\alpha(t)$, $\mathbf{x}_x(t)$, and $\mathbf{x}_y(t)$ result from the explicit initial value problem

$$\begin{aligned} \alpha'(t) &= \frac{\mathbf{R}'(t) \cdot \mathbf{X}'(t)}{\sqrt{|\mathbf{X}'(t)|^2 - |\mathbf{R}(t) \cdot \mathbf{X}'(t)|^2}} \\ \mathbf{x}_x'(t) &= (\mathbf{R}(t) \cdot \mathbf{X}'(t)) \cos\alpha(t) + \sqrt{|\mathbf{X}'(t)|^2 - |\mathbf{R}(t) \cdot \mathbf{X}'(t)|^2} \sin\alpha(t) \\ \mathbf{x}_y'(t) &= (\mathbf{R}(t) \cdot \mathbf{X}'(t)) \sin\alpha(t) - \sqrt{|\mathbf{X}'(t)|^2 - |\mathbf{R}(t) \cdot \mathbf{X}'(t)|^2} \cos\alpha(t). \end{aligned}$$

Next, we will verify that the given equations correspond to the constraints (1)–(4):

(1) The first constraint is trivially satisfied as $1 = |\mathbf{r}(t)| = |\mathbf{R}(t)|$.

(2) We compute $|\mathbf{x}'(t)|^2 = \mathbf{x}_x'(t)^2 + \mathbf{x}_y'(t)^2 = |\mathbf{X}'(t)|^2$, as all other terms cancel out.

[5] Recall that the first fundamental form I encodes the metric of a surface $\mathbf{S}(t,u)$. Its four coefficients of are defined as $E = I_{11} = \left(\frac{d}{dt}\mathbf{S}(t,u)\right)\left(\frac{d}{dt}\mathbf{S}(t,u)\right)$, $F = I_{12} = I_{21} = \left(\frac{d}{dt}\mathbf{S}(t,u)\right)\left(\frac{d}{du}\mathbf{S}(t,u)\right)$, and $G = I_{22} = \left(\frac{d}{du}\mathbf{S}(t,u)\right)\left(\frac{d}{du}\mathbf{S}(t,u)\right)$.

(3) We compute

$$\mathbf{r}(t)\cdot\mathbf{x}'(t) = \big(\mathbf{R}(t)\cdot\mathbf{X}'(t)\big)\cos^2\alpha(t) + \big(\mathbf{R}(t)\cdot\mathbf{X}'(t)\big)\sin^2\alpha(t) = \mathbf{R}(t)\cdot\mathbf{X}'(t).$$

(4) We have that

$$\mathbf{r}'(t)\cdot\mathbf{x}'(t) = \alpha'(t)\sqrt{|\mathbf{X}'(t)|^2 - |\mathbf{R}(t)\cdot\mathbf{X}'(t)|^2} = \mathbf{R}'(t)\cdot\mathbf{X}'(t).$$

Finally, note that $|\mathbf{R}(t)\cdot\mathbf{X}'(t)|$ represents the length of the projection of $\mathbf{X}'(t)$ onto $\mathbf{R}(t)$. Consequently, $|\mathbf{X}'(t)| > |\mathbf{R}(t)\cdot\mathbf{X}'(t)|$. □

Note that our computations of the development are solely based on the tangent continuity of both the directrix and the ruling directions (in contrast to other approaches, such as those in [75, 17], which require C^2 continuity). This is because the curvature of the (non-ruling) principal curvature lines is encoded in the first derivative of the ruling directions.

Next, we show that the developability condition is also sufficient:

Lemma 2.2. *If a tangent-continuous ruled surface has a development, the developability condition is satisfied for all $t \in T$.*

Proof. Let $\mathbf{s}(t,u) = \mathbf{x}(t) + u\mathbf{r}(t)$ denote the development of a tangent-continuous surface $\mathbf{S}(t,u) = \mathbf{X}(t) + u\mathbf{R}(t)$. It follows from isometry that the parametrization speeds of the two curves $\mathbf{x}(t)+\mathbf{r}(t)$ and $\mathbf{x}(t) + 2\mathbf{r}(t)$ are the same as the speeds of their respective 3D counterparts, that is,

$$0 = |\mathbf{x}'(t) + \mathbf{r}'(t)| - |\mathbf{X}'(t) + \mathbf{R}'(t)| = 2(\mathbf{r}'(t)\cdot\mathbf{x}'(t) - \mathbf{R}'(t)\cdot\mathbf{X}'(t)) + (|\mathbf{r}'(t)|^2 - |\mathbf{R}'(t)|^2),$$
$$0 = |\mathbf{x}'(t) + 2\mathbf{r}'(t)| - |\mathbf{X}'(t) + 2\mathbf{R}'(t)| = 4(\mathbf{r}'(t)\cdot\mathbf{x}'(t) - \mathbf{R}'(t)\cdot\mathbf{X}'(t)) + 4(|\mathbf{r}'(t)|^2 - |\mathbf{R}'(t)|^2).$$

Consequently, we have $|\mathbf{r}'(t)|^2 - |\mathbf{R}'(t)|^2 = 0$ and $\mathbf{r}'(t)\cdot\mathbf{x}'(t) - \mathbf{R}'(t)\cdot\mathbf{X}'(t) = 0$. Additionally, the isometry yields $\mathbf{R}(t)\cdot\mathbf{X}'(t) - \mathbf{r}(t)\cdot\mathbf{x}'(t) = 0$, and $|\mathbf{R}(t)|^2 = 1$ implies that $\mathbf{R}'(t)\cdot\mathbf{R}(t) = 0$.

We now examine the 3D configuration of the vectors $\mathbf{R}(t)$, $\mathbf{R}'(t)$, and $\mathbf{X}'(t)$, aiming to demonstrate that they are coplanar. It follows from $\mathbf{R}(t)\cdot\mathbf{X}'(t) = \mathbf{r}(t)\cdot\mathbf{x}'(t)$ and $\mathbf{R}'(t)\cdot\mathbf{X}'(t) = \mathbf{r}'(t)\cdot\mathbf{x}'(t)$ that $\mathbf{R}(t)$ and $\mathbf{R}'(t)$ are restricted to cones with axis direction $\mathbf{X}'(t)$. The cosine of their respective opening angle is defined by $\mathbf{r}(t)\cdot\mathbf{x}'(t)$ and $\mathbf{r}'(t)\cdot\mathbf{x}'(t)$, respectively. Therefore, given vectors $\mathbf{R}(t)$ and $\mathbf{X}'(t)$, the only vector satisfying $\mathbf{R}'(t)\cdot\mathbf{X}'(t) = \mathbf{r}'(t)\cdot\mathbf{x}'(t)$ and $\mathbf{R}(t)\cdot\mathbf{R}'(t) = \mathbf{r}(t)\cdot\mathbf{r}'(t)$ lies in the plane spanned by $\mathbf{R}(t)$ and $\mathbf{X}'(t)$.

□

Finally, we conclude:

Corollary 2.1. *A smooth ruled patch $\mathbf{S}(t,u) = \mathbf{X}(t) + u\mathbf{R}(t)$ is developable if and only if the developability condition is statisfied for all $t \in T$.*

In Section 3.2.3, we discuss an alternative approach for computing the development of a developable patch with a curvature-continuous directrix using patch characteristics.

2.2.2 Discrete Developability Condition and Development

A developable discrete ruled surface is characterized by the property that consecutive rulings are coplanar (and oriented correctly).

Lemma 2.3. *A discrete ruled surface* $\mathbf{S}(t,u) = \mathbf{X}(t)+u\mathbf{R}(t)$ *is developable if and only if it satisfies the* discrete developability condition *for all pairs of consecutive rulings,*

$$\det(\mathbf{R}(t_i), \mathbf{R}(t_{i+1}), \mathbf{X}(t_{i+1}) - \mathbf{X}(t_i)) = 0, \tag{2.6}$$

ensuring that two consecutive rulings are coplanar.

In the following, we assume that of the two possible orientations of the ruling vector $\mathbf{R}(t)$, the direction is chosen to point consistently towards one side of the directrix, that is,

$$(\mathbf{R}(t_i) \times (\mathbf{X}(t_{i+1}) - \mathbf{X}(t_i))) \cdot (\mathbf{R}(t_{i+1}) \times (\mathbf{X}(t_{i+1}) - \mathbf{X}(t_i))) > 0.$$

A discrete developable patch comprises a sequence of planar regions defined between two rulings. For practical considerations, we focus exclusively on finite regions. A development can be realized by sequentially placing planar quads and triangles in the xy-plane, while constructing the developed directrix $\mathbf{x}(t)$. Conversely, if a ruled patch has an development, the isometry forces two consecutive rule lines to be coplanar.

2.3 Singularities

2.3.1 Singularities on Smooth Patches

In this section, we provide an intuitive interpretation of the smooth developability condition and identify possible singular points of developable surfaces. Specifically, we show that the developability condition implies that, at points along a single ruling where the surface normal is defined, the tangent planes are constant. For each ruling, there exists at most one point where the tangent plane is undefined.

Recall that the normal vector $\mathbf{P}(t,u)$ of the surface $\mathbf{S}(t,u) = \mathbf{X}(t) + u\mathbf{R}(t)$ can be derived by normalizing the vector:

$$\tilde{\mathbf{P}}(t,u) = \left(\frac{d}{dt}\mathbf{S}(t,u)\right) \times \left(\frac{d}{du}\mathbf{S}(t,u)\right) = (\mathbf{X}'(t) + u\mathbf{R}'(t)) \times \mathbf{R}(t) = \mathbf{R}(t) \times \mathbf{X}'(t) + u\left(\mathbf{R}(t) \times \mathbf{R}'(t)\right).$$

If $\mathbf{R}'(t) = \mathbf{0}$, this vector simplifies to $\tilde{\mathbf{P}}(t,u) = \mathbf{R}(t) \times \mathbf{X}'(t) \neq \mathbf{0}$. Consequently, $\tilde{\mathbf{P}}(t,u)$ and $\mathbf{P}(t,u)$ are constant in u. This implies that the normal plane is the same for all points along the ruling at parameter t.

If on the other hand $\mathbf{R}'(t) \neq 0$, it follows from the developability condition that the vectors $\mathbf{R}(t)\times\mathbf{X}'(t)$ and $\mathbf{R}(t)\times\mathbf{R}'(t)$ are parallel and non-zero. Consequently, the normal vector is constant except for a unique parameter combination (t, u_t) where $\tilde{\mathbf{P}}(t,u_t) = \mathbf{0}$, that is,

$$u_t = -\frac{(\mathbf{X}'(t) \times \mathbf{R}(t)) \cdot (\mathbf{R}'(t) \times \mathbf{R}(t))}{|\mathbf{R}'(t) \times \mathbf{R}(t)|^2} = -\frac{\mathbf{X}'(t) \cdot \mathbf{R}'(t)}{|\mathbf{R}'(t)|^2}.$$

Note that this value is independent of the parametrization of the surface; thus, these points are (proper) singularities of the developable surface.

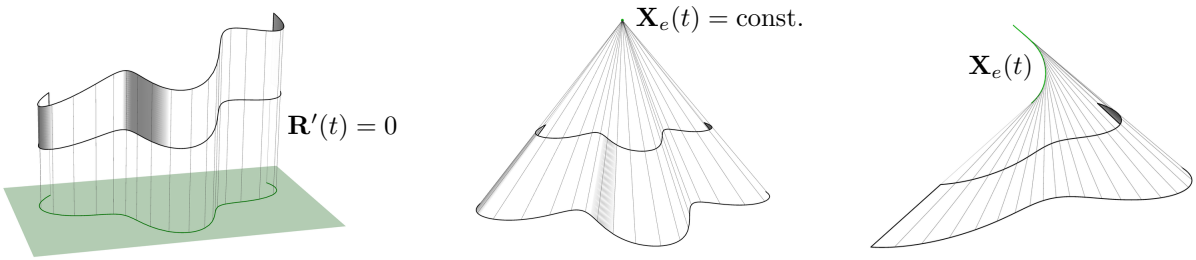

(a) Cylinder. (b) Cone. (c) Tangent developable.

Figure 2.3: Three basic types of a smooth developable patch.

Corollary 2.2. *Let $\mathbf{S}(t,u)$ be the parametrization of a smooth developable patch. For parameter values t where $|\mathbf{R}'(t)|^2 = 0$, the incident ruling is singularity-free. If on the other hand $|\mathbf{R}'(t)|^2 \neq 0$, the unique singular point of a ruling is located at*

$$\mathbf{X}_e(t) = \mathbf{X}(t) + e(t)\mathbf{R}(t),$$

where

$$e(t) = -\frac{(\mathbf{X}'(t) \times \mathbf{R}(t)) \cdot (\mathbf{R}'(t) \times \mathbf{R}(t))}{|\mathbf{R}'(t) \times \mathbf{R}(t)|^2} = -\frac{\mathbf{X}'(t) \cdot \mathbf{R}'(t)}{|\mathbf{R}'(t)|^2}. \tag{2.7}$$

Locally, a developable patch can be of one of three types: cylinder, cone, or general developable.

For open parameter intervals $J \subseteq T$ where $\mathbf{R}(t)$ is constant for all $t \in J$, the surface is locally a *cylinder* or *cylindrically ruled*. If there is an open parameter interval J where $\mathbf{X}_e(t)$ is constant, then the developable surface is locally a *cone* or *conically ruled*, with $\mathbf{X}_e(t)$ being its cone apex.

The third scenario arises when $\mathbf{X}_e(t)$ does not fit either of the prior descriptions for all open subintervals of an open interval $J \subseteq T$. If the surface is C^2 for all $t \in J$, the curve of singularities is termed the *edge of regression*. As the tangents of the edge of regression are parallel to the incident rulings, this surface type is also known as a *tangent developable*. For surfaces that are only C^1 for all values of $t \in J$, the curve $\mathbf{X}_e(t)$ is only continuous. Further analysis of this kind is left for future work.

2.3.2 Singularities on Discrete Patches

Another interpretation of the singularities in a smooth patch is that they are located at the intersections of two infinitesimally close rulings. In the case of a discrete patch, singularities occur at the intersections of two consecutive rulings. Specifically, when two consecutive ruling vectors are not parallel, that is $\mathbf{R}(t_{i+1}) \neq \mathbf{R}(t_i)$, we define $\mathbf{X}_e(t_{i+1})$ to be the intersection of rulings incident to $\mathbf{X}(t_i)$ and $\mathbf{X}(t_{i+1})$.

Lemma 2.4. *Let $\mathbf{S}(t,u)$ be the parametrization of a discrete developable patch. At parameters t_{i+1} with $|\mathbf{R}(t_{i+1}) - \mathbf{R}(t_i)|^2 = 0$, the incident ruling is singularity-free. If on the other hand $|\mathbf{R}(t_{i+1}) - \mathbf{R}(t_i)|^2 \neq 0$, the unique singular point of the ruling is located at*

$$\mathbf{X}_e(t) = \mathbf{X}(t) + e(t)\mathbf{R}(t),$$

where $e(t) : T\backslash\{t_0\} \to \mathbb{R}$ is

$$s(t_{i+1}) = -\frac{((\mathbf{X}(t_{i+1}) - \mathbf{X}(t_i)) \times \mathbf{R}(t_i)) \cdot (\mathbf{R}(t_{i+1}) \times \mathbf{R}(t_i))}{|\mathbf{R}(t_{i+1}) \times \mathbf{R}(t_i)|^2},$$

for $0 \leq i < n$.

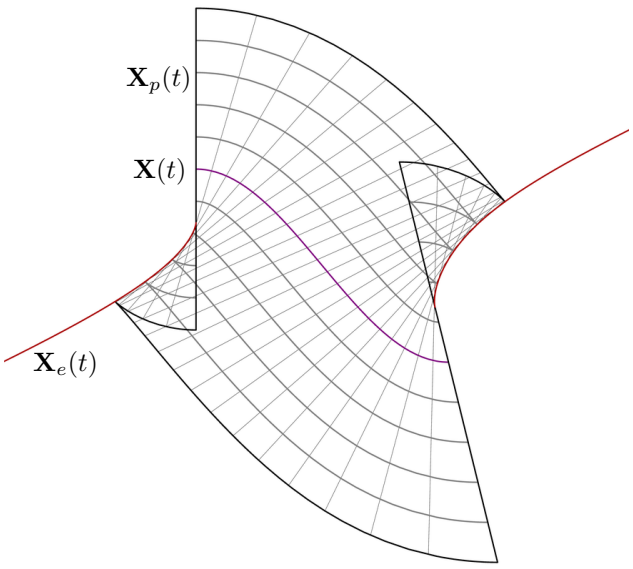

Figure 2.4: Developable patch with curve of regression $\mathbf{X}_e(t)$ (red) and parallel curves $\mathbf{X}_p(t)$ (gray) of the directrix $\mathbf{X}(t)$ (purple).

Proof. Since two consecutive rulings are coplanar, they have an real or ideal intersection. We compute this intersection by finding $e(t_i)$ and $e(t_{i+1})$ such that

$$\begin{aligned}\mathbf{0} &= (\mathbf{X}(t_{i+1}) + s(t_{i+1})\mathbf{R}(t_{i+1})) - (\mathbf{X}(t_i) + s(t_i)\mathbf{R}(t_i)) \\ &= \mathbf{X}(t_{i+1}) - \mathbf{X}(t_i) - s(t_i)\mathbf{R}(t_i) + s(t_{i+1})\mathbf{R}(t_{i+1}).\end{aligned}$$

For parameter values with $\mathbf{R}(t_{i+1}) \times \mathbf{R}(t_i) \neq \mathbf{0}$, the vector $\mathbf{X}(t_{i+1}) - \mathbf{X}(t_i) - s(t_i)\mathbf{R}(t_i)$ is not parallel to $\mathbf{R}(t_i)$ and has non-zero length. Consequently, we rewrite the constraint in terms of

$$\begin{aligned}\mathbf{0} &= (\mathbf{X}(t_{i+1}) - \mathbf{X}(t_i) + s(t_{i+1})\mathbf{R}_{i+1} - s(t_i)\mathbf{R}(t_i)) \times \mathbf{R}(t_i) \\ &= (\mathbf{X}(t_{i+1}) - \mathbf{X}(t_i)) \times \mathbf{R}(t_i) + s(t_{i+1})\,(\mathbf{R}(t_{i+1}) \times \mathbf{R}(t_i))\end{aligned}$$

Similar to above, the vectors $(\mathbf{X}(t_{i+1}) - \mathbf{X}(t_i)) \times \mathbf{R}(t_i)$ and $(\mathbf{R}(t_{i+1}) \times \mathbf{R}(t_i))$ are parallel to the incident tangent plane normal. Consequently, the above is the zero vector if and only if the product with a parallel non-zero vector is zero, that is,

$$0 = ((\mathbf{X}(t_{i+1}) - \mathbf{X}(t_i)) \times \mathbf{R}(t_i)) \cdot (\mathbf{R}(t_{i+1}) \times \mathbf{R}(t_i)) + s(t_{i+1})\,|\mathbf{R}(t_{i+1}) \times \mathbf{R}(t_i)|^2\,.$$

This implies the stated expression. □

Similar to the smooth case, we can distinguish between three types of discrete patches: cylinder, cone, or tangent developables.

Let J be a set of at least three consecutive parameters values t_i. If $\mathbf{R}(t)$ is constant for all $t_i \in J$, the surface is locally a *cylinder* or *cylindrically ruled*. If $\mathbf{X}_e(t)$ is constant for all $t \in J$, the patch is locally a *cone* or *conically ruled*, with $\mathbf{X}_e(t)$ being its cone apex.

The third scenario arises when the patch does not fit either of the prior descriptions for all subsets of at least size three of a set of parameter values J. Here, we refer to $\mathbf{X}_e(t)$ as the *(discrete) edge of regression*. As the discrete tangents of the polyline $\mathbf{X}_e(t)$ are parallel to the incident rulings, this surface type is also termed a *discrete tangent developable*.

2.4 Tangent-Parallel Curves

Given a developable patch $\mathbf{S}(t,u)$ by its directrix $\mathbf{X}(t)$ and ruling direction $\mathbf{R}(t)$, we study the curves whose tangents are parallel to the tangents of $\mathbf{X}(t)$. Specifically, we name a curve $\mathbf{X}_p(t) = \mathbf{X}(t) + p(t)\mathbf{R}(t)$ a *tangent-parallel curve* of $\mathbf{X}(t)$, if the tangents of $\mathbf{X}(t)$ and $\mathbf{X}_p(t)$ at the same parameter value are parallel; see Figure 2.4. These curves play an important role in the following chapters, in particular Section 3.5.2, as they share a similar kinematic behavior when incident patches are folded.

2.4.1 Tangent-Parallel Curves on Smooth Patches

In the following, we review selected properties of smooth parallel curves, and refer to Tachi [101] for another exposition.

Lemma 2.5. *Let $\mathbf{X}(t)$ be the directrix of a developable surface $\mathbf{S}(t,u)$. The tangent-parallel curves with respect to $\mathbf{X}(t)$ on $\mathbf{S}(t.u)$ can be parametrized by*

$$\mathbf{X}_p(t) = \mathbf{X}(t) + p(t)\mathbf{R}(t), \tag{2.8}$$

where $p(t)$ is specified by the initial value problem

$$\frac{p'(t)}{p(t)} = -\frac{(\mathbf{R}'(t)\times\mathbf{X}'(t))\cdot(\mathbf{R}(t)\times\mathbf{X}'(t))}{|\mathbf{R}(t)\times\mathbf{X}'(t)|^2} \qquad \textit{and} \qquad p(0) = p_0 \neq 0. \tag{2.9}$$

Proof. We are interested in length functions that satisfy $\mathbf{X}_p'(t)\times\mathbf{X}'(t) = \mathbf{0}$, that is,

$$\mathbf{0} = (\mathbf{X}'(t) + p(t)\mathbf{R}'(t) + p'(t)\mathbf{R}(t))\times\mathbf{X}'(t) = p(t)\left(\mathbf{R}'(t)\times\mathbf{X}'(t)\right) + p'(t)\left(\mathbf{R}(t)\times\mathbf{X}'(t)\right)$$

It follows from the developability condition that the vectors $\mathbf{R}'(t)\times\mathbf{X}'(t)$ and $\mathbf{R}(t)\times\mathbf{X}'(t)$ are parallel. Consequently, their sum is the zero vector if and only if the scalar product of their sum with a parallel non-trivial vector is zero. Since $\mathbf{R}(t)\times\mathbf{X}'(t) \neq \mathbf{0}$, the above expression is equivalent to

$$0 = p(t)\left(\left(\mathbf{R}'(t)\times\mathbf{X}'(t)\right)\cdot\left(\mathbf{R}(t)\times\mathbf{X}'(t)\right)\right) + p'(t)\left|\mathbf{R}(t)\times\mathbf{X}'(t)\right|^2,$$

which implies the above equation.

□

Lemma 2.6. *The solution to the initial value problem in Equation* (2.9) *reads*

$$p(t) = p_0 e^{-\int_0^t \frac{(\mathbf{R}'(u)\times\mathbf{X}'(u))\cdot(\mathbf{R}(u)\times\mathbf{X}'(u))}{|\mathbf{R}(u)\times\mathbf{X}'(u)|^2}du}. \tag{2.10}$$

2.4.2 Tangent-Parallel Polylines on Discrete Patches

In the discrete case, the tangent-parallel curves are polylines $\mathbf{X}_p(t) : T \to \mathbb{R}^3$ with vertices on the rule lines of $\mathbf{S}(t,u)$ such that $\mathbf{X}(t_{i+1}) - \mathbf{X}(t_i)$ and $\mathbf{X}_p(t_{i+1}) - \mathbf{X}_p(t_i)$ are parallel.

Lemma 2.7. *Let $\mathbf{X}(t)$ be a directrix of a developable surface $\mathbf{S}(t,u)$. The tangent-parallel curves with respect to $\mathbf{X}(t)$ can be parametrized by*

$$\mathbf{X}_p(t) = \mathbf{X}(t) + p(t)\mathbf{R}(t),$$

where $p(t)$ is specified by the difference equation, namely,

$$\frac{p(t_{i+1})}{p(t_i)} = \frac{(\mathbf{R}(t_i) \times (\mathbf{X}(t_{i+1}) - \mathbf{X}(t_i))) \cdot (\mathbf{R}(t_{i+1}) \times (\mathbf{X}(t_{i+1}) - \mathbf{X}(t_i)))}{|\mathbf{R}(t_{i+1}) \times (\mathbf{X}(t_{i+1}) - \mathbf{X}(t_i))|^2} \quad \textit{and} \quad p(t_0) = p_0 \neq 0. \tag{2.11}$$

Proof. Similar to above, we want the length function to satisfy

$$\mathbf{0} = (\mathbf{X}_p(t_{i+1}) - \mathbf{X}_p(t_i)) \times (\mathbf{X}(t_{i+1}) - \mathbf{X}(t_i)),$$

or, equivalently,

$$\begin{aligned}\mathbf{0} &= (\mathbf{X}(t_{i+1}) - \mathbf{X}(t_i) + p(t_{i+1})\mathbf{R}(t_{i+1}) - p(t_i)\mathbf{R}(t_i)) \times (\mathbf{X}(t_{i+1}) - \mathbf{X}(t_i)) \\ &= p(t_{i+1}) (\mathbf{R}(t_{i+1}) \times (\mathbf{X}(t_{i+1}) - \mathbf{X}(t_i))) - p(t_i) (\mathbf{R}(t_i) \times (\mathbf{X}(t_{i+1}) - \mathbf{X}(t_i))).\end{aligned}$$

Similar to the proof of Lemma 2.5, $\det(\mathbf{X}(t_{i+1}) - \mathbf{X}(t_i), \mathbf{R}(t_i), \mathbf{R}(t_{i+1})) = 0$, and the two vectors $\mathbf{R}(t_{i+1}) \times (\mathbf{X}(t_{i+1}) - \mathbf{X}(t_i))$ and $\mathbf{R}(t_i) \times (\mathbf{X}(t_{i+1}) - \mathbf{X}(t_i))$ are parallel. Consequently, assuming $\mathbf{R}(t_{i+1}) \times (\mathbf{X}(t_{i+1}) - \mathbf{X}(t_i)) \neq \mathbf{0}$, the expression is equivalent to

$$\begin{aligned}0 = p(t_{i+1}) &|\mathbf{R}(t_{i+1}) \times (\mathbf{X}(t_{i+1}) - \mathbf{X}(t_i))|^2 \\ &- p(t_i) (\mathbf{R}(t_i) \times (\mathbf{X}(t_{i+1}) - \mathbf{X}(t_i))) \cdot (\mathbf{R}(t_{i+1}) \times (\mathbf{X}(t_{i+1}) - \mathbf{X}(t_i))),\end{aligned}$$

resulting in the stated expression. □

Lemma 2.8. *The difference equation stated in Equation* (2.11) *allows for the following solution*

$$p(t_j) = p_0 \prod_{i=0}^{j-1} \frac{(\mathbf{R}(t_i) \times (\mathbf{X}(t_{i+1}) - \mathbf{X}(t_i))) \cdot (\mathbf{R}(t_{i+1}) \times (\mathbf{X}(t_{i+1}) - \mathbf{X}(t_i)))}{|\mathbf{R}(t_{i+1}) \times (\mathbf{X}(t_{i+1}) - \mathbf{X}(t_i))|^2},$$

for $0 \leq j < n$.

Part I

Curvature-Based Computation of Configurations

Chapter 3

Gluing and Creasing Using Patch Characteristics

The content of this chapter is unpublished and is based on discussions with Erik Demaine and Tomohiro Tachi.

Overview

In this chapter, we explore computational methods for joining multiple smooth patches with C^2 directrices along their curved boundaries. Initially, we introduce the patch characteristics, five functions that describe the geometry of a smooth ruled surface. We use these functions to express the developability condition and other useful geometric properties. Next, we discuss the process of joining two developed patches with specified rulings, emphasizing creasing as a special case. Subsequently, we address the problem of joining three developed patches along their curved boundaries when provided with only partial ruling information. Finally, we illustrate how to add additional patches to a pre-existing glued or creased structure, and highlight the special case of adding patches along tangent-parallel curves due to their special kinematic properties.

3.1 Introduction

Shapes that can be obtained by joining pieces of paper along curves allow the generation of intricate shapes. The parametric reconstruction of glued or creased shapes is a non-trivial task, for at least two reasons: First, it is hard to make a good guess about the rulings of the surface. Second, the underlying material allows imperfections, resulting in shapes that cannot be achieved with the provided crease pattern [16].

In this chapter, we provide a set of tools for the computational reconstruction of shapes obtained by gluing or creasing smooth patches. Up to this point, we have represented the ruling direction independently of the directrix. Particularly, in the smooth case, finding pairs of functions for the directrix and ruling direction that satisfy the developability condition (and are not cylinders and cones) is not very intuitive. Consequently, it is often more convenient to represent the ruling direction in relation to a local geometry-encoding coordinate system.

In Section 3.2, we build upon existing theoretical work, such as Fuchs and Tabachnikov [26] and Demaine et al. [17, 18], and use an orthonormal frame associated with the directrix to locate the ruling directions. As a result, we identify five scalar-valued functions which specify the configuration of a patch with specified rulings. These are termed as patch characteristics. Analogous to Chapter 2,

these patch characteristics must satisfy the developability condition to ensure that the patch is developable. Additionally, we discuss how other features, such as singularities and tangent-parallel curves, simplify in terms of patch characteristics. Furthermore, we explain how a subset of these five functions is capable of defining a configuration of a developable patch.

Next, in Section 3.3, we discuss the method of joining two developed patches with specified rulings. Although the methodology for determining the configuration of two glued patches is likely not novel, we believe our approach offers deeper insights into its computation. Specifically, we introduce a method to determine initial values based on a specified initial opening angle between the incident tangent planes of the two surfaces. Notably, in the unique case where both curves are identical and the patches represent opposite sides of the shared curve, the desired shapes can be achieved using a curved crease.

In Section 3.4, we consider the gluing of three patches along pairs of boundaries. As prescribing the rulings of all three patches would be overconstraining, we consider only partial ruling information as input. We provide three strategies how this partial ruling information can be specified. However, as of now the method is limited by the computational constraint that the relationship between the curve and its arc-length parametrized curvature of at least one pair of curves needs to be known.

Finally, in Section 3.5, we discuss how to append a patch to a curve on a patch of an already glued or creased pair. We highlight the special case where the patch is appended along tangent-parallel curves.

3.2 Patch Characteristics

3.2.1 Parametrization of Ruled Patches

We proceed with the definition of the five functions $K(t)$, $\tau(t)$, $s(t)$, $\varphi(t)$, and $\theta(t)$ comprising the *patch characteristics*. Three of the five functions describe a space curve, the directrix, equipped with an orthonormal frame, while the other two determine the ruling direction in relation to the local orthonormal frame.

We draw inspiration from existing work, such as Fuchs and Tabachnikov [26] or Demaine et al. [17, 18], that devise properties of the directrix and incident developable surfaces joined along a curved crease based on differentiation. While these existing approaches provide valuable insight into the geometry, when it comes to practical applications, they are limited by the requirement that the directrix needs to be properly curved. Consequently, cases where the curvature vanishes require special consideration. In this part of the thesis, our primary focus is on determining the 3D configuration based on a provided development, mostly using integration. As a result, we deviate a bit from the existing literature and approach the computations from another perspective.

Directrix and orthonormal frame

The first three patch characteristic functions $K(t) : [0, t_{\max}] \to \mathbb{R}$, $\tau(t) : [0, t_{\max}] \to \mathbb{R}$, and $s(t) : [0, t_{\max}] \to \mathbb{R}_{\geq 0}$ define the directrix $\mathbf{X}(t)$ and its orthonormal frame $(\mathbf{T}(t), \mathbf{N}(t), \mathbf{B}(t))$ through the Frenet-Serret formulas:

$$\begin{pmatrix} \mathbf{X}'(t) \\ \mathbf{T}'(t) \\ \mathbf{N}'(t) \\ \mathbf{B}'(t) \end{pmatrix} = s'(t) \begin{pmatrix} 1 & 0 & 0 \\ 0 & K(t) & 0 \\ -K(t) & 0 & \tau(t) \\ 0 & -\tau(t) & 0 \end{pmatrix} \begin{pmatrix} \mathbf{T}(t) \\ \mathbf{N}(t) \\ \mathbf{B}(t) \end{pmatrix}. \tag{3.1}$$

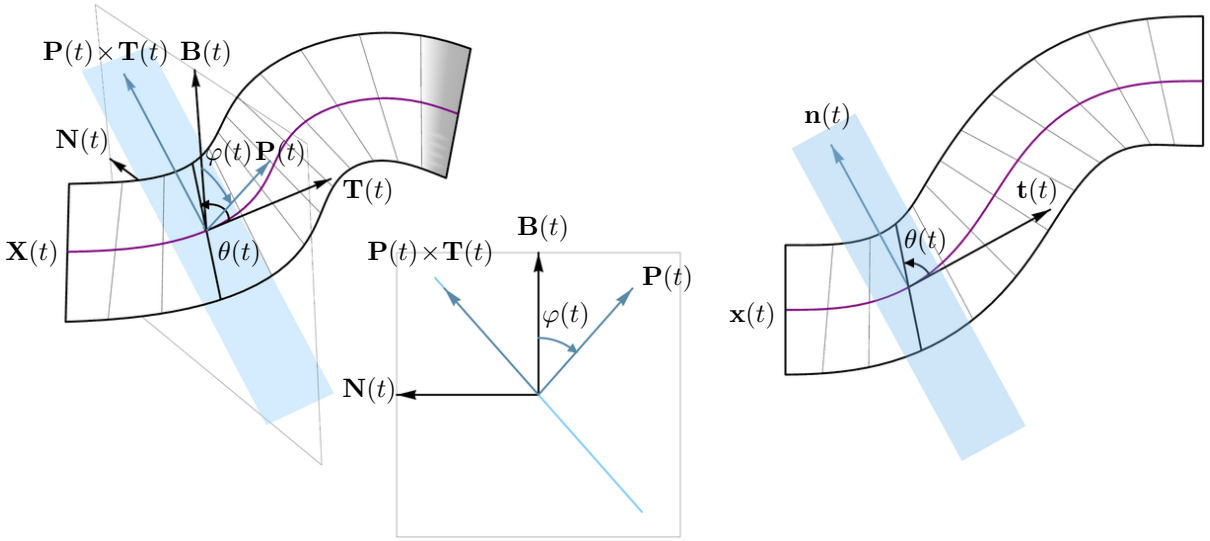

Figure 3.1: Illustration of the notation of a patch and its development involving patch characteristics.

Here we require that the $K(t)$, $\tau(t)$, and $s'(t)$ are continuous, and $s'(t) > 0$.

Note that we permit $K(t)$ to take negative values. Moreover, isolated points or intervals where $K(t) = 0$ or $\tau(t) = 0$ still yield a continuous frame $(\mathbf{T}(t), \mathbf{N}(t), \mathbf{B}(t))$. Consequently, this described frame is not a Frenet-frame. However, at parameter values where the Frenet-frame is defined, the computed frame coincides with the Frenet-frame up to sign. Additionally, $K(t)$ corresponds to the curvature of the directrix up to sign, while $\tau(t)$ is the torsion of the directrix when defined. We will refer to $K(t)$ as the *(signed) curvature* and to $\tau(t)$ as the *torsion*. Furthermore, $s(t)$ denotes the *arc length* of the directrix, and $s'(t)$ represents the *parametrization speed*.

Ruling direction

The remaining two patch characteristic functions, the *inclination angle* $\varphi(t) : [0, t_{\max}] \to (-\pi, \pi]$ and the *ruling angle* $\theta(t) : [0, t_{\max}] \to (0, \pi)$, parametrize the unit-length ruling vectors $\mathbf{R}(t)$ with respect to the local frame $(\mathbf{T}(t), \mathbf{N}(t), \mathbf{B}(t))$ of $\mathbf{X}(t)$; see Figure 3.1. The angle $\varphi(t)$ encodes the angle between the tangent plane and the local frame. Specifically, let $\Pi(t)$ be a tangent plane, then its normal vector $\mathbf{P}(t)$ can be represented as

$$\mathbf{P}(t) = \cos\varphi(t)\ \mathbf{B}(t) + \sin\varphi(t)\ \mathbf{N}(t), \tag{3.2}$$

where $\varphi(t)$ is the signed angle between $\mathbf{P}(t)$ and $\mathbf{B}(t)$.

Within the plane $\Pi(t)$, we locate the ruling direction using the ruling angle $\theta(t)$ as

$$\begin{aligned}\mathbf{R}(t) &= \cos\theta(t)\ \mathbf{T}(t) + \sin\theta(t)\ (\mathbf{P}(t) \times \mathbf{T}(t)) \\ &= \cos\theta(t)\ \mathbf{T}(t) + \sin\theta(t)\ (\cos\varphi(t)\ \mathbf{N}(t) - \sin\varphi(t)\ \mathbf{B}(t))\,.\end{aligned} \tag{3.3}$$

For the ruling direction to be at least C^1, we require $\theta(t)$ and $\varphi(t)$ to be C^1. Additionally, we exclude the undesirable cases where $\theta(t) \in \{0, \pi\}$, that is, cases where the ruling direction is parallel to the tangent direction.

3.2.2 Developability Condition and Development

The following lemma is a translation of Lemma 2.1 on the developability condition and the development.

Lemma 3.1. *A smooth ruled surface* $\mathbf{S}(t,u) = \mathbf{X}(t) + u\mathbf{R}(t)$ *parametrized using patch characteristics (as defined in Section 3.2.1) is developable if and only if the developability condition is satisfied for all* $t \in T$*,*

$$K(t)\sin\varphi(t)\cot\theta(t) = -\tau(t) + \frac{\varphi'(t)}{s'(t)}. \tag{3.4}$$

The development $\mathbf{s}(t,u) = \mathbf{x}(t) + u\mathbf{r}(t)$ *of such a developable patch* $\mathbf{S}(t,u)$ *can be obtained as* $\mathbf{r}(t) = (\cos\alpha(t), \sin\alpha(t), 0)$*, where*

$$\alpha'(t) = \frac{\theta'(t) + s'(t)K(t)\cos\varphi(t)}{\sin\theta(t)}$$

and $\mathbf{x}(t) = (\mathbf{x}_x(t), \mathbf{x}_y(t), 0)$*, where*

$$\begin{pmatrix}\mathbf{x}'_x(t)\\ \mathbf{x}'_y(t)\end{pmatrix} = \begin{pmatrix}s'(t)\cos\theta(t)\cos\alpha(t) + s'(t)\sin\theta(t)\sin\alpha(t)\\ s'(t)\cos\theta(t)\sin\alpha(t) - s'(t)\sin\theta(t)\cos\alpha(t)\end{pmatrix}.$$

Proof. We first simplify the developability condition (2.3). It follows from Equation (3.3) and $\mathbf{X}'(t) = s'(t)\mathbf{T}(t)$ that

$$\mathbf{X}'(t) \times \mathbf{R}(t) = s'(t)\sin\theta(t)\left(\cos\varphi(t)\ \mathbf{B}(t) + \sin\varphi(t)\ \mathbf{N}(t)\right).$$

Differentiating Equation (3.3) and using the Frenet-Serret equations (Equation (3.1)) yields

$$\begin{aligned}\mathbf{R}' \;=\; & -(\theta' + s'K\cos\varphi)\sin\theta\ \mathbf{T}\\ & + \left((\theta'\cos\varphi + s'K)\cos\theta + (-\varphi' + s'\tau)\sin\varphi\sin\theta\right)\mathbf{N}\\ & + \left(-\theta'\sin\varphi\cos\theta + (-\varphi' + s'\tau)\cos\varphi\sin\theta\right)\mathbf{B}\end{aligned} \tag{3.5}$$

Ultimately, we obtain

$$\begin{aligned}0 &= \det(\mathbf{X}'(t), \mathbf{R}(t), \mathbf{R}'(t))\\ &= (\mathbf{X}'(t)\times\mathbf{R}(t))\cdot\mathbf{R}'(t)\\ &= s'(t)^2\sin\theta(t)\left(\left(\tau(t) - \frac{\varphi'(t)}{s'(t)}\right)\sin\theta(t) + K(t)\sin\varphi(t)\cos\theta(t)\right)\end{aligned}$$

which results in the claimed equation.

Finally, inserting the above expressions in the differential equations that determine the development yields the above differential equations. □

3.2.3 Developed Curvature of the Directrix

In this section we consider the curvature of the directrix as a curve on $\mathbf{S}(t,u)$ and present another method for the computation of the development. In a sense, the approach for computing the development is the dual of the method presented earlier. While the prior method determined the ruling directions first, and determined the developed directrix in a second step, the method presented next first calculates the developed directrix and subsequently the rulings.

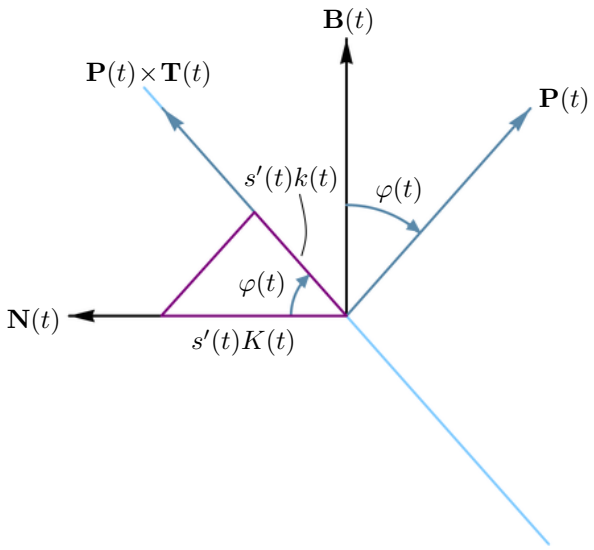

Figure 3.2: Illustration of the relationship between curvatures $K(t)$ and $k(t)$.

For a given developable surface $\mathbf{S}(t,u)$, the position of the tangent plane $\Pi(t)$ with respect to the directrix's frame influences the *geodesic curvature* $k(t)$ of $\mathbf{X}(t)$ as a curve on $\mathbf{S}(t,u)$, that is, the curvature of the projection of $\mathbf{X}(t)$ on $\Pi(t)$ at t,

$$k(t) = K(t)\cos\varphi(t); \tag{3.6}$$

see Figure 3.2. In particular, the geodesic curvature is zero if $\mathbf{P}(t) = \pm\mathbf{N}(t)$, and it is $\pm K(t)$ if $\mathbf{P}(t) = \pm\mathbf{B}(t)$.

Since $k(t)$ is an intrinsic quantity, computing the development amounts to constructing a curve $\mathbf{x}(t)$, the developed directrix, in the xy-plane with the same parametrization speed as $\mathbf{X}(t)$ and curvature $k(t)$. To be consistent with the 3D configuration, we consider $k(t)$ to be a signed curvature. Particularly, we define the normal $\mathbf{n}(t)$ of $\mathbf{x}(t)$ to be the tangent $\mathbf{t}(t)$ rotated by $\frac{\pi}{2}$, that is, $\mathbf{n}(t) = (0,0,1)\times\mathbf{t}(t)$ and require $\frac{1}{s'(t)}\mathbf{t}'(t) = k(t)\mathbf{n}(t)$. Consequently, $\mathbf{n}(t)$ is the *left-side normal*.

For a given geodesic curvature $k(t)$ and parametrization speed $s'(t)$, we now discuss how to obtain the corresponding developed curve. For this purpose, we assume that the tangent $\mathbf{t}(t)$ of the developed directrix $\mathbf{x}(t)$ is parametrized by an initially unknown angular function $\beta(t)$, that is,

$$\mathbf{t}(t) = (\cos\beta(t), \sin\beta(t), 0).$$

Note that the angular function $\beta(t)$ also specifies the normal $\mathbf{n}(t) = (0,0,1)\times\mathbf{t}(t)$. Since

$$\mathbf{t}'(t) = \beta'(t)(-\sin\beta(t), \cos\beta(t)) = \beta'(t)\mathbf{n}(t),$$

the curvature simplifies to

$$k(t) = \frac{1}{s'(t)}\mathbf{t}'(t)\cdot\mathbf{n}(t) = \frac{\beta'(t)}{s'(t)}.$$

We obtain the angular function $\beta(t)$ by integrating $s'(u)k(u)$, that is,

$$\beta(t) = \beta_0 + \int_0^t s'(u)k(u)\ du,$$

where $\beta_0 = \beta(0)$ influences the orientation of the initial tangent. Finally, we integrate the tangent direction to obtain the developed directrix

$$\mathbf{x}(t) = \mathbf{x}_0 + \int_0^t s'(u)\mathbf{t}(u)\ du,$$

where $\mathbf{x}_0 = \mathbf{x}(0)$ defines the initial position of the directrix.

As unrolling preserves the angles between rulings and tangents, the *developed ruling direction* is given by

$$\mathbf{r}(t) = \cos\theta(t)\ \mathbf{t}(t) + \sin\theta(t)\ \mathbf{n}(t).$$

3.2.4 Singularities

We now consider a statement analogous to Corollary 2.2 using patch characteristics:

Lemma 3.2. *Let $\mathbf{S}(t,u)$ be a parametrization of a smooth developable patch using patch characteristics. For parameter values t where $\theta'(t) + s'(t)k(t) = 0$, the incident ruling is singularity-free. If on the other hand $\theta'(t) + s'(t)k(t) \neq 0$, the unique singular point of a ruling is located at*

$$\mathbf{X}_e(t) = \mathbf{X}(t) + e(t)\mathbf{R}(t),$$

where

$$e(t) = \frac{s'(t)\sin\theta(t)}{\theta'(t) + s'(t)k(t)}. \tag{3.7}$$

Proof. Taking advantage of the isometry between 3D and 2D, we perform the necessary computations in 2D. First, we consider

$$\mathbf{r}'(t) = \left(\theta'(t) + s'(t)k(t)\right)\left(-\sin\theta(t)\ \mathbf{t}(t) + \cos\theta(t)\ \mathbf{n}(t)\right).$$

Since $|\mathbf{R}'(t)| = |\mathbf{r}'(t)|$, a singularity-free ruling is characterized by $\theta'(t) + s'(t)k(t) = 0$. For parameter values t where $\theta'(t) + s'(t)k(t) \neq 0$, we determine the location of $e(t)$ using the developed tangent and ruling direction using Corollary 2.2, namely,

$$e(t) = -\frac{\mathbf{x}'(t)\cdot\mathbf{r}'(t)}{|\mathbf{r}'(t)|^2} = -\frac{\left(-s'(t)\sin\theta(t)\right)\left(\theta'(t) + s'(t)k(t)\right)}{\left(\theta'(t) + s'(t)k(t)\right)^2} = \frac{s'(t)\sin\theta(t)}{\theta'(t) + s'(t)k(t)},$$

since $\mathbf{x}'(t) = s'(t)\mathbf{t}(t)$. □

3.2.5 Tangent-Parallel Curves

Next, we consider a statement analogous to Lemma 2.5 using patch characteristics:

Lemma 3.3. *Let $\mathbf{X}(t)$ be the directrix of a developable surface $\mathbf{S}(t,u)$ parametrized using patch characteristics. The tangent-parallel curves with respect to $\mathbf{X}(t)$ can be parametrized by*

$$\mathbf{X}_p(t) = \mathbf{X}(t) + p(t)\mathbf{R}(t),$$

where $p(t)$ is specified by the initial value problem

$$\frac{p'(t)}{p(t)} = -\cot\theta(t)\left(\theta'(t) + s'(t)k(t)\right) \qquad \text{and} \qquad p(0) = p_0. \tag{3.8}$$

Proof. Again, we use the 2D quantities to simplify the computations. First, note that

$$\frac{p'(t)}{p(t)} = -\frac{(\mathbf{r}'(t) \times \mathbf{x}'(t)) \cdot (\mathbf{r}(t) \times \mathbf{x}'(t))}{|\mathbf{r}(t) \times \mathbf{x}'(t)|^2} = -\frac{(\mathbf{r}(t) \cdot \mathbf{x}'(t))(\mathbf{r}'(t) \cdot \mathbf{x}'(t))}{|\mathbf{x}'(t)|^2 - |\mathbf{r}(t) \cdot \mathbf{x}'(t)|^2}.$$

Consequently, it follows that

$$\frac{p'(t)}{p(t)} = -\frac{(s'(t)\cos\theta(t))(-s'(t)\sin\theta(t)(\theta'(t) + s'(t)k(t))}{s'(t)^2 - (s'(t)\cos\theta(t))^2} = -\cot\theta(t)\left(\theta'(t) + s'(t)k(t)\right).$$

□

We use the patch characteristic functions to express the following relationship between the parametrization speeds $s'(t)$ and $s'_p(t)$ of the directrix and its tangent parallel counterpart; see Tachi [101].

Lemma 3.4. *The parametrization speed $s'(t)$ of $\mathbf{x}(t)$ and the parametrization speed $s'_p(t)$ of $\mathbf{x}_p(t)$ are related by*

$$s'_p(t) = s'(t) - \frac{\theta'(t) + s'(t)k(t)}{\sin\theta(t)}p(t) = \left(1 - \frac{p(t)}{e(t)}\right)s'(t). \tag{3.9}$$

where $e(t)$ is the distance to the singular point on a ruling from Equation (2.7).

Proof. Recall that with vanishing normal component, the first derivative of $\mathbf{x}_p(t)$ reads

$$\mathbf{x}'_p(t) = (s'(t) + p'(t)\cos\theta(t) - p(t)\sin\theta(t)(\theta(t) + s'(t)k(t)))\mathbf{t}(t).$$

Solving Equation (2.9) for $p'(t)$, and using the resulting expression in the previous equation results in

$$\mathbf{x}'_p(t) = \frac{1}{\sin\theta(t)}\left(s'(t)\sin\theta(t) - \left(\theta'(t) + s'(t)k(t)\right)p(t)\right)\mathbf{t}(t)$$

Note that we are interested in solutions were $\mathbf{x}'_p(t) \cdot \mathbf{r}^\perp(t) < 0$. With $\mathbf{r}^\perp(t) = -\sin\theta(t)\ \mathbf{t}(t) + \cos\theta(t)\ \mathbf{n}(t)$, this constraint simplifies to

$$\mathbf{x}'_p(t) \cdot \mathbf{r}^\perp(t) = p(t)\left(\theta'(t) + s'(t)k(t)\right) - s'(t)\sin\theta(t) < 0.$$

Since $\sin\theta(t) > 0$, the parametrization speed $s'_p(t) = \left|\mathbf{x}'_p(t)\right|$ of $\mathbf{x}_p(t)$ simplifies with the above inequality to

$$s'_p(t) = \left|\mathbf{x}'_p(t)\right| = s'(t) - \frac{\theta'(t) + s'(t)k(t)}{\sin\theta(t)}p(t).$$

□

Lemma 3.5. *For $s'_p(t) \neq 0$, the curvature $k_p(t)$ of $\mathbf{x}_p(t)$ relates to the curvature $k(t)$ of $\mathbf{x}(t)$ by*

$$s'_p(t)k_p(t) = s'(t)k(t).$$

Furthermore, the curvature and $K_p(t)$ and torsion $\tau_p(t)$ of $\mathbf{X}_p(t)$ relate to the curvature $K(t)$ and torsion $\tau(t)$ of $\mathbf{X}(t)$ by

$$s'_p(t)K_p(t) = s'(t)K(t) \qquad \textit{and} \qquad s'_p(t)\tau_p(t) = s'(t)\tau(t).$$

Proof. Since the first derivatives of $\mathbf{x}(t)$ and $\mathbf{x}_p(t)$ are parallel, their tangents and normals are the same. Therefore,

$$k_p(t) = \frac{1}{s_p(t)}\mathbf{t}'(t) \cdot \mathbf{n}(t) = \frac{s'(t)}{s'_p(t)}k(t).$$

Similar observations hold for their 3D counterparts. In particular, we have that $\mathbf{X}'(t)$ and $\mathbf{X}'_p(t)$ are parallel, and thus the tangent directions of $\mathbf{X}(t)$ and $\mathbf{X}_p(t)$ are the same. It follows that the first derivatives of the tangent vectors of $\mathbf{X}(t)$ and $\mathbf{X}_p(t)$ are the same. Consequently, the normal vectors of $\mathbf{X}(t)$ and $\mathbf{X}_p(t)$ are the same too. Thus the two curves have the same frame $(\mathbf{T}(t), \mathbf{N}(t), \mathbf{B}(t))$. We conclude

$$K_p(t) = \frac{1}{s_p(t)}\mathbf{T}'(t) \cdot \mathbf{N}(t) = \frac{s'(t)}{s'_p(t)}K(t) \qquad \text{and} \qquad \tau_p(t) = \frac{1}{s_p(t)}\mathbf{N}'(t) \cdot \mathbf{B}(t) = \frac{s'(t)}{s'_p(t)}\tau(t).$$

□

Corollary 3.1. *If $K(t) \neq 0$ and $K_p(t) \neq 0$, the ratio between torsion and curvature of parallel curves is constant along a ruling, that is,*

$$\frac{\tau_p(t)}{K_p(t)} = \frac{\tau(t)}{K(t)}.$$

3.2.6 Ruling Curvature

In later sections, we will consider configurations of developed patches with specified rulings. To show that two configurations of the same patch with specified rulings are identical, we follow the approach by Demaine et al. [17, 18] and define a measure for the amount of bending at each ruling, the so-called ruling curvature. This concept is closely related to principal curvature lines, which we will address first.

Principal curvature lines

If $\mathbf{S}(t, u)$ is a smooth developable patch, one of its principal curvature direction is aligned with the incident ruling direction [12, 75]. Consequently, one of the principal curvatures is zero, and the rulings compose one family of curvature lines.

As the principal curvature directions are perpendicular at non-umbilical points, the other principal direction is perpendicular to the rulings. The family of curves on the surface whose tangents are perpendicular to the rulings form the second family of curvature lines. Since their tangents enclose a constant angle with the ruling directions, namely $\frac{\pi}{2}$, they form a family of tangent parallel curves. The following lemma shows how to obtain the parametrization of a principal curvature line on a given developable surface.

Lemma 3.6. *Given a parametrization $\mathbf{S}(t, u) = \mathbf{X}(t) + u\mathbf{R}(t)$ of a smooth patch, a principal curvature line can be parametrized by*

$$\mathbf{X}_c(t) = \mathbf{X}(t) + c(t)\mathbf{R}(t) \tag{3.10}$$

where $c(t)$ is the solution to the initial value problem

$$c'(t) = -\mathbf{R}(t) \cdot \mathbf{X}'(t) \qquad \text{and} \qquad c(0) = c_0.$$

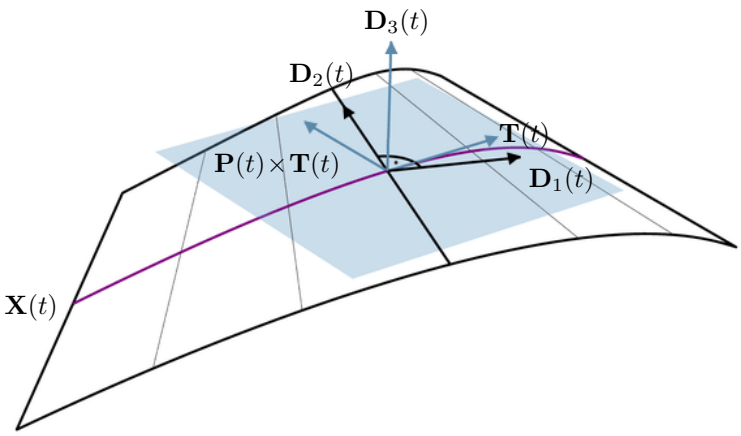

Figure 3.3: Illustration of the Darboux-frame of a principal curvature line of a patch.

Proof. We make the ansatz that a principal curvature is parametrized as stated in Equation (3.10) for an initially unknown length function $c(t)$. Since the tangent of $\mathbf{X}_c(t)$ is perpendicular to $\mathbf{r}(t)$, we require $\mathbf{X}_c'(t) \cdot \mathbf{R}(t) = 0$. Since $\mathbf{R}'(t) \cdot \mathbf{R}(t) = 0$, this constraint simplifies to

$$0 = \mathbf{X}_c'(t) \cdot \mathbf{R}(t) = \big(\mathbf{X}'(t) + c'(t)\mathbf{R}(t) + c(t)\mathbf{R}'(t)\big) \cdot \mathbf{R}(t) = \mathbf{X}'(t) \cdot \mathbf{R}(t) + c'(t),$$

which yields the differential equation stated above. □

A phrasing of Lemma 3.6 using patch characteristics is as follows:

Lemma 3.7. *Given a parametrization $\mathbf{S}(t,u) = \mathbf{X}(t) + u\mathbf{R}(t)$ of a smooth patch using patch characteristics, the length function of the principal curvature line in Equation* (3.10) *simplifies to*

$$c(t) = c_0 - \int_0^t s'(u) \cos\theta(u) du,$$

where $c_0 = c(0)$.

Proof. The above follows directly from the definition of the ruling direction in Equation (3.3) since $\mathbf{R}(t) \cdot \mathbf{X}'(t) = s'(t)\cos\theta(t)$. □

Principal curvatures

We continue our analysis by computing the non-trivial principal curvature of a developable strip.

For this purpose, recall that the *Darboux frame* of a curve on a surface is a frame that is aligned with the incident surface's tangent plane; see [90, Chapter 4]. Specifically, the Darboux frame of a curve $\mathbf{X}(t)$ on a surface $\mathbf{S}(t,u)$ consists of its tangent vector $\mathbf{D}_1(t)$, the incident tangent plane normal $\mathbf{D}_3(t)$, and the cross-product $\mathbf{D}_2(t) = \mathbf{D}_3(t) \times \mathbf{D}_1(t)$ of these two vectors. The Darboux-frame satisfies the following differential equations

$$\frac{1}{s'(t)} \begin{pmatrix} \mathbf{D}_1'(t) \\ \mathbf{D}_2'(t) \\ \mathbf{D}_3'(t) \end{pmatrix} = \begin{pmatrix} 0 & \kappa_g(t) & \kappa_n(t) \\ -\kappa_g(t) & 0 & \tau_r(t) \\ -\kappa_n(t) & -\tau_r(t) & 0 \end{pmatrix} \begin{pmatrix} \mathbf{D}_1(t) \\ \mathbf{D}_2(t) \\ \mathbf{D}_3(t) \end{pmatrix},$$

where $s'(t)$ is the curve's parametrization speed. In addition, $\kappa_g(t)$ denotes the *geodesic curvature*, $\kappa_n(t)$ the *normal curvature*, and τ_r the *relative torsion*.

We now consider the Darboux frames along a principal curvature line $\mathbf{X}_c(t)$ of a developable surface. For this purpose, we set $\mathbf{D}_3(t) = \mathbf{P}(t)$ to be the incident tangent plane normal, $\mathbf{D}_2(t) = \mathbf{R}(t)$, and $\mathbf{D}_1(t) = \mathbf{R}(t) \times \mathbf{P}(t)$; see Figure 3.3.

Note that since the normal along a ruling of a tangent developable is constant, the Darboux frame is the same for all points along a ruling. Consequently, the product of parametrization speed $s_c'(t)$ of $\mathbf{X}_c(t)$ and one of the three quantities, the geodesic curvature $\kappa_{g,c}(t)$, the normal curvature $\kappa_{n,c}(t)$, or relative torsion $\tau_c(t)$, are the same for all points of a ruling.

Before we proceed in computing the quantities, note that

$$\begin{aligned} \mathbf{R}(t) \times \mathbf{P}(t) &= \sin\theta(t)\ \mathbf{T}(t) - \cos\theta(t)\ (\mathbf{P}(t) \times \mathbf{T}(t)) \\ &= \sin\theta(t)\ \mathbf{T}(t) - \cos\theta(t)\ (\cos\varphi(t)\ \mathbf{N}(t) - \sin\varphi(t)\ \mathbf{B}(t))\,. \end{aligned} \tag{3.11}$$

Relative torsion. We first consider the relative torsion. Since

$$s_c'(t)\tau_c(t) = \mathbf{D}_3(t) \cdot \mathbf{D}_2'(t) = \mathbf{P}(t) \cdot \mathbf{R}'(t) = 0$$

This is not surprising, since the relative torsion vanishes for principal curvature lines.

Geodesic curvature of the (non-trivial) principal curvature lines. Using Equation (3.5) and Equation (3.11), we obtain

$$s_c'(t)\kappa_{g,c}(t) = -\mathbf{D}_3'(t) \cdot \mathbf{D}_1(t) = -\mathbf{R}'(t) \cdot (\mathbf{R}(t) \times \mathbf{P}(t)) = \theta'(t) + s'(t)k(t)$$

Consequently, observe that $|s_c'(t)\kappa_{g,c}(t)| = |\mathbf{R}'(t)| = |\mathbf{r}'(t)|$. Notably, the absolute value of the geodesic curvature of an arc-length parametrized principal curvature line only depends on the change of ruling directions, not their displacement.

Normal curvature of the (non-trivial) principal curvature lines. Finally, we compute the non-trivial curvature as the normal curvature of the specified Darboux-frame. Using Equation (3.4) for $\theta(t) \neq 0$, this curvature simplifies to

$$\begin{aligned} s_c'(t)\kappa_{n,c}(t) &= -\mathbf{D}_2'(t) \cdot \mathbf{D}_1(t) \\ &= -\mathbf{P}'(t) \cdot (\mathbf{R}(t) \times \mathbf{P}(t)) \\ &= -\cos\theta(t)(s'(t)\tau(t) - \varphi'(t)) + \sin\theta(t)s'(t)K(t)\sin\varphi(t) \\ &= s'(t)K(t)\sin\varphi(t)\frac{1}{\sin\theta(t)}. \end{aligned}$$

Ruling curvature

The quantity $s_c'(t)\kappa_{n,c}(t)$ encodes the bend of the surface perpendicular to the ruling direction. We therefore name it the *ruling curvature*:

$$V(t) = s_c'(t)\kappa_{n,c}(t) = s'(t)K(t)\sin\varphi(t)\frac{1}{\sin\theta(t)}. \tag{3.12}$$

In the next lemma, we demonstrate that (up to Euclidean motion) a 3D patch is specified by its development and a scalar-valued function $V(t)$. Upon successful construction, $V(t)$ will represent the patch's curvature. Consequently, we can use the ruling curvature to assess whether the bent states of a developed patch with specified rulings are the same, as we will do in the subsequent chapters.

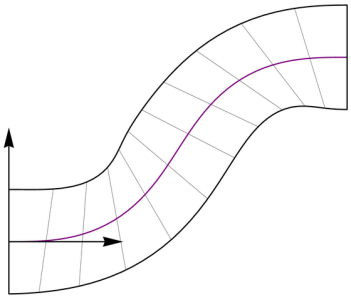

(a) Developed patch with specified rulings parametrized for $t \in [0, 2\pi]$ with an inflection point at $t = \pi$.

(b) Bending with prescribed torsion ($\tau(t) = 0$).
Successful bend (left) and premature termination with $\varphi(t') = \frac{\pi}{2}$ (right).

(c) Bending with prescribed inclination angle $\varphi(t)$.
Successful bend with $\varphi(\pi) = k(\pi) = 0$ (left) and premature termination with $\varphi(\pi - 0.1) = 0$ (right).

(d) Bending with prescribed curvature $K(t)$.
Successful bend with $K(\pi) = k(\pi) = 0$ (left) and premature termination because $|K(t')| < |k(t')|$.

Figure 3.4: Various configurations of a developed patch with specified rulings.

Lemma 3.8. *The configuration of a developable patch is defined by its development with specified rulings and the ruling curvature $V(t)$.*

Proof. Assuming that we are given a parametrization of a developed patch with specified rulings $\mathbf{s}(t,u) = \mathbf{x}(t) + u\mathbf{r}(t)$, where $s'(t) = |\mathbf{x}'(t)|$, we obtain a principal curvature line

$$\mathbf{x}_c(t) = \mathbf{x}(t) + c(t)\mathbf{r}(t)$$

and its parametrization speed $s_c'(t)$ using Lemma 3.6,

We obtain the space curve $\mathbf{X}_c(t)$ corresponding to $\mathbf{x}_c(t)$ by integrating the Darboux frame equations with normal curvature $\frac{1}{s_c'(t)}V(t)$, geodesic curvature $\frac{1}{s_c'(t)}\left(\theta'(t) + s'(t)k(t)\right)$, and zero relative torsion. Additionally, the ruling vector is the second vector of the integrated frame.

Ultimately, we obtain the directrix as $\mathbf{X}(t) = \mathbf{X}_c(t) - c(t)\mathbf{R}(t)$, resulting in the to $\mathbf{s}(t,u)$ isometric parametrization $\mathbf{S}(t,u) = \mathbf{X}(t) + u\mathbf{R}(t)$. □

3.2.7 Bending a Developed Patch with Specified Rulings

To summarize the previous considerations, the development of a patch with specified rulings is determined by the curvature $k(t)$ and the parametrization speed $s'(t)$ of its developed directrix $\mathbf{x}(t)$, along with a function that encodes the ruling angles $\theta(t) \in (0,\pi)$.

The 3D configuration is further characterized by three additional functions: the signed curvature $K(t)$ and torsion $\tau(t)$ of its directrix $\mathbf{X}(t)$, and the inclination angle $\varphi(t)$. All these quantities are subject to constraints that connect the curvatures and the inclination angle (see Equation (3.6)) and enforce developability (see Equation (3.4)).

In the following, we assume that the development of a patch with specified rulings is provided. We explore how to specify the range of shapes it can be bent into, in addition to Lemma 3.8. Specifically, we demonstrate how to retrieve the remaining quantities if one of the functions $K(t)$, $\tau(t)$, or $\varphi(t)$ is given.

Prescribed torsion $\tau(t)$

If we are given the torsion $\tau(t)$, the angular function is specified by the following initial value problem:

$$\varphi'(t) = \left(\cot\theta(t)k(t)\tan\varphi(t) + \tau(t)\right)s'(t), \qquad \text{where} \qquad \varphi(0) = \varphi_0.$$

However, the computation of a suitable inclination angle might encounter premature failure or not succeed at all. If $k(t') \neq 0$ or $\theta(t') \neq \frac{\pi}{2}$, the computed angle $\varphi(t)$ cannot exceed $\varphi(t') = \pm\frac{\pi}{2}$, as this would result in $\varphi(t') = \infty$. Specifically, we need the limit $\lim_{t\to t'}\cot\theta(t)k(t)\tan\varphi(t)$ to exist. This constraint is not easily achievable, as the trajectory of $\varphi(t)$ depends on the initial value φ_0.

Nevertheless, there usually exists a one-parameter family of solutions corresponding to suitable initial values for φ_0. Once a suitable $\varphi(t)$ is computed, the curvature is given by $K(t) = \frac{k(t)}{\cos\varphi(t)}$. Note that if $k(t') \neq 0$ and $\varphi(t') = \pm\frac{\pi}{2}$, it follows that $K(t') = \infty$. Consequently, we need $\lim_{t\to t'}\frac{k(t)}{\cos\varphi(t)}$ to be finite.

Prescribed inclination angle $\varphi(t)$

If we are given the inclination angle $\varphi(t)$, we obtain the curvature and torsion as follows

$$K(t) = \frac{k(t)}{\cos\varphi(t)} \qquad \text{and} \qquad \tau(t) = -k(t)\cot\theta(t)\tan\varphi(t) + \frac{\varphi'(t)}{s'(t)}.$$

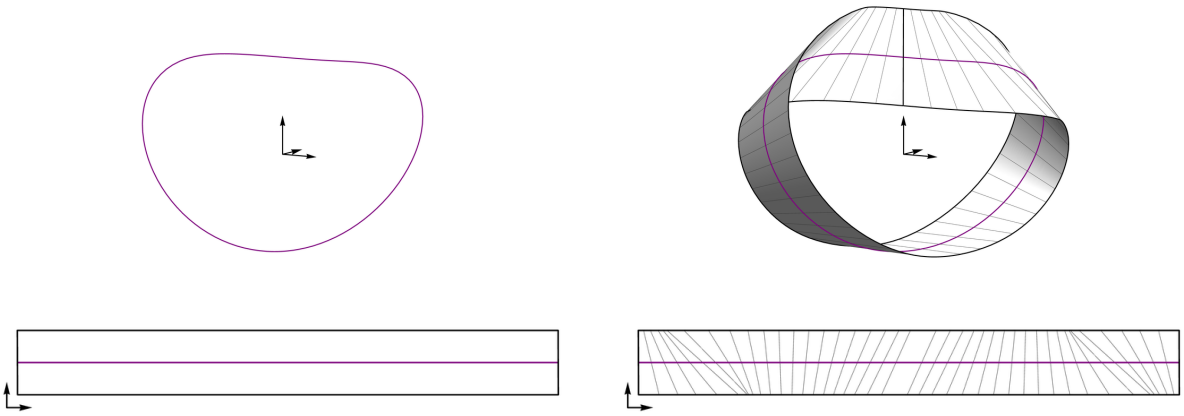

Figure 3.5: Parametrization of a Möbius-strip in equilibrium. Left: Space curve and developed patch with unspecified rulings. Right: Patch attached to the space curve. The parametrization of the space curve and the resulting developable surface was developed by Wunderlich [111] in the context of a parametrization of a Möbius band in equilibrium.

Consequently, if $\varphi(t') = \pm\frac{\pi}{2}$ and $k(t') \neq 0$, we obtain $K(t') = \infty$. Again we need $\lim_{t\to t'} \frac{k(t)}{\cos\varphi(t)}$ to be finite.

Prescribed curvature $K(t)$

If we are given the curvature $K(t)$, we first set without loss of generality $\varphi(t) = \arccos\left(\frac{k(t)}{K(t)}\right)$. It follows that we require $|K(t)| \geq |k(t)|$. Furthermore, if $K(t') = 0$, we require $\lim_{t\to t'} \frac{k(t)}{K(t)}$ to exist. However, this is usually the case since $|K(t)| \geq |k(t)|$. If $\varphi(t)$ is real-valued and differentiable along an interval, we can use it to compute the torsion as

$$\tau(t) = \frac{\varphi'(t)}{s'(t)} - K(t)\sin\varphi(t)\cot\theta(t).$$

3.2.8 Gluing a Patch to a Specified Curve

Gluing an patch with unspecified rulings to a space curve has been studied in differential geometric literature before, for instance, by Wunderlich [111] and Alese [3].

In the following, we assume that we are given a space curve $\mathbf{X}(t)$ and a directrix $\mathbf{x}(t)$ of a developed patch with unspecified rulings. Let the 3D curve $\mathbf{X}(t)$ be defined by the curvature function $K(t)$, the torsion $\tau(t)$, and the parametrization speed $s'(t)$. Additionally, without loss of generality, we assume that $\mathbf{x}(t)$ has the same parametrization speed $s'(t)$ as $\mathbf{X}(t)$ and its (signed) curvature is represented by $k(t)$.

Then, the two remaining degrees of freedom, the inclination angle $\varphi(t)$ and ruling angle $\theta(t)$, can be computed from the developability condition (Equation (3.4)) and curvature condition (Equation (3.6)). Specifically, for intervals where $|K(t)| > |k(t)|$, the inclination angle can be computed as

$$\varphi(t) = \pm\arccos\frac{k(t)}{K(t)}.$$

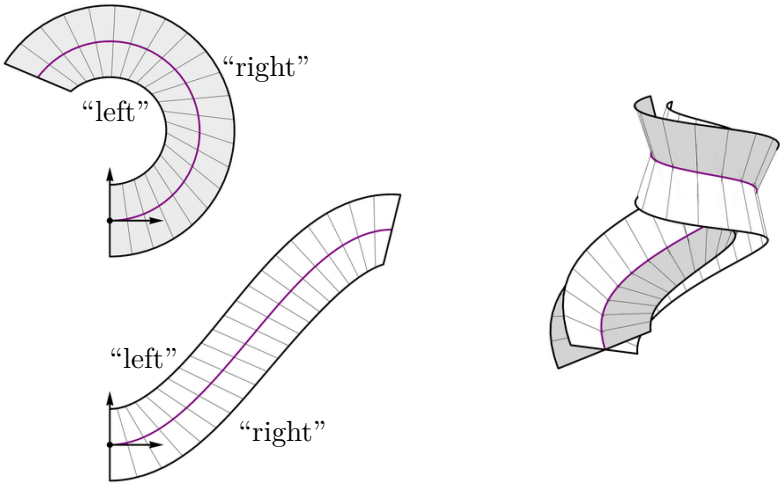

Figure 3.6: Two developed patches with specified rulings and their configuration when glued along their directrices.

Note that if $k(t) \neq 0$, the there are two possible inclination angles that in general (for curves with non-vanishing curvature) result in different surfaces.

Upon successful computation, the ruling angle can then be obtained from

$$\cot\theta(t) = -\frac{\tau - \frac{\varphi'(t)}{s'(t)}}{K(t)\sin\varphi(t)}.$$

Figure 3.5 shows an example developed by Wunderlich [111] for the parametrization of a Möbius strip in equilibrium.

3.3 Joining Two Patches Patches with Specified Rulings

In this section, we consider configurations obtained by gluing two developed patches with specified rulings along curves. We show that the configurations are determined up to initial opening angle of the configuration. We highlight the special case where the two gluing curves match in the development, as the resulting configuration can be achieved by folding along a curved crease.

3.3.1 Notation

In the following, we examine two developed patches with specified rulings, each parameterized by a directrix and a left-side ruling directions. Each directrix splits its respective developed patch into two subpatches, as depicted in Figure 3.6. Since combining both developed subpatches from each surface results in self-intersecting shapes, we focus on the case where we join two subpatches from distinct patches. Without loss of generality, we assume the two parts of interest to be associated with the left and right sides of the developed curves, respectively. More formally:

$$\mathbf{s}_L(t,u) = \mathbf{x}_L(t) + u\mathbf{r}_L(t) \qquad \text{and} \qquad \mathbf{s}_R(t,u) = \mathbf{x}_R(t) - u\mathbf{r}_R(t),$$

where $\mathbf{x}_L(t)$ and $\mathbf{x}_R(t)$ represent the two directrices that will be joined; see Figure 3.7. This assumption is valid, as the right-side subpatch is the left-side subpatch of a reflected patch. Without

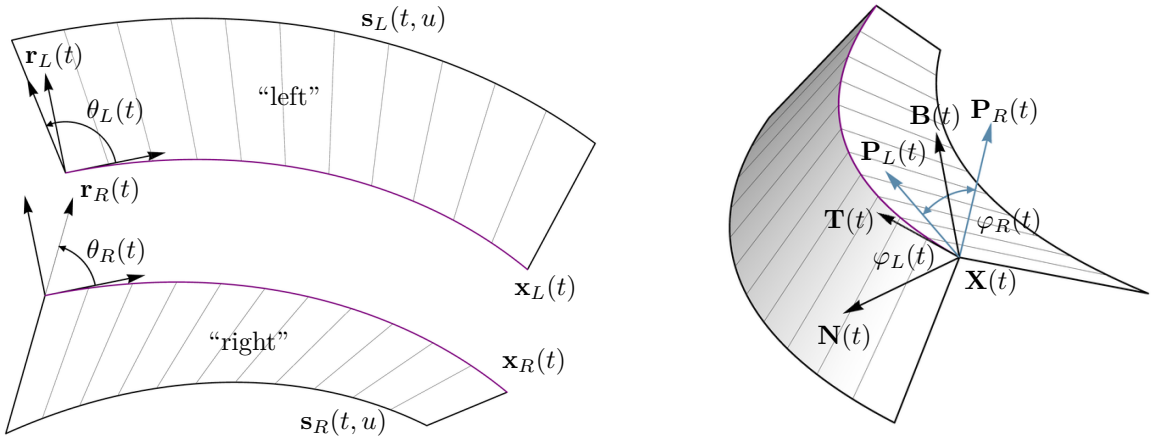

(a) Development. (b) Glued configuration.

Figure 3.7: Illustration of the notation used for gluing two patches with specified rulings in Section 3.3.

loss of generality, we assume that the two curves have the same parametrization speed, that is, $|\mathbf{x}_L'(t)| = |\mathbf{x}_R'(t)|$. The vectors $\mathbf{r}_L(t)$ and $\mathbf{r}_R(t)$ denote the (left-side) ruling directions of the patch. These are defined as

$$\mathbf{r}_L(t) = \cos\theta_L(t)\ \mathbf{t}_L(t) + \sin\theta_L(t)\ \mathbf{n}_L(t) \qquad \text{and} \qquad \mathbf{r}_R(t) = \cos\theta_R(t)\ \mathbf{t}_R(t) + \sin\theta_R(t)\ \mathbf{n}_R(t),$$

where $\mathbf{t}_i(t)$ are the tangents and $\mathbf{n}_i(t)$ are the left-side normals of $\mathbf{x}_i(t)$ as discussed in Section 3.2.3. Lastly, $k_L(t)$ and $k_R(t)$ denote the signed curvatures of the curves $\mathbf{x}_L(t)$ and $\mathbf{x}_R(t)$, respectively.

Typically, the gluing of two patches does not have a planar configuration. However, when the two curves are congruent, a planar arrangement of the joined patches is achievable. If the curves, $\mathbf{x}_L(t)$ and $\mathbf{x}_R(t)$, are not related by a reflection, the patches can be connected along opposite sides of the common curve, and the other glued states correspond to a creasing along the shared curve. In contrast, when the curves are congruent and related by a reflection, such a combination is referred to as a *geodesic pair*, as introduced in [74]. The planar configuration in this case corresponds to two patches whose directrices are related by a reflection.

In the following, we aim to determine the patch characteristics of the patches $\mathbf{S}_L(t,u)$ and $\mathbf{S}_R(t,u)$ corresponding to $\mathbf{s}_L(t,u)$ and $\mathbf{s}_R(t,u)$ with respect to the shared common glue curve $\mathbf{X}(t)$. Since the curve is incident to both patches, the curvature and torsion functions of both patch characteristics are the same, and we will denote them by $K(t)$ and $\tau(t)$. Additionally, the parametrization speed of $\mathbf{X}(t)$ is the same as of the developed curves, that is, $s'(t) = |\mathbf{x}_L'(t)| = |\mathbf{x}_R'(t)|$, and the ruling angles are also specified by the development, that is, $\theta_L(t)$ and $\theta_R(t)$. We denote the inclination angles with a corresponding subscript, $\varphi_L(t)$ and $\varphi_R(t)$. It therefore remains to compute the four unknown functions: $K(t)$, $\tau(t)$, $\varphi_R(t)$ and $\varphi_L(t)$.

3.3.2 Constraints

We derive the four quantities necessary to describe the 3D state from a differential-algebraic system of the following four equations, which arise from the developability constraint in Equation (3.4) for

each surface,

$$K(t)\sin\varphi_L(t)\cot\theta_L(t) = -\tau(t) + \frac{\varphi_L'(t)}{s'(t)} \qquad \text{and} \qquad K(t)\sin\varphi_R(t)\cot\theta_R(t) = -\tau(t) + \frac{\varphi_R'(t)}{s'(t)}, \tag{3.13}$$

and the curvature constraint in Equation (3.6) for each surface,

$$k_L(t) = K(t)\cos\varphi_L(t) \qquad \text{and} \qquad k_R(t) = K(t)\cos\varphi_R(t). \tag{3.14}$$

Before we discuss the computation of the 3D shape, we observe the following relationship between solutions of the given differential-algebraic system:

Lemma 3.9. *If $S_0 = (K(t), \tau(t), \varphi_L(t), \varphi_R(t))$ is a solution of the differential algebraic system in Equations* (3.13) *and* (3.14)*, then the following combinations are also solutions*

$$\begin{aligned} S_1 &= (K(t), -\tau(t), -\varphi_L(t), -\varphi_R(t)), \\ S_2 &= (-K(t), -\tau(t), \pi - \varphi_L(t), \pi - \varphi_R(t)), \\ S_3 &= (-K(t), \tau(t), \varphi_L(t) - \pi, \varphi_R(t) - \pi). \end{aligned}$$

The four corresponding solutions are related by Euclidean motions; see Figure 3.8.

Proof. The claim can be verified by inserting the quadruples of solutions into Equations (3.13) and (3.14). Simplification results in the same conditions as the respective change of signs cancel out. Furthermore, as the absolute value of the curvature and torsion are the same in all proposed solutions, the curves will be related by an Euclidean motion. In particular, S_0 and S_1 relate to S_2 and S_3 by a reflection about the initial rectifying plane. S_0 and S_2 relate to S_1 and S_3 by a reflection about the initial osculating plane. Finally, S_0 and S_1 relate to S_3 and S_2 by a rotation about the initial tangent direction by π. □

In the following, we first consider the general case of non-congruent curves. We then address the special case where the curves can be aligned, which corresponds to creasing the common curve.

3.3.3 Gluing: Joining Along Two Curves

In general, solving the differential-algebraic system presented in Equations (3.13) and (3.14) can be challenging. Even sophisticated programs like Mathematica encounter difficulties, even for relatively "simple" input functions $k_L(t)$, $k_R(t)$, $\theta_L(t)$, $\theta_R(t)$, and $s'(t)$. To address this challenge, we propose a rephrasing of this system, resulting in a single differential equation for one of the inclination angles, and three explicit equations for the remaining three unknown functions.

To solve the differential equation, an initial value for the inclination angle is required. This initial value determines the value of the other inclination angle, subsequently determining the overall opening angle between the first two tangent planes. This reflects the discrete counterpart of the problem, specifically the gluing of two PQ strips with equal edge lengths along the gluing polyline. When the gluing process begins, there is one degree of freedom for the angle between the initial two faces. As subsequent pairs of planar quads are attached, there are generally either two or no possible configurations. In cases where two possible solutions exist, one of them typically corresponds to the discrete counterpart of a smooth gluing.

In the subsequent discussion, we aim to derive a solution using an initial value problem for one of the inclination angles, beginning at $t = 0$. The asymmetric nature of the problem has led us to

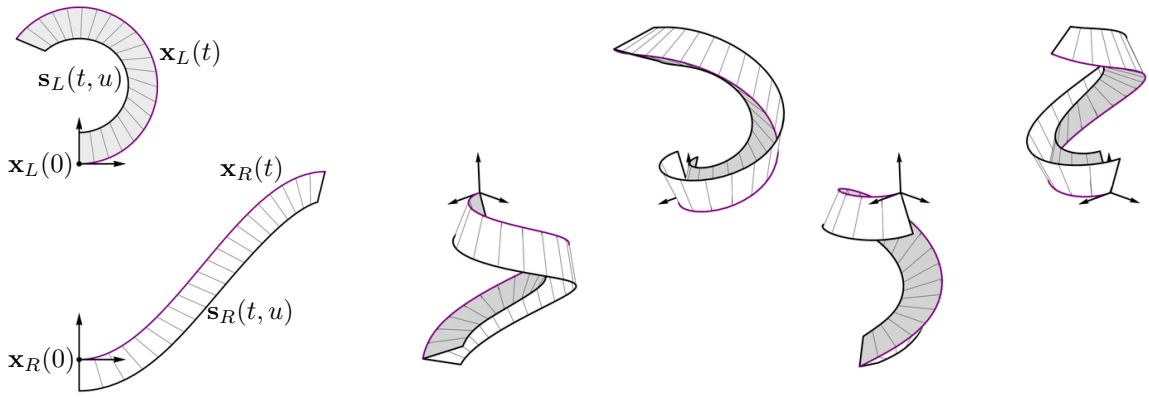

(a) Development. (b) Glued configurations corresponding to S_0, S_1, S_2, and S_3.

Figure 3.8: Four congruent solutions corresponding to the same development and same initial frame.

situations where solving for one inclination angle becomes infeasible, while integration for the other continues without issues. Specifically, points at which a curvature reaches zero present challenges for the corresponding inclination angle. For instance, consider the development in Figure 3.8 (left). Note that $\mathbf{x}_R(t)$ exhibits an inflection point, resulting in it vanishing curvature $k_R(t)$ at an intermediate value. Attempting to integrate $\varphi_R(t)$ would be problematic at this point. Yet, integration of $\varphi_R(t)$ with the right initial values results in the full gluing, as illustrated in Figures 3.8 and 3.10.

In the following, we will adaptively set either $(A, B) = (L, R)$ or $(A, B) = (R, L)$, and compute a solution for $\varphi_B(t)$ up to the point where integration meets an obstacle. Where feasible, we will switch the roles of L and R and continue. Observations suggest that it is possible to stitch together the integrated outcomes of the inclination angles alternately to achieve a solution for a larger interval.

Until now, the curvatures of the developed patches only required to be continuous. For the following simplifications, we require $k_A(t)$ and $k_B(t)$ to be C^1.

Lemma 3.10. *For $k_B(t) \neq 0$, the system of differential-algebraic equations in Equations* (3.13) *and* (3.14) *can be rephrased as the explicit initial value problem*

$$\varphi_B'(t) = \frac{\sigma(k_A k_B' - k_B k_A')\cos\varphi_B + s' k_B \left(\sigma(k_A^2 \cos\varphi_B - k_B^2 \sec\varphi_B)\cot\theta_A + k_B^2 x \tan\varphi_B \cot\theta_B\right)}{k_B^2 x - \sigma k_A k_B \sin\varphi_B}$$

where $\sigma \in \{-1, 1\}$ and $x(t) = \sqrt{1 - \frac{k_A^2(t)}{k_B^2(t)} \cos^2\varphi_B(t)}$.

The initial value problem is locally real-valued if the initial value $\varphi_B(0) \in [-\pi, \pi]$ satisfies

$$\left| \frac{k_A(0)}{k_B(0)} \cos\varphi_B(0) \right| \leq 1.$$

The inclination angle $\varphi_B(t)$ and its first derivative $\varphi'_B(t)$ specify the remaining functions as

$$\begin{aligned} K(t) &= \frac{k_B(t)}{\cos\varphi_B(t)}, \\ \tau(t) &= \frac{1}{s'(t)}\left(\varphi'_B(t) - s'(t)k_B(t)\cot\theta_B(t)\tan\varphi_B(t)\right), \\ \varphi_A(t) &= \sigma\arccos\left(\frac{k_A(t)}{k_B(t)}\cos\varphi_B(t)\right). \end{aligned}$$

Proof. First, we use equations in Equation (3.13) to solve for the curvature and torsion of $\mathbf{X}(t)$, resulting in

$$K(t) = \frac{\varphi'_A(t) - \varphi'_B(t)}{s'(t)\left(\cot\theta_A(t)\sin\varphi_A(t) - \cot\theta_B(t)\sin\varphi_B(t)\right)}, \tag{3.15}$$

$$\tau(t) = -\frac{\varphi'_A(t)\cot\theta_B(t)\sin\varphi_A(t) - \varphi'_B(t)\cot\theta_A(t)\sin\varphi_B(t)}{s'(t)\left(\cot\theta_A(t)\sin\varphi_A(t) - \cot\theta_B(t)\sin\varphi_B(t)\right)}. \tag{3.16}$$

If $k_B(t) \neq 0$, it follows from Equation (3.14, left) that $K(t) \neq 0$ and $\cos\varphi_B(t) \neq 0$. From the equations in Equation (3.14) we obtain

$$\cos\varphi_A(t) = \frac{k_A(t)}{k_B(t)}\cos\varphi_B(t) \qquad \Longrightarrow \qquad \varphi_A(t) = \sigma\arccos\left(\frac{k_A(t)}{k_B(t)}\cos\varphi_B(t)\right), \tag{3.17}$$

where $\sigma \in \{-1, 1\}$.

In order for the arccosine function to be real-valued, it is necessary for the absolute value of its argument to be less than or equal to 1. Additionally, to obtain continuous solutions, we need to be consistent in the choice of σ unless we encounter a point where $\left|\frac{k_A(t)}{k_B(t)}\cos\varphi_B(t)\right| = 1$.

Differentiation of $\varphi_A(t)$ yields

$$\varphi'_A(t) = \sigma\frac{(k_A(t)k'_B(t) - k_B(t)k'_A(t))\cos\varphi_B(t) + k_A(t)k_B(t)\sin\varphi_B(t)\varphi'_B(t)}{\sqrt{1 - \frac{k_A(t)^2}{k_B(t)^2}\cos^2\varphi_B(t)}k_B(t)^2}. \tag{3.18}$$

Finally, inserting Equations (3.15), (3.16), (3.17), and (3.18) in Equation (3.14, right) and solving for $\varphi'_B(t)$ results in the claimed equation.

The remaining functions are obtained in a straight-forward way. The expressions for curvature and torsion can be obtained by solving Equation (3.14, right) or Equation (3.13, right) for $K(t)$ or $\tau(t)$, respectively. The expression for $\varphi_A(t)$ follows Equation (3.17). □

Note that in the special case where $k_A(t) = k_B(t)$, it follows that $\varphi_A(t) = |\sigma\varphi_B(t)|$. Additionally, $x(t) = \sqrt{\sin^2\varphi_B(t)}$ and the differential equation in Lemma 3.10 simplifies to

$$\varphi'_B = \frac{s'(t)k_B(t)\left(-\sigma\sin\varphi_B(t)\cot\theta_A(t) + \sqrt{\sin^2\varphi_B(t)}\cot\theta_B(t)\right)}{\sqrt{\sin^2\varphi_B(t)} - \sigma\sin\varphi_B(t)}\tan\varphi_B(t).$$

If $\sqrt{\sin^2\varphi_B(t)} = \sigma\sin\varphi_B(t)$, it follows that $\varphi_A(t) = \varphi_B(t)$ and the expression is undefined. However, if $\sqrt{\sin^2\varphi_B(t)} = -\sigma\sin\varphi_B(t)$, it follows that $\varphi_A(t) = -\varphi_B(t)$ and the above simplifies to

$$\varphi'_B = \frac{1}{2}s'(t)k_B(t)\left(\cot\theta_A(t) + \cot\theta_B(t)\right)\tan\varphi_B(t). \tag{3.19}$$

In the next subsection, we will see that the latter case corresponds to the special case of creasing, and we will discuss a simpler derivation of Equation (3.19).

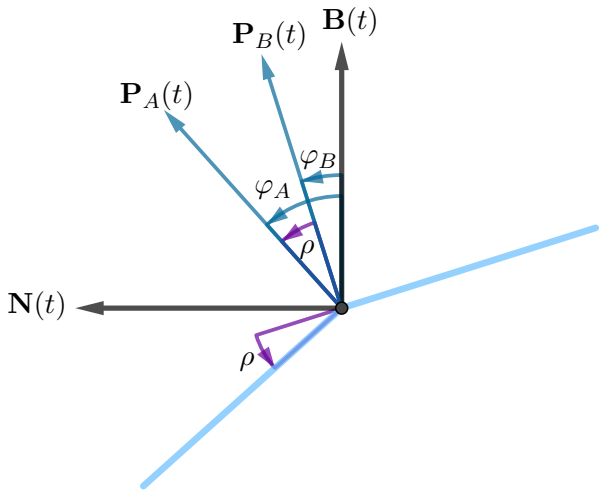

Figure 3.9: Illustration of the relationship between the fold angle ρ and the angles between the left and right surface patches.

Finding an initial value from a given opening angle

Instead of using the possibly unintuitive initial value for one of the inclination angles, $\varphi_B(0)$, we might prefer to specify an opening angle between the initial tangent planes normal vectors, and hence the tangent planes. Specifically, we may wish to specify $\rho_0 = \varphi_A(0) - \varphi_B(0)$ and subsequently find $\varphi_B(0)$ such that:

$$\varphi_B(0) = \arccos\left(c\cos(\varphi_B(0) + \rho_0)\right) \qquad \text{for} \qquad c = \frac{k_B(0)}{k_A(0)} \neq 0.$$

In the special case where the glue curve corresponds to a crease, $\rho(t) = \varphi_A(t) - \varphi_B(t)$ denotes the deviation from the flat stated and is often referred to as the *fold angle*; see Figure 3.9.

Without loss of generality, we assume $\rho_0 > 0$, which implies $\varphi_B(0) < \varphi_A(0)$. This assumption is made based on Lemma 3.9, which shows that every solution with $\varphi_B(0) < \varphi_A(0)$ corresponds to a solution with $\varphi_A(0) < \varphi_B(0)$ by replacing S_0 with S_2. This replacement involves considering the complements of $\varphi_A(t)$ and $\varphi_B(t)$, as well as changing the sign of the curvature and torsion.

Lemma 3.11. *For $c \neq 0$, $\rho_0 \in (0, \pi)$, and $1 + c^2 - 2c\cos\rho_0 > 0$, the equation*

$$\varphi_0 = \arccos\left(c\cos(\varphi_0 + \rho_0)\right) \tag{3.20}$$

has the following real-valued solutions: If $\rho_0 = \frac{\pi}{2}$, this equation has two solutions, namely

$$\varphi_0^{\mp} = \arccos\left(\mp\frac{c}{\sqrt{1+c^2}}\right).$$

Otherwise, the unique solution reads

$$\varphi_0 = \begin{cases} \arccos\left(-\frac{c\sin\rho_0}{\sqrt{1+c^2-2c\cos\rho_0}}\right), & \text{if } 1 - c\cos\rho_0 > 0, \\ 0, & \text{if } 1 - c\cos\rho_0 = 0, \\ \arccos\left(\frac{c\sin\rho_0}{\sqrt{1+c^2-2c\cos\rho_0}}\right), & \text{if } 1 - c\cos\rho_0 < 0. \end{cases}$$

Proof. We first rewrite Equation (3.20) as

$$\cos\varphi_0 = c\cos(\varphi_0 + \rho_0),$$

possibly introducing new solutions that we will later eliminate. We then use the addition formula for cosines to obtain the equivalent expression

$$\cos\varphi_0 = c(\cos\rho_0\cos\varphi_0 - \sin\rho_0\sin\varphi_0).$$

Using the tangent half-angle substitution $\varphi_0 = \tan\frac{p}{2}$, we obtain

$$\frac{(-1 + c\cos\rho_0)p^2 + 2(c\sin\rho_0)p + 1 - c\cos\rho_0}{1+p^2} = 0.$$

Since the denominator can not vanish, we distinguish two cases:

First, if $-1 + c\cos\rho_0 = 0$, the condition on p is linear. Furthermore, since $\rho_0 = \arccos\frac{1}{c}$, and $\sin\rho_0 = \sqrt{1-\frac{1}{c^2}}$, this constraint simplifies to

$$2\sqrt{1-\frac{1}{c^2}}p = 0.$$

Since $\rho_0 \neq 0$ and $\rho_0 \neq \pi$, we have that $c \neq \pm 1$. We thus require $p = 0$, resulting in $\varphi_0 = 2\arctan p = 0$.

Otherwise, assume $-1 + c\cos\rho_0 \neq 0$. In this case the constraint is quadratic, and its two solutions read

$$p^{\mp} = \frac{\mp\sqrt{1 + c^2 - 2c\cos\rho_0} - c\sin\rho_0}{-1 + c\cos\rho_0},$$

resulting in two possible solutions $\varphi_0^{\mp} = 2\arctan p^{\mp}$ of Equation (3.20).

To get a simpler expression, we note that $\arccos(\cos(2\arctan p)) = 2\arctan p$ since $\arctan : \mathbb{R} \mapsto [-\pi/2, \pi/2]$, and $\arccos(\cos x) = x$ for $x \in [-\pi, \pi]$. As furthermore

$$\cos(2\arctan p) = \frac{1-p^2}{1+p^2},$$

we ultimately obtain

$$\varphi_0^{\mp} = \arccos(\cos(2\arctan p^{\mp})) = \arccos\left(\frac{1-(p^{\mp})^2}{1+(p^{\mp})^2}\right) = \arccos\left(\mp\frac{c\sin\rho_0}{\sqrt{1+c^2-2c\cos\rho_0}}\right).$$

To eliminate the initially introduced solutions, we simplify

$$\begin{aligned}\arccos\left(c\cos(\varphi_0^{\mp} + \rho_0)\right) &= \arccos\left(c(\cos\rho_0\cos\varphi_0^{\mp} - \sin\rho\sin\varphi_0^{\mp})\right) \\ &= \arccos\left(\left(\frac{\mp c\cos\rho_0 - \sqrt{(1-c\cos\rho_0)^2}}{\sqrt{1+c^2-2c\cos\rho_0}}\right)c\sin\rho_0\right).\end{aligned}$$

If $\cos\rho = 0$, that is $\rho_0 = \frac{\pi}{2}$, we the above simplifies to

$$\arccos\left(c\cos\left(\varphi_0^{\mp} + \frac{\pi}{2}\right)\right) = \arccos\left(\pm\frac{c}{\sqrt{1+c^2}}\right) = \varphi_0^{\mp},$$

resulting in two possible solutions for φ_0.

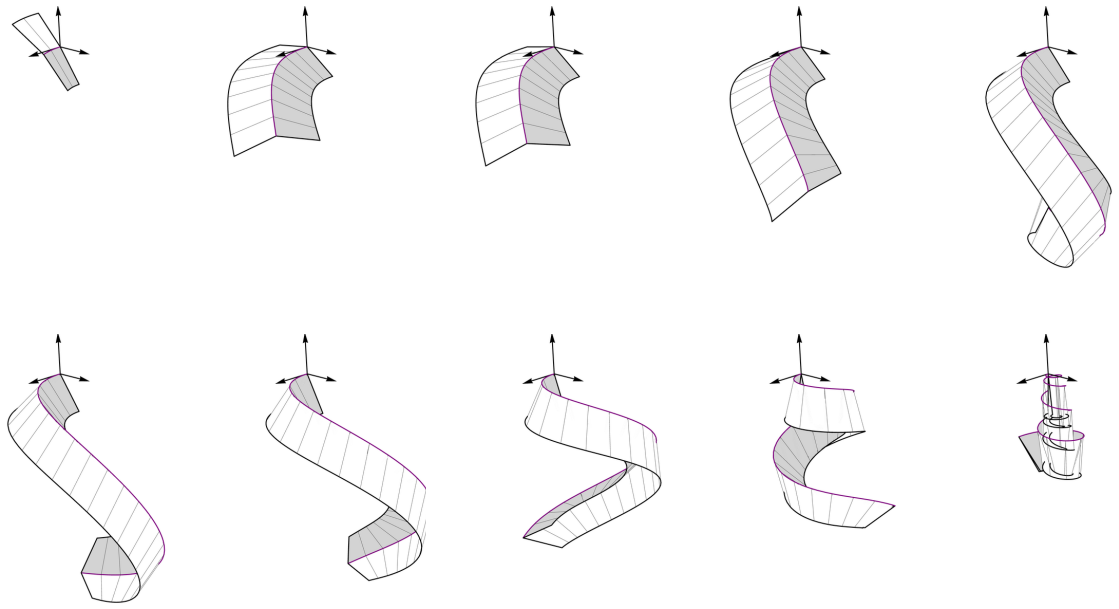

Figure 3.10: Gluing of the two patches depicted in Figure 3.8a for opening angles $\rho \in (0.95\pi, 0.85\pi, 0.75\pi, 0.65\pi, 0.55\pi, 0.45\pi, 0.35\pi, 0.25\pi, 0.15\pi, 0.05\pi)$. Integration stopped prematurely for the first three shapes and the last shape.

Otherwise, assume $\cos\rho_0 \neq 0$. If $1 - c\cos\rho_0 > 0$, we have

$$\arccos(c\cos(\varphi^- + \rho_0)) = \arccos\varphi^-,$$

in case of $1 - c\cos\rho_0 < 0$, we have

$$\arccos(c\cos(\varphi^+ + \rho_0)) = \arccos\varphi^+.$$

Finally, note that if $1 + c^2 - 2c\cos\rho_0 > 0$, the arccosines are real-valued since

$$\begin{aligned}\left(\mp\frac{c\sin\rho_0}{\sqrt{1+c^2-2c\cos\rho_0}}\right)^2 \leq 1 \quad &\iff \quad c^2\sin^2\rho_0 < 1 + c^2 - 2c\cos\rho_0 \\ &\iff \quad 0 \leq (1 - c\cos\rho_0)^2.\end{aligned}$$

□

Practical considerations

When employing the initial value obtained in Lemma 3.11 as an initial value for the differential equation in Lemma 3.10, it is important to choose the appropriate sign σ.

Figure 3.10 depicts gluings with varying opening angle ρ. It is worth noting that as the difference ρ approaches 0 or π, the solution interval typically becomes smaller if the glue curve does not correspond to a crease or a geodesic pair. This is due to the material struggling to compensate for the material loss or excess while maintaining developability; see Figure 3.10.

3.3.4 Creasing: Joining Along Two Matching Curves

We dedicate this subsection to a very prominent special case namely when the two curves match. In this case, we denote their common curvature by $k(t)$ and assume that $k(t)$ is non-zero except at isolated points. Then, Equation (3.14) implies that $\cos\varphi_L(t) = \cos\varphi_R(t)$, which leads to $\varphi_L(t) = \pm\varphi_R(t)$. The interesting scenario occurs when $\varphi_L(t) = -\varphi_R(t)$, as described in Lemma 3.13. For the sake of completeness, we also state the case when both angular functions are the same; see Lemma 3.12.

Lemma 3.12. *If $\varphi_L(t) = \varphi_R(t)$, two possible cases arise:*

- *If $\theta_L(t) \neq \theta_R(t)$, the system is overconstrained, resulting in the only solution being the flat configuration.*
- *If $\theta_L(t) = \theta_R(t)$, the system is underconstrained, resulting in multiple potential configurations of a doubly-covered patch with prescribed rulings (see Section 3.2.7).*

Proof. For $\varphi(t) = \varphi_L(t) = \varphi_R(t)$, we begin by expressing the torsion from both equations given in Equation (3.13). Using $K(t) = \frac{k(t)}{\cos\varphi(t)}$, we obtain

$$\tau(t) = \frac{\varphi'(t)}{s'(t)} - k(t)\cot\theta_L(t)\tan\varphi(t), \qquad \text{and} \qquad \tau(t) = \frac{\varphi'(t)}{s'(t)} - k(t)\cot\theta_R(t)\tan\varphi(t).$$

Subtracting one equation from the other, results in

$$0 = \left(\cot\theta_L(t) - \cot\theta_R(t)\right) k(t)\tan\varphi(t).$$

When the ruling angles differ and $k(t) \neq 0$ holds for almost all values of t, the above constraint implies $\varphi(t) = 0$. As a result, we also have $\tau(t) = 0$ and $K(t) = k(t)$. Consequently, this corresponds corresponds to a flat configuration.

Otherwise, if $\theta_L(t) = \theta_R(t)$, the above equation is trivially satisfied. As discussed in Section 3.2.7, there is a lot of flexibility when bending a patch with prescribed rulings. Recall that a bent patch is specified by the three functions: $K(t)$, $\tau(t)$ and $\varphi(t)$, which need to satisfy two constraints. Consequently, we have the flexibility to prescribe one of the three functions while determining the remaining two. □

We now proceed with the nontrivial case where $\varphi(t) = \varphi_L(t) = -\varphi_R(t)$, which for a given initial value of $\varphi(t)$ results in a uniquely defined 3D shape that corresponds to creasing along the common crease. Note that here we only require the common curvature function to be continuous.

Lemma 3.13. *If $\varphi(t) = \varphi_L(t) = -\varphi_R(t)$, the folded shape can be obtained by solving an initial value problem for the angular function $\varphi(t)$, namely,*

$$\varphi'(t) = \frac{1}{2}s'(t)k(t)\left(\cot\theta_L(t) + \cot\theta_R(t)\right)\tan\varphi(t), \qquad \textit{where} \qquad \varphi(0) = \varphi_0. \tag{3.21}$$

In addition, the directrix $\mathbf{X}(t)$ is specified by the following curvature and torsion,

$$K(t) = \frac{k(t)}{\cos\varphi(t)} \qquad \textit{and} \qquad \tau(t) = -\frac{1}{2}k(t)\left(\cot\theta_L(t) - \cot\theta_R(t)\right)\tan\varphi(t). \tag{3.22}$$

Proof. Using the definition of $\varphi(t)$ and $K(t) = \frac{k(t)}{\cos\varphi(t)}$, the equations in Equation (3.13) simplify to

$$k(t)\cot\theta_L(t)\tan\varphi(t) = -\tau(t) + \frac{\varphi'(t)}{s'(t)} \qquad \text{and} \qquad k(t)\cot\theta_R(t)\tan\varphi(t) = \tau(t) + \frac{\varphi'(t)}{s'(t)}. \tag{3.23}$$

Solving both equations for $\varphi'(t)$ and $\tau(t)$ results in the claimed expressions. □

Lemma 3.14. *The solution to the initial value problem in Equation* (3.21) *reads*

$$\varphi(t) = \arcsin\left(e^{\int_0^t f(u)du}\sin\varphi_0\right),$$

where

$$f(t) = \frac{1}{2}s'(t)k(t)\left(\cot\theta_A(t) + \cot\theta_B(t)\right).$$

Proof. The claim follows directly from

$$\int \frac{\varphi'(t)}{\tan\varphi(t)}dt = \ln\left(\sin\varphi(t)\right).$$

□

Planar creases

In the special case where $\theta_L(t) = \theta_R(t)$, we observe that $\tau(t) = 0$, which implies that the crease curve is planar. Under these conditions, the developed rulings corresponding to the same curve parameter are collinear, as illustrated in Figure 3.11 (left).

Planar creases can be constructed without the need for patch characteristics-based computations. One can form them by bisecting a patch with a plane and subsequently reflecting one of the resulting subpatches to the opposite side. This process ensures both connectivity and developability while introducing a curved crease.

Due to their simple construction, planar creases serve as a powerful design instrument [60, 58]. The above-mentioned method can be conveniently integrated into CAD software, enabling the design of shapes with multiple planar creases. In Chapter 14, we demonstrate the construction of spirals using cones and planar creases, showcasing examples of non-trivial designs achievable with this method.

Creases of constant fold angle

Another special case occurs when $\theta_L(t) = \pi - \theta_R(t)$, that is, when the developed rulings corresponding to the same curve parameter are reflected on the developed tangent. Note that this implies $\varphi'(t) = 0$, resulting in a crease with constant fold angle; see Figure 3.11 (right).

Prominent examples of such creases include constant fold angle creases between cylinders and cones. In this case, the developed creases are conic curves, with developed rule lines that converge at the conic's focal points. Combinations of conics as creases have been explored by Huffman in his designs [19, 43]. Some combinations of conic creases are compatible under rigid-ruling folding motion [18]. Chapter 10 provides a parametrization of those creases using elliptic integrals.

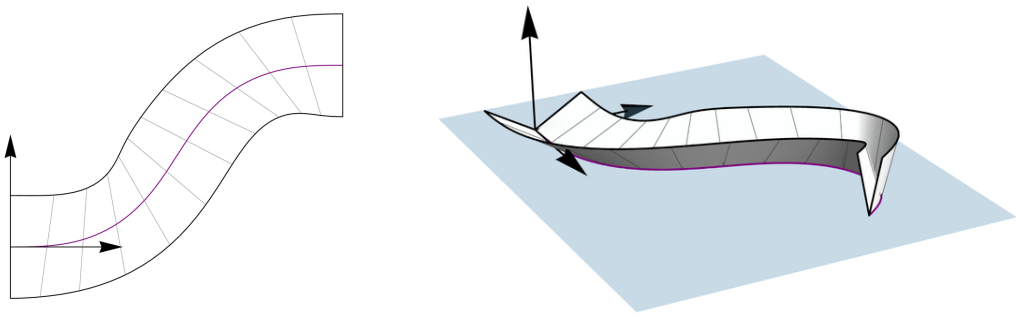

(a) A crease-rule pattern with pairwise collinear rulings ($\theta_L(t) = \theta_R(t)$) results in a planar crease.

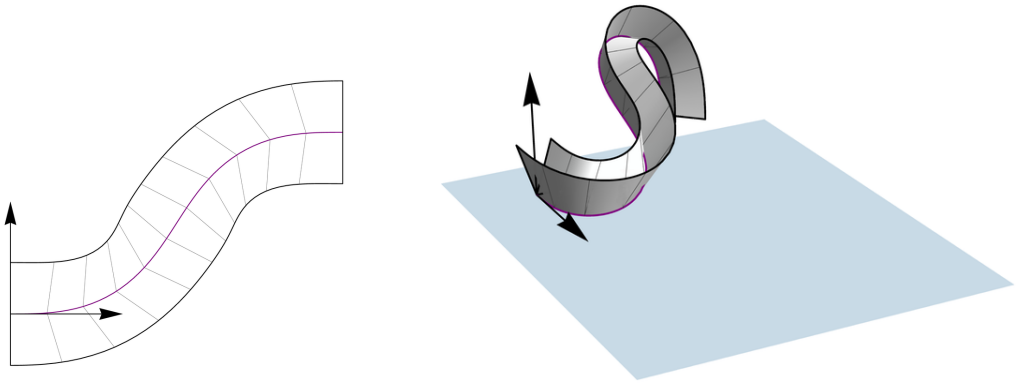

(b) A crease-rule pattern with pairwise tangent-reflected rulings ($\theta_L(t) = \pi - \theta_R(t)$) results in a crease with constant fold angle.

Figure 3.11: Illustration of the two special families of curved creases.

3.3.5 Practical Considerations

Unlike in the general case, a planar configuration always exists. This follows from Lemma 3.14 as $\varphi_0 = 0$ implies $\varphi(t) = 0$.

As noted before, $\rho(t) = \varphi_L(t) - \varphi_R(t) = 2\varphi(t)$ represents the deviation from the planar state. Consequently, $\varphi(t)$ denotes half of the fold angle $\rho(t)$.

3.4 Joining Three Patches with Partial Ruling Information

3.4.1 Notation

In what follows, we assume that we are given three patches, as depicted in Figure 3.12. The central patch is bounded on the right by $\mathbf{x}_{1L}(s)$ and on the left by $\mathbf{x}_{2R}(s)$. The right patch is bounded by $\mathbf{x}_{1R}(s)$, while the left patch is bounded by $\mathbf{x}_{2L}(s)$, as shown in Figure 3.12.

Our objective is to connect the right patch to the central patch along the curves $\mathbf{x}_{1R}(s)$ and $\mathbf{x}_{1L}(s)$. Similarly, we aim to join the central patch to the left patch along the curves $\mathbf{x}_{2R}(s)$ and $\mathbf{x}_{2L}(s)$. We assume, without loss of generality, that all four curves are parametrized by arc length. In subsequent discussions, let $k_{iL}(s)$ and $k_{iR}(s)$ represent the curvature of the curves $\mathbf{x}_{iL}(s)$ and

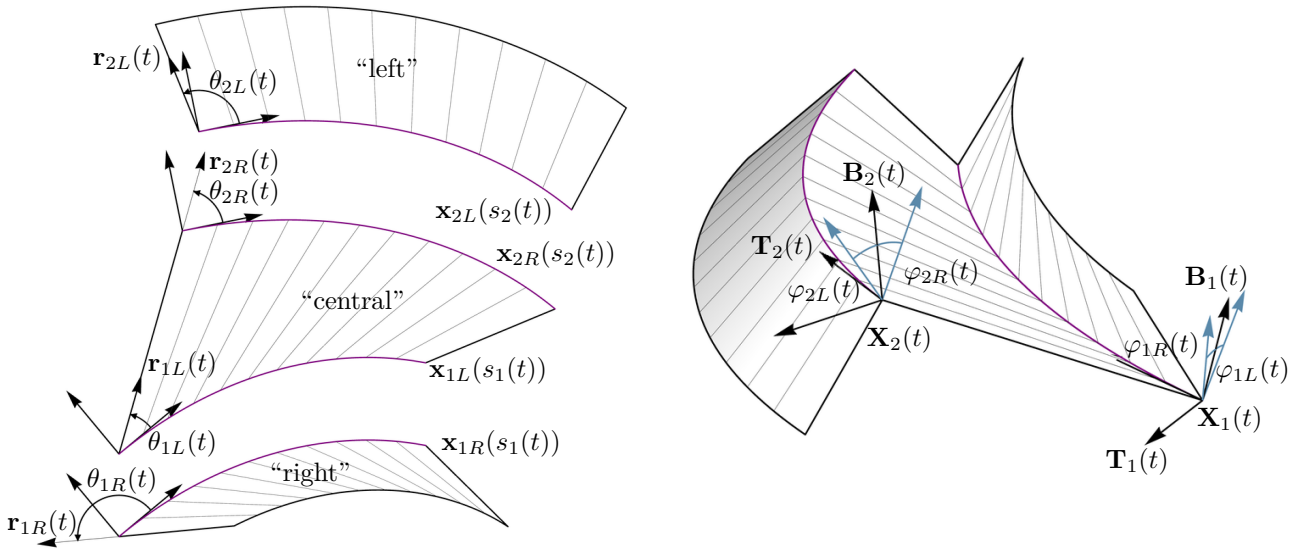

(a) Development.

(b) Glued configuration.

Figure 3.12: Illustration of the notation used for gluing three patches with partial ruling information in Section 3.4.

$\mathbf{x}_{iR}(s)$, respectively, at their arc-length parameters.

We represent the ruling directions using ruling angles. For a more streamlined notation and to ensure consistent ruling directions related to the central patch, we adopt the notation proposed by Demaine et al. [18] and use the parameter t to describe consecutive rulings. Specifically, we define two functions, $s_1(t)$ and $s_2(t)$, that encode the arc length of the curves corresponding to parameter t. Consequently, the ruling directions of the shared surface are given by

$$\mathbf{r}_{1L}(t) = \mathbf{r}_{2R}(t) = \frac{\mathbf{x}_{2R}(s_2(t)) - \mathbf{x}_{1L}(s_1(t))}{|\mathbf{x}_{2R}(s_2(t)) - \mathbf{x}_{1L}(s_1(t))|}. \tag{3.24}$$

It follows that the ruling angles of the central surface relative to either curve can be determined by the following

$$\theta_{1L}(t) = \arctan\left(\mathbf{t}_{1L}(s_1(t)) \cdot \mathbf{r}_{1L}(t), \mathbf{n}_{1L}(s_1(t)) \cdot \mathbf{r}_{1L}(t)\right). \tag{3.25}$$

$$\theta_{2R}(t) = \arctan\left(\mathbf{t}_{2R}(s_2(t)) \cdot \mathbf{r}_{2R}(t), \mathbf{n}_{2R}(s_2(t)) \cdot \mathbf{r}_{2R}(t)\right). \tag{3.26}$$

Here, $\mathbf{t}_i(t)$ represents the unit tangent, while $\mathbf{n}_i(t)$ stands for the left-normal of $\mathbf{x}_{1L}(s)$ and $\mathbf{x}_{2R}(s)$, respectively. Moreover, let $\theta_{1R}(t)$ and $\theta_{2L}(t)$ be the ruling angles incident to $\mathbf{x}_{1L}(s_1(t))$ and $\mathbf{x}_{2R}(s_2(t))$, respectively.

To describe the geometry of the two gluing curves $\mathbf{X}_1(t)$ and $\mathbf{X}_2(t)$ and the incident patches, it is left to determine their curvatures $K_1(t)$ and $K_2(t)$, torsions $\tau_1(t)$ and $\tau_2(t)$, and the inclination angles $\varphi_{1L}(t)$, $\varphi_{1R}(t)$, $\varphi_{2L}(t)$, and $\varphi_{2R}(t)$.

3.4.2 Constraints

We will now discuss the constraints required for a glued state to be valid. Specifically, we require that Equation (3.4) is satisfied for both adjacent patches of both curves. This results for $i \in \{1, 2\}$

in four equations,

$$K_i(t)\sin\varphi_{iR}(t)\cot\theta_{iR}(t) = -\tau_i(t) + \frac{\varphi'_{iR}(t)}{s'_i(t)}, \tag{3.27}$$

$$K_i(t)\sin\varphi_{iL}(t)\cot\theta_{iL}(t) = -\tau_i(t) + \frac{\varphi'_{iL}(t)}{s'_i(t)}. \tag{3.28}$$

In addition, we need to ensure that the geodesic curvatures of the surfaces match the given developed curvatures. Consequently, we require that Equation (3.6) is satisfied for both adjacent patches of both curves. This results for $i \in \{1, 2\}$ in four equations,

$$k_{iR}(s_i(t)) = K_{iR}(t)\cos\varphi_{iR}(t) \qquad \text{and} \qquad k_{iL}(s_i(t)) = K_{iL}(t)\cos\varphi_{iL}(t). \tag{3.29}$$

If all the above constraints are met, upon computational success, each pair of surfaces results in a valid glued state. However, we want to ensure that the common surface of the two pairs has the same curvature. Using Lemma 3.8, we consider the ruling curvature of the common patch with respect to the directrices $\mathbf{X}_1(t)$ and $\mathbf{X}_2(t)$, with the goal to ensure that

$$s'_1(t)K_1(t)\sin\varphi_{1L}(t)\frac{1}{\sin\theta_{1L}(t)} = s'_2(t)K_2(t)\sin\varphi_{2R}(t)\frac{1}{\sin\theta_{2R}(t)}. \tag{3.30}$$

In conclusion, the glued state is constrained by nine equations. However, the 3D shape is specified by eight functions: the curvatures $K_1(t)$ and $K_2(t)$, the torsions $\tau_1(t)$ and $\tau_2(t)$, and the inclination angles $\varphi_{1R}(t)$, $\varphi_{1L}(t)$, $\varphi_{2R}(t)$, and $\varphi_{2L}(t)$.

Thus, in general, specifying the developed patch with rulings would be overconstraining. Consequently, we introduce an additional "degree of freedom" in the development that influences the developed rulings, such as the relationship between the functions $s_1(t)$ and $s_2(t)$. For instance, we set $s_1(t) = t$ and $s_2(t) = u(t)$, and determine $u(t)$ so that all constraints are met.

In the following, we present three possible application strategies:

- Prescribe the ruling directions of the left and right patch with the goal to find the central patch's rulings. This strategy is used in the computation of a generalization of Tony Wills squaricle (Section 5.2) and David Huffman's tower (Section 5.3).
- Prescribe the type of crease curve, either planar or constant fold angle. An example where we solve for planar creases ($\theta_{iL}(t) = \theta_{iR}(t)$) is shown in Section 6.2, and an example where we consider constant angle creases ($\theta_{iL}(t) = \pi - \theta_{iR}(t)$) is shown in Section 6.3.
- Finally, we can also prescribe a general relationship between consecutive ruling polylines. An example is shown in the analysis of periodic circular creases (Section 7.2) and the attempt to analyze the circular spiral (Section 7.3).

3.4.3 Gluing: Joining Two Pairs of Curves

In this section, we outline a strategy to address the system of equations compiled in the previous section. As in earlier discussions, we work under the assumption that not both curves from a pair intended for joining exhibit vanishing curvature at the same parameter value.

Drawing parallels to Section 3.3.3, tackling this system directly might be challenging using standard mathematical software. As a result, we explore how to rephrase the nine constraints as a system of differential equations for three unknowns while expressing the remaining functions algebraically. Without loss of generality, we set $s_1(t) = t$ and discuss how to express the system in terms of only two inclination angles corresponding to different curves and the parametrization speed $s_2(t)$.

Initial values. Before determining the unknown patch characteristics, it is frequently advantageous to first establish the initial values for both the inclination angles and the curve's initial orthonormal frame. For simplicity, we typically specify these initial values at the parameter $t = 0$.

First, it is essential to establish a 2D ruling polyline. This can be achieved by setting the value of $s_2(0)$. We have encountered the following two scenarios:

- *Scenario 1:* In certain cases, such as in Section 5.2, the location of the corresponding initial 3D polyline is provided, along with appropriate tangent directions denoted by $\mathbf{T}_{1,0}$ and $\mathbf{T}_{2,0}$. In this case, it is necessary to compute the normal vectors and initial opening angles. This can be achieved by using the considerations presented in Section 3.3.3.

- *Scenario 2:* In other cases, we begin by freely specifying the initial values of the corresponding two inclination angles. However, this means that we need to determine the location of the corresponding initial 3D polyline and the initial orthonormal frames. It is important to note that specifying two inclination angles (corresponding to different curves) determines the other two inclination angles up to their sign. In this case, the location of the first orthonormal frame can be chosen freely, such as $\mathbf{X}_{1,0} = (0,0,0)$ and $\mathbf{T}_{1,0} = (1,0,0)$, $\mathbf{N}_{1,0} = (0,1,0)$, and $\mathbf{B}_{1,0} = (0,0,1)$. Let $\mathbf{P}_{1L,0} = \cos\varphi_{1L,0}\ \mathbf{B}_{1,0} + \sin\varphi_{1L,0}\ \mathbf{N}_{1,0}$ denote the initial normal vector of the left tangent plane. Then, the initial tangent direction of the second frame can be computed as $\mathbf{T}_{2,0} = R \cdot \mathbf{T}_{1,0}$ where R denotes the matrix that corresponds to a rotation by $\theta_{1L}(0) - \theta_{2R}(0)$ around $\mathbf{P}_{1L,0}$. Moreover, $\mathbf{B}_{2,0} = R' \cdot \mathbf{P}_{1L}(0)$ where R' is the matrix corresponding to a rotation by $-\varphi_{2R,0}$ around $\mathbf{T}_{2,0}$. Consequently, $\mathbf{N}_{2,0} = \mathbf{B}_{2,0} \times \mathbf{T}_{2,0}$. The initial point of the second curve can be obtained by

$$\mathbf{X}_{2,0} = \mathbf{X}_{1,0} + |\mathbf{x}_1(s_1(0)) - \mathbf{x}_2(s_2(0))|\,\mathbf{R}_{1L,0}$$

where $\mathbf{R}_{1L,0} = \cos\theta_{1L}(0)\ \mathbf{T}_{1,0} + \sin\theta_{1L}(0)\ (\mathbf{P}_{1L,0} \times \mathbf{T}_{1,0})$ is the initial ruling direction of the left patch incident to the first curve.

Simplification of the system. To simplify the system of equations, we follow the computations presented in Section 3.3.3. Under consideration of vanishing curvature functions as discussed in Section 3.3.3, we set either $A_i = L$ and $B_i = R$ or the other way round. Similar to before, for the subsequent simplifications, we require that $k_{iA_i}(t)$ and $k_{iB_i}(t)$ be C^1.

First, we solve Equation (3.27) and Equation (3.28) (with $i \in \{1,2\}$) for $K_i(t)$ and $\tau_i(t)$, resulting in

$$K_i(t) = \frac{\varphi'_{iA_i}(t) - \varphi'_{iB_i}(t)}{s'_i(t)\,(\cot\theta_{iA_i}(t)\sin\varphi_{iA_i}(t) - \cot\theta_{iB_i}(t)\sin\varphi_{iB_i}(t))} \tag{3.31}$$

$$\tau_i(t) = -\frac{\varphi'_{iA_i}(t)\cot\theta_{iB_i}(t)\sin\varphi_{iB_i}(t) - \varphi'_{iB_i}(t)\cot\theta_{iA_i}(t)\sin\varphi_{iA_i}(t)}{s'_i(t)\,(\cot\theta_{iA_i}(t)\sin\varphi_{iA_i}(t) - \cot\theta_{iB_i}(t)\sin\varphi_{iB_i}(t))}. \tag{3.32}$$

Next, similar to the gluing case, it follows from Equation (3.29) that

$$\cos\varphi_{iA_i}(t) = \frac{k_{iA_i}(s_i(t))}{k_{iB_i}(s_i(t))}\cos\varphi_{iB_i}(t).$$

Depending on the initial values of the inclination angles, we then choose $\sigma_i \in \{-1,1\}$ appropriately, resulting in

$$\varphi_{iA_i}(t) = \sigma_i \arccos\left(\frac{k_{iA_i}(s_i(t))}{k_{iB_i}(s_i(t))}\cos\varphi_{iB_i}(t)\right). \tag{3.33}$$

The corresponding derivative of the inclination function reads

$$\varphi'_{iA_i}(t) = \sigma_i \frac{(k_{iB_i}(s_i(t))k_{iA_i}(s_i(t)))' \cos\varphi_{iB_i}(t) + k_{iA_i}(s_i(t))k_{iB_i}(s_i(t))\varphi'_{iB_i}(t)\sin\varphi_{iB_i}(t) +}{\sqrt{1 - \frac{k_{iA_i}(s_i(t))^2}{k_{iB_i}(s_i(t))^2}\cos^2\varphi_{iB_i}(t)}k_{iB_i}(s_i(t))^2}. \quad (3.34)$$

Note that the only unknown functions occurring in the above two Equations are $\varphi_{iB_i}(t)$, the parametrization speeds, and their derivatives. Consequently, replacing $K_i(t)$ (Equation (3.31)), $\varphi_{iA_i}(t)$ (Equation (3.33)), and $\varphi'_{iA_i}(t)$ (Equation (3.34)) in Equations

$$k_{1B}(s_1(t)) = K_{1B_1}(t)\cos\varphi_{1B_1}(t) \qquad \text{and} \qquad k_{2B}(s_2(t)) = K_{2B_2}(t)\cos\varphi_{2B_2}(t)$$

and Equation (3.30) results in three equations that depend only on $\varphi_{iB_i}(t)$, $\varphi'_{iB_i}(t)$, and the parametrization speeds. Assuming $s_1(t) = t$ and $s_2(t) = u(t)$, the three equations have only three unknowns, possibly allowing to solve for $\varphi_{1B_1}(t)$, $\varphi_{2B_2}(t)$ and $u(t)$.

However, note that the system might not be explicit, that is, we might not be able to solve for the unknown derivatives. This is because the $u'(t) = s'_2(t)$ appears in both Equation (3.30) and the expression for $\varphi'_{2A_2}(t)$ in Equation (3.34).

Computation of the gluing curves and construction of surfaces. Upon successful computation of $\varphi_{1B_1}(t)$, $\varphi_{2B_2}(t)$, and $u(t)$ using appropriate initial values, the remaining inclination angles are given by Equation (3.33). The expressions for curvatures and torsions are as follows

$$K_i(t) = \frac{k_{iB_i}(t)}{\cos\varphi_{iB_i}(t)}, \qquad \tau_i(t) = \frac{\varphi'_{iB_i}(t)}{s'_i(t)} - k_{iB_i}(t)\cot\theta_{iB_i}(t)\tan\varphi_{iB_i}(t). \quad (3.35)$$

Subsequently, the Frenet-Serret equations, as presented in Equation (3.1), need to be integrated using the previously determined initial orthonormal frames along with appropriate starting points for the curves. Upon completion, we obtain the two gluing curves, $\mathbf{X}_1(t)$ and $\mathbf{X}_2(t)$.

Lastly, we construct the surfaces. The central surface is derived by lofting between $\mathbf{X}_1(t)$ and $\mathbf{X}_2(t)$. The ruling directions for the left and right surfaces can be determined using Equation (3.3). Specifically,

$$\mathbf{R}_{1R}(t) = \cos\theta_{1R}(t)\ \mathbf{T}_1(t) + \sin\theta_{1R}(t)\left(\cos\varphi_{1R}(t)\ \mathbf{N}_1(t) - \sin\varphi_{1R}(t)\ \mathbf{B}_1(t)\right),$$
$$\mathbf{R}_{2L}(t) = \cos\theta_{2L}(t)\ \mathbf{T}_2(t) + \sin\theta_{2L}(t)\left(\cos\varphi_{2L}(t)\ \mathbf{N}_2(t) - \sin\varphi_{2L}(t)\ \mathbf{B}_2(t)\right).$$

3.4.4 Creasing: Joining two Pairs of Matching Curves

We now discuss the special case where both curves match, allowing further simplifications of the equations. In this case, we denote the common curvatures by $k_i(t) = k_{iL}(t) = k_{iR}(t)$. In this case, however, it is sufficient for $k_i(t)$ to be C^0. Unlike the case of gluing, we assume that neither crease curve is straight, that is, $k_1(t) \neq 0$ and $k_2(t) \neq 0$.

As discussed in Section 3.3.4, the interesting curved-crease case occurs when $\varphi_i(t) = \varphi_{iL}(t) = -\varphi_{iR}(t)$. Consequently, the folded state is specified by $K_1(t)$, $K_2(t)$, $\tau_1(t)$ and $\tau_2(t)$, and the two inclination angles $\varphi_1(t)$ and $\varphi_2(t)$.

The computation of consistent initial values of the directrix and the frame is analogous to the gluing case.

Simplification of the system. The stated assumptions simplify the constraints discussed in Section 3.4.2. Specifically, the developability conditions (Equation (3.27) and Equation (3.28)) simplify to

$$K_i(t)\sin\varphi_i(t)\cot\theta_{iR}(t) = \tau_i(t) + \frac{\varphi_i'(t)}{s_i'(t)} \tag{3.36}$$

$$K_i(t)\sin\varphi_i(t)\cot\theta_{iL}(t) = -\tau_i(t) + \frac{\varphi_i'(t)}{s_i'(t)}, \tag{3.37}$$

the curvature constraints (Equation (3.29)) become

$$k_i(s_i(t)) = K_i(t)\cos\varphi_i(t),$$

and the compatibility constraint (Equation (3.30)) simplify to

$$s_1'(t)K_1(t)\sin\varphi_1(t)\frac{1}{\sin\theta_{1L}(t)} = -s_2'(t)K_2(t)\sin\varphi_2(t)\frac{1}{\sin\theta_{2R}(t)}. \tag{3.38}$$

Assuming that $s_1(t)$ is given (for example, $s_1(t) = t$), the seven stated equations allow solving for $\varphi_1'(t)$, $\varphi_2'(t)$, $s_2'(t)$, $K_1(t)$, $K_2(t)$, $\tau_1(t)$, and $\tau_2(t)$, resulting in the three differential equations

$$\begin{aligned}
s_2'(t) &= -s_1'(t)\frac{k_1(s_1(t))}{k_2(s_2(t))}\frac{\sin\theta_{2R}(t)}{\sin\theta_{1L}(t)}\frac{\tan\varphi_1(t)}{\tan\varphi_2(t)} \\
\varphi_1'(t) &= \frac{1}{2}s_1'(t)k_1(s_1(t))\left(\cot\theta_{1L}(t) + \cot\theta_{1R}(t)\right)\tan\varphi_1(t) \\
\varphi_2'(t) &= -\frac{1}{2}s_1'(t)k_1(s_1(t))\frac{\sin\left(\theta_{2L}(t)+\theta_{2R}(t)\right)}{\sin\theta_{1L}(t)\sin\theta_{2L}(t)}\tan\varphi_1(t).
\end{aligned} \tag{3.39}$$

and the four algebraic expressions

$$K_i(t) = \frac{k_i(s_i(t))}{\cos\varphi_i(t)} \qquad \text{and} \qquad \tau_i(t) = -\frac{1}{2}\left(\cot\theta_{iL}(t) - \cot\theta_{iR}(t)\right)k_i(s_i(t))\tan\varphi_i(t). \tag{3.40}$$

For reasonable input, the explicit system of differential equations in Equation (3.39) may be locally solved using initial values for $s_2(t)$, and the two inclination angles.

Computation of the gluing curves and construction of surfaces. Upon successful computation of the inclination angles and parametrization speed using Equation (3.39), we compute the curvatures and torsions from Equation (3.40).

Similarly to the previous section, it remains to integrate the Frenet-Serret equations (Equation (3.1)) for the previously computed initial orthonormal frame and the appropriate starting point of the curves to obtain the two gluing curves $\mathbf{X}_1(t)$ and $\mathbf{X}_2(t)$.

Finally, we construct the surfaces. Again, the central surface can be obtained by lofting between $\mathbf{X}_1(t)$ and $\mathbf{X}_2(t)$. The left and right surfaces' ruling directions follow from Equation (3.3), that is,

$$\mathbf{R}_{1R}(t) = \cos\theta_{1R}(t)\ \mathbf{T}_1(t) + \sin\theta_{1R}(t)\left(\cos\varphi_1(t)\ \mathbf{N}_1(t) + \sin\varphi_1(t)\ \mathbf{B}_1(t)\right), \tag{3.41}$$

$$\mathbf{R}_{2L}(t) = \cos\theta_{2L}(t)\ \mathbf{T}_2(t) + \sin\theta_{2L}(t)\left(\cos\varphi_2(t)\ \mathbf{N}_2(t) - \sin\varphi_2(t)\ \mathbf{B}_2(t)\right). \tag{3.42}$$

Next, we discuss how the system of differential equations in Equation (3.39) simplifies in two special cases: the combination of two planar creases and the combination of two creases with a constant fold angle.

Combination of two planar creases

When joining two planar creases, we have that $\theta_{iR}(t) = \theta_{iL}(t)$. Consequently,

$$s_2'(t) = -s_1'(t)\frac{k_1(s_1(t))}{k_2(s_2(t))}\frac{\sin\theta_{2L}(t)}{\sin\theta_{1L}(t)}\frac{\tan\varphi_1(t)}{\tan\varphi_2(t)} \tag{3.43}$$

$$\varphi_1'(t) = s_1'(t)k_1(s_1(t))\frac{1}{\tan\theta_{1L}(t)}\tan\varphi_1(t) \tag{3.44}$$

$$\varphi_2'(t) = -s_1'(t)k_1(s_1(t))\frac{\cos\theta_{2L}(t)}{\sin\theta_{1L}(t)}\tan\varphi_1(t)$$

In particular, it follows that

$$\frac{\varphi_1'(t)}{\varphi_2'(t)} = -\frac{\cos\theta_{1L}(t)}{\sin\theta_{2L}(t)}.$$

Note that this system is trivially satisfied for tangent parallel curves when $\varphi_1(t) = -\varphi_2(t)$. In this scenario, as discussed in Section 3.2.5, we have that $\theta_{1L}(t) = \theta_{2L}(t)$ and $s_1'(t)k_1(s_1(t)) = s_2'(t)k_2(s_2(t))$, and the two creases lie in parallel planes.

An example of a computation of the rulings connecting two planar creases can be found in Section 6.2.

Combination of two creases of constant fold angle

When joining two creases of constant fold angle, we have that $\theta_{iR}(t) = \pi - \theta_{iL}(t)$. Consequently, the last two equations in Equation (3.39) simplify to $\varphi_1'(t) = 0$ and $\varphi_2'(t) = 0$. Additionally, it follows that

$$s_2'(t) = -s_1'(t)\frac{k_1(s_1(t))}{k_2(s_2(t))}\frac{\sin\theta_{2L}(t)}{\sin\theta_{1L}(t)}\frac{\tan\varphi_{1,0}}{\tan\varphi_{2,0}} \tag{3.45}$$

where $\varphi_i(t) = \varphi_{i,0}$.

The above equation indicates that for appropriate initial values, we may obtain a rigid-ruling folding, as shown by Demaine et al. [18] (Theorem 2). Specifically, when we choose $s_2(0) = c_1$ and $\varphi_{2,0} = -\arctan(c_2\tan\varphi_{1,0})$ for some appropriate constants c_1 and c_2, a solution $s_2(t)$ corresponds multiple initial values, resulting in the same ruling layout for initial values where $c_2 = \frac{\tan\varphi_{2,0}}{\tan\varphi_{1,0}}$. Note that as $\varphi_{1,0}$ and $\varphi_{2,0}$ approach $\pm\frac{\pi}{2}$, $K_i(t)$ and $\tau_i(t)$ tend towards infinity, corresponding to a "smooth flat-folded state".

An example of a computation of the rulings connecting two constant fold angle creases is discussed in Section 6.3.

3.4.5 Towards Joining More Surfaces

Considerations similar to those discussed above can be extended to three or more glue or crease curves. However, the gluing scenario becomes increasingly computationally challenging, causing the generalization to be more relevant for the curved-crease case. It is important to note that the number of compatibility conditions can often conflict with the idea of closing a loop. If the geometry is not suitable, imposing a closure constraint is not supported.

Furthermore, we conjecture that there might be specific shapes, like D-forms, where rulings might spiral around the structure. Consequently, the computations we have presented might not directly apply to such cases. Investigating these unique shapes and formulating a computational method for their reconstruction remains a subject for future research.

3.5 Gluing Patches along Curves on Patches

In this section, we explore two approaches for gluing patches to a series of either glued or creased surfaces:

- *Gluing a patch with unspecified rulings to a curve on a patch:* The first method is based on attaching a patch with unspecified rulings to a space curve discussed in Section 3.5.1. It allows to specify the crease or glue curve and the corresponding 2D curvature. In this section, however, we tailor the computations specifically to patch characteristics. Through this approach, we identify two potential configurations for the appended surface and determine the ruling angles for each.
- *Gluing along a tangent-parallel curve on a patch:* The second method uses tangent-parallel curves discussed in Section 3.2.5. We demonstrate that it is possible to append a patch along a tangent parallel curve, with its rulings parallel to the penultimate patch. In a way, this method is dual to the previous one: while it calculates the gluing curve, it operates with predetermined ruling directions. This approach is noteworthy, as it enables the creation of patch combinations that allow a rigid-ruling folding motion.

In the following, we assume that we start with a gluing of two developed ruled patches and consider adding patches to the left side of the glue curve. However, adding patches to the right side works in a similar manner.

3.5.1 Gluing a Patch with Unspecified Rulings to a Curve on a Patch

In this case, the computations can be isolated to only quantities corresponding to the patch to which the new patch is appended. Consequently, we assume that we are given a patch by its characteristics $K_1(t)$, $\tau_1(t)$, $s_1(t)$, $\varphi_1(t)$ and $\theta_{1L}(t)$. Let $\mathbf{X}_1(t)$ denote the corresponding curve and $\mathbf{R}_{1L}(t)$ the corresponding ruling direction. We now discuss how to append a patch with unspecified rulings and developed curvature $k_{2R}(t)$ along the curve $\mathbf{X}_2(t) = \mathbf{X}_1(t) + l(t)\mathbf{R}_{1L}(t)$.

In Section 3.5.1, we described a method for attaching a curve to a space curve. However, this method necessitates the knowledge of both the curvature (including its sign) and the torsion of the space curve $\mathbf{X}_2(t)$. At parameters where $\mathbf{X}_2'(t)$ and $\mathbf{X}_2''(t)$ are linearly independent, we can derive the absolute value of the curvature and the torsion from the parametrization of $\mathbf{X}_2(t)$ using

$$K_2(t) = \frac{|\mathbf{X}_2'(t) \times \mathbf{X}_2''(t)|}{|\mathbf{X}_2'(t)|^3} \qquad \text{and} \qquad \tau_2(t) = \frac{(\mathbf{X}_2'(t) \times \mathbf{X}_2''(t)) \cdot \mathbf{X}_2'''(t)}{|\mathbf{X}_2'(t) \times \mathbf{X}_2''(t)|}.$$

However, special consideration is required for the sign of $K_2(t)$ and parameter values with vanishing curvature or undefined torsion.

To avoid a cumbersome case-analysis, we combine both 3D and 2D information and use the ruling curvature of the shared patch to compute the appropriate (signed) curvature $K_2(t)$ and torsion $\tau_2(t)$.

First, let $\mathbf{x}_1(t)$ and $\mathbf{r}_{1L}(t)$ denote the developed curve and ruling directions corresponding to $\mathbf{X}_1(t)$ and $\mathbf{R}_{1L}(t)$, and set $\mathbf{x}_2(t) = \mathbf{x}_1(t) + l(t)\mathbf{r}_{1L}(t)$. Let $s_2'(t)$ be the shared parametrization speed of $\mathbf{X}_2(t)$ and $\mathbf{x}_2(t)$. Furthermore, denote the tangent and left-side normal of $\mathbf{x}_2(t)$ by $\mathbf{t}_2(t)$ and $\mathbf{n}_2(t)$, respectively, and let $k_2(t)$ be the (signed) curvature.

First, we compute the ruling angle corresponding to the right patch of the second curve as

$$\theta_{2R}(t) = \arctan\left(\mathbf{r}_{1L}(t) \cdot \mathbf{t}_2(t), \mathbf{r}_{1L}(t) \cdot \mathbf{n}_2(t)\right).$$

Since the ruling curvature (Equation (3.12)) of the considered patch with respect to either curve must be same, we obtain an expression for the inclination angle of the common patch with respect to the frame of the second curve,

$$\varphi_{2R}(t) = \arctan\left(\frac{s_1'(t)\sin\theta_{2R}(t)}{s_2'(t)k_{2R}(t)\sin\theta_{1L}(t)}K_1(t)\sin\varphi_{1L}(t)\right) \tag{3.46}$$

It is important to note that the range of arctan is only $(-\frac{\pi}{2}, \frac{\pi}{2})$. At values where $k_{2R}(t) = 0$, special considerations are required to ensure the continuity of $\varphi_{2R}(t)$.

Upon successful computation of $\varphi_{2R}(t)$, the curvature and torsion read

$$K_2(t) = \frac{k_{2R}(t)}{\cos\varphi_{2R}(t)} \qquad \text{and} \qquad \tau_2(t) = -\frac{\varphi_2'(t)}{s_2'(t)} + \frac{1}{\cot\theta_{2R}(t)}k_{2R}(t)\tan\varphi_{2R}(t).$$

In addition, we obtain the other inclination angle as

$$\varphi_{2L}(t) = \pm\arccos\left(\frac{k_{2L}(t)}{k_{2R}(t)}\cos\varphi_{2R}(t)\right).$$

Finally, the other ruling angle is specified by the developability condition (Equation (3.4)) as

$$\theta_{2L}(t) = -\operatorname{arccot}\left(\cot\theta_{2R}(t) - \frac{2}{k_2(t)}\frac{\varphi_{2L}'(t)}{s_2'(t)}\cot\varphi_{2L}(t)\right) \pmod{\pi}. \tag{3.47}$$

This concludes the computations of the patch characteristics ($K_2(t)$, $\tau_2(t)$, $s_2'(t)$, $\varphi_{2L}(t)$, $\theta_{2L}(t)$) necessary to define the next patch.

To construct the next ruling direction $\mathbf{R}_{2L}(t)$, there are at least two possibilities:

- *Option 1:* One approach is to integrate the Frenet-Serret Equations with appropriate initial values to obtain the frame $(\mathbf{T}_2(t), \mathbf{N}_2(t), \mathbf{B}_2(t))$. Additionally, set $\mathbf{P}_{2R}(t) = \cos\varphi_2(t)\ \mathbf{B}_2(t) - \sin\varphi_2(t)\ \mathbf{N}_2(t)$.
- *Option 2:* Alternatively, we start with the left tangent plane normal of the first curve, $\mathbf{P}_{1L}(t) = \cos\varphi_{1L}(t)\ \mathbf{B}_1(t) + \sin\varphi_{1L}(t)\ \mathbf{N}_1(t)$, and compute the tangent plane normal of the appended patch, $\mathbf{P}_{2L}(t)$, by rotating $\mathbf{P}_{1L}(t)$ by $\varphi_{2R}(t) - \varphi_{2L}(t)$ about $\mathbf{X}_2'(t)$. Let $\mathbf{T}_2(t) = \frac{1}{s_2'(t)}\mathbf{X}_2'(t)$ denote the tangent of $\mathbf{X}_2(t)$.

In either case, the next next ruling direction is computed as

$$\mathbf{R}_{2L}(t) = \cos\theta_{2L}(t)\ \mathbf{T}_2(t) + \sin\theta_{2L}(t)\ \left(\mathbf{P}_{2R}(t) \times \mathbf{T}_2(t)\right).$$

While it has not been explicitly mentioned, the computations discussed can also be applied to append a curved crease. In this case, the computed expressions allow further simplifications.

3.5.2 Gluing Along a Tangent-Parallel Curve on a Patch

We have seen that in general, the ruling angles of the next surface depend on the ruling curvature of the previous surface. Thus, if the folded state of the initial patch is modified, the rulings of the appended patch usually need to adapt in response to these changes. In the following subsection, we show a special case that permits rigid-ruling folding motions for compositions of patches.

We consider a gluing curve $\mathbf{X}_1(t)$ of two planar patches $\mathbf{s}_{1L}(t) = \mathbf{x}_1(t) + u\mathbf{r}_L(t)$ and $\mathbf{s}_{1R}(t) = \mathbf{x}_1(t) - u\mathbf{r}_R(t)$, where $\mathbf{x}_{1L}(t)$ and $\mathbf{x}_{1R}(t)$ share the same parametrization speed $s_1'(t)$. Let $\mathbf{R}_L(t)$ and $\mathbf{R}_R(t)$ denote the (left-side) ruling vectors of the left and right patch, respectively, specified by the ruling angles $\theta_L(t)$ and $\theta_R(t)$, and inclination angles $\varphi_L(t)$ and $\varphi_R(t)$. Furthermore, let $k_{1L}(t)$ and $k_{1R}(t)$ denote the developed curvature of $\mathbf{x}_{1L}(t)$ and $\mathbf{x}_{1R}(t)$, respectively.

Lemma 3.15. *Let $\mathbf{X}_2(t) = \mathbf{X}_1(t) + p_L(t)\mathbf{R}_L(t)$ be a tangent parallel curve of $\mathbf{X}_1(t)$, that is, $p_L(t)$ is a solution to the initial value problem stated in Lemma 3.3,*

$$\frac{p_L'(t)}{p_L(t)} = -\cot\theta_{1L}(t)\left(\theta_{1L}'(t) + s_1'(t)k_{1L}(t)\right) \qquad \text{and} \qquad p_L(0) = p_{L,0}. \tag{3.48}$$

Then, $\mathbf{S}_{2L}(t,u) = \mathbf{X}_2(t) + u\mathbf{R}_R(t)$ is a developable patch. If $\mathbf{X}_1(t)$ is a curved crease, then $\mathbf{X}_2(t)$ is a curved crease connecting $\mathbf{S}_{2L}(t,u)$ and $\mathbf{S}_{2R}(t,u) = \mathbf{X}_2(t) - u\mathbf{R}_L(t)$.

Proof. In the following, let $K_i(t)$, $\tau_i(t)$, and $s_i(t)$ denote the curvature, torsion, and parametrization speed of the curves $\mathbf{X}_i(t)$. By Lemma 3.5, the curvature and torsion of $\mathbf{X}_2(t)$ are

$$K_2(t) = \frac{s_1'(t)}{s_2'(t)}K_1(t) \qquad \text{and} \qquad \tau_2(t) = \frac{s_1'(t)}{s_2'(t)}\tau_1(t).$$

Furthermore, the curvature of the curve $\mathbf{X}_2(t)$ with respect to $\mathbf{S}_{1L}(t,u)$ reads

$$k_{2R}(t) = \frac{s_1'(t)}{s_2'(t)}k_{1L}(t).$$

To verify the stated claim, we need to confirm the developability condition stated in Equation (3.4) for the appended patch. Before doing that, let us explore some similarities between the surfaces.

First, it is important to note that the tangents of $\mathbf{X}_1(t)$ and $\mathbf{X}_2(t)$ are parallel, resulting in the same angles between $\mathbf{R}_R(t)$ and the tangents of $\mathbf{X}_1(t)$ and $\mathbf{X}_2(t)$, namely $\theta_R(t)$. Since the frames of both curves are parallel (see proof of Lemma 3.5), the inclination angles of the tangent planes $\mathbf{P}_{1R}(t)$ and $\mathbf{P}_{2R}(t)$ and the frame of either curve are the same, namely $\varphi_R(t)$.

Using Equation (3.4), we finally confirm that the parametrization of $\mathbf{S}_{2R}(t,u)$ is developable,

$$-\frac{\tau_2(t) - \frac{\varphi_R'(t)}{s_2'(t)}}{K_2(t)\sin\varphi_R(t)} = -\frac{\frac{s_1'(t)}{s_2'(t)}\tau_1(t) - \frac{\varphi_R'(t)}{s_2'(t)}}{\frac{s_1'(t)}{s_2'(t)}K_1(t)\sin\varphi_R(t)} = -\frac{\tau_1(t) - \frac{\varphi_R'(t)}{s_1'(t)}}{K_1(t)\sin\varphi_R(t)} = \cot\theta_R(t).$$

Since $\cos\varphi_R(t) = \frac{k_{1R}(t)}{K_1(t)}$, we obtain the developed curvature $k_{2R}(t)$ of $\mathbf{X}_2(t)$ with respect to surface $\mathbf{S}_{2R}(t,u)$, as

$$k_{2R}(t) = K_2(t)\cos\varphi_R(t) = \frac{s_1'(t)}{s_2'(t)}K_1(t)\frac{k_{1R}(t)}{K_1(t)} = \frac{s_1'(t)}{s_2'(t)}k_{1R}(t). \tag{3.49}$$

Although each strip is bounded by two tangent-parallel curves, the strips corresponding to the same ruling directions will not necessarily be part of the same developed surface. Nevertheless, if we start with a curved crease, that is $k_{1L}(t) = k_{1R}(t)$, the above construction will result in tangent-parallel patches connected by curved creases, since

$$k_{2L}(t) = \frac{s_1'(t)}{s_2'(t)}k_{1L}(t) = \frac{s_1'(t)}{s_2'(t)}k_{1R}(t) = k_{2R}(t).$$

□

As discussed in Section 3.3, varying the initial opening angle between the glued patches while keeping the rulings rigid results in a 1-DOF mechanism of the two glued patches. Note that tangent parallel curves and ruling directions only depend on the developed state which remains rigid throughout this motion. As Lemma 3.15 holds for all configurations, we conclude:

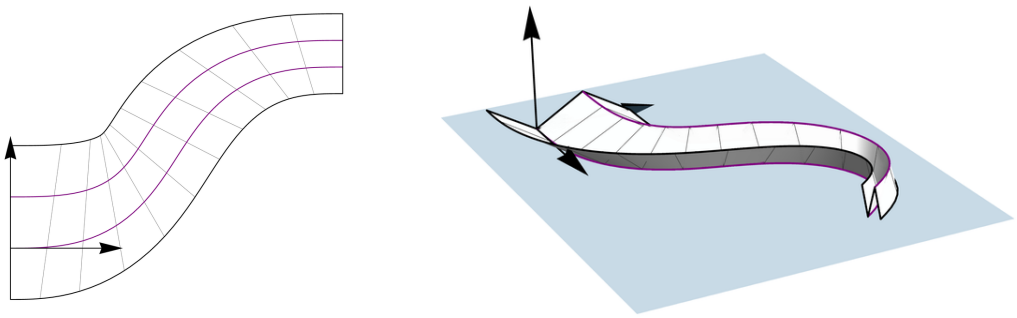

(a) Two tangent-parallel planar creases.

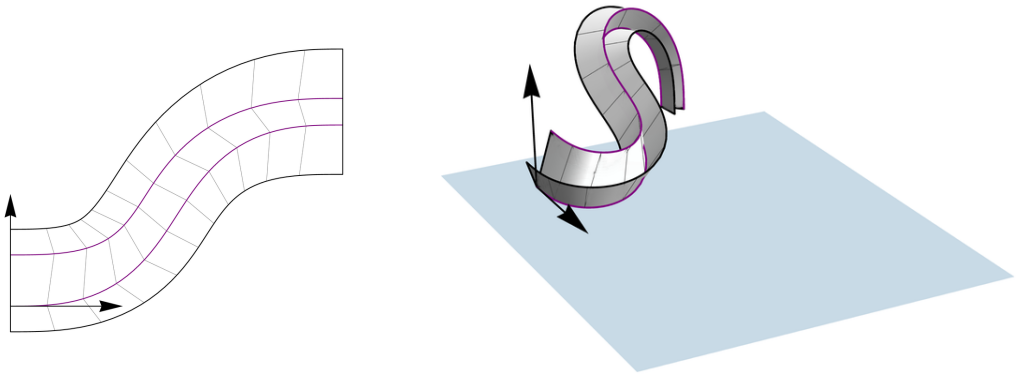

(b) Two tangent-parallel creases of constant fold angle.

Figure 3.13: Illustration of two rigidly-foldable crease-rule patterns with tangent-parallel crease curves.

Corollary 3.2. *The composition of patches described in Lemma 3.15 allows a rigid-ruling folding motion.*

Adding parallel creases to the resulting shapes introduces additional creases of the same type; see Figure 3.13. For combinations of two constant-angle creases (see Section 3.4.4), this is especially intriguing, as it enables the construction of crease rule patterns that fold with rigid rulings, even when some creases are not tangent-parallel.

3.5.3 Practical Considerations

By employing the discussed methods iteratively, one can construct intricate shapes with multiple glue or crease curves. In the case of tangent-parallel curves, this composition even allows a rigid-ruling bending motion. Chapter 4 demonstrates the application of the presented methods to add creases to shapes resulting from folds along an ellipse. However, as this construction does not directly influence the position of the edge of regression, the geometry of the shape constrains the number of times a subsequent patch can be added.

Chapter 4

Gluing and Creasing Ellipses

The content of this chapter is unpublished and is based on discussions with Erik Demaine and Tomohiro Tachi.

Overview

This chapter centers around the analytic reconstructions of two families of shapes: Anti D-forms and variations of the Bauhaus model with pleated ellipses. Both shapes result from either gluing or creasing elliptical curves into a closed space curve. We use a computational approach of prescribing the rulings of two adjacent patches and subsequently determining a folded state that results in a numerically closed shape.

4.1 Introduction

In this chapter, we provide two examples of the proposed theory from Chapter 3 applied to gluing or creasing ellipses.

In the first example, discussed in Section 4.2, we consider shapes inspired by Anti D-forms, which are shapes introduced by Tony Wills and John Sharp [108, 86, 87]. Here, two sheets with two holes with the same perimeter are glued along their boundaries. We examine the special case where the holes are congruent ellipses. Moreover, we glue the two elliptical holes in a manner such that one ellipse is a rotated version of the other by $\frac{\pi}{2}$.

The second example, discussed in Section 4.3, explores variations of the Bauhaus model, a shape obtained by folding paper along concentric circles using alternating mountain-valley assignments. We explore variations featuring at least one elliptical crease. The first example demonstrates scaled elliptical creases, while the other showcases pleats that are tangent parallel to an ellipse on a patch with periodic rulings.

At a high level, we compute the studied shapes by firstly determining the glued or folded state of the first curve, and then appending surfaces in the second step. For the computation of the proposed shapes, there exist at least two possible strategies:

- *Approach 1:* The first strategy involves specifying a space curve and using Section 3.2.8 to attach the surfaces. For this approach to be feasible, both developed curvatures must meet certain constraints, which is challenging to achieve. Furthermore, the resulting rulings might be undesirable since singularities could be positioned closely to the specified 3D curve. Ensuring the attached surfaces close properly also demands special attention.

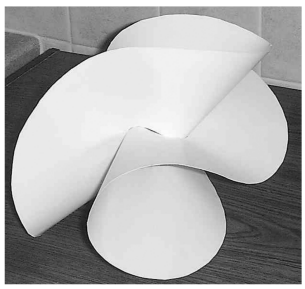

(a) Anti D-form
(Tony Wills, 2006)
Figure 6 in Wills [108].

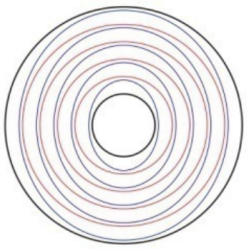

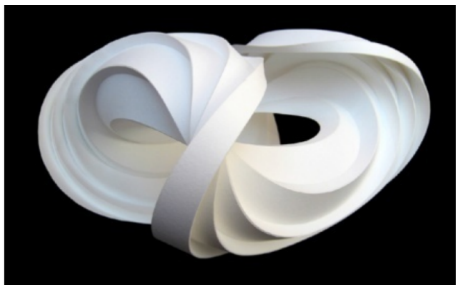

(b) Variations of Bauhaus model with ellipses and circles
(Duks Koschitz, 2015).
Parts of Figure 3 in Demaine et al. [15].

Figure 4.1: Shapes that inspired the content of Chapter 4.

- *Approach 2:* As an alternative, one might begin solely with 2D information. This involves estimating appropriate ruling directions of two neighboring patches and then examining rigid-ruling folding motions of the connected patches. When ruling angles are chosen appropriately, the curves might close for appropriate initial inclination angles and result in tangent-continuous surfaces.

In the following two examples, we follow Approach 2 to obtain a folded state of the first pair of patches. In the second set of considered examples, we subsequently append further creases as discussed in Section 3.5 or Section 3.5.2.

4.2 Joining two Ellipses to an Anti D-Form

Anti D-forms were introduced by Tony Wills and John Sharp [108, 86]. They are closely related to D-forms, that is, shapes that result from gluing two regions with equal perimeter along their boundaries. Examples of D-forms will be discussed in greater detail in Section 5.2 and Chapter 9.

The shape of a D-form, especially the unique convex realization, is generally not trivial to compute, as the gluing curve's points need to satisfy intrinsic distance constraints. This is not the case for Anti D-forms, allowing for flexibility in the shape that is constrained by the closure requirement only.

In this section, we study the gluing of two elliptical holes, where one ellipse is rotated by $\frac{\pi}{2}$ with respect to the other. Given that the glued shape is not fully determined by the closure constraint, there are many possible glued states. In the following, we devise a family of ruling angle combinations that result in numerically closed shapes. We believe that the proposed ruling family is only one of many feasible rulings.

4.2.1 Computation

Parametrization of the development

In this section, we consider a gluing of the following two elliptical curves, related by a rotation by $\frac{\pi}{2}$. To ensure that we combine a left and a right surface patch, we assume that the "left" patch is specified by a clockwise parametrized ellipse, and that the "right" patch is specified by a counterclockwise parametrized ellipse, that is,

$$\tilde{\mathbf{x}}_L(t) = (a\cos(-t), \sin(-t)) \qquad \text{and} \qquad \tilde{\mathbf{x}}_R(t) = (\sin t, a\cos t)\,,$$

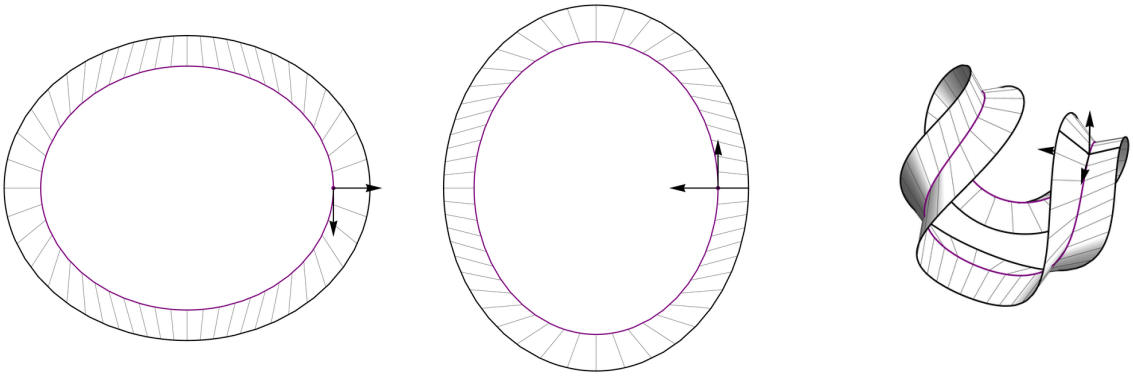

Figure 4.2: Two developed patches with specified rulings with $p = 0.8$ and a numerically closed gluing with $\varphi_R(0) = 1.1935$.

with common perimeter of length $2D$, see Figure 4.2.

We require both curves to have the same parametrization speed for the joining method discussed in Section 3.3 to be applicable. Consequently, we reparametrize both curves by arc length and denote the corresponding reparametrizations by $\mathbf{x}_L(t)$ and $\mathbf{x}_R(t)$. Moreover, let $k_L(t)$ and $k_R(t)$ be the curvature with respect to the arc-length parameter. Note that both curvatures are even periodic functions with period length D.

We select the ruling angles such that the cotangents of these angles form odd periodic functions with the same period length as the curvature functions,

$$\theta_L(t) = \frac{\pi}{2} - p\cos\left(\frac{4\pi}{D}\left(t - \frac{D}{8}\right)\right) \qquad \text{and} \qquad \theta_R(t) = \frac{\pi}{2} - p\cos\left(\frac{4\pi}{D}\left(t + \frac{D}{8}\right)\right),$$

where $p \in [0, \frac{\pi}{2})$; see Figure 4.2. Note that the parameter p influences the ruling angles and therefore the bending direction of the patches. If $p = 0$, the rulings are aligned with the normals of the ellipse, and in the undesirable case of $p = \frac{\pi}{2}$, the rulings become tangents of the ellipse at $t \equiv \frac{D}{4} \pmod{\frac{D}{2}}$.

Computation of the inclination angles, gluing curve, and surfaces

We now use Lemma 3.10 to find the solution for $\varphi_R(t)$ for $t \in [0, 2D]$ through the stated differential equation using appropriate initial values $\varphi_{R,0}$. The solution $\varphi_R(t)$ specifies the curvature $K(t)$, torsion $\tau(t)$, and the other inclination angle $\varphi_L(t)$.

Subsequently, we use the Frenet-Serret equations (Equation (3.1)) to determine the geometry of the glue curve $\mathbf{X}(t)$ for $t \in [0, 2D]$. Note that this curve will in general not be closed. However, we observe that the distance between its endpoints is influenced by the initial value for the opening angle $\varphi_{R,0}$; see Figure 4.3. Finally, we use Equation (3.3) to specify the ruling directions. For visualization, we trim the constructed surfaces so they are bounded by a scaled version of the elliptical glue curve.

4.2.2 Remarks on the Closure of the Gluing Curve

We observed that for appropriate parameter p, we were able to find initial values $\varphi_{R,0}$ that resulted in a numerically closed glue curve with tangent-continuous surfaces; see Figure 4.4. In the following,

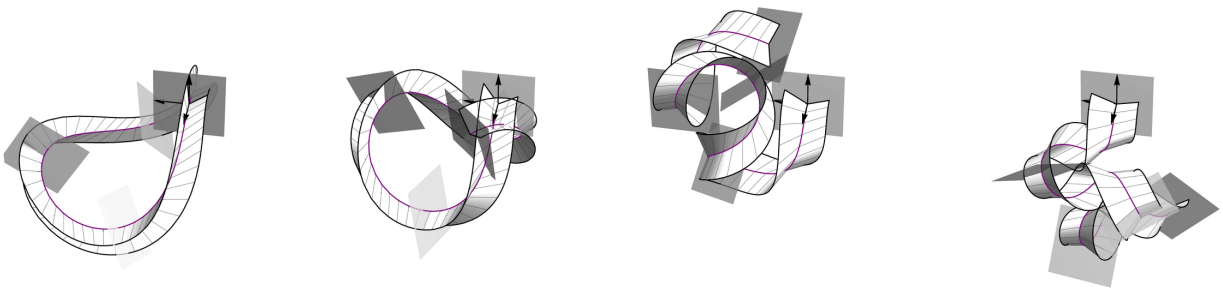

Figure 4.3: Illustration of the rigid-ruling folding motion for $a = 1.2$ and $\varphi_{R,0} \in (0.96, 1.06, 1.26, 1.36)$.

we use the periodicity of the developed curvatures and ruling angles to devise constraints for tangent-continuous closure of the gluing curve.

Periodicity of the inclination angle

We observe that if the computation of $\varphi_R(t)$ succeeds for $t \in [0, \frac{D}{2}]$, the computed inclination angles are periodic with period length D. Although we do not have a proof for the the existence and uniqueness of the solution $\varphi_R(t)$ of the differential equation in Lemma 3.10, we observe the following property of the solution:

Lemma 4.1. *The existence of a solution of the initial value problem for $\varphi_R(t)$ in Lemma 3.10 for $t \in [0, \frac{D}{2}]$ implies the existence of a periodic solution for $t \in \mathbb{R}$ with period length D.*

Proof. The differential equation in Lemma 3.10 can be expressed as $\varphi'_R(t) = f(t, \varphi_R(t))$. We show the following three properties:

- *Property 1:* $0 = f(0, \varphi(t)) = f\left(\frac{D}{2}, \varphi(t)\right)$,
- *Property 2:* $f(t, \varphi(t)) = -f(-t, \varphi(t))$,
- *Property 3:* $f(t, \varphi(t)) = f(t + D, \varphi(t))$.

As mentioned earlier, $k_L(t)$ and $k_R(t)$ are even periodic functions with period length D,

$$k_i(t) = k_i(-t), \qquad k_i(t) = k_i(t + D).$$

Consequently, their first derivatives are odd periodic functions with the same period length, that is,

$$k'_i(t) = -k'_i(-t), \qquad k'_i(t) = k'_i(t + D).$$

In addition, we have chosen the ruling angles such that their cotangents are odd periodic functions with period length D,

$$\cot\theta_i(t) = -\cot\theta_i(-t), \qquad \cot\theta_i(t) = \cot\theta_i(t + D).$$

Note that property 1 follows from $0 = k'_i(0) = k'_i\left(\frac{D}{2}\right)$ and $0 = \cot\theta_i(0) = \cot\theta_i\left(\frac{D}{2}\right)$. In addition, the above stated properties of $k_i(t)$, $k'_i(t)$, and $\cot\theta_i(t)$ imply properties 2 and 3.

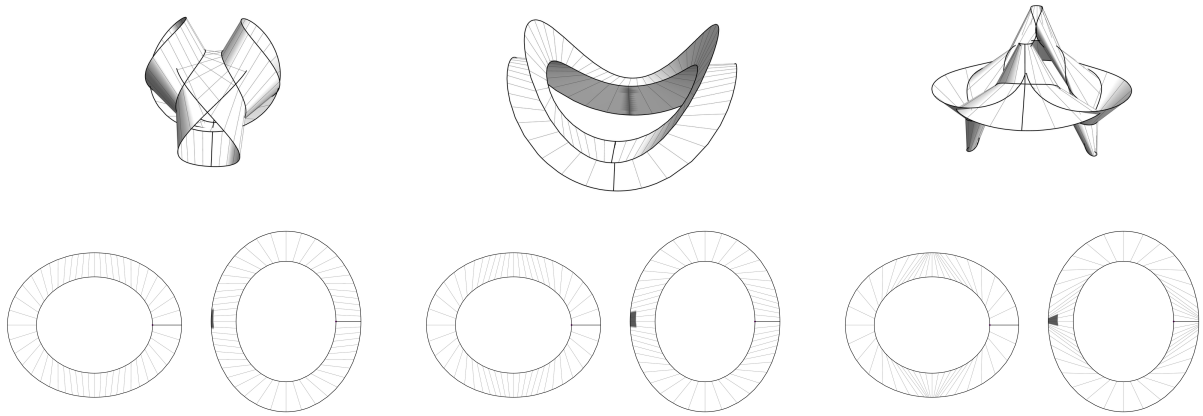

Figure 4.4: Numerically closed shapes for $p \in (0.6, 0.8, 1.2)$, $\varphi_R(0) \in (1.261728, 0.956301, 1.291588)$, and $a = 1.2$.

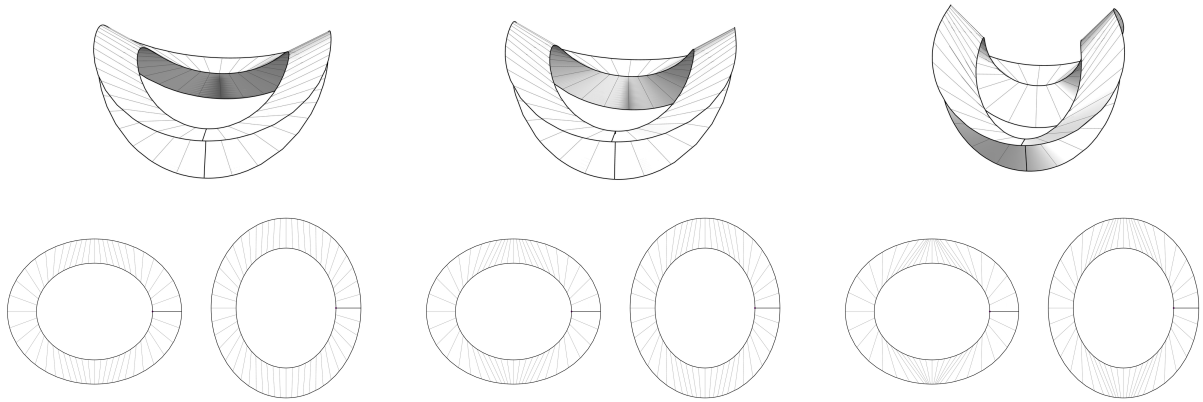

Figure 4.5: Numerically closed shapes with modified ruling directions from Equation (4.1) with $p \in (0.8, 1.0, 1.2)$, $\varphi_{R,0} \in (0.967000, 1.025101, 1.246270)$, and $a = 1.2$.

It follows that if $\varphi(t)$ is a solution of $\varphi_R'(t) = f(t, \varphi_R(t))$ for $t \in [0, \frac{D}{2}]$, a continuous continuation of the solution for $t \in [-\frac{D}{2}, 0]$ can be obtained using properties 1 and 2 by reflecting $\varphi(t)$ across $t = 0$. Utilizing properties 1 and 3, we can achieve continuation of the solution for $t \in \mathbb{R}$ through repetition. □

Periodicity of the gluing curve

Upon successful computation of a periodic function $\varphi_R(t)$, it follows that the curvature $K(t)$ and torsion $\tau(t)$ are also periodic functions with period length D. In particular, $K(t)$ is an even function, and $\tau(t)$ an odd function. Consequently, the integrated curve corresponding to $t \in [0, 2D]$ consists of four parts separated at $t = \frac{D}{2}$, $t = D$ and $t = \frac{3D}{2}$, where consecutive parts are related by a reflection on the normal plane at the common curve point; see Figure 4.3. It follows that if the normal planes at the endpoints are perpendicular, the overall curve is closed and curvature continuous. Additionally, the surfaces are also tangent-continuous.

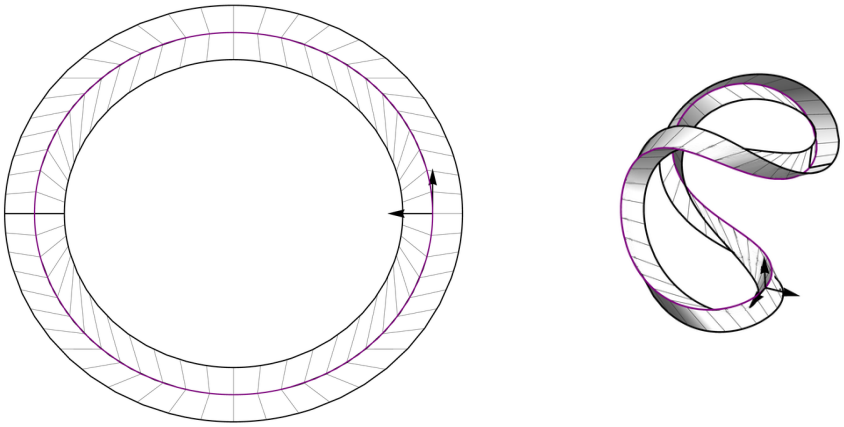

Figure 4.6: Numerically closed folding along a single elliptic crease with $a = 1.1$, $p = 0.9$, and $\varphi_{1,0} = 1.05181$.

To find numerically closed curves, we vary the initial fold angle for fixed values of p; see Figure 4.3. We observe that for suitable p, we were able to find initial opening angles that would result in closed curves.

4.2.3 Further Variations

There exist numerous families of rulings that lead to (numerically) closed curves. As an example, instead of using the same parameter p for both $\theta_L(t)$ and $\theta_R(t)$, variations in the shape can be achieved by substituting p with p_L and p_R (along with appropriate combinations of p_L and p_R).

In addition, we can also vary the sign in one of the cosine functions, such as

$$\bar{\theta}_L(t) = \theta_L(t) \qquad \text{and} \qquad \bar{\theta}_R(t) = \frac{\pi}{2} - p\cos\left(\frac{4\pi}{D}\left(t - \frac{D}{8}\right)\right). \tag{4.1}$$

Figure 4.5 shows corresponding (numerically) closed curves.

It would also be interesting to explore other shifts in parameters between the two ellipses $\mathbf{x}_L(t)$ and $\mathbf{x}_R(t)$. In this case, however, it is more challenging to find ruling angles that result in periodic solutions.

4.3 Elliptic Creases

We now turn to the second example where we study the shapes obtained by creasing along ellipse and adding further creases to the resulting folded shape. This section is inspired by the Bauhaus model, developed by a student of Josef Albers at the first Bauhaus in 1927 and 1928 [15, 2]. Over the years, it has been reinterpreted by multiple artists, including Irene Schawinsky, and Erik and Martin Demaine.

We follow a similar approach as in the previous section. First, we prescribe rulings that result in periodic curvature and torsion functions. Subsequently, by varying the initial angle, we find configurations that result in numerically closed shapes that correspond to creasing along a single elliptic crease. Finally, we explore examples of added pleats to the shape.

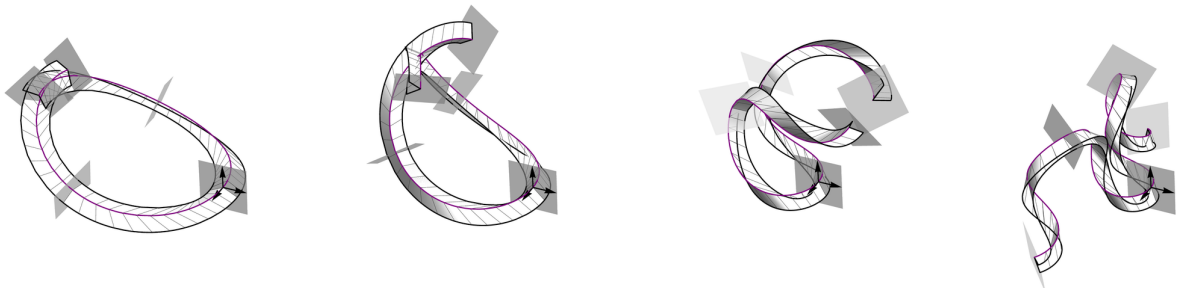

Figure 4.7: Illustration of the rigid-ruling folding motion of a single elliptic crease for $a = 1.2$, $p = 0.9$, and $\varphi_{1,0} \in (0.15\pi, 0.25\pi, 0.35\pi, 0.4\pi)$.

4.3.1 Computation of the First Curve

Parametrization of the development

We parameterize the first ellipse as follows

$$\mathbf{x}_1(t) = (a\cos t, \sin t, 0)\,,$$

where $t \in [-\pi, \pi]$. Unlike Section 4.2, there is no need for reparametrization by arc length in this case. The curvature function of $\mathbf{x}_1(t)$ is given by

$$k_1(t) = -\frac{a}{\sqrt{(\cos^2 t + a^2 \sin^2 t)^3}}.$$

Similar to the previous example, we define the ruling angles as

$$\theta_{1L}(t) = \frac{\pi}{2} + p\sin(2t) \qquad \text{and} \qquad \theta_{1R}(t) = \frac{\pi}{2} - \theta_{1L}(t),$$

where $p \in [0, \frac{\pi}{2})$.

Computation of the inclination angle, crease curve, and surfaces

First, we use Section 3.3.4 to compute the inclination angle. Since $\theta_{1L}(t)+\theta_{1R}(t) = \pi$, the fold angle is constant, hence $\varphi_1(t) = \varphi_{1,0}$. The curvature and torsion are then specified by Equation (3.22) as

$$K_1(t) = \frac{a}{(\cos^2 t + a^2 \sin^2 t)^{\frac{3}{2}} \cos\varphi_{1,0}} \qquad \text{and} \qquad \tau_1(t) = \frac{a\tan(p\sin(2t))}{(\cos^2 t + a^2 \sin^2 t)^{\frac{3}{2}}} \tan\varphi_{1,0}.$$

Subsequently, we use the Frenet-Serret equations (Equation (3.1)) to determine the geometry of the crease curve $\mathbf{X}_1(t)$ for $t \in [-\pi, \pi]$. Again, note that the distance between the curve's endpoints depends on the initial inclination angle $\varphi_{1,0}$. Finally, we use Equation (3.3) to specify the ruling directions. For visualization purposes, we trim the constructed surfaces so they are bounded by a scaled version of the elliptical glue curve.

4.3.2 Remarks on the Closure of the Crease Curve

Analogous to the previous example, the curvature of the developed ellipse and the cotangent of the ruling angles are periodic with period π. Specifically, $k_1(t)$ is even and $\cot\theta_i(t)$ are odd. Since the

inclination angle function is constant, the curvature $K_1(t)$ is an even function and the torsion $\tau_1(t)$ is an odd function with period length π.

Because of the periodicity of both curvature and torsion, the curve can once again be divided into four segments separated at $t = -\frac{\pi}{2}$, $t = 0$, and $t = \frac{\pi}{2}$, where adjacent segments are related through a reflection about the normal plane at the shared endpoint; see Figure 4.7.

Changing the initial value influences the angle between the normal planes at the endpoints of the quarter curve. We conjecture that, for suitable values of p, there exists a parameter value at which these two planes become orthogonal, consequently resulting in a closed shape.

4.3.3 Adding Pleats

In the subsequent discussion, we compare two approaches for adding further creases to the 3D shape, which bear a certain duality:

- First, we introduce pleats by attaching patches to curves on surfaces as described in Section 3.5. In this approach, we specify the 2D crease and then determine the rulings of the appended patch.
- Second, we add pleats along tangent parallel curves as described in Section 3.5.2. Here, the rulings of the upcoming patch are predetermined (they are parallel to the rulings of the penultimate patch), but the shape of the crease is constructed.

In both strategies, we lack the ability to directly control the edge of regression of the newly added surface. As a consequence, as we introduce an increasing number of creases, undesirable situations might arise where the edge of regression approaches the last crease.

Recall that we started from $\mathbf{x}_1(t)$ with rulings $\mathbf{r}_{1L}(t)$ and $\mathbf{r}_{1R}(t)$ (defined by $\theta_{1L}(t)$ and $\theta_{1R}(t)$), and computed their 3D counterparts, the curve $\mathbf{X}_1(t)$ and the 3D rulings $\mathbf{R}_{1L}(t)$ and $\mathbf{R}_{1R}(t)$, defined using the additional function $\varphi_1(t)$. Next, we will demonstrate how to add additional creases to the left patch of $\mathbf{x}_1(t)$ or $\mathbf{X}_1(t)$, respectively. The process of adding creases to patches to the right is analogous.

Scaled pleats

In this section, we discuss how to add pleats along scaled ellipses $c_i\mathbf{x}_1(t)$ where $c_i < c_{i-1}$ for $i > 1$. However, the computation for other appropriate curves works similarly.

In the following, we show how the curves $\mathbf{x}_{i-1}(t)$ and $\mathbf{X}_{i-1}(t)$, and the angles $\theta_{i-1,L}(t)$ and $\varphi_{i-1}(t)$ specify the next curves and angles $\mathbf{x}_i(t)$, $\mathbf{X}_i(t)$, $\theta_{i-1,L}(t)$, and $\varphi_{i-1}(t)$.

- *Step 1:* First, we determine an appropriate parametrization of the next curve. The parametrization $\mathbf{x}_{i-1}(t)$ and $\theta_{i-1,L}(t)$ specify the developed left ruling direction $\mathbf{r}_{i-1,L}(t)$. If the patch connecting $\mathbf{x}_{i-1}(t)$ and $c_i\mathbf{x}_1(t)$ is free of singularities, we trim the left rulings of $\mathbf{x}_{i-1}(t)$ with the next elliptic curve by solving

$$\mathbf{x}_{i-1}(t) + l_{i-1}(t)r_{i-1,L}(t) = c_i\mathbf{x}_1(u_i(t))$$

  for $l_{i-1}(t)$ and $u_i(t)$. When doing this computation in Mathematica, we use a fine sampling of $t \in [-\pi, \pi]$ and interpolate the corresponding values of $l_{i-1}(t)$ and $u_i(t)$. We then set $\mathbf{x}_i(t) = c_i\mathbf{x}_1(u_i(t))$ and define $\mathbf{X}_i(t) = \mathbf{X}_{i-1}(t) + l_{i-1}(t)\mathbf{R}_{i-1,L}(t)$

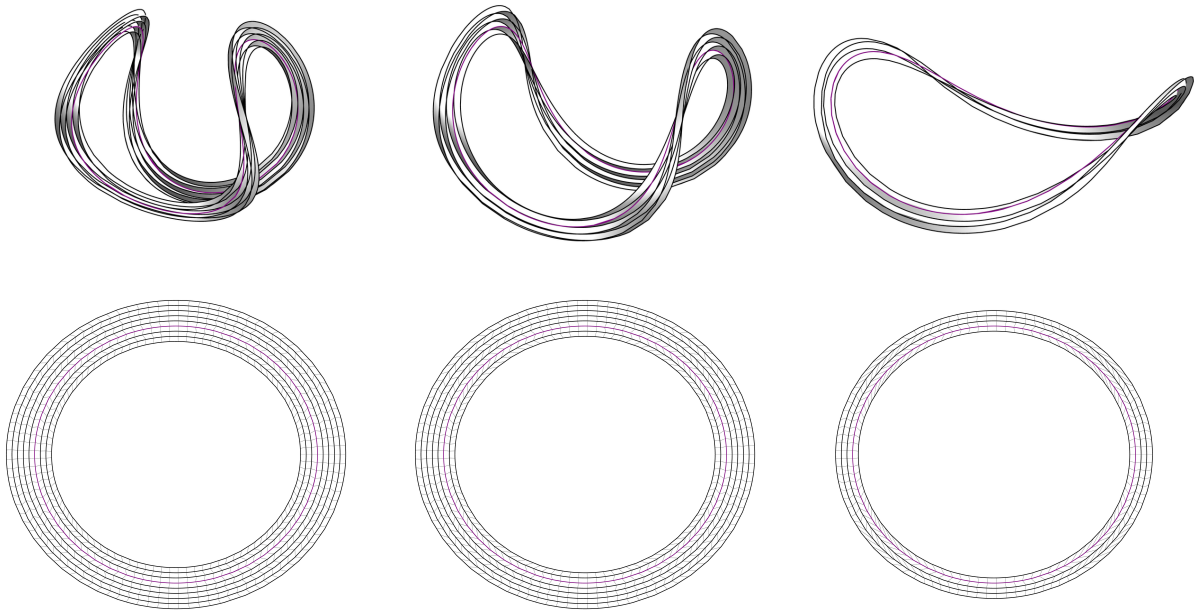

Figure 4.8: Numerically closed folded states of a pleated ellipse for $a = 1.1$, $p \in (0.8, 1, 1.2)$, and $\varphi_{1,0} \in (1.104801, 0.974231, 0.614106)$.

- *Step 2:* Next, we extract information from $\mathbf{x}_i(t)$. We set $s_i'(t) = |\mathbf{x}_i'(t)|$ and compute the curvature $k_i(t)$ of $\mathbf{x}_i(t)$ (at parameter t). Finally, we compute the ruling angle $\theta_{i,R}(t)$ using $\mathbf{r}_{i-1,L}(t)$ and the tangent and normal vectors of $\mathbf{x}_i(t)$ as

$$\theta_{i,R}(t) = \arctan(\mathbf{r}_{i-1,L}(t) \cdot \mathbf{t}_i(t), \mathbf{r}_{i-1,L}(t) \cdot \mathbf{n}_i(t)).$$

- *Step 3:* We determine the inclination angle $\varphi_i(t)$ from the computed quantities using the ruling curvature as stated in Equation (3.46), that is,

$$\varphi_i(t) = -\arctan\left(\frac{s_{i-1}'(t)\sin\theta_{i,R}(t)}{s_i'(t)k_i(t)\sin\theta_{i-1,L}(t)} K_{i-1}(t)\sin\varphi_{i-1}(t)\right).$$

- *Step 4:* Finally, we find the next ruling direction $\theta_{i,L}(t)$ using Equation (3.47), that is,

$$\theta_{i,L}(t) = -\operatorname{arccot}\left(\cot\theta_{i,R}(t) - \frac{2}{k_i(t)}\frac{\varphi_i'(t)}{s_i'(t)}\cot\varphi_i(t)\right) \pmod{\pi}.$$

Figure 4.8 illustrates the application of this method to both sides of the curve. Here, we intended to append four creases to either side of the curve, but failed to make much progress on the inner side of the ellipse.

Tangent parallel curves

In this section, we discuss the construction of pleats using tangent parallel curves. For this purpose, we first determine tangent-parallel curves to the left and right patch by solving the initial value

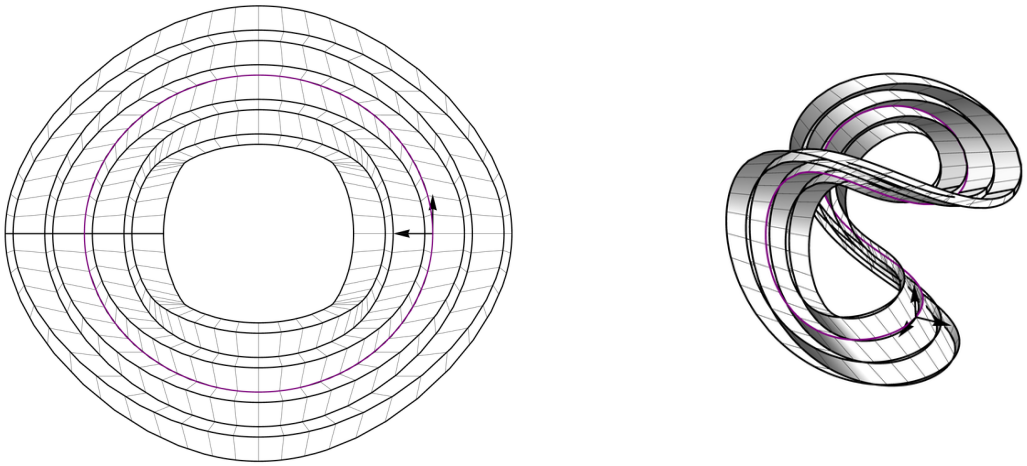

Figure 4.9: Elliptic crease depicted in Figure 4.6 with tangent-parallel pleats.

problem stated in Equation (2.9) for both sides, that is,

$$\frac{l_L'(t)}{l_L(t)} = \left(2\cos(2t) - \frac{a}{\cos^2 t + a^2 \sin^2 t}\right)\tan(\sin(2t)) \qquad \text{with} \qquad l_L(0) = l_{L,0},$$

and

$$\frac{l_R'(t)}{l_R(t)} = \left(2\cos(2t) + \frac{a}{\cos^2 t + a^2 \sin^2 t}\right)\tan(\sin(2t)) \qquad \text{with} \qquad l_R(0) = l_{R,0}.$$

Recall that the constructed surfaces consist of two families of parallel rulings. We therefore set $\mathbf{r}_L(t) = \mathbf{r}_{1L}(t)$, $\mathbf{r}_R(t) = \mathbf{r}_{1R}(t)$, $\mathbf{R}_L(t) = \mathbf{R}_{1L}(t)$, and $\mathbf{R}_R(t) = \mathbf{R}_{1R}(t)$. Lemma 3.15 implies how the curves $\mathbf{x}_{i-1}(t)$ and $\mathbf{X}_{i-1}(t)$ specify the next curves $\mathbf{x}_i(t)$ and $\mathbf{X}_i(t)$, that is,

$$\mathbf{x}_i(t) = \begin{cases} \mathbf{x}_{i-1}(t) + c_{i-1} l_L(t) \mathbf{r}_L(t), & \text{if } i \text{ is odd,} \\ \mathbf{x}_{i-1}(t) + c_{i-1} l_R(t) \mathbf{r}_R(t), & \text{if } i \text{ is even,} \end{cases}$$

and

$$\mathbf{X}_i(t) = \begin{cases} \mathbf{X}_{i-1}(t) + c_{i-1} l_L(t) \mathbf{R}_L(t), & \text{if } i \text{ is odd,} \\ \mathbf{X}_{i-1}(t) + c_{i-1} l_R(t) \mathbf{R}_R(t), & \text{if } i \text{ is even,} \end{cases}$$

where $c_{i-1} > 0$ are sufficiently small constants.

Figure 4.9 illustrates the application of this method to both sides of the curve. Here, we intended to append three curves to either side, but again failed to make much progress towards the center of the ellipse. Finally, note that Corollary 3.2 implies that a rigid-ruling folding motion as illustrated in Figure 4.7 induces the same crease-rule pattern when patches along tangent parallel curves are added; see Figure 4.11.

4.3.4 Further Variations

Similar to Section 4.2, this is not the only ruling angle combination that results in (numerically) closed shapes. Other variations can be obtained by considering

$$\theta_{1L}(t) = \frac{\pi}{2} + p_L \sin(2t) \qquad \text{and} \qquad \theta_{1R}(t) = \frac{\pi}{2} + p_R \sin(2t).$$

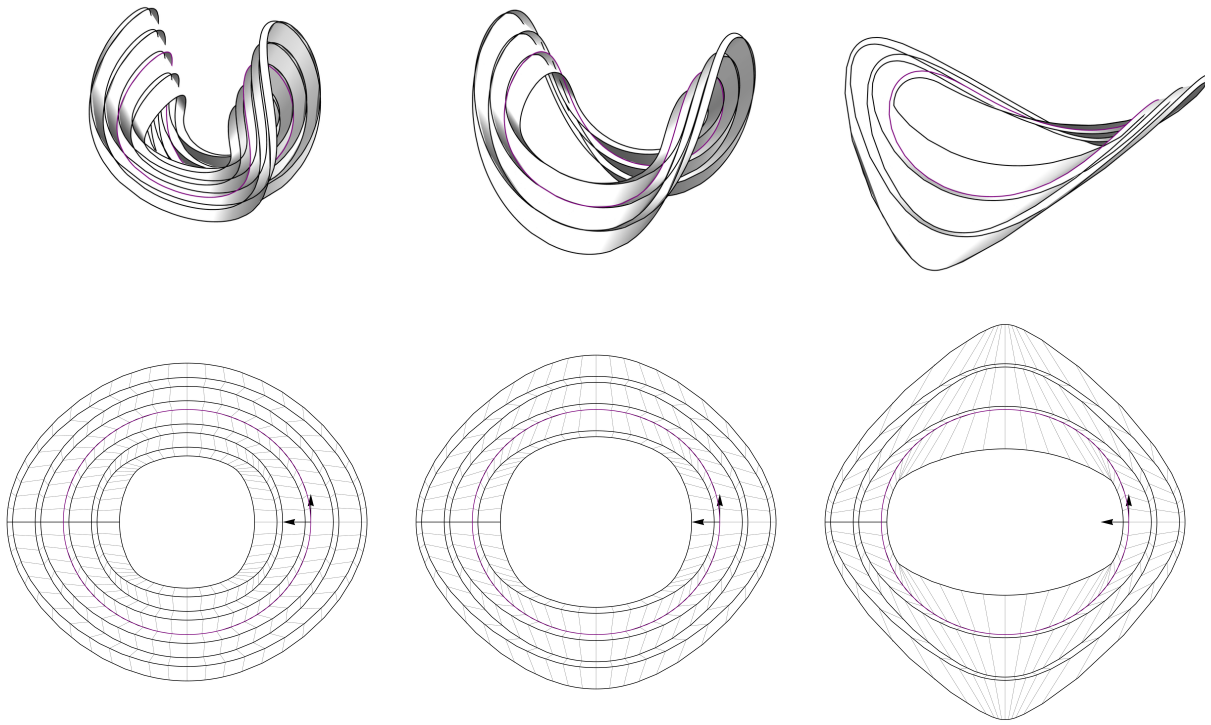

Figure 4.10: Numerically closed folded states of the pleated ellipse with tangent parallel pleats for the same folded states of curves as in Figure 4.8.

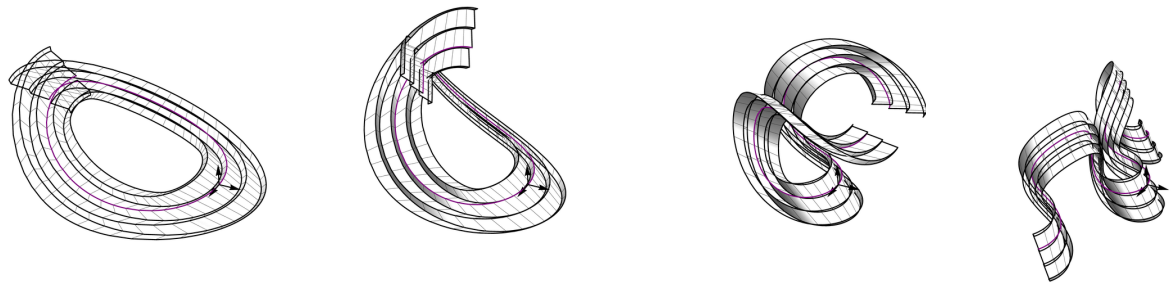

Figure 4.11: Illustration of the rigid-ruling folding motion in Figure 4.7 with tangent-parallel pleats.

for appropriate values of p_L and p_R. When $p_L \neq p_R$, the crease does not have constant fold angle. However, solving the corresponding initial value problem for $\varphi_1(t)$ results in an even periodic function. This allows a similar argument to the previous section implying periodic curves.

4.4 Final Remarks

We developed a strategy to derive (numerically) closed space curves from glued or folded ellipses. We suspect that similar considerations can be applied to other periodic convex crease or glue curves, provided the ruling angles are chosen appropriately. Specifically, in the case of circular curves, we are not limited by the curvature period of the developed curve. As a result, we can select the period length at will and construct shapes similar to those in Section 7.2.

Chapter 5

Connecting Two Patches with Specified Rulings to a Central Patch with Unspecified Rulings

The content of this chapter is unpublished and is based on discussions with Erik Demaine, Robert Lang, and Tomohiro Tachi.

Overview

In this chapter, we consider an application of gluing and creasing three patches with partial ruling information. Specifically, we highlight two examples in which the rulings of the left and right patches are deduced from the folded shape, while the rulings of the central patch remain initially undefined. These examples showcase variations of Tony Wills' squaricle and David Huffman's hexagonal column.

5.1 Introduction

This chapter illustrates the first application of the theory presented in Section 3.4. Specifically, we explore examples of how to join three patches where the rulings of the left and right patches are known. This is particularly interesting because the rulings of the side patches can sometimes be derived from symmetry or other properties of the folded shape. However, the central patch's rulings are initially unknown and not trivial to deduce. Consequently, prescribing the rulings of two patches and then attaching a third surface often does not yield the desired result.

We illustrate the corresponding computation using two examples. The first, discussed in Section 5.2, explores variations of the "squaricle", a shape introduced by Tony Wills [108]. A squaricle is a gluing of a square and a circle with equal perimeter length along their boundaries, as depicted in Figure 5.1a. The variations we consider in this chapter were suggested by John Sharp [86].

The second example, discussed in Section 5.3, analyzes one of David Huffman's designs: the hexagonal tower. Beyond Huffman codes, Huffman is known for a systematic study of the behavior of paper when folded along curves, specifically conic creases. Reconstructions of this crease pattern suggest that it consists of circles, parabolas, and lines [18]. Upon assembly, the pattern can be closed into a hexagonal shape, as shown in Figure 5.7. To the best of our knowledge, this section presents the first curved-crease analysis of this shape with a positive result.

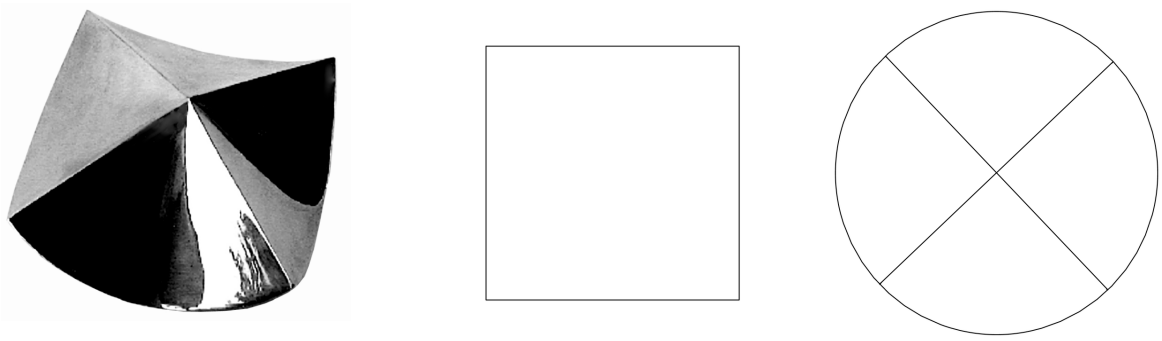

(a) A squaricle (Figure 4 in Wills [108]), which is obtained by gluing a circle with four creases and a square.

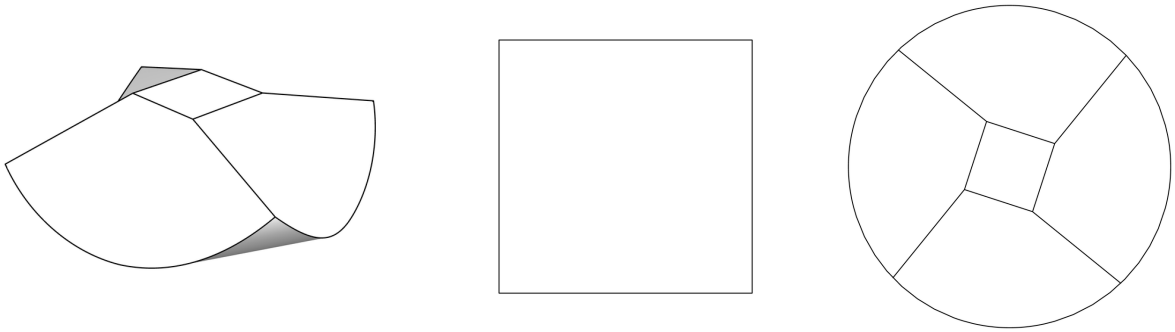

(b) A variation of the squaricle with a central planar square on the circular region.

Figure 5.1: The squaricle and its variations as considered in Section 5.2.

5.2 Variations of the Squaricle

The gluing of a square and a circle, as well as other planar regions, can result in various shapes. The final form can be altered by purposefully introducing creases on one or both surfaces. In the following, we consider squaricle variations proposed by John Sharp [86], illustrated in Figure 5.1b. In this context, we add eight creases to the circular region. Four of these create a planar square, with its midpoint coinciding with the circle's center. The other four creases connect the corners of the square with four evenly spaced points along the boundary of the circle. When folded, these designated points align with the corners of the square. In Chapter 9, we consider other variations of such gluings.

5.2.1 Ruling Analysis

When carefully constructing the proposed variation of the squaricle from paper, it is not obvious how the rulings are distributed. As one of the four bent regions of the circle is bounded by three straight edges and a curved edge, it requires further decomposition; see Figure 5.1b. In the following, we assume that an edge of the central square is part of a triangular region, dividing the patch into two cones on either side, with their apices coinciding with the corners of the creased square. Hence, the circular surface consists of a central square, four triangles, and eight cones as depicted in Figure 5.2. Due to the 4-fold rotational symmetry of the circular region, the square

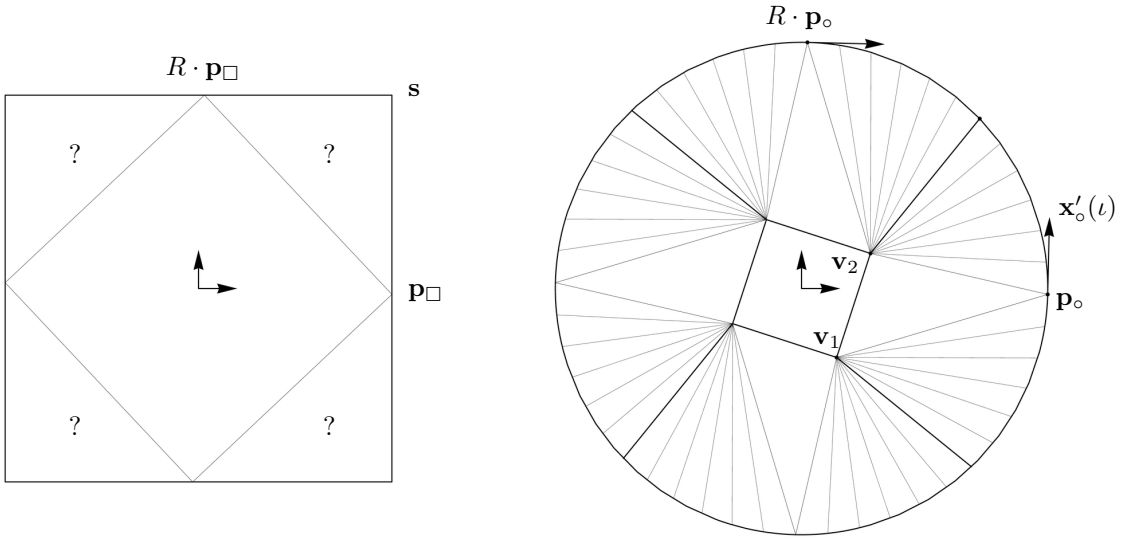

Figure 5.2: Crease pattern and notation.

region also requires 4-fold rotational symmetry. It consequently features a central plane. However, the alignment of rulings of the remaining triangular patches is unknown. In symmetric cases, these surfaces become cylinders, but for "twisted" squares, this assumption might not hold true.

In the following section, we demonstrate how to identify the rulings for the four patches, with each one connecting two cones.

5.2.2 Computation

Without loss of generality, we assume that the circle and square have unit boundary length. A circle and one side of the square can be parametrized by arc length as

$$\mathbf{x}_\circ(s) = \frac{1}{2\pi}\left(\cos(2\pi s), \sin(2\pi s), 0\right) \qquad \text{and} \qquad \mathbf{x}_\square(s) = \left(\frac{1}{8}, s, 0\right),$$

respectively. Assume that the circle and square are glued so that points corresponding to the same arc-length parameter value coincide. We parametrize the coordinates of the corners $\mathbf{v}_i$ of the creased shape using polar coordinates with radius r and angle α. We set $\mathbf{v}_1 = r\left(\cos\alpha, \sin\alpha, 0\right)$, and denote by $\mathbf{v}_2$, $\mathbf{v}_3$, and $\mathbf{v}_4$ the rotated copies of $\mathbf{v}_1$ by $\frac{\pi}{4}$, $\frac{\pi}{2}$, and $\frac{3\pi}{4}$ about the z-axis.

Initial values

Previously, we established the assumption that one of the bent patches consists of a triangle and two cones. However, we have not yet determined the third corner $\mathbf{p}_\circ$ of the triangle $\{\mathbf{v}_1, \mathbf{v}_2, \mathbf{p}_\circ\}$ that lies on the circular boundary.

Further careful analysis suggests that for a feasible combination of α and r there is only one possible solution for the location of $\mathbf{p}_\circ$. To obtain this location, we consider the initial tangent planes of the computed surfaces. As $\mathbf{p}_\circ$ might be any point on the circular boundary, we assume that $\mathbf{p}_\circ = \mathbf{x}_\circ(\iota)$ for some initially unknown arc-length parameter ι. Furthermore, we denote its corresponding counterpart on the square by $\mathbf{p}_\square = \mathbf{x}_\square(\iota)$. Finally, we denote the corner of the square by $\mathbf{s} = \mathbf{x}_\square\left(\frac{1}{8}\right)$.

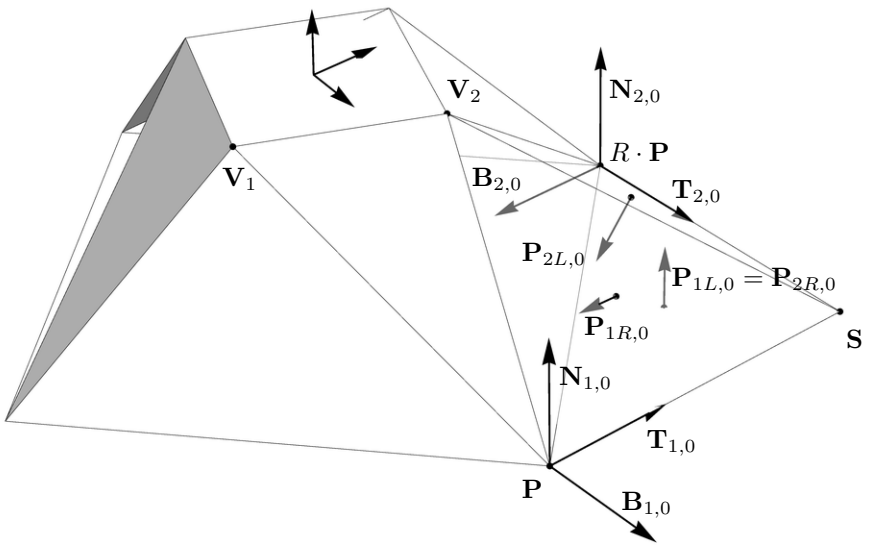

Figure 5.3: Notation of the quantities used in the analysis of the variation of a squaricle.

Without loss of generality, we assume that the 3D shape is positioned such that the corners of the creased square $\mathbf{V}_i$ coincide with their 2D counterparts, that is, $\mathbf{V}_i = \mathbf{v}_i$. Our goal is to locate point $\mathbf{P}$ that corresponds to the location of the points $\mathbf{p}_\square$ and $\mathbf{p}_\circ$, and point $\mathbf{S}$ that corresponds to the corner $\mathbf{s}$ on the initial tangent plane of the triangular patch of the square. In the following, we denote a rotation matrix corresponding to a rotation by $\frac{\pi}{4}$ about the z-axis by R.

The parameter ι and the location of the points $\mathbf{S}$ and $\mathbf{P}$ constitute seven unknowns. These can be determined from seven constraints derived from the isometry requirement between 2D and 3D. Specifically, we obtain five constraints from the following distance requirements,

$$\begin{aligned} &\operatorname{dist}(\mathbf{p}_\circ, \mathbf{v}_1) = \operatorname{dist}(\mathbf{P}, \mathbf{V}_1), \qquad \operatorname{dist}(\mathbf{p}_\circ, \mathbf{v}_2) = \operatorname{dist}(\mathbf{P}, \mathbf{V}_2), \qquad \operatorname{dist}(\mathbf{p}, \mathbf{s}) = \operatorname{dist}(\mathbf{P}, \mathbf{S}), \\ &\operatorname{dist}(\mathbf{p}_\square, R \cdot \mathbf{p}_\square) = \operatorname{dist}(\mathbf{P}, R \cdot \mathbf{P}), \quad \operatorname{dist}(R \cdot \mathbf{p}, \mathbf{s}) = \operatorname{dist}(R \cdot \mathbf{P}, \mathbf{S}). \end{aligned}$$

and two constraints from the angular constraints

$$\begin{aligned} \frac{(\mathbf{s} - \mathbf{p}) \cdot (\mathbf{v}_2 - \mathbf{p})}{|\mathbf{s} - \mathbf{p}|} &= \frac{(\mathbf{S} - \mathbf{P}) \cdot (\mathbf{V}_2 - \mathbf{P})}{|\mathbf{S} - \mathbf{P}|}, \\ \frac{(\mathbf{s} - R \cdot \mathbf{p}) \cdot (\mathbf{v}_2 - R \cdot \mathbf{p})}{|\mathbf{s} - R \cdot \mathbf{p}|} &= \frac{(\mathbf{S} - R \cdot \mathbf{P}) \cdot (\mathbf{V}_2 - R \cdot \mathbf{P})}{|\mathbf{S} - R \cdot \mathbf{P}|}. \end{aligned}$$

We solve the above seven constraints numerically, and for reasonable r and α, we obtain solutions for ι, $\mathbf{S}$, and $\mathbf{P}$. This defines the "scaffolding" consisting of the planar regions of the shape depicted in Figure 5.3. Additionally, the points of $\mathbf{P}$ and $\mathbf{S}$ define the initial tangent directions,

$$\mathbf{T}_1(0) = \mathbf{T}_{1,0} = \frac{\mathbf{S} - \mathbf{P}}{|\mathbf{S} - \mathbf{P}|} \qquad \text{and} \qquad \mathbf{T}_2(0) = \mathbf{T}_{2,0} = \frac{\mathbf{S} - R \cdot \mathbf{P}}{|\mathbf{S} - R \cdot \mathbf{P}|},$$

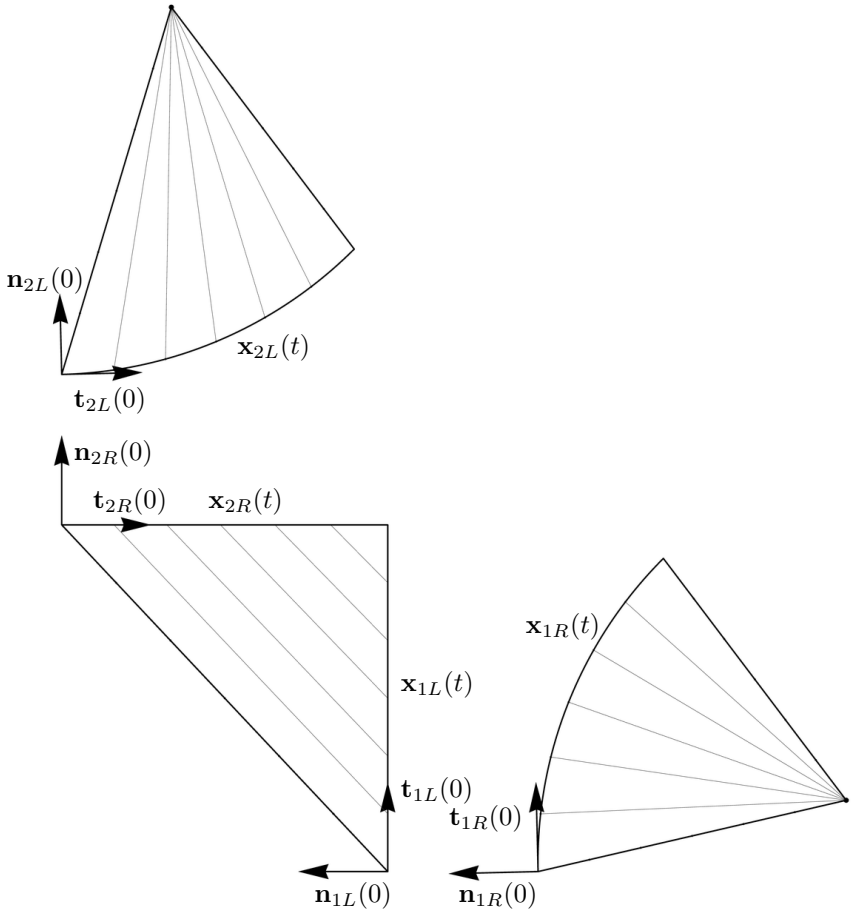

Figure 5.4: Illustration of the notation of the development.

and the normals of the incident tangent planes,

$$\begin{aligned}
\mathbf{P}_{1R,0} &= \frac{(\mathbf{P}-\mathbf{S})\times(\mathbf{V}_2-\mathbf{S})}{|(\mathbf{P}-\mathbf{S})\times(\mathbf{V}_2-\mathbf{S})|},\\
\mathbf{P}_{1L,0} = \mathbf{P}_{2R,0} &= -\frac{(\mathbf{P}-\mathbf{S})\times(R\cdot\mathbf{P}-\mathbf{S})}{|(\mathbf{P}-\mathbf{S})\times(R\cdot\mathbf{P}-\mathbf{S})|},\\
\mathbf{P}_{2L,0} &= -\frac{(R\cdot\mathbf{P}-\mathbf{S})\times(\mathbf{V}_2-\mathbf{S})}{|(R\cdot\mathbf{P}-\mathbf{S})\times(\mathbf{V}_2-\mathbf{S})|}.
\end{aligned}$$

Parametrization of the development

We now proceed in discussing the parametrization of the development to set up the computation of the gluing curves; see Figure 5.4.

Following the notation of Section 3.4.3, we let the central triangular patch be bounded by curves

$$\mathbf{x}_{1L}(s) = \mathbf{x}_{\square}(\iota + s) \qquad \text{and} \qquad \mathbf{x}_{2R}(s) = R\cdot\mathbf{x}_{\square}(\iota - s);$$

see Figure 5.4. For simplicity, we work with reflected versions of $\mathbf{x}_{1R}(s)$ and $\mathbf{x}_{2L}(s)$, denoting them

using a tilde superscript ($\sim$):

$$\tilde{\mathbf{x}}_{1R}(s) = \mathbf{x}_\circ(\iota + s) \qquad \text{and} \qquad \tilde{\mathbf{x}}_{2L}(s) = R \cdot \mathbf{x}_\circ(\iota - s).$$

This reflection needs to be taken in account when computing the corresponding ruling directions and curvatures.

In the following, analogous to Section 3.4.3, we assume that the rulings of the central patch connect $\mathbf{x}_{1L}(s_1(t))$ with $\mathbf{x}_{2R}(s_2(t))$, where we assume without loss of generality that the parametrization speeds are $s_1(t) = t$ and $s_2(t) = u(t)$ for an initially unknown function $u(t)$.

The (reflected) ruling directions can be obtained from

$$\tilde{\mathbf{r}}_{1R}(t) = \frac{\mathbf{v}_2 - \tilde{\mathbf{x}}_{1R}(t)}{|\mathbf{v}_2 - \tilde{\mathbf{x}}_{1R}(t)|}, \quad \mathbf{r}_{1L}(t) = \mathbf{r}_{2R}(t) = \frac{\mathbf{x}_{2R}(u(t)) - \mathbf{x}_{1L}(t)}{|\mathbf{x}_{2R}(u(t)) - \mathbf{x}_{1L}(t)|}, \quad \tilde{\mathbf{r}}_{2L}(t) = \frac{\mathbf{v}_2 - \tilde{\mathbf{x}}_{2L}(u(t))}{|\mathbf{v}_2 - \tilde{\mathbf{x}}_{2L}(u(t))|}.$$

Considering the reflection, the corresponding ruling angles read

$$\begin{aligned}
\theta_{1R}(t) &= \pi - \arctan\left(\tilde{\mathbf{r}}_{1R}(t) \cdot \tilde{\mathbf{t}}_{1R}(t), \tilde{\mathbf{r}}_{1R}(t) \cdot \tilde{\mathbf{n}}_{1R}(t)\right) \\
&= \pi - \arctan\left(\frac{2\pi r\cos(\alpha - 2\pi(\iota + t))}{\sqrt{1 + 4\pi^2 r^2 + 4\pi r \sin(\alpha - 2\pi(\iota + t))}}, \frac{1 + 2\pi r \sin(\alpha - 2\pi(\iota + t))}{\sqrt{1 + 4\pi^2 r^2 + 4\pi r \sin(\alpha - 2\pi(\iota + t))}}\right) \\
\theta_{2L}(t) &= -\arctan\left(\tilde{\mathbf{r}}_{2L}(t) \cdot \tilde{\mathbf{t}}_{2L}(u(t)), \tilde{\mathbf{r}}_{2L}(t) \cdot \tilde{\mathbf{n}}_{2L}(u(t))\right) \\
&= -\arctan\left(\frac{-2\pi r\sin(\alpha - 2\pi(\iota - u(t)))}{\sqrt{1 + 4\pi^2 r^2 + 4\pi r \cos(\alpha - 2\pi(\iota - u(t)))}}, \frac{-1 + 2\pi r \cos(\alpha - 2\pi(\iota - u(t)))}{\sqrt{1 + 4\pi^2 r^2 + 4\pi r \cos(\alpha - 2\pi(\iota - u(t)))}}\right),
\end{aligned}$$

where $\tilde{\mathbf{t}}_{1R}(s)$ and $\tilde{\mathbf{t}}_{2L}(s)$ are the tangents, and $\tilde{\mathbf{n}}_{1R}(s)$ and $\tilde{\mathbf{n}}_{2L}(s)$ the normals of $\tilde{\mathbf{x}}_{1R}(s)$ and $\tilde{\mathbf{x}}_{2L}(s)$, respectively. The remaining ruling angles follow the definition in Equation (3.25) and Equation (3.26), that is,

$$\begin{aligned}
\theta_{1L}(t) &= \arctan\left(\frac{\frac{1}{8} - \iota - t}{\sqrt{(\frac{1}{8} - \iota - t)^2 + (\frac{1}{8} + \iota - u(t))^2}}, \frac{\frac{1}{8} + \iota - u(t)}{\sqrt{(\frac{1}{8} - \iota - t)^2 + (\frac{1}{8} + \iota - u(t))^2}}\right) \\
\theta_{2R}(t) &= \arctan\left(\frac{-\frac{1}{8} - \iota + u(t)}{\sqrt{(\frac{1}{8} - \iota - t)^2 + (\frac{1}{8} + \iota - u(t))^2}}, \frac{\frac{1}{8} - \iota - t}{\sqrt{(\frac{1}{8} - \iota - t)^2 + (\frac{1}{8} + \iota - u(t))^2}}\right)
\end{aligned}$$

using the tangents $\mathbf{t}_{1L}(s)$ and $\mathbf{t}_{2R}(s)$, and normals $\mathbf{n}_{1L}(s)$ and $\mathbf{n}_{2R}(s)$ of $\mathbf{x}_{1L}(s)$ and $\mathbf{x}_{2R}(s)$, respectively.

Finally, the curvatures of the developed curves are $k_{1R}(s) = -2\pi$, $k_{1L}(s) = k_{2R}(s) = 0$, and $k_{2L}(s) = 2\pi$.

Initial values of frame and inclination angles

It follows from $k_{1L}(t) = 0$ and $k_{2R}(u(t)) = 0$ that $\varphi_{1L}(t) = \pm\frac{\pi}{2}$ and $\varphi_{2L}(t) = \pm\frac{\pi}{2}$. In both cases, we decide to use the positive branch[1]. Furthermore, it follows that $\varphi'_{1L}(t) = \varphi'_{2R}(t) = 0$.

These two inclination angles determine the initial normal vectors of both frames, since by Equation (3.2), we have that

$$\begin{aligned}
\mathbf{P}_{1L}(0) &= \cos\varphi_{1L}(0)\ \mathbf{B}_1(0) + \sin\varphi_{1L}(0)\ \mathbf{N}_1(0) = \mathbf{N}_1(0) = \mathbf{N}_{1,0}, \\
\mathbf{P}_{2R}(0) &= \cos\varphi_{2R}(0)\ \mathbf{B}_2(0) + \sin\varphi_{2R}(0)\ \mathbf{N}_2(0) = \mathbf{N}_2(t) = \mathbf{N}_{2,0}.
\end{aligned}$$

[1]Experimentation suggests that this is the only valid choice, but we do not have an argument for that

Consequently, the initial binormal vectors read $\mathbf{B}_i(0) = \mathbf{B}_{i,0} = \mathbf{T}_{i,0} \times \mathbf{N}_{i,0}$.

The initial values of the frame specify the initial values of the other inclination angles as

$$\varphi_{1R,0} = \arctan\left(\mathbf{P}_{1R,0} \cdot \mathbf{B}_{1,0}, \mathbf{P}_{1R,0} \cdot \mathbf{N}_{1,0}\right) \quad \text{and} \quad \varphi_{2L,0} = \arctan\left(\mathbf{P}_{2L,0} \cdot \mathbf{B}_{2,0}, \mathbf{P}_{2L,0} \cdot \mathbf{N}_{2,0}\right).$$

Computation of the inclination angles and parametrization speed

Since $k_{1L}(t) = 0$, we use the approach discussed in Section 3.4.3 for $(A_1, B_1) = (L, R)$ and $(A_2, B_2) = (R, L)$, that is, $\varphi_{1A}(t) = \varphi_{1L}(t)$, $\varphi_{1B}(t) = \varphi_{1R}(t)$, $\varphi_{2A}(t) = \varphi_{2R}(t)$, and $\varphi_{2B}(t) = \varphi_{2L}(t)$.

Inserting $\varphi_{1L}(t) = \frac{\pi}{2}$ and $\varphi_{2R}(t) = \frac{\pi}{2}$ simplifies the three equations discussed in Section 3.4.3 in a system of three differential equations, that can be stated explicitly as follows

$$\begin{aligned}
u'(t) &= \frac{k_{1R}(t)}{k_{2L}(u(t))} \frac{\cos\varphi_{2L}(t)}{\cos\varphi_{1R}(t)} \frac{\sin\theta_{2R}(t)}{\sin\theta_{1L}(t)} \\
\varphi'_{1R}(t) &= k_{1R}(t) \left(-\frac{\sec\varphi_{1R}(t)}{\tan\theta_{1L}(t)} + \frac{\tan\varphi_{1R}(t)}{\tan\theta_{1R}(t)} \right) \\
\varphi'_{2L}(t) &= -k_{1R}(t) \frac{\sin\theta_{2R}(t)}{\sin\theta_{1L}(t)} \left(\frac{1}{\tan\theta_{2R}(t)} - \frac{\sin\varphi_{2L}(t)}{\tan\theta_{2L}(t)} \right) \sec\varphi_{1R}(t)
\end{aligned}$$

For $t \in [0, \frac{1}{8} - \iota)$, we then solve these three equations using the initial values $u(0) = 0$, $\varphi_{1R}(0) = \varphi_{1R,0}$ and $\varphi_{2L}(0) = \varphi_{2L,0}$.

Computation of the gluing curves and construction of surfaces

Upon a successful computations of the inclination angles and parametrization speed, we define the curvatures, $K_1(t)$ and $K_2(t)$, and torsions, $\tau_1(t)$ and $\tau_2(t)$, using Equation (3.35).

Finally, we integrate the corresponding Frenet-Serret equations (see Equation (3.1)). The first curve is parametrized by arc-length and starts at $\mathbf{X}_1(0) = \mathbf{P}$. Its Frenet frame has the initial values $(\mathbf{T}_{1,0}, \mathbf{N}_{1,0}, \mathbf{B}_{1,0})$. The second curve starts at $\mathbf{X}_2(0) = R \cdot \mathbf{P}$ and its parametrization speed is $u(t)$. Additionally, its frame has initial values $(\mathbf{T}_{2,0}, \mathbf{N}_{2,0}, \mathbf{B}_{2,0})$.

Finally, we construct the surfaces as a loft between the two curves $\mathbf{X}_1(t)$ and $\mathbf{X}_2(t)$, and either curve and $\mathbf{V}_2$.

5.2.3 Conclusion

Although we anticipated the integration to terminate prematurely, our observations indicated that upon successful computation of the scaffolding, that is, ι, $\mathbf{P}$, and $\mathbf{S}$, we usually also managed to derive solutions for the two systems of differential equations.[2] This suggest (numerical) existence of these variations of the squaricle. This could be attributed to the observation that the rulings of the central patch are almost parallel (appearing to be strictly parallel only in the symmetric case).

For cases with symmetric configurations, specifically when $\alpha = \frac{\pi}{4}$, it follows that $\iota = 0$, allowing for a constructive computation of the scaffolding. In such instances, the join-and-fan method explained in Section 8 can be employed to achieve a more straightforward computation, as discussed in Chapter 9 for cases where $r = 0$.

[2]Given the singularity of the system at $t = \frac{1}{8} - \iota$, our typical integration range was up to $t_{\max} = \frac{1}{8} - \iota - 10^{-6}$.

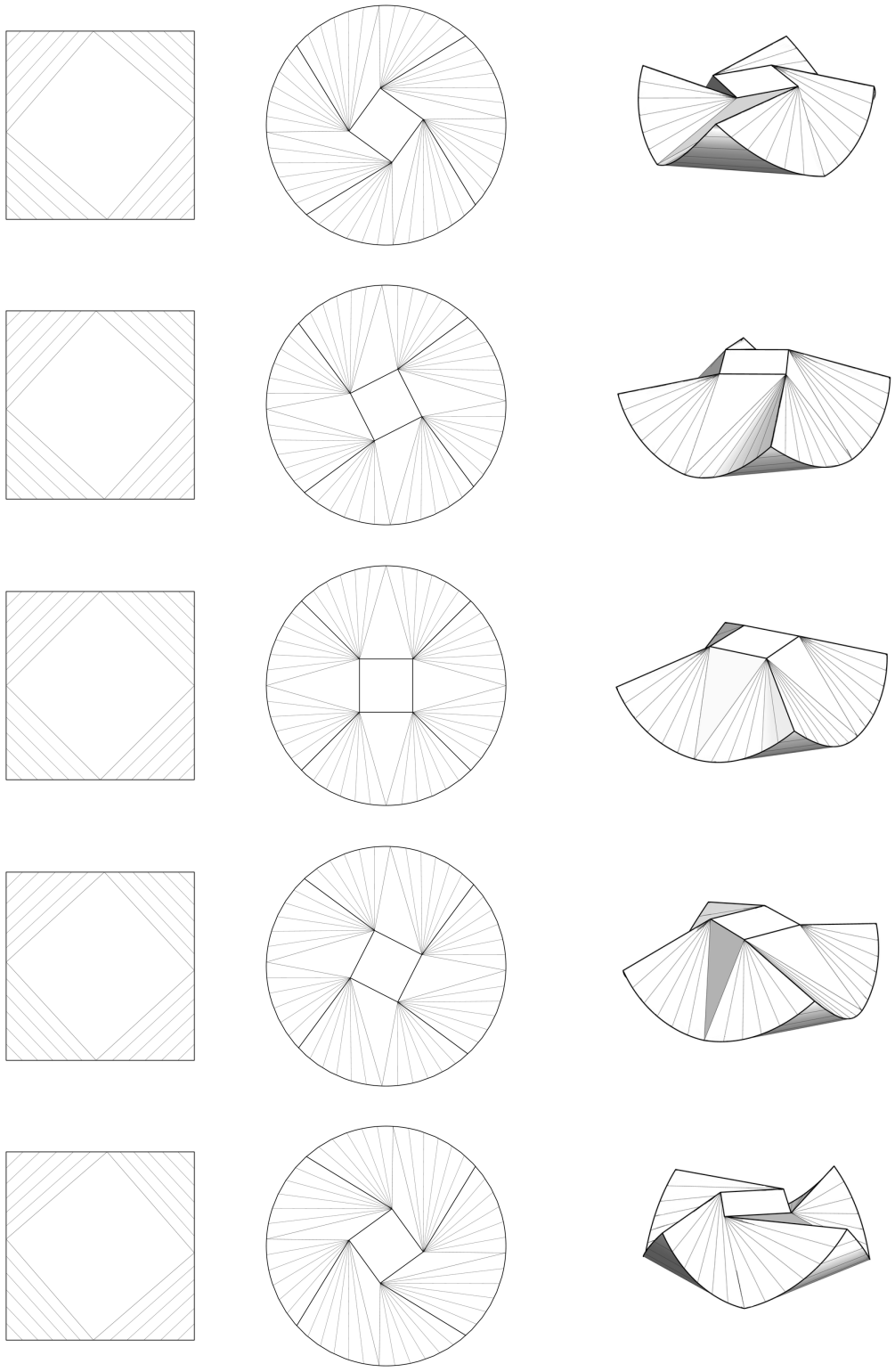

Figure 5.5: Squaricle variations for $r = 0.05$ and $\alpha \in (0.05\pi, -0.1\pi, -0.25\pi, -0.4\pi, -0.55\pi)$.

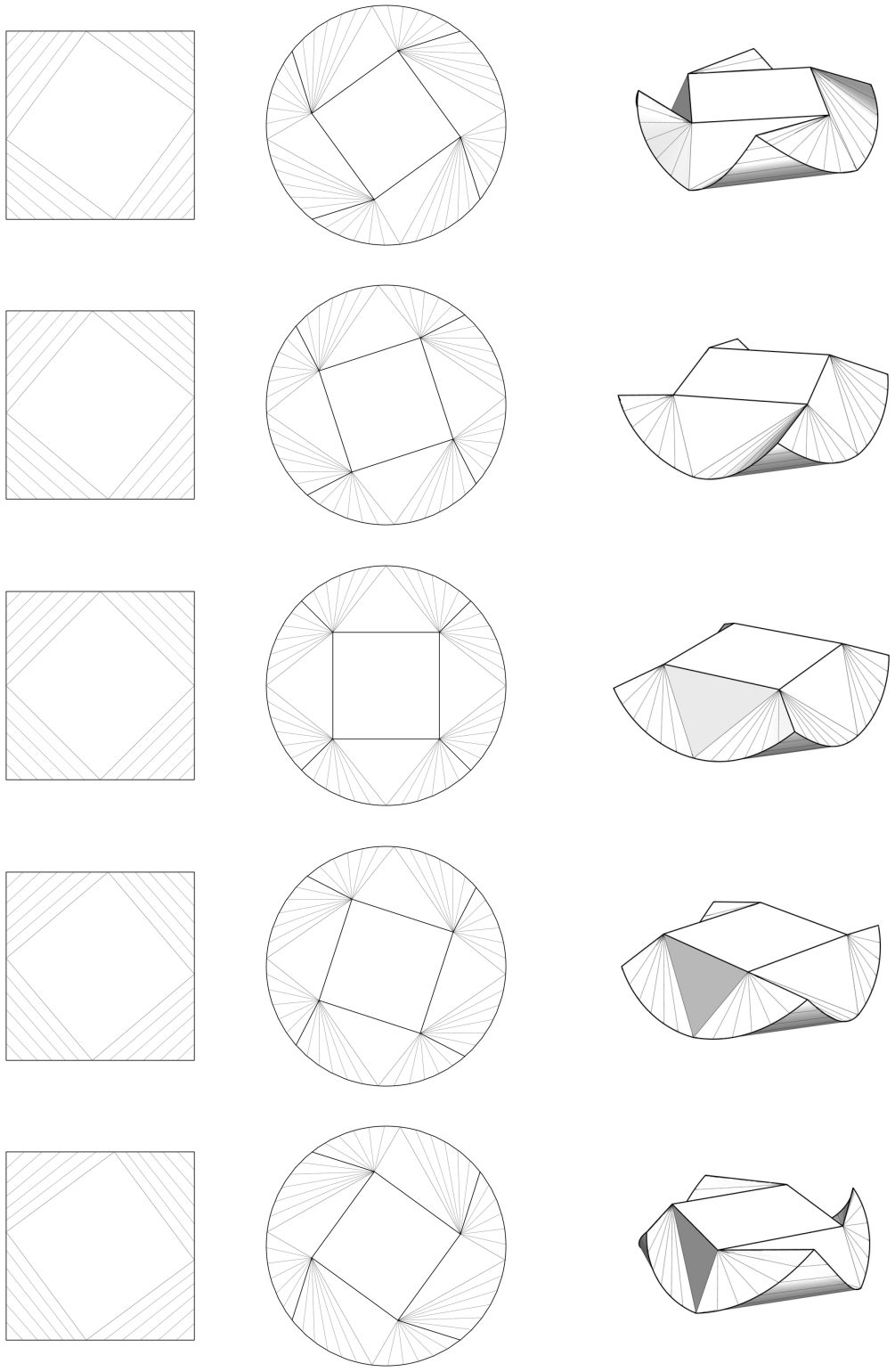

Figure 5.6: Squaricle variations for $r = 0.1$ and $\alpha \in (-0.05\pi, -0.15\pi, -0.25\pi, -0.35\pi, -0.45\pi)$.

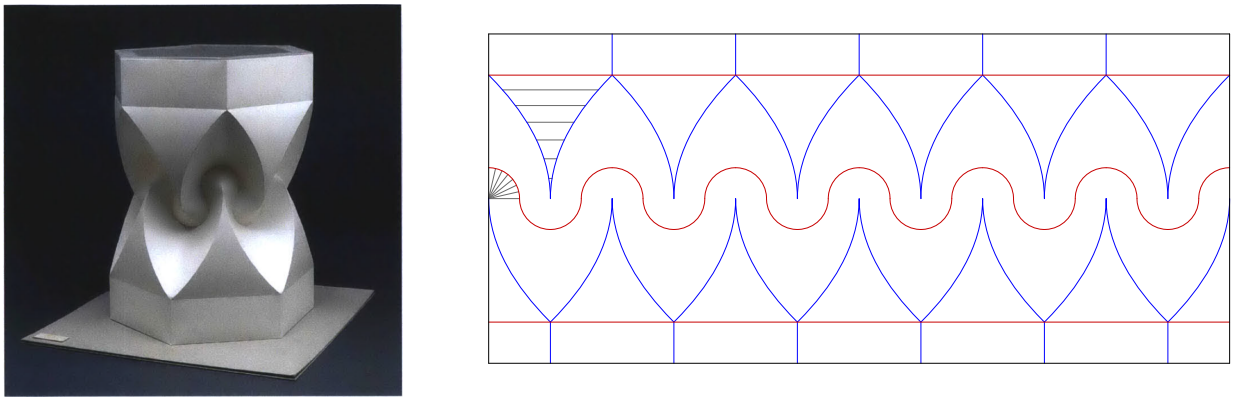

Figure 5.7: Left: Hexagonal tower with cusps (David Huffman, 1978), Figure 4.4.48 in Koschitz [43]. Not for reproduction. Right: Reconstructed crease pattern with guessed rulings.

5.3 Huffman's Hexagonal Tower

David Huffman's hexagonal tower is a result of his investigation into folding paper along conic creases. The studied shape's crease pattern consists of pairs of circular and parabolic arcs, which are positioned such that the parabola's focal point aligns with the circle's center. The circle's radius is selected to be half the focal length of the parabola, allowing for the regular tessellation of the pattern. In addition to the tessellation that produces a hexagonal tower, Huffman also experimented with a quadrangular base [43].

5.3.1 Ruling Analysis

We begin by analyzing the folded shape to form an informed hypothesis about the ruling patterns of the patches; see Figure 5.7 (right). Given that the folded shape exhibits rotational symmetry indicates that the area between two adjacent parabolic arches is cylindrically ruled. On the other hand, the section connecting the intersection of two neighboring parabolas to the circular arc must be, at the very least, locally conically ruled. In the subsequent discussion, we will assume that the entire half-circle is a cone, in line with the indications from the folded shape and existing analysis of Koschitz [43] and Demaine et al. [18].

In the upcoming computation, our initial focus will be only on one of the modules of the shape. One module consists the conical and cylindrical patches, along with the central patch whose ruling pattern is unknown. In the computation, our goal is to determine the rulings of the central patch to create a compatible connection between the cylinder and a cone. Our computations provide a family of folded states that can be influenced by the initial values of the fold angles.

Ultimately, our goal is to achieve complete closure of the shape corresponding to an appropriate arrangement of folded modules. First, we encounter the problem that fully covering the computed surface with a single singularity-free developable patch may not achieve the curvature required for full closure. Consequently, we follow the same strategy as Demaine et al. [18] in the discretized simulation. Specifically, we allow the rulings to come closer together (on the side closer to the circle), resulting in a not fully covered circular crease. To avoid gaps in the shape, we append two cones connected by a circular curved crease to either side, whose apices align with the endpoints of the parabola. This strategic combination of rulings ensures the necessary curvature of the patches and, upon proper assembly, results in a (numerically) closed tower.

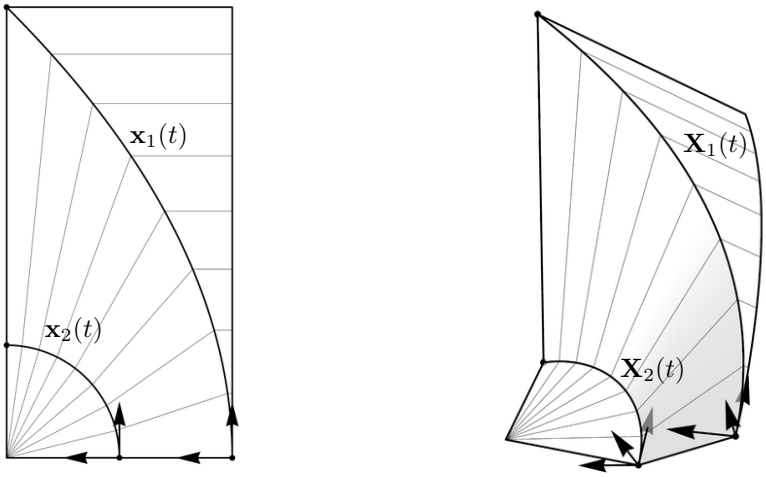

Figure 5.8: Folding of the first module.

5.3.2 Computation

Parametrization of the development

In the following, we study the creasing of a part of a crease pattern that consists of a single parabolic and circular arc that share the same center and focal point respectively; see Figure 5.8. Specifically, we choose the common center to coincide with the origin, the circle to have radius one, and the parabola to pass through point $(2, 0, 0)$.

To apply the discussed method, we parametrize the rulings with a parameter t. Since a closed-form of the arc-length parametrization of a parabola is not known (to the best of my knowledge), we want to avoid solving for a function that needs to be evaluated at the arc-length parametrization of the parabola's curvature. Therefore, we assume that the function $s_2(t)$, which corresponds to the arc-length parameter of the circle, is unknown. Specifically, we let $\mathbf{x}_1(t)$ be the (numerically approximated) arc-length parametrization of the parabola[3] starting at point $\mathbf{x}_1(0) = (2, 0, 0)$ and ending at point $\mathbf{x}_1(t_{\max}) = (0, 4, 0)$. Furthermore, let $\mathbf{x}_2(s)$ denote the arc-length parametrization of the circle,

$$\mathbf{x}_2(s) = (\cos s, \sin s, 0)\,.$$

In the following, we parametrize the ruling polylines by $s_1(t) = t$ and $s_2(t) = u(t)$.

Additionally, we set the ruling directions of the left and right patch to be

$$\mathbf{r}_{1R}(t) = (-1, 0, 0) \qquad \text{and} \qquad \mathbf{r}_{2L}(t) = -\frac{\mathbf{x}_2(u(t))}{|\mathbf{x}_2(u(t))|}.$$

[3] A parabola can be parametrized by polar coordinates by

$$\tilde{\mathbf{x}}_1(\phi) = \frac{4}{1+\cos\phi}\,(\cos\phi, \sin\phi, 0)\,.$$

Then the parametrization speed is

$$\tilde{s}'(\phi) = 2\sec^3\frac{\phi}{2} \qquad \text{resulting in} \qquad \tilde{s}(\phi) = 2\left(\operatorname{arctanh}\left(\sin\frac{\phi}{2}\right) + \sec\frac{\phi}{2}\tan\frac{\phi}{2}\right).$$

In the following computations, we set $\mathbf{x}_1(s) = \tilde{\mathbf{x}}_1(\tilde{s}^{-1}(\tau))$. A closed form of the inverse is not known (I think).

Consequently, the corresponding ruling angles read

$$\theta_{1R}(t) = \arctan\left(\mathbf{r}_{1R}(t) \cdot \mathbf{t}_1(t), \mathbf{r}_{1R}(t) \cdot \mathbf{n}_1(t)\right)$$
$$\theta_{2L}(t) = \arctan\left(\mathbf{r}_{2L}(t) \cdot \mathbf{t}_2(u(t)), \mathbf{r}_{2L}(t) \cdot \mathbf{n}_2(u(t))\right)$$

where $\mathbf{t}_i(s)$ and $\mathbf{n}_i(s)$ denote the tangent and normal vectors of $\mathbf{x}_i(s)$. In addition, we use Equation (3.24) to define the ruling direction $\mathbf{r}_{1L}(t) = \mathbf{r}_{2R}(t)$ of the central patch, and Equation (3.25) and Equation (3.26) to define their corresponding ruling angles $\theta_{1L}(t)$ and $\theta_{2R}(t)$.

Finally, we denote the curvature of the parabolic arc $\mathbf{x}_1(s)$ at arc-length parameter by $k_1(s)$. The curvature of the circle is $k_2(s) = 1$.

Computation of the inclination angles and parametrization speed

We use the system of differential equations in Equation (3.39) to compute the inclination angles and the unknown parametrization speed. To cover the full central area, we set $u(0) = 0$. The combination of initial values of the inclination angles influences the value of $u(t_{\max})$. To get a full covering of the central patch, we aim for $u(t_{\max}) = \frac{\pi}{2}$; see Figure 5.8. It appears that if the initial value of one inclination angle remains the same, changing the other appropriately results in solutions with the desired property.

Computation of the crease curves and construction of surfaces

Upon a successful computation of $u(t)$, $\varphi_1(t)$, and $\varphi_2(t)$, we define the curvatures $K_i(t)$ and torsions $\tau_i(t)$ using Equation (3.40).

To obtain a suitable combination of the initial points and vectors of the curves and their frames, we follow the strategy outlined in Section 3.4.3, Scenario 2.

Arranging surfaces

Finally, we attempt to arrange the surfaces to form the full shape. To do that, we first rotate all three surfaces by π about the bisector of the first two rulings of the central and right patch, that is, the line with direction $\mathbf{D} = \mathbf{R}_{2L}(0) - \mathbf{R}_{1R}(0)$ passing through $\mathbf{X}_2(0)$. Let $T : \mathbf{X} \mapsto R_\pi \cdot (\mathbf{X} - \mathbf{X}_1(0)) + \mathbf{X}_1(0)$ denote the corresponding transformation, where R_π indicates the corresponding rotation matrix about π around $\mathbf{D}$. Furthermore, let Π be the base plane of the cylinder, that is, a plane perpendicular to $\mathbf{R}_{1R}(t)$ (which is constant) passing through $\mathbf{X}_1(0)$.

For the folded patches to form a closed shape, we require the following four constraints to be met (see Figure 5.3.2):

- *Constraint 1:* As mentioned, to cover the full area of the central patch, we require $u(t_{\max}) = \frac{\pi}{2}$.
- *Constraint 2:* To allow for the surfaces to be reflected and aligned in a polar array, we require that $T(\mathbf{X}_1(t_{\max})) \in \Pi$.
- *Constraint 3:* Additionally, to ensure that there is no gap or intersection along the reflected surfaces, we also need $T(\mathbf{X}_2(u(t_{\max}))) \in \Pi$.
- *Constraint 4:* Finally, for the shape to close up, we require that the angle between consecutive cylinders is appropriate. In the case of an hexagonal column, the angle between $\mathbf{R}_{1L}(0)$ and $R_\pi \cdot \mathbf{R}_{1L}(0)$ should be $\frac{5\pi}{6}$.

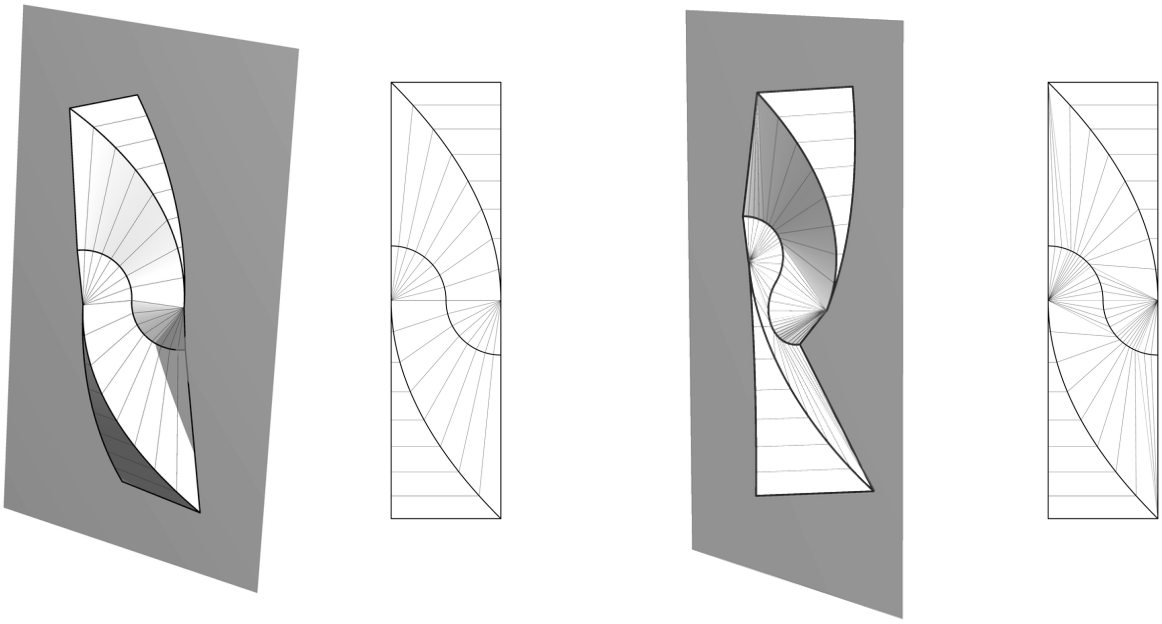

(a) Not aligned boundaries.

(b) Aligned boundaries.

Figure 5.9: Composition of two modules of Huffman's tower.

Within our assumptions, these four conditions can only be influenced by two initial values for the inclination angles. Experimentally, we were not able to find values that would satisfy all four constraints. Consequently, we resorted to the following approach to allow for more flexibility in the design.

Modified approach with circular creases

In this modified approach, we let the initial value $u(0)$ vary too (within reasonable bounds $0 < u(0) < \frac{\pi}{2}$). This results in a potentially not fully covered circle. To avoid gaps, we fill the holes with two cones connected by circular creases to either side. In the following, we assume that we have obtained a folding of parts of the three patches, and proceed with discussing how to compute and append the remaining conical patches.

We divide the circular arc into three parts. In the following, we use subscripts "S" and "E" to indicate whether the newly introduced circular creases between cones belong to the "start", that is, the circular segment $\mathbf{x}_S(s) = \mathbf{x}_2(s)$ where $s \in [0, u(0)]$, or "end", that is, the circular segment $\mathbf{x}_E(s) = \mathbf{x}_2(s)$ where $s \in [u(t_{\max}), \frac{\pi}{2}]$.

Parametrization of the development. We define the the left ruling directions of both patches to be

$$\mathbf{r}_{S,L}(s) = \mathbf{r}_{E,L}(s) = -\frac{\mathbf{x}_2(s)}{|\mathbf{x}_2(s)|}.$$

In addition, we define the right ruling directions as

$$\mathbf{r}_{S,R}(s) = \frac{\mathbf{x}_2(s) - \mathbf{x}_1(0)}{|\mathbf{x}_2(s) - \mathbf{x}_1(0)|}, \qquad \text{and} \qquad \mathbf{r}_{E,R}(s) = \frac{\mathbf{x}_2(s) - \mathbf{x}_1(t_{\max})}{|\mathbf{x}_2(s) - \mathbf{x}_1(t_{\max})|}.$$

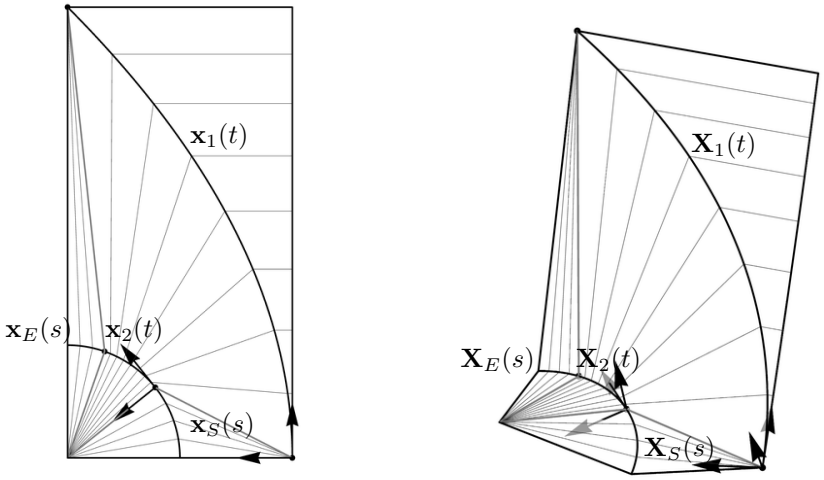

Figure 5.10: Notation and folding of the modified module.

The corresponding ruling angles $\theta_{S,R}(t)$, $\theta_{S,L}(t)$, $\theta_{E,R}(t)$ and $\theta_{E,L}(t)$ follow similar to Equation (3.25) and Equation (3.26).

Computation of the inclination angles and parametrization speed. For the beginning and end, we compute $\varphi_S(t)$ and $\varphi_E(t)$ from Equation (3.21).

To obtain (tangent) continuous transitions, we set the initial values of the inclination angles to match the corresponding start and end values of $\varphi_2(t)$. Specifically, we set $\varphi_S(u(0)) = \varphi_2(0)$ and $\varphi_E(u(t_{\max})) = \varphi_2(t_{\max})$.

Computation of the crease curves and construction of surfaces. We use Equation (3.22) to define the curvatures $K_S(t)$ and $K_E(t)$, and torsions $\tau_S(t)$ and $\tau_E(t)$.

To obtain tangent-continuous transitions, we start the integration of the Frenet-Serret equations at the respective frames at the end points of $\mathbf{X}_2(t)$. Specifically, we set set $\mathbf{X}_S(u(0)) = \mathbf{X}_2(0)$, $\mathbf{X}_E(u(t_{\max})) = \mathbf{X}_2(t_{\max})$, and

$$(\mathbf{T}_S(u(0)), \mathbf{N}_S(u(0)), \mathbf{B}_S(u(0))) = (\mathbf{T}_2(0), \mathbf{N}_2(0), \mathbf{B}_2(0))$$
$$(\mathbf{T}_E(u(t_{\max})), \mathbf{N}_E(u(t_{\max})), \mathbf{B}_E(u(t_{\max}))) = (\mathbf{T}_2(t_{\max}), \mathbf{N}_2(t_{\max}), \mathbf{B}_2(t_{\max})).$$

Upon successful computation, we construct the cones using the ruling directions (Equation (3.41) and Equation (3.42)) or as a central extrusion between the curve and corresponding apices.

Numerical closure of shape

With the modified approach we have one more degree of freedom, the initial value of $u(t)$, while no longer requiring the first constraint (we no longer require $u(t_{\max}) = \frac{\pi}{2}$). The second and fourth constraint remains unchanged, while the third is modified to $T(\mathbf{X}_E(\pi)) \in \Pi$. Note that transformation T is modified to rotate by π about the bisector of the first rulings of the cones adjacent to $\mathbf{X}_S(s)$.

To measure the suitability of a configuration, we introduce the following error measurements:

- *Error corresponding to Constraint 2:* $e_1 = \mathbf{R}_{1R} \cdot \frac{T(\mathbf{X}_1(t_{\max})) - \mathbf{X}_1(0)}{|T(\mathbf{X}_1(t_{\max})) - \mathbf{X}_1(0)|}$

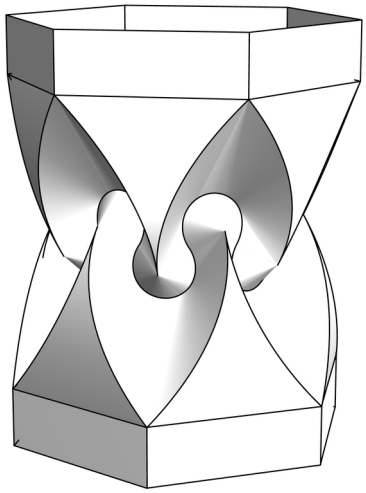

Figure 5.11: Final assembled Huffman's hexagonal tower.

- *Error corresponding to Constraint 3:* $e_2 = \mathbf{R}_{1R} \cdot \frac{T(\mathbf{X}_E(\frac{\pi}{2})) - \mathbf{X}_1(0)}{\left|T(\mathbf{X}_E(\frac{\pi}{2})) - \mathbf{X}_1(0)\right|}$
- *Error corresponding to Constraint 4:* $e_3 = \mathbf{R}_{1R} \cdot (R \cdot \mathbf{R}_{1R}) - \cos\frac{5\pi}{6}$.

Using numerical minimization in Mathematica (with manual help to find a good initial guess), we obtain the following initial values

$$(u_0, \varphi_{1,0}, \varphi_{2,0}) = \{0.6015913936768009, -0.7753374025984491, 0.6754673354175101\}.$$

A computation with $u(0) = u_0$, $\varphi_1(0) = \varphi_{1,0}$, and $\varphi_2(0) = \varphi_{2,0}$, results in a solution where

$$(e_1, e_2, e_3) = (1.4 \cdot 10^{-9}, -1.02 \cdot 10^{-10}, 6.22 \cdot 10^{-15}).$$

Consequently, appropriately assembling the modules results in a (numerically) closed shape. To better match David Huffman's design, we add planar faces at the top and bottom of the shape.

5.3.3 Conclusion

We were able to obtain a precise numerical approximation of Huffman's shape that closes up to numerical error. Consequently, we conjecture that the shape exists with the proposed ruling pattern.

Variations of this shape can be obtained by changing the shapes of the involved creases, such as replacing the parabolic crease with circular creases [19]. Figure 5.12 shows two variations with strategically positioned circles. The shapes are computed with an analogous approach to the presented method.

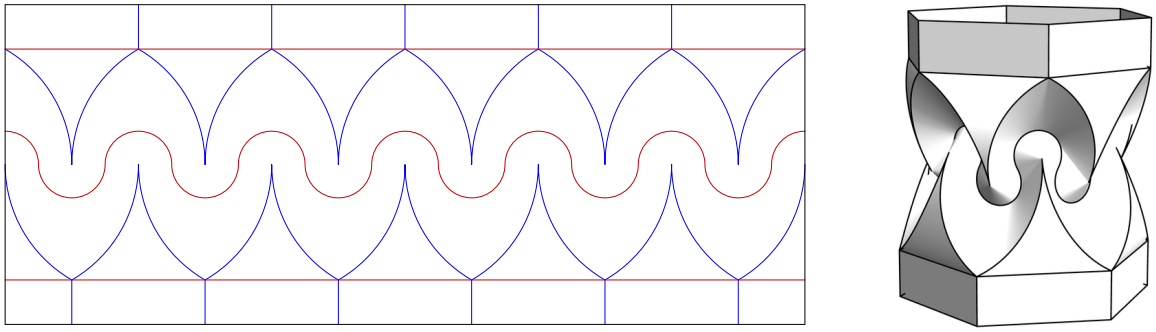

(a) Circular creases with radius $r = 4$.

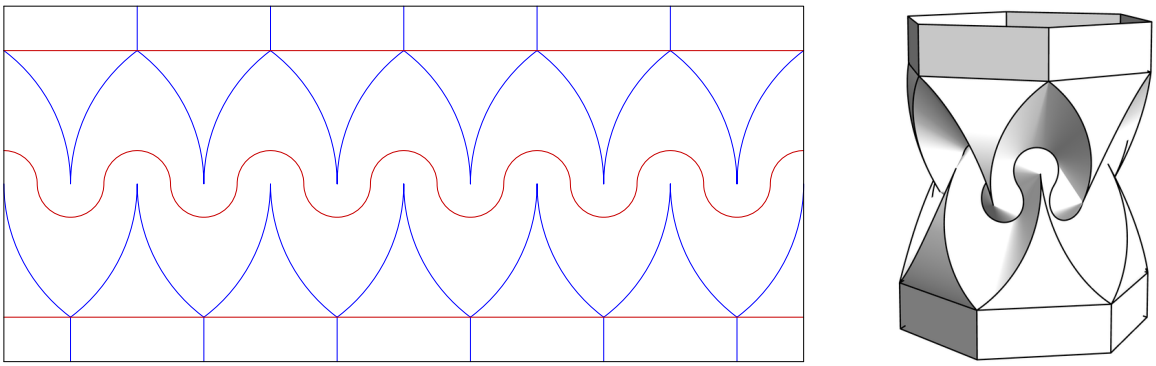

(b) Circular creases with radius $r = 5$.

Figure 5.12: Variations of David Huffman's hexagonal tower with circular creases.

Chapter 6

Connecting Two Planar or Constant Fold Angle Creases

The content of this chapter is unpublished.

Overview

In this chapter, we focus on the second application, which involves joining three patches using partial ruling information and specifying the glue curves to be either planar creases or creases with a constant fold angle. In the case of the latter, appropriate combinations of inclination angles result in a rigid folding motion. The examples considered include Maximilian Klammer's kinetic sculpture "Polyannular Cyclide" and two logarithmic spiral curves folded with constant fold angle.

6.1 Introduction

In certain applications, prescribing the type of crease has practical implications. For instance, as demonstrated in the following examples, defining a patch to be bounded by two planar creases allows for patches to be wedged between planes and arranged using reflections. On the other hand, prescribing constant angle creases facilitates rigid-ruling folding motions.

However, achieving a scenario where both creases are either planar or of constant angle is not straightforward. For a single crease, selecting a specific ruling angle function, along with the crease type (either planar or of constant angle), determines the direction of the other incident ruling. When adding a second patch along a specified curve, the ruling angles of this new patch may not correspond to a planar or constant-angle crease. As a result, insisting on both creases being planar or of constant angle defines the rulings of the three patches. While it is possible to combine both types – asking for one crease to be planar and the other to maintain a constant fold angle – this may not always be practical.

In Section 6.2, we examine the kinetic sculpture shown in Figure 6.1. Maximilian Klammer designed this sculpture for his Master's thesis at the Academy of Fine Arts Vienna [42]. The sculpture consists of twenty-four circular segments, alternately joined along their curved boundaries. Without further constraints, this configuration permits numerous degrees of freedom. In our discussion, we will focus on instances where the gluing curves are constrained to lie in rotationally symmetric planes, all enclosing equal angles. The motion proposed by Max Klammer is steered by a circular opening, as illustrated in Figure 6.1. By reconstructing this shape, we observe that the circular

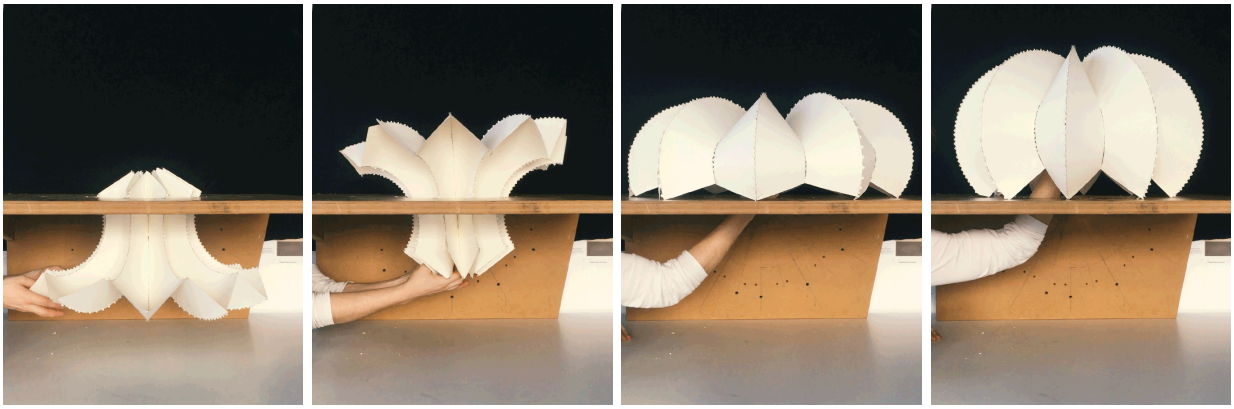

Figure 6.1: Kinetic sculpture “Polyannular Cyclide” from annuli designed by Maximilian Klammer.

patches move on developable surfaces whose shape is determined by the opening angle of the two planes and the radius of the opening.

In the second example, we focus on creasing along two logarithmic spirals. We chose this particular example for two reasons: first, unlike the previous examples, here both curves do not exhibit a constant curvature; second, we aimed to experimentally validate our intuition concerning a fully folded state. We conjecture that, in the limit, two constant-angle creases allow a fully folded state where all rulings become parallel. This would be analogous to the flat folded state of discretizations of curved-crease patterns that have rows of flat-foldable vertices.

6.2 Kinetic Sculpture from Annuli

In the upcoming sections, we use the discussed methods to compute the developable surfaces involved in the kinetic sculpture displayed in Figure 6.3. Specifically, we will demonstrate how to position a region bounded by two concentric circles such that the circular boundaries lie in two intersecting planes. By arranging the resulting bent patches appropriately, we obtain a configuration of the kinematic sculpture. We show that, given a circular opening, the developable patches move along fixed developable surfaces throughout the motion, provided they are sufficiently constrained to do so.

6.2.1 Computation

Since we constrain the overall shape to exhibit n-fold rotational symmetry, we would like to ensure that the gluing curves are planar. However, finding an appropriate ruling layout based solely on a paper model is not straightforward. Simply connecting the two curves with rulings perpendicular to both curves results in a conical ruling. When the corresponding conical patch is bent, both boundary curves lie in parallel planes. The boundaries of the patches involved in the sculpture, however, are contained in intersecting planes.

To find appropriate rulings, we apply the approach of joining three patches along curved creases, as described in Section 3.4.4. Specifically, we view the circular boundary curves as planar creases, as depicted in Figure 6.2. In the following section, we assume that one circular crease (or boundary) is parametrized by arc length and demonstrate how to determine the parametrization of the second curve that results in a valid combination of two curved creases.

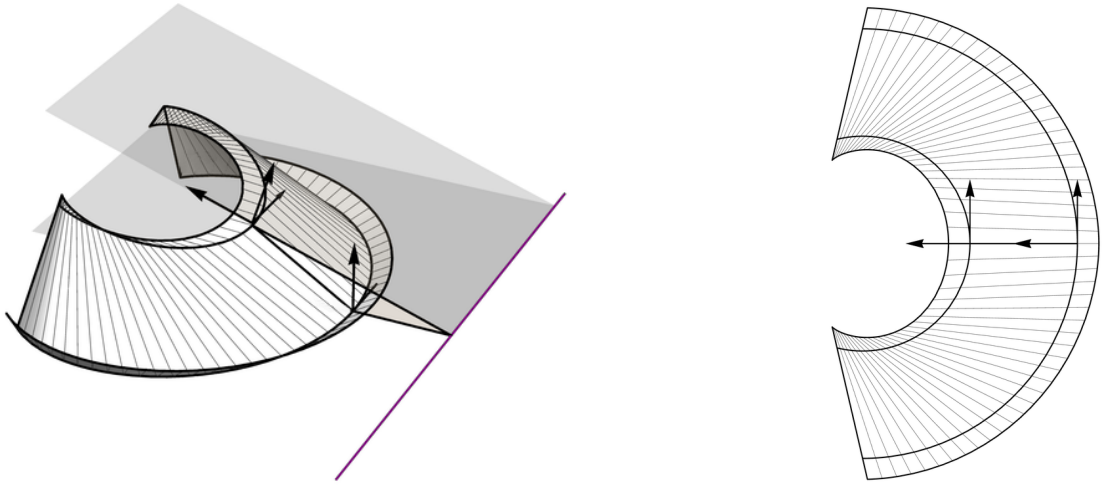

Figure 6.2: Illustration of the computational approach for the analysis of the kinetic sculpture.

Parametrization of the development

In the following, we consider the patch between two developed circles with radius r_1 and r_2. These circles can be parametrized by arc length as follows:

$$\mathbf{x}_i(s) = r_i \left(\cos \frac{s}{r_i}, \sin \frac{s}{r_i}, 0 \right).$$

There are multiple possible ways to set-up the assumption about the parametrization to use the method discussed in Section 3.4.4. In the following, we assume $s_1(t) = r_1 t$ and $s_2(t) = r_2(t + u(t))$ for some unknown function $u(t)$.

Since we consider planar creases, all ruling directions are the same and can be parametrized by

$$\mathbf{r}(t) = \mathbf{r}_{1R}(t) = \mathbf{r}_{1L}(t) = \mathbf{r}_{2R}(t) = \mathbf{r}_{2L}(t) = \frac{\mathbf{x}_2(s_2(t)) - \mathbf{x}_1(s_1(t))}{|\mathbf{x}_2(s_2(t)) - \mathbf{x}_1(s_1(t))|}.$$

To compute the ruling angles, recall that the tangent and normal of $\mathbf{x}_i(s)$ read

$$\mathbf{t}_i(s) = \left(-\sin \frac{s}{r_i}, \cos \frac{s}{r_i}, 0 \right) \qquad \text{and} \qquad \mathbf{n}_i(s) = -\left(\cos \frac{s}{r_i}, \sin \frac{s}{r_i}, 0 \right).$$

To simplify the equations, we assume without loss of generality that $r_1 = 1$ and $r_2 = r$ for some $0 < r < 1$. Then, the ruling angles in Equation (3.25) and Equation (3.26) can be expressed as follows:

$$\theta_{1L}(t) = \theta_{1R}(t) = \arctan\left(r \sin u(t), 1 - r \cos u(t)\right), \tag{6.1}$$

$$\theta_{2L}(t) = \theta_{2R}(t) = \arctan\left(\sin u(t), \cos u(t) - r\right). \tag{6.2}$$

Initial values

The function $u(t)$ measures the deviation of the ruling directions from being perpendicular to both curves. To avoid undesired artifacts such as intersecting rulings or rulings that exceed the circular region, we aim for the absolute value of $u(t)$ to be small.

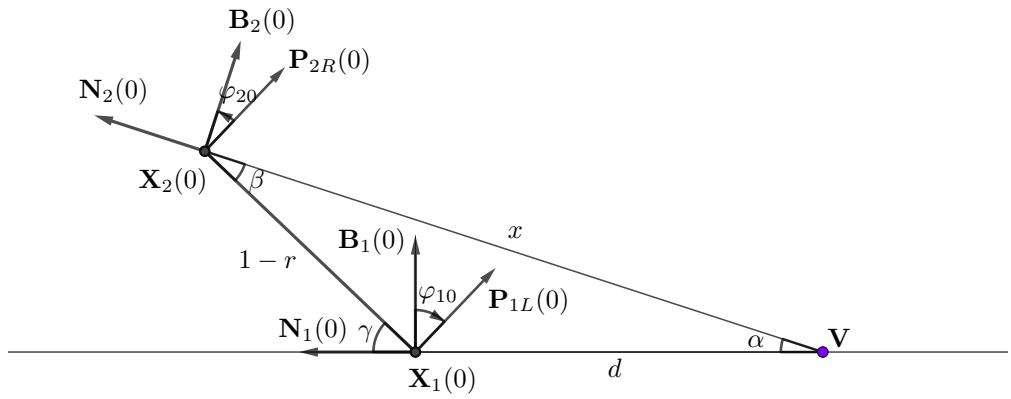

Figure 6.3: Illustration of the construction of the initial values in Section 6.2.1.

For reasonable initial values, the system of equations provides a local solution. To facilitate a geometric interpretation of the resulting curves, we consider solutions corresponding to symmetric initial values at $t = 0$. Specifically, we set $u(0) = 0$, resulting in parallel developed tangents at $t = 0$, which imply parallel tangents in 3D. Since these tangents lie in the two base planes, the 3D ruling corresponding to $t = 0$ lies in a plane perpendicular to the intersection of the two base planes; see Figure 6.2.

We connect the initial values of the inclination angles to the angle α between the two base planes and the distance d between the initial point $\mathbf{X}_1(0)$ and the common axis. For this purpose, we study the triangle composed of $\mathbf{X}_1(0)$, $\mathbf{X}_2(0)$, and $\mathbf{V}$, the base point of $\mathbf{X}_i(0)$ on the intersection of the base planes.

Note that the distance between $\mathbf{X}_1(0)$ and $\mathbf{X}_2(0)$, the length of the ruling at $u(0)$, is $1 - r$. Consequently, using trigonometric identities (see Figure 6.3), we can obtain the remaining length of the triangle:

$$x = \operatorname{dist}(\mathbf{V}, \mathbf{X}_2(0)) = d\cos\alpha + \sqrt{(1-r)^2 - \frac{d^2}{2}\left(1 - \cos(2\alpha)\right)}$$

and the angles:

$$\gamma = \arcsin\left(\frac{x}{1-r}\sin\alpha\right) \qquad \text{and} \qquad \beta = \pi - \alpha - (\pi - \gamma).$$

The (oriented) initial angles are $\varphi_{10} = -\gamma$ and $\varphi_{20} = \beta$.

In our computations, we use $\mathbf{T}_{1,0} = (1, 0, 0)$, $\mathbf{N}_{1,0} = (-1, 0, 0)$, $\mathbf{B}_{1,0} = \mathbf{T}_{1,0} \times \mathbf{N}_{1,0}$. Additionally, we set $\mathbf{T}_{2,0} = \mathbf{T}_{1,0}$, $\mathbf{B}_{2,0} = \cos\delta\, \mathbf{N}_{1,0} + \sin\delta\, \mathbf{B}_{1,0}$, where $\delta = \frac{\pi}{2} - \varphi_{1,0} + \varphi_{2,0}$, and $\mathbf{N}_{2,0} = \mathbf{B}_{2,0} \times \mathbf{T}_{2,0}$. Finally, let $\mathbf{X}_1(0) = (-d, 0, 0)$ and $\mathbf{X}_2(0) = \mathbf{X}_1(0) + (1 - r)(\cos\gamma\, \mathbf{N}_{1,0} + \sin\gamma\, \mathbf{B}_{1,0})$.

Figure 6.4a shows configurations with common angle α but varying distances d. On the other hand, Figure 6.4b shows shapes sharing a common distance d that vary in angle α.

Computation of the inclination angles and parametrization speed

Using Equation (6.1), Equation (6.2), and the assumptions about the arc-length parameters $s_1(t)$ and $s_2(t)$, the system of differential equations for $u(t)$, $\varphi_1(t)$, and $\varphi_2(t)$ in Equation (3.44) simplifies

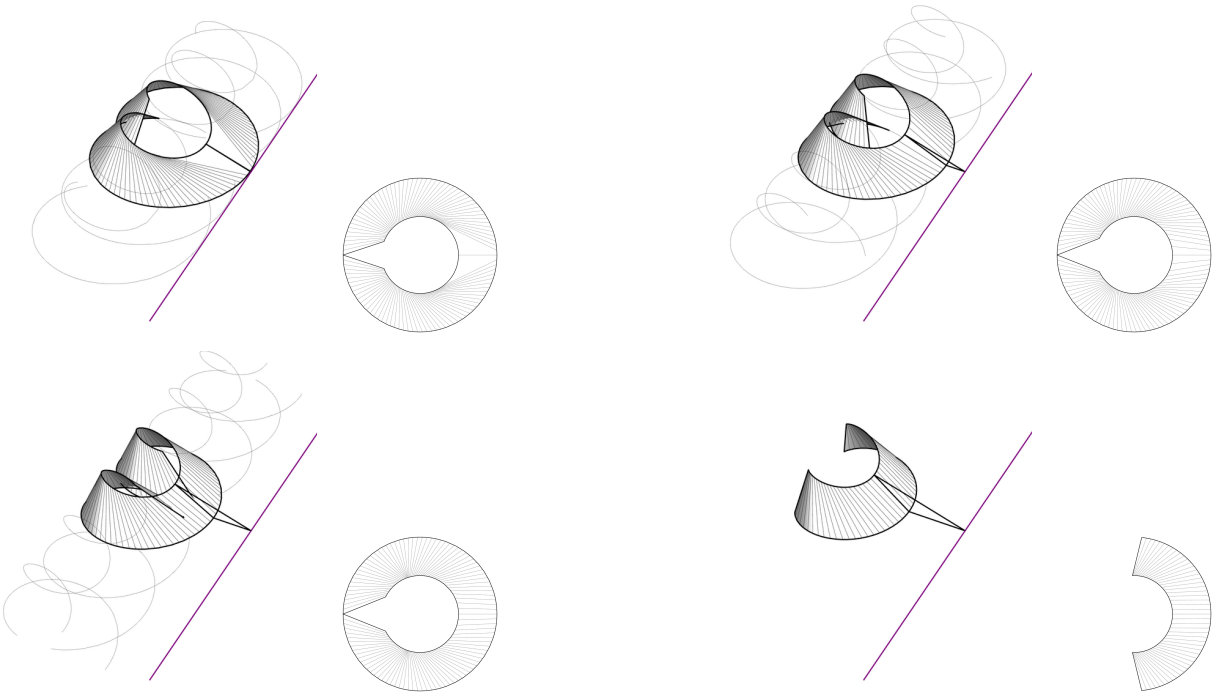

(a) Opening angle $\alpha = \frac{\pi}{10}$ and distances $d \in (0.01, 0.2, 0.4, 0.6)$.

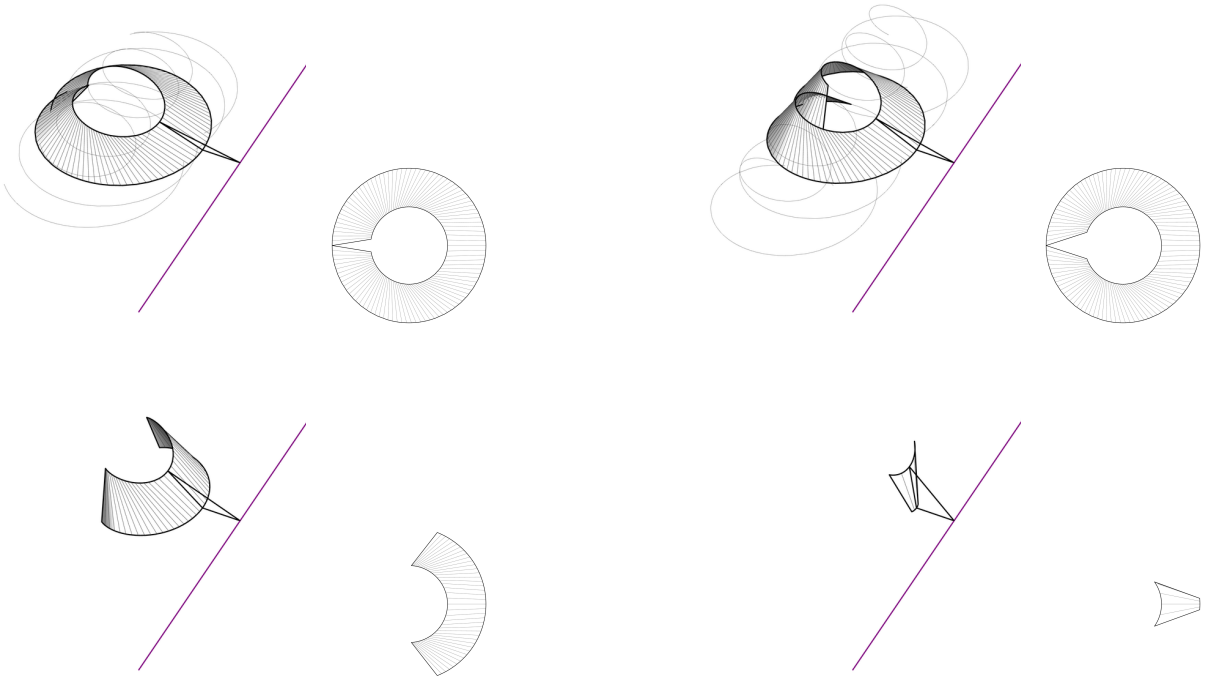

(b) Opening angles $\alpha \in \left(\frac{2\pi}{32}, \frac{2\pi}{24}, \frac{2\pi}{16}, \frac{2\pi}{8}\right)$ and distance $d = 0.4$.

Figure 6.4: Illustration of solutions for $r = \frac{1}{2}$ corresponding to different initial values.

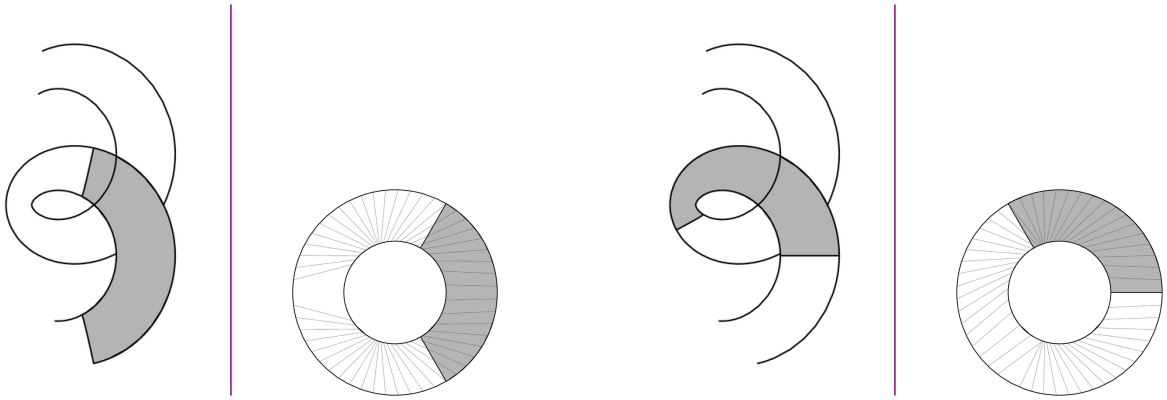

Figure 6.5: Illustration of a motion of a circular patch.

to

$$\begin{aligned} u'(t) &= -1 - \frac{(\cos u(t) - r)\tan\varphi_1(t)}{(1 - r\cos u(t))\tan\varphi_2(t)} \\ \varphi_1'(t) &= \frac{r\sin u(t)}{1 - r\cos u(t)}\tan\varphi_1(t) \\ \varphi_2'(t) &= -\frac{\sin u(t)}{1 - r\cos u(t)}\tan\varphi_1(t). \end{aligned} \tag{6.3}$$

Note that $\varphi_1'(t) = -r\varphi_2'(t)$, which yields $\varphi_1(t) = -r\varphi_2(t) + c$. However, despite this relationship, we could not find a closed-form solution of the given system.

We also observe that the existence of a unique real-valued solution implies that it is periodic. An argument for this property of the system follows from Kotin [45]. Firstly, note that the system of equations in Equation (6.3) can be expressed using a function $f(\mathbf{x}) : \mathbb{R}^6 \to \mathbb{R}^3$ as follows:

$$f(u(t), \varphi_1(t), \varphi_2(t), u'(t), \varphi_1'(t), \varphi_2'(t)) = \mathbf{0}. \tag{6.4}$$

Additionally, functions that satisfy Equation (6.4) also satisfy

$$f(-u(t), \varphi_1(t), \varphi_2(t), u'(t), -\varphi_1'(t), -\varphi_2'(t)) = \mathbf{0}.$$

Furthermore, we have the initial condition $u(0) = 0$. It follows from Lemma 1 in Kotin [45] that $u(t) = -u(-t)$, $\varphi_1(t) = \varphi_1(-t)$, and $\varphi_2(t) = \varphi_2(-t)$. Moreover, if there exists a parameter D with $u\left(\frac{D}{2}\right) = 0$, then $u(t+D) = \varphi_1(t+D) = \varphi_2(t+D) = 0$ by Theorem 1 in Kotin [45]. We numerically solve the system and observe that, given suitable initial values, the obtained solutions were unique and periodic.

Figure 3-6: Illustration of a motion of a circular patch.

Computation of the crease curves and construction of surfaces

We obtain the 3D curvatures with Equation (3.40) (the torsion of a planar curve is zero). Finally, we find the curves by integrating the Frenet-Serret equations with appropriate initial orthonormal frames and points as discussed earlier (see Figure 6.3). Finally, we construct the surface by computing a linear loft between $\mathbf{X}_1(t)$ and $\mathbf{X}_2(t)$.

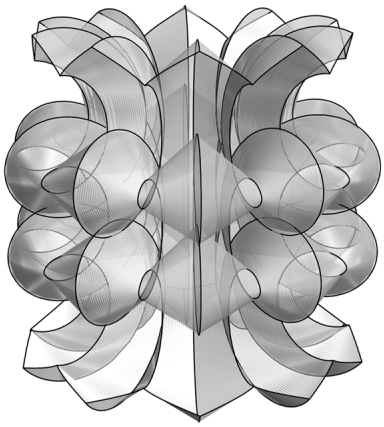

Figure 6.6: Shape from periodic developable patches that contains the configurations of a variation of the sculpture.

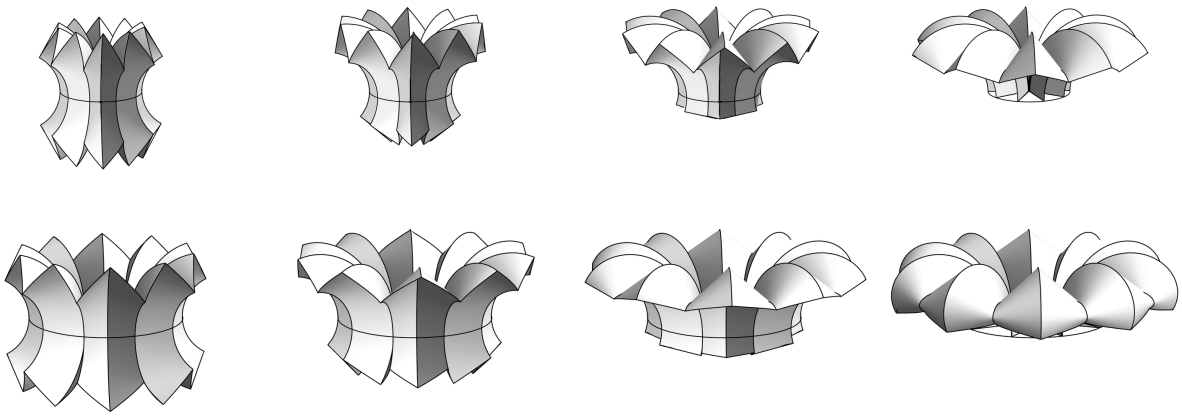

Figure 6.7: Illustration of the kinetic motion of two variations of the the sculpture.

6.2.2 Kinetic Motion

Three or two of the four solutions presented in Figure 6.4a and Figure 6.4b, respectively, result in (numerically computed) periodic solutions that allow infinite propagation. However, in reality, we only consider a finite segment, such as a circular segment with an opening angle of $\frac{2\pi}{3}$.

Due to the circular shape of the development, we can trace out the computed global developable surface with such a finite circular patch; see Figure 6.5 and Figure 6.6. In the sculpture by Max Klammer, this motion is guided by the circular opening, as shown in Figure 6.7, until the point where one of the boundaries reaches the circular opening.

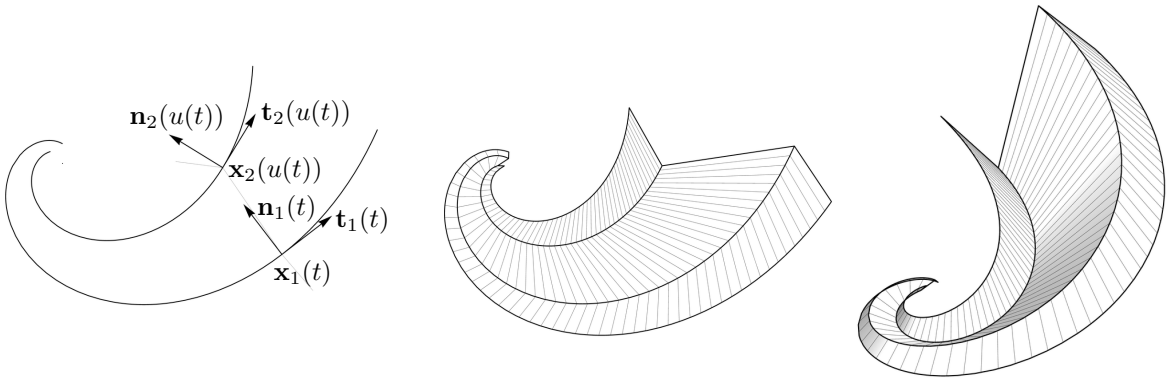

(a) Notation. (b) Computed developed rulings and folded state.

Figure 6.8: Illustration of the computations in Section 6.3.

6.3 Constant Angle Creases Along Logarithmic Spirals

In the following, we consider two spiral curves to illustrate how to apply the method discussed in Section 3.4.4 to compute the rulings of two creases with constant fold angle.

6.3.1 Computation

Parametrization of the development

In the following, we parametrize the first arc-length parametrized logarithmic spiral by

$$\mathbf{x}_1(s) = \left(\frac{1}{2}s\cos(\sqrt{3}\log s), \frac{1}{2}s\sin(\sqrt{3}\log s)\right)$$

and define the second curve to be a by $\frac{\pi}{3}$ rotated copy of $\mathbf{x}_1(s)$, that is, $\mathbf{x}_2(s) = R_{\frac{\pi}{3}} \cdot \mathbf{x}_1(s)$, where $R_{\frac{\pi}{3}}$ denotes a rotation of $\frac{\pi}{3}$ about the z-axis. The curvatures of both curves are $k_1(s) = k_2(s) = \frac{\sqrt{3}}{s}$.

Similar to before, we assume that the central rulings are parametrized by a parameter t. The rulings connect the two curves at arc-length parameter values $s_1(t) = t$ and $s_2(t) = u(t)$, respectively, where $u(t)$ is an initially unknown function. Using Equation (3.24), we obtain the ruling angles as

$$\sin\theta_{1L}(t) = \mathbf{n}_1(t)\cdot\mathbf{r}(t) = -\frac{\sqrt{3}t - 2u(t)\sin X(t)}{2\sqrt{t^2 - t(\cos X + \sqrt{3}\sin X)u(t) + u(t)^2}},$$
$$\sin\theta_{2R}(t) = \mathbf{n}_2(u(t))\cdot\mathbf{r}(t) = \frac{(\sqrt{3}\cos X(t) + \sin X(t))t - \sqrt{3}u(t)}{2\sqrt{t^2 - t(\cos X(t) + \sqrt{3}\sin X(t))u(t) + u(t)^2}},$$

where $X(t) = \sqrt{3}(\log t - \log u(t))$ and $\mathbf{t}_i(s)$ and $\mathbf{n}_i(s)$ denote the tangent and normal of the respective curve at arc-length parameter.

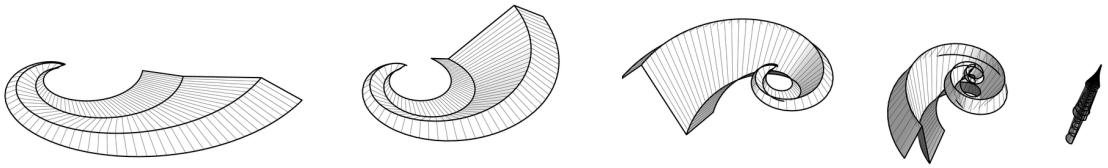

Figure 6.9: Rigid-ruling folding motion of the spiral for $\varphi_{1,0} \in (0.1\pi, 0.2\pi, 0.3\pi, 0.4\pi, 0.49\pi)$ with $c = 0.917$.

Computation of the inclination angles and parametrization speed

Substituting the above ruling angles and curvatures in Equation (3.45) simplifies to

$$u'(t) = \frac{(3t\cos X(t) + \sqrt{3}t\sin X(t) - 3u(t))u(t)}{(3t - 2\sqrt{3}u(t)\sin X(t))t}\frac{\tan\varphi_{1,0}}{\tan\varphi_{2,0}}.$$

As the right hand side of the above expression is unbounded at $t = 0$, we choose to start our integration at some value other than 0, for example $t_0 = 2$. We choose a value for $u(t_0)$, and the inclination angles $\varphi_1(t) = \varphi_{1,0}$ and $\varphi_2(t) = \varphi_{2,0}$.

As highlighted in the previous section, we obtain the same ruling layout for combinations of inclination angles where $c = \frac{\varphi_{1,0}}{\varphi_{2,0}}$.

Computation of the crease curves and surfaces

Upon successful computation of the function $u(t)$, we obtain the curvatures and torsions using Equation (3.40).

To obtain the consistent initial points and vectors of the curves and orthonormal frames we follow the strategy outlined in Section 3.4.3, Scenario 2.

6.3.2 Conclusion

Upon successful computation, we obtain folded states of the two spiral curves with constant angle. We experimentally confirm our conjecture that the folded states converge towards a thin line with parallel rulings as the fold angles of both creases converge to a complete fold.

Chapter 7

Parametrization of Ruling Polylines

The content of this chapter is unpublished and is based on discussions with Erik Demaine, Robert Lang, and Tomohiro Tachi.

Overview

In this chapter, we present the last application of joining three patches with partial ruling information along two creases. Specifically, we define the shape of the ruling polylines up to a single parameter, which is then determined by the common ruling curvature of the shared patches. We demonstrate this approach on closed periodic shapes with two circular creases, and discuss an unsuccessful attempt to analyze circular spirals.

7.1 Introduction

In this chapter, we explore other variations of the method for joining three patches with partial ruling information along two creases. The examples presented in this chapter lean more towards the experimental side and may not directly contribute to new theoretical insights. Nevertheless, we find them to be interesting applications that highlight potential and constraints of the discussed method.

In our first example, discussed in Section 7.2, we consider closed circular pleats. This subsequent analysis differs from that presented in Section 4.3, which was also applicable to circular curves. In that context, we determined a two-parameter family of shapes corresponding to closed elliptic pleats by guessing appropriate ruling directions. However, in this chapter, we take a different approach. We obtain the ruling directions by making an assumption about the shape of consecutive rule segments, which is determined up to scaling. We use the ruling curvature to find the scale factor for each ruling parameter, which identifies ruling directions that correspond to periodic shapes with two circular creases. Given suitable initial values, we achieve periodic shapes with numerical closure. However, as noted in Section 4.3, the addition of more patches to the folded shape is similarly constrained by both geometric and numerical factors.

Our second example, discussed in Section 7.3, is based on David Huffman's circular spirals, as discussed in Koschitz [43] or Demaine et al. [19]. In this chapter, we make a similar assumption about the rulings of the crease pattern, which leads to a folded state comprising three patches. However, since the compatibility holds only for the shared patch and not for the left and right patches, we are unable to complete the spiral. The rulings necessary to close and complete the spiral towards the center are unknown and may not be retrievable with the discussed approach. A construction for a special family of folded states of spirals is shown in Chapter 14.

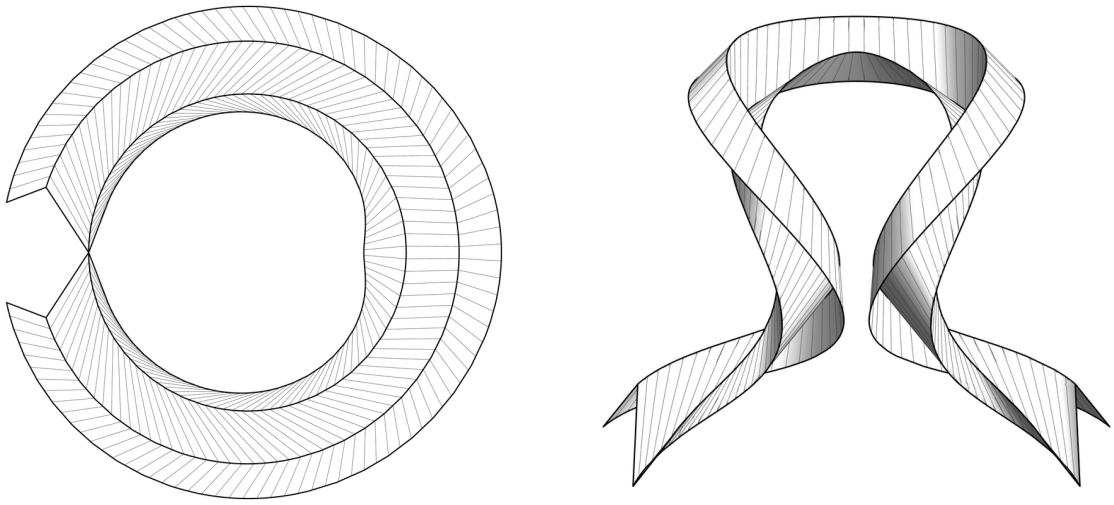

Figure 7.1: Two concentric circles with constant fold angle computed with the method discussed in Section 6.3.

7.2 Pleated Annulus

Folding circles in an alternating pattern of mountain and valley creases produces intricate shapes. Yet, describing these forms is a non-trivial task. Alese [3] explores examples by carefully constructing surfaces around closed curves and introducing additional creases.

When folding concentric circles, a seemingly "natural" state emerges. Nonetheless, in most cases, these shapes remain flexible and can be guided into various configurations. In our pursuit to parametrize such shapes, we conducted experiments to identify rulings that appeared as "natural" as possible. We conducted many experiments. For example, our attempt to assume that two curves are folded along constant angle creases proved unsuccessful as we could not achieve a closed shape, as shown in Figure 7.1. In what follows, we detail one of our more successful approaches.

7.2.1 Computation

In the following, we assume that the four circles, corresponding to two circular creases and two circular boundaries, are parametrized by arc length by

$$\mathbf{x}_i(s) = \left(r_i \cos \frac{s}{r_i}, r_i \sin \frac{s}{r_i}, 0 \right),$$

where $r_0 > r_1 > r_2 > r_3$.

The method defines the layout of the polyline of consecutive rulings, constrained by a scale factor $u(t)$, which represents the yet-to-be-determined degree of freedom. This scale factor is encoded in the arc lengths $s_i(t)$ of the circles $\mathbf{x}_i(s)$,

$$s_i(t) = r_i(t + p_i u(t)),$$

where p_i are four constants. The shape of the ruling polylines $(\mathbf{x}_0(s_0(t)), \mathbf{x}_1(s_1(t)), \mathbf{x}_2(s_2(t)), \mathbf{x}_3(s_3(t)))$ is then specified up to parameter $u(t)$.

The four constants determine the shape of the polyline. Since a common scale factor can be incorporated in the function $u(t)$, they comprise three shape parameters.

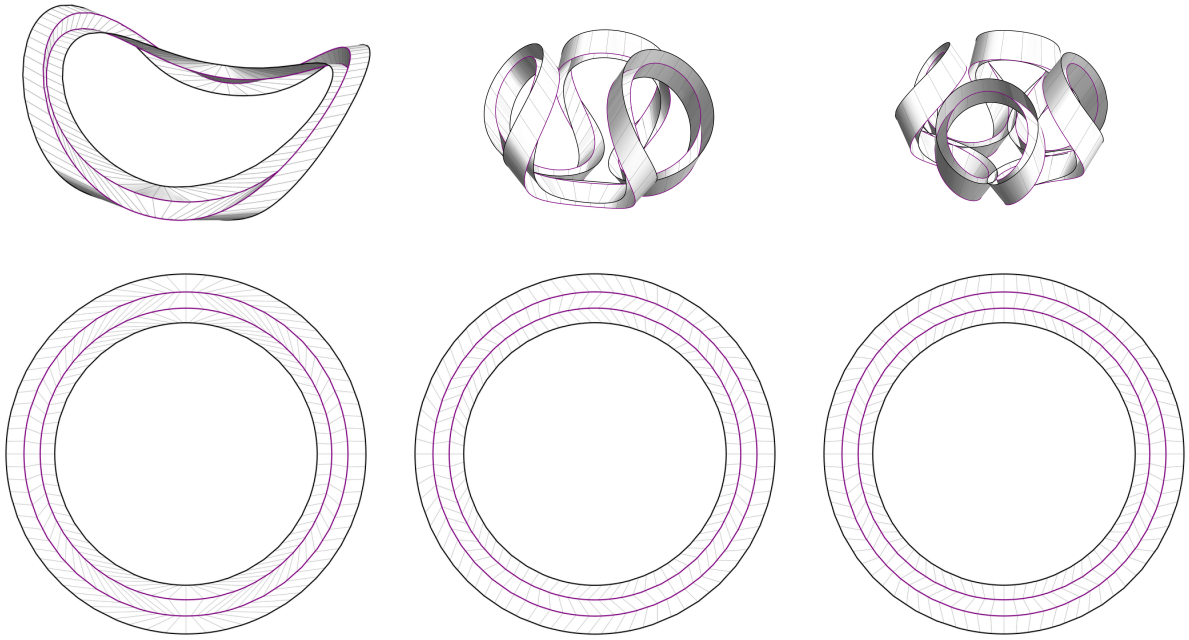

(a) Folded shapes with $s = 0.9$.

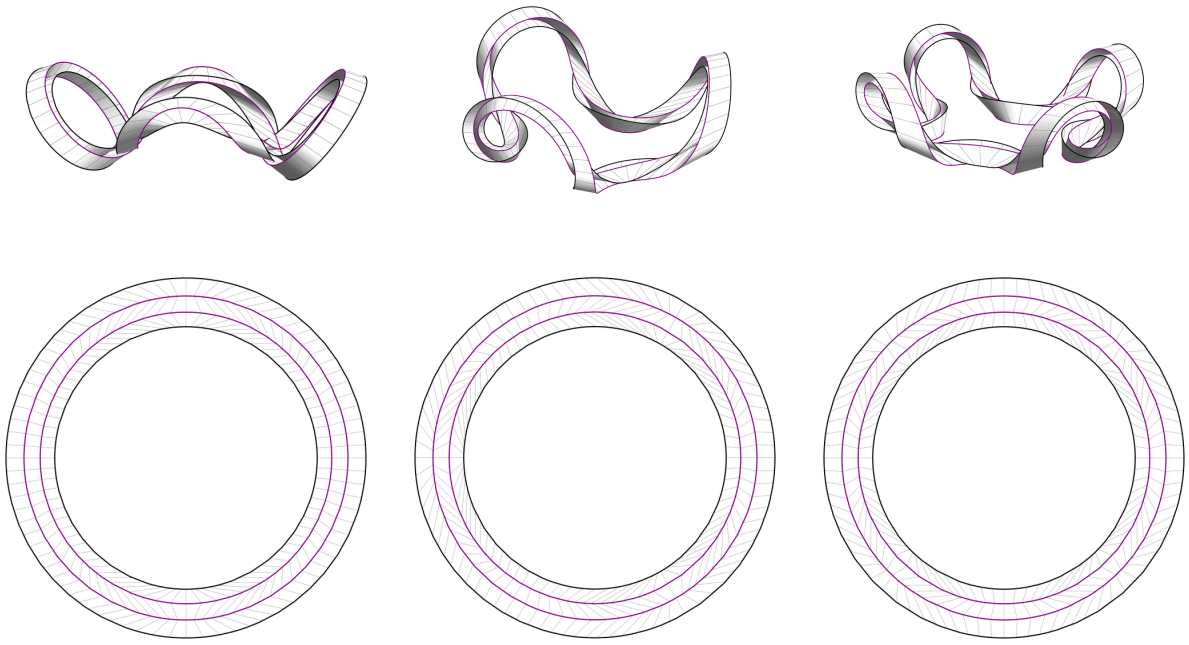

(b) Folded shapes with $s = 0.8$.

Figure 7.2: Illustration of shapes obtained from the computations in Section 7.2.

Parametrization of the development

Using Equation (3.24), the ruling directions for $i < 3$ read

$$\mathbf{r}_{iL}(t) = \left(\frac{-r_i \cos(t + p_i u(t)) + r_{i+1} \cos(t + p_{i+1} u(t))}{\sqrt{r_i^2 + r_{i+1}^2 - 2 r_i r_{i+1} \cos((p_i - p_{i+1}) u(t))}}, \frac{-r_i \sin(t + p_i u(t)) + r_{i+1} \sin(t + p_{i+1} u(t))}{\sqrt{r_i^2 + r_{i+1}^2 - 2 r_i r_{i+1} \cos((p_i - p_{i+1}) u(t))}}, 0 \right).$$

Consequently, the ruling angles simplify to

$$\begin{aligned}
\theta_{iR}(t) &= \arctan\left(\mathbf{r}_{i-1,L}(t) \cdot \mathbf{t}_i(s_i(t)), \mathbf{r}_{i-1,L}(t) \cdot \mathbf{n}_i(s_i(t))\right) \\
&= \arctan\left(-\frac{-r_{i-1} \sin((p_{i-1} - p_i) u(t))}{\sqrt{r_{i-1}^2 + r_i^2 - 2 r_{i-1} r_i \cos((p_{i-1} - p_i) u(t))}}, \frac{-r_i + r_{i-1} \cos((p_{i-1} - p_i) u(t))}{\sqrt{r_{i-1}^2 + r_i^2 - 2 r_{i-1} r_i \cos((p_{i-1} - p_i) u(t))}} \right)
\end{aligned}$$

and

$$\begin{aligned}
\theta_{iL}(t) &= \arctan\left(\mathbf{r}_{i+1,L}(t) \cdot \mathbf{t}_i(s_i(t)), \mathbf{r}_{i+1,L}(t) \cdot \mathbf{n}_i(s_i(t))\right) \\
&= \arctan\left(-\frac{-r_{i+1} \sin((p_i - p_{i+1}) u(t))}{\sqrt{r_i^2 + r_{i+1}^2 - 2 r_i r_{i+1} \cos((p_i - p_{i+1}) u(t))}}, \frac{-r_i + r_{i+1} \cos((p_i - p_{i+1}) u(t))}{\sqrt{r_i^2 + r_{i+1}^2 - 2 r_i r_{i+1} \cos((p_i - p_{i+1}) u(t))}} \right).
\end{aligned}$$

Additionally, the curvatures of the curves $\mathbf{x}_i(t)$ are $k_i(t) = \frac{1}{r_i}$.

Computation of the inclination angles and parametrization speed

The equations in Equation (3.39) simplify to

$$\begin{aligned}
u'(t) &= \frac{(-r_2 + r_1 \cos((p_1 - p_2) u(t))) \tan\varphi_1(t) + (r_1 - r_2 \cos((p_1 - p_2) u(t))) \tan\varphi_2(t)}{p_1 (r_2 - r_1 \cos((p_1 - p_2) u(t))) \tan\varphi_1(t) + p_2 (-r_1 - r_2 \cos((p_1 - p_2) u(t))) \tan\varphi_2(t)} \\
\varphi_1'(t) &= -\frac{(p_1 - p_2)\left(r_0 r_1 \sin((p_0 - p_1) u(t)) - r_1 r_2 \sin((p_1 - p_2) u(t)) + r_0 r_2 \sin((p_0 - 2p_1 + p_2) u(t))\right)}{2(r_1 - r_0 \cos((p_0 - p_1) u(t))) X(t)} \\
\varphi_2'(t) &= -\frac{(p_1 - p_2)\left(r_1 r_2 \sin((p_1 - p_2) u(t)) - r_2 r_3 \sin((p_2 - p_3) u(t)) + r_1 r_3 \sin((p_1 - 2p_2 + p_3) u(t))\right)}{2(r_2 - r_3 \cos((p_2 - p_3) u(t))) X(t)}
\end{aligned}$$

where $X(t) = p_2 (r_1 - r_2 \cos((p_1 - p_2) u(t))) \cot\varphi_1(t) + p_1 (-r_2 + r_1 \cos((p_1 - p_2) u(t)) \cot\varphi_2(t))$.

Computation of the crease curve and surfaces

Upon successful computation, the curvatures and torsion follow from Equation (3.40). Additionally, the consistent initial values for the curve and frame can be obtained as described in Section 3.4.3, Scenario 2.

7.2.2 Remarks on the Closure of the Shape

Similar to Chapter 4 and Section 6.2, we observed that a successful numerical computation results in three periodic functions with respect to the same period length D. Specifically, an odd function $u(t)$, and two even solution $\varphi_1(t)$ and $\varphi_2(t)$.

An informal argument, neglecting the requirement of a unique solution, again invokes the theory presented by Kotin [45]. We interpret the initial value problem for the functions $u(t)$, $\varphi_1(t)$, and $\varphi_2(t)$ as

$$\mathbf{0} = f(u(t), \varphi_1(t), \varphi_2(t), u'(t), \varphi_1'(t), \varphi_2'(t)). \tag{7.1}$$

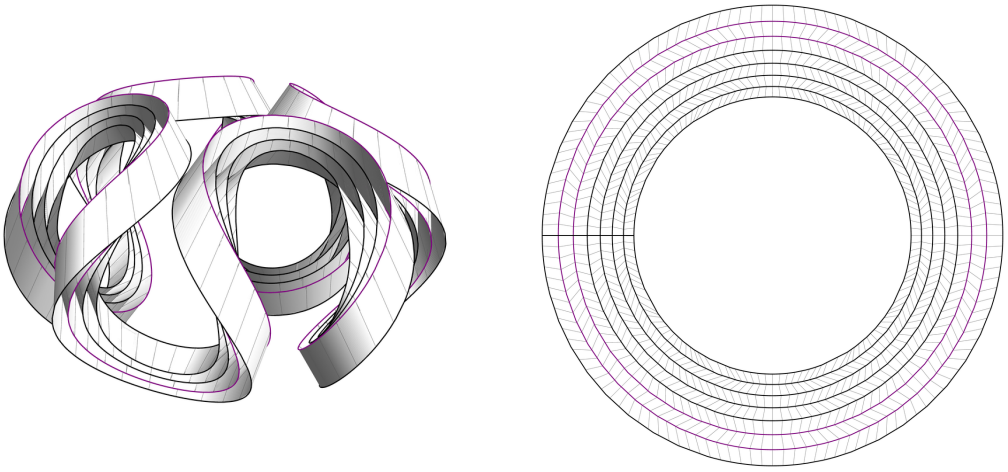

Figure 7.3: Numerically closed circular creases with $n = 4$ with added circular pleats towards the center of the shape.

Since a solution of Equation (7.1) also satisfies

$$\mathbf{0} = f(-u(t), \varphi_1(t), \varphi_2(t), u'(t), -\varphi_1'(t), -\varphi_2'(t)),$$

it follows from Kotin [45] that, if the solution is unique, $u(t) = -u(-t)$, $\varphi_1(t) = \varphi_1(-t)$, and $\varphi_2(t) = \varphi_2(-t)$. Moreover, if there exists a parameter D with $u\left(\frac{D}{2}\right) = 0$, then $u(t + D) = u(t)$, $\varphi_1(t + D) = \varphi_1(t)$, and $\varphi_2(t + D) = \varphi_2(t)$.

If the above holds true, similar to Chapter 4, it follows that also $K_i(t)$ and $\tau_i(t)$ are periodic functions with respect to the same period D. Specifically, $K_i(t)$ are even functions, and $\tau_i(t)$ are odd functions. Upon successful integration of the Frenet-Serret equations for $t \in [-\frac{D}{2}, \frac{D}{2}]$, the resulting curve is symmetric with respect to the normal plane at $t = 0$. Additionally, the normal planes at $t = \pm\frac{D}{2}$ contain the incident ruling directions and are perpendicular to the tangent planes. As a result, copies of this curve segment can be arranged by reflecting on the endpoint's normal planes, as discussed in Chapter 4. When the opening angle between the normal planes at $t = \pm\frac{D}{2}$ is $\frac{2\pi}{n}$ for some n, the curve closes up. When in addition the period length is also $\frac{2\pi}{n}$, the full shape allows a closed folded state without a cut.

Through experimentation, we observe that the choice of $\varphi_1(0)$ and $\varphi_2(0)$ influences the period length D and the opening angle between the normal planes at $t = \pm\frac{D}{2}$. We conjecture that for appropriate values p_i, we are able to achieve numerically closed shapes for different values of n.

To navigate the three-dimensional parameter space, we experimented with different parameter combinations, for example setting $p_0 = c^3$, $p_1 = -c^2$, $p_2 = c$ and $p_3 = -1$ for some parameter c, resulting in a one-parameter family of solutions parametrized by c. Figure 7.2 shows numerically closed shapes obtained for appropriate initial values resulting in $n \in \{2, 3, 4\}$ and $D \in \{\pi, \frac{2\pi}{3}, \frac{2\pi}{4}\}$, where $c = 0.9$ (first row) and $c = 0.8$ (second row).

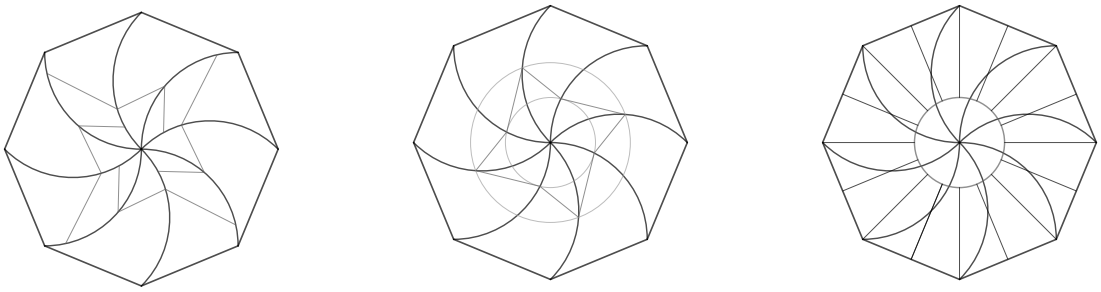

(a) Spiral with "spiraling" rulings. (b) Spiral with "closed" rulings. (c) Spiral with "conical" rulings.

Figure 7.4: Possible ruling layouts for origami spirals.

7.2.3 Limitations

Our still unresolved primary objective is to demonstrate that circular creases can be propagated infinitely many times. To achieve this, we studied crease patterns that are scaled versions of one another. Yet, while the ruling curvature condition ensures compatibility for the central patch, it does not guarantee it for the left and right patches. At present, our capability to introduce creases is as discussed in Section 3.2.8. An example of a shape with added circular pleats is shown in Figure 7.3.

We also made an attempt to generalize the described approach for a greater number of creases. Unfortunately, we were unable to identify periodic solutions in this context.

7.3 Circular Spiral

In the following, we discuss another application of the approach outlined in the previous section, using Huffman's design of circular spirals as an example.

7.3.1 Ruling Analysis

Folding eight circular arcs arranged in a polar array, with alternating mountain and valley patterns, results in an origami spiral. Among the numerous possible configurations, we, for the sake of analysis, assume that the spiral is folded such that the patches exhibit 4-fold rotational symmetry. As a result, the rulings of the developed patches also possess rotational symmetry. The alignment of these rulings can be categorized into at least the following three possibilities:

- *Spiraling rulings:* One approach is for the ruling polylines to form infinite "spiraling" polylines, as indicated in David Huffman's other spiral designs [43, Figure 4.11.7]. However, without further assumptions, this approach does not allow for a direct application of the methods previously discussed. To date, we have not managed to find compatible spiraling rulings. We conjecture that a successful computation of this nature requires a well-informed initial guess.
- *Closed rulings:* There is also the theoretical possibility that the rulings create closed polygons. This assumption can be analyzed using the previously discussed method and will be elaborated on below. Nevertheless, attempts at application have been unsuccessful.

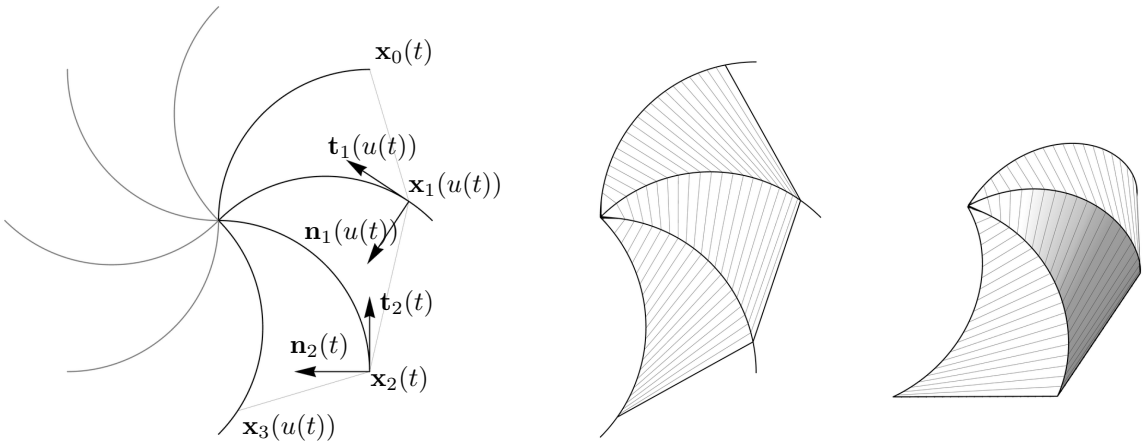

(a) Notation. (b) Computed developed rulings and folded state.

Figure 7.5: Illustration of the computations in Section 7.3.

- *Conical rulings:* Another option is for all rulings to intersect at the spiral's center. In this scenario, the patches are to cones connected by planar creases. However, parts of the spiral must be trimmed since the "D"-shaped areas, bounded by a crease and a ruling, need to remain planar. Drawing from this observation, we developed a construction tool for such spirals, introduced in Chapter 14.

7.3.2 Computation

Parametrization of the development

We follow the notation of the previous section. In particular, we parametrize the developed curves as circular arcs in the xy-plane of unit radius centered at $(1, 0, 0)$ and their $n-1$ copies, that is,

$$\mathbf{x}_i(t) = R_{\frac{i\pi}{n}} \cdot (1 - \sin t, \cos t, 0)\,,$$

where $R_{\frac{i\pi}{n}}$ denotes the rotation about the z-axis by $\frac{i\pi}{n}$; see Figure 7.5a.

We make the assumption that $s_0(t) = s_2(t) = t$ and $s_1(t) = s_3(t) = u(t)$, a and compute ruling angles with Equation (3.24) as discussed in the previous sections. Additionally, we have that $k_1(t) = k_2(t) = 1$.

Computation of the inclination angles and parametrization speed

For the system of differential equations discussed in Section 3.4, we must determine initial values for $u(t)$, $\varphi_1(t)$, and $\varphi_2(t)$. Our calculations tend to be more successful when initiated at $t = \frac{\pi}{4}$, aiming to reach the limits at $t_{\min} = 0$ and $t_{\max} = \frac{\pi}{2}$. However, in many instances, the computation ends prematurely or $u(t)$ reverses its direction, leading to overlaps.

Computation of the gluing curves and construction of surfaces

Upon successful computation, the curvatures and torsion follow from Equation (3.40). Additionally, the consistent initial values for the curve and frame can be obtained as described in Section 3.4.3, Scenario 2.

7.3.3 Conclusion

Figure 7.5b displays a promising result from our computations for three patches. However, it is important to note that our calculations made only the central patch compatible. In general, the outer patches possess differing ruling curvatures. Despite numerous experiments with various combinations of initial values, we were unable to achieve a consistent ruling curvature.

In Chapter 14, we present a construction for spirals where the rulings converge toward the shape's center. However, this construction cannot be extended right up to the center. The question of whether a complete origami spiral, with creases that converge to the center – even if they are circular – remains an open problem.

Part II

Ruling-Length-Based Computation of Configurations of Cylinders and Cones

Chapter 8

Join-and-Fan Method

The content of this chapter is unpublished and is based on discussions with Erik Demaine.

Overview

We consider the special case of gluing two surfaces that are either cylinders or cones. We introduce the *join-and-fan method*, a technique designed to compute the glue or crease curves between cylinders or cones using a single integration step. Through this method, we simplify the computational process, enabling a deeper understanding of the underlying geometry. Additionally, in the context of discrete creases, we explore a linkage-based approach that offers further insights into the existence of rigid folding motions.

8.1 Introduction

Many naturally occurring or intentionally designed shapes from developable surfaces exhibit symmetries. In many cases these shapes consist of cylinders and cones. Notable examples of such designs can be found in the works of David Huffman [19, 43] and Jeannine Mosely [61].

When the geometry consists of cylinders or cones, the complexity of the involved surfaces is significantly reduced. This reduction arises from the simplified requirement of developability, which translates to the requirement that the rulings of the involved surfaces either converge to a single point or remain parallel. Consequently, the corresponding shapes can be constrained by intrinsic distances.

In this section, we formalize a simplified computational approach for the case of gluing two (smooth or discrete) surfaces that are either cylinders or cones. We introduce the *join-and-fan method*, which computes the glue or crease curve of two cylinders or cones using two steps: the *joining step* amounts to solving two algebraic equations, the *fanning step* requires solving a first-order differential equation in the smooth case or a difference equation in the discrete case. This approach offers a straightforward computation, providing deeper insights into the geometric characteristics of the constructed shapes. This approach can be seen as a generalization of a method employed by Mosely [61] in the analysis of the Orb, a modular curved-crease origami shape, and by Demaine et al. [17] in the analysis of curved-crease tessellations.

Furthermore, in the case of discrete creases, we use a linkage-based approach to analyze the rigid folding behavior, without the requirement of flat foldability. In particular, we present an intuitive interpretation of sufficient conditions for the existence of a rigid folding motion of a single crease.

The use of the join-and-fan method helps the mathematical description of various shapes. In Chapter 9, we use this method to derive closed-form parametrizations for different variations of gluings between a polygon and a circle. Additionally, in Chapter 10, we apply this method to demonstrate the rigid foldability of two discretizations of conic crease patterns with reflecting rule lines. This finding is particularly noteworthy as conventional methods typically require the patterns to be flat foldable, which is not always the case for the studied crease patterns.

8.2 Smooth Join-and-Fan Method

8.2.1 Input

The smooth join-and-fan method's input consists of two surface patches, denoted by $\mathbf{s}_1(t,u)$ and $\mathbf{s}_2(t,u)$, each of which can be either conical or cylindrical, and are assumed to be parameterized by

$$\mathbf{s}_i(t,u) = \mathbf{x}_i(t) + u\mathbf{r}_i(t),$$

where, in the case of a cone, all rulings converge at a point $\mathbf{v}_i$, and in the case of a cylinder, all rulings are parallel.

The goal of this section is to determine the 3D shape resulting from joining the two surfaces along $\mathbf{x}_1(t)$ and $\mathbf{x}_2(t)$. Without loss of generality, we assume that the curves $\mathbf{x}_1(t)$ and $\mathbf{x}_2(t)$ have the same parametrization speed, meaning that $|\mathbf{x}_1'(t)| = |\mathbf{x}_2'(t)|$.

Furthermore, if surface $\mathbf{s}_i(t,u)$ is a cone, we assume that we are given the target 3D apex $\mathbf{V}_i$. If surface $\mathbf{s}_i(t,u)$ is a cylinder, we assume that we are given an oriented *base line* π_i of the developed cylinder, that is, a line perpendicular to the cylinder's ruling direction $\mathbf{r}_i$ specified by an incident point $\mathbf{p}_i$, and its 3D target position, the *base plane* Π_i of the 3D cylinder, specified by the 3D ruling direction $\mathbf{R}_i$ and an incident point $\mathbf{P}_i$.

8.2.2 Unknowns

In the smooth join-and-fan method, we encode the three unknowns of the gluing or folding curve $\mathbf{X}(t)$ as three functions, for example, the three coordinate function in a parametrization with Cartesian coordinates

$$\mathbf{X}(t) = (\mathbf{X}_x(t), \mathbf{X}_y(t), \mathbf{X}_z(t)), \tag{8.1}$$

or the distance and angle functions in a parametrization with polar coordinates, such as

$$\mathbf{X}(t) = l(t)\left(\cos\zeta(t)\cos\eta(t), \cos\zeta(t)\sin\eta(t), \sin\zeta(t)\right), \tag{8.2}$$

where $l(t) \geq 0$, $\eta(t) \in [0, 2\pi]$, and $\zeta(t) \in [-\frac{\pi}{2}, \frac{\pi}{2}]$.

8.2.3 Constraints

The smooth join-and-fan method solves for the three unknown functions in two steps:

Joining step

In the joining step, we deduce two functions from two algebraic constraints from the distances imposed by the conical or cylindrical surfaces. In particular, if $\mathbf{s}_i(t,u)$ is a cone, we want the distance between the glue curve and the 3D apex to be the same as in the development, which yields

$$|\mathbf{X}(t) - \mathbf{V}_i|^2 = |\mathbf{x}_i(t) - \mathbf{v}_i|^2. \tag{8.3}$$

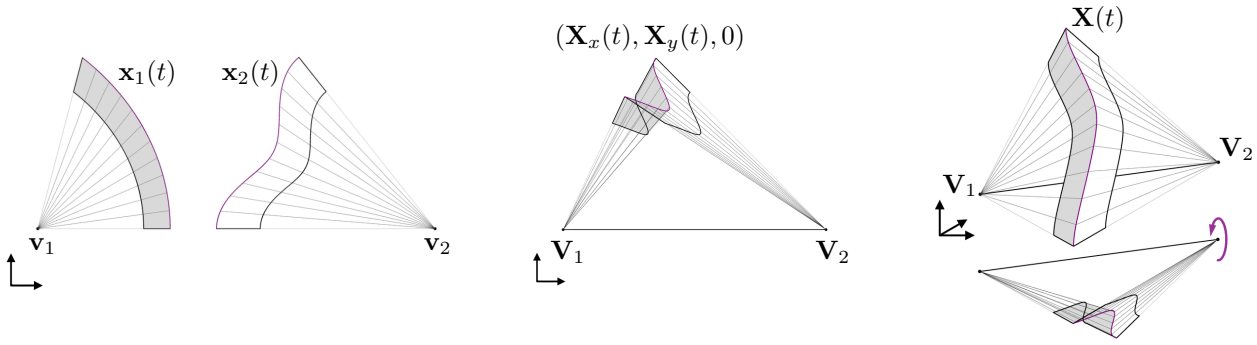

(a) Input: Two developed cones. (b) Joining step. (c) Fanning step.

Figure 8.1: Illustration of the smooth join-and-fan method for two cones.

If $\mathbf{s}_i(t, u)$ is a cylinder, we constrain the distances between the glue curve and the base line π_i and base plane Π_i to be the same, resulting in

$$(\mathbf{X}(t) - \mathbf{P}_i) \cdot \mathbf{R}_i = (\mathbf{x}_i(t) - \mathbf{p}_i) \cdot \mathbf{r}_i, \tag{8.4}$$

where $\mathbf{p}_i \in \pi_i$ and $\mathbf{P}_i \in \Pi_i$ are two points incident to the base line or plane of the cylinder.

Using two constraints, one from each surface, we are able to compute two out of the three unknown functions (for details see Section 8.2.4). The two resulting functions allow for the interpretation of an intermediate planar solution as depicted in Figure 8.1 (middle).

Fanning step

Second, to obtain isometric surfaces, we need to ensure that the parametrization speeds of $\mathbf{X}(t)$ and the corresponding developed curves match. In the *fanning step*, we therefore find the third function from the differential constraint

$$\left|\mathbf{X}'(t)\right|^2 = \left|\mathbf{x}_1'(t)\right|^2 = \left|\mathbf{x}_2'(t)\right|^2.$$

In case of Cartesian coordinates, this constraint can be written as

$$\mathbf{X}_x'(t)^2 + \mathbf{X}_y'(t)^2 + \mathbf{X}_z'(t)^2 = \left|\mathbf{x}_1'(t)\right|^2 = \left|\mathbf{x}_2'(t)\right|^2. \tag{8.5}$$

In case of a parametrization with polar coordinates, this constraint reads

$$l'(t) + l(t)^2 \left(\eta'(t)^2 \cos^2 \zeta(t) + \zeta'(t)^2\right) = \left|\mathbf{x}_1'(t)\right|^2 = \left|\mathbf{x}_2'(t)\right|^2. \tag{8.6}$$

This step can be visualized as spreading or "fanning" out the planes containing consecutive ruling lines, which were computed in the previous step. This process results in the final 3D shape, as depicted in Figure 8.1 (right).

8.2.4 Computation Details

There are many ways to apply this method to a given problem, but not all approaches result in explicit solutions for two of the three unknown functions in the joining step. In the following, we present approaches for choosing the parametrization of the gluing curve and the location and orientation of the coordinate systems for the three different cases (cylinder-cylinder, cone-cylinder, and cone-cone) that result in explicit solutions for two of the three involved functions in the joining step.

Cylinder-cylinder gluing

If $\mathbf{s}_1(t,u)$ and $\mathbf{s}_2(t,u)$ are both cylinders, it is convenient to parametrize the glue curve with Cartesian coordinates as given in Equation (8.1). Additionally, we assume that the ruling directions $\mathbf{R}_1$ and $\mathbf{R}_2$ are parallel to the xy-plane, that is, $0 = \mathbf{R}_1 \cdot (0,0,1) = \mathbf{R}_2 \cdot (0,0,1)$.

1. *Joining step:* By imposing the constraint in Equation (8.4) for both surfaces, we obtain expressions for the first two coordinates of the glue curve, namely,

$$\begin{pmatrix} \mathbf{X}_x(t) \\ \mathbf{X}_y(t) \end{pmatrix} = \begin{pmatrix} \mathbf{R}_{1,x} & \mathbf{R}_{1,y} \\ \mathbf{R}_{2,x} & \mathbf{R}_{2,y} \end{pmatrix}^{-1} \begin{pmatrix} (\mathbf{x}_1(t) - \mathbf{p}_1) \cdot \mathbf{r}_1 + \mathbf{P}_1 \cdot \mathbf{R}_1 \\ (\mathbf{x}_2(t) - \mathbf{p}_2) \cdot \mathbf{r}_2 + \mathbf{P}_2 \cdot \mathbf{R}_2 \end{pmatrix}. \tag{8.7}$$

2. *Fanning step:* The third coordinate function is determined from the parametrization speed constraint in Equation (8.5), which yields two solutions that are related by a reflection on a xy-parallel plane.

Cylinder-cone gluing

If $\mathbf{s}_1(t,u)$ is a cone and $\mathbf{s}_2(t,u)$ is a cylinder, it is convenient to parametrize the glue curve $\mathbf{X}(t)$ in polar coordinates as in Equation (8.2). Without loss of generality we assume that the cone apex $\mathbf{V}_1$ coincides with the origin and that $\mathbf{R}_2 = (0,0,1)$. Note that the ruling vector $\mathbf{R}_2$ is chosen so that the scalar product $\mathbf{R}_2 \cdot \mathbf{X}(t)$ depends on only one angular function.

1. *Joining step:* Using the conical constraint in Equation (8.3) for the first surface in polar coordinates results in $l(t) = r_1(t)$. The cylindrical constraint in Equation (8.4) yields[1]

$$\zeta(t) = \arcsin\left((\mathbf{x}(t) - \mathbf{p}_2) \cdot \mathbf{r}_2 - \mathbf{P}_2 \cdot \mathbf{R}_2\right). \tag{8.8}$$

2. *Fanning step:* The remaining angular function $\eta(t)$ can be computed from the parametrization constraint in Equation (8.6), resulting in

$$\eta'(t) = \pm\sqrt{\frac{|\mathbf{x}_1'(t)|^2 - r_1'(t) - r_1(t)^2\zeta'(t)^2}{r_1(t)^2\cos^2\zeta(t)}}. \tag{8.9}$$

   When solving this initial value problem with $\eta(0) = \eta_0$, the resulting two shapes vary by a reflection on a vertical plane.

Cone-cone gluing

If $\mathbf{s}_1(t,u)$ and $\mathbf{s}_2(t,u)$ are both cones, it is convenient to assume that the glue curve is again parametrized by polar coordinates as given in Equation (8.2). Without loss of generality, assume that the two apices are located at $\mathbf{V}_1 = (0,0,0)$ and $\mathbf{V}_2 = (0,0,h)$.

1. *Joining step:* Using the conical constraint in Equation (8.3) for the first surface in polar coordinates results in $l(t) = r_1(t)$. Consequently, the conical constraint in Equation (8.3) for the second surface in polar coordinates yields

$$\zeta_1(t) = \arcsin\left(\frac{h^2 + r_1(t)^2 - r_2(t)^2}{2hr_1(t)}\right). \tag{8.10}$$

2. *Fanning step:* Similar to before, the second angular function is determined from the parametrization speed constraint (see Equation (8.9)).

[1] Recall that we limited $\zeta(t)$ to $[-\frac{\pi}{2}, \frac{\pi}{2}]$.

8.2.5 Limitations

When employing the smooth join-and-fan method with suitable initial values and realistic input, it typically yields a local solution. However, it's important to note that, similar to the gluing process described in Section 3.3, there is a possibility of encountering geometric challenges that may cause the solution computation to fail prematurely in either of the two steps.

Geometric limitations in the joining step. For the cylinder-cylinder combination, it is necessary for the two 3D ruling directions to be non-parallel to ensure the existence of the inverse in Equation (8.7). In the cone-cylinder case, the corresponding plane should not be too close or too far away from the common vertex to ensure a successful (local) computation in Equation (8.8). In the cone-cone case, it is required that the 3D vertices are neither too close nor too far away from each other to find a (local) solution in Equation (8.10).

Geometric limitations in the fanning step. To obtain intuition about the functionality of the fanning step, we consider the planar curves that corresponds to intermediate "solutions", namely,

$$\mathbf{x}_{\text{temp}}(t) = (\mathbf{X}_x(t), \mathbf{X}_y(t), 0) \qquad \text{or} \qquad \mathbf{x}_{\text{temp}}(t) = (l(t)\cos\eta(t), l(t)\sin\eta(t), 0),$$

respectively. To ensure the success of the fanning step, we require that the parametrization speed of the intermediate curves $\mathbf{x}_{\text{temp}}(t)$ is smaller than the common parametrization speed of $\mathbf{x}_1(t)$ and $\mathbf{x}_2(t)$.

8.3 Discrete Join-and-Fan Method

8.3.1 Input

In the following, we discuss how the smooth join-and-fan method can be adapted to the discrete setting. Let $T = (t_0, t_1, \ldots, t_n)$ be an array of discrete parameter values. We parametrize two discrete surfaces $\mathbf{s}_1(t,u) = \mathbf{x}_1(t) + u\mathbf{r}_1(t)$ and $\mathbf{s}_2(t,u) = \mathbf{x}_2(t) + u\mathbf{r}_2(t)$ using two polylines that are parametrized as discrete 3D functions $\mathbf{x}_1(t)$ and $\mathbf{x}_2(t)$ defined over the same domain T. Similarly to the smooth case, we require that their discrete "parametrization speeds" are the same, that is,

$$|\mathbf{x}_1(t_i) - \mathbf{x}_1(t_{i+1})| = |\mathbf{x}_2(t_i) - \mathbf{x}_2(t_{i+1})|\,,$$

for all consecutive pairs of parameter values. Additionally, we encode the incident unit-length ruling vectors as discrete 3D functions $\mathbf{r}_1(t)$ and $\mathbf{r}_2(t)$ defined over domain T, such that $|\mathbf{r}_1(t_i)| = 1$. The surface $\mathbf{s}_i(t,u)$ is a (discrete) cylinder, if all discrete rulings are parallel, that is, $\mathbf{r}_i(t)$ is constant. The surface $\mathbf{s}_i(t,u)$ is a (discrete) cone, if all discrete rulings converge at a point $\mathbf{v}_i$, the apex of the cone.

In addition, we assume that in case of a cone, we are given the corresponding target cone apex $\mathbf{V}_i$. In case of a cylinder, we assume that we are given an oriented base line π_i perpendicular to $\mathbf{r}_i$ by its incident point $\mathbf{p}_i$, and its 3D counterpart, the oriented base plane Π_i, specified by a point $\mathbf{P}_i$ and a target ruling direction $\mathbf{R}_i$.

8.3.2 Unknowns

Similar to the smooth case, for each parameter value in T, the glue or crease polyline has three unknown discrete coordinate functions. These unknowns can be encoded as the three discrete

coordinate functions defined over T of a three-dimensional polyline

$$\mathbf{X}(t) = (\mathbf{X}_x(t), \mathbf{X}_y(t), \mathbf{X}_z(t)).$$

Alternatively, we may use a polar coordinate representation, such as

$$\mathbf{X}(t) = l(t)\,(\cos\zeta(t)\cos\eta(t), \cos\zeta(t)\sin\eta(t), \sin\zeta(t))\,. \tag{8.11}$$

Here the three unknowns are encoded as the three discrete functions $l(t) \geq 0$, $\eta(t) \in [0, 2\pi]$, and $\zeta(t) \in [-\frac{\pi}{2}, \frac{\pi}{2}]$ that are defined over T.

8.3.3 Constraints

The values of the three unknown functions are again constrained by three equations, corresponding to the smooth steps described above.

Joining step

If either of the surfaces is a cone with 3D apex $\mathbf{V}_i$ and 2D apex $\mathbf{v}_i$, we write

$$|\mathbf{X}(t) - \mathbf{V}_i|^2 = |\mathbf{x}(t) - \mathbf{v}_i|^2\,.$$

If either surface is a cylinder with corresponding base line π_i and base plane Π_i, we require

$$(\mathbf{X}(t) - \mathbf{P}_i) \cdot \mathbf{R}_i = (\mathbf{x}(t) - \mathbf{p}_i) \cdot \mathbf{r}_i.$$

Using analogous representation assumptions and coordinate system locations as in discussed for the smooth case in Section 8.2.4, we can obtain explicit expressions for two of the three discrete functions.

Fanning step

Finally, we need to ensure that the distances between two consecutive points on the polyline are the same in 2D as in 3D, that is,

$$|\mathbf{X}(t_{i+1}) - \mathbf{X}(t_i)|^2 = |\mathbf{x}_1(t_{i+1}) - \mathbf{x}_1(t_i)|^2 = |\mathbf{x}_2(t_{i+1}) - \mathbf{x}_2(t_i)|^2\,.$$

Note that, starting from an initial value for the remaining unknown function, there are in general two or no real-valued solution. If there are two real-valued solutions, only one consistent choice results in the discrete counterpart of a smooth gluing. If there is no real-valued solution, continuation is not possible.

8.4 Rigid-Ruling Folding Motions

Both in the smooth and discrete case, the join-and-fan method allows us to explore a family of glued states with rigid rulings.

Recall that if the incident surface is a cone, all corresponding points are constrained to meet at a single point, the 3D apex. On the other hand, if the incident surface is a cylinder, the rule segments are constrained to be perpendicular to an arbitrary but fixed plane, the base plane of the cylinder. Consequently, rigid-ruling folding motions can be induced as follows:

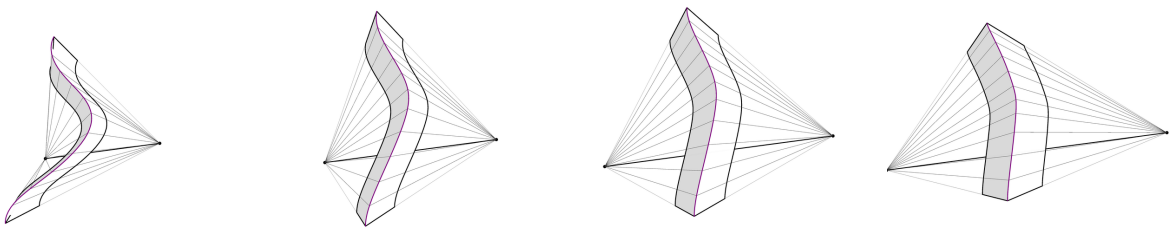

Figure 8.2: Rigid-ruling folding motion of the two cones from Figure 8.1.

- In the cone-cone case, a motion can be obtained by varying the distance between the cone apices; see Figure 8.2.
- In the cylinder-cone case, a motion can be obtained by varying the the distance between the cylinder's base plane with respect to the 3D cone apex.
- In the cylinder-cylinder case, a motion can be obtained by varying the opening angle of the cylinder's base planes.

Note that every glued state can be considered computationally in the two separate steps of the join-and-fan method.

8.5 Rigid Foldability of Discrete Creases between Cylinders and Cones

In this section, we use a linkage interpretation to get further insights into the geometry of shapes obtained from gluing two conical or cylindrical surfaces along discrete congruent curves $\mathbf{x}_1(t)$ and $\mathbf{x}_2(t)$. Recall that the resulting gluings correspond to either a discretized curved fold or a geodesic gluing.

Without loss of generality, we assume that the considered cylindrical or conical surfaces $\mathbf{s}_1(t, u)$ and $\mathbf{s}_2(t, u)$ are positioned such that the two curves $\mathbf{x}_1(t)$ and $\mathbf{x}_2(t)$ are aligned. We define linkages formed by bars that correspond to the discrete rulings of these surfaces, where the bars are connected at vertices located on the discrete glue or crease curve. Additionally, bars corresponding to the rulings of a cone are joint at the apex, and bars corresponding to the rulings of a cylinder are constrained to be perpendicular to a line. The precise definition of these extracted linkages is provided in Section 8.5.2.

As previously discussed, for a folded state of the crease pattern to exist, both steps of the join-and-fan method need to be successful. Consequently, the joining step needs to result in a configuration in which the distances between neighboring vertices along the common curve are smaller than in the initial configuration. We call such a configuration a *contracted diagonals configuration*.

When starting from an extracted linkage, usually only one motion results in a contracted diagonals configuration. In the example shown in Figure 8.3, only decreasing the distances between the apices results in a decrease of the distance between adjacent points on the glue or crease curve.

The contributions of this section are two-fold. First, we study how the previously discussed motions affect the distances between neighboring points on the common curve, with the goal to classify contracted diagonals motions. Second, we show that for a given extracted linkage X_0, the existence of a contracted diagonals configuration X_1 implies the existence of a one-parameter

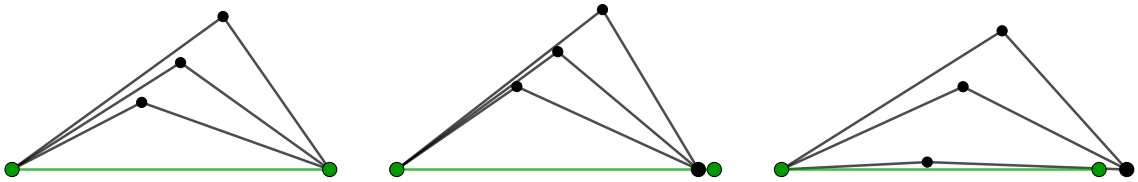

Figure 8.3: Illustration of a linkage derived from a crease between two cones. Left: Initial configuration. Middle: Configuration with decreased distance between the cone apices. Right: Configuration with increased distance between the cone apices.

family of intermediate contracted diagonals configurations X_t. Finally, we specify which contracted configurations allow a successful fanning step.

8.5.1 Diagonal Property of Four-bar Linkages

Before we continue, let us review the diagonal property that describes the behavior of diagonals of a four-bar linkage. Recall that four-bar linkages come in three different types (Figure 8.4): convex, crossing or non-crossing concave.

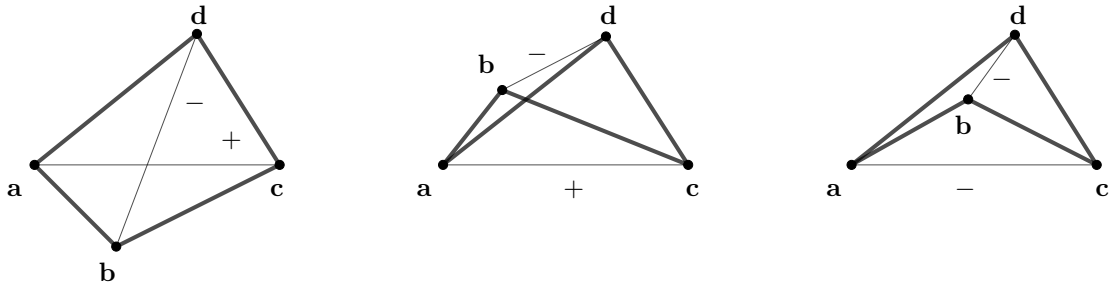

Figure 8.4: The three types of a four-bar linkage $X = \{\mathbf{a}, \mathbf{b}, \mathbf{c}, \mathbf{d}\}$: convex (left), crossing (middle), non-crossing concave (right). The signs indicate whether the diagonal **ac** increases (convex or crossing) or decreases (non-crossing concave) as the diagonal **bd** decreases in length.

The relationship between modifications of the linkage and changes in diagonal lengths can be expressed as follows:

Theorem 8.1 (Diagonal property of a four-bar linkages (from [105]))**.** *Let $X = \{\mathbf{a}, \mathbf{b}, \mathbf{c}, \mathbf{d}\}$ be a four-bar linkage in general position, that is, no three of its vertices are collinear.*

- *If X is a* convex *or a* crossing *four-bar linkage, one diagonal increases if and only if the other decreases.*
- *If X is a* non-crossing concave *four-bar linkage, one diagonal increases if and only if the other also increases.*

In the discussion below, we will examine four-bar linkages that correspond to either a combination of a cylinder and a cone or two cylinders. In this context, the intersection point of the two

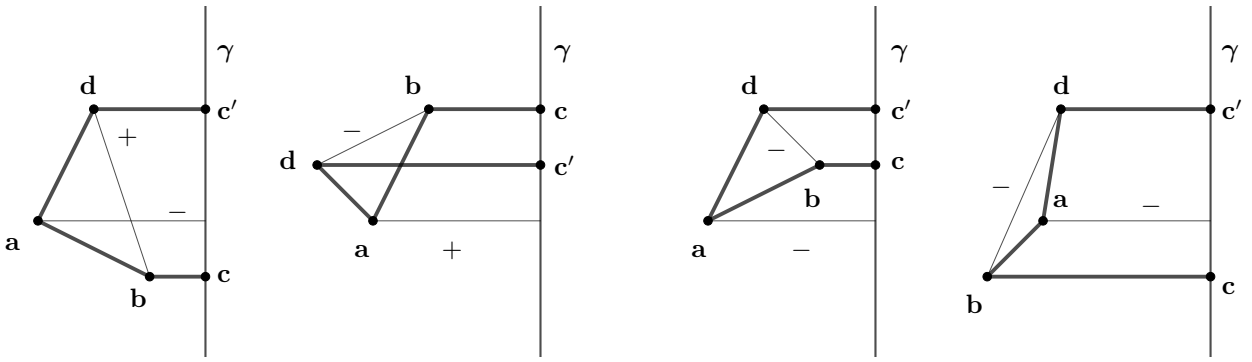

Figure 8.5: The three types of a four-bar linkage with a pair of parallel bars (from left to right): convex, crossing, and two concave non-crossing configurations.

bars lies at infinity. Rather than working with infinitely long parallel bars, we will truncate these bars using an oriented perpendicular line. As a result, instead of moving the intersection point, we adjust the location of the line. Through careful case analysis, we will confirm behavior analogous to these linkages.

In the following, we will consider four-bar linkages that correspond to a combination of a cylinder and cone, that is, four-bar linkages with a pair of parallel bars. In this case, the four-bar linkage consists of an open sequence of bars connecting the vertices $(\mathbf{c}, \mathbf{b}, \mathbf{a}, \mathbf{d}, \mathbf{c}')$. Additionally, the bars $\mathbf{bc}$ and $\mathbf{dc}'$ are constrained to be perpendicular to an oriented line $\boldsymbol{\gamma}$. Specifically, points $\mathbf{b}$ and $\mathbf{d}$ will be situated in the left-hand side half plane bounded by $\boldsymbol{\gamma}$, while points $\mathbf{c}$ and $\mathbf{c}'$ represent the base points of $\mathbf{b}$ and $\mathbf{d}$ on γ. Consequently, we will indicate a four-bar linkage with two parallel bars by three points and an oriented line, such as $X = \{\mathbf{a}, \mathbf{b}, \boldsymbol{\gamma}, \mathbf{d}\}$.

Similar to the previous linkage type, these linkages can be categorized into three types: convex, concave non-crossing, and crossing, as depicted in Figure 8.5. The diagonal property of these linkages can be expressed as follows. For a proof, please refer to Section 8.6.

Theorem 8.2 (Diagonal property of a four-bar linkage with a pair of parallel bars)**.** *Let* $X = \{\mathbf{a}, \mathbf{b}, \boldsymbol{\gamma}, \mathbf{d}\}$ *be a four-bar linkage with a pair of parallel bars in general position, that is, the three vertices* $\mathbf{a}$*,* $\mathbf{b}$*,* $\mathbf{d}$ *are not collinear and* $\mathbf{ac}$ *and* $\mathbf{ad}$ *are not perpendicular to* $\boldsymbol{\gamma}$*.*

- *If* X *is in a* convex *or* crossing *four-bar linkage, the distance between* $\mathbf{b}$ *and* $\mathbf{d}$ *decreases when the distance between* $\mathbf{a}$ *and* $\boldsymbol{\gamma}$ *increases.*
- *If* X *is in a* non-crossing and concave *four-bar linkage, the distance between* $\mathbf{b}$ *and* $\mathbf{d}$ *decreases when the distance between* $\mathbf{a}$ *and* $\boldsymbol{\gamma}$ *decreases.*

Finally, we also introduce four-bar linkages with two pairs of parallel bars. These will be useful for further analysis of the linkages corresponding to combinations of two cylinders. In this case, the four-bar linkage consists of two pairs of bars, connecting the vertices $(\mathbf{a}, \mathbf{b}, \mathbf{c})$ and $(\mathbf{a}', \mathbf{d}, \mathbf{c}')$. Additionally, the bars $\mathbf{ab}$ and $\mathbf{a}'\mathbf{d}$ are constrained to be perpendicular to an oriented line $\boldsymbol{\alpha}$, and the bars $\mathbf{bc}$ and $\mathbf{dc}'$ are constrained to be perpendicular to an oriented line $\boldsymbol{\gamma}$. Specifically, the vertices $\mathbf{b}$ and $\mathbf{d}$ will be located on the left-hand side half planes of $\boldsymbol{\alpha}$ and $\boldsymbol{\gamma}$. Consequently, we will indicate a four-bar linkage with two pairs of parallel bars by two points and two planes, such as $X = \{\boldsymbol{\alpha}, \mathbf{b}, \boldsymbol{\gamma}, \mathbf{d}\}$.

In this case, however, the linkages come only in two types: concave non-crossing and crossing; see Figure 8.6. To specify when a four-bar linkage with two pairs of parallel bars is crossing or

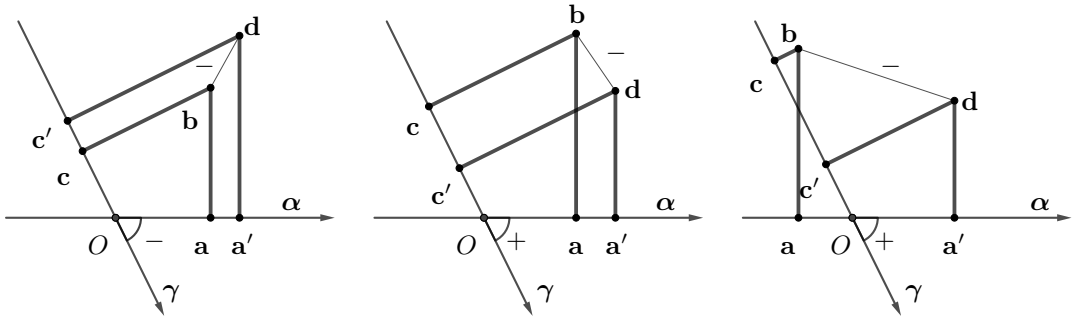

Figure 8.6: The three types of four-bar linkage with two pairs of parallel bars: convex (left), and two crossing configurations (center and right).

non-crossing, we consider the oriented distances of the intersection O of the base lines $\boldsymbol{\alpha}$ and $\boldsymbol{\gamma}$ to the respective foot-points $\mathbf{a}$, $\mathbf{a}'$, or $\mathbf{c}$, $\mathbf{c}'$ of $\mathbf{b}$ and $\mathbf{d}$. In particular, let $d_{\mathbf{a}}$, $d_{\mathbf{a}'}$, $d_{\mathbf{c}}$, $d_{\mathbf{c}'}$ denote the corresponding oriented distances. We compute

$$D = (d_{\mathbf{a}'} - d_{\mathbf{a}})(d_{\mathbf{c}'} - d_{\mathbf{c}}).$$

If $D > 0$, we say that the linkage is *non-crossing*, and if $D < 0$, we say that the linkage is *crossing*. Note that if the vertices are in general position, $D \neq 0$.

The diagonal property can be expressed as follows. Again, the corresponding proof can be found in Section 8.6.

Theorem 8.3 (Diagonal property of four-bar linkages with two pairs of parallel bars)**.** *Let $X = \{\boldsymbol{\alpha}, \mathbf{b}, \boldsymbol{\gamma}, \mathbf{d}\}$ be a four-bar linkage with two pairs of parallel bars in general position, that is, $\mathbf{b} \neq \mathbf{c}$ and $\boldsymbol{\alpha}$ and $\boldsymbol{\gamma}$ not parallel.*

- *If X is a* crossing *four-bar linkage, the distance between $\mathbf{b}$ and $\mathbf{d}$ decreases when the angle between the lines $\boldsymbol{\alpha}$ and $\boldsymbol{\gamma}$ increases.*
- *If X is a* non-crossing *(and concave) four-bar linkage, the distance between $\mathbf{b}$ and $\mathbf{d}$ decreases when the angle between the lines $\boldsymbol{\alpha}$ and $\boldsymbol{\gamma}$ decreases.*

8.5.2 Extracting Linkages from Crease Pattern

We now provide the definition of an extracted linkage of a developed configuration. For this purpose, let $\mathbf{x}_j$ denote the vertices of the common planar discrete glue curve, that is, $\mathbf{x}_j = \mathbf{x}_1(t_j) = \mathbf{x}_2(t_j)$. If $\mathbf{s}_j(t, u)$ is a cone, let $\mathbf{v}_j$ be the location of its apex. If $\mathbf{s}_j(t, u)$ is a cylinder, let π_j be its (oriented) base line, such that all points $\mathbf{x}_j$ lie to the left-hand side of π_j. (If we combine a cylinder and a cone, without loss of generality, let $\mathbf{s}_1(t, u)$ be the cone.)

We define the bars of the *extracted linkage* to be as follows. Let a_j denote the bars that connect $\mathbf{x}_j$ with $\mathbf{v}_1$ or the corresponding base point on π_1, and let b_j denote the bars that connect $\mathbf{x}_j$ with $\mathbf{v}_2$ or the corresponding base point on π_2. In addition, we will use a_j or b_j to refer to the bar lengths too.

Additionally, we assume that the extracted linkages are positioned in the plane in *standard position*, defined as follows:

- If both surfaces are cones, let the apex of the first cone coincide with the origin, and the apex of the second cone be located on the positive x-axis.
- If one surface is a cone and the other a cylinder, assume that the cone apex $\mathbf{v}_1$ is located at the origin, and that the cylinder's base line π_2 is perpendicular to the x-axis, specifically, $\pi_2 : x = v$ for some $v > 0$.
- If both surfaces are cylinders, let the linkage be positioned such that the intersection of base lines coincides with the origin. In addition, let π_1 be aligned with the x-axis.

If the vertices $\mathbf{x}_j$ of the common polyline have both positive and negative y-coordinates, reflect the linkage points with negative y-coordinates on the x-axis to arrive at a linkage with vertices that have non-negative y-coordinates.

An *extracted four-bar linkage* consists of two consecutive rule polylines, that is, (a_i, b_i) and (a_{i+1}, b_{i+1}), that are joined at their common endpoints. These four-bar linkages can be categorized into three types:

- *Cone-cone combination:* If the extracted linkage corresponds to a gluing of two cones, the obtained linkage is a (standard) four-bar linkage. Due to the above assumptions, the linkage is either non-crossing concave, crossing, or has at most two collinear bars that correspond to different surfaces.
- *Cylinder-cone combination:* If the extracted linkage corresponds to a gluing of a cylinder and a cone, the linkage is a four-bar linkage with a pair of parallel bars. Due to the above assumptions, the linkage is either non-crossing concave, crossing, or has at most two collinear bars that correspond to different surfaces.
- *Cylinder-cylinder combination:* If the extracted linkage corresponds to a gluing of two cylinders, the linkage is a four-bar linkage with two pairs of parallel bars. Due to the above assumptions, the linkage is either non-crossing, or crossing.

Note that in the context of the extracted linkages, we assume that consecutive bars corresponding to the same surface, such as a_i and a_{i+1}, or b_i and b_{i+1}, are not collinear.

Given that none of the considered linkages are convex, we will focus our discussion on distinguishing between non-crossing and crossing linkages. Additionally, we will use the term *cable distance* to refer to the distance between $\mathbf{x}_i$ and $\mathbf{x}_{i+1}$. This term intuitively captures our objective of considering configurations where the distance between $\mathbf{x}_i$ and $\mathbf{x}_{i+1}$ is either smaller or equal to the distance in the initial configuration.

8.5.3 Collinear Linkage Configurations

In the following analysis, we explore the configuration space of linkages and investigate the relationships between bar lengths and diagonals. Additionally, we consider contracted motions of all types of linkages. In particular, we show contracted motions of extracted collinear configurations (see Lemma 8.3 and Lemma 8.5). Finally, we classify which types of extracted four-bar linkages of the same type are compatible to ensure the existence of a local contracted motion (see Corollary 8.1, Corollary 8.2, and Corollary 8.3).

Before we continue, we make note of the following:

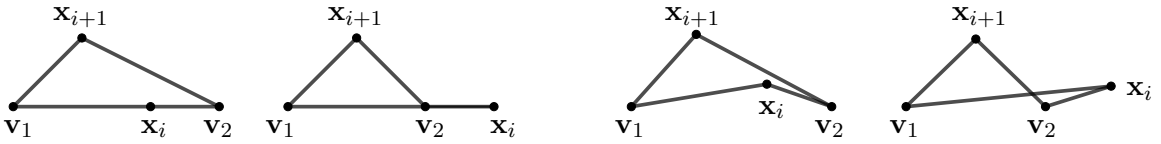

Figure 8.7: Illustration of two collinear configurations of extracted linkages corresponding to cone-cone combinations (left) and the configurations after contracted motions (right).

Lemma 8.1. *Let a and a' be two lengths. There exists a triangle with side lengths (a, a', d) if and only if $|a - a'| \leq d \leq a + a'$. For $a \neq a'$, there exists a (possibly degenerated) right trapezoid[2], whose parallel edges have length a and a' and whose non-perpendicular edge has length d if and only if $|a - a'| \leq d$.*

Proof. The first claim follows directly from the triangle inequalities.

For the second claim, we construct the trapezoid from an inscribed right triangle with side length $|a - a'|$ and hypotenuse d. It follows, that such a triangle exists if and only if $d \geq |a - a'|$. □

Cone-cone combination

Let $X = \{\mathbf{v}_1, \mathbf{x}_i, \mathbf{v}_2, \mathbf{x}_{i+1}\}$ be an extracted four-bar linkage of a cone-cone combination.

Since $\{\mathbf{v}_1, \mathbf{v}_2, \mathbf{x}_i\}$ and $\{\mathbf{v}_1, \mathbf{v}_2, \mathbf{x}_{i+1}\}$ form triangles, it follows from the triangle inequalities described in Lemma 8.1 that the diagonal distances need to satisfy

$$v_{\min} = \max\{|a_i - b_i|, |a_{i+1} - b_{i+1}|\} \leq |\mathbf{v}_1 - \mathbf{v}_2| \leq \min\{a_i + b_i, a_{i+1} + b_{i+1}\} = v_{\max}.$$

Similarly, the triangles $\{\mathbf{v}_1, \mathbf{x}_i, \mathbf{x}_{i+1}\}$ and $\{\mathbf{v}_2, \mathbf{x}_i, \mathbf{x}_{i+1}\}$ yield

$$d_{\min} = \max\{|a_i - a_{i+1}|, |b_i - b_{i+1}|\} \leq |\mathbf{x}_i - \mathbf{x}_{i+1}| \leq \min\{a_i + a_{i+1}, b_i + b_{i+1}\} = d_{\max}.$$

Lemma 8.2. *Given four bar lengths a_i, a_{i+1}, b_i and b_{i+1}, and a distance $v = |\mathbf{v}_A - \mathbf{v}_B|$ with $v_{\min} \leq v \leq v_{\max}$, a configuration of an extracted linkage corresponding to a cone-cone combination in standard position is uniquely defined.*

Proof. Given the distance v, we can first position the points $\mathbf{v}_1 = (0, 0)$ and $\mathbf{v}_2 = (v, 0)$. Since both points $\mathbf{x}_i$ and $\mathbf{x}_{i+1}$ should have non-negative y-coordinate, their location is uniquely defined from the incident bar lengths. □

It follows that there are only two cases where a_i and b_i become collinear: either when $|\mathbf{v}_1 - \mathbf{v}_2| = a_i + b_i$ or when $|\mathbf{v}_1 - \mathbf{v}_2| = |a_i - b_i|$, as depicted in Figure 8.7. In the following, we will also refer to these configurations as *non-crossing* and *crossing* cone-cone combinations, respectively. A justification of this is provided by the next lemma:

Lemma 8.3. *Given an extracted four-bar linkage corresponding to a collinear non-crossing cone-cone combination, that is, $|\mathbf{v}_1 - \mathbf{v}_2| = a_i + b_i$, decreasing the distance between $\mathbf{v}_1$ and $\mathbf{v}_2$ such that $\mathbf{x}_i$ and $\mathbf{x}_{i+1}$ lie on the same side of $\mathbf{v}_1\mathbf{v}_2$ decreases the distance between the points $\mathbf{x}_i$ and $\mathbf{x}_{i+1}$.*

Given an extracted four-bar linkage corresponding to a collinear crossing cone-cone combination, that is, $|\mathbf{v}_1 - \mathbf{v}_2| = |a_i - b_i|$, increasing the distance between $\mathbf{v}_A$ and $\mathbf{v}_B$ such that $\mathbf{x}_i$ and $\mathbf{x}_{i+1}$ lie on the same side of $\mathbf{v}_1\mathbf{v}_2$ decreases the distance between the points $\mathbf{x}_i$ and $\mathbf{x}_{i+1}$.

[2] A *right trapezoid* is a trapezoid with two right angles.

Proof. First, we consider the case where $|\mathbf{v}_1 - \mathbf{v}_2| = a_i + b_i < a_{i+1} + b_{i+1}$ and argue that this configuration behaves like a non-crossing linkage.

We consider the configurations obtained by slightly rotating the bar a_i towards a_{i+1}, hereby decreasing the cable distance, that is, the distance between $\mathbf{x}_i$ and $\mathbf{x}_{i+1}$. As the initial configuration is a triangle, the initial cable distance d between $\mathbf{x}_i$ and $\mathbf{x}_{i+1}$ satisfies

$$d > \max\{|a_i - a_{i+1}|, |b_i - b_{i+1}|\} = d_{\min}.$$

As the cable distance varies smoothly with the rotation angle ε, we obtain a one-parameter family of shapes where the cable distance monotonically decreases while staying greater than $d_{\min}$, ensuring that neither a_i and a_{i+1}, or b_i and b_{i+1} become collinear. In addition, a_i and b_i are not collinear since we decrease the angle between a_i and a_{i+1}. Furthermore, a_{i+1} and b_{i+1} cannot become collinear due to length constraints corresponding to the triangle inequalities. For all intermediate shapes, we find the location of vertex $\mathbf{v}_2$, such that $\mathbf{v}_1$ and $\mathbf{v}_2$ lie on opposite sides of $\mathbf{x}_i$ and $\mathbf{x}_{i+1}$.

It remains to show that the distance between $\mathbf{v}_1$ and $\mathbf{v}_2$ decreases, and that the obtained linkage configuration's vertices $\mathbf{x}_i$ and $\mathbf{x}_{i+1}$ lie on one side of $\mathbf{v}_1$ and $\mathbf{v}_2$.

Since we smoothly varied the initial linkage, the motion is reversible. When considering the reversed motion, we observe that the resulting shape cannot be crossing. This is because a crossing linkage in general position with increasing distances between vertices $\mathbf{x}_i$ and $\mathbf{x}_{i+1}$ decreases the distance between $\mathbf{v}_1$ and $\mathbf{v}_2$, as stated in Theorem 8.1. As the initial configuration started with the maximal possible distance between $\mathbf{v}_1$ and $\mathbf{v}_2$, this is not possible. An analogous argument yields that the intermediate configurations are not convex.

Therefore, the intermediate configurations are concave and non-crossing, and thus a motion with decreasing distance between $\mathbf{x}_i$ and $\mathbf{x}_{i+1}$ decreases distance $\mathbf{v}_1\mathbf{v}_2$. Note that this also implies that both $\mathbf{x}_i$ and $\mathbf{x}_{i+1}$ lie on one side of $\mathbf{v}_1\mathbf{v}_2$.

Second, we consider the case where $|\mathbf{v}_1 - \mathbf{v}_2| = |a_i - b_i| > |a_{i+1} - b_{i+1}|$, and argue that this configuration behaves like a crossing linkage. Again, we consider the motion obtained by slightly rotating the bar a_i towards a_{i+1}, hereby decreasing the cable distance. As the initial configuration satisfies the corresponding triangle inequalities, we have that the initial cable distance d satisfies

$$d > \max\{|a_i - a_{i+1}|, |b_i - b_{i+1}|\} = d_{\min}.$$

Analogous to the previous case, by smoothly varying the rotation angle ε, we obtain a one-parameter family of shapes whose cable distances monotonically decrease while staying greater than $d_{\min}$, that is, no other bars become collinear. For all intermediate shapes, we find the location of vertex $\mathbf{v}_2$ such that $\mathbf{v}_1$ and $\mathbf{v}_2$ lie on the same side of the diagonal $\mathbf{x}_i$ and $\mathbf{x}_{i+1}$. Unlike above, this already implies that vertices $\mathbf{x}_i$ and $\mathbf{x}_{i+1}$ lie on the same side of $\mathbf{v}_1$ and $\mathbf{v}_2$. Furthermore, the intermediate configurations can only be non-crossing concave or crossing.

It remains to show that the distance between $\mathbf{v}_1$ and $\mathbf{v}_2$ increases, and that the shapes are crossing. For this purpose, we again consider the reversed motion. If this would be a non-crossing linkage, reversing the motion would increase the distance between points $\mathbf{v}_1$ and $\mathbf{v}_2$, as stated in Theorem 8.1. However, as the initial configuration started with the minimal possible distance between $\mathbf{v}_1$ and $\mathbf{v}_2$, this is not possible.

Therefore, the intermediate configurations are crossing, and thus decreasing distance between $\mathbf{x}_i$ and $\mathbf{x}_{i+1}$ increases distance between $\mathbf{v}_1$ and $\mathbf{v}_2$.

□

It follows from Theorem 8.1 and Lemma 8.3 that extracted linkages allow a contracted diagonals motion if and only if they consist of four-bar linkages of the same type:

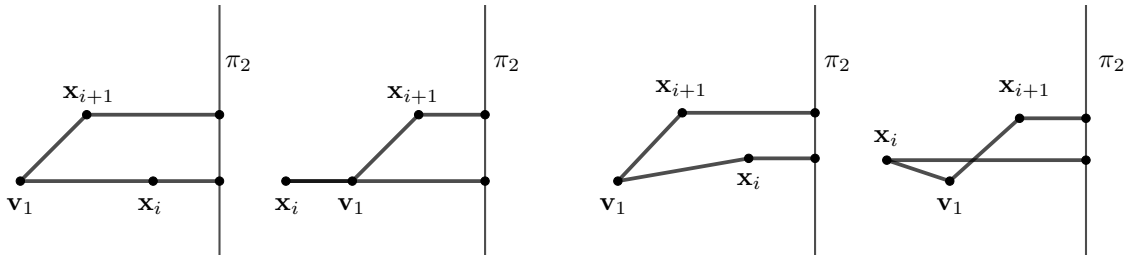

Figure 8.8: Illustration of two collinear configurations of extracted linkages corresponding to cylinder-cone combinations (left) and the configurations after a contracted motion (right).

Corollary 8.1. *An extracted linkage of a cone-cone combination allows a contracted motion by decreasing the distance between the cone apices if and only if all extracted four-bar linkages are non-crossing.*

Conversely, an extracted linkage of a cone-cone combination allows a contracted motion by increasing the distance between the cone apices if and only if all extracted four-bar linkages are crossing.

Cylinder-cone combination

Let $X = \{\mathbf{v}_1, \mathbf{x}_i, \pi_2, \mathbf{x}_{i+1}\}$ be an extracted four-bar linkage of a cylinder-cone combination.

Since the sum of connected bars cannot be smaller than the distance between the apex and the base line, and the difference cannot be bigger than the distance between the apex and the base line, we have

$$v_{\min} = \max\{|a_i - b_i|, |a_{i+1} - b_{i+1}|\} \leq \operatorname{dist}(\mathbf{v}, \pi_2) \leq \min\{a_i + b_i, a_{i+1} + b_{i+1}\} = v_{\max}.$$

Similarly, to the previous section, the cable distance is limited by applications of the statements in Lemma 8.1. Specifically, triangle inequalities corresponding to triangle $\{\mathbf{v}_1, \mathbf{x}_i, \mathbf{x}_{i+1}\}$, and the constraint of the existence of a right trapezoid with parallel edge lengths b_i, b_{i+1} result in

$$d_{\min} = \max\{|a_i - a_{i+1}|, |b_i - b_{i+1}|\} \leq |\mathbf{x}_i - \mathbf{x}_{i+1}| \leq a_i + a_{i+1} = d_{\max}.$$

Lemma 8.4. *Given four bar lengths a_i, a_{i+1}, b_i, and b_{i+1}, and the distance $v = \operatorname{dist}(\mathbf{v}_1, \pi_2)$ where $v_{\min} \leq v \leq v_{\max}$, a configuration of an extracted linkage corresponding to a cylinder-cone combination in standard position is uniquely defined.*

Proof. When positioning apex $\mathbf{v}_1$ at the origin and $\pi_2 : x = v$, we obtain

$$\mathbf{x}_j = \left(v - b_j, \sqrt{a_j^2 - (v - b_j)^2}\right);$$

see the proof of Theorem 8.2. Note that these points are well-defined, since $a_j^2 - (v - b_j)^2 \geq 0$ for $v \in [|a_j - b_j|, a_j + b_j]$. □

It follows that there are only two cases where a_i and b_i become collinear: either when $\operatorname{dist}(\mathbf{v}_1, \pi_2) = a_i + b_i$ or when $\operatorname{dist}(\mathbf{v}_1, \pi_2) = |a_i - b_i|$, as depicted in Figure 8.8. As before, we will also refer to these configurations as *non-crossing* and *crossing* cylinder-cone combinations, respectively. A justification of this is provided by the next lemma:

Lemma 8.5. *Given an extracted four-bar linkage corresponding to a collinear cylinder-cone combination with* $\operatorname{dist}(\mathbf{v}_1, \pi_2) = a_i + b_i$*, decreasing the distance between* $\mathbf{v}_1$ *and* π_2 *such that* $\mathbf{x}_i$ *and* $\mathbf{x}_{i+1}$ *lie on the same side of the normal of* π_2 *through* $\mathbf{v}_1$ *decreases the distance between the points* $\mathbf{x}_i$ *and* $\mathbf{x}_{i+1}$*.*

Given an extracted four-bar linkage corresponding to a collinear cylinder-cone combination with $\operatorname{dist}(\mathbf{v}_1, \pi_2) = |a_i - b_i|$*, decreasing the distance between* $\mathbf{v}_1$ *and* π_2 *such that* $\mathbf{x}_i$ *and* $\mathbf{x}_{i+1}$ *lie on the same side of the normal of* π_2 *through* $\mathbf{v}_1$ *decreases the distance between the points* $\mathbf{x}_i$ *and* $\mathbf{x}_{i+1}$*.*

Proof. The proof is analogous to the proof of Lemma 8.3. In particular, we start with the corresponding configuration and modify it by rotating a_i towards a_{i+1}. We obtain the location of the base line from the construction of a corresponding right trapezoid.

Again, we argue that the corresponding configurations are non-crossing or crossing respectively, as it would otherwise contradict the maximality or minimality of the initial lengths. □

Similar to Corollary 8.1, it follows from Theorem 8.2 and Lemma 8.5 that extracted linkages allow a contracted diagonals motion if and only if they consist of four-bar linkages of the same type:

Corollary 8.2. *An extracted linkage of a cylinder-cone combination allows a contracted motion by decreasing the distance between the cone apex and base line if and only if all extracted four-bar linkages are non-crossing.*

Conversely, an extracted linkage of a cylinder-cone combination allows a contracted motion by increasing the distance between the cone apex and the base line if and only if all extracted four-bar linkages are crossing.

Cylinder-cylinder combination

Let $X = \{\pi_1, \mathbf{x}_i, \pi_2, \mathbf{x}_{i+1}\}$ be an extracted four-bar linkage of a cylinder-cylinder combination.

In the following, we limit our considerations only to the case where $a_i \neq a_{i+1}$ or $b_i \neq b_{i+1}$. We therefore require that

$$0 < \angle(\pi_1, \pi_2) < \pi.$$

Furthermore, it follows from the existence of right trapezoids in Lemma 8.1 that

$$d_{\min} = \max\{|a_i - a_{i+1}|, |b_i - b_{i+1}|\} \leq |\mathbf{x}_i - \mathbf{x}_{i+1}|.$$

Lemma 8.6. *Given four bar lengths* a_i*,* a_{i+1}*,* b_i *and* b_{i+1}*, and an angle* $\varphi \in (0, \pi)$ *between the base line* π_1 *and* π_2*, a configuration of an extracted linkage corresponding to a cylinder-cylinder combination in standard position is uniquely defined.*

Proof. It follows from the proof of Theorem 8.3, that

$$\mathbf{x}_j = \left(\frac{1}{\sin\varphi}(b_j - a_j\cos\varphi), a_j\right),$$

resulting in the statement. □

In the following, we exclude collinear bars a_j and b_j in the case of cylinder-cylinder combinations, since the considered linkage is not well-defined for parallel planes. We therefore only claim:

Corollary 8.3. *An extracted linkage of a cylinder-cylinder combination allows a contracted motion by decreasing the angle between the base lines if all extracted four-bar linkages are non-crossing.*

Conversely, an extracted linkage of a cylinder-cylinder combination allows a contracted motion by increasing the angle between the base lines if all extracted four-bar linkages are crossing.

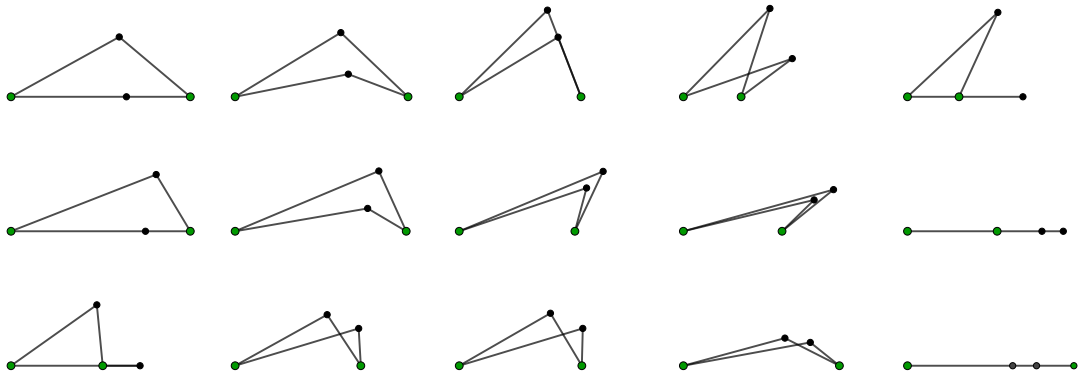

Figure 8.9: Motions of an extracted four-bar linkage corresponding to a cone-cone combination in standard position. First row: Non-crossing configuration changes to crossing configuration. Second row: Non-crossing configuration remains non-crossing. Third row: Crossing configuration remains crossing.

8.5.4 Linkage Motions and the Joining Step

In this section, we examine the range of motion of extracted four-bar linkages and analyze the behavior of the cable distance. We establish that the cable distance undergoes a change from increasing to decreasing or vice versa at most once.

By the end of this section, we conclude that for any two linkage configurations, where the second configuration has a smaller cable length than the first, it is possible to smoothly transition from the first linkage to the second while maintaining contracted diagonals of the intermediate configurations (Corollary 8.4).

Cone-cone combinations

We first consider the motion that starts with collinear non-crossing configuration, that is at $|\mathbf{v}_1 - \mathbf{v}_2| = v_{\max} = a_i + b_i$; see Figure 8.9 (first and second row). Using Lemma 8.3, decreasing the distance between the points $\mathbf{v}_1$ and $\mathbf{v}_2$, decreases the cable distance. We decrease the distance between points $\mathbf{v}_1$ and $\mathbf{v}_2$ until three points become collinear:

- If the three points $\{\mathbf{v}_1, \mathbf{x}_i, \mathbf{v}_2\}$ or $\{\mathbf{v}_1, \mathbf{x}_{i+1}, \mathbf{v}_2\}$ become collinear, we have that $|\mathbf{v}_1 - \mathbf{v}_2| = v_{\min}$ and no further motion is possible; see Figure 8.9 (second row).
- If on the other hand the three points $\{\mathbf{v}_1, \mathbf{x}_i, \mathbf{x}_{i+1}\}$ or $\{\mathbf{v}_2, \mathbf{x}_i, \mathbf{x}_{i+1}\}$ become collinear, we are at a transition point to a crossing configuration; see Figure 8.9 (first row). This is because remaining collinear is not possible, and remaining non-crossing would result in a decrease of the cable distance beyond feasible values by Theorem 8.1. Thus, decreasing the distance between $\mathbf{v}_1$ and $\mathbf{v}_2$ more leads to an increase of the cable distance. The remaining motion then increases the cable distance until $|\mathbf{v}_1 - \mathbf{v}_2| = v_{\min}$.

Second, we consider the motion that starts with a collinear crossing configuration with $|\mathbf{v}_1 - \mathbf{v}_2| = v_{\min} = |a_i - b_i|$; see Figure 8.9 (first and third row), from right to left. Using Lemma 8.3, increasing the distance between the points $\mathbf{v}_1$ and $\mathbf{v}_2$ decreases the cable distance. Similar to before, we increase the distance between points $\mathbf{v}_1$ and $\mathbf{v}_2$ until three points become collinear:

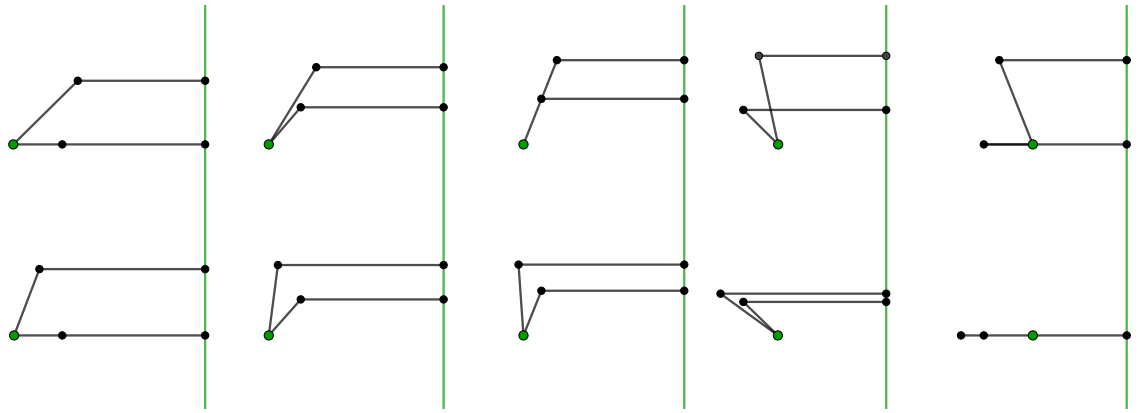

Figure 8.10: Motions of an extracted four-bar linkage corresponding to a cylinder-cone combination in standard position. First row: Non-crossing configuration changes to crossing configuration. Second row: Non-crossing configuration remains non-crossing.

- If the three points $\{\mathbf{v}_1, \mathbf{x}_i, \mathbf{v}_2\}$ or $\{\mathbf{v}_1, \mathbf{x}_{i+1}, \mathbf{v}_2\}$ become collinear, we have that $|\mathbf{v}_1 - \mathbf{v}_2| = v_{\min}$ and no further motion is possible; see Figure 8.9 (third row).
- If on the other hand the three points $\{\mathbf{v}_1, \mathbf{x}_i, \mathbf{x}_{i+1}\}$ or $\{\mathbf{v}_2, \mathbf{x}_i, \mathbf{x}_{i+1}\}$ become collinear, we are at a transition point to a non-crossing configuration; see Figure 8.9 (first row). This is because remaining collinear is not possible, and remaining non-crossing would result in an increase of the cable distance beyond feasible values by Theorem 8.2. Thus, increasing the distance between $\mathbf{v}_1$ and $\mathbf{v}_2$ more leads to a decrease of the cable distance. The remaining motion then decreases the cable distance until $|\mathbf{v}_1 - \mathbf{v}_2| = v_{\max}$.

Cylinder-cone combinations

Analogous observation can be done also in the cylinder-cone case; see Figure 8.10. Instead of decreasing the distance between $\mathbf{v}_1$ and $\mathbf{v}_2$, we decrease the distance between $\mathbf{v}_1$ and π_2.

We first consider the motion that starts with a collinear non-crossing configuration, that is at $\operatorname{dist}(\mathbf{v}_1, \pi_2) = v_{\max} = a_i + b_i$. Using Lemma 8.5, decreasing the distance between the point $\mathbf{v}_1$ and the line π_2, decreases the cable distance. We decrease the distance between the point $\mathbf{v}_1$ and the line π_2 until the two bars become collinear:

- If the bars a_i and b_i or a_{i+1} and b_{i+1} become collinear, we have that $\operatorname{dist}(\mathbf{v}_1, \pi_2) = v_{\min}$ and no further motion is possible; see Figure 8.10 (second row).
- If on the other hand the bars a_i and a_{i+1} become collinear, we are at a transition point to a crossing configuration; see Figure 8.10 (first row). This is because remaining collinear is not possible, and remaining non-crossing would result in a decrease of the cable distance beyond feasible values by Theorem 8.2. Thus, decreasing the distance between $\mathbf{v}_1$ and π_2 more leads to an increase of the cable distance. The remaining motion then increases the cable distance until $\operatorname{dist}(\mathbf{v}_1, \pi_2) = v_{\min}$.

Every non-crossing configuration of a cylinder-cone combination corresponds to a crossing cylinder-cone combination. Thus, reversing the argument yields a motion that starts from a collinear crossing configuration and results in a collinear non-crossing or fully collinear configuration.

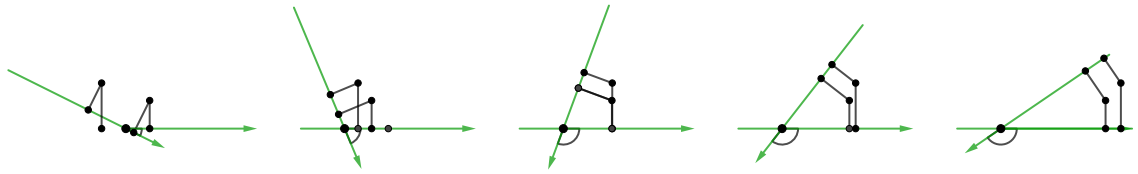

Figure 8.11: Motion of a four-bar linkage corresponding to a cylinder-cylinder combination.

Cylinder-cylinder combinations

In the case of two cylinders, our consideration begins at $\varphi = \frac{\pi}{2}$; see Figure 8.11. Let us first examine the scenario where the linkage is non-crossing at $\varphi = \frac{\pi}{2}$. According to Theorem 8.3, increasing the angle φ leads to an increase in the cable distance. Consequently, the linkage will remain non-crossing as we continue the motion in this manner.

Conversely, starting at $\varphi = \frac{\pi}{2}$, we consider the motion induced by decreasing φ. This causes the cable distance to decrease, resulting in two possibilities:

- While decreasing φ, we do not reach a collinear state.
- While decreasing φ, we reach a collinear state. This occurs at the smallest possible cable distance. Since further decreasing the cable distance is not feasible, the linkage transitions into a crossing state. Subsequently, as the angle is further decreased, the cable distance increases and the linkage remains in a crossing state until the end of the motion.

Hence, it can be concluded that there is at most one transition from a crossing to a non-crossing configuration throughout the motion that involves a non-crossing configuration.

The motion of the linkage behaves similarly when initiated from a crossing state. In other words, during the motion, there is at most one transition to a non-crossing configuration.

Interpolation between linkages

In all cases, we observe that a transition from decreasing to increasing cable length or vice versa can occur at most once. Therefore, when considering the cable distance throughout the motion, there can be at most one local minimum. Based on this observation, we draw the following conclusion:

Lemma 8.7. *Given an initial four-bar extracted linkage configuration X_0 with a cable distance of d_0, and a target configuration X_1 with a cable distance of d_1, if $d_1 \leq d_0$, there exists a smooth transition of linkages X_t between X_0 and X_1 with cable distance d_t, such that $d_t \leq d_0$.*

Recall that for a given set of bar lengths and diagonal distance, the corresponding extracted four-bar linkage configuration in the standard position is uniquely defined. This allows us to combine multiple four-bar linkages, leading to the following result:

Corollary 8.4. *Given an initial extracted linkage configuration X_0 with cable distances $d_{0,i}$, and a target configuration X_1 with cable distances $d_{1,i}$, if $d_{1,i} \leq d_{0,i}$ for all i, there exists a smooth transition of linkages X_t between X_0 and X_1 with cable distances $d_{t,i}$ such that $d_{t,i} \leq d_{0,i}$.*

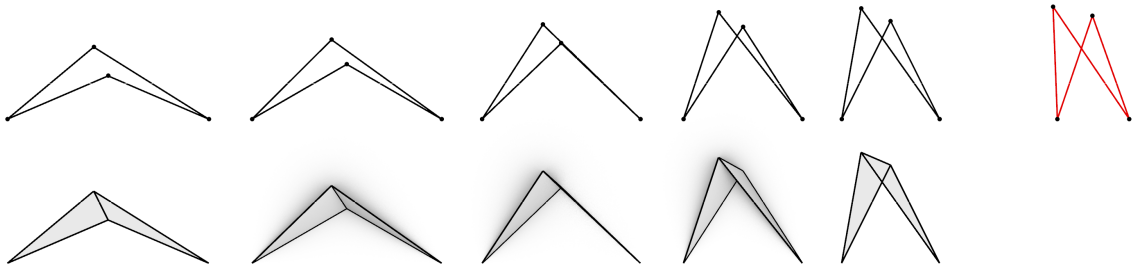

(a) Case 1: Cable length increases beyond the configuration corresponding to the flat-folded state.

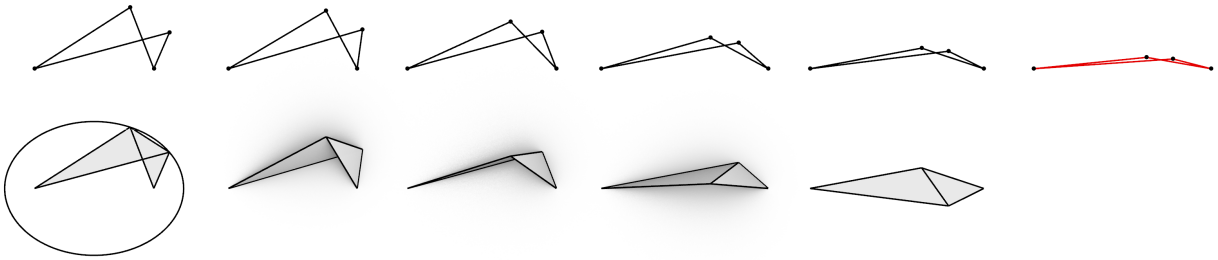

(b) Case 2: Cable length decreases beyond the configuration corresponding to the flat-folded state.

Figure 8.12: Illustration of linkages obtained from the joining step (top rows) and their corresponding configurations after the fanning step (bottom rows).

8.5.5 Linkage Motions and the Fanning Step

In contrast to the smooth case, the discrete fanning step during the construction of linkages imposes an additional requirement to ensure feasibility. Apart from reducing cable lengths, it is necessary to consider the realizability of the proposed linkages.

Specifically, let us consider the two faces corresponding to a (planar) four-bar linkage; as depicted in Figure 8.12a. During the folding motion corresponding to the fanned-out linkage motion, one face rotates with respect to the other, until the rotation angle of π is reached. If the initial linkage configuration is non-crossing, the resulting configuration becomes crossing, and vice versa. The extracted four-bar linkage corresponding to this extremal configuration represents a bound on the distance between the two apices, the apex and the base line, or the angle between the baselines.

To determine the maximum achievable configuration for each four-bar linkage given the initial state, we reflect one face about the corresponding edge of the discrete glue curve. If the linkage was initially crossing, this reflected configuration represents the maximum achievable distance or angle for that particular four-bar linkage. If the linkage was initially non-crossing, this reflected configuration represents the minimum achievable distance or angle for that particular four-bar linkage. To obtain a feasible configuration for the entire pattern, we take the corresponding minimum or maximum over these distances.

In many cases, the configuration obtained by reflecting one face onto the other side is a configuration of the other type with equal cable length and part of the motion. Therefore, usually continuing the motion beyond this configuration would result in not feasible cable lengths anyhow; see Figure 8.12a. However, this is not always the case. In Figure 8.12b, there are configurations of the linkage that satisfy the cable distance requirement, but fail to construct the fanning step when the apices are too far apart.

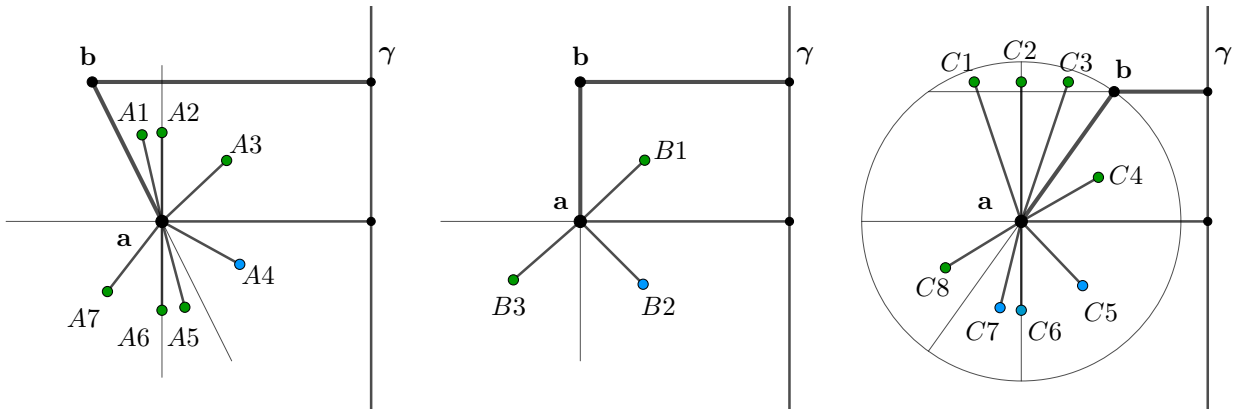

Figure 8.13: Illustration of the case analysis from the proof of Theorem 8.2.

Theorem 8.4. *Given an extracted linkage X_0 and a configuration X_1 with contracted cable lengths corresponding to an appropriate distance or angle, there exists a rigid motion connecting X_0 with a fanned-out version of X_1.*

In Chapter 10, we use the discrete join-and-fan method and Theorem 8.4 to prove rigid foldability of two discretizations of conic crease patterns with reflecting rule lines. It is worth noting that the conventional method of proving rigid foldability in quadrivalent patterns, which involves fold angle multipliers [24], cannot be directly applied in this context as some of the studied patterns have non-flat-foldable vertices.

8.6 Selected Proofs from Section 8.5

Considering the length and potential diversion caused by the inclusion of certain proofs in Section 8.5, we have relocated them to this dedicated section.

Proof of Theorem 8.2. Let a_1 and a_2 be the lengths of the bars **ab** and **ad** corresponding to the cone, and b_1 and b_2 be the lengths of the bars **b** and **dc′** corresponding to the cylinder. Without loss of generality, let $\mathbf{a} = (0, 0)$ be the cone apex and $\boldsymbol{\gamma} : x = v$ be the the cylinder's base line.

From the distance constraints

$$|\mathbf{b}|^2 = a_1^2 \qquad \text{and} \qquad \mathbf{b} \cdot (1, 0) = v - b_1,$$
$$|\mathbf{d}|^2 = a_2^2 \qquad \text{and} \qquad \mathbf{d} \cdot (1, 0) = v - b_2,$$

we obtain the locations of the vertices

$$\mathbf{b} = \left(v - b_1, \sigma_1 \sqrt{a_1^2 - (v - b_1)^2}\right),$$

and

$$\mathbf{d} = \left(v - b_2, \sigma_2 \sqrt{a_2^2 - (v - b_2)^2}\right),$$

where $\sigma_j \in \{-1, 1\}$.

In the following, we are interested in the change of the squared distance $d(v)$ between the points, that is,

$$d(v) = |\mathbf{a} - \mathbf{d}|^2 = (b_1 - b_2)^2 + \left(\sigma_1 \sqrt{a_1^2 - (v - b_1)^2} - \sigma_2 \sqrt{a_2^2 - (v - b_2)^2}\right)^2.$$

To see the infinitesimal behavior, we consider the fist derivative,

$$d'(v) = 2F_1F_2,$$

where

$$F_1 = \sigma_1\sqrt{a_1^2 - (v-b_1)^2} - \sigma_2\sqrt{a_2^2 - (v-b_2)^2}$$

and

$$F_2 = \frac{\sigma_2(v-b_2)}{\sqrt{a_2^2 - (v-b_2)^2}} - \frac{\sigma_1(v-b_1)}{\sqrt{a_1^2 - (v-b_1)^2}}.$$

If $d'(v) > 0$, the length between $\mathbf{b}$ and $\mathbf{d}$ increases for increasing distance between $\mathbf{a}$ and $\boldsymbol{\gamma}$, which we show to happen in the non-crossing concave case. If $d'(v) < 0$, the length between $\mathbf{b}$ and $\mathbf{d}$ decreases for increasing distance between $\mathbf{a}$ and $\boldsymbol{\gamma}$, which we show to happen in the crossing or convex case.

We first consider the non-crossing cases, and assume without loss of generality $a_1 > a_2$, and that $\sigma_1 = 1$, that is, $\mathbf{b}$ to be located in the upper half plane. In the following, we will use a (slightly lengthy) case-analysis to analyze the signs of F_1 and F_2, and therefore determine the sign of $d'(v)$; see Figure 8.13.

- *Case A:* Here, we assume that $\mathbf{b}_x = v - b_1 < 0$. Note that since we assume that $a_1 > a_2$, we obtain non-crossing configurations only when $\mathbf{b}_y > \mathbf{d}_y$, and thus, $F_1 > 0$. We now consider the following seven cases for the location of $\mathbf{d}$:
  - *Case A1:* Here $\mathbf{d}$ and has negative x-coordinate, that is, $v - b_2 < 0$, but positive y-coordinate, that is, $\sigma_2 = 1$. As vertex $\mathbf{d}$ it additionally lies to "the right" of the line $\mathbf{ab}$, we have that
  $$\frac{\sqrt{a_1^2 - (v-b_1)^2}}{\sqrt{a_2^2 - (v-b_2)^2}} = \frac{\mathbf{b}_y}{\mathbf{d}_y} < \frac{a_1}{a_2} < \frac{\mathbf{b}_x}{\mathbf{d}_x} = \frac{\sigma_1(v-b_1)}{\sigma_2(v-b_2)}.$$
  For the corresponding concave configuration, it follows that $F_2 > 0$ and $d'(v) > 0$.
  - *Case A2:* Here, we have that $v - b_2 = 0$ and $\sigma_2 = 1$.
  For the corresponding concave configuration, it follows that $F_2 > 0$ and $d'(v) > 0$.
  - *Case A3:* In this case, we have that $v - b_2 > 0$ and $\sigma_2 = 1$.
  For the corresponding concave configuration, it follows that $F_2 > 0$ and $d'(v) > 0$.
  - *Case A4:* In this case, $\sigma_2 = -1$ and $v - b_2 > 0$. In addition, we have that $\mathbf{d}$ lies to "the right" of line $\mathbf{ab}$, resulting in
  $$\frac{\sqrt{a_1^2 - (v-b_1)^2}}{\sqrt{a_2^2 - (v-b_2)^2}} = \frac{\mathbf{b}_y}{-\mathbf{d}_y} > \frac{a_1}{a_2} > \frac{\mathbf{b}_x}{-\mathbf{d}_x} = \frac{\sigma_i(v-b_1)}{\sigma_2(v-b_2)}.$$
  For the corresponding convex configuration, it follows that $F_2 < 0$ and $d'(v) < 0$.
  - *Case A5:* In this case, again $\sigma_2 = -1$ and $v - b_2 > 0$. In addition, we have that $\mathbf{d}$ lies to "the left" of line $\mathbf{ab}$, resulting in
  $$\frac{\sqrt{a_1^2 - (v-b_1)^2}}{\sqrt{a_2^2 - (v-b_2)^2}} = \frac{\mathbf{b}_y}{-\mathbf{d}_y} < \frac{a_1}{a_2} < \frac{\mathbf{b}_x}{-\mathbf{d}_x} = \frac{\sigma_1(v-b_1)}{\sigma_2(v-b_2)}.$$
  For the corresponding concave configuration, it follows that $F_2 > 0$ and $d'(v) > 0$.

- *Case A6:* Again $\sigma_2 = -1$, but in this case we have that $v - b_2 = 0$. For the corresponding concave configuration, it follows that $F_2 > 0$ and $d'(v) > 0$.
- *Case A7:* Finally, consider the case where $v - b_2 < 0$ and $\sigma_2 = -1$. For the corresponding concave configuration, it again follows that $F_2 > 0$ and $d'(v) > 0$.

- *Case B:* In this case, we assume that $v - b_1 = 0$. As in the previous case, we can only obtain non-crossing configurations for point combinations where $\mathbf{b}_y > \mathbf{d}_y$, and thus, $F_1 > 0$.
  - *Case B1:* Assume $v - b_2 > 0$ and $\sigma_2 = 1$.
  - For the corresponding concave configuration, it follows that $F_2 > 0$ and $d'(v) > 0$.
  - *Case B2:* Assume $v - b_2 > 0$ and $\sigma_2 = -1$.
    For the corresponding convex configuration, it follows that $F_2 < 0$ and $d'(v) < 0$.
  - *Case B3:* Assume $v - b_2 < 0$ and $\sigma_2 = -1$.
    For the corresponding concave configuration, it follows that $F_2 > 0$ and $d'(v) > 0$.

- *Case C:* Finally, we consider the cases where $v - b_1 > 0$. Unlike in the previous cases, it can happen $\mathbf{b}_y < \mathbf{d}_y$, and thus we consider both factors separately.
  - *Case C1:* Let $v - b_2 < 0$ and $\sigma_2 = 1$. To arrive at a non-crossing configuration, we require $\mathbf{b}_y < \mathbf{d}_y$, and thus $F_1 < 0$. In addition, it follows that $F_2 < 0$.
    For the corresponding concave configuration, we therefore have $d'(v) > 0$.
  - *Case C2:* Let $v - b_2 = 0$ and $\sigma_2 = 1$. To arrive at a non-crossing configuration, we require $\mathbf{b}_y < \mathbf{d}_y$, and thus $F_1 < 0$. In addition, it follows that $F_2 < 0$.
    For the corresponding concave configuration, we therefore have $d'(v) > 0$.
  - *Case C3:* Let $v - b_2 > 0$ and $\sigma_2 = 1$. To arrive at a non-crossing configuration, we again require $\mathbf{b}_y < \mathbf{d}_y$, and thus $F_1 < 0$. As $\mathbf{d}$ lies to "the left" of $\mathbf{ab}$, we have that
    $$\frac{\sqrt{a_1^2 - (v - b_1)^2}}{\sqrt{a_2^2 - (v - b_2)^2}} = \frac{\mathbf{b}_y}{\mathbf{d}_y} < \frac{a_1}{a_2} < \frac{\mathbf{b}_x}{\mathbf{d}_x} = \frac{\sigma_1(v - b_1)}{\sigma_2(v - b_2)},$$
    which implies that $F_2 < 0$.
    For the corresponding concave configuration, we therefore have $d'(v) > 0$.

  In the remaining cases, we have that $\mathbf{b}_y > \mathbf{d}_y$, and thus $F_1 > 0$.

  - *Case C4:* Let $v - b_2 > 0$ and $\sigma_2 = 1$. As $\mathbf{d}$ lies to "the right" of $\mathbf{ab}$, we have that
    $$\frac{\sqrt{a_1^2 - (v - b_1)^2}}{\sqrt{a_2^2 - (v - b_2)^2}} = \frac{\mathbf{b}_y}{\mathbf{d}_y} > \frac{a_1}{a_2} > \frac{\mathbf{b}_x}{\mathbf{d}_x} = \frac{\sigma_1(v - b_1)}{\sigma_2(v - b_2)},$$
    which implies that $F_2 > 0$.
    For the corresponding concave configuration, we again have $d'(v) > 0$.
  - *Case C5:* Let $v - b_2 > 0$ and $\sigma_2 = -1$, which implies that $F_2 < 0$.
    For the corresponding convex configuration, it follows that $d'(v) < 0$.
  - *Case C6:* Let $v - b_2 = 0$ and $\sigma_2 = -1$, which implies that $F_2 < 0$.
    For the corresponding convex configuration, it follows that $d'(v) < 0$.

– *Case C7:* In this case, we have that $v - b_2 < 0$ and $\sigma_2 = -1$. As $\mathbf{d}$ lies to "the right" of $\mathbf{ab}$, we have that

$$\frac{\sqrt{a_1^2 - (v-b_1)^2}}{\sqrt{a_2^2 - (v-b_2)^2}} = \frac{\mathbf{b}_y}{-\mathbf{d}_y} < \frac{a_1}{a_2} < \frac{\mathbf{b}_x}{-\mathbf{d}_x} = \frac{\sigma_1(v-b_1)}{\sigma_2(v-b_2)},$$

which implies that $F_2 < 0$.

For the corresponding convex configuration, it follows that $d'(v) < 0$.

– *Case C8:* Finally, we consider the case where $v - b_2 < 0$ and $\sigma_2 = -1$. As $\mathbf{d}$ lies to "the left" of $\mathbf{ab}$, we have that

$$\frac{\sqrt{a_1^2 - (v-b_1)^2}}{\sqrt{a_2^2 - (v-b_2)^2}} = \frac{\mathbf{b}_y}{-\mathbf{d}_y} > \frac{a_1}{a_2} > \frac{\mathbf{b}_x}{-\mathbf{d}_x} = \frac{\sigma_1(v-b_1)}{\sigma_2(v-b_2)},$$

which implies that $F_2 > 0$.

For the corresponding concave configuration, it follows that $d'(v) > 0$.

Ultimately, the case-analysis above confirms the statement for the non-crossing cases, that is, convex and concave non-crossing.

Note that every concave non-crossing linkage corresponds to a crossing linkage. The crossing linkage can be obtained by replacing the horizontal bars with bars of appropriate length to the other side, and reflecting the whole linkage across the y-axis. A non-crossing linkage configuration obtained by moving the base plane towards the apex corresponds to a crossing linkage configuration with the base plane moved away from the apex.

This concludes our proof. □

Proof of Theorem 8.3. As previously, we use a parametrization to study the behavior of the linkage. In particular, without loss of generality, assume that $\boldsymbol{\alpha}$ and $\boldsymbol{\gamma}$ coincide with the origin. In addition, assume that the base lines have direction vectors $\mathbf{r}_{\boldsymbol{\alpha}} = (1, 0)$ and $\mathbf{r}_{\boldsymbol{\gamma}} = (\cos\varphi, -\sin\varphi)$, resulting in the normals $\mathbf{n}_\alpha = (0, 1)$ and $\mathbf{n}_{\boldsymbol{\gamma}} = (\sin\varphi, \cos\varphi)$, where $\varphi \in [0, \pi]$. Finally, let a_1 and a_2 be the lengths of the cylinder bars corresponding to the first surface, that is, $\mathbf{ab}$ and $\mathbf{a'd}$, respectively. Similarly, let b_1 and b_2 be the lengths of the bars $\mathbf{bc}$ and $\mathbf{dc'}$.

Then, the vertices of the linkages satisfy

$$\begin{aligned} \mathbf{b} \cdot \mathbf{n}_\alpha &= a_1 \qquad \text{and} \qquad \mathbf{b} \cdot \mathbf{n}_{\boldsymbol{\gamma}} = b_1, \\ \mathbf{d} \cdot \mathbf{n}_\alpha &= a_2 \qquad \text{and} \qquad \mathbf{d} \cdot \mathbf{n}_{\boldsymbol{\gamma}} = b_2, \end{aligned}$$

resulting in the coordinates

$$\mathbf{b} = \left(\frac{1}{\sin\varphi}\left(b_1 - a_1\cos\varphi\right), a_1\right) \qquad \text{and} \qquad \mathbf{d} = \left(\frac{1}{\sin\varphi}\left(b_2 - a_2\cos\varphi\right), a_2\right).$$

Consequently, the diagonal distance reads

$$D(\varphi) = |\mathbf{b} - \mathbf{d}|^2 = (a_1 - a_2)^2 + \frac{1}{\sin^2\varphi}\left(-b_1 + b_2 + (a_1 - a_2)\cos\varphi\right)^2.$$

We compute the first derivative of $D'(\varphi)$ as

$$D'(\varphi) = \frac{2}{\sin^3\varphi}\left(-b_1 + b_2 + (a_1 - a_2)\cos\varphi\right)\left(-a_1 + a_2 + (b_1 - b_2)\cos\varphi\right).$$

Since $\varphi \in [0, \pi]$, the first factor is positive. In addition, we now show that the other factors correspond to $d_{\mathbf{a}} - d_{\mathbf{a}'}$ and $d_{\mathbf{c}} - d_{\mathbf{c}'}$, respectively.

First, the base points are

$$\mathbf{a} = \mathbf{b} - a_1 \mathbf{n}_{\boldsymbol{\alpha}} = \left(\frac{1}{\sin \varphi} (b_1 - a_1 \cos \varphi), 0 \right),$$
$$\mathbf{a}' = \mathbf{d} - a_2 \mathbf{n}_{\boldsymbol{\alpha}} = \left(\frac{1}{\sin \varphi} (b_2 - a_2 \cos \varphi), 0 \right).$$

and

$$\mathbf{c} = \mathbf{b} - b_1 \mathbf{n}_{\boldsymbol{\gamma}} = \left((b_1 \cos \varphi - a_1) \cot \varphi, a_1 - b_1 \cos \varphi \right),$$
$$\mathbf{c}' = \mathbf{d} - b_2 \mathbf{n}_{\boldsymbol{\gamma}} = \left((b_2 \cos \varphi - a_2) \cot \varphi, a_2 - b_2 \cos \varphi \right).$$

Consequently, the oriented distances from of the base points to the origin read

$$d_{\mathbf{a}} = \mathbf{a} \cdot \mathbf{r}_{\boldsymbol{\alpha}} = \frac{1}{\sin \varphi} (b_1 - a_1 \cos \varphi) \qquad d_{\mathbf{c}} = \mathbf{c} \cdot \mathbf{r}_{\boldsymbol{\gamma}} = \frac{1}{\sin \varphi} (b_1 \cos \varphi - a_1)$$
$$d_{\mathbf{a}'} = \mathbf{a}' \cdot \mathbf{r}_{\boldsymbol{\alpha}} = \frac{1}{\sin \varphi} (b_2 - a_2 \cos \varphi) \qquad d_{\mathbf{c}'} = \mathbf{c}' \cdot \mathbf{r}_{\boldsymbol{\gamma}} = \frac{1}{\sin \varphi} (b_2 \cos \varphi - a_2)$$

It follows that

$$D'(\varphi) = -\frac{1}{\sin \varphi} (d_{\mathbf{a}'} - d_{\mathbf{a}}) (d_{\mathbf{c}'} - d_{\mathbf{c}})$$

Thus, $D'(\varphi) > 0$ if the linkage is non-crossing and $D'(\varphi) < 0$ if the linkage is crossing, confirming the statement of the lemma. □

Chapter 9

Rotationally Symmetric Polygircles

The contents of this chapter are not published and are based on discussions with Erik Demaine, Robert Lang, Tomohiro Tachi, and Tony Wills.

Overview

Based on Tony Wills' squaricle design, we explore families of "polygircles", that is, shapes that can be obtained by gluing a polygon and a circle along their entire perimeter such that the resulting shapes consist of cylinders, cones, and planes. Using the join-and-fan method from Chapter 8, we find closed-form expressions for certain types of these gluings, which provide insights into the shape's geometry. In particular, we show that the gluing of a circle and polygon consisting of cylinders and planes results in a convex shape.

9.1 Introduction

D-forms are shapes that can be created by joining two convex regions of equal perimeter along their boundary. These forms were discovered by Tony Wills, a designer based in London [108, 86]. According to the Alexandrov–Pogorelov theorem [4], there exists a unique convex shape that can be obtained by joining two regions along their boundaries. Demaine et al. [21] show that this convex shape is the convex hull of its seam, and if the boundaries are smooth, the flat components of the shape do not have any creases.

In addition to the convex realizations, there are also other interesting non-convex configurations that can be obtained by joining two regions. One example is the *Squaricle* [108], which is formed by joining a square and a circle, while adding four straight creases to the circular region; see Figure 5.1a.

Determining the shape resulting from joining the boundaries of two convex regions is generally a non-trivial task, as discussed by Kane et al. [40] in the context of the discrete case. However, in this section, we demonstrate how the computations described earlier can be applied to simplify the parametrization of four families of n-fold rotationally symmetric gluings of a circle and a regular n-gon that consist of cylinders and cones. However, it is important to note that this parametrization approach has the potential to be extended for other configurations as well.

Building upon Tony Wills' concept of the squaricle, we adopt the term "polygircles" to refer to the resulting gluings of a polygon and a circle. By employing the join-and-fan method, we are able to derive closed-form expressions for certain types of polygircle gluings. This analytical approach not only provides closed-form parametrizations of non-trivial curves parametrized by arc

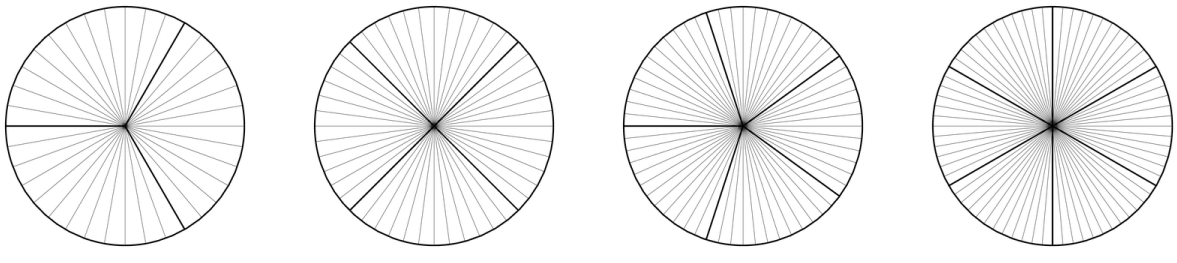

(a) Circles with conical rulings.

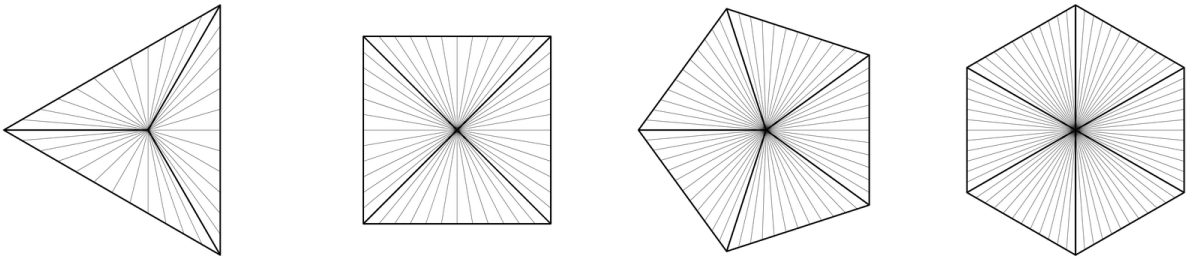

(b) Polygons with conical rulings.

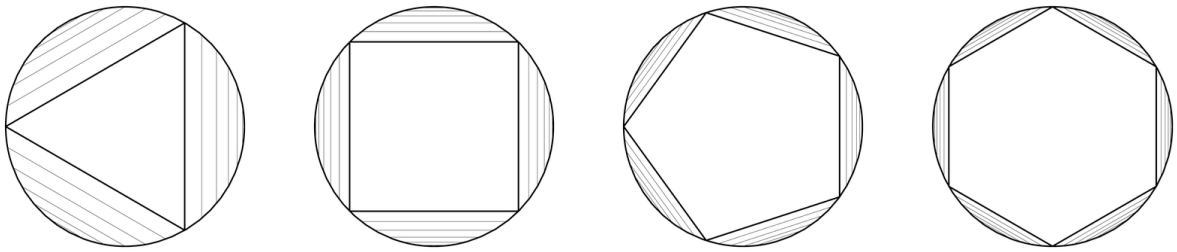

(c) Circles with cylindrical rulings.

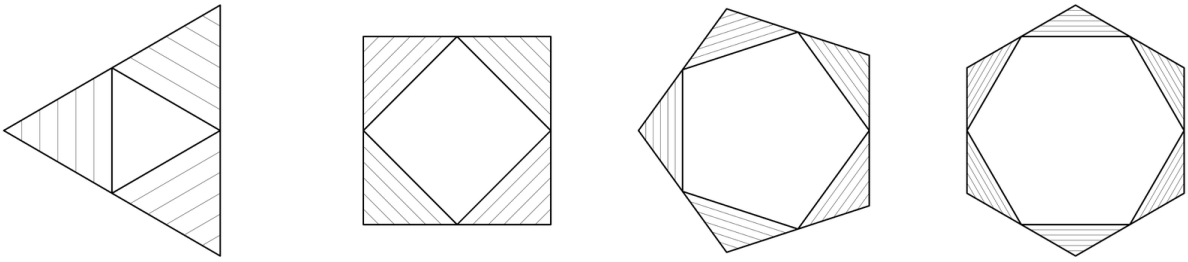

(d) Polygons with cylindrical rulings.

Figure 9.1: Considered ruling variations of circles and n-gons for $n \in \{3, 4, 5, 6\}$.

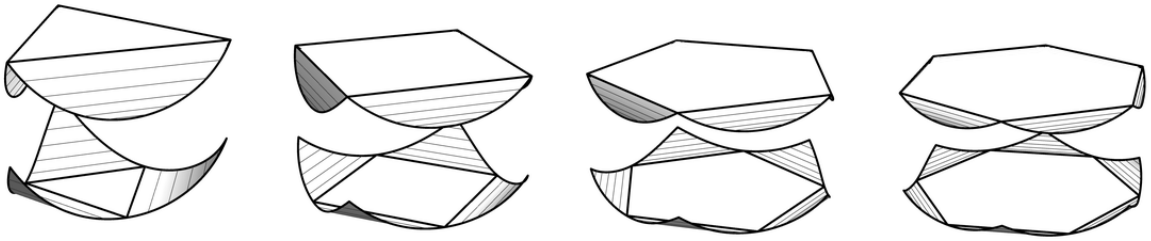

(a) Convex gluing of a cylindrically-ruled circle and n-gon.

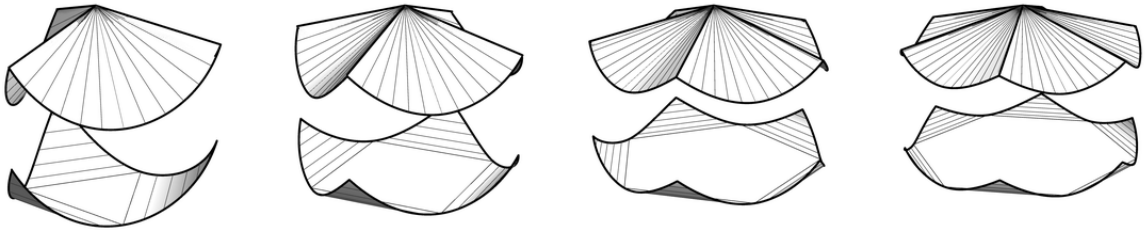

(b) Gluing of a conically-ruled circle and cylindrically-ruled n-gon.

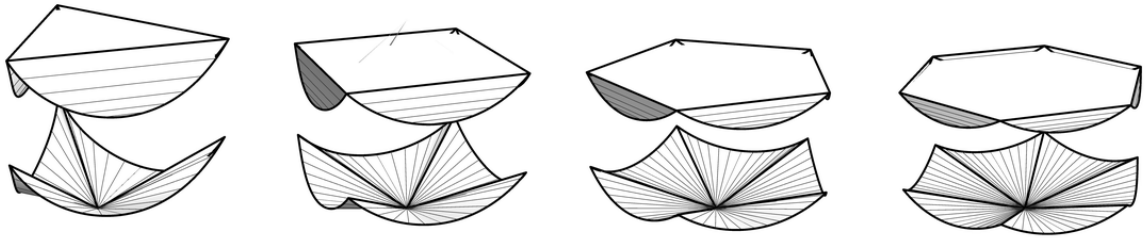

(c) Gluing of a cylindrically-ruled circle and conically-ruled n-gon.

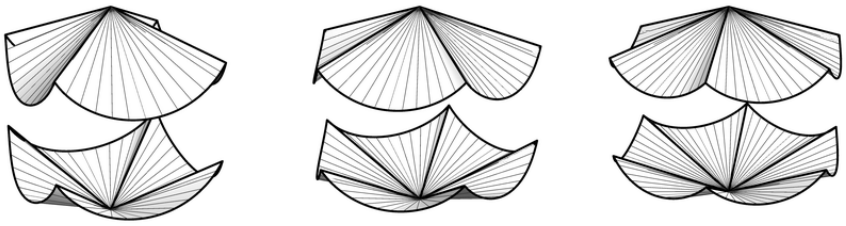

(d) Gluing of a conically-ruled circle and n-gon.

Figure 9.2: Considered gluings of a n-gon and a circle for $n \in \{3, 4, 5, 6\}$. For visualization, the surfaces are shown separated.

length, but also allows us to establish the convexity of the resulting shape in one of the closed form parametrizations.

In the following, we call a circular or n-gonal region *conically ruled* if all its rulings are incident to the center of the region which corresponds to the location of the cone apex; see first two rows of Figure 9.1. We call a circular or n-gonal region *cylindrically ruled*, if it consists of a planar region whose vertices are equally spaced along the boundary (circle) or the midpoints of its boundary edges (n-gon), and n cylinders whose rulings are parallel to the adjacent edge of the planar patch, see last two rows of Figure 9.1. We study the following four possible combinations of the proposed rulings of the circle and n-gon:

(1) Both circular and n-gonal regions are cylindrically ruled (Section 9.3 and first row of Figure 9.2). This combination results in a convex gluing.

(2) The circular region is conically ruled and the n-gonal region is cylindrically ruled (Section 9.4 and second row of Figure 9.2). This combination results in a generalization of Tony Wills' squaricle.

(3) The circular region is cylindrically ruled and the n-gonal region is conically ruled (Section 9.5 and third row of Figure 9.2).

(4) Both circular and n-gonal regions are conically ruled (Section 9.6 and fourth row of Figure 9.2).

9.2 Notation

In the following, we consider a circular region $R_\circ$ and an n-gonal region $R_\square$ with unit boundary length which we parametrize without loss of generality by arc length. Our goal in the following is to construct closed 3D shapes with n-fold rotational and mirror symmetry. Since the length of the boundaries of both glued regions is one, the length of the overall gluing curve will also be one. As a result, we only consider the portion of the gluing curve $\mathbf{X}(t)$ that corresponds to parameter values t in the interval $\left[0, \frac{1}{2n}\right]$. We can then obtain the remaining shape by applying appropriate reflections and rotations. To simplify notation, we denote the upper limit of the parameter as $t_{\max} = \frac{1}{2n}$.

In the following subsections, we parametrize for $t \in [0, t_{\max}]$ the respective 2D gluing curves as

$$\mathbf{x}_\circ(t) = \left(\frac{1}{2\pi}\cos(2\pi t), \frac{1}{2\pi}\sin(2\pi t), 0\right) \qquad \text{and} \qquad \mathbf{x}_\square(t) = \left(\frac{1}{2n}\cot\frac{\pi}{n}, t, 0\right),$$

where $\mathbf{x}_\square(t)$ parametrizes the segment of the n-gon that is perpendicular to the x-axis.

If the surfaces are cylindrically ruled, the developed surface's rulings are $\mathbf{r}_\circ = (0,1,0)$ and $\mathbf{r}_\square = \left(\sin\frac{\pi}{n}, -\cos\frac{\pi}{n}, 0\right)$. In addition, we set the points defining the cylinder's base plane to $\mathbf{p}_\circ = \mathbf{p}_\square = (0,0,0)$. Additionally, we also want the corresponding 3D profile curves to be containing in planes passing through the origin. We therefore set $\mathbf{P}_\circ = \mathbf{P}_\square = (0,0,0)$.

If the surfaces are conically ruled, the apices $\mathbf{v}_\circ$ and $\mathbf{v}_\square$ coincide with the origin. Similar to the previous section, we can use a polar parametrization centered at the origin. In this case, the parametrizations can be written as $\bar{\mathbf{x}}_\circ(t) = r_\circ(t)\bar{\mathbf{r}}_\circ(t)$ and $\bar{\mathbf{x}}_\square(t) = r_\square(t)\bar{\mathbf{r}}_\square(t)$, with distance functions

$$r_\circ(t) = \frac{1}{2\pi} \qquad \text{and} \qquad r_\square(t) = \sqrt{t^2 + \frac{1}{4n^2}\cot^2\frac{\pi}{n}},$$

and ruling vectors

$$\bar{\mathbf{r}}_\circ(t) = (\cos(2\pi t), \sin(2\pi t), 0) \qquad \text{and} \qquad \bar{\mathbf{r}}_\square(t) = \frac{1}{\sqrt{t^2 + \frac{1}{4n^2}\cot^2\frac{\pi}{n}}}\left(\frac{1}{2n}\cot\frac{\pi}{n}, t, 0\right).$$

9.3 Convex Gluing of a Cylindrically-ruled Circle and Polygon

Lemma 9.1. *For $t \in \left[0, \frac{1}{2n}\right]$, the gluing curve $\mathbf{X}(t)$ of a cylindrically-ruled circle and cylindrically-ruled n-gon allows the following arc-length parametrization,*

$$\begin{aligned}
\mathbf{X}_x(t) &= \frac{\pi - 2n\pi t + n\sin(2\pi t)}{2n\pi\tan\frac{\pi}{n}},\\
\mathbf{X}_y(t) &= \frac{\sin(2\pi t)}{2\pi},\\
\mathbf{X}_z(t) &= \frac{1}{\pi}\left(1 + \left(\operatorname{arctanh}\left(\frac{\sqrt{2}\cos(\pi t)}{x(t)}\right) - \operatorname{arctanh}\left(\csc\frac{\pi}{n}\right)\right)\frac{\cos\frac{\pi}{n}}{\tan\frac{\pi}{n}} - \frac{x(t)\cos(\pi t)}{\sqrt{2}\sin\frac{\pi}{n}}\right),
\end{aligned}$$

where $x(t) = \sqrt{\cos(2\pi t) - \cos\frac{2\pi}{n}} > 0$. The remaining parts of the gluing curve can be obtained by reflecting $\mathbf{X}(t)$ on the xz-plane and constructing an n-fold polar array of both curves.

Proof. We follow the explanation in Section 8.2 and use the Cartesian coordinate representation of $\mathbf{X}(t)$. In this case, we set $\mathbf{R}_\circ = \mathbf{r}_\circ$ and $\mathbf{R}_\square = \mathbf{r}_\square$. In addition, we let the corresponding base planes be incident to the origin, resulting in $\mathbf{P}_\square = \mathbf{P}_\circ = (0,0,0)$. Therefore, in the joining step, simplifying Equation (8.7) results the provided expression for $\mathbf{X}_x(t)$ and $\mathbf{X}_y(t)$.

In the fanning step, solving Equation (8.5) with $\mathbf{X}_z(0) = 0$ results up to sign in the provided expression for the third coordinate function of the glue curve. □

Lemma 9.2. *The parametrization of the gluing of a cylindrically-ruled circle and n-gon provided by Lemma 9.1 yields a convex shape.*

Proof. The computed shape consists of two horizontal n-gons and $2n$ n-fold rotationally symmetric cylinders with horizontal rulings. To prove convexity of the gluing, we follow a constructive approach, and represent the gluing as a union of a convexity-preserving arrangement of (convex) intersections of convex shapes.

On a high-level, our proof can be decomposed in the following three steps:

- *Step 1:* We define two shapes $S_\circ$ and $S_\square$, see Figure 9.3.
- *Step 2:* We show that $S_\circ$ and $S_\square$ are convex.
- *Step 3:* We define S as the intersection of $S_\circ$ and $S_\square$, and show that its assembly into the final gluing results in a convex shape.

Before we proceed, let us recall that $\Pi_\circ$ and $\Pi_\square$ are the two planes passing through the origin that are perpendicular to the ruling directions $\mathbf{R}_\circ$ and $\mathbf{R}_\square$, respectively. Additionally, let $\mathbf{C}_\circ(t)$ and $\mathbf{C}_\square(t)$ be the profile curves of the cylinders incident to $\Pi_\circ$ and $\Pi_\square$, respectively. Specifically, we can write their parametrizations as

$$\mathbf{C}_\circ(t) = \mathbf{X}(t) - (\mathbf{x}_\circ(t)\cdot\mathbf{r}_\circ)\mathbf{R}_\circ \qquad \text{and} \qquad \mathbf{C}_\square(t) = \mathbf{X}(t) - (\mathbf{x}_\square(t)\cdot\mathbf{r}_\square)\mathbf{R}_\square.$$

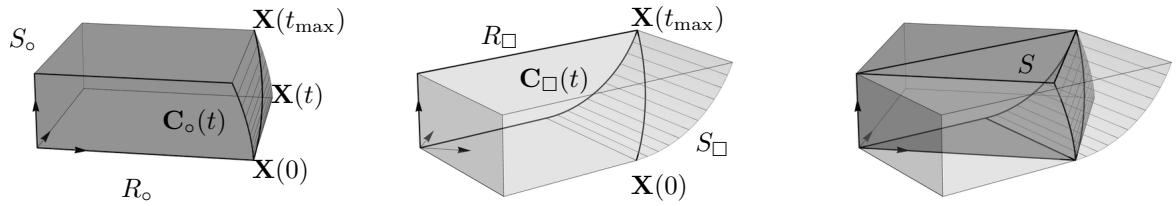

Figure 9.3: Convex shapes used in the proof of Lemma 9.2.

Step 1. We start our proof by defining the two shapes $S_\circ$ and $S_\square$, see Figure 9.3. For $\times \in \{\bigcirc, \square\}$, let $S_\times$ be the shape that is bounded by:

- the two xy-parallel planes denoted by Π_1 and Π_2 that contain the points $\mathbf{X}(0)$ and $\mathbf{X}(t_{\max})$, respectively,
- the two planes denoted by Π_3 and Π_4 perpendicular to the ruling direction $\mathbf{R}_\times$ that contain the points $\mathbf{X}(0)$ and $\mathbf{X}(t_{\max})$, respectively,
- the cylinder with profile curve $\mathbf{C}_\times(t)$ and ruling direction $\mathbf{R}_\times$, and
- a vertical plane containing the origin and the ruling direction $\mathbf{R}_\times$.

For this definition to be meaningful, it is necessary for the intersections of Π_1, Π_2, Π_3, and Π_4 with $\mathbf{X}(t)$ to occur only at the points $\mathbf{X}(0)$ or $\mathbf{X}(t_{\max})$. This condition ensures that the gluing curve is monotonous with respect to the ruling directions and the vertical axis, justifying the bounding of the curve by the vertical and horizontal planes.

To verify this, we compute the dot product of the curve's tangent and the ruling direction, resulting in the following expressions:

$$\mathbf{X}'(t) \cdot \mathbf{R}_\circ = \cos(2\pi t), \qquad -\mathbf{X}'(t) \cdot \mathbf{R}_\square = \cos\frac{\pi}{n}, \qquad \mathbf{X}'(t) \cdot (0,0,1) = \sqrt{2}x(t)\frac{\sin(\pi t)}{\sin\frac{\pi}{n}}.$$

It can be observed that for $n \geq 3$ and $t \in [0, t_{\max}]$, all three expressions are non-negative, indicating that the gluing curve is bounded from below, above, and on two sides.

Step 2. We now show that the shapes $S_\circ$ and $S_\square$ are convex. Let $R_\circ$ and $R_\square$ be the regions obtained from intersecting $S_\circ$ and $S_\square$ with $\Pi_\circ$ and $\Pi_\square$, respectively. Since the shapes $S_\circ$ and $S_\square$ result from orthogonal extrusion of $R_\circ$ and $R_\square$ with respect to the corresponding ruling direction, we show the convexity of $S_\circ$ and $S_\square$ by showing that the regions $R_\circ$ and $R_\square$ are convex. Note that both region are bounded by a polyline and a profile curve of one of the cylinders. In the following we show that the cylinder's profile curves are bend consistently in one direction by computing their curvatures; see Figure 9.4.

First, we consider $R_\circ$. The tangents of $\mathbf{C}_\circ(t)$ read

$$\mathbf{T}_\circ(t) = \frac{\mathbf{C}'_\circ(t)}{|\mathbf{C}'_\circ(t)|} = \left(-\frac{\sin^2(\pi t)}{\sin(2\pi t)\tan\frac{\pi}{n}}, 0, \frac{\sqrt{(\cos\frac{2\pi}{n} - \cos(2\pi t))(-1+\cos(4\pi t))}}{4\sin\frac{\pi}{n}\sin(\pi t)\cos^2(\pi t)} \right).$$

Since $\mathbf{C}_\circ(t)$ lies in the xz-plane, its left-sided normal can be obtained by rotating $\mathbf{T}_\circ(t)$ by $+\frac{\pi}{2}$ around $(0,-1,0)$. Computing the curvature results in

$$\kappa_\circ(t) = \mathbf{T}'_\circ(t) \cdot \mathbf{N}_\circ(t) = \frac{\sqrt{2}\pi}{x(t)} \cos\frac{\pi}{n} \sec(\pi t).$$

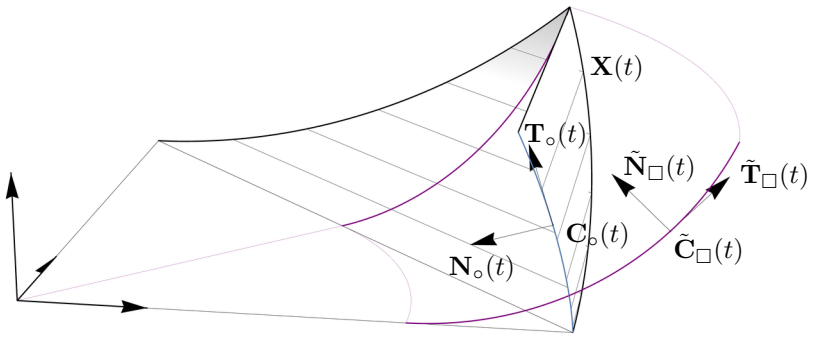

Figure 9.4: Illustration of the notation in the proof of Lemma 9.2 on a part of a gluing of a circle and a square.

Note that for $t \in [0, t_{\max}]$ and $n \geq 3$, $\kappa_\circ(t) \geq 0$ and thus the region $R_\circ$ is convex.

Second, we consider $R_\square$. To allow simpler computations of the curvature, we position $\mathbf{C}_\square(t)$ in the xz-plane using a rotation by $\frac{\pi}{n}$ around $(0, 0, 1)$, and denote the rotated profile curve by $\tilde{\mathbf{C}}_\square(t)$. The tangent of $\tilde{\mathbf{C}}_\square(t)$ simplifies to

$$\tilde{\mathbf{T}}_\square(t) = \frac{\tilde{\mathbf{C}}'_\square(t)}{\left|\tilde{\mathbf{C}}'_\square(t)\right|} = \left(-\frac{1 + \cos\frac{2\pi}{n} - 2\cos(2\pi t)}{2\sin^2\frac{\pi}{n}}, 0, \frac{\sqrt{2}x(t)\sin(\pi t)}{\sin^2\frac{\pi}{n}} \right).$$

Again, we obtain the normal $\tilde{\mathbf{N}}_\square(t)$ by rotating $\tilde{\mathbf{T}}_\square(t)$ by $+\frac{\pi}{2}$ around $(0, -1, 0)$. The curvature then simplifies to

$$\kappa_\square(t) = \mathbf{T}'_\square(t) \cdot \mathbf{N}_\square(t) = \tilde{\mathbf{T}}'_\square(t) \cdot \tilde{\mathbf{N}}_\square(t) = \frac{2\sqrt{2}\pi}{x(t)} \cos(\pi t).$$

Again, note that for $t \in [0, t_{\max}]$ and $n \geq 3$, $\kappa_\square(t) \geq 0$ and thus the region $R_\square$ is convex. Consequently, the shapes $S_\circ$ and $S_\square$ are convex.

Step 3. To this end, we have verified that the two shapes $S_\circ$ and $S_\square$ are convex. Therefore, their intersection S is convex. To obtain the full shape, we reflect the shape about the plane $\Pi_\circ$ to obtain shape S' and form a n-fold polar array of the union of S and S' around the origin. We now demonstrate that these operations maintain convexity by ensuring that the transitions between assembled copies of S and S' remain convex.

Firstly, it is important to note that since S is bounded from below and above by xy-parallel planes, the final assembly will also be bounded by these planes, preserving convexity. Additionally, the non-horizontal boundary transitions maintain convexity because the surfaces are cylinders with rulings that are perpendicular to the reflecting planes.

We conclude that the proposed parametrization results in a family of convex shapes for $n \geq 3$. □

9.4 Gluing of a Conically-ruled Circle and a Cylindrically-ruled Polygon

We follow the description for the cone-cylinder case in Section 8.2.4, and set $\mathbf{V}_\circ = (0, 0, 0)$ and $\mathbf{R}_\square = (0, 0, 1)$.

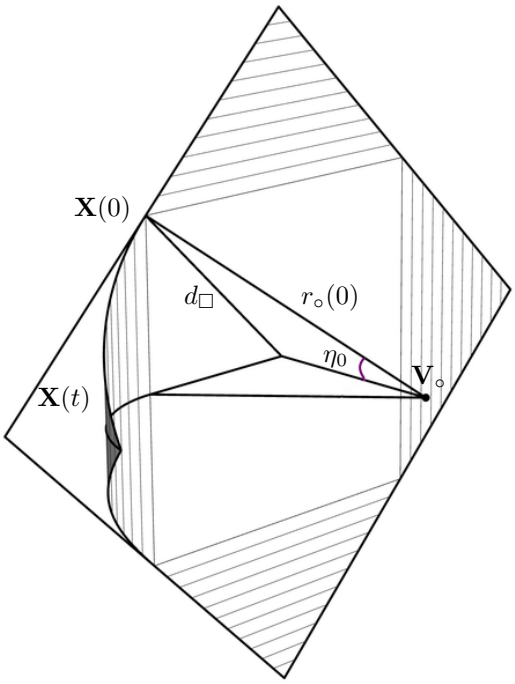

Figure 9.5: Notation describing the parametrization of the glue curve between a cylindrically-ruled n-gon and a conically-ruled circle, as used in Section 9.4.

Joining step. The joining step yields the two functions

$$l(t) = r_\circ(t) = \frac{1}{2\pi} \qquad \text{and} \qquad \zeta(t) = \arcsin\left(\frac{\pi}{n}(1-2nt)\cos\frac{\pi}{n}\right).$$

Fanning step. We first compute the first derivative of $\zeta(t)$, that is,

$$\zeta'(t) = -\frac{2\pi\cos\frac{\pi}{n}}{\sqrt{1-\frac{\pi^2}{n^2}(1-2nt)^2\cos^2\frac{\pi}{n}}}.$$

Then Equation (8.9) simplifies to

$$\begin{aligned}\eta'(t) &= 2\sqrt{2}n\pi\frac{\sqrt{n^2(1-\cos\frac{2\pi}{n})-\pi^2(1+\cos\frac{2\pi}{n})(1-2nt)^2}}{-2n^2+\pi^2(1+\cos\frac{2\pi}{n})(1-2nt)^2} \\ &= A\frac{\sqrt{B-C(1-2nt)^2}}{D+C(1-2nt)^2}, \end{aligned} \tag{9.1}$$

where

$$A = 2\sqrt{2}n\pi, \qquad B = n^2\left(1-\cos\frac{2\pi}{n}\right), \qquad C = \pi^2\left(1+\cos\frac{2\pi}{n}\right), \qquad D = -2n^2.$$

Solving the initial value problem in Equation (9.1) with $\eta(0) = \eta_0$ results in

$$\eta(t) = \eta_0 + A\left(\sqrt{B+D}\left(\arctan\frac{\sqrt{C}\sqrt{B+D}}{\sqrt{D}\sqrt{B-C}} - \arctan\frac{\sqrt{C}\sqrt{B+D}(1-2nt)}{\sqrt{D}\sqrt{B-C(1-2nt)^2}}\right)\right.$$
$$\left. - \sqrt{D}\left(\arctan\frac{\sqrt{C}}{\sqrt{B-C}} - \arctan\frac{\sqrt{C}(1-2nt)}{\sqrt{B-C(1-2nt)^2}}\right)\right).$$

Computation of η_0. Finally, it remains to determine the initial value η_0 that yields the desired shape; see Figure 9.5. First note, that the cylindrically-ruled n-gon has an inscribed planar n-gonal region whose circumradius is the inradius of the n-gon, that is,

$$d_\square = \frac{1}{2n}\cot\frac{\pi}{n}.$$

This polygon forms the base of an n-sided pyramid with vertex $\mathbf{V}_\circ$ whose non-base edge lengths equal half of the diameter of the circle, that is, $r_\circ(0) = \frac{1}{2\pi}$. Consequently, we obtain that

$$\eta_0 = \arcsin\frac{d_\square}{r_\circ(0)}.$$

The second row of Figure 9.2 shows the resulting shapes, which were rotated by $\frac{\pi}{2}$ about the y-axis to have consistent orientation with the other gluings.

9.5 Gluing of a Cylindrically-ruled Circle and a Conically-ruled Polygon

Again, we follow the description for the cone-cylinder case in Section 8.2.4, and set $\mathbf{V}_\square = (0,0,0)$ and $\mathbf{R}_\circ = (0,0,1)$.

Joining step. The joining step yields the two functions

$$l(t) = \sqrt{t^2 + \frac{\cot^2\frac{\pi}{n}}{4n^2}} \qquad \text{and} \qquad \zeta(t) = \arcsin\frac{\sin(2\pi t)}{\pi\sqrt{t^2 + \frac{\cot^2\frac{\pi}{n}}{4n^2}}}.$$

Fanning step. We first compute the first derivative of $\zeta(t)$, that is,

$$\zeta'(t) = \frac{2\pi\cos(2\pi t)\left(4n^2t^2 + \cot^2\frac{\pi}{n}\right) - 4n^2t\sin(2\pi t)}{(4n^2t^2 + \cot^2\frac{\pi}{n})\sqrt{4\pi^2t^2 + \frac{\pi^2}{n^2}\cot^2\frac{\pi}{n} - \sin^2(2\pi t)}}$$

Then, Equation (8.9) simplifies to

$$\eta'(t) = \frac{2n\pi\sqrt{\pi^2\cot^2\frac{\pi}{n}\sin^2(2\pi t) - n^2(\sin(2\pi t) - 2\pi t\cos(2\pi t))^2}}{\pi^2\cot^2\frac{\pi}{n} + n^2(4\pi^2t^2 - \sin^2(2\pi t))}.$$

We have encountered difficulties in finding a closed-form solution for this or other approaches. Therefore, we will proceed by solving the initial value problem numerically for $\mathbf{X}(t_{\max}) = \eta_{\max}$.

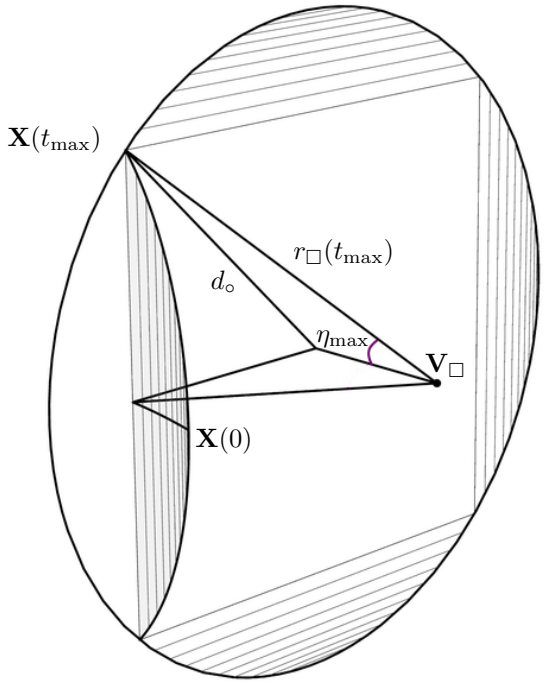

Figure 9.6: Notation describing the parametrization of the glue curve between a cylindrically-ruled n-gon and a conically-ruled circle, as used in Section 9.5.

Computation of $\eta_{\max}$. It remains to compute the initial value for $\eta_{\max}$; see Figure 9.6. Similarly to before, note that the cylindrically-ruled circle has an inscribed planar n-gonal region whose circumradius is the circular boundary of the region. Therefore,

$$d_\circ = \frac{1}{2\pi}.$$

Again, this polygon forms the base of an n-sided pyramid with vertex $\mathbf{V}_\square$ whose non-base edge lengths equal half of the diameter of the n-gon, that is, $r_\square(t_{\max})$. Consequently, the opening angle can be obtained as

$$\eta_{\max} = \arcsin \frac{d_\circ}{r_\square(t_{\max})}.$$

The third row of Figure 9.2 shows the resulting shapes, which were rotated by $\frac{\pi}{2}$ about the y-axis to have consistent orientation with the other gluings.

9.6 Gluing of a Conically-ruled Circle and Polygon

In this case, we follow the cone-cone case in Section 8.2.4, and set $\mathbf{V}_\circ = (0, 0, 0)$ and $\mathbf{V}_\square = (0, 0, h)$. Unlike in the previous cases, it is not obvious to determine the parameter h that results in a closed parametrization. We resort in computing this value at the end of this section numerically.

n	3	4	5	6	7
h	–	0.145527	0.130935	0.120127	0.111651

n	8	9	10	100	1000
h	0.1047600	0.0990101	0.0941159	0.0302579	0.0095841

Table 9.1: Numerically found solutions of $\eta(t_{\max}) = \frac{\pi}{n}$ for h and different n.

Joining step. From the joining step for the two cones, we obtain the two functions

$$l(t) = \frac{1}{2\pi} \qquad \text{and} \qquad \zeta(t) = \arcsin\left(\frac{(1 + 4h^2\pi^2 - 4\pi^2t^2)n^2 - \pi^2\cot^2\frac{\pi}{2}}{4hn^2\pi}\right).$$

Fanning step. The first derivative of the angular function $\zeta(t)$ reads

$$\zeta'(t) = -\frac{2\pi t}{h\sqrt{1 - \left(\frac{(1+4h^2\pi^2-4\pi^2t^2)n^2-\pi^2\cot^2\frac{\pi}{2}}{4hn^2\pi}\right)^2}}.$$

With this, Equation (8.10) can be be rewritten as

$$\eta'(t) = 2\pi\frac{\sqrt{1 - at^2 - (b - ct^2)^2}}{1 - (b - ct^2)^2},$$

where

$$a = \frac{1}{h^2}, \qquad b = \frac{n^2 + 4h^2n^2\pi^2 - \pi^2\cot^2\frac{\pi}{n}}{4hn^2\pi^2}, \qquad c = -\frac{\pi}{h}.$$

For $\eta(0) = 0$, the solution of the initial value problem can be written in terms of the elliptic integral of the first kind[1], and the incomplete integral of the third kind[2]

$$\eta(t) = x(t)\left(2c\,\mathrm{F}\left(\phi(t), \frac{n_-}{n_+}\right) + a\left(\Pi\left(\frac{n_-}{2c(b+1)}, \phi(t), \frac{n_-}{n_+}\right) - \Pi\left(\frac{n_-}{2c(b-1)}, \phi(t), \frac{n_-}{n_+}\right)\right)\right),$$

where

$$n_\pm = a + 2bc \pm \sqrt{a^2 + 4abc + 4c^2}$$

and

$$\phi(t) = -\sinh\left(\sqrt{-\frac{2c^2}{n_-}}t\right) \qquad \text{and} \qquad x(t) = -\frac{\sqrt{1 + \frac{2c^2t^2}{n_-}}\sqrt{1 + \frac{2c^2t^2}{n_+}}}{c\sqrt{-\frac{2c^2}{n_-}}\sqrt{1 - at^2 - (b + ct^2)^2}}.$$

Computing h. The value of $\eta(t_{\max})$ is influenced by the parameter h. Given that $\eta(0) = 0$, our objective is to find a solution where $\eta(t_{\max}) = \frac{\pi}{n}$. Through numerical computations, we have obtained values of h for different values of $n \geq 4$; see Table 9.1. However, no numerical solution was found for $n = 3$.

As the number of polygonal edges increases, the numerically determined height decreases. This observation is consistent with the intuition that gluing a polygon with numerous sides to a circle will yield a shape with a relatively small volume. In Figure 9.2, the resulting shapes are depicted in the last row.

[1] $\mathrm{F}(\phi, m) = \int_0^\phi \frac{1}{\sqrt{1 - m\sin^2\theta}}d\theta$

[2] $\Pi(n, \phi, m) = \int_0^\phi \frac{1}{1 - n\sin^2\theta}\frac{1}{\sqrt{1 - m\sin^2\theta}}d\theta$

Chapter 10

Conic Creases with Reflecting Rule Lines

This chapter is based on the paper "Flat and Rigidly Foldable Discretizations of Conic Crease Patterns with Reflecting Rule Lines" that the thesis author coauthored with Erik Demaine and Tomohiro Tachi. This paper appeared in the proceedings of the International Conference in Geometry and Graphics [20].

Overview

Conic curved creases with reflected rule lines, first explored by David Huffman, offer one-degree-of-freedom folding motions with rigid rule lines that remain the same throughout the folding motion. We employ the join-and-fan method from Chapter 8 to provide a parametrization of these creases. Furthermore, we present two general methods for discretizing such curved-crease patterns into straight-line crease patterns. In particular, we replace each curve with either an inscribing or circumscribing polygonal line, and show in both cases that the resulting discretized crease patterns are rigidly foldable. Additionally, the circumscribed discretization yields locally flat-foldable crease patterns, while only careful sampling in the inscribed method achieves the same result.

10.1 Introduction

Many of David Huffman's curved-crease origami designs use conics sharing focal points as the creases and lines passing through the focal points as rulings of the curved surfaces [43]; see Figure 10.1. Demaine et al. [18] call these *natural rule lines*. Because of properties of conics, natural rule lines reflect at the creases, and if such creases can fold, they fold with constant fold angles [26]. Demaine et al. [18] characterize valid combinations of conic creases with natural rule lines and show that compatible conic creases produce a rigid-ruling folding motion. As the rulings are rigid throughout the motion, the fold angles along a crease are constant.

Rigid-ruling folding is a curved-crease analogue of rigid folding; see Figure 10.2. Therefore, rigid-ruling folding of conics naturally raises the question: can we discretize conic curved creases such that they rigidly fold? Tachi [101] and Lang et al. [48] discretize (using a locally flat-foldable inscribed discretization as explained later) a specific family of multi-crease curved origami and a single-crease curved origami, respectively. However, whether such a discretization exists for crease patterns with multiple conic creases, and if it exists whether it is rigidly foldable, were unknown.

Our contribution in this section is two-fold. First, we use the join-and-fan method discussed in

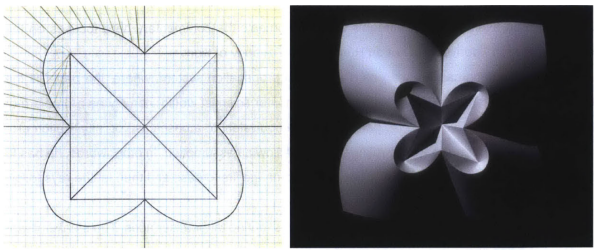

(a) 4-lobed cloverleaf design (1977). Figure 5.3.3. in Koschitz [43].

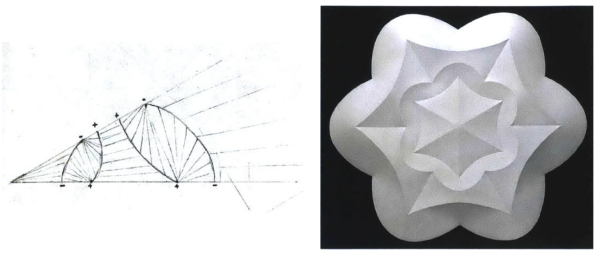

(b) Starburst design (undated). Figure 5.8.23 in Koschitz [43].

Figure 10.1: Two designs by David Huffman using conic creases with crease-rule pattern sketches. Not for reproduction.

Section 8.2 to provide an, up to elliptic integrals, closed form parametrization of conic creases with reflecting rule lines that does not rely on the computation of the Frenet-frame. Our computations confirm the crease compatibilities as discussed in [18].

Second, we show how the join-and-fan method is used to analyze two discretization approaches [20]: (1) the *inscribed discretization* samples curve points and connects them consecutively to form an inscribed polyline, and (2) the *circumscribed discretization* samples conic tangents and ends them at consecutive intersections to form a circumscribed polyline. With both methods, the sampling parameters of a single curve can be freely specified, but need to be propagated to other creases with *discrete natural rule lines*, that is, the vertices of neighboring compatible creases and their common focal point need to be collinear. Both discretizations result in rigidly foldable patterns. In addition, we also show that circumscribed discretization ensures that each vertex is locally flat foldable, whereas inscribed discretization achieves this property only with careful sampling. When each vertex is locally flat foldable, the fold angle along the original curved crease is constant, preserving the original properties of conic curved-crease folding with natural rule lines.

A common approach to proving rigid foldability of a quadrivalent pattern (as produced by our discretization methods) is to show the compatibility of fold angles based on fold angle multipliers [24, 102], but this approach requires that each vertex is locally flat foldable. As our inscribed discretization method does not always produce locally flat-foldable vertices, we instead prove rigid foldability by using the join-and-fan method, resulting in a constructive approach based on a compatible series of planar linkages using the properties of conics.

10.2 Review of Properties of Conic Sections

We begin by introducing the notation, and review some of the key properties of conic sections. Recall that a conic can be described by two parameters: the shape of a conic is determined by its *eccentricity* e, and the conic's scale is determined by a scale parameter a. Specifically, we call a conic an *ellipse* if $|e| < 1$, a *parabola* if $|e| = 1$, and a *hyperbola* if $|e| > 1$. Analytically, conic sections are quadratic curves and can be described as follows

$$\text{ell or hyp: } \frac{x^2}{a^2} + \frac{y^2}{a^2(1-e^2)} = 1, \qquad \text{par: } y^2 = -4ax. \tag{10.1}$$

A conic has two focal points. In case of an ellipse or hyperbola, both focal points are real-valued. If the ellipse or hyperbola are given by Equation (10.1) (left), the focal points are located at $\mathbf{f}_{1,2} = (\pm ae, 0)$. In case of a parabola, one focal point is real-valued and the other focal point is

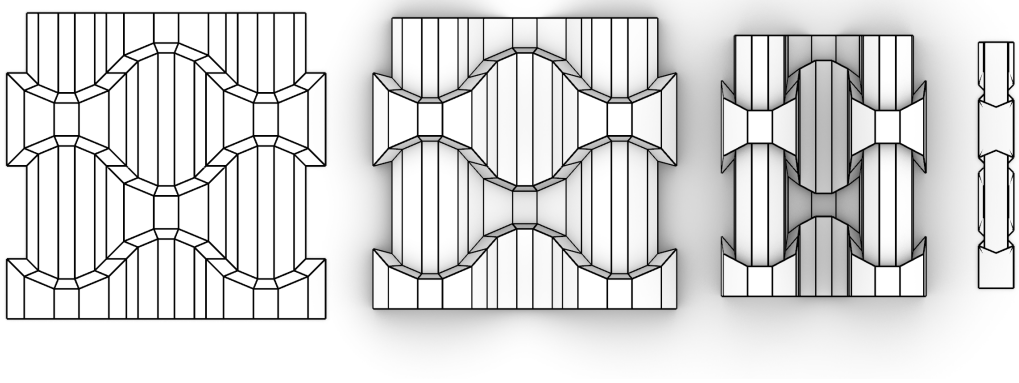

Figure 10.2: A locally flat and rigidly foldable discretization of one of David Huffman's designs with scaled and reflected parabolas.

ideal. If the parabola is given by Equation (10.1) (right), one focal point is located at $\mathbf{f}_1 = (-a, 0)$ and the other is the ideal point of the x-axis.

10.2.1 Conics as Loci of Points

Alternatively, conic sections can be defined as sets of points that satisfy the following properties with respect to their focal points:

- An *ellipse* is the set of points, for which the sum of distances to the two focal points is constant.
- A *hyperbola* is the set of points, for which the absolute difference of distances to the two focal points is constant.
- A *parabola* is the set of points, for which the orthogonal distance to a line equals the distance to the real-valued focal point. This line is also referred to as the *directrix* of the parabola.

10.2.2 Parametrization of Conics with Polar Coordinates

In the following, we position conics such that one real focal point coincides with the origin, and use the polar parametrization, that is, a parametrization in form of $\mathbf{c}(t) = r(t)\mathbf{r}(t)$, where $\mathbf{r}(t) = (\cos t, \sin t)$, to describe the conic. The proofs of the following two Lemmas can be found in Section 10.9.

Lemma 10.1. *An ellipse or hyperbola with eccentricity e and major axis length $a \neq 0$ can be parametrized by polar coordinates centered at one of its foci by*

$$\mathbf{c}(t) = \frac{a(1-e^2)}{1 + e\cos t}\mathbf{r}(t) \tag{10.2}$$

where $t \in [-\pi, \pi]$. Note that in case of a hyperbola, the conic has two ideal points at $t_\pm = \pm\arccos\left(-\frac{1}{e}\right)$. When $e > 0$, $t \in (t_-, t_+)$ parametrizes the branch closer to the origin, and the branch further from the origin if $e < 0$. The second focal point is located at $(-2ae, 0)$.

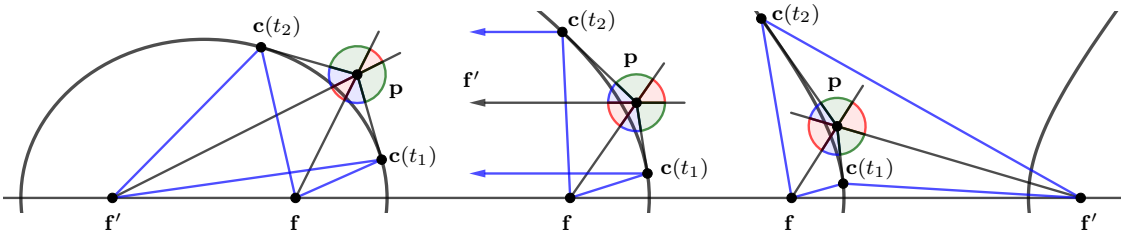

Figure 10.3: Illustration of Lemma 10.4.

Lemma 10.2. *A parabola with scale factor a can be parametrized by polar coordinates centered at the real-valued focal point by*

$$\mathbf{c}(t) = \frac{2a}{1+\cos t}\mathbf{r}(t). \tag{10.3}$$

10.2.3 Intersections of Tangents of Conics

Lemma 10.3. *Let $\mathbf{c}(t)$ be a conic section with focal points $\mathbf{f}$ and $\mathbf{f}'$ parametrized using Equation (10.2) or Equation (10.3), respectively. The intersection $\mathbf{p}$ of its tangents at parameter values τ_1 and τ_2 is the intersection of the angle bisector of $\{\mathbf{c}(\tau_1), \mathbf{f}, \mathbf{c}(\tau_2)\}$ and the angle bisector of $\{\mathbf{c}(\tau_1), \mathbf{f}', \mathbf{c}(\tau_2)\}$, that is,*

$$\mathbf{p} = \begin{cases} \frac{a(1-e^2)}{\cos t^- + e\cos t}\left(\cos t, \sin t\right), & \text{in case of an ellipse or hyperbola.} \\ \frac{2a}{\cos t^- + e\cos t}\left(\cos t, \sin t\right), & \text{in case of an parabola,} \end{cases}$$

where $t = \frac{\tau_1+\tau_2}{2}$ and $t^- = \frac{\tau_2-\tau_1}{2}$; see Figure 10.3.

Proof. The claim can be readily verified by showing that the stated point $\mathbf{p}$ lies on the tangents of the respective conics at parameters τ_1 and τ_2:

A vector parallel to the normal vector of the conic can be obtained by rotating and scaling $\mathbf{c}'(t)$ by $\frac{\pi}{2}$, resulting in

$$\mathbf{n}(\tau) = \begin{cases} \left(e + \cos\tau, \sin\tau\right), & \text{in case of an ellipse or hyperbola,} \\ \left(-e + \cos\tau, \sin\tau\right), & \text{in case of a parabola.} \end{cases}$$

In both cases, we confirm the claim by simplifying for $i \in \{1, 2\}$,

$$(\mathbf{c}(\tau_i) - \mathbf{p}) \cdot \mathbf{n}(\tau_i) = 0.$$

□

Note that as τ_2 moves towards τ_1, t^- converges to zero, and t converges to τ_1. Thus the obtained equations converge to the expressions in Equation (10.2) and Equation (10.3).

10.2.4 Reflection Properties of Conics

It is known, that conic section have a reflecting property. Specifically, a line incident with one focal point is reflected on the intersection of the conic about its incident tangent in a line that passes through the other focal point.

The following Lemma extends this property to intersections of conic tangents (see Figure 10.3), and can be found in classical literature on descriptive geometry, such as Steiner's Lecture Notes [93].

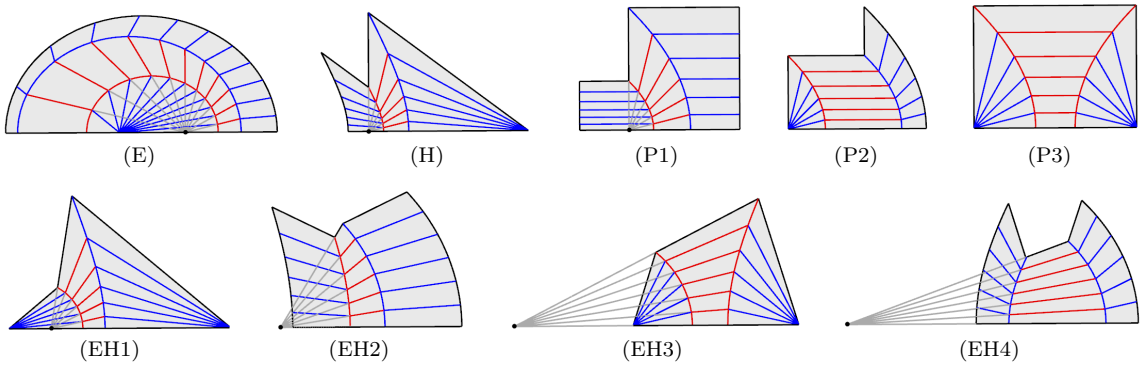

Figure 10.4: The nine distinct cases of compatible conic creases with reflecting rule lines sharing a focal point. Red and blue indicate mountain and valley creases, respectively. Note that the entire MV assignment can also be inverted.

Lemma 10.4. *Let* $\mathbf{c}(t)$ *be a conic section with focal points* $\mathbf{f}$ *and* $\mathbf{f}'$*, and* $\mathbf{p}$ *the intersection of its tangents at* τ_1 *and* τ_2*. Then,* $\angle(\mathbf{f}, \mathbf{p}, \mathbf{c}(\tau_1)) = \angle(\mathbf{c}(\tau_2), \mathbf{p}, \mathbf{f}')$ *in case of an ellipse or parabola, and* $\angle(\mathbf{f}, \mathbf{p}, \mathbf{c}(\tau_1)) + \angle(\mathbf{f}', \mathbf{p}, \mathbf{c}(\tau_2)) = \pi$ *in case of a hyperbola.*

10.3 Smooth Conic Crease Patterns with Reflecting Rule Lines

In the following, we consider conic creases with *natural rule lines*, that is, rule lines that pass through the focal points of the conic. When combining conics with natural rule lines, the combined conics need to share a focal point. Specifically, Demaine et al. show that naturally ruled crease pattern of two conic creases $\mathbf{c}_1(t)$ and $\mathbf{c}_2(t)$ sharing a focal point fold if and only if the conics have the same or reciprocal eccentricity. Figure 10.4 shows the nine distinct cases of two conics: (E), (H), (P1), (P2), (P3), (EH1), (EH2), (EH3), and (EH4).

If two conics have the same eccentricity, they are scaled versions of each other if the common focal point is real (cases (E), (H), and (P1)), and are translated or reflected if the common focal point is a point at infinity (cases (P2) and (P3)). This can only happen in case of a parabola.

If two conics have reciprocal eccentricities, they are a combination of an ellipse $\mathbf{c}_1(t)$ and a hyperbola $\mathbf{c}_2(t)$. Figure 10.4 shows the resulting valid combinations. In the following case analysis, let without loss of generality $a_1 = 1$ and $e = e_1 = \frac{1}{e_2}$, with $|e| < 1$.

- If $0 < e < 1$, the ellipse can only be combined with the branch of the hyperbola that is closer to the origin. There are two cases that do not result in intersecting rulings that depend on the scaling of the hyperbola with respect to the scaling of the ellipse:
  - Case (EH1): If $0 < 1 - e = \mathbf{c}_1(0) \leq \mathbf{c}_2(0)$, we require $a_2 \leq -e$.
  - Case (EH2): If $0 < \mathbf{c}_2(0) < \mathbf{c}_1(0) = 1 - e$, we require $-e < a_2 < 0$.
- If $-1 < e < 0$, the ellipse can only be combined with the branch of the hyperbola that is further away from the origin. Again, there are two cases that do not result in intersecting rulings that depend on the scaling of the hyperbola with respect to the scaling of the ellipse:
  - Case (EH3): If $0 < 1 + e = \mathbf{c}_1(0) \leq \mathbf{c}_2(0)$, we require $a_2 \geq -e$.
  - Case (EH4): If $0 < \mathbf{c}_2(0) < \mathbf{c}_1(0) = 1 - e$, we require $-e < a_2 < 0$.

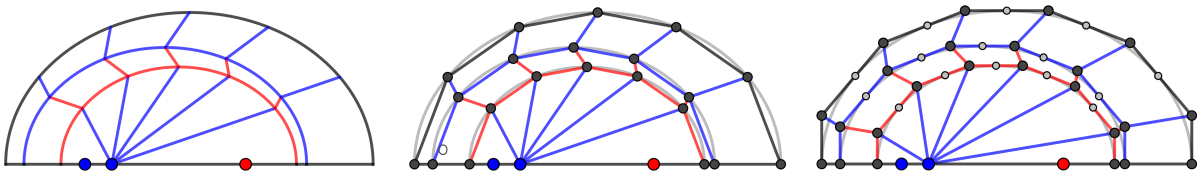

(a) Smooth crease pattern. (b) Inscribed discretization. (c) Circumscribed discretization.

Figure 10.5: Illustration of the considered crease patterns, exemplified by two scaled ellipses with reflecting rule lines.

In cases (EH2) and (EH3) the two conics intersect. This effects the direction of the reflected outer rule lines. In the following we only consider parameter intervals $(t_{\min}, t_{\max})$, where either $|\mathbf{c}_1(t)| \leq |\mathbf{c}_2(t)| < \infty$ for all $t \in (t_{\min}, t_{\max})$ or $|\mathbf{c}_2(t)| \leq |\mathbf{c}_1(t)| < \infty$ for all $t \in (t_{\min}, t_{\max})$.

10.4 Discretized Conic Crease Patterns with Reflecting Rule Lines

In addition to the smooth case, we examine two discretizations, as illustrated in Figure 10.5. In this section, we provide a formal description of the proposed discretizations.

Let $\mathbf{c}(t)$ be a conic and T and T_τ two ordered lists of appropriate parameter values. The two discretizations under study are as follows:

- *Inscribed discretization:* The vertices of the inscribed discretization method are points on the conic corresponding to parameters in T, and vertices corresponding to adjacent parameters are connected with edges.
- *Circumscribed discretization:* The vertices of the circumscribed discretization method are intersections of tangents of the conics at parameters in T_τ, and vertices corresponding to adjacent parameters are connected with edges.

We propagate the two discretizations with *discrete natural rule lines*: In case of the inscribed discretization, the sampling of the conics is propagated such that the sampled vertices of two compatible conics and the shared focal point are collinear; see Figure 10.5b. In case of the circumscribed discretization, the sampling of the points of contact is propagated such the sampled points of contact of two compatible conics and their shared focal point are collinear; see Figure 10.5c. It follows from Lemma 10.4 that the vertices obtained by intersecting neighboring tangents and the shared focal point are again collinear. Thus the discretized rulings in both discretization methods essentially sample the rulings in the smooth case.

When sampling the input curve, it is important to comply with the following constraints. When dealing with a hyperbola, sampling should be limited to a single branch. Furthermore, it is crucial to position the sampled points in such a way that all angles formed by the discretization remain smaller than π. Specifically, the parameter values of the sampled points must not differ by more than π in with respect to either apex.

10.5 Local Flat Foldability of Discretized Conic Crease Patterns

Prior to applying the join-and-fan method to determine the parametrization of the smooth crease curves and demonstrate the existence of a rigid folding motion, we first examine the flat foldability of vertices.

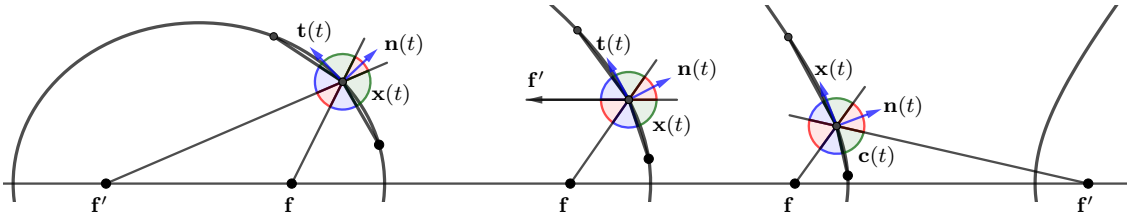

Figure 10.6: Illustration of the angles around a locally flat-foldable inscribed vertex. A vertex in the inscribed discretization is locally flat foldable, if the discretized creases are reflected on the normal of the conic. Note that this allows a decomposition in three pairs of equal angles around a vertex as in Lemma 10.4.

For a degree-4 vertex to be flat foldable, the sum of opposite angles must be π. It is known that when folding a flat-foldable degree-4 vertex, the fold angles along the opposite creases with same MV assignment are the same. Thus, if a pattern consist of flat-foldable degree-4 vertices, the fold angles along polylines with same MV assignment are constant.

As the rule lines of smooth conic curved creases are reflected on the crease, the resulting folded creases will have constant fold angle. In the following, we show when this property is preserved in our studied discretizations, that is, when all vertices are flat foldable. We show that the circumscribed discretization gives flat-foldable vertices for any (reasonable) parameter sampling. Furthermore, we show that carefully chosen parameter samplings in the inscribed discretization method result in locally flat-foldable crease patterns.

10.5.1 Circumscribed Discretizations

With Lemma 10.4, the angle around a vertex in a circumscribed discretization decomposes into three pairs of equal angles, that is, $2\pi = 2\alpha + 2\beta + 2\gamma$. Note that for discrete natural rule lines the sum of opposite angles is $\alpha + \beta + \gamma = \pi$, resulting in flat-foldable vertices for any sampling of points of contact. This trivially holds for all compatible conics.

10.5.2 Inscribed Discretizations

It is known, that the bisectors of opposite creases in a flat-foldable degree-4 vertex are perpendicular, and thus are referred to as *axes* of the flat-foldable vertex. In case of the inscribed discretization method, it follows from the reflection property of the conic that the axes of a flat-foldable inscribed vertex are the tangent and normal of the conic, as shown by Lang et al. [48]; see Figure 10.6.

Lemma 10.5. *A vertex $\mathbf{x}_i = \mathbf{x}(t)$ of an inscribed discretization of a conic section $\mathbf{x}(t)$ is flat-foldable if and only if its axes are the tangent $\mathbf{t}(t)$ and normal direction $\mathbf{n}(t)$ of the conic.*

For a single crease, we can therefore construct a set of parameters that result in flat-foldable vertices in the following way. Initially, we choose two sampling parameters. Reflecting the connecting lines on the incident conic normal and choosing the intersection with the conic as the next vertex, makes the central vertex flat-foldable. Iterating this construction results in a discretization with flat-foldable vertices.

The following lemma establishes a connection between the flat-foldable vertices of the inscribed discretization and the vertices of the circumscribed discretization method; see Figure 10.7:

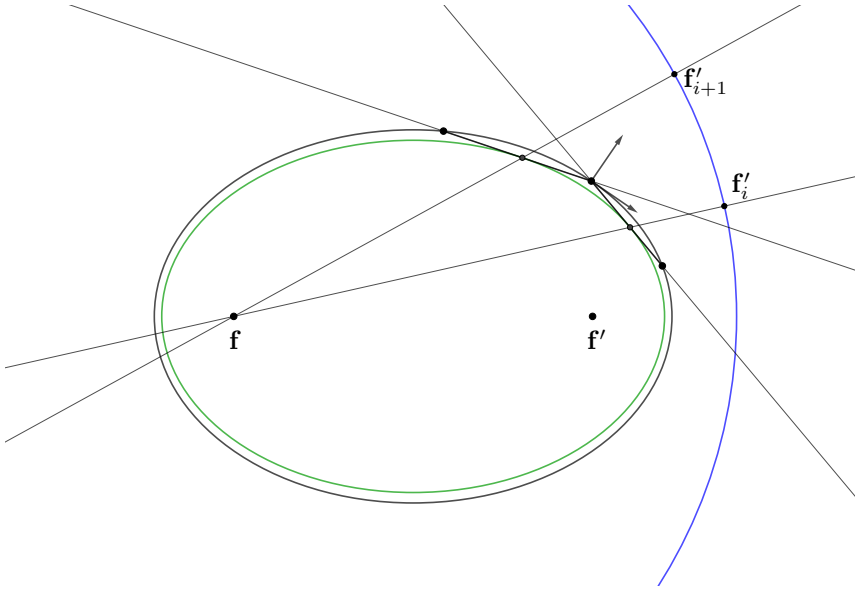

Figure 10.7: Illustration of Lemma 10.6.

Lemma 10.6. *The segments of a flat-foldable inscribed discretization are tangents to a conic of the same type.*

It remains to show that flat foldability of vertices propagates to compatible conics. In case of scaled or translated conics, the discretized creases of neighboring conics are parallel. Thus, opposite enclosing angles still sum up to π. In case of reflected parabolas with flat-foldable vertices, the reflected vertices are also still flat foldable.

The only non-trivial case is the combination of conics with reciprocal eccentricities. The proof of the following lemma is provided in Section 10.9.

Lemma 10.7. *A vertex in an inscribed discretization of two conics with reciprocal eccentricities is flat-foldable if and only if its neighboring vertex on the other conic is flat-foldable.*

10.6 Conic Creases and the Join-and-Fan Method

In the following, we first consider a crease-rule pattern consisting of only a single conic crease with reflecting rule lines, that is, a conic crease that connects a cone with a cylinder, or two cones, whose apices or ruling direction coincide with the (real or ideal) focal points $\mathbf{f}$ and $\mathbf{f}'$.

Using the join-and-fan method, we compute the parametrization of the resulting smooth crease curve (see Figure 10.8), and argue rigid foldability of the pattern consisting of one discrete curve.

10.6.1 Input

Parametrization of the development

In the following, we assume without loss of generality that the first surface $\mathbf{s}_1(t, u)$ in our construction is a cone with apex $\mathbf{v}_1$ located at the origin, that is connected to a cylinder or another cone with a conic crease.

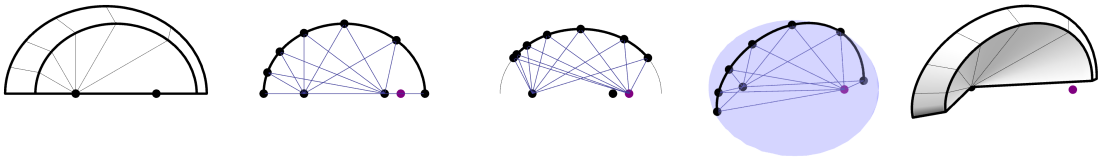

(a) Elliptic crease.

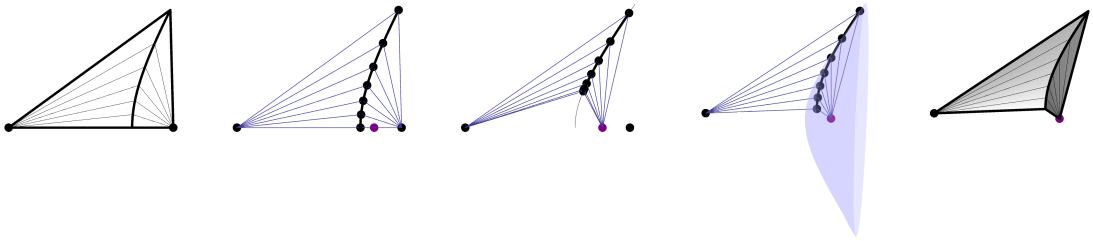

(b) Hyperbolic crease.

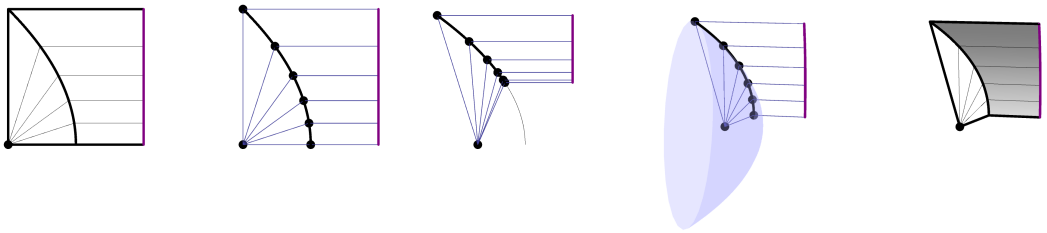

(c) Parabolic crease.

Figure 10.8: Illustration of the join-and-fan method for conic crease curves. From left to right: Crease pattern, extracted linkages, joining step, fanning step, and extraction of creases and surfaces.

Since the joining step is similar for both the smooth and discrete cases, we use a common notation to describe all considered cases: smooth, inscribed, and circumscribed. The main distinction lies in whether the points corresponding to the studied conic crease lie on the conic itself (smooth parametrization or inscribed discretization) or not (circumscribed discretization). We call the lengths associated with the two cases *inscribed* or *circumscribed*, respectively.

To cover both cases, we introduce a continuous or discrete domain T, which we use to define the functions associated with either the smooth or discrete parametrization. Specifically, we parametrize the smooth or discrete conics with a case-specific distance function $r_1(t) : T \to \mathbb{R}$ (defined below), and unit length ruling directions $\mathbf{r}_1(t) : T \to \mathbb{R}^3$ with $\mathbf{r}_1(t) = (\cos t, \sin t, 0)$. Consequently, for $t \in T$, the parametrization of the conic is given by $\mathbf{x}(t) = r_1(t)\mathbf{r}_1(t)$.

Inscribed lengths. In the smooth case, we set $T = (t_{\min}, t_{\max})$. In case of the inscribed discretization, we set let the parameter domain be a ordered list of points $T = (t_0, t_1, \ldots, t_m)$ where $t_i \in (t_{\min}, t_{\max})$. We parametrize the crease with polar coordinates using the parametrization given in Lemma 10.1 and Lemma 10.2 as

$$r_1(t) = \begin{cases} \frac{a(1-e^2)}{1+e\cos t}, & \text{if } \mathbf{x}(t) \text{ is an ellipse or hyperbola,} \\ \frac{2a}{1+\cos t}, & \text{if } \mathbf{x}(t) \text{ is a parabola.} \end{cases}$$

Circumscirbed lengths. In case of the circumscribed discretization, we assume that we are given a list of parameter values $T_\tau = (\tau_0, \tau_1, \ldots, \tau_m)$. We define T to be the array of the averages of two consecutive values, that is, $T = \left(\frac{\tau_0+\tau_1}{2}, \ldots, \frac{\tau_{m-1}+\tau_m}{2}\right)$, and set $T^- = \left(\frac{\tau_1-\tau_0}{2}, \ldots, \frac{\tau_m-\tau_{m-1}}{2}\right)$. Using the description given in Lemma 10.3, we set

$$r_1(t) = \begin{cases} \frac{a(1-e^2)}{\cos t^- + e\cos t}, & \text{if } \mathbf{x}(t) \text{ is an ellipse or hyperbola,} \\ \frac{2a}{\cos t^- + \cos t}, & \text{if } \mathbf{x}(t) \text{ is a parabola,} \end{cases}$$

where $t^- \in T^-$ shares a common index with $t \in T$.

Location of the developed apices and cylinder base lines. If $\mathbf{x}(t)$ is an ellipse or hyperbola, we consider a cone-cone combination where the second cone apex is $\mathbf{v}_2 = \mathbf{f}_2$. Note that this implies that $r_2(t) = |\mathbf{x}(t) - \mathbf{f}_2|$. If $\mathbf{x}(t)$ is a parabola, we consider a cone-cylinder combination where we choose the cylinders base line π_2 to be the directrix of the parabola, which is perpendicular to the cylinders ruling direction $\mathbf{r}_2 = (1, 0, 0)$, and coincides with point $\mathbf{p}_2 = (2a, 0)$.

Parametrization of the folded state

To be closer to the notation of [20], we modify the ansatz for the parametrization of the 3D crease curve. In particular, we assume that the 3D counterpart $\mathbf{X}(t)$ of $\mathbf{x}(t)$, defined over the same domain T, can be represented as

$$\mathbf{X}(t) = l(t)\left(\cos\zeta(t), \sin\zeta(t)\sin\eta(t), \sin\zeta(t)\cos\eta(t)\right), \tag{10.4}$$

where $l(t)$ is a length function, $\zeta(t) \in [0, \pi]$ denotes the opening angle between the ruling and the x-axis, and $\eta(t) \in [0, 2\pi]$ encodes the ruling's rotation around the x-axis.

Note that if two curves have a parametrization that has the same opening angle $\zeta(t)$ and rotation angle $\eta(t)$, they lie on the same conical surface.

Location of 3D apices and cylinder base planes. In the following, we study the configurations obtained by keeping the apex of the first cone fixed at the origin, that is, $\mathbf{V}_1 = (0, 0, 0)$, while moving the second apex $\mathbf{V}_2$ or base-plane Π_2, respectively.

We parametrize the motion using a *fold parameter* s as follows:

- *Ellipse or hyperbola:* We induce a folding motion by changing the distance between the focal points. Specifically, we move the second vertex from $\mathbf{v}_2 = (-2ae, 0, 0)$ to $\mathbf{V}_2 = (-2as, 0, 0)$ where $es > 0$. We increase the distance in case of an ellipse, and we decrease that distance in case of a hyperbola. We will see that in the smooth case and in case of the circumscribed discretization, folded states exists for $0 < |e| \leq |s| < 1$ in case of an ellipse, or $|e| \geq |s| > 1$ in case of a hyperbola.
- *Parabola:* In case of a parabola, we move the base plane Π_2 of the cylinder towards $\mathbf{V}_1$. Since the directrix of the parabola reads $x = 2a$, we parametrize the positions of the yz-parallel plane Π_2 by varying the incident point $\mathbf{P}_2 = (2as, 0, 0)$, where $0 < s \leq 1$.

10.6.2 Joining Step

In this section, we perform the joining step of a single conic crease for both inscribed and circumscribed points, resulting in closed-form expressions for the length function $l(t)$ and the opening angle $\eta(t)$.

Elliptic and hyperbolic creases

For the cone-cone combination, the two conical constraints in Equation (8.3) applied to the parametrization assumption in Equation (10.4), yield

$$l(t) = r_1(t) \qquad \text{and} \qquad \cos\zeta(t) = \frac{r_1(t)^2 - r_2(t)^2 + 4s^2}{4r_1(t)s}. \tag{10.5}$$

Inscribed lengths. For an inscribed point at parameter $t \in T$, the distance functions simplify to

$$r_1(t) = \frac{1-e^2}{1+e\cos t} \qquad \text{and} \qquad r_2(t) = \frac{1+e^2-2e\cos t}{1+e\cos t}.$$

Inserting into Equation (10.5) yields the following two solutions

$$l(t) = \frac{1-e^2}{1+e\cos t} \qquad \text{and} \qquad \cos\zeta(t) = \frac{s^2-e^2+e(1-s^2)\cos t}{(1-e^2)s}. \tag{10.6}$$

Note that since the bar lengths come from ellipses or hyperbolas, their sum or absolute difference of consecutive bar lengths is constant. This property is preserved when changing the position of one of the apices. Consequently, the resulting points will still lie on conics of the same type and same major axis length but varying eccentricity.

Circumscribed lengths. For a circumscribed point at parameter $t \in T$, the distance functions simplify to

$$r_1(t) = \frac{1-e^2}{\cos t^- + e\cos t} \qquad \text{and} \qquad r_2(t) = \sqrt{\frac{(2e\cos t^- + (1-e^2)\cos t)^2 + (-1+e^2)^2\sin^2 t}{(\cos t^- + e\cos t)^2}},$$

where $t^- \in T^-$ is the value corresponding to $t \in T$ (sharing the same array index). Inserting into Equation (10.5) yields the following two solutions

$$l(t) = \frac{1-e^2}{\cos t^- + e\cos t} \qquad \text{and} \qquad \cos\zeta(t) = \frac{(s^2-e^2)\cos t^- + e(1-s^2)\cos t}{(1-e^2)s}. \tag{10.7}$$

Compatibility of creases with reciprocal eccentricities. Before we continue, we make the following observation:

Lemma 10.8. *Substituting e with $\frac{1}{e}$ and s with $\frac{1}{s}$ in the expressions for $\zeta(t)$ in Equation* (10.6) *and Equation* (10.7) *gives the same result.*

Parabolic creases

In the parabolic case, the join step results using the conical constraint in Equation (8.3) for the first surface, and the cylindrical constraint in Equation (8.4) for the second surface, result in

$$l(t) = r_1(t) \qquad \text{and} \qquad \cos\zeta(t) = \cos t - \frac{2a(1-s)}{r_1(t)}.$$

Inscribed lengths. For an inscribed point at parameter $t \in T$, we obtain

$$l(t) = \frac{2a}{1+\cos t} \qquad \text{and} \qquad \cos\zeta(t) = \cos t - (1-s)(1+\cos t). \tag{10.8}$$

Again, note that since the bar lengths come from a parabola, consecutive bar lengths are equal. This property is preserved when changing the position of the base plane. As a result, the obtained points will still lie on a parabola, although it may be differently scaled.

Circumscribed lengths. For an circumscribed point at parameter $t \in T$, we obtain

$$l(t) = \frac{2a}{\cos t^- + \cos t} \qquad \text{and} \qquad \cos\zeta(t) = \cos t - (1-s)(\cos t^- + \cos t),$$

where $t^- \in T^-$ is the value corresponding to $t \in T$ (sharing the same array index).

10.6.3 Smooth Fanning Step: Parametrization of Conic Creases

The resulting 2D and 3D cones are isometric if $|\mathbf{X}'(t)| = |\mathbf{x}'(t)|$. This constraint is satisfied when

$$\zeta'(t)^2 + \eta'(t)^2 \sin^2\zeta(t) = 1 \qquad \Longrightarrow \qquad \eta'(t) = \pm\frac{\sqrt{1-\zeta'(t)^2}}{\sin\zeta(t)}, \tag{10.9}$$

a first-order differential equation for the function $\eta(t)$, the rotation angle about the x-axis. Without loss of generality, we consider only the positive branch and choose $\eta(0) = 0$.

Recall that the curves obtained from the inscribed joining step are located on conic sections. As a result, the curves produced during the smooth fanning step will lie on corresponding rotational quadrics, as illustrated in Figure 10.8.

Elliptic and hyperbolic creases

Inserting the solution of $\zeta(t)$ from Equation (10.6) into the positive root of Equation (10.9) simplifies to

$$\eta'(t) = \frac{(e^2-1)\sqrt{1+e^2-2e\cos t}}{(e^2-s+e(-1+s)\cos t)(e^2+s-e(1+s)\cos t)}\sqrt{\frac{(e^2-s^2)s^2}{-1+s^2}},$$

For $\delta = 1$ in case of an ellipse and $\delta = -1$ in case of a hyperbola, the above can be rewritten as

$$\eta'(t) = \frac{k\delta\phi'(t)}{\sqrt{1-m\sin^2\phi(t)}}\left(\frac{1}{1-n_1\sin^2\phi(t)} - \frac{1}{1-n_2\sin^2\phi(t)}\right)$$

where

$$\phi(t) = \arcsin\left(\frac{\sqrt{1+e^2-2e\cos t}}{1+e}\right),$$

and

$$k = \frac{2}{1-e}\sqrt{\frac{(e-s)(e+s)}{(1-s^2)}}, \qquad n_1 = \frac{(1+e)(-1+s)}{(-1+e)(1+s)},$$
$$m = \left(\frac{1+e}{1-e}\right)^2, \qquad n_2 = \frac{(1+e)(1+s)}{(-1+e)(-1+s)}.$$

Note that $\phi(t)$ has a continuous derivative for $t \in (-\pi, \pi)$. Using integral substitution, the solution of the differential equation with $\zeta(0) = 0$ can be written in terms of the incomplete elliptic integral of the third kind[1],

$$\begin{aligned}\eta(t) &= \int_0^t \eta'(\theta) d\theta \\ &= \delta k \int_{\phi(0)}^{\phi(t)} \frac{1}{\sqrt{1 - m \sin^2 \theta}} \left(\frac{1}{1 - n_1 \sin^2 \theta} - \frac{1}{1 - n_2 \sin^2 \theta} \right) d\theta \\ &= \delta k \left(\Pi(n_1; \phi(t)|m) - \Pi(n_2; \phi(t)|m) - (\Pi(n_1; \phi(0)|m) - \Pi(n_2; \phi(0)|m)) \right)\end{aligned} \tag{10.10}$$

Lemma 10.9. *For the relevant combinations of e and s, namely $es > 0$ and $0 < |e| \leq |s| < 1$ for an ellipse, or $|e| \geq |s| > 1$ for a hyperbola, the parametrization of $\eta(t)$ provided in Equation* (10.10) *is real-valued.*

Proof. By a case analysis on the possible valid combinations of e and s, we observe that k is a imaginary part of a complex number.

Nevertheless, the overall solution for $\eta(t)$ is real-valued. This is a consequence of the sum of the stated complex-valued elliptic integrals being a complex number whose real-part is zero. Since

$$1 - m \sin^2 \theta \begin{cases} > 0, & \text{for } 0 < \theta < \phi(0), \\ = 0, & \text{for } \theta = \phi(0), \\ < 0, & \text{for } \phi(0) < \theta < \phi(\pi), \end{cases}$$

the real-valued parts, that is, $\int_0^{\phi(0)} (1 - m \sin^2 \theta)^{-1/2} (1 - n_{1,2} \sin^2 \theta)^{-1} d\theta$, of the elliptic integrals cancel out. □

Parabolic creases

Inserting the solution of $\zeta(t)$ from Equation (10.8) into the positive root of Equation (10.9) simplifies to

$$\eta'(t) = \frac{\sqrt{2} c}{\sqrt{s(1 + \cos t)} \, (2 - s(1 + \cos t))}$$

where $c = \sqrt{1 - s}$. Consequently, the solution to the initial value problem with $\eta(0) = 0$ reads

$$\eta(t) = \frac{\left(\sqrt{s} \left(\arctan\left(-\sqrt{s} \sin \tfrac{t}{2}, c \right) - \arctan\left(\sqrt{s} \sin \tfrac{t}{2}, c \right) \right) + 4c \operatorname{arctanh}\left(\tan \tfrac{t}{4} \right) \right) \cos \tfrac{t}{2}}{\sqrt{2} \sqrt{s(1 + \cos t)}}.$$

Note that the above expression is real-valued for $t \in (-\pi, \pi)$ and $s \in (0, 1)$.

10.6.4 Discrete Fanning Step: Rigidly Foldable Discretizations

In this section, we use the tools presented in Section 8.5 to show the existence of rigid folding motions for both discretizations of a single conic crease.

We now consider an extracted linkage from a discretized conic crease pattern corresponding to a single conic crease as discussed in Section 8.5. In the following, we specify case-specific

[1] $\Pi(n; \phi|m) = \int_0^{\phi} (1 - m \sin^2 \theta)^{-1/2} (1 - n \sin^2 \theta)^{-1} d\theta$.

contracted diagonal configurations and use Corollary 8.4 to argue the existence of linkage motions with contracted diagonals. We conclude with an discussion of the fanning step, in particular the the application of Theorem 8.4. In the case of the circumscribed discretization, we confirm the existence of a complete rigid folding motion to the flat folded state. For the inscribed discretization, we reach the same conclusion until the first pair of faces fold flat. If the inscribed discretization is flat foldable, it yields the same result as the circumscribed case.

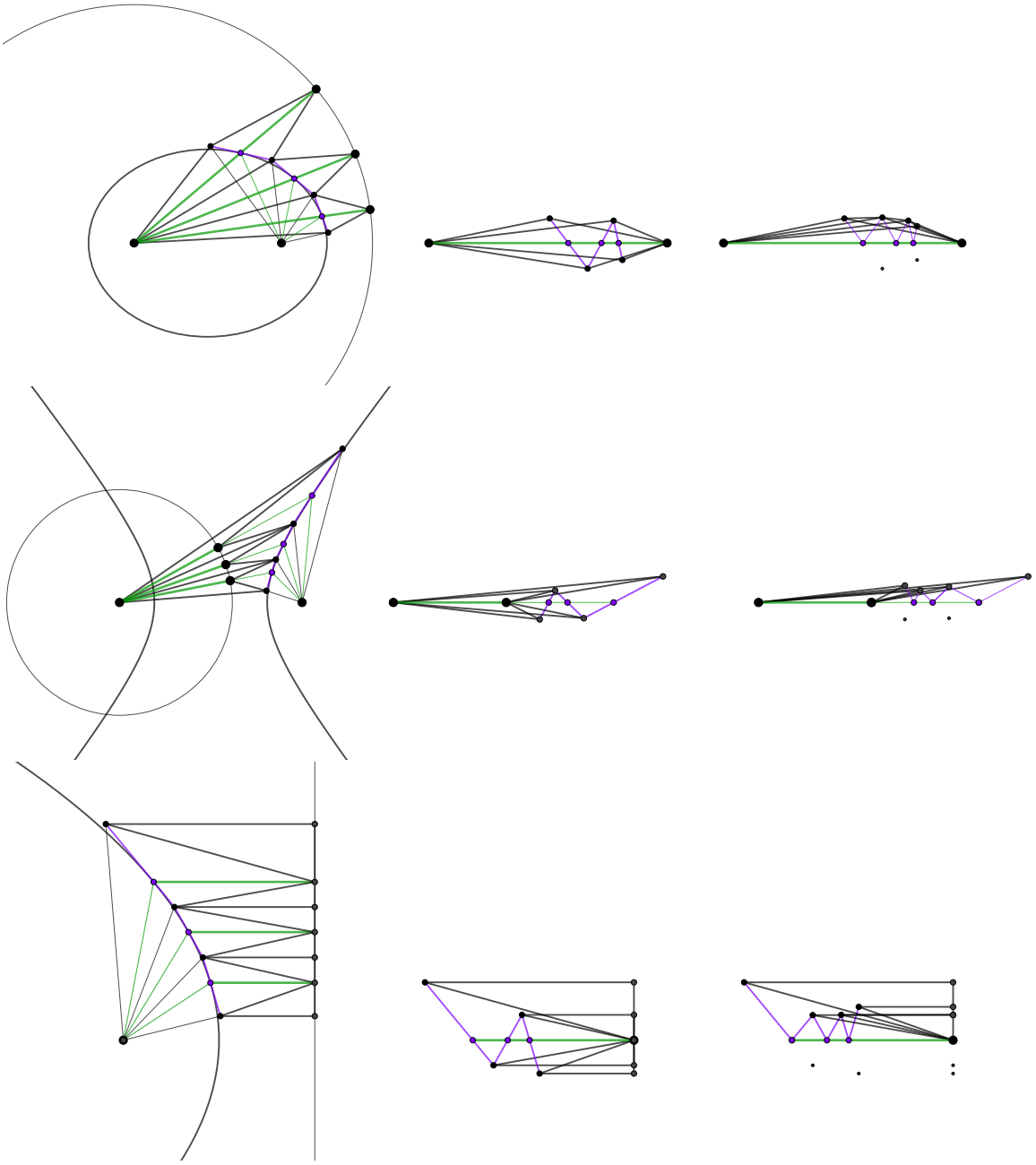

Figure 10.9: Illustration of the argument for the existence of a contracted configuration of the circumscribed discretization. Left: Crease pattern with overlaid fully folded faces across crease edges. Middle: Flat-folded state. Right: Flat-folded state folded along the central line to obtain a contracted linkage configuration.

Circumscribed discretization

For either conic crease type, we define the extracted linkages following the definition provided in Section 8.5; see Figure 10.9 (left). In case of an ellipse or hyperbola with major axis length a, note that reflecting a focal point on a sampled tangent results in a point on a circle centered at the other focal point with radius $2a$. In case of a parabola, reflecting the real focal point on a sampled tangent results in a point on the directrix. The reflection property of the conic ensures that the lines connecting the incident tangent point with either the focal point or its reflection are collinear.

In this case, we can find a suitable linkage configuration by positioning the pairs consisting of two adjacent triangles (ellipse or hyperbola) or a triangle and a quad (parabola) form the flat folded state of the pattern (as we will see, circumscribed discretizations are always flat foldable); see Figure 10.9 (middle). In case of an ellipse or hyperbola, $|\mathbf{v}_1 - \mathbf{v}_2| = 2a$, and in case of a parabola, $\operatorname{dist}(\mathbf{v}_1, \pi_2) = 0$.

To obtain the target linkage configuration, we "fold" the aligned faces along the x-axis. The face boundaries and the connections between neighboring vertices form a configuration of the extracted linkage; see Figure 10.9 (right). Note that this configuration has shorter cable distances than the initial pattern, as folding along the x-axis only brings neighboring linkage points closer together.

We therefore conclude the existence of a rigid folding motion that connects the development with a fully folded state.

Inscribed discretization

Again, for either conic crease type, we define the extracted linkages of an inscribed discretization following the definition provided in Section 8.5; see Figure 10.10 (left).

As discussed in Section 10.6.2, recall that the vertices of the modified linkages again lie on conics. Specifically, in case of an ellipse or hyperbola, these conics have the same major axis length, but have varying eccentricity. In case of a parabola, the vertices again lie on a scaled version of the parabola. It follows, that the linkages allow a "fully collapsed" configuration where all bars are aligned, at $|\mathbf{v}_1 - \mathbf{v}_2| = 2a$ in case of an ellipse or hyperbola, and $\operatorname{dist}(\mathbf{v}_1, \pi_2) = 0$ in case of a parabola; see Figure 10.10 (right). Note that these fully collapsed configurations correspond to the minimal possible cable length distance. Thus, with Corollary 8.4, there exists a one-parameter family of configurations whose cable lengths are shorter than the initial cable lengths. (In fact, in this case the motion monotonically decreases the cable lengths.)

As discussed in Section 8.5, we need to take the extremal feasible distances between apices or apex and base line into account; see Figure 10.10 (middle). In cases where the pattern cannot be flat-folded, we continue folding until the first discretized crease edge is completely folded. As discussed in Section 8.5.5 we can use the following strategy to determine the corresponding extremal distance. Let $\mathbf{v}_{1,i}$ be the vertices obtained by reflecting $\mathbf{v}_1$ about the crease segment $\mathbf{x}_i\mathbf{x}_{i+1}$.

- A folding of an elliptic crease is induced by moving the apices further away from each other. Therefore, the maximal distance between apices equals $\min_i |\mathbf{v}_2 - \mathbf{v}_{1,i}|$.
- A folding of a hyperbolic crease is induced by moving the apices closer together. Therefore, the minimal distance between apices equals $\max_i(\mathbf{v}_2, \mathbf{v}_{1,i})$.
- A folding of a parabolic crease is induced by moving the base plane closer to the apex. Therefore, the minimal distance between the base plane and the apex equals $\max_i \operatorname{dist}(\pi_2, \mathbf{v}_{1,i})$.

Note that in case of a locally flat-foldable inscribed discretization, the points $\mathbf{v}_{1,i}$ again lie on a circle centered at $\mathbf{v}_2$ (see Lemma 10.6).

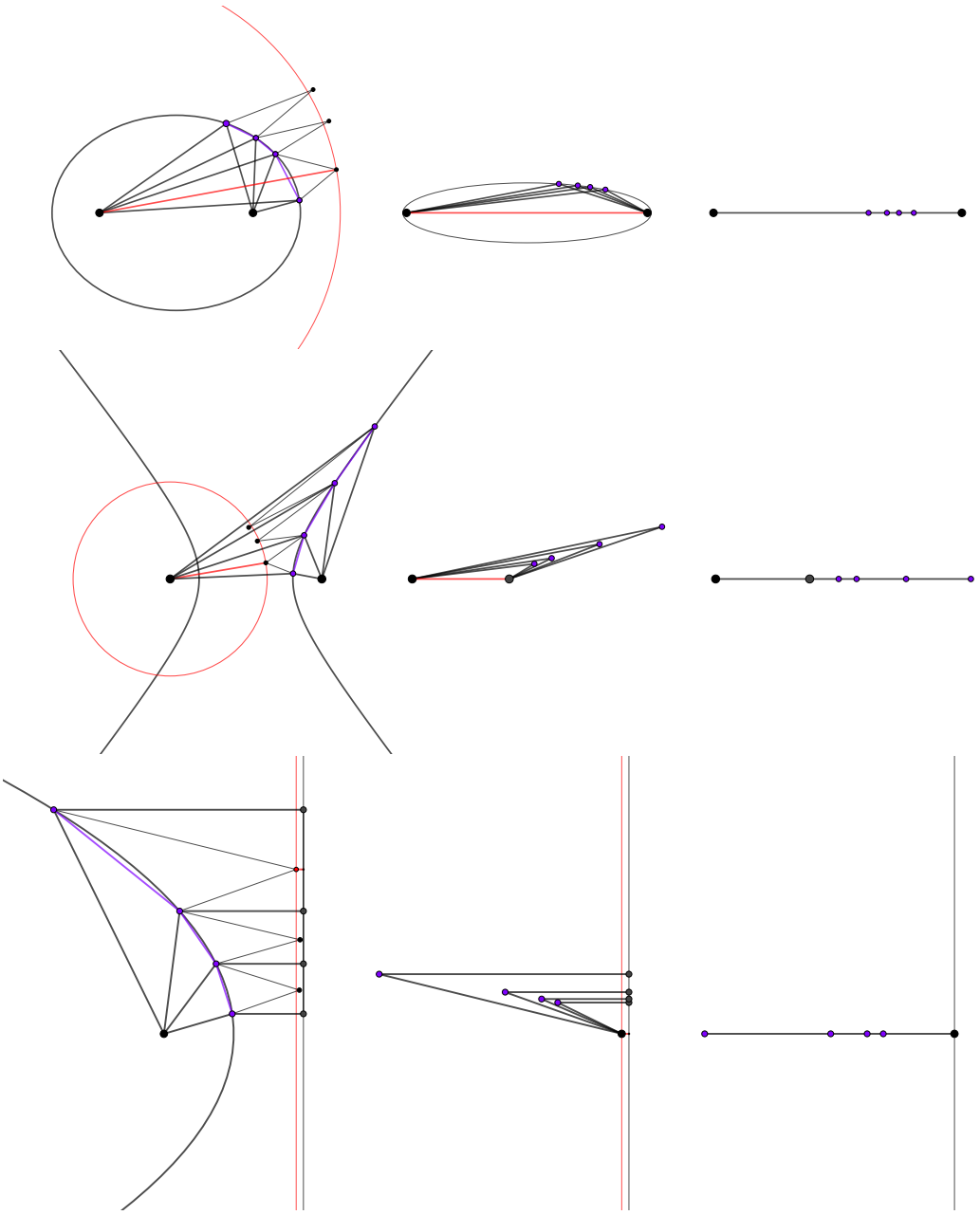

Figure 10.10: Illustration of the argument on the existence of a contracted configuration of the inscribed discretization. Left: Crease pattern with overlaid fully folded faces across the crease edges (the maximal/minimal distance between apices or apex and base line is depicted in red). Middle: Folded state corresponding to the maximal valid folding. Right: Fully folded configuration of the linkage.

We conclude that a rigid folding motion exists until the corresponding extremal distance between the apices or the apex and base line is reached.

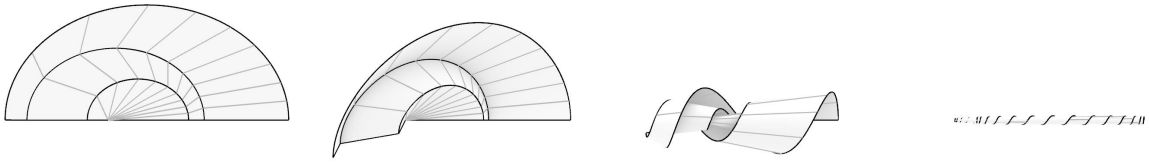

(a) Smooth creases with a rigid-ruling folding motions.

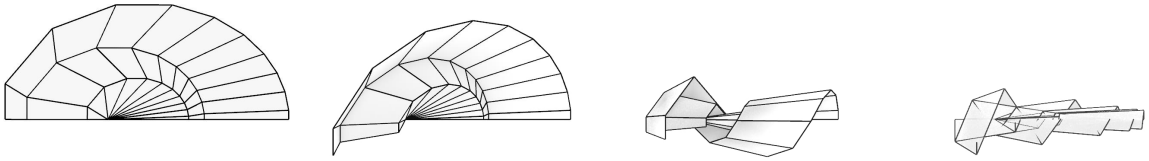

(b) Locally flat and rigidly-foldable circumscribed discretization.

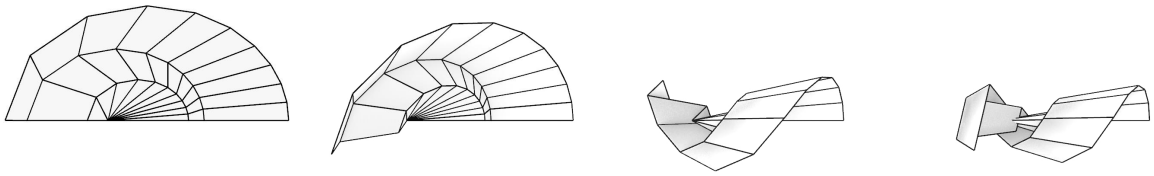

(c) Rigidly-foldable inscribed discretization.

Figure 10.11: Illustration of the folding motion of compatible elliptic creases.

10.7 Compatibility of Conic Creases

Finally, we confirm with our computations that the crease combinations stated in Section 10.3 share a common surface and are therefore compatible.

10.7.1 Conic Creases Connected by a Cylinder

First, let us consider the case where the smooth or discrete creases are connected by a cylindrical surface, which corresponds to cases (P2) and (P3). When we have a curve on a cylinder, translating this curve along a vector parallel to the ruling direction or reflecting it about a plane perpendicular to the ruling direction results in another curve on the same cylinder. The same operations can also be applied to the ruling vectors corresponding to the cone, resulting in a conical surface that is connected to the cylindrical surface with a smooth or discrete curved crease.

10.7.2 Conic Creases Connected by a Cone

In the remaining cases, the two conic creases are connected by a cone. Recall that the conics lie on the same cone when their angular functions $\eta(t)$ and $\zeta(t)$ match.

It follows from the computations in Section 10.6.2 that conic sections with (1) matching eccentricities and identical fold parameters, as well as (2) reciprocal eccentricities and reciprocal fold parameters (see Lemma 10.8), share the same opening angle $\zeta(t)$.

As a result, if two conics have the same $\zeta(t)$, they also share the same $\eta(t)$. Specifically, in the case of smooth curves, the differential equations are identical. In the discrete case, let us consider

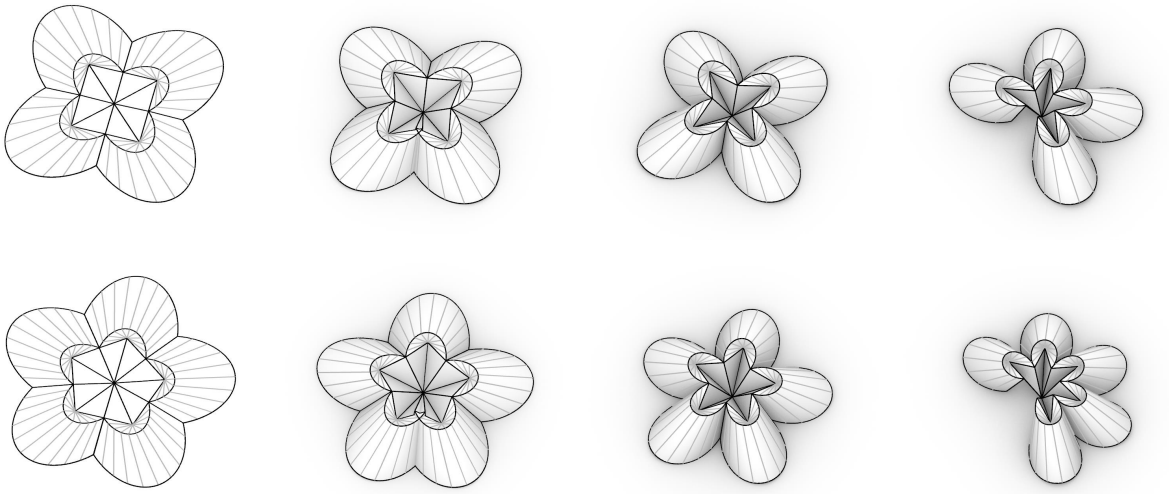

(a) David Huffman's "4-lobed cloverleaf design" (see Figure 10.1a) and a variation featuring five leaves. The crease patterns require a cut to be rigidly-foldable.

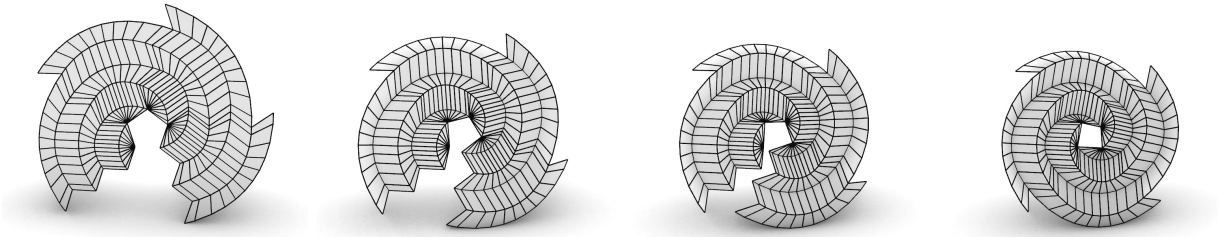

(b) Rigidly-foldable spiral with parabolic creases. The crease pattern requires a cut to be rigidly foldable.

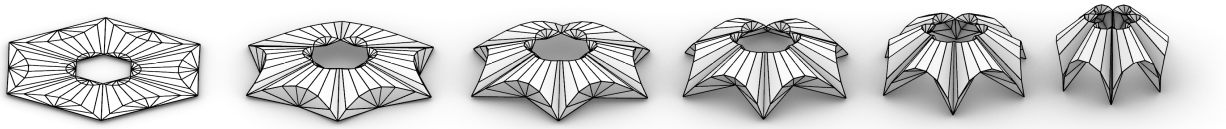

(c) Rigidly-foldable modification of David Huffman's "starburst design" (see Figure 10.1b). The crease pattern is rigidly foldable without an additional cut.

Figure 10.12: Illustration of folding motion computed using our implementation.

two conic sections $\mathbf{X}_1(t)$ and $\mathbf{X}_2(t)$ that are compatible and connected by a shared cone. Since

$$\begin{aligned}\angle(\mathbf{X}_1(t_i), \mathbf{V}_1, \mathbf{X}_1(t_{i+1})) &= \angle(\mathbf{x}_1(t_i), \mathbf{v}_1, \mathbf{x}_1(t_{i+1})) \\ &= \angle(\mathbf{x}_2(t_i), \mathbf{v}_1, \mathbf{x}_2(t_{i+1})) = \angle(\mathbf{X}_2(t_i), \mathbf{V}_1, \mathbf{X}_2(t_{i+1})),\end{aligned}$$

it can be observed that the second angular function $\eta(t)$ is likewise identical.

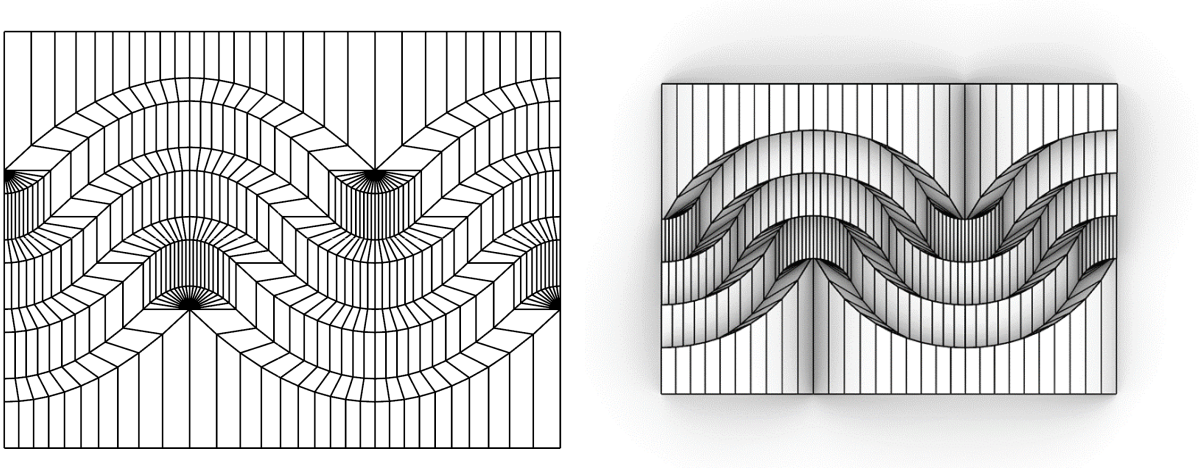

Figure 10.13: Rigidly foldable design with parabolic creases.

10.8 Implementation

We implemented the linkage-based construction as an interactive design tool for Grasshopper / Rhino. The plug-in allows the user to construct folded states of sequences of compatible conics. Rhino's and Grasshopper's environment allows to combine the obtained folded states, resulting in the possibility to explore folded states and folding motions, as depicted in Figure 10.12 and Figure 10.13.

10.9 Selected Proofs from Chapter 10

Proof of Lemma 10.1. First, consider the equation for an ellipse or hyperbola with unit major axis length centered at the one of the focal points,

$$(x+e)^2 + \frac{y^2}{1-e^2} = 1.$$

Specifically, if $e > 0$, the above conic is centered at the right focal point. If $e = 0$, the conic is a circle and the two focal points coincide with the origin. Otherwise, if $e < 0$, the conic is centered at the left focal point.

Replacing the two coordinates (x, y) with $r(t)\mathbf{r}(t)$, results in a quadratic equation for $r(t)$, namely,

$$\left(\frac{\sin^2 t}{1-e^2} + \cos^2 t\right) r(t)^2 + 2(e\cos t)r(t) + e^2 - 1 = 0.$$

Solving for $l(t)$ results in two solutions,

$$r_1(t) = \frac{1-e^2}{1+e\cos t} \qquad \text{and} \qquad r_2(t) = \frac{1-e^2}{-1+e\cos t}.$$

The resulting two parametrizations are related by a change of parameters, since

$$r_1(\pi+t)\,(\cos(\pi+t), \sin(\pi+t)) = r_2(t)\,(\cos t, \sin t)\,.$$

Setting $t \in [-\pi, \pi]$, we choose without loss of generality only one of them.

Finally, it follows from the parametrization that the second focal point is located at $(-2e, 0)$. Scaling by the factor a with respect to the origin yields the claimed results. □

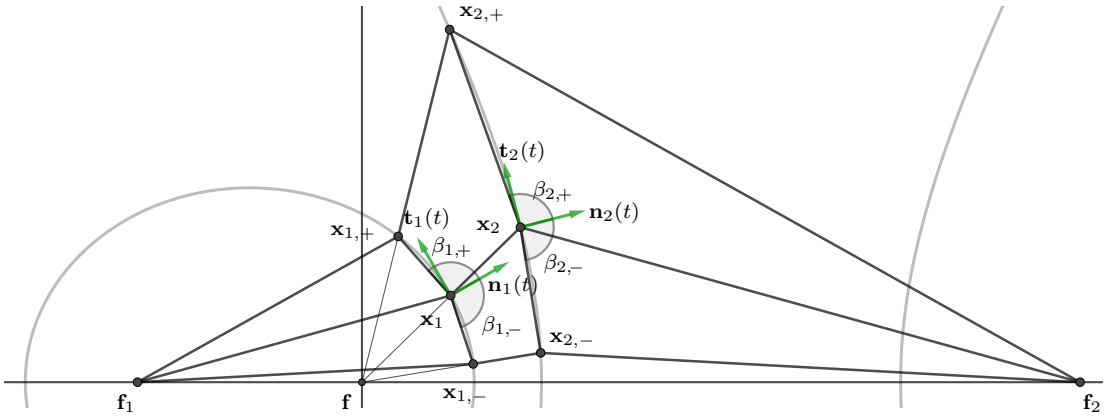

Figure 10.14: Notation used in the proof of Lemma 10.7 (case (EH1)).

Proof of Lemma 10.2. First, again consider the parabola centered at its focal point with scale factor $a = 1$,

$$y^2 = -4(x - 1).$$

Again, substituting (x, y) by $r(t)\mathbf{r}(t)$, yields a quadratic equation for $r(t)$, namely,

$$\left(\sin^2 t\right) r(t)^2 + (4\cos t)\, r(t) + 4 = 0.$$

Solving for $r(t)$ yields two solutions,

$$r_1(t) = -\frac{1}{\sin^2 \frac{t}{2}} \qquad \text{and} \qquad r_2(t) = \frac{1}{\cos^2 \frac{t}{2}}.$$

Analogously to before, we have that

$$r_1(\pi + t)\,(\cos(\pi + t), \sin(\pi + t)) = r_2(t)\,(\cos t, \sin t)\,,$$

thus we may choose to use only one of the solutions. Finally, note that

$$r(t) = \frac{1}{\cos^2 \frac{t}{2}} = \frac{2}{1 + \cos t}.$$

Scaling the conic by factor a yields the claimed result. □

Proof of Lemma 10.7. Let $0 < |e| < 1$ and let the two compatible conics be an ellipse $\mathbf{x}_1(t)$ and a hyperbola $\mathbf{x}_2(t)$ with eccentricity e and $\frac{1}{e}$, respectively. Assume without loss of generality that both conics are parametrized as in Equation (10.1) and denote their normal vectors by $\mathbf{n}_i$. Let $\mathbf{x}_i = \mathbf{x}_i(t)$ for $t \in (t_{\min}, t_{\max})$ be two adjacent vertices of the crease pattern. For $\delta_+ > 0$ and $\delta_- > 0$ such that $t \pm \delta_\pm \in (t_{\min}, t_{\max})$, we denote the neighboring vertices on the crease by $\mathbf{x}_{i,\pm} = \mathbf{x}_i(t \pm \delta_\pm)$.

In the following, let $\cos\beta_{i,\pm} := \cos(\angle(\mathbf{n}_i(t), \mathbf{x}_{i,\pm} - \mathbf{x}_i))$. We show $\mathbf{x}_1$ is flat-foldable if and only if vertex $\mathbf{x}_2$ by showing

$$\cos\beta_{1,-} = \cos\beta_{1,+} \qquad \Longleftrightarrow \qquad \cos\beta_{2,-} = \cos\beta_{2,+}.$$

Using the parametrization in (10.1), we obtain

$$\cos\beta_{1,\pm} = \frac{\sqrt{2}(1+e\cos t)\sin\frac{\delta_\pm}{2}}{\sqrt{(1+e^2+2e\cos t)(2+e^2(1+\cos\delta_\pm)+2e(\cos t+\cos(t\pm\delta_\pm)))}}$$
$$\cos\beta_{2,\pm} = \frac{\sqrt{2}e(e+\cos t)\sin\frac{\delta_\pm}{2}}{\sqrt{(1+e^2+2e\cos t)(2e^2+1+\cos\delta_\pm+2e(\cos t+\cos(t\pm\delta_\pm)))}}.$$

Note that $\cos\beta_{1,-}=\cos\beta_{1,+}$ is equivalent to $B_{1,-}=B_{1,+}$, where

$$B_{1,\pm} = \frac{\sin\frac{\delta_\pm}{2}}{\sqrt{2+e^2(1+\cos\delta_\pm)+2e(\cos t+\cos(t\pm\delta_\pm))}},$$

and $\cos\beta_{2,-}=\cos\beta_{2,+}$ is equivalent to $B_{2,-}=B_{2,+}$, where

$$B_{2,\pm} = \frac{\sin\frac{\delta_\pm}{2}}{\sqrt{2e^2+1+\cos\delta_\pm+2e(\cos t+\cos(t\pm\delta_\pm))}}.$$

Note that $B_{i,\pm}>0$, and thus $B_{i,-}=B_{i,+}$ if and only if $\frac{1}{B_{i,-}^2}=\frac{1}{B_{i,+}^2}$. Because

$$\frac{1}{B_{1,+}^2}-\frac{1}{B_{2,+}^2}=\frac{1}{B_{1,-}^2}-\frac{1}{B_{2,-}^2}=2(1-e^2),$$

we conclude that

$$\cos\beta_{1,-}=\cos\beta_{1,+} \iff \frac{1}{B_{1,-}^2}=\frac{1}{B_{1,+}^2} \iff \frac{1}{B_{2,-}^2}=\frac{1}{B_{2,+}^2} \iff \cos\beta_{2,-}=\cos\beta_{2,+}.$$

□

Chapter 11

Sliding Developables and Planar Creases

The contents of this chapter are based on discussions with Erik Demaine, Riccardo Foschi, Robby Kraft, Rupert Maleczek, Georg Nawratil, Tomohiro Tachi, and Helmut Pottmann, and are partially published [64, 65].

Overview

Designing developable surfaces while simultaneously preserving their developability, controlling the regression curve, and providing an intuitive user interface poses a significant challenge. We present an approach based on a special case of the join-and-fan method that is suited for generating one-parameter families of bend states of developable surfaces with rigid rulings. This method, referred to as "sliding", maintains the planarity of a fixed curve and results in a sliding-like motion. Consequently, it is closely related to rigid-ruling folding motions of planar creases.

11.1 Introduction

Among all deformations of a planar patch, preserving a given layout of ruling lines has the advantage of avoiding the introduction of new singularities through folding motions. In this section, we employ a method where the deformation is guided by maintaining the planarity of a curve that intersects all ruling lines exactly once.

The construction of such surfaces has a single degree of freedom, which corresponds to the amount of bending of the surface. If the curve used for guiding the motion is one of the curved boundaries of the developable patch, adjusting this parameter resembles a sliding motion of the patch. Consequently, we call it a "sliding motion"; see Figure 11.3. Discrete sliding developables are studied also in the context of kinematics as they are related to the T-hedra construction [85, 84].

For a given patch with specified rulings, we have previously discussed a Frenet frame based approach for the computation of states in which a specified curve is planar (see Section 3.3.3). However, in this section, our focus shifts to methods that do not rely on computing the Frenet frame. In particular, for cases involving cylinders and cones, this computation can be accomplished with a single integration step, as opposed to the at least four integrations necessary when using the Frenet frame-based approach. Moreover, similar to our previous discussion, this alternative method allows us to gain a deeper understanding of the space of achievable shapes. In addition to

the cylinder and cone case, we review a connection between deformations of tangent developables and cones.

11.2 Sliding Cylinders and Cones and the Join-and-Fan Method

In the following, we explore the application of the join-and-fan method to bent cylinders and cones while maintaining the planarity of a fixed curve. Specifically, we focus on the case where we start with two copies of a developed cylinder or cone and employ the join-and-fan method to achieve a symmetric shape with a planar glue curve. Then, one half of the shape will be the desired slided cylinder or cone. To help intuitive understanding, we modify the setup of the join-and-fan method to reflect a sliding where the sliding plane is the xy-plane.

11.2.1 Input

In the following, we assume that we are given a smooth or discrete cylindrical or conical patch, $\mathbf{s}(t,u) = \mathbf{x}(t) + u\mathbf{r}(t)$, where $\mathbf{x}(t)$ is a smooth or discrete curve that will be constrained to be planar.

To arrive at a symmetric shape, we set the two surfaces $\mathbf{s}_1(t,u)$ and $\mathbf{s}_2(t,u)$ involved in the join-and-fan method to $\mathbf{s}(t,u)$. In particular, we define $\mathbf{x}(t) = \mathbf{x}_1(t) = \mathbf{x}_2(t)$ and $\mathbf{r}(t) = \mathbf{r}_1(t) = \mathbf{r}_2(t)$.

Cylinders

In case of a cylinder, we set without loss of generality $\mathbf{p}_1 = \mathbf{p}_2 = (0,0,0)$. In addition, we use $\rho \in [\frac{\pi}{2}, \pi]$ to denote the angle between the cylinder base plane's normal and the xy-plane. Specifically, we define the base-planes normals, the 3D ruling vectors, to be $\mathbf{R}_1 = (\cos\rho, 0, -\sin\rho)$ and $\mathbf{R}_2 = (\cos\rho, 0, \sin\rho)$. Furthermore, let $\mathbf{P}_1 = \mathbf{P}_2 = (0,0,0)$. In this case, similarly to Section 8.2.4, it is convenient to make the assumption that $\mathbf{X}(t)$ is parametrized with Cartesian coordinates, as in Equation (8.1). Note that the opening angle of the planes is $\varphi = 2(\pi - \rho)$.

Cones

In case of a cone, we assume that the corresponding 2D cone are located at $\mathbf{v}$. Without loss of generality, we set the location of the 3D apices to be $\mathbf{V}_1 = (0,0,h)$ and $\mathbf{V}_2 = -\mathbf{V}_1$, where $h > 0$ is denoted as the *height* of the cone apex. We use a polar parametrization for the glue curve, centered at the cone apex $\mathbf{V}_1$, that is, $\mathbf{X}(t) = \mathbf{V}_1 + l(t)\mathbf{R}(t)$ where

$$\mathbf{R}(t) = (\cos\eta(t)\cos\zeta(t), \sin\eta(t)\cos\zeta(t), \sin\zeta(t)),$$

for $l(t) \geq 0$, $\eta \in [0,\pi]$, and $\zeta(t) \in [0, 2\pi]$.

11.2.2 Joining Step

We now perform the joining step for both configurations.

Cylinders

Applying the cylindrical constraints (Equation (8.4)) to each of the two surfaces yields

$$\mathbf{X}_x(t) = \frac{\mathbf{x}(t)\cdot\mathbf{r}}{\cos\rho} \qquad \text{and} \qquad \mathbf{X}_z(t) = 0.$$

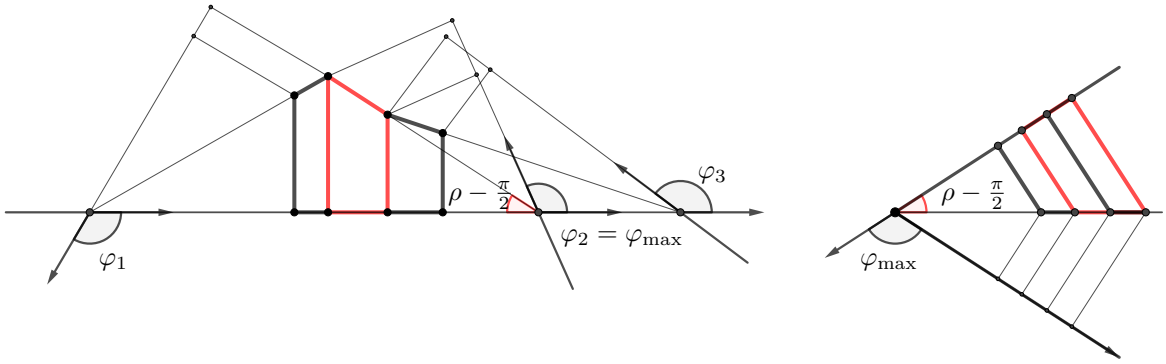

Figure 11.1: Illustration of the extremal angle $\varphi_{\max}$ used in the sliding cylinder computation. Left: Discrete planar cylinder in the sliding cylinder computation. Right: Side view of the configuration where $\varphi = \varphi_{\max}$. Here, the limiting red plane lies in a plane perpendicular to the base planes.

Cones

Applying the conical constraints (Equation (8.3)) to each of the two surfaces yields

$$l(t) = r(t) \qquad \text{and} \qquad \zeta(t) = -\arcsin\frac{h}{r(t)}.$$

11.2.3 Discrete Fanning Step: Existence of a Motion

Next, let us examine the discrete fanning step, using the extracted linkages from the surface. In the case of a cylinder, the extracted linkage consists of four-bar linkages that have two pairs of parallel bars. On the other hand, in the case of a cone, the extracted linkage consists of regular four-bar linkages.

Since the involved surfaces are identical, the consecutive lengths of the bars are the same. As a result, in both cases, the extracted linkages form families of non-crossing four-bar linkages. Furthermore, the linkages again are symmetric with respect to the bisecting plane of the base lines or apices.

Cylinders

Since the non-collinear linkages are non-crossing, increasing the angle between the base planes increases the cable lengths. Therefore, the cable distances only increase during the motion. The maximal realizable angle $\rho_{\max}$ again corresponds to half of the corresponding extremal angle between the cylinders base plane and its reflection on $\mathbf{x}(t_i)\mathbf{x}(t_{i+1})$, that is,

$$\rho_{\max} = \max_i \left|\arccos\left(\frac{\mathbf{r}\cdot(\mathbf{x}(t_{i+1}) - \mathbf{x}(t_i))}{|\mathbf{x}(t_{i+1}) - \mathbf{x}(t_i)|}\right)\right|,$$

With Theorem 8.4, we conclude a rigid sliding motion for $\rho \in [0, \rho_{\max}]$.

Cones

Since the non-collinear linkages are non-crossing, increasing the distance between the apices increases the cable distance. Therefore, the cable distances only increase during the motion. The

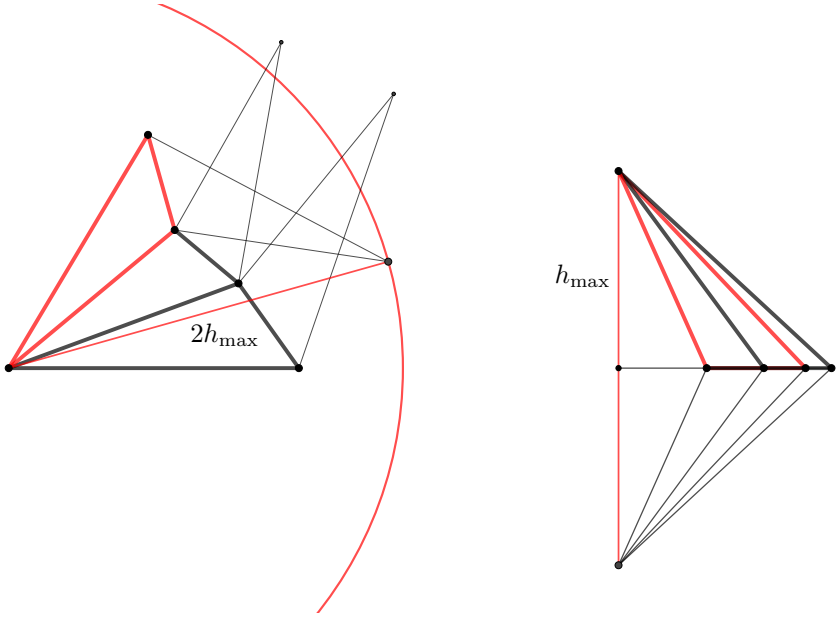

Figure 11.2: Illustration of the extremal height h used in the sliding cone computation. Left: discrete planar cone. Right: Side view of the configuration where $h = h_{\max}$. Here, the limiting red plane lies in a plane perpendicular to the base planes.

maximal realizable height $h_{\max}$ again corresponds to half of the minimal distance between the apex and its reflection on $\mathbf{x}(t_i)\mathbf{x}(t_{i+1})$, that is,

$$h_{\max} = \min_i \sqrt{1 - \frac{(\mathbf{r}(t) \cdot (\mathbf{x}(t_{i+1}) - \mathbf{x}(t_i)))^2}{|\mathbf{x}(t_{i+1}) - \mathbf{x}(t_i)|^2}} l(t_i).$$

With Theorem 8.4, we conclude a rigid sliding motion for $h \in [0, h_{\max}]$.

11.2.4 Smooth Fanning Step: Existence of a Motion

Cylinder

In case of a cylinder, we obtain the remaining function from the parametrization speed requirement in Equation (8.5), that is,

$$\mathbf{X}'_y(t) = \pm\sqrt{|\mathbf{x}'(t)|^2 - \frac{(\mathbf{r} \cdot \mathbf{x}'(t))^2}{\cos^2 \rho}}.$$

Note that this derivative is real-valued for $\rho \in [0, \rho_{\max}]$, where

$$\rho_{\max} = \max_{t \in [0, t_{\max}]} \left| \arccos\left(\frac{\mathbf{r} \cdot \mathbf{x}'(t)}{|\mathbf{x}'(t)|} \right) \right|. \tag{11.1}$$

Note that this is a smooth counterpart of the expression for $\rho_{\max}$ in the discrete case, that is, we the maximal angle between the ruling direction and the curve's tangent.

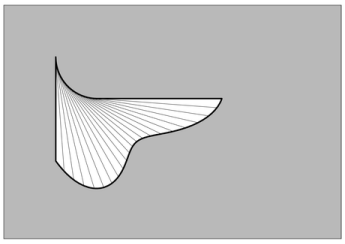

(a) Tangent developable $\mathbf{s}(t, u)$.

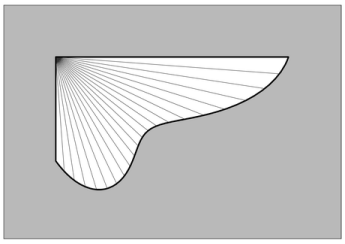

(b) Cone $\mathbf{s}_\triangle(t, u)$.

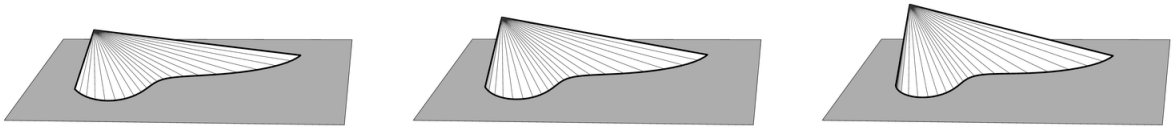

(c) Slided configurations $\mathbf{S}_\triangle(t, u)$ of the cone $\mathbf{s}_\triangle(t, u)$.

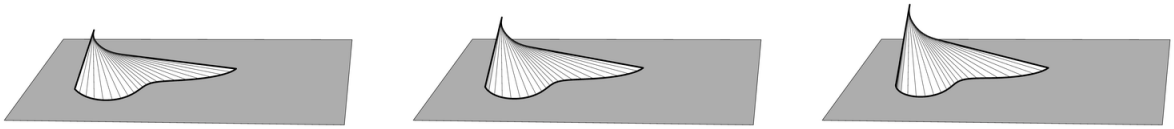

(d) Slided configurations $\mathbf{S}(t, u)$ of the tangent developable $\mathbf{s}(t, u)$.

Figure 11.3: Illustration of the connection between sliding cylinders and sliding tangent developables.

Cone

In case of a cone, we obtain the remaining function from the parametrization speed requirement in Equation (8.6), that is,

$$\eta'(t) = \pm\frac{\sqrt{|\mathbf{r}'(t)| - \zeta'(t)}}{\sin\zeta(t)} = \pm\frac{\sqrt{r(t)^2\,|\mathbf{r}'(t)|^2\,(r(t)^2 - h^2) - h^2 r'(t)^2}}{l(t)^2 - h^2}$$

Note that this derivative is real-valued for $h \leq h_{\max}$ where

$$h_{\max} = \min_{t\in[0,t_{\max}]} \frac{r(t)^2\,|\mathbf{r}'(t)|}{\sqrt{r'(t)^2 + r(t)^2\,|\mathbf{r}'(t)|^2}}.$$

Like in the previous case, note that this is a smooth counterpart of the expression for $h_{\max}$, that is, the minimal distance between the apex and its reflection on the glue curve's tangent.

11.3 From Sliding Cones to Sliding Tangent Developables

Sauer [82] presents a method to reduce the sliding motion of a discrete tangent developable to the sliding motion of a discrete cone. In the following, we review the corresponding discrete approach and formulate its smooth analogue.

11.3.1 Discrete Case

Sauer proposes the following approach. Let $\mathbf{s}(t,u) = \mathbf{x}(t) + u\mathbf{r}(t)$ be a discrete tangent developable surface and $\mathbf{c}(t)$ its discrete edge of regression, that is, $\mathbf{c}(t_i)\mathbf{c}(t_{i+1})$ and $\mathbf{r}(t_i)$ are collinear. Furthermore, let $\mathbf{x}(t) = \mathbf{c}(t) + l(t)\mathbf{r}(t)$ be a polyline on $\mathbf{s}(t,u)$. Our goal is to construct a surface $\mathbf{S}(t,u)$ isometric to $\mathbf{s}(t,u)$ such that the curve $\mathbf{X}(t)$ corresponding to $\mathbf{x}(t)$ is planar.

In the following, let $\mathbf{s}_\triangle(t) = \mathbf{v} + u\mathbf{r}(t)$ be a cone with apex $\mathbf{v}$ sharing the same ruling directions as $\mathbf{s}(t,u)$. Define $\mathbf{x}_\triangle(t) = \mathbf{c}(t) + l_\triangle(t)\mathbf{r}(t)$, where $l_\triangle(t)$ is such that $l_\triangle(0) = l(0)$ and $\mathbf{x}_\triangle(t_i)\mathbf{x}_\triangle(t_{i+1})$ are parallel to $\mathbf{x}(t_i)\mathbf{x}(t_{i+1})$. Furthermore, let $\mathbf{S}_\triangle(t,u) = \mathbf{V} + l_{\triangle(t)}\mathbf{R}(t)$ be a cone isometric to $\mathbf{s}_\triangle(t,u)$ such that $\mathbf{X}_\triangle = \mathbf{V} + l_\triangle(t)\mathbf{R}(t)$ is planar.

Saurer shows that one can construct a 3D configuration of $\mathbf{S}(t,u)$ from $\mathbf{S}_\triangle(t,u)$, by reconstructing the discrete edge of regression. Specifically, let $\mathbf{C}(0) = \mathbf{V}$ and $\mathbf{C}(t_{i+1}) = \mathbf{C}(t_i) + |\mathbf{c}(t_i) - \mathbf{c}(t_{i+1})|\,\mathbf{R}(t_i)$ and set $\mathbf{S}(t,u) = \mathbf{C}(t) + u\mathbf{R}(t)$. It follows that $\mathbf{X}(t) = \mathbf{C}(t) + l(t)\mathbf{R}(t)$ is planar.

11.3.2 Smooth Case

To phrase a smooth analogue of the discrete construction, We consider a tangent developable surface given by its edge of regression, that is, $\mathbf{s}(t,u) = \mathbf{c}(t) + u\mathbf{r}(t)$ where $\mathbf{c}'(t) = s'(t)\mathbf{r}(t)$, and a curve $\mathbf{x}(t) = \mathbf{c}(t) + l(t)\mathbf{r}(t)$ on $\mathbf{s}(t,u)$.

Analogous to the discrete case, we consider the planar cone $\mathbf{s}_\triangle(t,u) = \mathbf{v} + u\mathbf{r}(t)$ and the curve $\mathbf{x}_\triangle(t) = \mathbf{v} + l_\triangle(t)\mathbf{r}(t)$, where $l_\triangle(t)$ is chosen such that $\mathbf{x}'(t)$ and $\mathbf{x}'_\triangle(t)$ are parallel. The length function $l_\triangle(t)$ can be computed from

$$\Big(\mathbf{x}'(t) \times \mathbf{x}'_\triangle(t)\Big) \cdot (0,0,1) = 0.$$

For $|\mathbf{r}'(t)| \neq 0$, this equation simplifies to

$$\frac{l'_\triangle(t)}{l_\triangle(t)} = \frac{s'(t) + l'(t)}{l(t)}. \tag{11.2}$$

For $l_\triangle(0) = l(0)$ the solution of the corresponding initial value problem reads

$$l_\triangle(t) = l(0)\; e^{\int_0^t \frac{s'(\theta)+l'(\theta)}{l(\theta)} d\theta}.$$

In the following, let $\mathbf{S}_\triangle(t,u) = \mathbf{V} + l_\triangle(t)\mathbf{R}(t)$ be a cone isometric to $\mathbf{s}_\triangle(t,u)$ such that $\mathbf{X}_\triangle(t) = \mathbf{V} + l_\triangle(t)\mathbf{R}(t)$ is planar. We now prove:

Lemma 11.1. *Let $\mathbf{C}(t)$ a curve such that $\mathbf{C}'(t) = s'(t)\mathbf{R}(t)$. Then, $\mathbf{S}(t,u) = \mathbf{C}(t) + u\mathbf{R}(t)$ is isometric to $\mathbf{s}(t,u)$ and $\mathbf{X}(t) = \mathbf{C}(t) + l(t)\mathbf{R}(t)$ is a planar curve on $\mathbf{S}(t,u)$.*

Proof. First, we show that $\mathbf{S}(t,u)$ and $\mathbf{s}(t,u)$ are isometric. Note that the developability of $\mathbf{S}(t,u)$ follows from its definition as a tangent developable. Consequently, it is sufficient select two curves on $\mathbf{S}(t,u)$, and show that (1) two curves on $\mathbf{s}(t,u)$ have the same parametrization speed as their 2D counterparts, and (2) that the two curves enclose the same angle with the ruling vectors as their 2D counterparts with the developed rulings.

For this purpose, consider the two curves $\mathbf{C}(t)$ and $\mathbf{X}(t)$ and their 2D counterparts $\mathbf{c}(t)$ and $\mathbf{x}(t)$. The 3D curves have the same parametrization speed as their 2D counterparts, since $|\mathbf{C}'(t)| = s'(t) = |\mathbf{c}'(t)|$ and $|\mathbf{X}'(t)|^2 = (1 + l'(t))^2 + l(t)^2 = |\mathbf{x}'(t)|^2$. In addition, we have that $\mathbf{C}'(t) \cdot \mathbf{R}(t) =$

$s'(t) = \mathbf{c}'(t) \cdot \mathbf{r}(t)$ and $\mathbf{X}'(t) \cdot \mathbf{R}(t) = 1 + l'(t) = \mathbf{x}'(t) \cdot \mathbf{r}(t)$. Consequently, $\mathbf{S}(t, u)$ and $\mathbf{s}(t, u)$ are isometric.

Finally, we show that $\mathbf{X}(t)$ is planar by confirming that $\mathbf{X}'(t)$ and $\mathbf{X}'_{\triangle}(t)$ are parallel. Analogous to the above, for $|\mathbf{r}'(t)| \neq 0$, this condition translates to Equation (11.2) which is satisfied by definition of $l_{\triangle}(t)$. □

Overall, this approach solves four integrals, that is, one to obtain the angular function $\eta(t)$ and three more to determine $\mathbf{C}(t)$ from $\mathbf{R}(t)$. Therefore, it is not a significant improvement to the construction with the Frenet-frame based approach proposed in Section 3.3.3, where the number of computed integrals is also at least four. Specifically, we need one integration step to determine $\varphi(t)$, one integration step to determine the 2D tangent from the curvature function, and two to conclude the trajectory of the planar crease. Although it is the same number of integrals, they need to be performed in three consecutive steps. On the other hand, the smooth counterpart to Saurer's construction approach allows a computation of the four integrals in two steps.

Moreover, the sliding based approach offers a better understanding of attainable shapes. Specifically, for a given patch, constructing the corresponding cone is the major limitation, as integrating an appropriately scaled tangent vector does not cause problems. See Section 11.2.4 for a discussion on the geometric limitations on the height of the cone apex.

11.4 Folding Motion of Planar Creases

For each slided configuration, extending and reflecting the extended part on the sliding plane results in a planar crease. If done for each slided state, this gives a rigid-ruling folding motion of the planar crease. As discussed in Section 3.5.2, a pleated structure can be obtained by adding parallel creases, which in this case will lie in planes parallel to the sliding plane; see Figure 11.4.

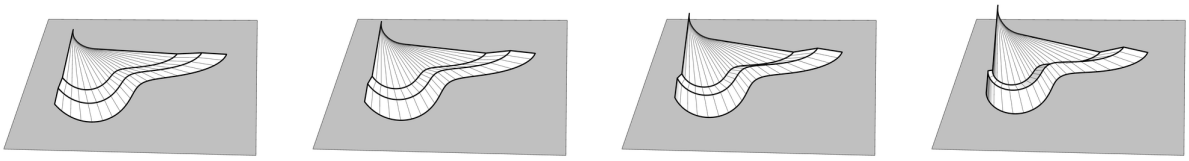

Figure 11.4: Illustration of a rigid-ruling folding motion with planar parallel pleats.

Part III

Ruling-Length-Based Computation of Creases

Chapter 12

Patch-to-Patch Construction

This chapter introduces the patch-to-patch construction method and provides a summary of relevant considerations used in its applications, such as [63, 67, 55, 46, 65]. Most of the presented work is based on discussions and collaborations with corresponding coauthors, particularly Erik Demaine and Tomohiro Tachi.

Overview

We present a construction method that enables the computation of creases between a smooth or discrete developable patch and a cylinder or a cone. The proposed patch-to-cylinder and patch-to-cone constructions do not rely on optimization techniques and are suitable for parametrized interactive additive design of folded shapes. Furthermore, we demonstrate the combination of both methods into a unified approach, the patch-to-projective-cone construction. By employing this unified method, we show how to approximate a curved crease between two developable patches.

12.1 Introduction

The digital reconstruction of folded shapes plays an important role in the design process, offering designers the ability to verify tolerances and integrate models into other digital projects. This is especially relevant in engineering applications such as architecture. An editable and parametric digital model is highly desirable as it allows for easy manipulation, exploration of various configurations, and the ability to meet specific constraints and requirements. However, designing complex folded shapes presents significant challenges, often requiring a strong background in optimization or geometry. Moreover, existing methods for parametric design are limited, as discussed by Foschi et al. [25].

In this chapter, we present a ruling-based constructive approach for the computation and design of creases that connect smooth or discrete developable patches with cylinders or cones. Additionally, we demonstrate how the patch-to-cylinder and patch-to-cone construction can be used to approximate a curved crease between two developable patches. This approach is implemented as a user-friendly plug-in named Lotus for Rhino/Grasshopper, enabling interactive additive parametrized design of folded shapes.

The subsequent chapters illustrate further applications of the patch-to-cylinder and patch-to-cone method. Chapter 13 showcases two geometric shapes reconstructed and designed using the patch-to-cylinder and patch-to-cone constructions. Chapter 15 and Chapter 16 discuss two strategies for algorithmically generating complex shapes with smooth or discrete creases. Finally, Chapter 17 demonstrates how the presented ideas can be applied to the subdivision of regular planar quad meshes.

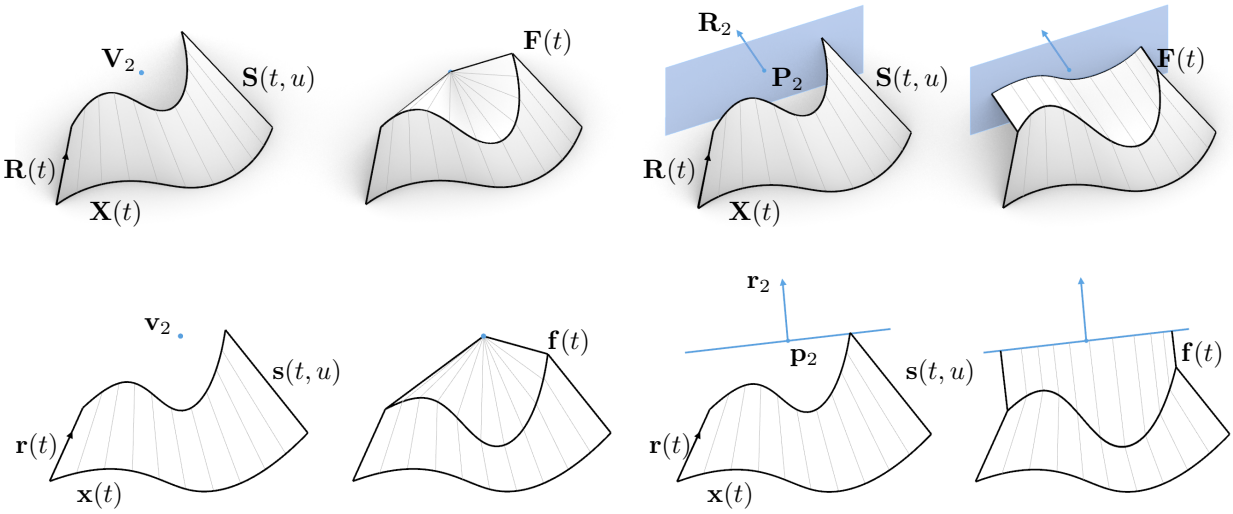

(a) Input and result of the patch-to-cone construction.

(b) Input and result of the patch-to-cylinder construction.

Figure 12.1: Illustration of the notation for the patch-to-cone and patch-to-cylinder constructions.

We begin this chapter by introducing the patch-to-cylinder and patch-to-cone constructions to illustrate the key concept of the construction. Next, in Section 12.4, we present a unified generalization that enables numerically stable computations through the utilization of scaling transformations. While the presented constructions do not prevent surface intersections, we address this issue by presenting a sufficient constraint for surface intersection prevention in Section 12.5. Additionally, in Section 12.6, we explore the conditions under which two patch-to-projective-cone constructions can be connected in a tangent-continuous manner. Finally, we demonstrate the practical application of combining patch-to-projective-cone constructions to approximate a crease between two patches in Section 12.7.

12.2 Notation

As in the previous part, we parametrize a (smooth or discrete) developable patch as a ruled surface with normalized ruling directions $\mathbf{R}(t)$, that is,

$$\mathbf{S}(t,u) = \mathbf{X}(t) + u\mathbf{R}(t),$$

where $\mathbf{X}(t)$ is a curve on $\mathbf{S}(t,u)$ that can degenerate to a single point in the case of a cone's apex. The surface is a cylinder if the ruling direction $\mathbf{R}(t)$ is constant. Let $\mathbf{s}(t,u)$ denote an isometric parametrization of the development of $\mathbf{S}(t,u)$ in the xy-plane, that is,

$$\mathbf{s}(t,u) = \mathbf{x}(t) + u\mathbf{r}(t),$$

as discussed in Section 2.1. In particular, $|\mathbf{r}(t)| = 1$ and $|\mathbf{x}'(t)| = |\mathbf{X}'(t)|$ in the smooth case or $|\mathbf{X}(t_i) - \mathbf{X}(t_{i+1})| = |\mathbf{x}(t_i) - \mathbf{x}(t_{i+1})|$ in the discrete case, respectively.

To find the crease curve between $\mathbf{S}(t,u)$ and a cylinder or a cone, we make the assumption that the crease curve $\mathbf{F}(t)$ is parametrized with an initially unknown length function $l(t)$ as

$$\mathbf{F}(t) = \mathbf{X}(t) + l(t)\mathbf{R}(t). \tag{12.1}$$

Consequently, its developed counterpart reads

$$\mathbf{f}(t) = \mathbf{x}(t) + l(t)\mathbf{r}(t). \tag{12.2}$$

The main idea behind the computation of the location of the crease curve is to identify pairs of corresponding points for each ruling that satisfy specific distance constraints. In the following, we will provide algebraic expressions for the resulting length function $l(t)$.

12.3 Patch-to-Cylinder and Patch-to-Cone Constructions

12.3.1 Locating the Crease

In this section, we locate the crease that connects a given patch with a cylinder or a cone specified by the position of the cylinder's base plane or the cone's apex location, respectively.

Lemma 12.1. *The crease connecting a developable patch $\mathbf{S}(t,u)$ with a cone, specified by the 3D cone apex $\mathbf{V}_2$ and 2D cone apex $\mathbf{v}_2$, is uniquely specified by the length function*

$$l(t) = \frac{1}{2}\frac{|\mathbf{v}_2 - \mathbf{x}(t)|^2 - |\mathbf{V}_2 - \mathbf{X}(t)|^2}{(\mathbf{v}_2 - \mathbf{x}(t)) \cdot \mathbf{r}(t) - (\mathbf{V}_2 - \mathbf{X}(t)) \cdot \mathbf{R}(t)}, \tag{12.3}$$

if $(\mathbf{x}(t) - \mathbf{v}_2) \cdot \mathbf{r}(t) - (\mathbf{X}(t) - \mathbf{V}_2) \cdot \mathbf{R}(t) \neq 0$. Otherwise, there are no solutions (when $|\mathbf{v}_2 - \mathbf{x}(t)|^2 - |\mathbf{V}_2 - \mathbf{X}(t)|^2 \neq 0$) or infinitely many solutions (when $|\mathbf{v}_2 - \mathbf{x}(t)|^2 - |\mathbf{V}_2 - \mathbf{X}(t)|^2 = 0$).

Proof. If $\mathbf{F}(t)$ is a valid crease between the patch and the cone, then each point on $\mathbf{F}(t)$ will be connected to the cone apex $\mathbf{V}_2$ through a ruling segment. Similarly, in the 2D case, $\mathbf{f}(t)$ is connected to the the cone apex $\mathbf{v}_2$ with corresponding rule line segments. To ensure isometry, we aim for the corresponding rule line segments in both 2D and 3D to have equal lengths, that is,

$$|\mathbf{F}(t) - \mathbf{V}_2|^2 = |\mathbf{f}(t) - \mathbf{v}_2|^2 .$$

By substituting the assumptions for $\mathbf{F}(t)$ and $\mathbf{f}(t)$ (Equation (12.1) and Equation (12.2)), we obtain

$$|\mathbf{X}(t) - \mathbf{V}_2 + l(t)\mathbf{R}(t)|^2 = |\mathbf{x}(t) - \mathbf{v}_2 + l(t)\mathbf{r}(t)|^2 ,$$

a quadratic equation in $l(t)$. However, simplifications lead to the elimination of the quadratic terms in $l(t)$, resulting in a linear equation for $l(t)$,

$$0 = -2\left((\mathbf{v}_2 - \mathbf{x}(t)) \cdot \mathbf{r}(t) - (\mathbf{V}_2 - \mathbf{X}(t)) \cdot \mathbf{R}(t)\right) l(t) + |\mathbf{v}_2 - \mathbf{x}(t)|^2 - |\mathbf{V}_2 - \mathbf{X}(t)|^2 .$$

Consequently, if the coefficient of $l(t)$ is not equal zero, we obtain the unique solution stated above. If the coefficient of $l(t)$ is zero, the number of solutions depends on whether the constant term is zero or not. □

In the following, we assume that a 3D plane Π_2 is specified by the normal direction $\mathbf{R}_2$ and an incident point $\mathbf{P}_2$. Similarly, assume that a 2D line is specified by the normal direction $\mathbf{r}_2$ such that $|\mathbf{r}_2| = |\mathbf{R}_2| \neq 0$, and the incident point π_2.

Lemma 12.2. *The crease connecting a developable patch $\mathbf{S}(t,u)$ with a cylinder, specified by an oriented 3D base plane Π_2 and oriented 2D base line π_2, is uniquely specified by the length function*

$$l(t) = \frac{(\mathbf{p}_2 - \mathbf{x}(t)) \cdot \mathbf{r}_2 - (\mathbf{P}_2 - \mathbf{X}(t)) \cdot \mathbf{R}_2}{\mathbf{r}(t) \cdot \mathbf{r}_2 - \mathbf{R}(t) \cdot \mathbf{R}_2}, \tag{12.4}$$

if $\mathbf{r}(t)\cdot\mathbf{r}_2 - \mathbf{R}(t)\cdot\mathbf{R}_2 \neq 0$. Otherwise, there are no solutions (when $(\mathbf{p}_2 - \mathbf{x}(t))\cdot\mathbf{r}_2 - (\mathbf{P}_2 - \mathbf{X}(t))\cdot\mathbf{R}_2 \neq 0$) or infinitely many solutions (when $(\mathbf{p}_2 - \mathbf{x}(t)) \cdot \mathbf{r}_2 - (\mathbf{P}_2 - \mathbf{X}(t)) \cdot \mathbf{R}_2 = 0$).

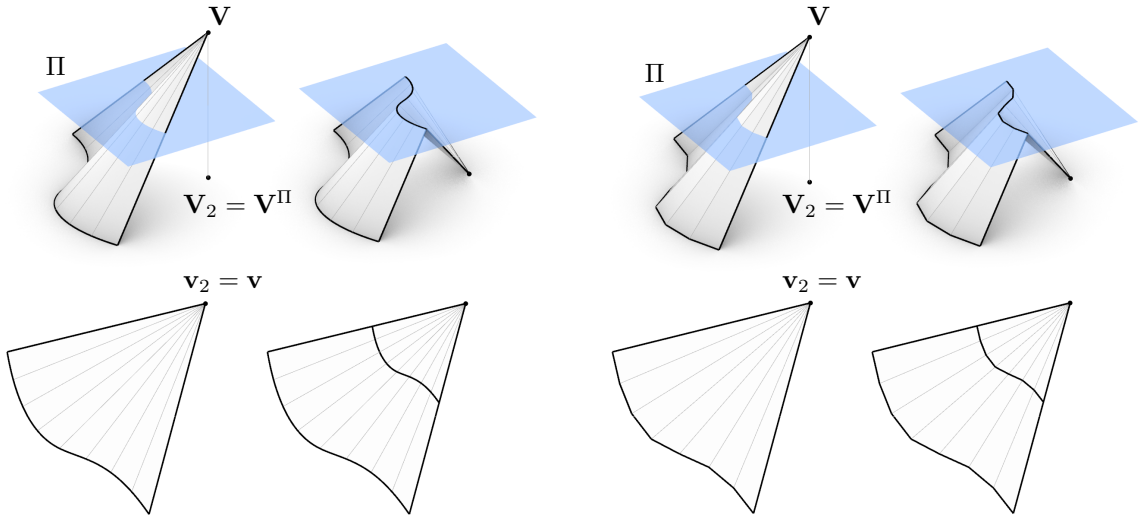

Figure 12.2: Illustration of how the patch-to-cone construction can be used to locate a planar crease in both the smooth (left) and discrete (right) cases.

Proof. If $\mathbf{F}(t)$ is a valid crease between the patch and the cylinder, then each point on $\mathbf{F}(t)$ will be connected to the base plane Π_2 by a ruling segment that is perpendicular to Π_2. Similarly, in the 2D case, $\mathbf{f}(t)$ is connected to π_2 with corresponding rule line segments that are perpendicular to π_2. To ensure isometry, we aim for the corresponding oriented distances in both 2D and 3D to be the same, that is,

$$(\mathbf{F}(t) - \mathbf{P}_2) \cdot \mathbf{R}_2 = (\mathbf{f}(t) - \mathbf{p}_2) \cdot \mathbf{r}_2.$$

By substituting the assumptions for $\mathbf{F}(t)$ and $\mathbf{f}(t)$ (Equation (12.1) and Equation (12.2)), we obtain

$$(\mathbf{X}(t) - \mathbf{P}_2 + l(t)\mathbf{R}(t)) \cdot \mathbf{R}_2 = (\mathbf{x}(t) - \mathbf{p}_2 + l(t)\mathbf{r}(t)) \cdot \mathbf{r}_2,$$

a linear equation for $l(t)$, that is,

$$0 = (\mathbf{r}(t) \cdot \mathbf{r}_2 - \mathbf{R}(t) \cdot \mathbf{R}_2)\, l(t) - ((\mathbf{p}_2 - \mathbf{x}(t)) \cdot \mathbf{r}_2 - (\mathbf{P}_2 - \mathbf{X}(t)) \cdot \mathbf{R}_2)\,.$$

Consequently, if the coefficient of $l(t)$ is not equal zero, we obtain the unique solution stated above. If the coefficient of $l(t)$ is zero, the number of solutions depends on whether the constant term is zero or not. □

Note that Equation (12.4) yields the same result for pairs of points $\mathbf{P}_2$ and $\mathbf{p}_2$ where $-\mathbf{r}_2 \cdot \mathbf{p}_2 + \mathbf{P}_2 \cdot \mathbf{R}_2 = \text{const}$. This implies that if a plane Π' and a line π' are parallel to Π_2 and π_2 and share the same oriented distance with respect to Π_2 and π_2, they will result in the same crease.

12.3.2 Planar Creases

Recall from Section 3.3.4 that planar creases can be obtained by splitting a developable patch along a plane Π into two parts, and then reflecting one of those parts across Π. In instances where the patch is either a cylinder or a cone, and given the appropriate input, the patch-to-cylinder and patch-to-cone constructions can be used to locate planar crease curves.

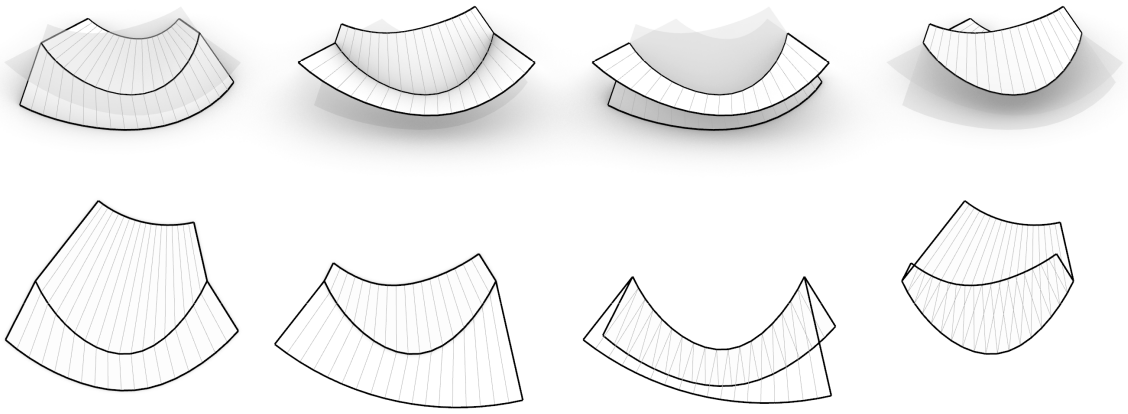

Figure 12.3: Four possible combinations of subpatches obtained by intersecting two patches along a curved crease. Left: Two combinations achievable through folding. Right: Two geodesic pair combinations.

If $\mathbf{S}(t,u)$ represents a cone with its apex at $\mathbf{V}$, and $\mathbf{s}(t,u)$ is its development with an apex of $\mathbf{v}_2$, we obtain a planar crease by setting $\mathbf{V}_2$ as the vertex achieved by reflecting $\mathbf{V}$ across Π and $\mathbf{v}_2 = \mathbf{v}$, as illustrated in Figure 12.2.

In the case where $\mathbf{S}(t,u)$ is a cylinder with its base plane determined by the point $\mathbf{P}$ and a normal $\mathbf{R}$, and its development $\mathbf{s}(t,u)$ has a corresponding base plane defined by points $\mathbf{p}$ and $\mathbf{v}$, we obtain a planar crease by setting both $\mathbf{P}_2$ and $\mathbf{R}_2$ as the reflections of $\mathbf{P}$ and $\mathbf{R}$ across Π and defining $\mathbf{p}_2 = \mathbf{p}$ and $\mathbf{v}_2 = \mathbf{v}$, respectively.

12.3.3 Valid Patch Combinations

The computed crease curve divides the input developable surface patch $\mathbf{S}(t,u)$ and the cylinder or cone into two surface parts each. Figure 12.3 illustrates the four possible combinations. Among these combinations, two can be achieved through *folding* along a curve, while the remaining two form a *geodesic pair* (discussed in Section 3.3.3). The geodesic pair consists of two surfaces with congruent boundaries that cannot be created by folding along a single crease. We refer to pairs of surfaces that can be achieved by folding as *compatible*.

In this section, we demonstrate how to computationally characterize compatible patches by utilizing the contraction property. This property states that the distance between two points on a shape can only decrease through folding.

In the following, let $\mathbf{S}_2(t,u)$ denote the surface patch obtained through a $\mathbf{V}_2$-central extrusion in the case of a cone or a $\mathbf{R}_2$-parallel extrusion in the case of a cylinder. The next lemma shows the connection between the ruling direction of the patch $\mathbf{S}(t,u)$ that is compatible with $\mathbf{S}_2(t,u)$ and the denominator of $l(t)$.

Lemma 12.3. *Let $D(t) \neq 0$ denote the denominator of $l(t)$ as given in Equation* (12.3) *and Equation* (12.4)*, that is,*

$$D(t) = \begin{cases} (\mathbf{v}_2 - \mathbf{x}(t)) \cdot \mathbf{r}_2 - (\mathbf{V}_2 - \mathbf{X}(t)) \cdot \mathbf{R}_2, & \text{if } \mathbf{S}_2(t,u) \text{ is a cylinder} \\ \mathbf{r}(t) \cdot \mathbf{r}_2 - \mathbf{R}(t) \cdot \mathbf{R}_2, & \text{if } \mathbf{S}_2(t,u) \text{ is a cone.} \end{cases}$$

The surface patch $\mathbf{S}_2(t,u)$ is compatible with the ruling direction $-\operatorname{sign}(D(t))\mathbf{R}(t)$.

Proof. Conical case: For a fixed parameter t we consider the following parametrizations of two corresponding rulings,

$$\mathbf{G}(u) = \mathbf{X}(t) + u\mathbf{R}(t) \qquad \text{and} \qquad \mathbf{g}(u) = \mathbf{x}(t) + u\mathbf{r}(t).$$

In the conical case, we consider the difference between the distances of points on the rulings and the corresponding apices, that is,

$$\begin{aligned} K(u) &= |\mathbf{g}(u) - \mathbf{v}_2|^2 - |\mathbf{G}(u) - \mathbf{V}_2|^2 \\ &= -2\left((\mathbf{v}_2 - \mathbf{x}(t)) \cdot \mathbf{r}(t) - (\mathbf{V}_2 - \mathbf{X}(t)) \cdot \mathbf{R}(t)\right) u + |\mathbf{x}(t) - \mathbf{v}_2|^2 - |\mathbf{X}(t) - \mathbf{V}_2|^2 . \end{aligned}$$

Note that $K(u)$ is a linear function in u, and by definition of the crease, $K(l(t)) = 0$. Assuming that $K(u)$ is not constant, the sign of $K(u)$ changes at $u = l(t)$.

For values u where $K(u) < 0$, the distance between points on the rulings and the corresponding apex in 3D is greater than in 2D. Consequently, the points corresponding to those parameters can not lie on the part of the ruling that is connected to $\mathbf{S}_2(t, u)$ by a fold. Parameters corresponding to the admissible part of the ruling therefore satisfy $K(u) > 0$.

Since $K(u)$ is a linear function in u, we consider (half of) the coefficient of u, the denominator $D(t)$ of $l(t)$:

- If $D(t) > 0$, we have $K(u) \geq 0$ if $u \leq l(t)$, resulting in the compatible ruling direction $-\mathbf{R}(t)$.
- If $D(t) < 0$, we have $K(u) \geq 0$ if $u \geq l(t)$, resulting in the compatible ruling direction $+\mathbf{R}(t)$.

Consequently, the compatible ruling direction can be stated as $-\operatorname{sign}(D(t))\mathbf{R}(t)$.

Cylindrical case: In the cylindrical case, we consider the angles between the rulings. Note that folding can only decrease the angle between lines. Therefore, consider the denominator

$$D(t) = \mathbf{r}(t) \cdot \mathbf{r}_2(t) - \mathbf{R}(t) \cdot \mathbf{R}_2(t).$$

If $D(t) > 0$, the angle between ruling segments in 3D is bigger than in 2D, making the direction $-\mathbf{R}(t)$ a compatible segment direction. If $D(t) < 0$, the angle between the ruling segments in 3D is smaller than in 2D, making the direction $+\mathbf{R}(t)$ a compatible segment direction. □

12.3.4 Alternative User Input

While specifying cone apices $\mathbf{V}_2$ and $\mathbf{v}_2$ or cylinder base planes Π_2 and π_2 can be practical in certain applications, it is not always intuitive. Additionally, it is desirable to have an input that relies solely on the 3D configuration, allowing for a proper determination of the corresponding 2D configurations. A solely 3D input is beneficial in the implementation, as it does not require keeping track between 2D and 3D configurations. In this section, we introduce two alternative specifications that we use as user-input in our implementation of the Lotus plug-in for Grasshopper/Rhino [57, 81].

Both types of input require the 3D surface $\mathbf{S}(t, u)$, a point $\mathbf{A}$ on $\mathbf{S}(t, u)$ and a point $\mathbf{V}$ not on the surface. If the second surface is a cylinder, its base plane Π_2 is specified by its normal, the ruling direction $\mathbf{R}_2 = \frac{\mathbf{V}-\mathbf{A}}{|\mathbf{V}-\mathbf{A}|}$, and the incident point $\mathbf{P}_2 = \mathbf{V}$. On the other hand, if the second surface is a cone, $\mathbf{V}$ corresponds to the 3D apex position $\mathbf{V}_2$.

- In addition to the two points, the *user-input 3pt* requires a second point $\mathbf{B}$ on $\mathbf{S}(t, u)$. If feasible, the resulting crease will pass through $\mathbf{A}$ and $\mathbf{B}$. The corresponding developed points $\mathbf{a}$, $\mathbf{b}$, and $\mathbf{v}$ will be oriented in counter-clockwise direction.

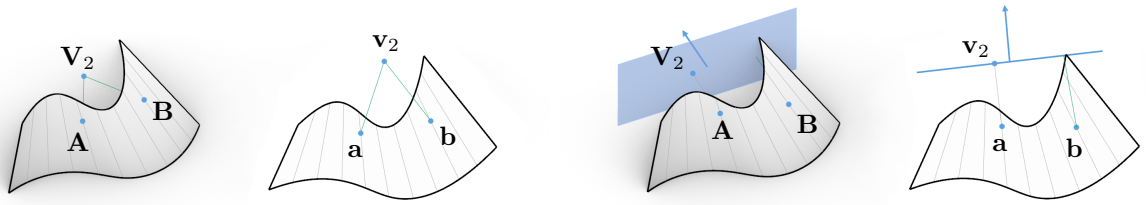

(a) User-input 3pt.

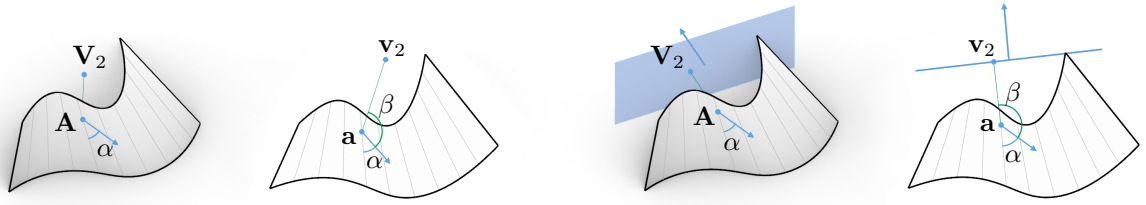

(b) User-input Tan.

Figure 12.4: Illustration of the notation for user-input 3pt and user-input Tan in the patch-to-cone (left) and patch-to-cylinder (right) constructions.

- In addition to the two points, the *user-input Tan* requires an input angle $\alpha \in [0, 2\pi)$. The resulting crease will pass through point $\mathbf{A}$, and the tangent of the crease curve and the incident ruling of the input surface will enclose the user-specified angle α. The corresponding developed point $\mathbf{v}$ will lie to the left of the oriented developed tangent.

Note that the user-input 3pt and user-input Tan do only depend on 3D information.

Corollary 12.1. *User-input Tan uniquely specifies the location of the point* $\mathbf{v}$*. If feasible, user-input 3pt also uniquely specifies the location of* $\mathbf{v}$*. Consequently, both inputs, if feasible, specify the location of the 2D base line* π_2 *or 2D apex* $\mathbf{v}_2$*, and thus the crease uniquely.*

Proof. From the given input, we first compute the developed surface $\mathbf{s}(t, u)$, and locate the point $\mathbf{a}_1$, and if given, the point $\mathbf{a}_2$.

User-input 3pt: First, let us consider the case of the patch-to-cylinder construction with the aim to determine π_2. As the distances between points on surfaces in 3D and their developed counterparts must be the same, we have

$$\operatorname{dist}(\mathbf{A}, \Pi_2) = \operatorname{dist}(\mathbf{a}, \pi_2) \qquad \text{and} \qquad \operatorname{dist}(\mathbf{B}, \Pi_2) = \operatorname{dist}(\mathbf{b}, \pi_2).$$

Thus, π_2 is a common tangent of the two circles $\mathbf{c}_A$ and $\mathbf{c}_B$ centered at $\mathbf{a}$ and $\mathbf{b}$ with radii $\operatorname{dist}(\mathbf{A}, \Pi)$ and $\operatorname{dist}(\mathbf{B}, \Pi)$, respectively. In general, there are two suitable solutions for the outer tangents, candidates for π_2 on opposite sides of $\mathbf{a}$ and $\mathbf{b}$, which determine two solutions for $\mathbf{v}$. We choose π_2 such that $(\mathbf{a}, \mathbf{b}, \mathbf{v})$ are positioned counterclockwise.

Second, let us consider the case of the patch-to-cone construction with the aim to determine $\mathbf{v}_2$. As the distances between points on surfaces in 3D and their developed counterparts must be the same, the location of $\mathbf{v}_2$ is constrained by two distances,

$$\operatorname{dist}(\mathbf{A}, \mathbf{V}_2) = \operatorname{dist}(\mathbf{a}, \mathbf{v}_2) \qquad \text{and} \qquad \operatorname{dist}(\mathbf{B}, \mathbf{V}_2) = \operatorname{dist}(\mathbf{b}, \mathbf{v}_2).$$

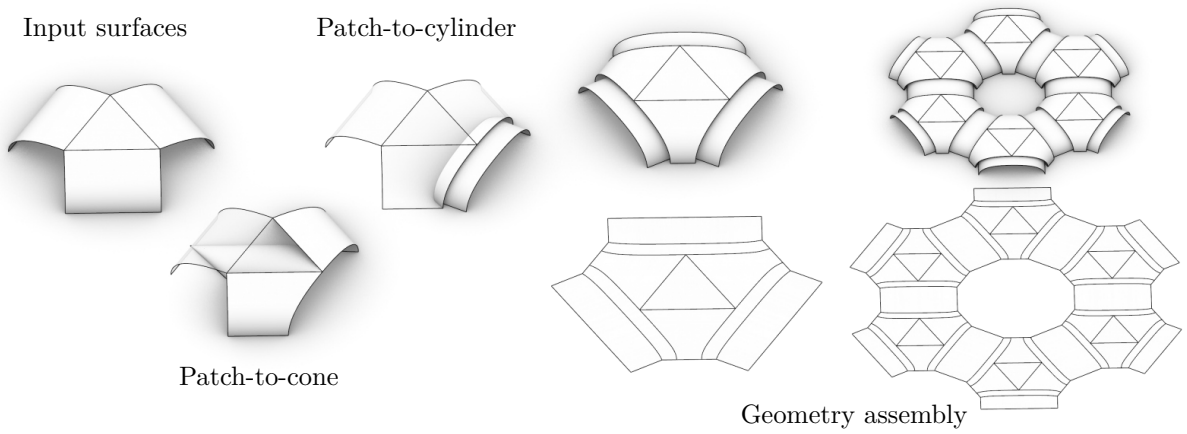

Figure 12.5: Example of a design process with Lotus 1.0.

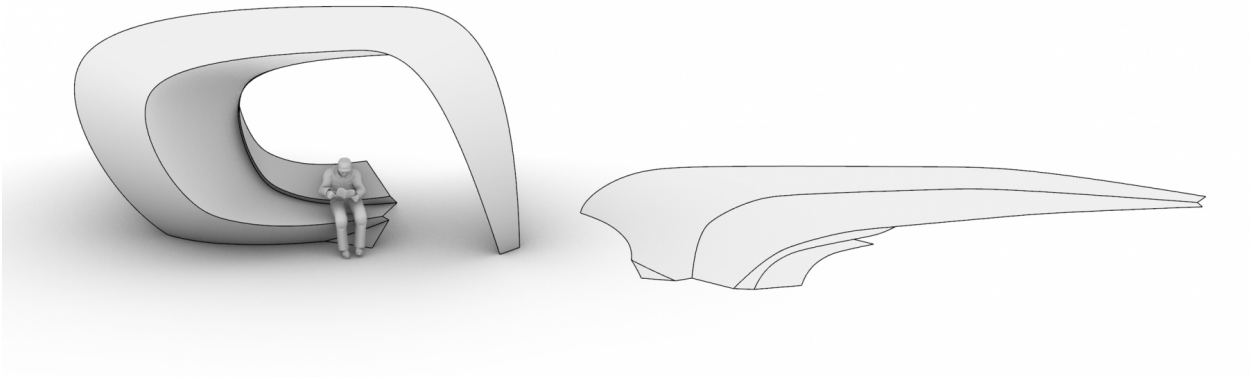

Figure 12.6: Example of a bus stop designed with Lotus 1.0 (Figure 1 in [65]).

Thus, $\mathbf{v}_2$ is an intersection point of two circles $\mathbf{c}_A$ and $\mathbf{c}_B$ centered at $\mathbf{a}$ and $\mathbf{b}$ with radii $\text{dist}(\mathbf{A}, \mathbf{V}_2)$ and $\text{dist}(\mathbf{B}, \mathbf{V}_2)$, respectively. If feasible, there are two solutions for $\mathbf{v}_2$ on opposite sides of the line spanned by $\mathbf{a}$ and $\mathbf{b}$. Again, we choose the solution such that $(\mathbf{a}, \mathbf{b}, \mathbf{v}_2)$ are positioned counterclockwise.

User-input Tan: After finding the location of $\mathbf{a}$, we reconstruct the 3D tangent line in the incident tangent plane and 2D tangent line using the counterclockwise angle that they enclose with the ruling. Let β be the angle between the tangent and $\mathbf{A}$, $\mathbf{V}_2$. As developing a surface preserves angles and distances, we find $\mathbf{v}_2$ as the endpoint of the line segment of length $\text{dist}(\mathbf{A}, \mathbf{V}_2)$ enclosing the counterclockwise angle β with the 2D tangent line. □

12.3.5 Lotus 1.0

The described constructions are implemented as components in the interactive design tool Lotus for Grasshopper / Rhino. With this, the user can interactively and intuitively design shapes with multiple patches joined along curved creases.

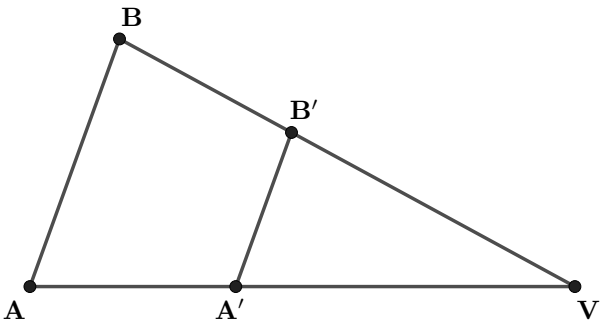

Figure 12.7: Illustration of a scaling transformation. If $\mathbf{AB} \parallel \mathbf{A'B'}$, the four points $\{\mathbf{A}, \mathbf{A'}, \mathbf{B}, \mathbf{B'}\}$ determine a scaling where $\mathbf{A} \mapsto \mathbf{A'}$ and $\mathbf{B} \mapsto \mathbf{B'}$.

12.4 Patch-to-Projective-Cone

In certain applications presented later, we may encounter apices that are located at greater distances, which can pose numerical challenges during computation of the crease curve. To address this issue, we introduce an alternative computation based on (projective) scaling transformations. Specifically, we consider the newly constructed cylinders and cones as surfaces that can be obtained by scaling the crease with respect to infinite or finite apices. To describe these transformations, we employ an approach that allows us to represent the scaling transformation without explicitly specifying the cone apex. As a result, this method provides a unified expression for both the patch-to-cylinder and patch-to-cone constructions.

12.4.1 Scaling Transformations

Before we proceed, let us review some scaling properties. In the following, we will represent scaled images by adding a prime symbol. For example, the scaled version of $\mathbf{A}$ will be denoted as $\mathbf{A'}$, and the scaled version of $\mathbf{a}$ will be denoted as $\mathbf{a'}$.

It is important to note that a scaling can be specified in multiple ways, including some that do not explicitly use the center of scaling. In our approach, we use mappings of two points $\mathbf{A} \mapsto \mathbf{A'}$ and $\mathbf{B} \mapsto \mathbf{B'}$ to represent the scaling transformation. It is required that the line segments $\mathbf{AB}$ and $\mathbf{A'B'}$ are parallel in order to ensure a valid scaling, as illustrated in Figure 12.7.

It is worth mentioning that if the line segments $\mathbf{AA'}$ and $\mathbf{BB'}$ are also parallel, the transformation represents a scaling with respect to a point at infinity, which is essentially a translation.

The following lemma demonstrates that the condition $\mathbf{AB} \parallel \mathbf{A'B'}$ is sufficient to uniquely represent a scaling transformation. A detailed proof is provided in the Section 12.8.

Lemma 12.4. *Let* $\{\mathbf{A}, \mathbf{A'}, \mathbf{B}, \mathbf{B'}\}$ *be four distinct points such that* $\mathbf{AB}$ *and* $\mathbf{A'B'}$ *are parallel. The scaling that maps* $\mathbf{A} \mapsto \mathbf{A'}$ *and* $\mathbf{B} \mapsto \mathbf{B'}$ *can be computed as*

$$\mathbf{P} \mapsto \mathbf{P'} = s(\mathbf{P} - \mathbf{A}) + \mathbf{A'} = s(\mathbf{P} - \mathbf{B}) + \mathbf{B'} \text{ where } s = \frac{(\mathbf{B'} - \mathbf{A'}) \cdot \mathbf{N}}{(\mathbf{B} - \mathbf{A}) \cdot \mathbf{N}}$$

for some vector $\mathbf{N}$ *with* $|\mathbf{N}| > 0$ *and* $(\mathbf{B} - \mathbf{A}) \cdot \mathbf{N} \neq 0$. *If* $\mathbf{AA'}$ *and* $\mathbf{BB'}$ *are parallel,* $s = 1$. *If* $s \neq 1$, *the scaling center* $\mathbf{V}$ *is*

$$\mathbf{V} = \frac{\mathbf{A'} - s\mathbf{A}}{1 - s} = \frac{\mathbf{B'} - s\mathbf{B}}{1 - s}.$$

We highlight the following:

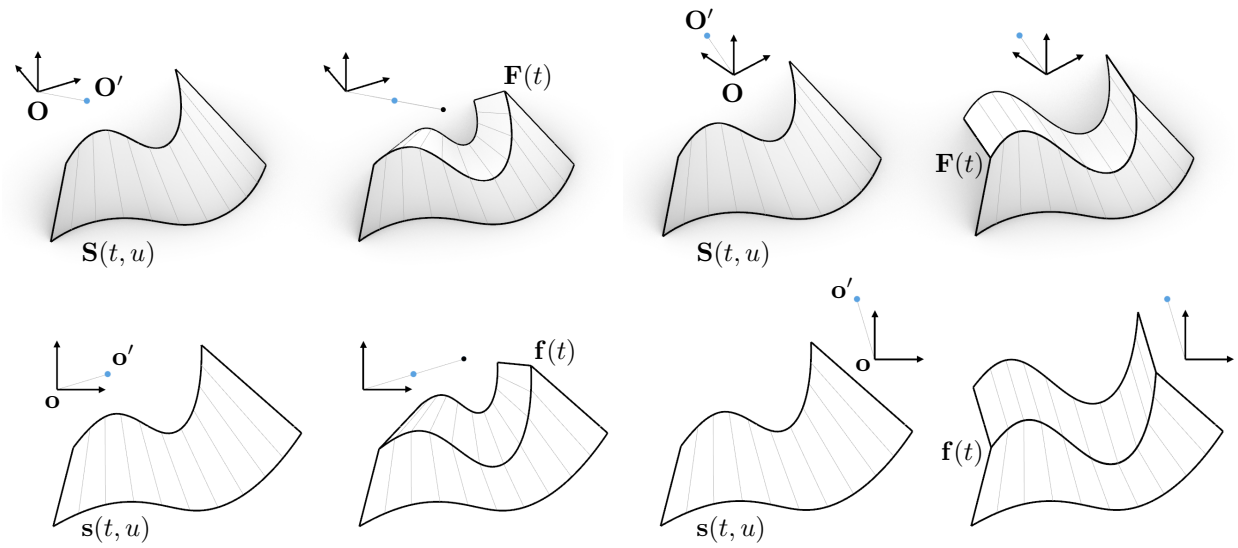

(a) Input and result of the patch-to-projective-cone construction with $s = \frac{1}{2}$.

(b) Input and result of the patch-to-projective-cone construction with $s = 1$.

Figure 12.8: Notation of the patch-to-projective-cone construction.

Corollary 12.2. *Two distinct points* $\mathbf{A}$, $\mathbf{A}'$ *and a scale factor* $s \in \mathbb{R}$ *determine a scale transformation with* $\mathbf{A} \mapsto \mathbf{A}'$ *as follows*

$$\mathbf{P} \mapsto \mathbf{P}' = s(\mathbf{P} - \mathbf{A}) + \mathbf{A}'.$$

12.4.2 Locating the Crease

The following theorem provides a unified approach, based on scaling transformations, that combines the results of Lemma 12.1 and Lemma 12.2.

Theorem 12.1. *The crease connecting a developable patch* $\mathbf{S}(t, u)$ *with a projective cone, specified by a 3D scaling transformation* Σ *and a 2D scaling transformation* σ *sharing the same scale factor* s*, is uniquely specified by the length function*

$$l(t) = \frac{1}{2} \frac{|\mathbf{o}' - (1-s)\mathbf{x}(t)|^2 - |\mathbf{O}' - (1-s)\mathbf{X}(t)|^2}{(\mathbf{o}' - (1-s)\mathbf{x}(t)) \cdot \mathbf{r}(t) - (\mathbf{O}' - (1-s)\mathbf{x}(t)) \cdot \mathbf{R}(t)}, \tag{12.5}$$

$$= \frac{1}{2} \frac{(1-s)\left(|\mathbf{x}(t)|^2 - |\mathbf{X}(t)|^2\right) - 2(\mathbf{o}' \cdot \mathbf{x}(t) - \mathbf{O}' \cdot \mathbf{X}(t))}{\mathbf{o}' \cdot \mathbf{r}(t) - \mathbf{O}' \cdot \mathbf{R}(t) - (1-s)(\mathbf{x}(t) \cdot \mathbf{r}(t) - \mathbf{X}(t) \cdot \mathbf{R}(t))}, \tag{12.6}$$

if $(\mathbf{o}' - (1-s)\mathbf{x}(t)) \cdot \mathbf{r}(t) - (\mathbf{O}' - (1-s)\mathbf{x}(t)) \cdot \mathbf{R}(t) \neq 0$*. Here,* $\mathbf{O}'$ *and* $\mathbf{o}'$ *with* $|\mathbf{O}'| = |\mathbf{o}'|$ *are the images of the origin with respect to* Σ *or* σ*, respectively.*

Proof. We distinguish between two cases:

Crease connecting a cone ($s \neq 1$)*:* Similarly to before, during the construction of the crease, corresponding bars of the newly constructed cylinders or cones need to have equal lengths. In this case, we require the distance between points on the crease and their scaled counterparts to be the same in both 3D and 2D, that is,

$$\left|\mathbf{f}(t) - \mathbf{f}(t)'\right|^2 = \left|\mathbf{F}(t) - \mathbf{F}(t)'\right|^2.$$

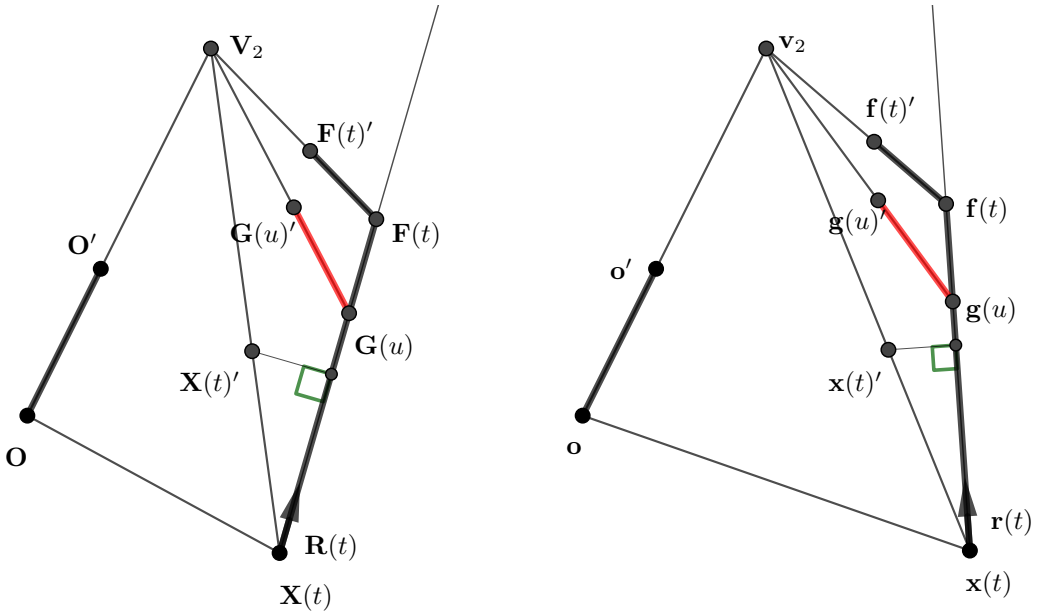

Figure 12.9: Illustration of the notation used in Lemma 12.5.

Substituting the identities for $\mathbf{F}(t)$, $\mathbf{f}(t)$, $\mathbf{F}(t)' = s\mathbf{F}(t) + \mathbf{O}'$, and $\mathbf{f}(t)' = s\mathbf{f}(t) + \mathbf{o}'$ results in the quadratic equation for $l(t)$, that is,

$$0 = \left|(1-s)\mathbf{x}(t) - \mathbf{o}' + (1-s)l(t)\mathbf{r}(t)\right|^2 - \left|(1-s)\mathbf{X}(t) - \mathbf{O}' + (1-s)l(t)\mathbf{R}(t)\right|^2.$$

However, simplifications cancel out the quadratic terms, resulting in a linear equation for $l(t)$ whose solution is stated above.

Note that the above expression can also be obtained by inserting $\mathbf{V}_2 = \frac{\mathbf{O}'}{1-s}$ and $\mathbf{v}_2 = \frac{\mathbf{o}'}{1-s}$ into Equation (12.3). In particular, for $s = 0$, we have that $\mathbf{V}_2 = \mathbf{O}'$ and $\mathbf{v}_2 = \mathbf{o}'$, and the expressions in Equation (12.3) and Equation (12.6) are equal.

Crease connecting a cylinder ($s = 1$)*:* In this case, the scaling transformation corresponds to a translation parallel to $\mathbf{O}'$ and $\mathbf{o}'$. Consequently, the cone is specified by base planes that are perpendicular to $\mathbf{O}'$ and base lines that are perpendicular to $\mathbf{o}'$, sharing a common oriented distance from the origin. To obtain the crease, we use Lemma 12.2 where Π_2 and π_2 are set to contain the origin and have the normals $\mathbf{R}_2 = \frac{1}{k}\mathbf{O}'$ and $\mathbf{r}_2 = \frac{1}{k}\mathbf{o}'$, respectively, where $k = |\mathbf{O}'| = |\mathbf{o}'|$.

Inserting into Equation (12.4) gives the stated expression for $s = 1$, that is,

$$l(t) = \frac{\mathbf{o}' \cdot \mathbf{x}(t) - \mathbf{O}' \cdot \mathbf{X}(t)}{\mathbf{o}' \cdot \mathbf{r}(t) - \mathbf{O}' \cdot \mathbf{R}(t)}.$$

□

12.4.3 Valid Patch Combination

Similarly to before, we now consider the compatible surface combinations that result in a crease and not in a geodesic gluing.

In the following, let $\mathbf{S}_2(t, u)$ be the patch between the computed crease and $\mathbf{F}(t)'$, that is, its scaling with respect to the scaling transformation Σ. Again, the compatible direction depends on the denominator of the length function $l(t)$.

Lemma 12.5. *Let $D(t)$ denote the (half of the) denominator of the length function as given in Equation* (12.6)*, that is,*

$$D(t) = (\mathbf{o}' - (1-s)\mathbf{x}(t)) \cdot \mathbf{r}(t) - (\mathbf{O}' - (1-s)\mathbf{x}(t)) \cdot \mathbf{R}(t).$$

If $s \neq 1$, the surface patch $\mathbf{S}_2(t,u)$ is compatible with the ruling direction $-\operatorname{sign}((1-s)D(t))\mathbf{R}(t)$. If $s = 1$, the surface patch $\mathbf{S}_2(t,u)$ is compatible with the ruling direction $-\operatorname{sign}(D(t))\mathbf{R}(t)$.

Proof. Again, we distinguish between two cases:

Crease connecting a cone ($s \neq 1$): Similar to the proof of Lemma 12.3, we consider two corresponding parametrizations of two rulings at a fixed parameter t,

$$\mathbf{G}(u) = \mathbf{X}(t) + u\mathbf{R}(t) \qquad \text{and} \qquad \mathbf{g}(u) = \mathbf{x}(t) + u\mathbf{r}(t).$$

Analogously to the proof of Lemma 12.3, the distances between points on the compatible ruling segments need to contract during folding, that is, only parameters u with $K(u) > 0$, where

$$K(u) = |\mathbf{g}(u) - \mathbf{v}_2|^2 - |\mathbf{G}(u) - \mathbf{V}_2|^2$$

are compatible with the corresponding ruling segments of the surfaces $\mathbf{S}_2(t,u)$ or $\mathbf{s}_2(t,u)$, respectively.

To show the stated claim, we define

$$K_s(u) = |\mathbf{g}(u) - \mathbf{g}(u)'|^2 - |\mathbf{G}(u) - \mathbf{G}(u)'|^2.$$

and show that $K(u) > 0$ if and only if $K_s(u) > 0$.

When connecting $K_s(u)$ to $K(u)$, it is important to note that $\mathbf{G}(u)'$ and $\mathbf{g}(u)'$ may not lie on the surfaces $\mathbf{S}_2(t,u)$ and $\mathbf{s}_2(t,u)$, respectively. Refer to Figure 12.9 for visualization.

To address this issue, recall that $|\mathbf{O}'| = |\mathbf{o}'|$. Additionally, it follows that $|\mathbf{V}_2| = \left|\frac{1}{1-s}\right| |\mathbf{O}'| = \left|\frac{1}{1-s}\right| |\mathbf{o}'| = |\mathbf{v}_2|$. We therefore define the a k as follows

$$k = \frac{|\mathbf{V}_2|}{|\mathbf{O}'|} = \frac{|\mathbf{v}_2|}{|\mathbf{o}'|}.$$

From the intercept theorem applied to the points $(\mathbf{O}, \mathbf{O}', \mathbf{V}_2)$ and $(\mathbf{G}(u), \mathbf{G}(u)', \mathbf{V}_2)$ where $\mathbf{O}$ denotes the origin, we deduce that

$$\frac{|\mathbf{V}_2 - \mathbf{G}(u)|}{|\mathbf{G}(u)' - \mathbf{G}(u)|} = \frac{|\mathbf{V}_2|}{|\mathbf{O}'|} = k.$$

Similarly, for the points $(\mathbf{o}, \mathbf{o}', \mathbf{v}_2)$ and $(\mathbf{g}(u), \mathbf{g}(u)', \mathbf{v}_2)$ where $\mathbf{o}$ denotes the origin, we have

$$\frac{|\mathbf{v}_2 - \mathbf{g}(u)|}{|\mathbf{g}(u)' - \mathbf{g}(u)|} = \frac{|\mathbf{v}_2|}{|\mathbf{o}'|} = k.$$

Consequently, we can conclude that

$$K(u) = kK_s(u),$$

which implies that $K_s(u) > 0$ if and only if $K(u) > 0$ since $k > 0$.

Finally, we analyze the sign of $K_s(u)$. Similarly to before, note that $K_s(u)$ is a linear function in u, and that $K_s(l(t)) = 0$. Consequently, its sign depends on the coefficient of the linear term as stated above, since

$$\begin{aligned} K_s(u) \;=\; & -2(1-s)\left((\mathbf{o}' - (1-s)\mathbf{x}(t)) \cdot \mathbf{r}(t) - (\mathbf{O}' - (1-s)\mathbf{x}(t)) \cdot \mathbf{R}(t)\right) u \\ & + |\mathbf{o}' - (1-s)\mathbf{x}(t)|^2 - |\mathbf{O}' - (1-s)\mathbf{X}(t)|^2. \end{aligned}$$

Crease connecting a cylinder ($s = 1$): This case directly follows from the Lemma 12.3.

□

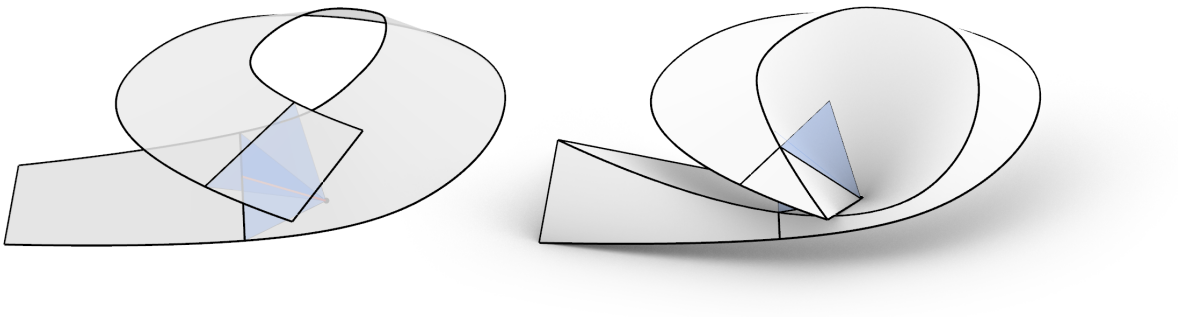

Figure 12.10: This figure illustrates that non-intersecting (projective) triangles are only a sufficient, not necessary, condition for surface non-intersection. While the triangles intersect here, the surfaces do not.

12.4.4 Alternative User-Input

Similarly to the other constructions, specifying a crease using a 3D and a 2D scale transformations may not be very intuitive. Therefore, we discuss an alternative input for the patch-to-projective-cone construction, which is based on either prescribing two points on the crease (user-input 3pt) or one point and the tangent direction (user-input Tan). Once again, these input specifications only require 3D quantities and allow us to determine the necessary 2D information.

In addition to the 3D surface $\mathbf{S}(t,u)$, in both cases, we prescribe a point $\mathbf{A}$ on $\mathbf{S}(t,u)$, a point $\mathbf{A}'$ not on $\mathbf{S}(t,u)$, and a scalar $s \in \mathbb{R}$. Consequently, the scalar transformation Σ is specified by the pair of points $\mathbf{A} \mapsto \mathbf{A}'$ and the scale factor s.

- In addition to the previous specifications, the *user-input 3pt* requires a second point $\mathbf{B}$ on $\mathbf{S}(t,u)$. If feasible, the resulting crease will pass through $\mathbf{A}$ and $\mathbf{B}$, and the points $(\mathbf{a}, \mathbf{b}, \mathbf{a}')$ will be oriented counterclockwise.
- In addition to the previous specifications, the *user-input Tan* requires of an angle $\alpha \in [0, 2\pi)$. If feasible, the resulting crease will pass through $\mathbf{A}$, and the (smooth or discrete) tangent of the crease at $\mathbf{A}$ and the incident ruling of $\mathbf{S}(t,u)$ will enclose the angle α. In the development, $\mathbf{a}'$ will lie to the left of the oriented developed tangent.

We make note of the following lemma, whose proof can be found in in Section 12.8:

Lemma 12.6. *If feasible, both user-input 3pt and user-input Tan uniquely specify the scalar transformation σ.*

Finally, it is important to note that for the application of the formulas in the patch-to-projective-cone construction (Lemma 12.1), it is essential to ensure that the surfaces $\mathbf{S}(t,u)$ and $\mathbf{s}(t,u)$ (as well as the points $\mathbf{A}'$ and $\mathbf{a}'$) are positioned such that $\mathbf{A}$ and $\mathbf{a}$ coincide with the origin.

12.5 Preventing Local Surface Intersections

In addition to the valid patch combination, it is often desirable to avoid self-intersections in the folded surfaces. Self-intersections can occur when the base plane's normal $\mathbf{R}_2$ or the apex $\mathbf{V}_2$ are

chosen improperly. In the following, we discuss sufficient conditions that ensure non-intersecting surfaces obtained through the patch-to-cylinder and patch-to-cone construction.

Let $\mathbf{S}(t,u)$ be a bounded patch defined as $\mathbf{S}(t,u) = \mathbf{X}(t) + u\ w(t)\mathbf{R}(t)$, where $t \in [0, t_{\max}]$ and $u \in [0,1]$. The function $w(t)$ represents the width along the rulings of the patch. We assume that there are no singularities within the interior of the patch, and the crease points are located within $\mathbf{S}(t,u)$, satisfying $0 < l(t) < w(t)$.

When computing the crease curve between a developable surface and a cylinder or a cone, we consider the (projective) triangles $T_\triangle$, where each triangle is bounded by a ruling segment of $\mathbf{S}(t,u)$ and either $\mathbf{V}_2$ or $\mathbf{R}_2$. If all (projective) triangles intersect only at $\mathbf{V}_2$ or $\mathbf{R}_2$, then the surfaces do not have self-intersections, as each pair of consecutive rule lines lies in triangles that only meet at the desired common point. This condition can be intuitively understood as the rule segments being consistently illuminated by a light source located at $\mathbf{V}_2$ or $\mathbf{R}_2$. An example for why this constraint is sufficient but not necessary is given in Figure 12.10.

In the case where the first surface is a cylinder or a cone, we can test for the absence of surface intersections as follows. When the first surface is a cylinder, we consider the ruling planes T, that is, the planes that contain the ruling and $\mathbf{V}_2$ or $\mathbf{R}_2$. When the first surface is a cone, we consider only ruling half-planes T, that is, planes spanned by the ray starting at the cone apex of $\mathbf{S}(t,u)$ containing the rule segment of $\mathbf{S}(t,u)$ and the $\mathbf{V}_2$ or $\mathbf{R}_2$. Note that in both cases, the planes share a common line L, which is spanned by the apices or ruling directions of both surfaces. Now, we may choose a plane Π that does not contain L. If $\Pi \cap T$ consists of lines that only meet at $L \cap T$, the planes in T and thus the triangles in $T_\triangle$ are distinct.

Equivalently, in case of the first surface being a cylinder or a cone, we may consider the normals of the tangent planes incident to the rulings. Define

$$X(t) = \begin{cases} \mathbf{N}(t) \cdot (\mathbf{V}_2 - \mathbf{X}(t)), & \text{for a cone} \\ \mathbf{N}(t) \cdot \mathbf{R}_2, & \text{for a cylinder.} \end{cases}$$

It follows that there are no surface intersections if either $X(t) > 0$ for all $t \in [0, t_{\max}]$ or $X(t) < 0$ for all $t \in [0, t_{\max}]$.

12.6 Tangent Continuity

To expand the range of design possibilities, it can be advantageous to connect two or more patch-to-cylinder or patch-to-cone constructions. For many applications, achieving tangent continuity of the combined crease curves is desirable. The following section focuses on tangent-continuous combinations of creases obtained by patch-to-cylinder and patch-to-cone constructions.

12.6.1 Computing Tangents

In this section, we consider a pair of corresponding consecutive 2D and 3D ruling directions. We show that if one of the 3D tangent planes is given, the incident crease curve's tangent direction is uniquely specified. To simplify our analysis, we explore the tangent direction in the context of a patch-to-projective-cone construction. However, note that analogous behavior holds in the context of the patch-to-cylinder and patch-to-cone constructions.

In the following, we consider a surface pair obtained from a patch-to-projective-cone construction specified by the two scaling transformations Σ and σ, where $\mathbf{O}'$ and $\mathbf{o}'$ are the images of the origin and s the scale parameter.

We focus on the ruling directions and tangent plane incident to a parameter t_0, and denote the tangent direction of the base curve of the first surface at t_0 by $\mathbf{X}'(t_0)$, and the corresponding 2D counterpart by $\mathbf{x}'(t_0)$.

Lemma 12.7. *The 3D and 2D tangents of the crease at t_0 can be parametrized by*

$$\mathbf{T}_{t_0}(t) = \mathbf{X}(t_0) + t\mathbf{X}'(t_0) + l_T(t)\mathbf{R}(t_0) \qquad \textit{and} \qquad \mathbf{t}_{t_0}(t) = \mathbf{x}(t_0) + t\mathbf{x}'(t_0) + l_T(t)\mathbf{r}(t_0),$$

respectively, where

$$l_T(t) = -\frac{\mathbf{o}' \cdot \mathbf{x}(t_0) - \mathbf{O}' \cdot \mathbf{X}(t_0)}{\mathbf{o}' \cdot \mathbf{r}(t_0) - \mathbf{O}' \cdot \mathbf{R}(t_0)} + \frac{\mathbf{o}' \cdot \mathbf{x}'(t_0) - \mathbf{O}' \cdot \mathbf{X}'(t_0)}{\mathbf{o}' \cdot \mathbf{r}(t_0) - \mathbf{O}' \cdot \mathbf{R}(t_0)} t. \tag{12.7}$$

Proof. We obtain a parametrization of the tangent line of $\mathbf{F}(t)$ at t_0 by applying the patch-to-projective-cone construction with respect to the same scaling transformations to two corresponding parametrizations of the tangent plane in 3D and 2D. The latter is just a special parametrization of the xy-plane. Here, we define the base curves to be $\mathbf{X}_T(t) = \mathbf{X}(t_0) + t\mathbf{X}'(t_0)$ and $\mathbf{x}_T(t) = \mathbf{X}(t_0) + t\mathbf{x}'(t_0)$. Furthermore, set $\mathbf{R}_T = \mathbf{R}(t_0)$ and $\mathbf{r}_T = \mathbf{r}(t_0)$. Then, simplifying Equation (12.6) results in the stated expression since $|\mathbf{X}'(t_0)|^2 = |\mathbf{x}'(t_0)|^2 = 1$ and $\mathbf{X}'(t_0) \cdot \mathbf{R}(t_0) = \mathbf{x}'(t_0) \cdot \mathbf{r}(t_0)$.

The result is a linear curve that does not depend on the scale factor s, that is, the direction of the tangent does not depend on the (real or infinite) location of the projective cone apex. Consequently, this is the unique solution to that ensures that all points on the parametrization of the linear curve have the property that their distance to the tangent plane's base curve and to any pair of corresponding points on the second ruling are the same in 2D and 3D. Consequently, this curve parametrizes the tangent of the crease curve incident to $\mathbf{F}(t_0)$. □

Note that the denominator of $l_T(t)$ equals the denominator of $l(t_0)$, that is, $D(t_0)$. Thus, the valid patch combinations of the tangent planes incident to t_0 and the local surface behavior at $\mathbf{F}(t_0)$ is the same.

Corollary 12.3. *Two corresponding 3D and 2D ruling directions and an incident tangent plane determine the location of the incident crease curve's tangent direction uniquely.*

12.6.2 Combinations of Patch-to-Projective-Cone Constructions

We now explore tangent-continuous combinations of patch-to-cylinder and patch-to-cone constructions. To simplify the analysis, we again consider two patch-to-projective-cone constructions.

Consider two surface patches $\mathbf{S}_1(t, u)$ and $\mathbf{S}_2(t, u)$ that share a common (oriented) tangent plane at the incident rulings $\mathbf{S}_1(t_1, u)$ and $\mathbf{S}_2(t_2, u)$. Let $\mathbf{A}$ be a point on the common ruling. Without loss of generality, let us assume that $\mathbf{A} = \mathbf{S}_1(t_1, u_0) = \mathbf{S}_2(t_2, u_0)$, and that the surfaces are positioned such that $\mathbf{A}$ coincides with the origin.

Furthermore, let $\mathbf{s}_1(t, u)$ and $\mathbf{s}_2(t, u)$ denote the development of the two surfaces, and let $\mathbf{a} = \mathbf{s}_1(t_1, u_0) = \mathbf{s}_2(t_2, u_0)$. Without loss of generality, we assume that the developed surfaces are aligned at the common rulings and that they are positioned such that $\mathbf{a}$ coincides with the origin.

Finally, let Σ_i and σ_i for $i \in \{1, 2\}$ be two scaling transformations given by the images of the origin, $\mathbf{O}'_i$ and $\mathbf{o}'_i$, where $|\mathbf{O}_i| = |\mathbf{o}'_i|$, and the scale factors $s_i \in \mathbb{R}$. Let $\mathbf{F}_i(t)$ be the crease obtained by applying the patch-to-projective-cone construction to $\mathbf{S}_i(t, u)$ and $\mathbf{s}_i(t, u)$ with respect to the scaling transformations Σ_i and σ_i.

Lemma 12.8. *If $\mathbf{O}'_1 = k\mathbf{O}'_2$ and $\mathbf{o}'_1 = k\mathbf{o}'_2$ for some constant $k \neq 0$, then the tangents of the crease curves incident with $\mathbf{A}$ are the same.*

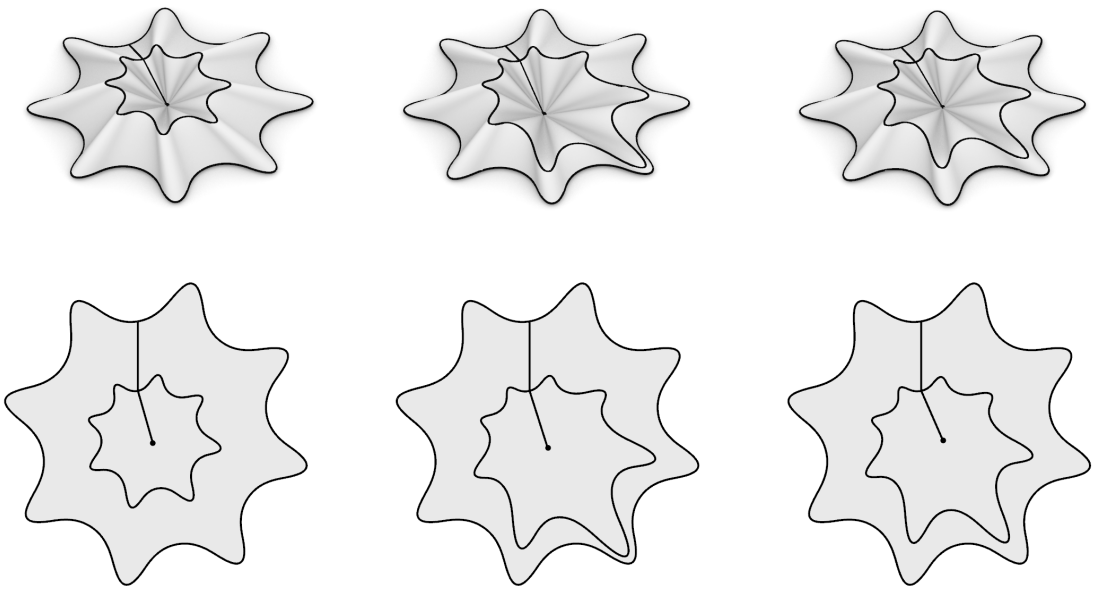

Figure 12.11: Illustration of the tangent-continuity condition for closed crease curves in cases where the first surface is a closed ring that is developable without additional cuts. Upon successful computation, the crease curve is tangent continuous for arbitrary combinations of 2D and 3D apices.

Proof. Using Lemma 12.7, we observe that both choices for the image of the origin result in the same tangent directions, as the factor k cancels out. □

We can also phrase the above stated lemma more intuitively as follows:

Corollary 12.4. *The two computed creases are tangent-continuous at t_0 if the two incident 3D ruling directions are identical and the incident 2D ruling directions are also identical.*

Note that the converse is not true, since by Lemma 12.7 the tangent's inclination with respect to the tangent of $\mathbf{X}(t)$ is the same for points $\mathbf{O'}$ where $\mathbf{O'} \cdot \mathbf{X}'(t_0) = \text{const}$. This implies that there is a one-parameter family of directions $\mathbf{O'}$ that result in the same tangent direction.

12.6.3 Closed Developable Rings and Tangent-continuous Creases

We now consider the special case where we apply a single patch-to-cone or patch-to-cylinder construction to a closed ring of tangent-continuous developable patches $\mathcal{R} = (\mathbf{S}_1(t,u), \ldots, \mathbf{S}_n(t,u))$, that are joined along common rule lines tangent-continuously. There are two cases to consider, depending on whether the development $\mathcal{r} = (\mathbf{s}_1(t,u), \ldots, \mathbf{s}_n(t,u))$ of $\mathcal{R}$ is closed or not, that is, whether the first ruling of $\mathbf{s}_1(t,u)$ is the same as the last ruling of $\mathbf{s}_n(t,u)$.

Closed development

If the development is closed, it follows that any (valid) combination of a 3D and a 2D cone apex results in a tangent-continuous crease. This follows from Corollary 12.4 as we ensure that at all potential transition rulings between $\mathbf{S}_i(t,u)$ and $\mathbf{S}_{i+1}(t,u)$, their developments, and the tangent planes align.

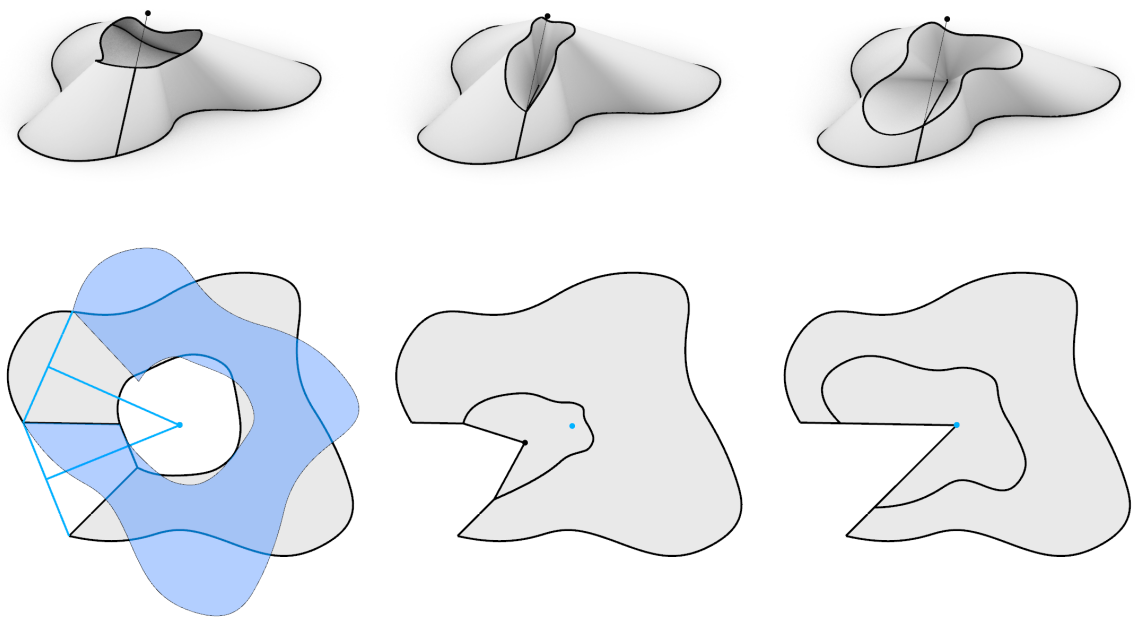

Figure 12.12: Illustration of the tangent-continuity condition for closed crease curves in cases where the first surface is a closed ring that requires a cut to be developable. In this case, there is only one location of the 2D apex that results in tangent-continuous closed crease curves.

On the other hand, when constructing a patch-to-cylinder combination, we cannot obtain a closed crease curve that would result in a consistent valid patch combination, since the developed ruling directions cannot point consistently towards one side of the developed closed crease curve.

Open development

Note however, that if the development is open – that is, there is a gap between the end rulings of the development – then the situation changes. In particular, choosing an arbitrary 2D apex might not result in the same angle between consecutive 2D ruling directions of the start and end ruling.

Consequently, a patch-to-cylinder or patch-to-cone construction typically results in creases that are not tangent-continuous at the gap (refer to Figure 12.12). To achieve tangent continuity, we need to ensure that the angle between the ruling directions at the boundaries are the same. Consequently, if the boundary rulings of the developed ring surface are not parallel, we choose the apex to be the unique center of rotation that transforms the first ruling of $\mathbf{s}_1(t, u)$ to the last ruling of $\mathbf{s}_n(t, u)$. Consequently, no patch-to-cylinder construction will result in closed tangent-continuous creases.

If on the other hand the end rulings are parallel, only a patch-to-cylinder construction can result in tangent-continuous creases. Here, as long as valid, the developed ruling direction of the cylinder can be chosen freely to ensure tangent continuity. However, we observed that these cases usually result in intersecting surfaces.

12.7 Patch-to-Piecewise-Projective-Cone Construction

In this section, we show how to apply a sequence of tangent-continuous patch-to-projective-cone constructions to obtain an approximation of a crease between two general developable surfaces.

Starting from a tangent-continuous developable patch, we ensure that the crease is tangent-continuous by finding the apices of the projective cones such that the 3D ruling directions and 2D ruling directions match at the transition points.

In this section, we explore two construction strategies for the separation of the second surface into projective cones:

- *Ruling planes:* We use a sequence of user-specified ruling planes to separate the (projective) cones. This approach offers the advantage of allowing the user to directly control the singularities of the second surface, as they occur at the intersections of these ruling planes. However, the shape of the crease can only be influenced indirectly.
- *Crease points:* We use a sequence of user-specified points that, if possible, will lie on the crease and separate the (projective) cones. This approach offers the advantage of allowing the user to directly control the shape of the crease. However, the location of the apices of the projective cones, and therefore the singularities of the constructed patch, can only be influenced indirectly.

In Chapter 17, we show how the approximation of patch-to-patch constructions can be used for developable subdivision of regular planar quad meshes.

12.7.1 Input

The input for our construction is as follows:

- a developable strip $\mathbf{S}(t,u) = \mathbf{X}(t) + u\mathbf{R}(t)$ (without loss of generality assume $0 \leq t \leq 1$ and $u \geq 0$) and its development $\mathbf{s}(t,u) = \mathbf{x}(t) + u\mathbf{r}(t)$;
- two points $\mathbf{A}_0 \in \mathbf{S}(t,u)$ (without loss of generality $\mathbf{A}_0 = \mathbf{S}(0,u)$) and $\mathbf{A}_0' \notin \mathbf{S}(t,u)$ that determine the initial ruling direction $\mathbf{A}_0' - \mathbf{A}_0$;
- their developed counterparts $\mathbf{a}_0$ and $\mathbf{a}_0'$; and
- either:
  - a list of *ruling planes*, that is, a sequence of planes E_i containing rulings $\mathbf{X}(t_i) + u\mathbf{R}(t_i)$ with $0 < t_i < t_{i+1}$ for $1 \leq i \leq n$, or
  - a list of *crease points*, that is, a sequence of planes $\mathbf{A}_i$ coincident with the surface points $\mathbf{S}(t_i, u_i)$ with $0 < t_i < t_{i+1}$ for $1 \leq i \leq n$.

If desired, the position of $\mathbf{a}_0'$ can be indirectly specified using either the user-input 3pt or Tan methods. However, it is important to note that when using the user-input 3pt method, it is preferable for the second crease point to be sufficiently close to $\mathbf{A}$.

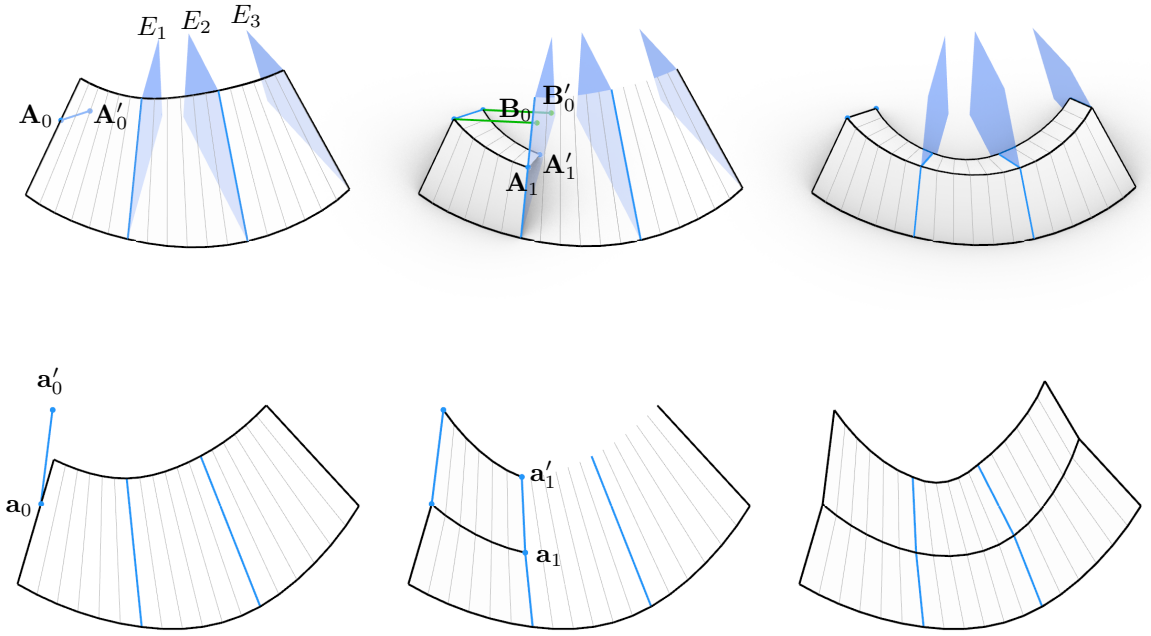

Figure 12.13: IIlustration of the patch-to-piecewise-projective-cone construction using ruling planes.

12.7.2 Patch-to-Piecewise-Projective-Cone Construction using Ruling Planes

We now discuss the case where the separation between projective cones is specified through a sequence of ruling planes; see Figure 12.13. Specifically, we show how points $\mathscr{A}_i = \{\mathbf{A}_i, \mathbf{A}'_i, \mathbf{a}_i, \mathbf{a}'_i\}$ and the next ruling plane E_{i+1} specify the scale parameter s_i and the points $\mathscr{A}_{i+1} = \{\mathbf{A}_{i+1}, \mathbf{A}'_{i+1}, \mathbf{a}_{i+1}, \mathbf{a}'_{i+1}\}$ used for the next construction.

Suppose we are given the input points $\mathscr{A}_i$ and a plane E_{i+1}. For E_{i+1} to be a ruling plane, it needs to contain the (finite or infinite) apex $\mathbf{V}_i$ of the second surface corresponding to the interval $[u_i, u_{i+1}]$. As $\mathbf{V}_i$ needs to also lie on the ruling $\mathbf{A}_i\mathbf{A}'_i$, $\mathbf{V}_i$ is the intersection of $\mathbf{A}_i\mathbf{A}'_i$ with E_{i+1}.

If $\mathbf{A}_i\mathbf{A}'_i$ is almost parallel to E_{i+1}, computing the intersection might be numerically challenging. However, with Lemma 12.4, we do not need to know the intersection $\mathbf{V}_i$, rather it is sufficient to only determine the corresponding scale factor. To do that, we use an orthogonal projection of points $\mathbf{A}_i$ and $\mathbf{A}'_i$ onto E_{i+1} to obtain points $\mathbf{B}_i$ and $\mathbf{B}'_i$. Setting $\mathbf{N}_i = \mathbf{B}_i - \mathbf{A}_i$, we use Lemma 12.4 to compute the scale factor s_i from the four points $\{\mathbf{A}_i, \mathbf{A}'_i, \mathbf{B}_i, \mathbf{B}'_i\}$.

Alternatively, if $\mathbf{A}_i\mathbf{A}'_i$ is almost orthogonal to E_{i+1}, we can compute the intersection $\mathbf{V}_i$ directly and obtain the scale factor s_i using $s_i = \frac{(\mathbf{V}_i - \mathbf{A}'_i)\cdot\mathbf{N}_i}{(\mathbf{V}_i - \mathbf{A}_i)\cdot\mathbf{N}_i}$, where $\mathbf{N}_i$ is some vector not orthogonal to $\mathbf{V}_i - \mathbf{A}$, such as $\mathbf{A}'_i - \mathbf{A}_i$.

Having computed the scale factor s_i, we use Lemma 12.1 to compute the crease curve $\mathbf{F}_i(u)$ for the the surface patch $\mathbf{S}(u, v)$ with $u_i \le u \le u_{i+1}$. To continue, we let $\mathbf{A}_{i+1} = \mathbf{F}_i(u_{i+1})$ be the crease point incident to the next ruling plane and $\mathbf{a}_{i+1}$ its development. Furthermore, we define $\mathbf{A}'_{i+1}$ and $\mathbf{a}'_{i+1}$ to be the scaled versions of $\mathbf{A}_{i+1}$ or $\mathbf{a}_{i+1}$, specified by $\mathbf{A}_i \mapsto \mathbf{A}'_i$ and s_i.

We can now iterate the above described procedure starting at $\mathscr{A}_{i+1}$ and E_{i+2} to obtain the remaining scale factors and creases.

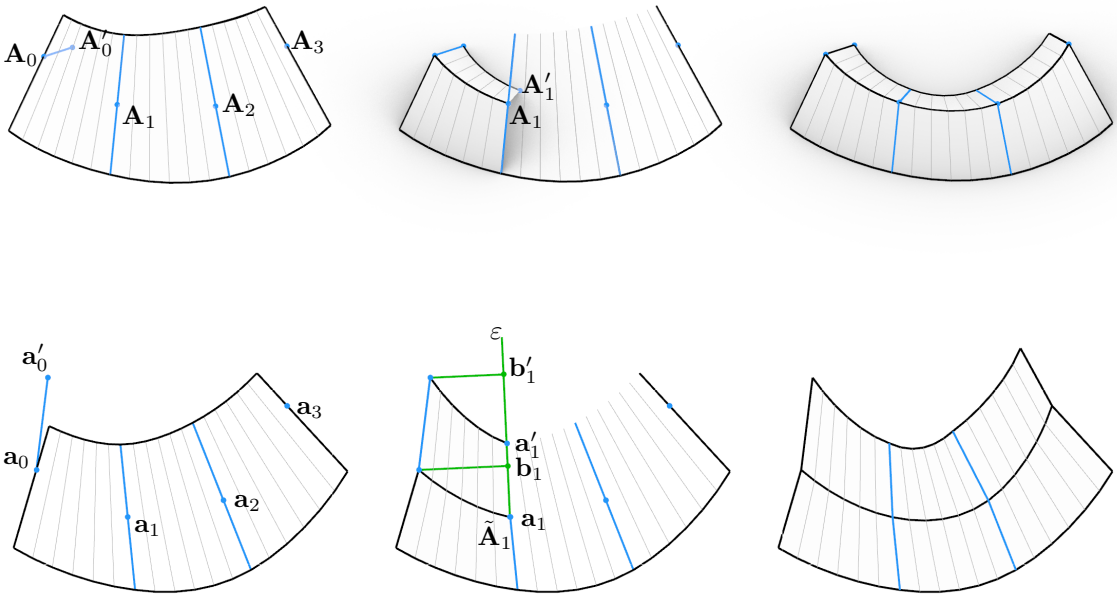

Figure 12.14: IIlustration of the patch-to-piecewise-projective-cone construction using crease points.

12.7.3 Patch-to-Piecewise-Projective-Cone Construction using Crease Points

Second, we discuss the case where the separation of projective cones is specified by a sequence of crease points; see Figure 12.14. Again, we show how the points $\mathcal{A}_i = \{\mathbf{A}_i, \mathbf{A}'_i, \mathbf{a}_i, \mathbf{a}'_i\}$ and the next crease point $\mathbf{A}_{i+1}$ specify the scale parameter and the points $\mathcal{A}_{i+1} = \{\mathbf{A}_{i+1}, \mathbf{A}'_{i+1}, \mathbf{a}_{i+1}, \mathbf{a}'_{i+1}\}$ used for the next construction.

Suppose we are given the input points $\mathcal{A}_i$ and the next crease point $\mathbf{A}_{i+1}$. Let $\mathbf{a}_{i+1}$ be the development of $\mathbf{A}_{i+1}$. To determine the location of the cone apex, and therefore the scale parameter s_i, we need to find a parameter u that describes the location of the 3D apex $\mathbf{V}_i = (1-u)\mathbf{A}_i + u\mathbf{A}'_i$ and its developed counterpart, i.e., $\mathbf{v}_i = (1-u)\mathbf{a}_i + u\mathbf{a}'_i$, such that $|\mathbf{A}_{i+1} - \mathbf{V}_i| = |\mathbf{a}_{i+1} - \mathbf{v}_i|$.

Suppose, we "unroll" the plane containing points $\{\mathbf{A}_i, \mathbf{A}'_i, \mathbf{A}_{i+1}\}$ to the 2D plane to obtain $\{\tilde{\mathbf{A}}_i, \tilde{\mathbf{A}}'_i, \tilde{\mathbf{A}}_{i+1}\}$ such that $\tilde{\mathbf{A}}_i$ coincides with $\mathbf{a}_i$ and $\tilde{\mathbf{A}}'_i$ coincides with $\mathbf{a}'_i$. As the point $\mathbf{v}_i$ lies on $\mathbf{a}_i\mathbf{a}'_i$ and is equidistant to $\tilde{\mathbf{A}}_{i+1}$ and $\mathbf{a}_{i+1}$, it must be the intersection of the perpendicular bisector ε of $\tilde{\mathbf{A}}_{i+1}$ and $\mathbf{a}_{i+1}$ with $\mathbf{a}_i\mathbf{a}'_i$.

If the angle between ε and $\mathbf{a}_i\mathbf{a}'_i$ is small, computing u explicitly might result in numerical difficulties. Instead of computing this intersection, we can again compute the projections $\mathbf{b}_i$ and $\mathbf{b}'_i$ of $\mathbf{a}_i$ and $\mathbf{a}'_i$ on ε and use the four points $\{\mathbf{a}_i, \mathbf{a}'_i, \mathbf{b}_i, \mathbf{b}'_i\}$ and normal $\mathbf{n}_i = \mathbf{b}_i - \mathbf{a}_i$ to compute the scale factor s_i with Lemma 12.4.

Alternatively, if ε and $\mathbf{a}_i\mathbf{a}'_i$ are almost perpendicular, we can also just compute the intersection $\mathbf{v}_i$ directly and employ the above discussed methods to retrieve the scale factor s_i.

Having computed the scale factor s_i, we use Lemma 12.1 to compute the crease curve $\mathbf{F}_i(u)$ for the the surface patch $\mathbf{S}(u, v)$ with $u_i \leq u \leq u_{i+1}$. To continue, we define $\mathbf{A}'_{i+1}$ and $\mathbf{a}'_{i+1}$ to be the scaled versions of $\mathbf{A}_{i+1}$ or $\mathbf{a}_{i+1}$, specified by $\mathbf{A}_i \mapsto \mathbf{A}'_i$ and s_i.

We can now iterate the above described procedure starting at $\mathcal{A}_{i+1}$ and $\mathbf{A}_{i+2}$ to obtain the

remaining scale factors and crease points.

Limitations

The approximation of a patch-to-patch construction using crease points has the major disadvantage of needing to construct the perpendicular bisector of two points that are potentially very close. In particular, when points $\tilde{\mathbf{A}}_{i+1}$ and $\mathbf{a}_{i+1}$ are the same, that is, the 3D patch is almost straight, any point on the line $\mathbf{a}_i\mathbf{a}_i'$ is a candidate for the apex of the next projective cone.

12.7.4 Lotus 2.0

We are currently developing an extension of Lotus 1.0, Lotus 2.0, to incorporate the patch-to-piecewise-projective-cone constructions.

12.8 Selected Proofs from Chapter 12

Proof of Lemma 12.4. A scaling that maps $\mathbf{P} \mapsto \mathbf{P}'$ can be described as

$$\mathbf{P} \mapsto \mathbf{P}' = s(\mathbf{P} - \mathbf{T}_1) + \mathbf{T}_2,$$

where $\mathbf{T}_1, \mathbf{T}_2$ are two translation vectors and s a scale factor. Using $\mathbf{A} \mapsto \mathbf{A}'$ and $\mathbf{B} \mapsto \mathbf{B}'$, we obtain

$$\mathbf{A}' = s(\mathbf{A} - \mathbf{T}_1) + \mathbf{T}_2 \qquad \text{and} \qquad \mathbf{B}' = s(\mathbf{B} - \mathbf{T}_1) + \mathbf{T}_2.$$

One of the equations is trivially satisfied if $(\mathbf{T}_1, \mathbf{T}_2) = (\mathbf{A}, \mathbf{A}')$ or $(\mathbf{T}_1, \mathbf{T}_2) = (\mathbf{B}, \mathbf{B}')$, resulting in the other simplifying to

$$s(\mathbf{B} - \mathbf{A}) = \mathbf{B}' - \mathbf{A}'.$$

Since $s(\mathbf{B} - \mathbf{A})$ and $\mathbf{B}' - \mathbf{A}'$ are parallel vectors, they are the same if and only if their non-trivial projection to a vector is the same. Thus the above equation is equivalent to

$$s(\mathbf{B} - \mathbf{A}) \cdot \mathbf{N} = (\mathbf{B}' - \mathbf{A}') \cdot \mathbf{N},$$

for some vector $\mathbf{N}$ with $|\mathbf{N}| > 0$ and $(\mathbf{B} - \mathbf{A}) \cdot \mathbf{N} \neq 0$, resulting in the claimed expression for s.

Note that if $s \neq 1$, we obtain the scaling center as a point that is mapped onto itself,

$$\mathbf{V} = s(\mathbf{V} - \mathbf{A}) + \mathbf{A}' = s(\mathbf{V} - \mathbf{B}) + \mathbf{B}',$$

resulting in the claimed expression. □

Proof of Lemma 12.6. We first locate point $\mathbf{a}$, that is, the point corresponding to $\mathbf{A}$ on $\mathbf{s}(t, u)$, the development of $\mathbf{S}(t, u)$.

Type 3pt. Let $\mathbf{B}' = s(\mathbf{B} - \mathbf{A}) + \mathbf{A}'$, and $\mathbf{b}$ the development of $\mathbf{B}$. We want to find the location of $\mathbf{a}'$ and $\mathbf{b}'$, such that

$$\text{dist}(\mathbf{a}, \mathbf{a}') = \text{dist}(\mathbf{A}, \mathbf{A}') \qquad \text{and} \qquad \text{dist}(\mathbf{b}, \mathbf{b}') = \text{dist}(\mathbf{B}, \mathbf{B}').$$

In addition, we require that $\mathbf{b}' = s(\mathbf{b} - \mathbf{a}) + \mathbf{a}'$.

For the following computations, we make the assumption that $\mathbf{a}' = \mathbf{a} + r_a(\cos\phi, \sin\phi)$ where $r_a = |\mathbf{A} - \mathbf{A}'|$.

- *Case 1 ($s \neq 1$):* In the case of constructing a crease that connects to a cone, we write $\mathbf{b}' = s(\mathbf{b} - \mathbf{a}) + \mathbf{a}'$ and compute the unknown variable ϕ from

$$\left|\mathbf{b} - \mathbf{b}'\right|^2 = \left|\mathbf{B} - \mathbf{B}'\right|^2 =: r_b^2.$$

- *Case 2 ($s = 1$):* In the case of constructing a crease that connects to a cylinder, the lengths of the segments between the points on the ruling are trivially the same, as the transformation is a translation.

  However, to ensure that both vectors $\mathbf{a}' - \mathbf{a}$ and $\mathbf{b}' - \mathbf{b}$ are perpendicular to the same line, we introduce the planes $\Pi_{\mathbf{A}}$ and $\Pi_{\mathbf{B}}$, which are perpendicular to $\mathbf{A}' - \mathbf{A}$ and pass through $\mathbf{A}$ or $\mathbf{B}$, respectively. Similarly, we define the lines $\pi_{\mathbf{a}}$ and $\pi_{\mathbf{b}}$, which are perpendicular to $\mathbf{a}' - \mathbf{a}$ and pass through $\mathbf{a}$ or $\mathbf{b}$, respectively. In order to satisfy the desired constraints, we require that the oriented distances of the planes (with respect to $\mathbf{A}' - \mathbf{A}$ or $\mathbf{a}' - \mathbf{a}$) are the same. This can be expressed as

$$(\mathbf{A}' - \mathbf{A}) \cdot (\mathbf{B} - \mathbf{A}) = (\mathbf{a}' - \mathbf{a}) \cdot (\mathbf{b} - \mathbf{a}).$$

In both cases, the equations can be simplified to

$$\begin{pmatrix} x_1 \\ x_2 \end{pmatrix} \cdot \begin{pmatrix} \cos\phi \\ \sin\phi \end{pmatrix} = x_3,$$

where

$$\begin{aligned} \begin{pmatrix} x_1 \\ x_2 \end{pmatrix} &= \begin{cases} 2r_a(1-s)(\mathbf{b} - \mathbf{a}), & \text{if} s \neq 1 \\ r_a(\mathbf{b} - \mathbf{a}) & \text{if } s = 1 \end{cases} \\ x_3 &= \begin{cases} r_a^2 - r_b^2 + (1-s)^2|\mathbf{b} - \mathbf{a}|^2 & \text{if} s \neq 1 \\ (\mathbf{A}' - \mathbf{A}) \cdot (\mathbf{B} - \mathbf{A}) & \text{if} s = 1 \end{cases} \end{aligned}$$

If $x_1^2 + x_2^2 - x_3^2 > 0$, the two solutions modulo 2π read

$$\phi = \arctan\left(\frac{x_1 x_3 \mp \sqrt{x_2^2(x_1^2 + x_2^2 - x_3^2)}}{x_1^2 + x_2^2}, \frac{x_2^2 x_3 \pm x_1\sqrt{x_2^2(x_1^2 + x_2^2 - x_3^2)}}{x_2(x_1^2 + x_2^2)} \right),$$

and the resulting two solutions for $\mathbf{a}'$ are related by a reflection about a line spanned by $\mathbf{a}$ and $\mathbf{b}$. Note that a solution might not always exist (for more details refer to Section 3.3. of [65]).

In case of input-type 3pt, the two solutions of $\mathbf{a}'$ in general result in two different crease curves. We use the solution in which the points $\mathbf{a}$, $\mathbf{b}$, and $\mathbf{a}'$ are oriented counter-clockwise. The other solution can be obtained by exchanging the roles of $\mathbf{a}$ and $\mathbf{b}$.

Type Tan. First we locate the initial crease tangent direction $\mathbf{T}$ by rotating the rule line direction $\mathbf{R}$ of the ruling incident with $\mathbf{A}$ by α about the ruling's normal plane normal $\mathbf{N}$. Similarly, we obtain its development $\mathbf{t}$ by rotating the incident developed ruling direction $\mathbf{r}$ about α. Define $\beta = \angle(\mathbf{A}' - \mathbf{A}, \mathbf{T})$. We locate the point $\mathbf{a}'$ such that $|\mathbf{a} - \mathbf{a}'| = |\mathbf{A} - \mathbf{A}'|$ and $\beta = \angle(\mathbf{a}' - \mathbf{a}, \mathbf{t})$. □

Chapter 13

Analytic Parametrization of Geometric Shapes

This chapter presents the results from two papers: "Folding the Vesica Piscis," co-authored with Tony Wills, which was presented at the Bridges Conference in 2018 [67], and "Curved Crease Folds of Spherical Polyhedra with Regular Faces," which was also presented at the Bridges Conference in 2019 [63].

Overview

The parametrization of shapes that incorporate curved creases can be challenging, as explicit parametrizations are rarely obtained through Frenet-based methods. In the following, we parametrize two families of shapes: generalizations of the folded Vesica Piscis and spherical regular polyhedra. This work initiated the formalization of the patch-to-cylinder and patch-to-cone constructions.

13.1 Introduction

Analyzing real-world shapes created from flat materials presents challenges due to the potential introduction of small imperfections during the fabrication process. Moreover, determining the rulings of the involved developable surfaces is typically approached through trial-and-error methods, lacking a straightforward analytical solution. As a result, describing these shapes mathematically becomes non-trivial, and traditional Frenet-based methods often do not provide explicit parametrizations for them. In this chapter, we present two families of shapes that allow an up to elliptic integrals closed form parametrization, obtained by the patch-to-cylinder and patch-to-cone methods.

We first consider a family of shapes that generalize the folded Vesica Piscis, used in the sculpture "Attraction" by Susan Latham; see Figure 13.1 (left) and Figure 13.3. These shapes are created by folding two overlapping circles such that their boundaries align, resulting in configurations composed of cylinders and cones. By determining the parametrizations of the crease curves, we establish the geometric existence of these shapes. Moreover, we identify a one-parameter subfamily of shapes that have circular creases.

In the second application, we examine shapes consisting of cylinders, cones, and planes that resemble the structure of a spherical polyhedron with regular faces; see Figure 13.1 (right). We provide explicit formulas to parametrize the crease curves of these shapes.

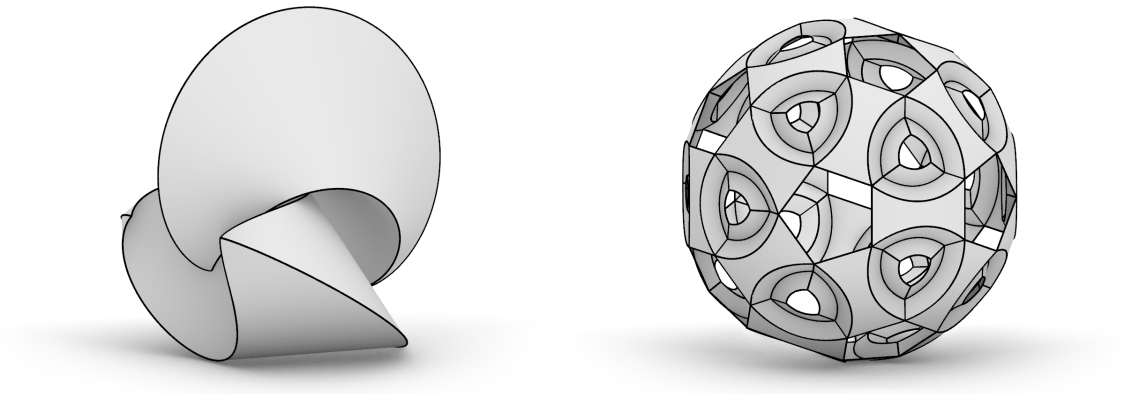

(a) Reconstruction of Susan Latham's sculpture "Attraction".

(b) Curved-crease design of an icosahedron.

Figure 13.1: Two shapes with curved creases discussed in Chapter 13.

13.2 Parametrization of the Folded Vesica Piscis

13.2.1 Vesica Piscis

The *Vesica Piscis* is a geometric shape formed by the intersection of two congruent circles, where the centers of the circles lie on the respective other circle. This simple formation has found various applications throughout history. For example, it is used in Euclid's Elements to construct an equilateral triangle, as shown in Figure 13.2.

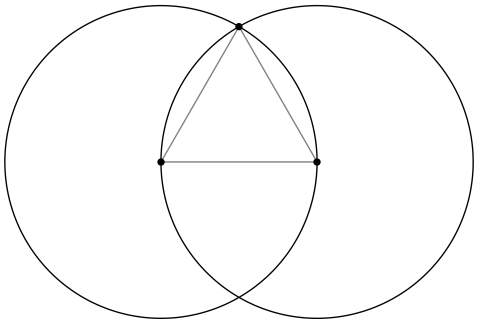

Figure 13.2: Vesica Piscis in Euclid's Elements.

Our interest in the folded Vesica Piscis shape was sparked by the sculpture "Attraction" created by artist Susan Latham. In her sculpture, two Vesica Piscae are cut out of sheet bronze and each folded along the inner circle segments in such a way that the outer segments coincide, as depicted in Figure 13.3. While manually creating this shape may be relatively simple, its geometric reconstruction is not supported in common CAD software. This led us to explore the design space of closed shapes that are formed by gluing developable surfaces with curved creases along their perimeters.

We initiated the analysis of the folded Vesica Piscis through numerical experiments, which provided indications that the object can be represented using cylindrical and conical surface patches. To further investigate and confirm this observation, we proceed by determining explicit parametriza-

Figure 13.3: Susan Latham's "Attraction", Santa Fe (2008). Figure from author's homepage [49]. Not for reproduction.

tions for the shape.

In this section, we extend our analysis to developments composed of two overlapping discs with varying overlap, allowing us to obtain a two-parameter family of closed shapes. The advantage of this approach lies in the availability of (up to elliptic integrals) explicit parametrizations, enabling us to explore the shapes of the developed crease curves. In particular, we demonstrate the existence of a one-parameter family of shapes with circular creases.

13.2.2 Notation

In the following, we investigate the shapes consisting of one cylindrical and two conical surface patches that are isometric to the union D^u of two discs of unit radius and centers $(\pm u, 0, 0)$ located in the xy-plane. Assuming that the seam curve remains planar and the developed cones' vertices coincide with the origin, we determine the parametrization of the 3D seam and crease curves. Due to the symmetry of this shape, we consider only the half of the region D^u, which is bounded by the y-axis and the circle

$$\mathbf{x}_u(t) = (\cos t + u, \sin t, 0) \quad \text{with} \quad t \in [t_0, t_1] = [-\arccos(-u), \arccos(-u)].$$

The Vesica Piscis corresponds to the special case of $u = \frac{1}{2}$.

13.2.3 Parametrization of the Seam Curve

To begin, we determine the cone with an apex at $\mathbf{V}_h = (0, 0, h)$ and a planar boundary curve $\mathbf{X}_{u,h}(t)$ that corresponds to the given half of D^u. We employ the concept of sliding with a modified parametrization assumption. Specifically, we use polar coordinates to parameterize $\mathbf{X}_{u,h}(t)$ as

$$\mathbf{X}_{u,h}(t) = r_{u,h}(t)(\cos \alpha_{u,h}(t), \sin \alpha_{u,h}(t), 0) \quad \text{and} \quad \mathbf{X}_{u,0}(t) = \mathbf{x}_u(t).$$

As isometry preserves the lengths of the cones' rulings we deduce

$$r_{u,h}(t) = \sqrt{\mathbf{x}_u^2(t) - h^2} = \sqrt{2u \cos t + u^2 + 1 - h^2} \tag{13.1}$$

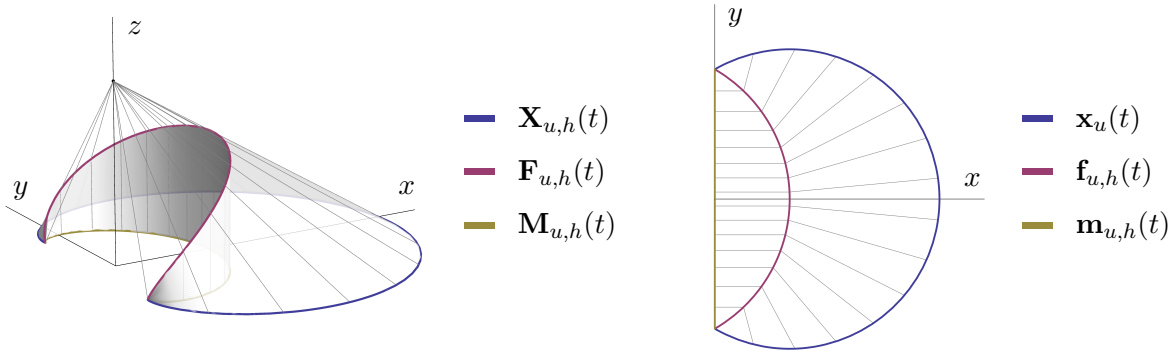

Figure 13.4: Parametric setup for the folded configuration and development of $D^u|_{x\geq 0}$

Moreover, the parametrization speed of $\mathbf{X}_{u,h}(t)$ and $\mathbf{x}_{u,h}(t)$ need to match, resulting in

$$|\mathbf{X}'_{u,h}(t)| = \sqrt{r'_{u,h}(t)^2 + r_{u,h}(t)^2 \alpha'_{u,h}(t)^2} = 1 = |\mathbf{x}'_u(t)|.$$

From this, we deduce

$$\alpha'_{u,h}(t)^2 = \frac{1}{r_{u,h}(t)^2}\left(1 - r'_{u,h}(t)^2\right).$$

Inserting the expression for $r_{u,h}(t)$ in Equation (13.1) and simplification yield that $\alpha_{u,h}$ is up to the orientation of parametrization and rotation determined by

$$\alpha'_{u,h}(t) = \frac{\sqrt{(u\cos t + h + 1)\,(u\cos t - h + 1)}}{2u\cos t + u^2 - h^2 + 1}.$$

The corresponding integral is real-valued for $0 \leq h \leq h_{\max}(u) = 1 - u^2$ and can be written as a linear combination of elliptic integrals of the third kind[1], namely

$$\alpha_{u,h}(t) = \frac{1}{2}\left(\gamma_0 \Pi(\delta_0, \phi(t), m) + \gamma_1 \Pi(\delta_1, \phi(t), m)\right),$$

where the Jacobi amplitude and elliptic modulus are given by

$$\phi(t) = \arctan\left(\sqrt{\frac{1-u+h}{1+u+h}}\tan\frac{t}{2}\right) \qquad \text{and} \qquad m = \frac{4uh}{1-(u-h)^2}.$$

Additionally, the elliptic characteristics and coefficients read

$$\delta_0 = \frac{-2u}{1-u+h}, \qquad \delta_1 = \frac{2u}{1+u-h}, \qquad \gamma_0 = \frac{2(1+u+h)}{\sqrt{1-(u-h)^2}}, \qquad \gamma_1 = \gamma_0\frac{1-u-h}{1+u+h}.$$

[1] $\Pi(l;\phi,k) = \int_0^\phi \frac{1}{(1-l\sin^2\theta)\sqrt{1-k\sin^2\theta}}d\theta$

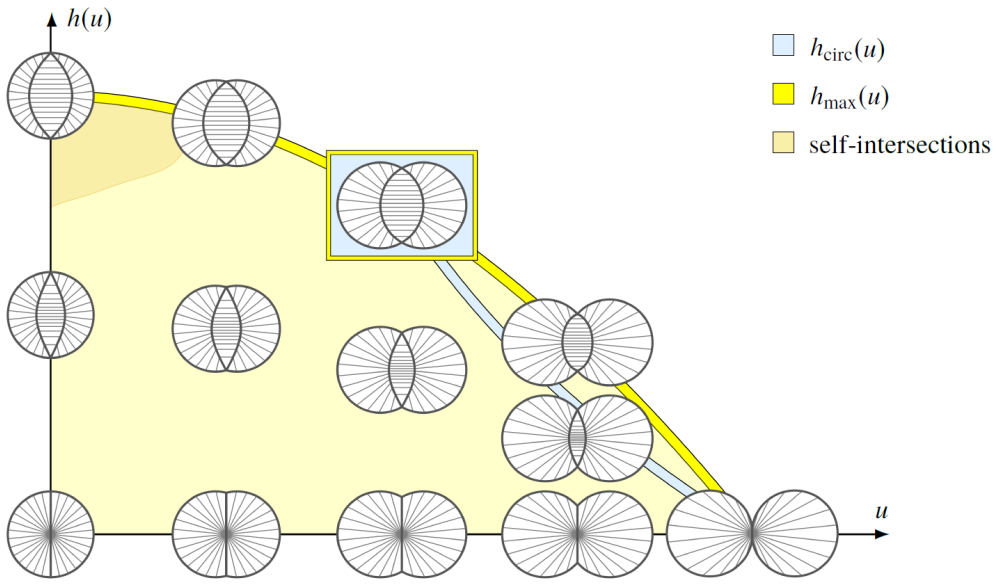

Figure 13.5: Diagram representing the crease curves of the two-parameter family of closed shapes. It follows from numerical computations that $\alpha_{u,h}(s_1)$ exceeds π for $u \leq 0.19$ and high values of h. The corresponding folded shapes exhibit self-intersections.

13.2.4 Parametrization of the Crease Curve

In the following, we use a modified approach to the patch-to-cylinder construction method. Specifically, we assume that the crease curve $\mathbf{F}_h(t)$ and its development $\mathbf{f}_h(t)$ are represented by

$$\mathbf{F}_{u,h}(s) = (1 - t_{u,h}(s))\mathbf{V}_h + t_{u,h}(s)\mathbf{X}_{u,h}(s) \quad \text{and} \quad \mathbf{f}_{u,h}(s) = t_{u,h}(s)\mathbf{x}_{u,0}(s), \tag{13.2}$$

where $t_{u,h}(t)$ is an initially unknown length function.

When looking for the location of the crease that connects the cone with a cylinder with vertical rulings, we are interested in the points of the ruling where the z-value of $\mathbf{F}_{u,h}(s)$ equals the x-value of $\mathbf{f}_{u,h}(s)$. Consequently, it follows that

$$t_{u,h}(s) = \frac{h}{\cos s + u + h}. \tag{13.3}$$

Note that the resulting crease curves are generally non-planar. Figure 13.5 provides an illustration of the computed developed crease curves, showcasing their behavior dependent on the parameters u and h, where $u \in [0, 1]$ and $h \in [0, h_{\max}(u)]$.

13.2.5 Circular Crease Curves

Finally, we note that this construction results in a one-parameter family of circular crease curves; see Figure 13.6 and Figure 13.5. Specifically, the creases are circular when the cone's apices are at height

$$h_{\text{circ}}(u) = \frac{1 - u^2}{2u} \quad \text{for} \quad u \in \left[\frac{1}{2}, 1\right].$$

The original folded Vesica Piscis is the special case of $u = \frac{1}{2}$ and $h = h_{\text{circ}}\left(\frac{1}{2}\right) = h_{\max}\left(\frac{1}{2}\right) = \frac{3}{4}$.

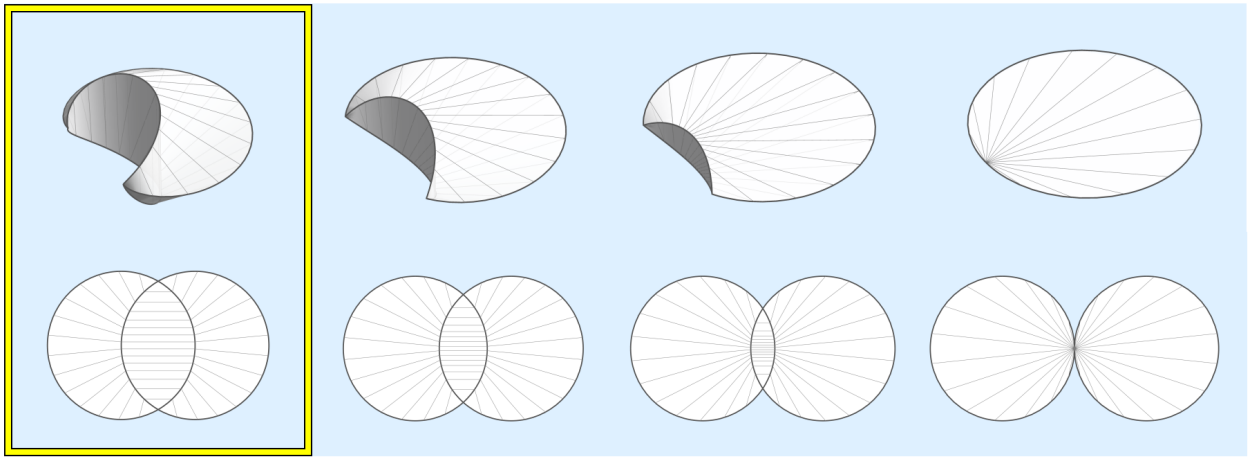

Figure 13.6: Examples of folded closed shapes with circular creases.

13.3 Curved-Crease Designs from Spherical Polyhedra with Regular Faces

13.3.1 Spherical Polyhedra with Regular Faces

We now introduce the second class of shapes where the patch-to-cone construction can be used to achieve an explicit parametrization. The resulting creases are not tangent-continuous. For a discussion on a shapes with smooth creases that cover a wider range of polyhedra, refer to Chapter 15.

We begin by providing an overview of the definitions and properties of the considered class of polyhedra. A polyhedron is called *regular* or a *Platonic solid* if all its faces are identical regular polygons. On the other hand, a polyhedron is called *semi-regular* or an *Archimedean solid* if all its faces are regular polygons and all its vertices are equal. Finally, the dual polyhedra of the Archimedean solids are called *Catalan solids*. It is important to note that the faces of Catalan solids are not necessarily regular. It is known that the vertices of Platonic, Archimedean, and Catalan solids lie on on a sphere.

When discussing a *spherical polyhedron*, we refer to a tessellation of a unit sphere (denoted as S), in which the surface is divided into bounded regions known as *spherical polygons* using great arcs on S. It is established that Platonic, Archimedean, and Catalan solids can be projected onto the sphere, resulting in spherical polyhedra. However, in general, only Platonic and Archimedean solids yield spherical polyhedra with regular faces.

In the following, we present a construction that transforms a spherical polyhedron with regular faces into a modular curved-crease design; see Figure 13.7 and Figure 13.8.

13.3.2 Construction Overview

In the following, let $\mathscr{P}$ be spherical polyhedron with regular faces. Note that this implies that all spherical "edges", have the same length which we will denote by $2t_{\max}$. Furthermore, let $t_{\text{ini}} \in (0, t_{\max})$ be a user-specified parameter.

The construction of the curved-crease folded polygon can be broken down into three distinct steps, as depicted in Figure 13.9:

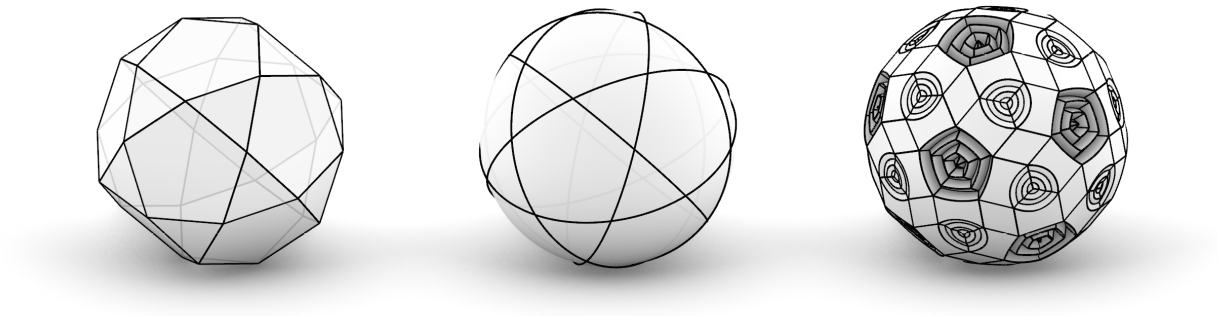

Figure 13.7: Curved-crease design from a icosidodecahedron. Left to right: The Archimedean solid icosidodecahedron, its projection to a sphere, and a proposed curved-crease approximation.

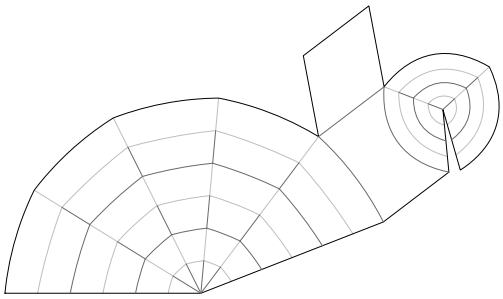

Figure 13.8: Part of the curved-folded Icosidodecahedron's development (darker gray depicts the mountain, lighter gray the valley folds).

- *Step 1:* Initially, we align right circular cylinders along the edges of $\mathscr{P}$ and connect them using planar patches. The size of these planar patches is determined by the user-specified parameter t_{ini}.
- *Step 2:* Next, we use the patch-to-cone construction to compute the crease curves that connect the given cylinders with cones with suitable apices.
- *Step 3:* As an optional step, we have the flexibility trim or introduce additional creases to the cones, such as by reflecting them at planes.

The subsequent section provides a detailed description of each of these individual steps.

13.3.3 Construction Details

In the following section, we outline the process of incorporating a curved-crease design onto a single face of the spherical polyhedron. By employing identical cylinders along each edge, we ensure that the individual faces can be seamlessly connected to form the completed curved-crease design.

Step 1: Constructing the cylinders

Let $P = (\mathbf{P}_1, \dots, \mathbf{P}_n)$ be a regular spherical n-gon of $\mathscr{P}$. We parametrize the edges $\mathbf{P}_i\mathbf{P}_{i+1}$ of P, which are the great circles of the underlying (unit) sphere $\mathcal{S}$, using arc-length parametrized curves $\mathbf{X}_i(t)$ for $t \in [-t_{\max}, t_{\max}]$, such that $\mathbf{X}_i(-t_{\max}) = \mathbf{P}_{i-1}$ and $\mathbf{X}_i(t_{\max}) = \mathbf{P}_i$. Let $\mathbf{R}_i$

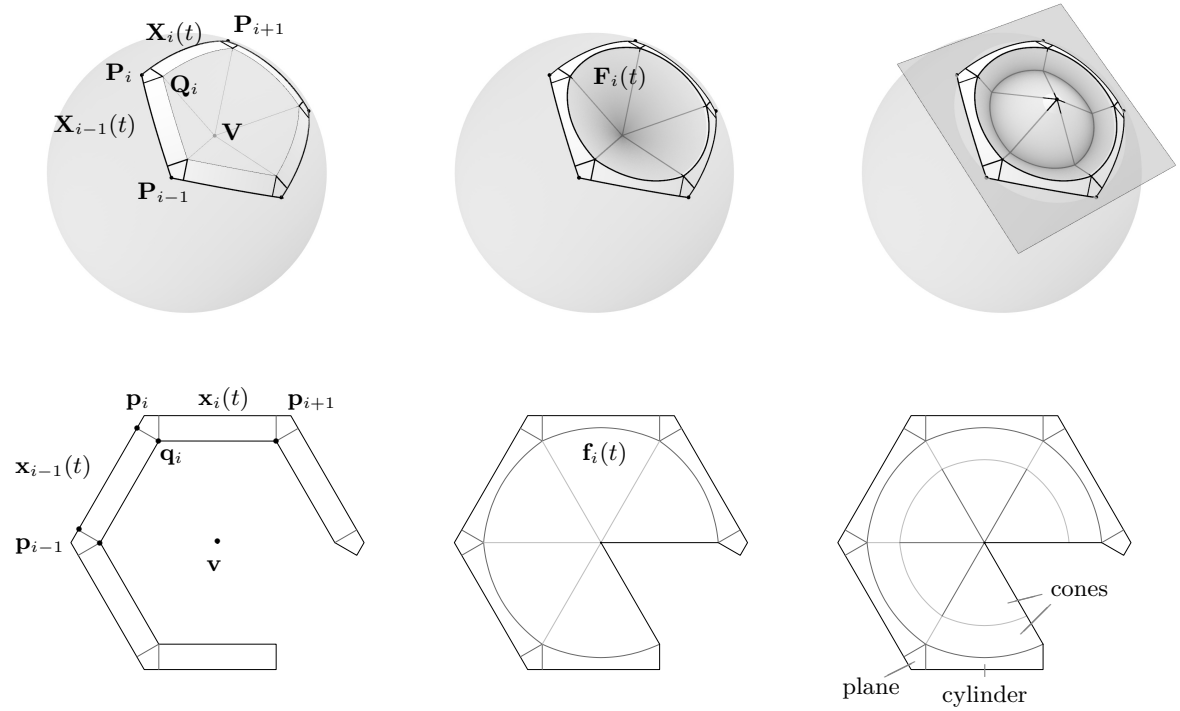

Figure 13.9: Illustration of the proposed three steps in the construction of a folded spherical regular polygon.

denote the normal of the base plane of the curve $\mathbf{X}_i(t)$, pointing towards the interior of P. Then, $\mathbf{S}_i(t,u) = \mathbf{X}_i(t) + u\mathbf{R}_i$ for $u \geq 0$ and $t \in [-t_{\text{ini}}, t_{\text{ini}}]$ parametrizes a cylindrical patch that is tangential to $\mathcal{S}$.

Next, we determine the intersection point $\mathbf{Q}_i$ between the two adjacent rulings incident to $\mathbf{X}_{i-1}(t_{\text{ini}})$ and $\mathbf{X}_i(-t_{\text{ini}})$, and fill the area between these rulings with a planar patch. It is important to note that the connections between the cylindrical and planar patches are not tangent-continuous. We represent the resulting poly-arc as $Q = (\mathbf{Q}_1, \ldots, \mathbf{Q}_n)$.

We then sequentially unroll the composition of cylinders and planes into the xy-plane, resulting in a polyline denoted by $q = \{\mathbf{q}_1, \ldots, \mathbf{q}_n\}$. We denote the development of $\mathbf{S}_i(t,u)$ by $\mathbf{s}_i(t,u) = \mathbf{x}_i(t) + u\mathbf{r}_i$.

Since the polyline q has equal edge lengths and angles, it possesses a circumcircle with center $\mathbf{v}$, which we will use as the developed cone apex. To determine the location of a suitable 3D apex $\mathbf{V}$, we locate the point $\mathbf{V}$ that satisfies $|\mathbf{V} - \mathbf{Q}_i| = |\mathbf{v} - \mathbf{q}_i|$ for all $1 \leq i \leq n$. Generally, there will be two solutions, and we select the one that is closer to the center of the sphere.

Step 2: Folding the cylinders into cones

In the next step, we determine the crease between each cylinder $\mathbf{S}_i(t,u)$ and a cone with a 3D apex $\mathbf{V}$ and a 2D apex $\mathbf{v}$. It is important to note that the points $\mathbf{Q}_i$ lie on the crease curve, as their distances to the apex are the same in 3D as in 2D.

To simplify the computation, we choose a local coordinate system. Specifically, we set $\mathbf{X}_i(t) = (\cos t, \sin t, 0)$ and $\mathbf{R}_i = (0,0,1)$ for the 3D cylinder. For the development, we choose $\mathbf{x}_i(t) = (t,0,0)$ and $\mathbf{r}_i = (0,1,0)$. Since both $\mathbf{V}$ and $\mathbf{v}$ lie in the perpendicular bisector of $\mathbf{X}_i(-t_{\text{ini}})$ and $\mathbf{X}_i(t_{\text{ini}})$ or

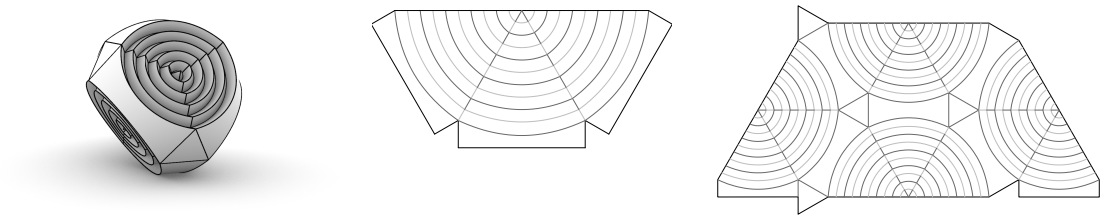

(a) Spherical tetrahedron with curved creases.

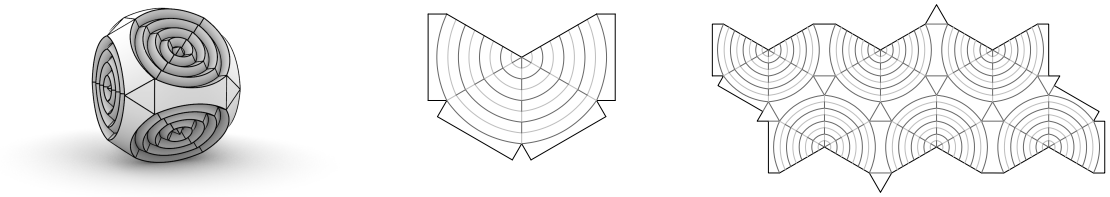

(b) Spherical hexahedron with curved creases.

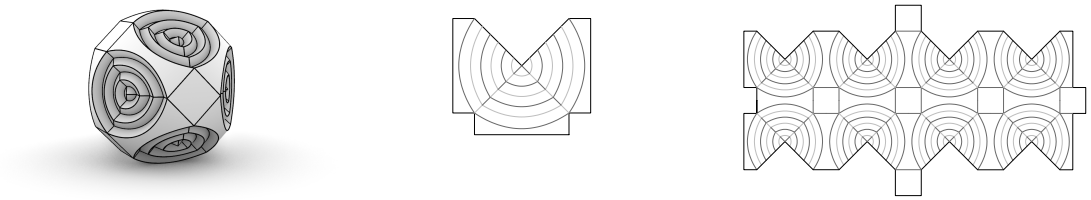

(c) Spherical octahedron with curved creases.

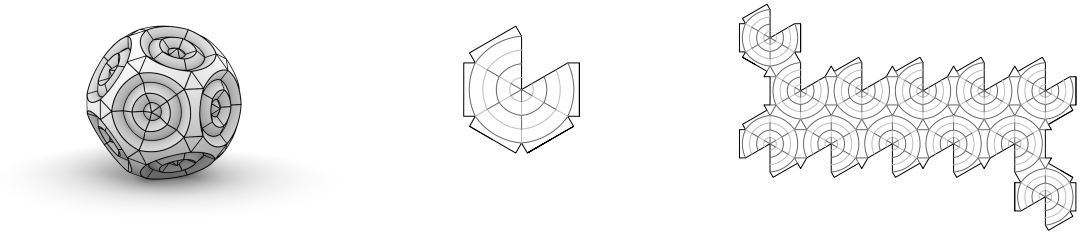

(d) Spherical dodecahedron with curved creases.

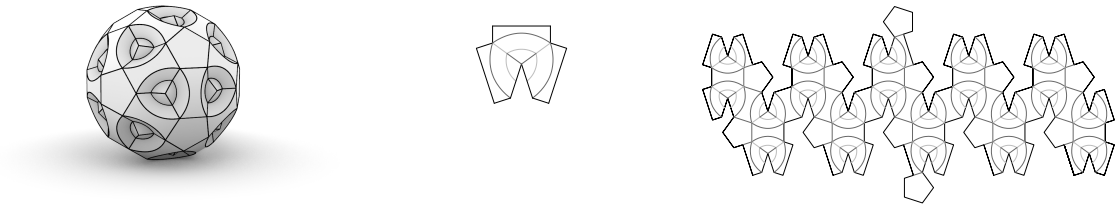

(e) Spherical icosahedron with curved creases.

Figure 13.10: Spherical Platonic solids with curved creases and their developments.

Figure 13.11: Spherical icosahedron fabricated from Hylite, in collaboration with RnKOLEKTIVE, displayed at the MIT MediaLab in Summer 2023.

$\mathbf{x}_i(-t_{\text{ini}})$ and $\mathbf{x}_i(t_{\text{ini}})$, we assume $\mathbf{V} = (\mathbf{V}_x, 0, \mathbf{V}_z)$ and $\mathbf{v} = (0, \mathbf{v}_y)$.

The length functions of the crease $\mathbf{F}_i(t) = \mathbf{X}_i(t) + l_i(t)\mathbf{R}_i$ and its development $\mathbf{f}_i(t) = \mathbf{x}_i(t) + l_i(t)\mathbf{r}_i$ can then be computed using Lemma 12.1 as follows

$$l(t) = \frac{1}{2}\frac{1 - t^2 - 2\mathbf{V}_x \cos t + \mathbf{V}_x^2 + \mathbf{V}_z^2 - \mathbf{v}_y^2}{\mathbf{v}_y - \mathbf{V}_z}.$$

We conjecture that the valid patch condition is always satisfied, that is, $\mathbf{v}_y - \mathbf{V}_z > 0$. However, two creases incident to the same cylinder might intersect. This can usually be prevented by choosing a smaller parameter t_{ini}. It is important to note that since the cylindrical surfaces and adjacent planes are not tangent-continuous, the computed crease curves will also not be tangent continuous. Chapter 15 discusses an approach that results in tangent developable surfaces and creases.

Step 3: Adding further creases

Optionally, these hereby constructed cones can either be trimmed or folded. In our examples we reflect the cones along planes that are perpendicular to the axis of P, that is, the line spanned by the origin and the barycenter of P.

13.3.4 Fabrication

As part of the RnKOLEKTIVE [69], we successfully fabricated a spherical icosahedron with a diameter of 2.2m; see Figure 13.11. To construct this structure, we used Hylite, a 1.2mm aluminum composite panel by 3A Composites. This panel consists of a 0.8mm polypropylene core sandwiched between two layers of 0.2mm aluminum. The fabrication process involved milling the creases from both sides using a Zünd machine, followed by manual folding.

To optimize material usage during fabrication, we divided the crease pattern into pieces corresponding to the edges of the polyhedron. Each piece consisted of a cylindrical surface and four conical patches. Additionally, thin flaps were added along the sides of the pieces to enhance structural integrity, assist in the fabrication process, and conceal the electronics used in the project.

Chapter 14

Design of Conic Spirals with Planar Creases

The content of this chapter is based on the paper "Design of Conic Spirals with Planar Creases" that the thesis author coauthored with Erik Demaine, Robert Lang, and Tomohiro Tachi. This paper appeared in the Bridges 2023 conference proceedings [66].

Overview

We describe two exact geometric constructions of *origami spirals* obtained by creasing a flat sheet of paper along $2n$ curves, alternating mountain and valley, where the 2D crease pattern and resulting 3D folding are $2n$-fold rotationally symmetric about the center. Both constructions use conical developable surfaces and planar creases. In one construction (conical spirals), the cone patches all share an apex (the center), effectively forming one big (creased) cone. In the second construction, inspired by David Huffman's "exploded vertex" designs, the cone apices are the vertices of a central regular polygon. Both constructions have planar creases and, in addition to their rotational symmetry, are reflectionally symmetric through the base plane.

14.1 Introduction

Origami with curved creases forms beautifully intricate geometries using relatively few creases. One family of designs, which we call *spirals*, folds $2n$ rotationally symmetric curves, alternating mountain and valley [53, 59]. While in many designs the curves meet at the center, David Huffman [43] introduced a variation with an "exploded" central vertex, replacing the central vertex by a regular $2n$-gon; see Figure 14.1.

Origami spirals are related to origami flashers, a family of straight-crease rigidly foldable deployable structures that result from wrapping material around a polygonal base [47]. Their compact folded state makes them suitable for applications such as star-shaders in space-exploration [6].

Material imperfections make it nontrivial to determine whether a real-world folded shape mathematically *exists*, i.e., preserves the intrinsic distances on the surface (no stretching or tearing). In this chapter, we give two geometric constructions for spirals made from smooth or discrete cones with planar creases, resulting in shapes that are guaranteed to (mathematically) exist. We construct only the folded geometries, conjecturing that the constructed spirals in general do not have rigid-ruling folding motions.

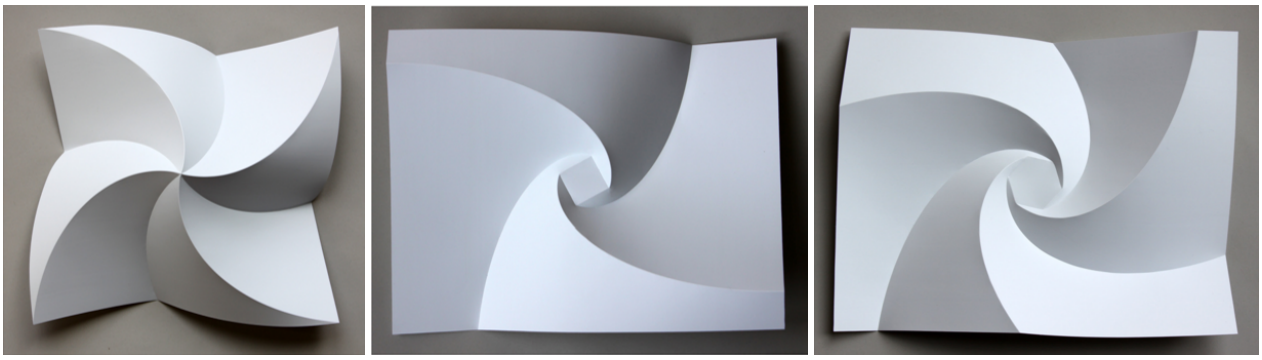

Figure 14.1: David Huffman's variations with (un)exploded vertices reconstructed by Duks Koschitz. Figures 5, 7, and 8 in [19].

14.2 Triangle Wreaths

The first step in our construction is to position $2n$ congruent triangles in a rotationally symmetric way; see Figure 14.2. Precisely, a *triangle wreath* consists of $2n$ congruent triangles $(\triangle_0, \triangle_1, \ldots, \triangle_{2n-1})$ such that consecutive triangles $\triangle_i, \triangle_{i+1}$ share a vertex $\mathbf{P}_i$ and are related by the rotation $\mathbf{R}_n$ by $\frac{\pi}{n}$ about the z-axis and the reflection $\mathbf{M}_{xy}$ through the xy-plane:

$$\triangle_{i+1 \pmod{2n}} = \mathbf{M}_{xy}\left(\mathbf{R}_n\left(\triangle_{i \pmod{2n}}\right)\right) \quad \text{for all } 0 \le i < 2n.$$

Lemma 14.1. *Given a triangle $\triangle = (a, b, c)$, up to rotation about the z-axis, there exists a two-parameter family of triangle wreaths in which the endpoints of triangle edge a are joined.*

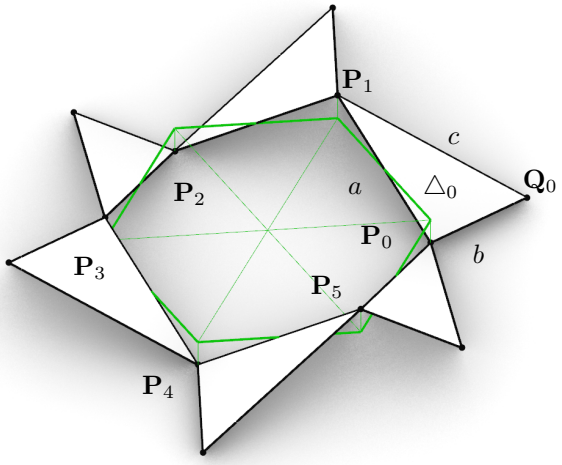

Figure 14.2: Triangle wreath.

Proof. Let $\mathscr{P} = (\mathbf{P}_0, \mathbf{P}_1, \ldots, \mathbf{P}_{2n-1})$ be the polyline formed by consecutive vertices that coincide with two triangles in a triangle wreath. Because $\mathbf{P}_0$ and $\mathbf{P}_1$ are related by rotation $\mathbf{R}_n$ and reflection $\mathbf{M}_{xy}$, their coordinates can be written as $\mathbf{P}_0 = \left(r\cos\frac{\pi}{n}, -r\sin\frac{\pi}{n}, -h\right)$ and $\mathbf{P}_1 = \mathbf{M}_{xy}\left(\mathbf{R}_n\left(\mathbf{P}_0\right)\right) = \left(r\cos\frac{\pi}{n}, r\sin\frac{\pi}{n}, h\right)$ for some $h > 0$ and $r > 0$. Because $|\mathbf{P}_0 - \mathbf{P}_1| = a$, it follows

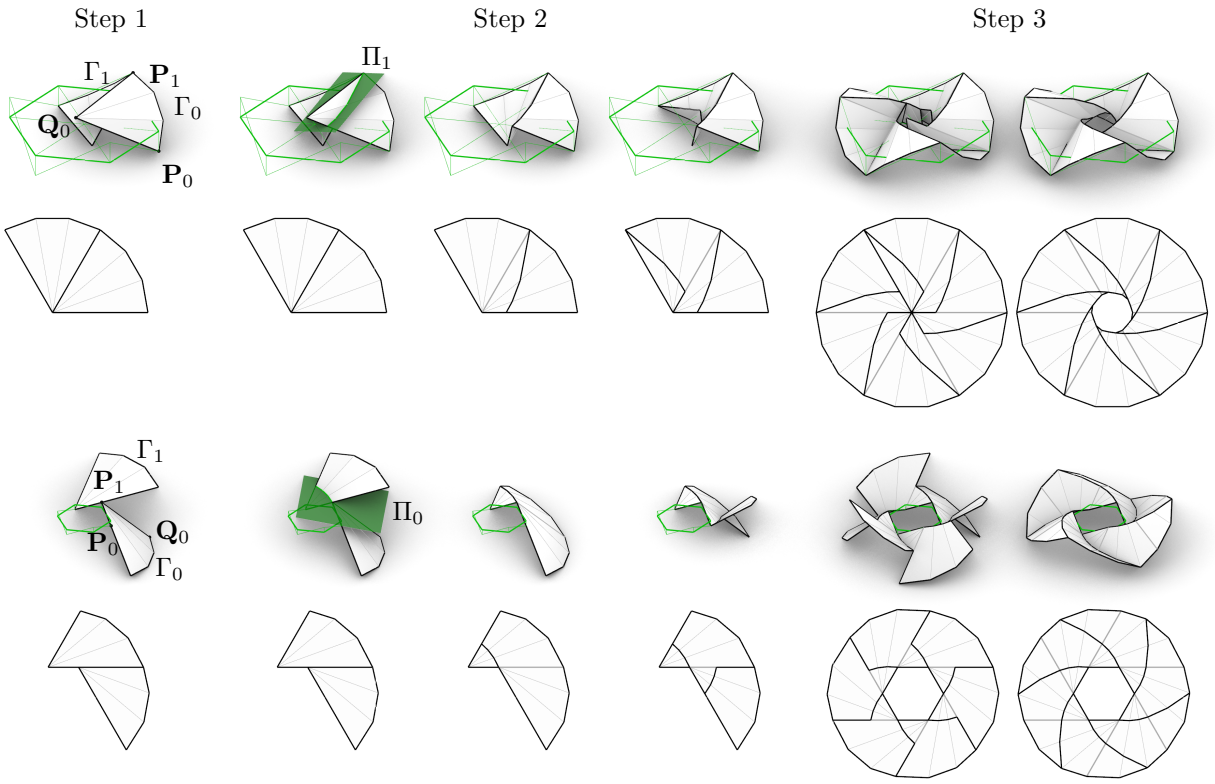

Figure 14.3: Construction steps for the conical spiral (top) and the exploded-vertex spiral (bottom).

that $r = \frac{1}{2}\sqrt{a^2 - 4h^2}\left(\sin\frac{\pi}{n}\right)^{-1}$ for $h \in [0, \frac{a}{2})$. Thus we have one degree of freedom for the configuration of the polyline $\mathscr{P}$. In addition, we have another degree of freedom corresponding to the location of the third vertex of the first triangle $\triangle_0 = (\mathbf{P}_0, \mathbf{P}_1, \mathbf{Q}_0)$ of the wreath, corresponding to a rotation about $\mathbf{P}_0\mathbf{P}_1$. □

14.3 Curved Spiral Construction

We now discuss how to construct a conical or an exploded-vertex spiral by attaching cones to the triangles of a triangle wreath and them reflecting appropriately. In the following, let Γ be a (smooth or discrete) cone with developed opening angle $\frac{\pi}{n}$, specified by an apex $\mathbf{V}$ and a (smooth or discrete) boundary curve $\mathbf{C}(t)$ where $t \in [0, 1]$. Without loss of generality, we assume that the first and last ruling of Γ are of the same length, $1 = |\mathbf{V} - \mathbf{C}(0)| = |\mathbf{V} - \mathbf{C}(1)|$. The two proposed constructions of spirals with $2n$ cones can be divided into three steps:

- *Step 1:* Use points on Γ to define a triangle $\triangle = (\mathbf{P}_0, \mathbf{P}_1, \mathbf{Q}_0)$. Using Lemma 14.1 and two input parameters, we construct a wreath of triangles congruent to $\triangle$. Position a copy Γ_0 of Γ at the corresponding points on the first triangle $\triangle_0$ of the triangle wreath. Define a second cone $\Gamma_1 = \mathbf{M}_{xy}\left(\mathbf{R}_n\left(\Gamma_0\right)\right)$.
  - *Conical spiral:* Let $\mathbf{P}_0 = \mathbf{C}(0)$, $\mathbf{P}_1 = \mathbf{C}(1)$ and $\mathbf{Q}_0 = \mathbf{V}$.
  - *Exploded-vertex spiral:* Let $\mathbf{P}_0$ be some non-apex point on the first cone ruling, that is, $\mathbf{P}_0 = (1-t)\mathbf{V} + t\mathbf{C}(0)$ for $t \in (0, 1)$, $\mathbf{P}_1 = \mathbf{V}$ and $\mathbf{Q}_0 = \mathbf{C}(1)$. Because we extend the cones in Step 3 anyhow, the choice of t influences the scale. In our implementation, we use $t = \frac{1}{4}$.

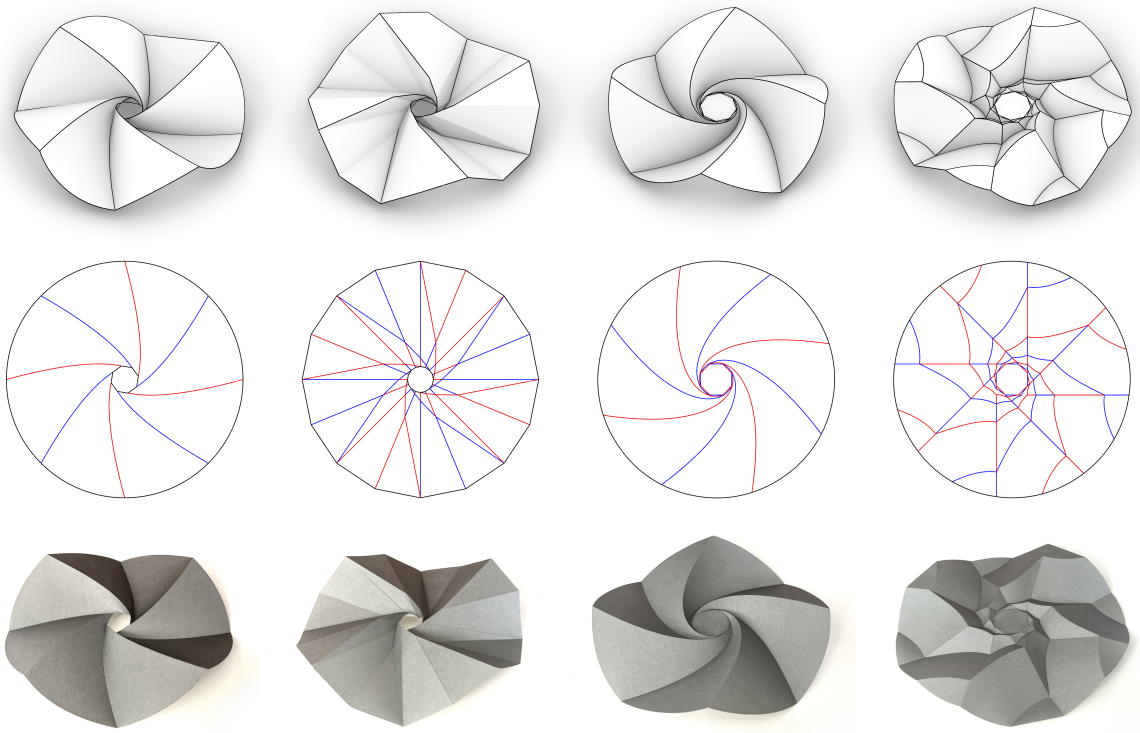

Figure 14.4: Examples of spirals designed using our plug-in and folded from paper.

- *Step 2:* Construct a plane to connect a subpatch of Γ_0 with the other subpatch of Γ_1 using a planar crease. The crease curve can be computed using the considerations in Section 12.3.2. Fold the other cone analogously.
  - *Conical spiral:* Let Π_0 be the bisecting plane of $\mathbf{P}_0$ and $\mathbf{P}_1$. We split Γ_0 with Π_0 into two subpatches, and reflect the subpatch containing the apex by Π_0.
  - *Exploded-vertex spiral:* Define Π_1 to be the bisecting plane of $\mathbf{C}_0(1)$ and $\mathbf{C}_1(0)$. We split Γ_1 with Π_1 into two subpatches, and reflect the subpatch not containing the apex by Π_1.

  Both reflections join a subpatch of Γ_1 with the other subpatch of Γ_0, resulting in four connected surface patches.
- *Step 3:* Arrange copies of the two cones in a polar array to obtain a closed ring of $2n$ creased cones. If possible, extend the creases to neighboring cones by using their incident planes for splitting and reflecting, and trim the surfaces appropriately.

Note that this construction might fail for unrealistic parameter combinations, or result in intersecting cones. Upon success, this construction results in closed developable rings of patches joined along creases; see Figure 14.4 and Figure 14.5. Note, that even if the involved cones are smooth, the connection between Γ_0 and Γ_1 might not be tangent-continuous. In many cases, tangent continuity can be achieved by tweaking the parameters of the wreath construction. We conjecture that the conical spiral construction can be generalized to patches other than cones, in which singularities of the surface might need special treatment. If the polyline of the wreath is planar, we can close the center of the spiral with a planar polygonal face.

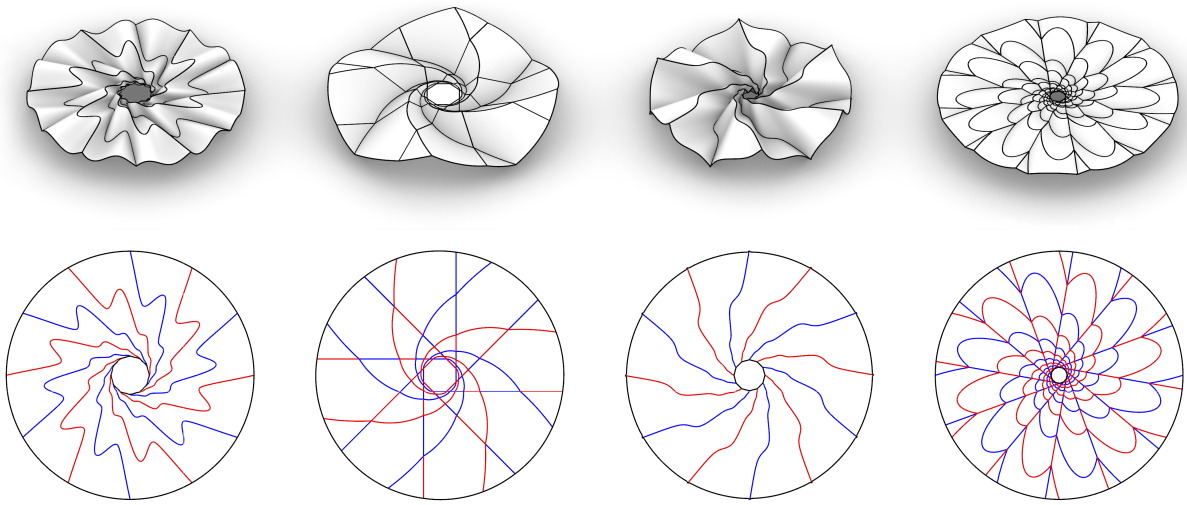

Figure 14.5: Examples of more complex spirals designed using our plug-in.

14.4 Software Implementation

We implemented the described construction as an interactive design tool for Grasshopper / Rhino. To construct smooth or discrete cones with appropriate opening angle, we use the sliding developable method (discussed in Section 11 and [64]) and its implementation described in [65]. The position of the first triangle $\triangle_0 = (\mathbf{P}_0, \mathbf{P}_1, \mathbf{Q}_0)$ of the wreath can be influenced by the user with two angles: angle φ describes the inclination of $\mathbf{P}_0\mathbf{P}_1$ w.r.t. the xy-plane, angle ψ describes the angle between $\triangle_0$ and the plane spanned by the x-axis and $\mathbf{P}_0\mathbf{P}_1$. We use an external plug-in named Goat [79] to optimize for tangent continuity.

Chapter 15

Rounded Corner Polyhedra

This chapter presents results from the paper titled "Curved Crease Edge Rounding of Polyhedral Surfaces" that the thesis author coauthored with Rupert Maleczek and Tomohiro Tachi. This paper has been presented at the Advances of Architectural Geometry Conference (AAG) [55], 2020.

Overview

We show a method to design a curved-crease folding that constructs the edge-rounded, i.e., filleted, version of a given polyhedral surface. We replace each edge with a smoothly rounded cylinder and each vertex with a generalized cone, such that the surfaces joined through curved creases form a single developable surface. Because the curved crease can be explicitly computed from the isometry of corresponding line segments for given locations of the cone apex in 2D and 3D, our problem reduces to identifying the locations of the apices. We characterize the conditions for the apex positions and provide a numerical scheme to find the apices for the given mesh by solving a nonlinear optimization problem. In general, the rounding of edges reduces the surface area, resulting in a shape that is not guaranteed to be foldable from a single piece of uncut paper. We solve this problem by computing consistent material loss caused by rounding radii.

15.1 Introduction

Generating complex shapes with curved creases poses a significant challenge. While a patch-by-patch folding technique offers design flexibility, the resulting shape's complexity is often limited by the time required for manual creation by a designer.

One approach to address this challenge is to automate the construction process by approximating a given shape using curved-crease designs. For instance, Chandra et al. [14] approximate polyhedra by smoothing creases, while Jiang et al. [38] employ multiple curved pleats for surface approximation through optimization.

In this chapter and the subsequent one, we introduce two design approaches that use polyhedra to construct folded shapes, particularly modular ones. In the following, we present a method for designing folded shapes that represent an edge-rounded or filleted version of the original polyhedral surface (refer to Figure 15.1). Each vertex of the input polyhedron corresponds to a dimple surrounded by closed curved creases, which function as structural ribs. Our method can be considered a generalization of existing artworks in curved folding. For example, Mosely [61] computes modular origami from a rounded cube with circular dimples at the corners, and Section 13.3 (see also Mundilova [63]) applies a similar approach to regular polyhedra. However, our method extends to

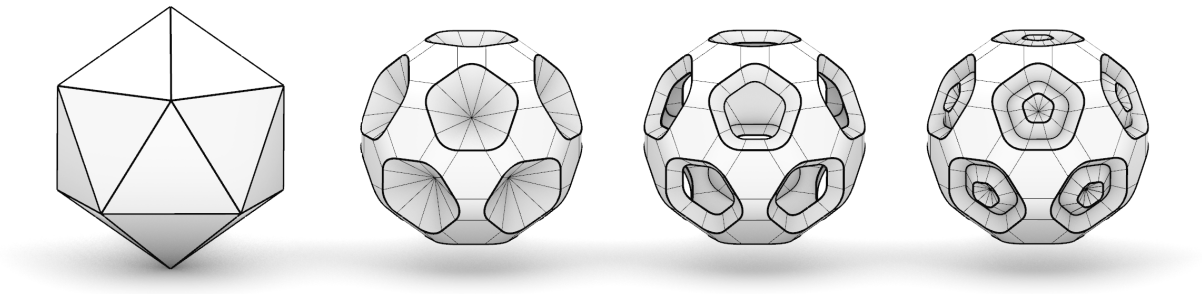

Figure 15.1: Illustration of an edge-rounded icosahedron. From left to right: Input polyhedron; edge-rounded version with curved creases; edge-rounded version with trimmed cones; and edge-rounded version with additional planar creases.

non-regular (albeit not arbitrary) polyhedral surfaces and ensures tangent continuity of the surfaces when they are not joined by a curved crease.

Overview

The overview of our design approach is as follows:

1. We first replace each edge of the polyhedron with a smoothly rounded cylinder.
2. We replace each vertex by a general cone meeting the incident cylinders and faces with curved and straight creases respectively, such that the developability is maintained at the creases. This further decomposes into two steps.
   (a) For each vertex, we first locate the positions of the apex in 2D and 3D. A desirable location results in a collection of valid, non-self-intersecting patches whose tangent-continuous crease curve are in a valid range.
   (b) We then compute the curved crease explicitly using the patch-to-cone construction in Lemma 12.1.

Therefore, the main task is to locate the apices (2a) while maintaining the specified constraints. In Section 15.3, we gather the necessary constraints to identify suitable apices, and subsequently, in Section 15.4, we present a method for formulating a local optimization problem. It is important to acknowledge that there might be instances where the intersection of valid regions, linked to the established conditions, does not exist. Specifically, we demonstrate in Section 15.3.4 that our construction cannot be applied to vertices with saddle shapes. To determine the positions of the apices, we employ numerical techniques to solve a nonlinear constrained optimization problem based on the given conditions. The particulars of this process are outlined in Section 15.4.

In general, the rounding of edges reduces the surface area, so the resulting curved folded surface is not isometric to the original polyhedron. In particular, even if the original polyhedral surface is developable, the resulting curved-crease surface is in general not closed around the cone apices. In Section 15.5, we show the constraints for the valid rounding radii used in Step 1 so that the resulting surface is also developable when applied to an originally developable surfaces. We solve this problem as a linear constrained optimization problem for a given general polygonal mesh. In particular, we prove the existence of a consistent edge-rounding and cone apex construction for a limited class of polyhedral surfaces, namely, a conical convex mesh (Section 15.6).

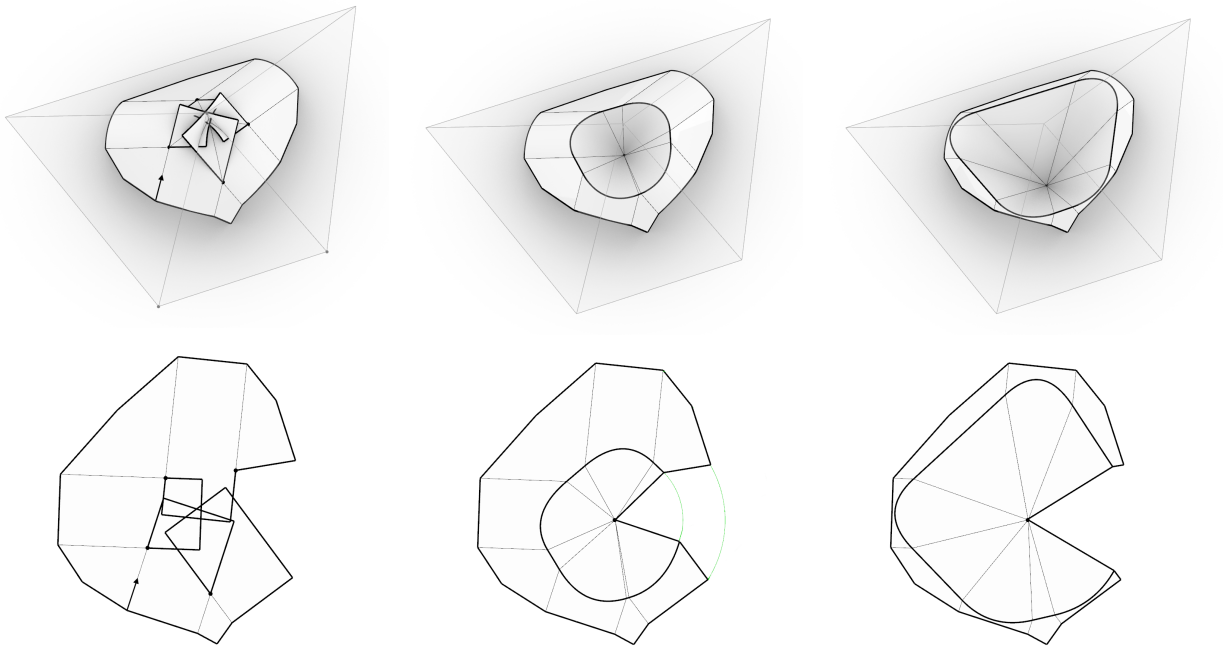

(a) Step 1: Replace edges with right circular cylinders.

(b) Step 2: Determine the cone that is connected to incident cylinders with curved creases. The crease's shape can be influenced by the user.

Figure 15.2: Overview of the proposed method for edge-rounding a polyhedron.

We implemented our construction method including the optimization as a component for Grasshopper / Rhino [81, 57], so the designer can interactively design curved crease folding by modeling an initial mesh and adjusting other design parameters. Section 15.7 shows how the parameters in each process affect the results. Furthermore, we show design variations using our methods that have potential architectural applications.

15.2 Notation

Let M be a user-specified mesh, which is defined by its vertices P and faces F. Additionally, let R represent a list of rounding radii r_i defined for each edge in the mesh. Note that it is important to ensure that the rounding radii assigned to the edges incident to a face are compatible, in order to avoid intersecting surfaces. Furthermore, we assume the availability of a half-edge data structure for M.

In the following discussion, we focus on the 1-star neighboring vertices of a vertex $\mathbf{P}_k$; see Figure 15.3. For each half-edge of the mesh M that ends at vertex $\mathbf{P}_k$ and originates from a vertex $\mathbf{P}_i$, we attach a right-circular cylinder with a user-specified radius that is tangent-continuous to its adjacent faces. These cylinders cover half of each edge and will be folded into a cone at the end-vertex $\mathbf{P}_k$.

Let $\mathbf{X}_{ik}(t)$ represent the base curve of such a filleted cylinder, where t is an arc-length parameter ranging from $-t_{ik}^{\max}$ to $t_{ik}^{\max}$. This base curve is a circular arc that lies in the plane bisecting the two endpoints $\mathbf{P}_i$ and $\mathbf{P}_k$. Additionally, we define $\mathbf{R}_{ik}$ as the normalized ruling direction, given by $\mathbf{R}_{ik} = \frac{\mathbf{P}_k - \mathbf{P}_i}{|\mathbf{P}_k - \mathbf{P}_i|}$. Consequently, the parametric representation of the cylinders can be expressed as $\mathbf{S}_{ik}(t, u) = \mathbf{X}_{ik}(t) + u\mathbf{R}_{ik}$.

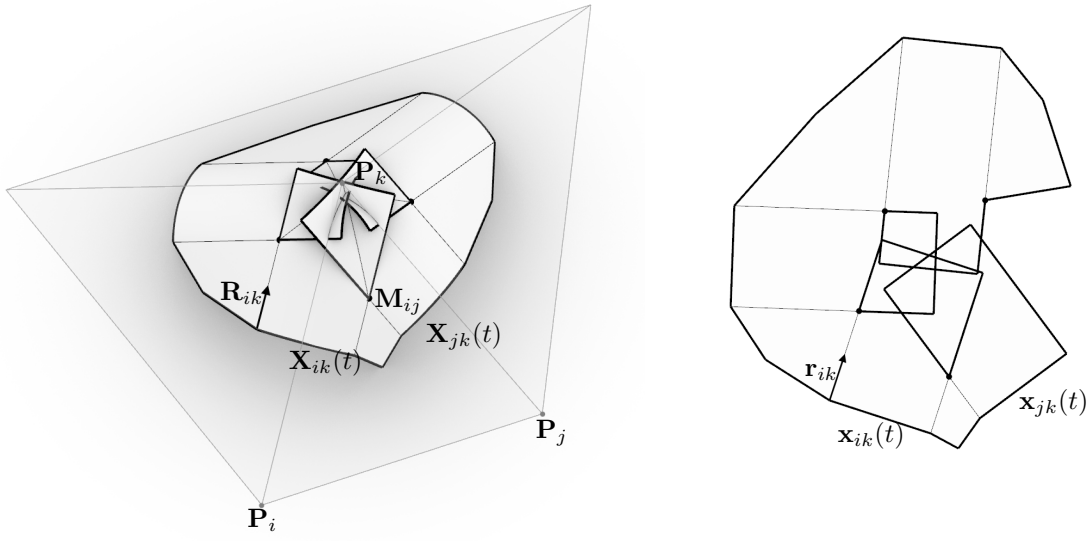

Figure 15.3: Illustration of the notation of the edge-rounded area around a vertex.

The first and last rulings of two neighboring cylinders, $\mathbf{S}_{ik}(t,u)$ and $\mathbf{S}_{jk}(t,u)$, corresponding to the same face, intersect each other. Let $\mathbf{M}_{ij}$ represent the intersection of these rulings. We fill the space between the two adjacent cylinders $\mathbf{S}_{ik}(t,u)$ and $\mathbf{S}_{jk}(t,u)$ with planar patches τ_{ij}.

To obtain the development of the constructed surfaces, we flatten and unfold the cylinders and planes in the 1-star neighborhood of $\mathbf{P}_k$. This involves sequentially positioning them in the xy-plane. Note that the base curves $\mathbf{X}_{ik}(t)$ for the cylinders $\mathbf{S}_{ik}(t,u)$ result in straight line segments when unfolded, represented as $\mathbf{x}_{ik}(t)$. The rulings $\mathbf{r}_{ik}$ associated with these unfolded line segments are perpendicular to their respective tangents.

To apply the patch-to-cone construction, as described in Section 12.3, we need to determine the positions of the apices $\mathbf{V}_k$ and $\mathbf{v}_k$ that satisfy certain constraints for all cylinders associated with half-edges whose endpoints are $\mathbf{P}_k$.

15.3 Constraints on the Location of the Cone Apices

15.3.1 Valid Surface Patch Combinations and Valid Range

Let us first consider a single cylinder $\mathbf{S}_{ik}(t,u)$. For an apex location $\mathbf{V}_k$ and its 2D counterpart $\mathbf{v}_k$, the denominator and numerator of the length function $l_{ik}(t)$ computed using the patch-to-cone construction for the crease $\mathbf{F}_{ik}(t) = \mathbf{X}_{ik}(t) + l_{ik}(t)\mathbf{R}_{ik}$ and its development, $\mathbf{f}_{ik}(t) = \mathbf{x}_{ik}(t) + l_{ik}(t)\mathbf{r}_{ik}$, have a geometric interpretation that is linked to the valid surface patch combination (discussed in Section 12.3.3) and range of the length function.

Valid surface patch combination

First, we require that the cone apex location is such that the contraction happens on the desired side of the cylinder. Using Lemma 12.3, we require the denominator to be positive, that is,

$$D(t) = (\mathbf{x}_{ik} - \mathbf{v}_k) \cdot \mathbf{r}_{ij} - (\mathbf{X}_{ik}(t) - \mathbf{V}_k) \cdot \mathbf{R}_{ik} > 0.$$

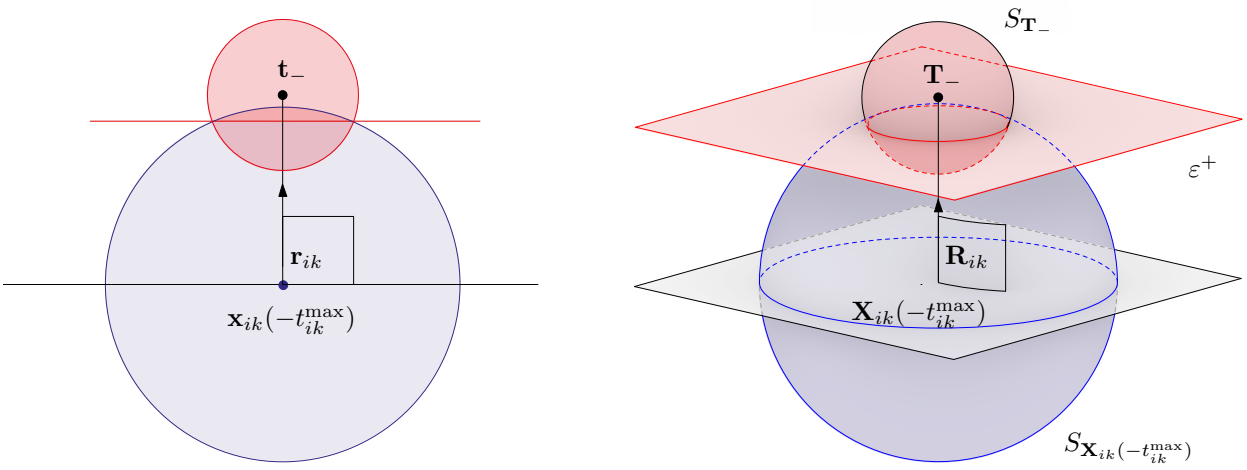

Figure 15.4: Given a developed apex, the desirable region for the spatial apex for $0 \leq l(-t_{ik}^{\max})$ is $S^+_{\mathbf{X}_{ik}(-t_{ik}^{\max})} \cap \varepsilon^+$ and for $0 \leq l(-t_{ik}^{\max}) \leq |\mathbf{x}_{ik}(-t_{ik}^{\max}) - \mathbf{t}_-|$ it is $S^+_{\mathbf{X}_{ik}(-t_{ik}^{\max})} \backslash S^+_{\mathbf{T}_-}$.

Valid range

Recall that we set the base curve at the midpoint of the rounded edge, so $l_{ik}(t) \geq 0$ for all $t \in [-t_{ik}^{\max}, t_{ik}^{\max}]$ ensures that the creases from two incident vertices of a rounded crease will not affect each other. (However, this constraint is not always necessary, as is the case in Figure 15.10.) Furthermore, we want to upper bound the length of the boundary rulings to not exceed the intersection of cylinders around a vertex at the curve's endpoints. In other words, we impose the condition $l_{ik}(\pm t_{ik}^{\max}) \leq m_\pm$, where $m_\pm$ represent the corresponding maximum distances.

Apex locations that result in $l_{ik}(t) \geq 0$. For valid surface patch combinations, the denominator is positive and thus the sign of the length function $l_{ik}(t)$ is determined by the numerator. The numerator is positive, if and only if the distances between the base curve and apex contract after folding, i.e., $l_{ik}(t) \geq 0$ if

$$|\mathbf{v}_k - \mathbf{x}_{ik}(t)|^2 - |\mathbf{V}_k - \mathbf{X}_{ik}(t)|^2 \geq 0.$$

Apex locations that result in $l_{ik}(\pm t_{ik}^{\max}) \leq m_\pm$. We can rewrite the desired inequality as

$$|\mathbf{v}_k - \mathbf{t}_\pm|^2 - |\mathbf{V}_k - \mathbf{T}_\pm|^2 \leq 0,$$

where $\mathbf{t}_\pm = \mathbf{x}(\pm t_{ik}^{\max}) + m_\pm \mathbf{r}_{ik}(\pm t_{ik}^{\max})$ and $\mathbf{T}_\pm = \mathbf{X}(\pm t_{ik}^{\max}) + m_\pm \mathbf{R}_{ik}(\pm t_{ik}^{\max})$[1]. Consequently, the distances between the apices and the upper bounds need to expand during folding to prevent the crease from escaping the intended range at the first and last rulings.

Geometric interpretation

For the purpose of easier explanation, we temporarily position $\mathbf{S}_{ik}(t,u)$ such that $\mathbf{X}_{ik}(t)$ coincides with the xy-plane and $\mathbf{R}_{ik}$ is vertical. Similarly, we position $\mathbf{s}_{ik}(t,u)$ such that $\mathbf{x}_{ik}(t)$ aligns with the x-axis, and $\mathbf{r}_{ik} = (0,1,0)$.

[1]This detail differs slightly from Maleczek et al. [55], where the bound was assumed to be symmetric.

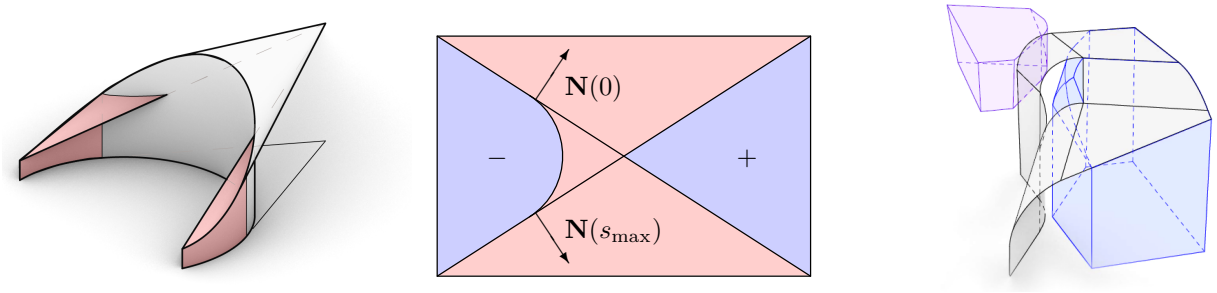

(a) Curved crease with self-intersections and top view of admissible and forbidden regions for the location of the 3D apex (blue and red, respectively) for a given cylindrical patch.

(b) Illustration of the intersection of all admissible regions.

Figure 15.5: Illustration of the considerations to prevent intersecting surfaces.

Given a developed apex $\mathbf{v}_k = (v_x, v_y, 0)$, let $S_{\mathbf{X}_{ik}(t)}$ denote the sphere with center at $\mathbf{X}_{ik}(t)$ and radius $|\mathbf{v}_k - \mathbf{x}_{ik}(t)|$. Additionally, let $S_{\mathbf{T}_\pm}$ denote the spheres with centers at $\mathbf{T}_\pm$ and radii $|\mathbf{v}_k - \mathbf{t}_\pm|$, as illustrated in Figure 15.4. In the following, we refer to the interior of a sphere S is by S^+, and the exterior by S^-.

An apex $\mathbf{V}_k$ satisfies the valid patch condition if it lies in the half-space defined by $\varepsilon^+ : z < v_y$. Furthermore, an apex $\mathbf{V}_k$ satisfies the lower bound $l_{ik}(t) \geq 0$ of the valid range condition if it lies within the spheres $S_{\mathbf{X}_{ik}(t)}$ for all $t \in [-t_{ik}^{\max}, t_{ik}^{\max}]$. In the implementation, we approximate the intersection of the spherical location constraints along the base curve by the intersections of three spheres corresponding to the boundary and center points of the curve, that is, $t = \pm t_{ik}^{\max}$ and $t = 0$.

Lastly, an apex $\mathbf{V}_k$ satisfies the upper bounds of the valid range condition at the first and last rulings if it lies in the regions $S^-_{\mathbf{T}_-}$ and $S^-_{\mathbf{T}_+}$, respectively.

15.3.2 Preventing Self-intersection

In addition to the valid patch and valid range constraints, an improper choice of the apex $\mathbf{V}_k$ can cause intersections between the cylinder and cone as depicted in Figure 15.5. Consider, for example, the construction of a crease curve on a cylinder, whose base curve is a half of a circle, for an apex lying outside the cylinder as in Figure 15.5. As discussed in Section 12.5, directly applying the above-mentioned geometric construction yields a self-intersection of the paper when the ruling emanating from the apex goes past the point of tangency as the crease curve wraps around the cylinder. At the points of tangency, the rulings emanating from the apex transition from the convex to the concave side of the cylinder, and thus the crease assignment changes between mountain and valley while passing through complete 180° folding.

As discussed in Section 12.5, locating such a transition point is equivalent to locating the shade line of the cylinder when we put a point light source at the cone apex. Therefore the target cylinder region needs to be constantly lit or shaded with respect to the light source. Denoting the surface normals of the cylinders along $\mathbf{X}_{ik}(t)$ by $\mathbf{N}(t)$, the *non-intersection condition* reads

$$\begin{aligned}&(\mathbf{V}_k - \mathbf{X}_{ik}(t)) \cdot \mathbf{N}(t) > 0 \text{ for all } t \in [-t_{ik}^{\max}, t_{ik}^{\max}] \text{ or,}\\ &(\mathbf{V}_k - \mathbf{X}_{ik}(t)) \cdot \mathbf{N}(t) < 0 \text{ for all } t \in [-t_{ik}^{\max}, t_{ik}^{\max}].\end{aligned} \tag{15.1}$$

For each rounded crease, this determines the feasible regions for the candidate apex as depicted in Figure 15.5 (right).

Consequently, the regions of admissible points the non-intersection condition are obtained by taking the intersection of admissible regions for all incident rounded edges of an vertex. This is equivalent to taking the apex consistently on the front normal side or back normal side measured from any point on the surface. The existence of such a region depends on the types of vertices as we illustrate in Section 15.3. We potentially get two portions of the solution space on the outside and the inside of the vertex, corresponding to whether a light source constantly illuminates and shades the surface, respectively; see Figure 15.5b. However, when combined with the valid patch condition, at most one of these components is feasible as explained in Section 15.3.4.

15.3.3 Tangent Continuity

In our design, we are rounding edges of polyhedral surfaces with tangent-continuous cylinders. Therefore, we are ultimately interested in crease curves between tangent-continuous combinations of cylinders and planes and cones or triangles, respectively. To prevent possibly undesirable kinks in the crease curve, we require the crease curve to be tangent-continuous in the transitions between every cylinder and plane.

As discussed in Section 12.6.3, there are two cases to consider. If the development of the combination of cylinders and planes has a gap, we need to choose the 2D cone apex to be the center of rotation, which transforms one end ruling to the other end ruling. If on the other hand, if the development is closed, the 2D apex can be freely specified.

15.3.4 Feasible Apex Directions

We characterize the feasible regions for $\mathbf{V}_k$ given by the intersection of constraints for each vertex, namely the valid patch and the non-intersection conditions. We omit the valid range condition because we can move the base curve sufficiently far away from the apex (or appropriately decrease the rounding radii), as we consider each vertex separately. In addition, we focus on a simplified necessary condition for those conditions under an assumption described below, which is also sufficient in the limit case with rounding radius approaching to 0.

Here, we assume that the height to the developed apex position is smaller than or equal the height of the original vertex position, that is,

$$(\mathbf{v}_k - \mathbf{x}_{ik}(t)) \cdot \mathbf{r}_{ik} \leq (\mathbf{P}_k - \mathbf{X}_{ik}(t)) \cdot \mathbf{R}_i, \tag{15.2}$$

for admissible t. We conjecture that the assumption is true for our construction in cases where the vertices are non-developable and exhibit consistent material loss. This is due to the uniqueness of the developed apex positions, which are derived from the tangent continuity constraint (as described in Section 15.3.3) in combination with the material loss considerations (as explained in Section 15.5).

Valid patch conditions. It follows from the assumption in Equation (15.2) that the intersection of the valid patch conditions,

$$0 < (\mathbf{v}_k - \mathbf{x}_{ik}(t)) \cdot \mathbf{r}_{ik} - (\mathbf{V}_k - \mathbf{X}_{ik}(t)) \cdot \mathbf{R}_{ik},$$

is contained in

$$0 < (\mathbf{P}_k - \mathbf{X}_{ik}(t)) \cdot \mathbf{R}_{ik} - (\mathbf{V}_k - \mathbf{X}_{ik}(t)) \cdot \mathbf{R}_{ik} = (\mathbf{P}_k - \mathbf{V}_k) \cdot \mathbf{R}_{ik}.$$

Using $\mathbf{D} := \mathbf{V}_k - \mathbf{P}_k$, the condition is represented as

$$\mathbf{D} \cdot (-\mathbf{R}_{ik}) > 0. \tag{15.3}$$

Finding a vector $\mathbf{D}$ that satisfies Equation (15.3) is equivalent to finding a plane of normal $\mathbf{D}$ passing through $\mathbf{P}_k$ such that all adjacent faces lie on one side of this plane. An important consequence is that the construction does not work for *saddle* vertices, that is, a vertex without such a plane. Note that while the sum of incident face angles of a saddle vertex is at least 2π and thus has negative integral curvature, not all negative vertices are saddles. For example, consider a negative vertex corrugated to approximate a convex vertex. In addition, since a developable vertex, that is, a vertex whose sum of sector angles is 2π, folds to a half plane either by popping up or down as shown in Abel et al. [1], it is always possible to find a direction $\mathbf{D}$ satisfying Equation (15.3).

Non-intersection approximations. In addition, we sample the non-intersection conditions given by Equation (15.1) at the extrema $s = 0$ for each edge, where the surface normal equals the face normal $\mathbf{N}_{i,j}$ between edges i and j adjacent to the same face. Because the corresponding end point of $\mathbf{X}_{ij}(t)$ and $\mathbf{P}_k$ are both on face i, j, Equation (15.1) yields

$$\mathbf{D} \cdot \sigma\mathbf{N}_{i,j} > 0 \text{ for all } i, j, \tag{15.4}$$

for either $\sigma = \pm 1$. Note that at most one of the signs σ can be satisfied. The half-plane discussion corresponding to Equation (15.3) predicts the correct candidate of σ as follows. Consider the solid angle Ω of the vertex $\mathbf{P}_k$ on M on the front side defined by $\mathbf{N}_i$, then the back side has solid angle of $4\pi - \Omega$. Because of the half-plane property, the solid angle of the vertex on $\mathbf{D}$ side needs to be smaller than 2π. So, we choose $\sigma = 1$ if $\Omega < 2\pi$, and $\sigma = -1$ if $\Omega > 2\pi$.

We call the direction $\mathbf{D}$ computed from both Equation (15.3) and Equation (15.4) the *vertex normal* (Figure 15.6). In Section 15.4.1, we start our computation by constructing the normal from given edge directions and face normals. Once a valid normal is found, the vector can be arbitrarily scaled to find other candidates for apex positions. Because the effect of rounding becomes relatively small by scaling up the vector, there is a sufficiently distant position of apex along the normal that creates a valid folding.

15.4 Locating Cone Apices Through Optimization

For every interior vertex $\mathbf{P}_k$ of the mesh, we solve an optimization problem to find the location of

- the apex $\mathbf{V}_k$, if the development is open, or
- the apices $\mathbf{V}_k$ and $\mathbf{v}_k$, if the development is closed,

that fold the incident cylinders and planes along tangent-continuous curves into cones and triangles. We implement the constraints collected in Section 15.3 to avoid invalid surface patch combinations and intersections.

15.4.1 Vertex Normals

Before we start the optimization, we determine a normal direction $\mathbf{D}$ of the vertex as explained in Section 15.3.4 through optimization; we later locate the initial apex on the computed normal. We find directions satisfying Equation (15.3) and Equation (15.4) by maximizing the minimum dot product of a unit vector with the adjacent edge directions $-\mathbf{R}_{ik}$ and face normal directions $\sigma\mathbf{N}_{ij}$.

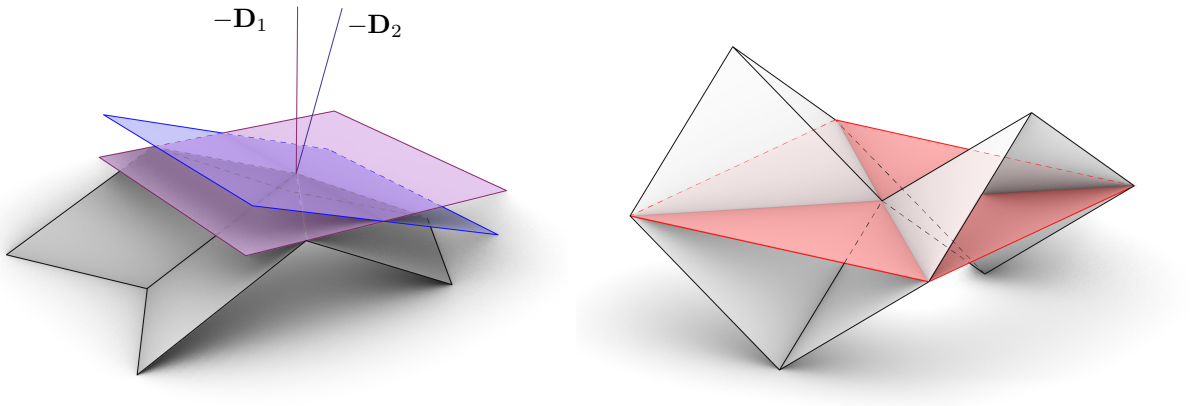

(a) Non-saddle vertex. While the average $\mathbf{D}_1$ of face normals does not satisfy Equation (15.3), $\mathbf{D}_2$ is a valid vertex normal.

(b) Saddle vertex.

Figure 15.6: Illustration of the constraint for valid patch combinations.

Variables: The variables are the three coordinates of the vertex normal and a scalar b which is going to be the lower bound that we maximize.

Equality constraint: To prevent unboundedness of variables, we keep $\mathbf{D} \cdot \mathbf{D} = 1$.

Inequality constraint: We bound $\mathbf{D} \cdot \mathbf{R}_{ik} \geq b$ and $\mathbf{D} \cdot (\sigma \mathbf{N}_{ij}) \geq b$ for every adjacent edge and face.

Objective: We maximize the lower bound b.

Initialization: As an initial guess, we take the normalized mean over all edge directions and oriented face normals.

15.4.2 Optimization Setup

To locate the apices, we solve a non-linearly constrained optimization problem. We use hard inequality constraints given from Section 15.3 and minimize the objective function to achieve regularity. Specifically, we sample the quadratic inequality constraints resulting from the valid range condition, by evaluating the base curve at sampled points, e.g., at the beginning, middle and end of a cylindrical arc. For every incoming edge, we let $\mathbf{X}_{ik}(t_0)$, $\mathbf{X}_{ik}(t_1)$ and $\mathbf{X}_{ik}(t_2)$ denote the points on the central circle of the cylinder corresponding to the start, middle and end parameters, and $\mathbf{x}_{ik}(t_0)$, $\mathbf{x}_{ik}(t_1)$ and $\mathbf{x}_{ik}(t_2)$ denote their developed locations. Let furthermore $\mathbf{T}_{\pm}$ be the intersection at the start and end parameter of the cylinder with the neighboring cylinder and $\mathbf{R}_{ik}$ the ruling direction towards the vertex. The corresponding developments are again indicated by lower cases.

Variables: The variables are the three coordinates of $\mathbf{V}_k$ and the two coordinates of $\mathbf{v}_k$ if the development is closed.

Inequality constraints: For every adjacent edge, we add five quadratic and two linear inequality constraints, namely:

- We require that the developed height of the cone apex $\mathbf{v}_k$ to with respect to the base plane of the cylinder is larger than the corresponding distance in 3D. As all profile curve points lie in the base plane, we can enforce this constraint by specifically applying it to $t = 0$ only. In other words, we require

$$(\mathbf{V}_k - \mathbf{X}_{ik}(0)) \cdot \mathbf{R}_{ik} \leq (\mathbf{v}_k - \mathbf{x}_{ik}(0)) \cdot \mathbf{r}_{ik}.$$

- We require that the current combination for $(\mathbf{V}_k, \mathbf{v}_k)$ lies in the respective spheres $S^+(t_i)$ at the three parameter values, i.e.,

$$|\mathbf{V}_k - \mathbf{X}_{ik}(t_j)|^2 \leq |\mathbf{v}_k - \mathbf{x}_{ik}(t_j)|^2 \qquad \text{for } j \in \{0, 1, 2\}.$$

- We require that the lengths do not exceed the distance between the base point to the intersection of cylinders, i.e., $l_{ik}(t_j) \leq |\mathbf{T}_\pm - \mathbf{X}_{ik}(t_j)|$ for $j \in \{0, 2\}$, or equivalently,

$$|\mathbf{v}_k - \mathbf{t}_\pm|^2 \leq |\mathbf{V}_k - \mathbf{T}_\pm|^2 .$$

- We linearize the rounding depicted in Figure 15.5 by a plane through $\mathbf{X}(t_0)$ or $\mathbf{X}(t_2)$ and $\mathbf{T}_-$ or $\mathbf{T}_+$. We believe that this is not too constraining as candidates close to the cylinders are not very desirable. This yields

$$(\mathbf{V}_k - \mathbf{T}_-) \cdot \sigma \mathbf{N}_e > 0 \quad \text{where} \quad \mathbf{N}_e = \frac{(\mathbf{X}_{ik}(t_2) - \mathbf{X}_{ij}(t_0)) \times (\mathbf{T}_- - \mathbf{X}_{ik}(t_0))}{|(\mathbf{X}_{ik}(t_2) - \mathbf{X}_{ik}(t_0)) \times (\mathbf{T}_- - \mathbf{X}_{ik}(t_0))|}.$$

Furthermore, for every adjacent face, we want the vertex to lie on the correct side of the faces to ensure non-intersections as described in 15.3.2. This amounts in

$$(\mathbf{V}_k - \mathbf{T}_\pm) \cdot \mathbf{N}_{ij} > 0,$$

where $\mathbf{T}_+$ or $\mathbf{T}_-$ is the corresponding is the intersection of cylinders in the current face.

Initialization: We initialize the the spatial apex $\mathbf{V}_k$ as $\mathbf{V}_{\text{ini}} = \mathbf{V}_k + d\mathbf{D}$ on the vertex normal, where $d > 0$ is the user-specified *depth* along the vertex normal. If the development is closed, we initialize $\mathbf{v}_k$ as the intersection $\mathbf{v}_{\text{ini}}$ of the central rulings of two consecutive developed cylinders.

Objective: We use the objective for regularization. Depending whether the development is open or closed, we minimize

$$\min_{\mathbf{V}_k} (\mathbf{V}_k - \mathbf{V}_{\text{ini}})^2 \qquad \text{or} \qquad \min_{(\mathbf{V}_k, \mathbf{v}_k)} (\mathbf{V}_k - \mathbf{V}_{\text{ini}})^2 + (\mathbf{v}_k - \mathbf{v}_{\text{ini}})^2 .$$

This objective function tries keep the original depth d; Figure 15.2b shows the same rounding using another initial vertex depth.

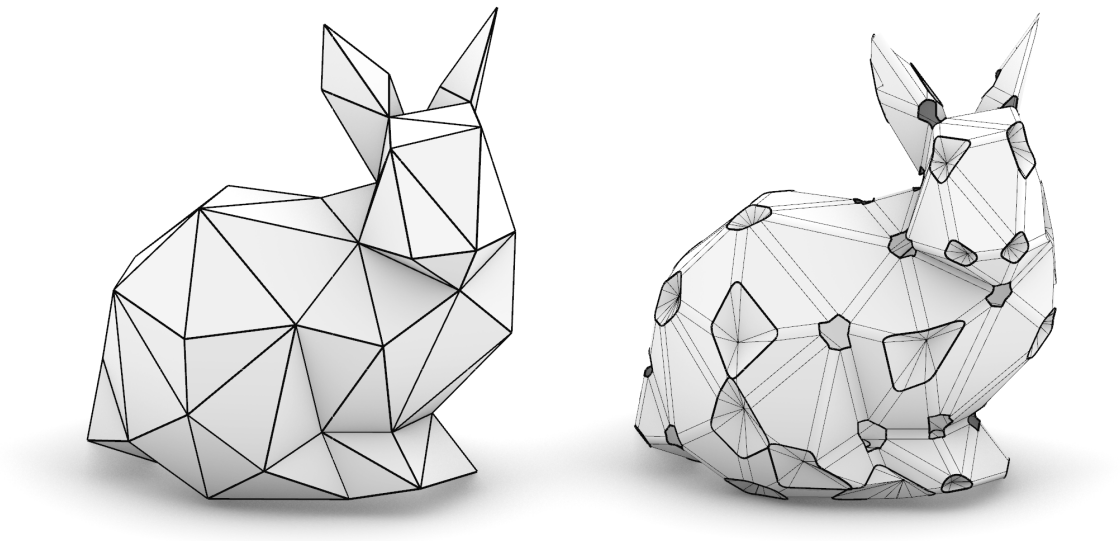

Figure 15.7: Edge-rounded low-poly Stanford bunny computed with our Grasshopper component. Notice that only non-saddle shaped vertices can connected to cones with curved creases.

15.5 Consistent Material Loss

Through edge rounding, the intrinsic distance between adjacent faces on a polyhedral surface decreases. As a result, the target polyhedral surface can be visualized as the folding of a "shrunk" version of the original surface. However, it is crucial to ensure that a consistent "shrunk" paper can be defined. This consistency is disrupted if the material loss around each rounded edge adjacent to a vertex is not uniform. When there is arbitrary material loss, the original sheet of paper loses its consistent disk topology, resulting in a non-fillable hole around the vertex.

In this section, our goal is to determine a consistent material loss that enables the "shrunk" polyhedral paper to fold into the desired rounded and curved-creased shape without requiring any cuts. This consistency is particularly important when the target polyhedral surface is initially a developable surface, such as an origami tessellation, as it allows the entire shape to be created by folding a single sheet of paper while preserving its developability.

15.5.1 Material Loss

First, we compute the material loss when rounding an edge with a right circular cylinder; see Figure 15.8a. Let us denote the half angle between the adjacent surface normals by γ and the radius of rounding by r. Then the length a of the rounded edge and the original length A can be expressed as

$$a = 2r\gamma \quad \text{and} \quad A = 2r\tan\gamma.$$

We call $w = A - a$ the *material loss* induced by rounding an edge. In the following process, we first compute a consistent amount of material loss, which conversely, determines the radius of rounding. For given w and γ, the remaining quantities read

$$a = \frac{w\gamma}{\tan\gamma - \gamma}, \qquad A = \frac{w\tan\gamma}{\tan\gamma - \gamma}, \qquad r = \frac{w}{2(\tan\gamma - \gamma)}.$$

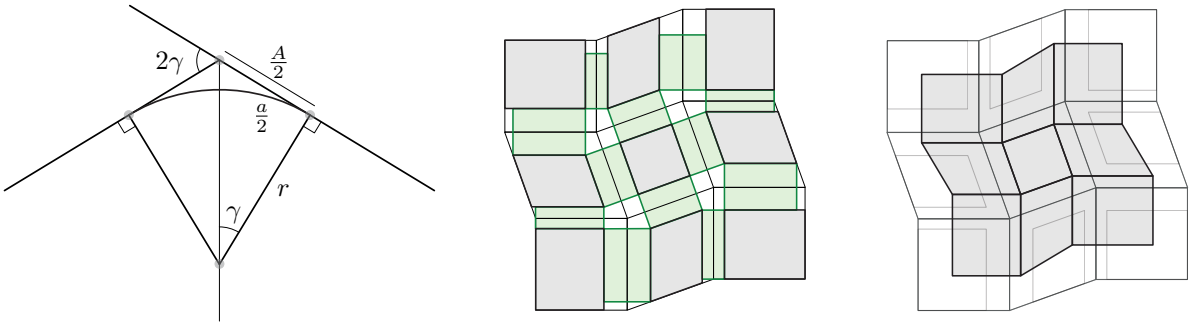

(a) Illustration of the material loss induced by rounding an edge.

(b) Developable tessellation with contracting cycles and regions before and after contraction.

Figure 15.8: Illustrations highlighting considerations to achieve consistent material loss during the edge-rounding step.

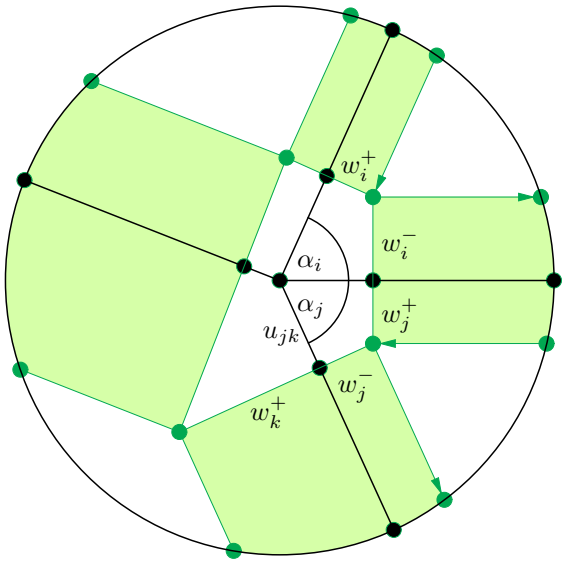

Figure 15.9: Illustration showcasing the notation used for constraints at a vertex.

15.5.2 Consistency Condition

The central concept is as follows: Imagine walking on the surface around a vertex in a direction perpendicular to the adjacent edges, covering a distance equal to the material loss. For the contracted distances to result in consistent material loss, our objective is to return to the same starting point; see Figure 15.8b. This forms a closed polygonal cycle around each vertex. For each polyhedral edge, we can draw a rectangular region (colored green in Figure 15.8b) between the corresponding congruent edge of the cycles on both ends. The material loss is equivalent to contracting these cycles to points and rectangles to segments, where points and segments correspond to vertices and edges of polyhedral sheet of paper that is then folded to a curved-crease folding.

If the original polyhedron is developable, the process of constructing such polygonal cycles perpendicular to the edges of the polyhedral surface is analogous to creating a reciprocal diagram

on the polyhedral development. Specifically, the edge graph must form a *spiderweb* configuration, that is, a reciprocal diagram with positive edge lengths.

15.5.3 Optimization Setup

The consistent material loss is given as the following linear programming problem.

Variables: We identify the contracting regions by determining cycles around each vertex, as illustrated in Figure 15.9. In each sector, the corner of a cycle can be represented by the perpendicular distances w_i^- and w_i^+ to the incident edges.

For interior edges connecting sectors i and j, the variables w_i^- and w_j^+ represent the material loss on the respective sides of the edges, contributing to the overall material loss of the edge $w = w_i^- + w_j^+$. We adopt the notation based on the half-edge data structure, where w_i^+ corresponds to the incoming adjacent oriented edge and w_i^- corresponds to the outgoing adjacent edge associated with a sector angle α_i of a vertex.

Additionally, we introduce a variable b as a lower bound that we aim to maximize.

Linear equality constraints: Along every vertex, the perpendicular widths should close up. For every adjacent face, we set the widths u_{ij} along the quad to be the same, see Figure 15.9. This results in the linear equality constraint

$$\left(w_i^+ + w_i^- \cos\alpha_i\right) \frac{1}{\sin\alpha_i} = \left(w_j^- + w_j^+ \cos\alpha_j\right) \frac{1}{\sin\alpha_j}.$$

Linear inequality constraints: Before we start the optimization problem, we compute the maximal rounding width for every edge and upper bound the sum of the widths of two opposite half edges by this maximal rounding loss. Furthermore, we require the widths $w_i > b$.

Objective function: We maximize b subject to the above constraints. The solution is feasible, if $b > 0$.

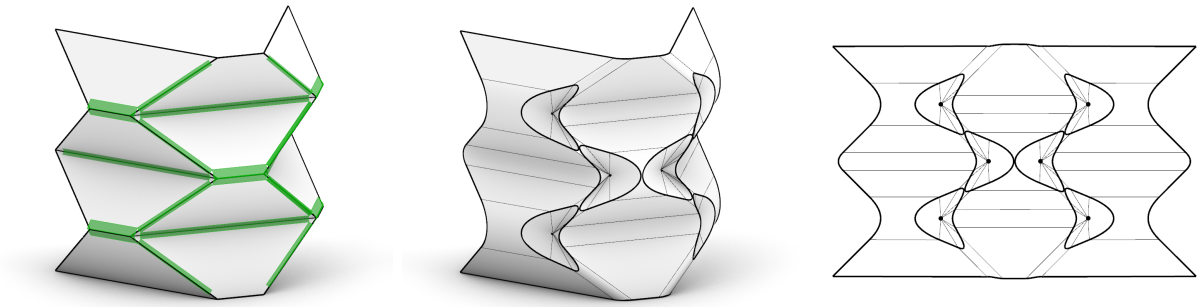

(a) Computed material loss. (b) Computed developable edge-rounded shape. (c) Development.

Figure 15.10: Developable edge-rounded chicken wire tesselation.

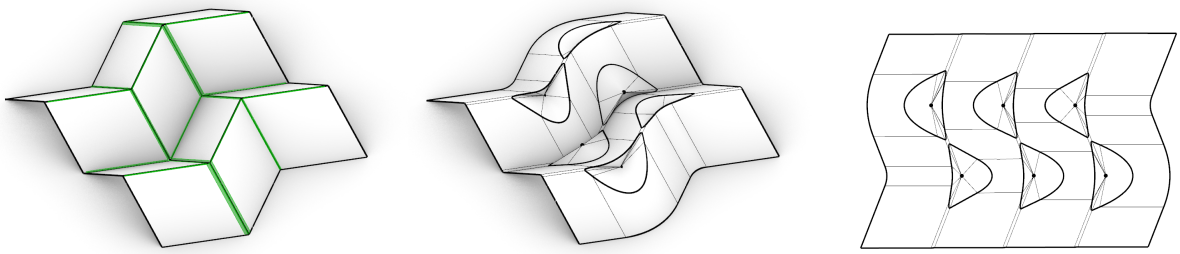

(a) Computed material loss.

(b) Computed developable edge-rounded shape.

(c) Development.

Figure 15.11: Developable edge-rounded Miura-ori tessellation. Note how the cylinder radii decrease or increase in one direction, limiting the number of possible rows.

15.6 Conical Convex Mesh

In the special case of conical convex meshes, we can construct the consistent material loss along vertices and location of apices, see Figure 15.12.

Conical meshes are characterized by having faces tangent to a cone of revolution whose axis is the intersection of the bisectors of two neighboring faces. This in particular implies, that conical meshes have a family of constant face offsets whose vertices lie on the axes of the tangent cones. We use the offset mesh to construct the consistent material loss and the axis as the vertex normal to locate the apex.

Suppose we fix an offset distance and project the faces perpendicular to the original faces. Then, this locates the contracting regions, from which we compute the rounding applied to the original mesh, so the offset mesh is the piece of paper we fold.

For this material loss, we find good candidates for apices on the axis. By the tangent continuity condition, the developed apex corresponds to the vertex of the offset mesh. If we intersect the common lines of the cone and the offset faces with a plane perpendicular to its axis, we find that the intersection points $\mathbf{p}_i$ lie on a circle of radius r with center on the axis. If this plane is sufficiently far away from the apex, we can find a point on the axis whose distance to the corresponding points $\mathbf{P}_i$ on the original surface is again r.

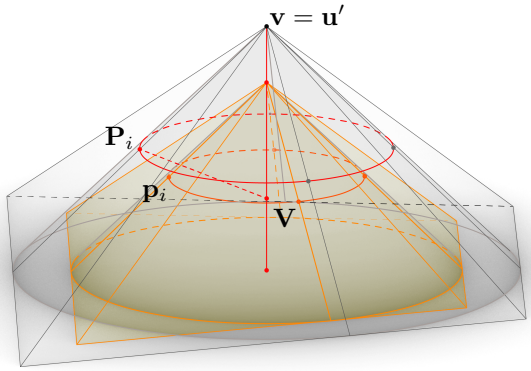

Figure 15.12: Illustration of the construction of consistent material loss and apex location.

Figure 15.13: Variation of the edge-rounded icosahedron in Figure 15.1, crafted from oak veneer, in collaboration with Alfonso Parra Rubio and other participants of Haystack Labs 2023.

15.7 Design Examples, Limitations, and Future Work

We implemented our construction method as a component for Grasshopper / Rhino [81, 57] to create an interactive design system. The user specifies the input mesh, the preferred rounding radii, preferred depth of apex, which are used as the initial conditions for the optimization. We implemented the component in C# using *ALGLIB* [10] for optimization using Augmented Lagrangian (AUL). Furthermore, we used the half-edge data structure of *Plankton* [73] for mesh operations.

Figure 15.7 illustrates the application of the method to a low-resolution version of the Stanford bunny. Note that at the saddle points, it is not possible to locate the normal and thus the apices as described in Section 15.3.4.

Figure 15.10 showcases a developable curved folded origami, which was computed from a folded shape of the chicken-wire tessellation. It is worth highlighting that there is a noticeable difference between the rounding radii in this case. Exploring the impact of material loss and investigating additional heuristics the optimized material loss could be beneficial in future research.

Figure 15.11 exhibits another developable curved folded origami, which was computed from a folded shape of a part of the Miura-ori origami tessellation. In addition to significant differences in rounding radii, it is notable that the rounding radii decrease in one direction, potentially hindering rounding additional columns of the pattern. One possible solution could involve working with cone-rounded edges. Again, this remains a topic for future investigation.

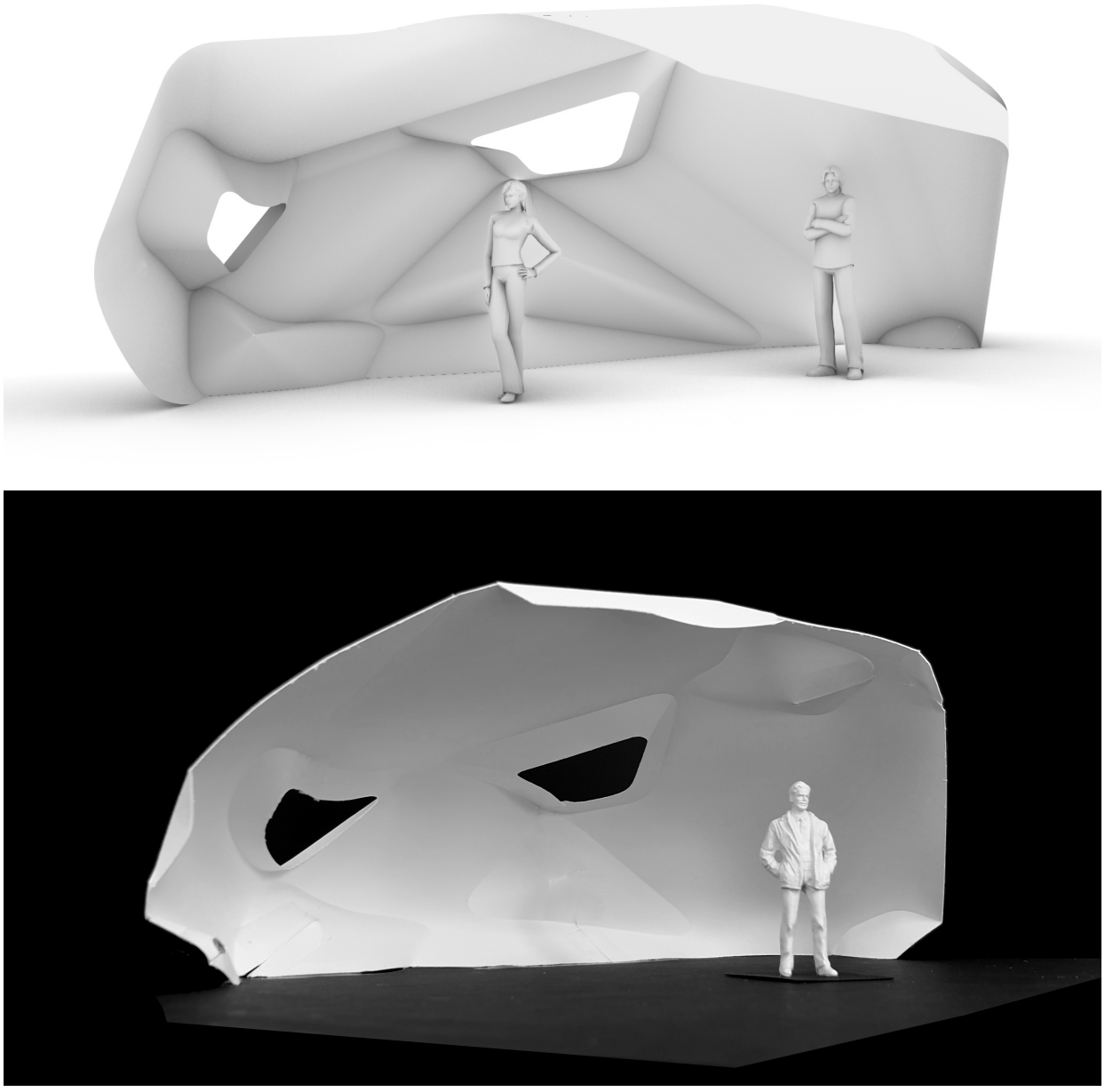

Figure 15.14: Curved origami based shell structure and folded model.

Chapter 16

Wrinkling Paper

This chapter presents results from the paper titled "From Quad Filling to Wrinkled Surfaces" that the thesis author coauthored with Robby Kraft, Rupert Maleczek, and Tomohiro Tachi. This paper has been accepted to the Advances of Architectural Geometry Conference (AAG) [46], 2023.

Overview

Inspired by David Huffman's curved-crease lens tessellations, we present an approach for transforming polyhedral shapes into modular smooth or discretized curved-crease designs. Specifically, we use two types of molecules, the lens and the cone-cone molecule, to fill the faces of a non-planar quad mesh. Furthermore, we investigate techniques for optimizing the target shape to achieve a global origami development, eliminating the need for additional slits or holes.

16.1 Introduction

David Huffman's design collection [19] features a variety of captivating designs, including curved-crease tessellations. Among these tessellations, one notable example is Huffman's creation that incorporates repeated horizontal lenses formed by circular arcs. Demaine et al. [17] further explore and analyze a generalized version of these curved-crease lens tessellations. Their research demonstrates the existence of such tessellations for convex curved-crease lenses. Within their investigations, the authors identify individual quadrangular kite molecules composed of cylinders and cones.

Subsequent work by Stern et al. [94] explores architectural applications of a freeform assembly using these kites as molecules. Building upon their work, we further extend the research by using the patch-to-cone construction to fill non-planar quadrangular faces of a polyhedron with two types of quadrangular molecules: the lens molecule and the cone-cone molecule; see Figure 16.1. Our contribution includes the development of a plug-in for Grasshopper/Rhino [81, 57], which enables users to customize these molecules using multiple parameters. The individual molecules possess polygonal boundaries and consist of either two cones or a cylinder and two cones, pairwise joined along creases. In both cases, the cylinders or cones can be smooth or discrete. In addition, we demonstrate constraints for the generation of globally developable freeform tessellated shapes.

This chapter is organized as follows. In Section 16.2, we show how to fill a quadrangular face with two curved-crease designs: the cone-cone and the lens. We then propose a subdivision scheme to prepare an arbitrary mesh for our surface-filling algorithm in Section 16.3. Finally, we explain how to optimize towards global development without holes in Section 16.4.

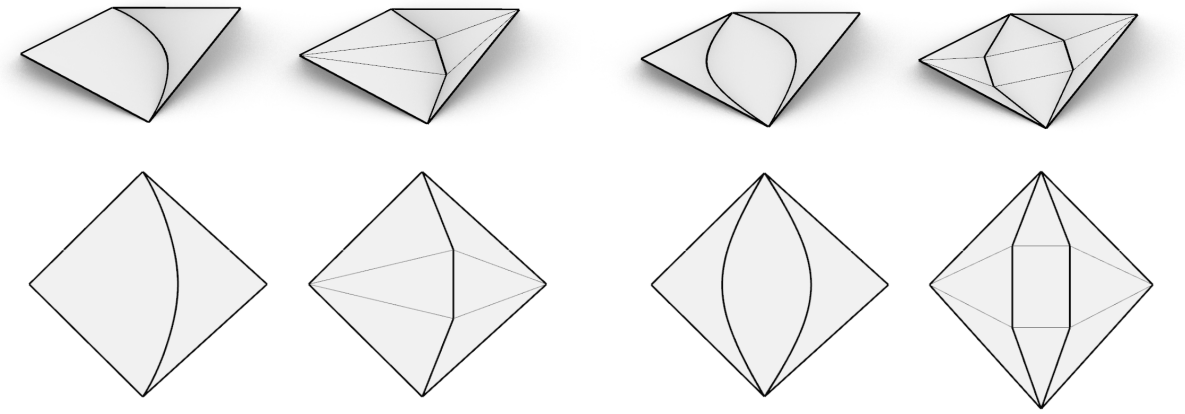

(a) Smooth and discrete cone-cone molecule.

(b) Smooth and discrete lens molecule.

Figure 16.1: Illustration of the two molecule types suitable for filling a non-planar quad.

16.2 Quad Filling

In this section, we show how to fill a single non-planar quad $Q = \{\mathbf{V}_1, \mathbf{V}_2, \mathbf{V}_3, \mathbf{V}_4\}$ with a (smooth or discrete) curved-crease design. In particular, we consider two developable surface layouts (see Figure 16.2):

- *Cone-cone:* A smooth or discrete cone with apex $\mathbf{V}_1$ and rulings $\mathbf{V}_1\mathbf{V}_2$ and $\mathbf{V}_1\mathbf{V}_4$ is folded into a cone with apex $\mathbf{V}_3$ such that the crease passes through the points $\mathbf{V}_2$ and $\mathbf{V}_4$.
- *Lens:* A smooth or discrete central cylinder is folded into two cones with apices $\mathbf{V}_1$ and $\mathbf{V}_3$ such that both creases between the cylinder and the cone pass through points $\mathbf{V}_2$ and $\mathbf{V}_4$.

In both cases, our method consists of two steps:

1. *Construct first surface:* First, we construct a smooth or discrete cylindrical or conical surface $\mathbf{S}(t, u)$ inside the quad. A curve which defines the shape of this surface and further parameters can be specified by the user. Details are provided in Section 16.2.1.
2. *Construct remaining surface(s):* Then, we construct the fold between $\mathbf{S}(t, u)$ and a cone with apex $\mathbf{V}_4$ (cone-cone), or two cones with apices $\mathbf{V}_1$ and $\mathbf{V}_4$ (lens). Details are provided in Section 16.2.4.

16.2.1 Construction of the First Surface

Intuitively, we obtain the first surface $\mathbf{S}(t, u)$ by extruding a not self-intersecting smooth or discrete planar curve $\mathbf{P}(t)$ with start point $\mathbf{V}_2$ and end point $\mathbf{V}_4$. In the following, we will call $\mathbf{P}(t)$ the *base curve*. In particular, when constructing a cone, $\mathbf{P}(t)$ is extruded to the point $\mathbf{V}_1$. When constructing a cylinder, $\mathbf{P}(t)$ is extruded in the direction that is perpendicular to the curve's incident plane. The resulting surface can therefore be parametrized as

$$\mathbf{S}(t, u) = \mathbf{X}(t) + u\mathbf{R}(t),$$

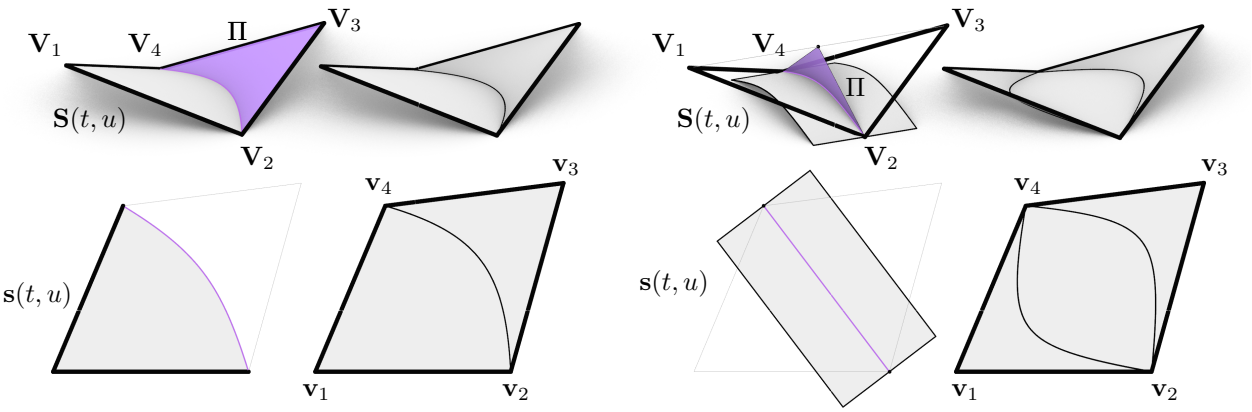

Figure 16.2: Two steps of the quad filling method for the cone-cone molecule (left) and the lens molecule (right).

where in case of a cone we set $\mathbf{X}(t) = \mathbf{V}_1$ and $\mathbf{R}(t) = \frac{\mathbf{P}(t)-\mathbf{V}_1}{|\mathbf{P}(t)-\mathbf{V}_1|}$, and in case of a cylinder we set $\mathbf{X}(t) = \mathbf{P}(t)$ and $\mathbf{R}$ to be the normalized vector perpendicular to Π.

The choice of $\mathbf{P}(t)$ influences not only the shape of the first surface $\mathbf{S}(t, u)$, but also the shape of the second, constructed cone $\mathbf{S}_2(t, u)$ that connects to $\mathbf{S}(t, u)$ with a curved crease. When choosing the planar curve $\mathbf{P}(t)$ arbitrarily, we might observe some undesired artifacts, such as local self-intersections of $\mathbf{S}_2(t, u)$; see Figure 16.3 (left).

In the following, we discuss how to apply the theory of Section 12.5 to modify a user-specified input curve $\mathbf{Q}(t)$ using projective transformations.

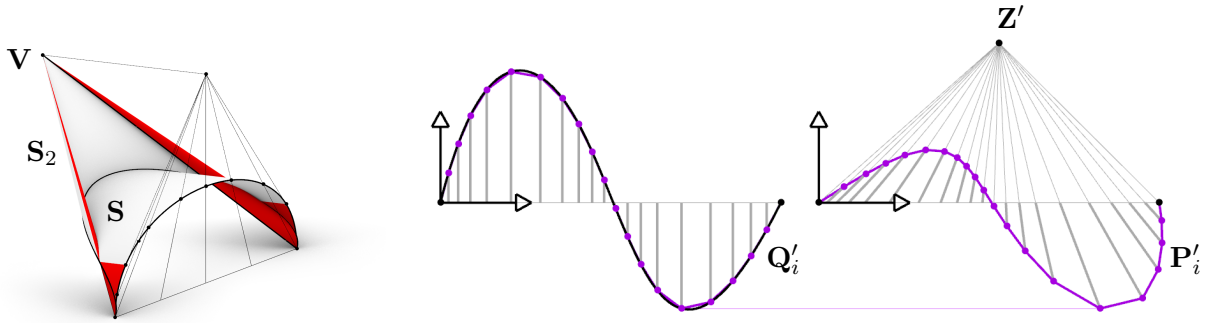

(a) Intersecting surfaces.

(b) Projective mapping used for the construction of the base curve of the first surface.

Figure 16.3: Illustration highlighting considerations to avoid creating intersecting surfaces.

16.2.2 Non-Self-Intersecting Cones and Central Functions

Suppose we aim to determine the fold between a developable surface $\mathbf{S}(t, u)$ and a cone with apex $\mathbf{V}$. As discussed in Section 12.5, the ruling planes form a pencil of planes T. If $\mathbf{S}(t, u)$ is a conical surface with apex $\mathbf{V}_1$, the family of planes constitutes a pencil of planes with the axis $\mathbf{V}_1\mathbf{V}$. On the other hand, if $\mathbf{S}(t, u)$ is a cylindrical surface with a ruling direction $\mathbf{R}$, the family of planes is a pencil of planes with its axis passing through $\mathbf{V}$ and having the direction $\mathbf{R}$.

Since the rulings continuously vary along $\mathbf{S}(t, u)$, the planes in the pencil also vary. To avoid self-intersections of the second surface, it is crucial that all planes in the pencil are distinct and

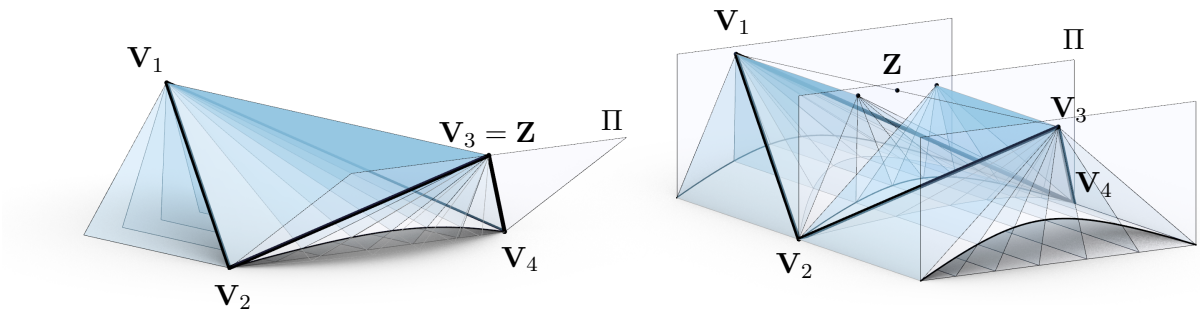

Figure 16.4: Illustration of the pencil of ruling planes used in the argumentation in Section 16.2.2 for the cone-cone molecule (left) and lens molecule (right).

do not "double back", as illustrated in Figure 16.3 (left). To check for repeating ruling planes, we consider a planar section of the pencil of planes using a plane Π that passes through $\mathbf{V}$ and intersects all surfaces at least once. If all intersecting lines of $\Pi \cap T$ are unique, the planes in the pencil are also unique.

Consequently, when locating the base curve $\mathbf{P}(t)$, our objective is to induce non-repeating planes, resulting in a curve that has unique connecting lines with the apex. In the following, we refer to such a curve as a *central function*[1]. To obtain a central function with center $\mathbf{Z}$, we can transform the graph of a function using a projective transformation that maps the ideal point of the y-axis to the center $\mathbf{Z}$, as depicted in Figure 16.3 (right).

In case of the cone-cone design, we construct the first surface $\mathbf{S}(t, u)$ such that its base curve is a $\mathbf{V}_3$-central function. In case of a lens design, we determine the fold between the cylinder and two cones on either side. Thus we would need a central function with respect to two centers (the orthogonal projections of $\mathbf{V}_1$ and $\mathbf{V}_3$ on Π). If the orthogonal projections are not the same, we observed in our experiments that it is usually sufficient to approximate this "doubly-central" function by a $\mathbf{Z}$-central function, where $\mathbf{Z}$ is the intersection of the line spanned by $\mathbf{V}_1$ and $\mathbf{V}_3$ with Π.

16.2.3 Surface Fitting

On a high level, the construction of the first conical or cylindrical surface involves locating a plane Π and constructing an appropriate central base curve $\mathbf{P}(t) \in \Pi$ that resembles the shape of a given input curve.

In addition to the coordinates of the 3D quad, the input for the surface fitting includes:

- A *shape-defining curve*, that is a curve $\mathbf{Q}(t) = (t, f(t), 0)$ where $f(t)$ is a function with $f(0) = f(1) = 0$.
- A scale parameter s.
- When constructing the lens design, an additional parameter ϕ that influences the orientation of Π.

Although the following operations can be performed analytically, we explain the following in terms of our implementation using a sampling of the input curve. Our proposed algorithm works as follows, see Figure 16.5:

[1]This terminology is based on the concept of "common" 2D functions, which are central functions with respect to the point at infinity of the z-axis.

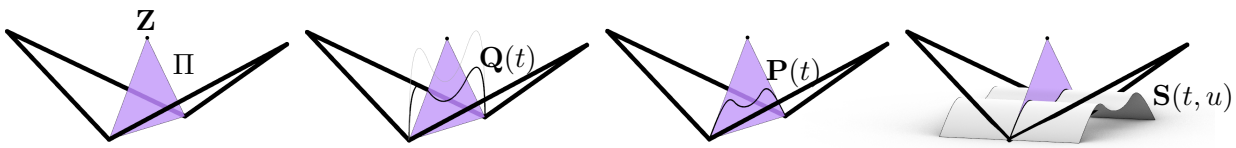

Figure 16.5: Surface fitting. Illustration of the construction steps 1(a) – 1(d).

(a) *Locate plane* Π*:* For a given 3D quad, we define the design-dependent base plane Π. In case of a cone, let Π be the plane containing the points $\mathbf{V}_2$, $\mathbf{V}_3$ and $\mathbf{V}_4$. In case of a cylinder, let Π be a plane containing $\mathbf{V}_2$ and $\mathbf{V}_4$, whose orientation can be influenced by a parameter ϕ (the rotation about $\mathbf{V}_2\mathbf{V}_4$). In both cases, let $\mathbf{V}$ be the intersection of Π with the line spanned by $\mathbf{V}_1$ and $\mathbf{V}_3$ (in the cone design, $\mathbf{Z} = \mathbf{V}_3$).

(b) *Scale and orient* $\mathbf{Q}(t)$*:* We scale the user defined curve so that the distance between its endpoints equals $|\mathbf{V}_2 - \mathbf{V}_4|$. In addition, we scale the curve in y-direction by the user-specified parameter s. Finally, we move the curve from the xy-plane to Π, such that $\mathbf{Q}(0) = \mathbf{V}_2$ and $\mathbf{Q}(1) = \mathbf{V}_4$, such that $\mathbf{Z}$ lies in the $y > 0$ half-plane. Note that the resulting polyline might not be $\mathbf{Z}$-central and thus not suitable for the fold construction without self-intersections.

(c) *Projective transformation:* We apply a projective mapping to transform $\mathbf{Q}(t)$ into a $\mathbf{Z}$-central function. In the following, we use a local 2D coordinate system where $\mathbf{V}_2$ corresponds to the origin, $\mathbf{V}_4 - \mathbf{V}_2$ to the x-axis, and $\mathbf{Z}$ lies on the half-plane with $y > 0$. Let $\mathbf{Z}'$ denote the coordinates of $\mathbf{Z}$ in this local coordinate system. Moreover, let $\mathcal{Q}' = (\mathbf{Q}'_1, \mathbf{Q}'_2, \ldots, \mathbf{Q}'_n)$ be a sampling of curve $\mathbf{Q}(t)$ in this local coordinate system (if the curve is a polyline, let $\mathcal{Q}$ contain its vertices). We use the following projective transformation to turn $\mathcal{Q}'$ in a $\mathbf{Z}'$-central polyline $\mathcal{P}' = (\mathbf{P}'_1, \mathbf{P}'_2, \ldots, \mathbf{P}'_n)$, that is,

$$(\mathbf{Q}'_x, \mathbf{Q}'_y) \mapsto \mathbf{P}' = \left(\frac{k\mathbf{Q}'_x + \mathbf{Z}'_x\mathbf{Q}'_x}{k + \mathbf{Q}'_y}, \frac{\mathbf{Z}'_y\mathbf{Q}'_y}{k + \mathbf{Q}'_y} \right) \quad \text{where} \quad k = \mathbf{Z}'_y - \min_i \mathbf{Q}'_{i,y}.$$

Note that because of the choice of k, the points are bounded. In particular, the lowest y-coordinate of $\mathbf{P}'_i$ is the lowest y-coordinate of

(d) Finally, depending on the application, we can either smoothly or linearly interpolate the points of $\mathcal{P}$ to obtain $\mathbf{X}(t)$ (in world-coordinates) and construct the design-dependent initial surface $\mathbf{S}(t, u)$.

16.2.4 Construction of the Remaining Surface(s)

Lastly, we employ the patch-to-cone method, as described in Lemma 12.1, to determine the location of the crease between the constructed patch $\mathbf{S}(t, u)$ and a cone with apex $\mathbf{V}_3$. This is achieved by utilizing the user-input 3pt, to ensure that $\mathbf{V}_2$ and $\mathbf{V}_4$ lie on the crease.

When creating a lens molecule, we calculate an additional crease that connects the cylindrical patch $\mathbf{S}(t, u)$ with a cone having apex $\mathbf{V}_1$. This is done using the user-input 3pt to ensure that the crease is incident with $\mathbf{V}_2$ and $\mathbf{V}_4$.

As discussed in Section 12.3 in more detail, a "good" crease point connecting a developable surface patch and a cone has the following characteristics:

- *Valid patch combination:* The computed crease separates a the given developable surface and the constructed cone into four surface patches. Out of the four possible combinations,

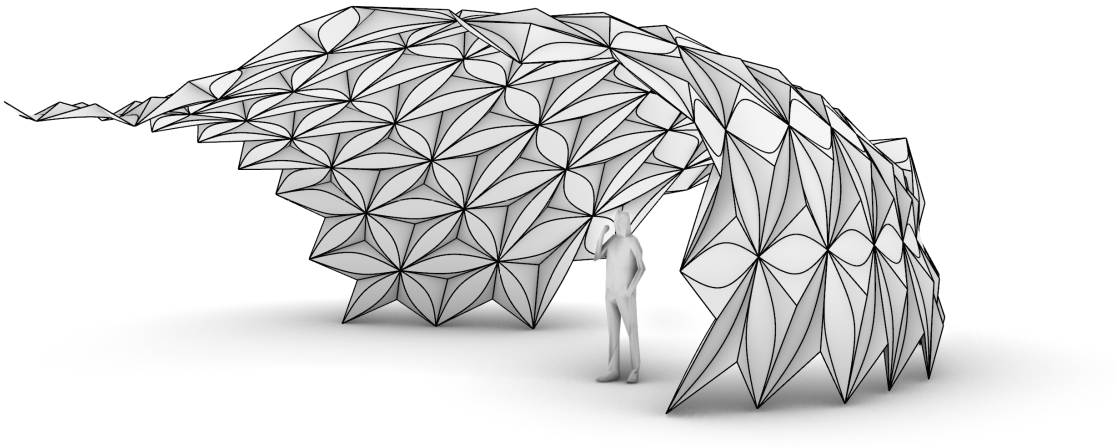

Figure 16.6: Pavilion structure designed with modular quads with lenses.

only two are developable. As discussed in Section 12.3.3, we require that the denominator is greater zero for the values of each ruling, resulting in $(\mathbf{v} - \mathbf{x}_i) \cdot \mathbf{r}_i > (\mathbf{V} - \mathbf{X}_i) \cdot \mathbf{R}_i$, where $\mathbf{X}_i$ is a sampled point of $\mathbf{X}(t)$ and $\mathbf{x}_i$ its development.

- *Valid range:* We want to make sure that the crease exists in a suitable range of the developable surface (e.g., does not pass through the apex to the other part of the cone). This property translates to the numerator of $l(t)$ being greater than zero, that is, $|\mathbf{v} - \mathbf{x}_i|^2 > |\mathbf{V} - \mathbf{X}_i|^2$, where $\mathbf{X}_i$ is a sampled point of $\mathbf{X}(t)$ and $\mathbf{x}_i$ its development.

When the above inequalities are satisfied for all sampled points, we have found a valid curved crease. In case of a cone-cone design, we then (smoothly or linearly) interpolate the crease and construct extrusions to $\mathbf{V}_1$ and $\mathbf{V}_2$. In case of the lens design, we compute the crease for the other cone with apex $\mathbf{V} = \mathbf{V}_1$. We then extrude both creases to the corresponding cone apices and construct the cylinder as a loft with parallel rulings between the two curves.

16.3 Modular Curved-Crease Designs

Equipped with the theory of the previous section, we apply the quad-filling method to each face of a non-planar quad mesh. If the faces of the mesh are planar or not all quads, we can apply the following planarity-breaking "subdivision" scheme to construct a mesh M' with non-planar faces from the given mesh M.

1. Initialize M' with the set of vertices of M and an empty face set.
2. For every face, add a new vertex at a user-specified amount in normal direction from the face's center. The corresponding parameter establishes the degree of non-planarity.
3. For every interior edge, create a face containing the edge's endpoints and the two vertices corresponding to its adjacent faces.

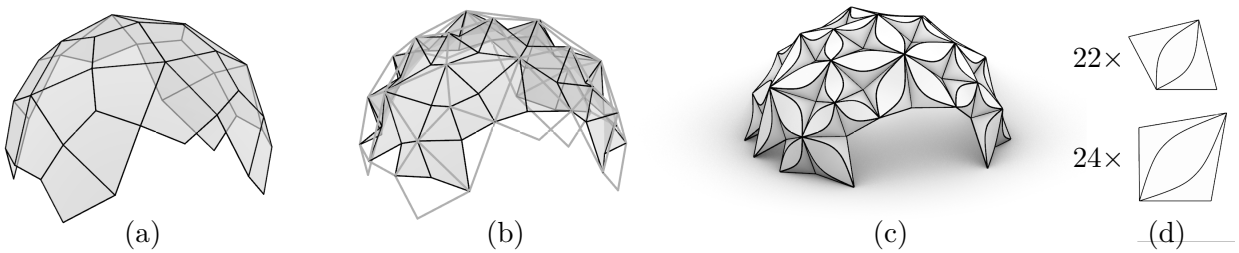

Figure 16.7: Illustration of the modular curved-crease design workflow: (a) Initial mesh M. (b) Subdivided mesh M'. (c) Quads filled with curved-crease molecules. (d) Development consisting of two different types of developed molecules.

Development. Applying the quad-filling method from Section 16.2 to a non-planar quad mesh results in a shape comprised of curved-crease modules. Each curved-crease module can be unrolled, resulting in a set of curved-crease patterns with quadrangular boundaries. However there is no guarantee that the sum of intrinsic angles incident to a common vertex is exactly 2π, and thus the shape might not be globally developable. For fabrication purposes, the decomposition into smaller pieces can be beneficial. Alternatively, knowing the dimensions of the unrolled quads allows the use of other positioning heuristics of the quads, such as polygon nesting [7] or Origamizer-based Kirigami patterns [22].

Design variations. Tiling entire surfaces with foldable modules is a design approach used in many fields. Some design variations of foldable lenses are shown in Maleczek et al. [94]. In our setup, each non-planar quad of a mesh can be filled with one of six curved-crease molecule types (see Figure 16.8). In addition, there is the freedom of changing the shape-defining curve. Our implementation can be used to explore patterns generated by the composition of curved creases in quads.

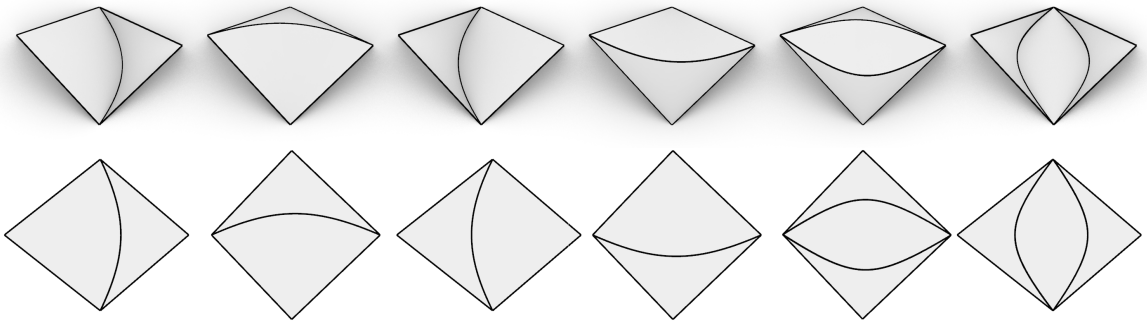

Figure 16.8: For each non-planar quad and fixed curve, we can select the molecule's orientation and type. This leads to six potential curved crease molecule designs (four cone-cone molecules and two lens molecules).

16.4 Towards Global Origami Development

In the previous sections, we considered the non-planar faces of a quad mesh as individual folded patches, the final mesh being a joining of these parts. However, for admissible shapes, we might

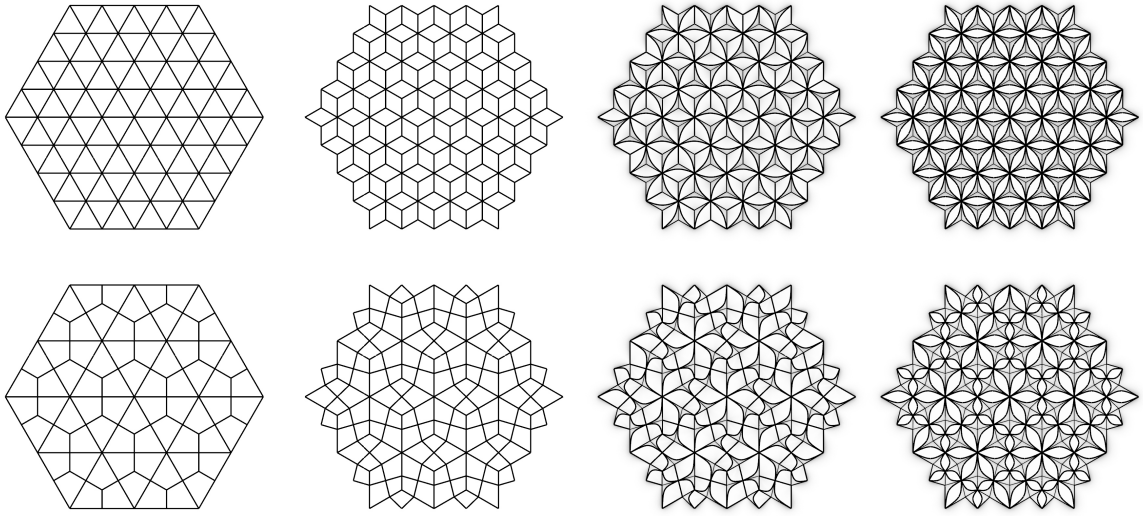

Figure 16.9: Patters generated by subdivision and quad filling. From left to right: initial pattern, subdivided pattern, filled cone-cone molecules, and filled lens molecules.

aim for a globally developable design that can be fabricated from a single large sheet of material without any slits. To accomplish this, we formulated an optimization problem and implemented it using Kangaroo, a dynamic relaxation engine plugin for Rhino/Grasshopper. Upon success, the resulting shape often times looks wrinkled, hence the name; see Figure 16.10.

To begin, we must generate a topologically identical mesh to our given 3D mesh to serve as our crease pattern. This mesh must be planar and should not contain overlapping faces or edges. For simple geometries, this can be manually generated, or it can be obtained through a Tutte embedding [106] or the ARAP method [89, 52].

The variables in the optimization problem include the positions of the 3D mesh vertices, and optionally, the positions of the vertices in the developed mesh. In certain cases, it is desirable to find a mesh that is compatible with a predetermined crease pattern, further limiting the space of feasible solutions.

16.4.1 Constraints

To obtain suitable geometries, we impose the following constraints on the 3D (and optionally 2D) vertices of the meshes:

1. Every mesh edge must have identical length in 3D and 2D.
2. Corresponding quad diagonals must be shorter in 3D than in 2D.
3. Every 2D quad's diagonal length should be bounded by above to ensure that the constructed first surface can be realized from a suitable **Z**-central function.

To prevent significant deviations from the initial configuration, we incorporate regularization constraints into the optimization process, such as anchoring certain points to their original positions. Moreover, it can be beneficial to restrict a sparse set of vertices to remain on the design surface, preserving proximity to the original shape. Similarly, constraining boundary vertices to stay on

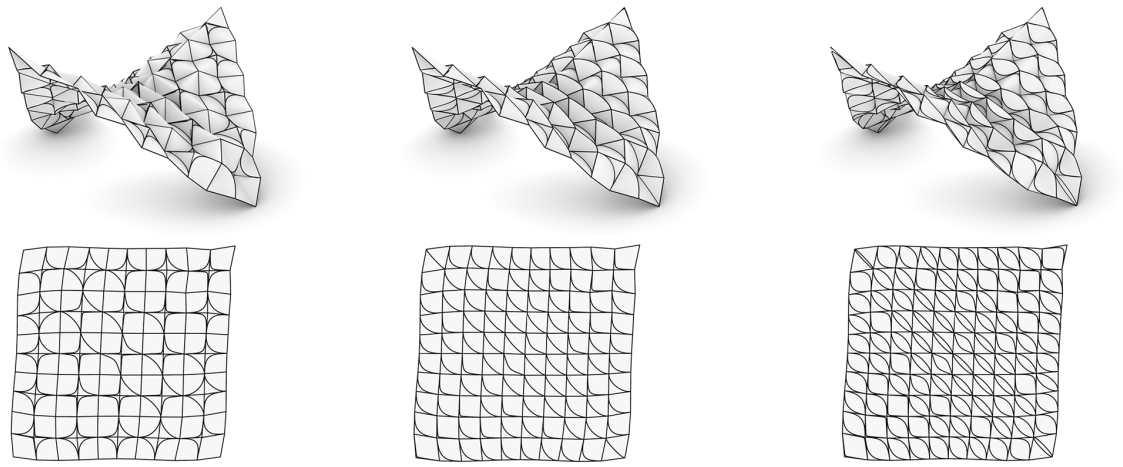

Figure 16.10: Three globally developable curved-crease designs that are based on the same mesh and their crease patterns.

the boundary edges helps prevent them from collapsing to a single point. For more details on the implementation, refer to Kraft et al. [46].

16.4.2 Filling a 3D Quad with a Prescribed Development

Upon success of the above described optimization process of the 3D and 2D mesh, we aim to fill each 3D non-planar quad with a curved-crease molecule whose development fits the corresponding 2D face. The scale parameter s, as discussed in Section 16.2.3, provides a degree of design flexibility. Adjusting this scale parameter affects the intrinsic opening angle of the cone in the case of the cone-cone design, or the intrinsic distance between two points on a cylinder in the case of a lens design.

Determining an appropriate scale parameter that corresponds to the desired opening angle or diagonal distance of the target 2D quad can be framed as finding the root of a scalar function. We have observed that in most valid configurations, this scalar function demonstrates monotonic behavior.

16.5 Fabrication

Figure 16.12 displays two shapes designed by the methods of this chapter that were fabricated using paper-backed veneer.

In collaboration with the RnKOLEKTIVE [69], our implementation was used to construct a tower using discretized folded panels made from 1.2mm Hylite. The tower was fabricated using milling on the Zünd machine and was showcased at the MIT MediaLab in Summer 2023, as depicted in Figure 16.11.

Figure 16.11: A tower with discretized lens molecules, displayed at the MIT MediaLab during summer 2023.

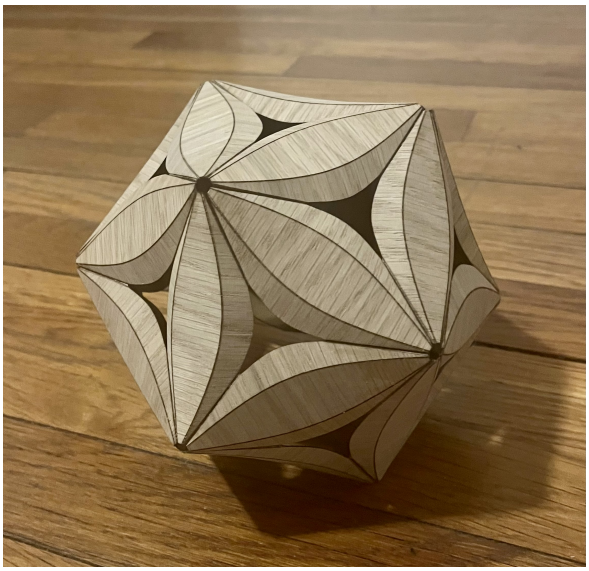

(a) A curved-crease icosahedron made from oak veneer consisting of 30 trimmed lenses.

(b) An ornament fabricated from four types of paper-backed veneer.

Figure 16.12: Two shapes made from paper-backed veneer.

Chapter 17

Developable Regular Planar Quad Mesh Subdivision

This chapter presents unpublished results of discussions with Erik Demaine and Tomohiro Tachi.

Overview

In this chapter, we present an approach for subdividing regular planar quad (PQ) meshes while preserving the planarity of faces without requiring an additional optimization step. Our method involves replacing each face of the mesh with a generalized cylinder or cone. We demonstrate how our approach can be modified using the patch-to-projective-cone construction to maintain the overall developability of the PQ mesh when the input mesh is close to being developable.

By using this construction technique, we propose a framework for the interactive design of precise discretizations of curved folding. Specifically, we use a coarse PQ mesh as the control geometry to efficiently compute the subdivided approximation. The time required for our approach scales linearly with the number of rulings, which eliminates the typical trade-off between surface fineness and interactivity encountered in optimization-based methods.

17.1 Introduction

Curved-crease origami is widely used for design and engineering applications given its simplicity of fabrication and aesthetic expression [31, 15], resulting in demand for interactively exploring the design space of shapes possible by folding sheets along curves. However, the curved-crease design process is challenging given the complicated geometric constraints on feasible solutions [17, 18].

Past work has developed constructive and optimization-based approaches for interactively designing curved folding. Constructive approaches can robustly produce precise and fine results but have been limited to a small family of curved folding, namely, curved origami that can be constructed by reflection of a single developable surface [60], curved folding produced from a single curve [100], or curved folding with a prescribed position of singularities of rulings using the patch-to-cylinder and patch-to-cone constructions [64]. Optimization-based approaches can handle a wider variety of origami patterns through the discretization of developable surfaces. Planar-quad (PQ) meshes are discrete analogues of developable surfaces [82], but they are generally prone to jaggy artifacts and computation instability when rulings change drastically. Despite various approaches to tackle these problems, there is a persistent trade-off between the fineness of the surface and interactivity.

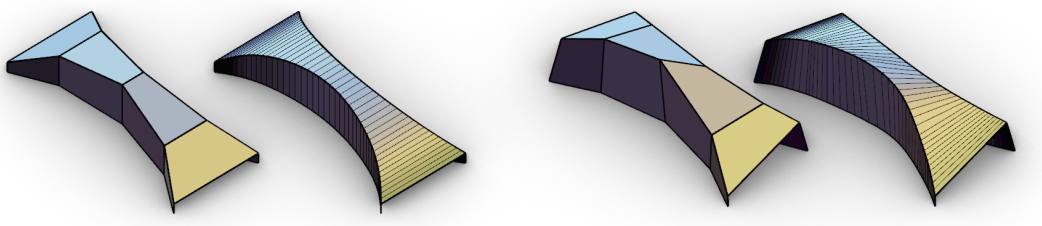

Figure 17.1: Illustration of the robust behavior of our method for significantly changing rulings.

In this chapter, we present a constructive approach for subdividing a coarse regular origami pattern, resulting in a finely discretized curved-crease origami design without the need for further optimization. Using a coarse pattern as the control geometry, this approach efficiently computes exact developable PQ meshes in linear time. Through this method, we achieve improved interactivity, both in terms of computation time and robustness, as illustrated in Figure 17.1. This advancement significantly broadens the range of achievable curved-crease origami designs using constructive techniques.

To begin, we demonstrate how scaling transformations can be used for the subdivision of a PQ strip in Section 17.2. Next, we showcase how the subdivision of the PQ strip can be propagated throughout the regular PQ mesh without the requirement of additional optimization in Section 17.3. Finally, we explore the application of the patch-to-projective-cone construction in Section 17.4, enabling the generation of developable meshes when the input mesh is already close to being developable.

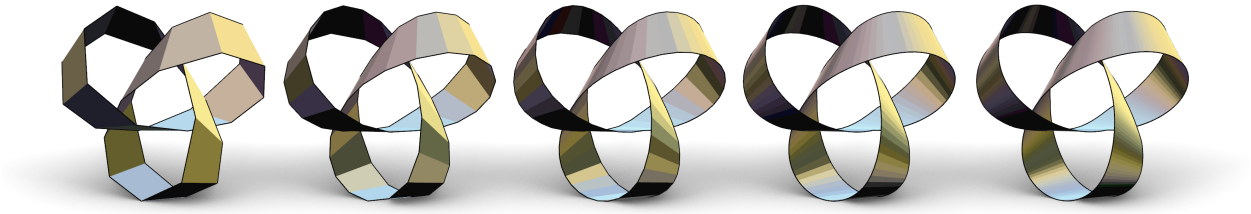

Figure 17.2: Illustration of the proposed subdivision scheme on a PQ strip in the shape of a trefoil knot.

17.2 PQ Strip Subdivision

We first consider a construction that subdivides a PQ strip using a sequence of discrete cylinders and cones.

The main idea of the proposed construction is to subdivide one of the boundary curves of the PQ strip using scaling with respect to the intersection of the incident interior edges. This process determines the subdivided edge directions, resulting in rulings of piece-wise discrete cylinders and cones. This idea can be formalized as follows:

Let $\mathscr{P}_1 = \{\mathbf{P}_{1,0}, \ldots, \mathbf{P}_{1,n-1}\}$ and $\mathscr{P}_2 = \{\mathbf{P}_{2,0}, \ldots, \mathbf{P}_{2,n-1}\}$, where $n > 3$, represent the bounding polylines of the strip, and let m be the desired number of subdivisions we aim to introduce per face.

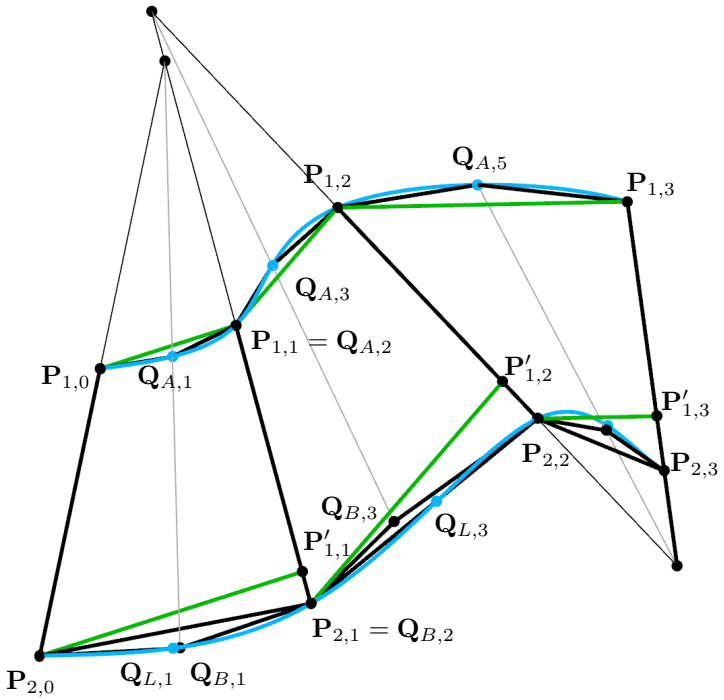

Figure 17.3: Illustration of the PQ strip subdivision notation.

As a result of this subdivision process, the subdivided PQ strip's boundary polylines will possess $(n-1)m+1$ vertices.

First, we interpolate the boundary polylines $\mathcal{P}_1$ and $\mathcal{P}_2$ with two smooth cubic splines $\mathbf{X}_1(t)$ and $\mathbf{X}_2(t)$ such that $\mathbf{X}_1(t_{1,i}) = \mathbf{P}_{1,i}$ and $\mathbf{X}_2(t_{2,i}) = \mathbf{P}_{2,i}$ for $0 \leq i < n$, where $t_{j,i}$ are some appropriately chosen knot values.

We then evaluate the curves at intermediate parameters, resulting in polylines $\mathcal{Q}_1$ and $\mathcal{Q}_2$ with $(n-1)m+1$ vertices. Specifically, we evaluate the curve at m equidistant convex combinations of the interpolated parameter values, that is, for $0 \leq im+j < (n-1)m+1$, where $0 \leq i < n-1$ and $0 \leq j \leq m$, define for $k \in \{1,2\}$

$$\mathbf{Q}_{k,im+j} = \mathbf{X}_k\left(\frac{m+1-j}{m+1}t_{k,i} + \frac{j}{m+1}t_{k,i+1}\right).$$

Note that the original input points are contained in the subdivided polylines.

The mesh obtained by lofting $\mathcal{Q}_1$ and $\mathcal{Q}_2$ does not necessarily have planar faces. Instead of choosing both boundary polylines, we choose one of them to be the *shape-defining polyline* $\mathcal{Q}_A$, and the other to be the *length-defining polyline* $\mathcal{Q}_L$. The points of the shape-defining polylines will be the vertices of the final subdivided mesh, and we use scale transformation to obtain the points of the second boundary curve $\mathcal{Q}_B$ of the subdivided PQ mesh.

For each face, consider a scale transformation defined by two corresponding pairs of points (as discussed in Lemma 12.4): $\mathbf{P}_{1,i} \mapsto \mathbf{P}_{2,i}$ and $\mathbf{P}_{1,i+1} \mapsto \mathbf{P}'_{1,i+1}$, where $\mathbf{P}'_{1,i+1}$ denotes the intersection of $\mathbf{P}_{1,i+1}\mathbf{P}_{2,i+1}$ with the line parallel to $\mathbf{P}_{1,i}\mathbf{P}_{1,i+1}$ incident to $\mathbf{P}_{2,i}$. For each point $\mathbf{Q}_{A,l} \in \mathcal{Q}_A$ corresponding to that face (resp. interval $[t_{A,i}, t_{A,i+1}]$), we choose the incident ruling to be spanned by $\mathbf{Q}_{A,l}$ and its scaled counterpart $\mathbf{Q}'_{A,l}$.

We then use the length-defining polyline to appropriately "trim" the computed ruling, resulting in the corresponding point $\mathbf{Q}_{B,l} \in \mathcal{Q}_B$. For example, we can choose $\mathbf{Q}_{B,l}$ to be the closest point

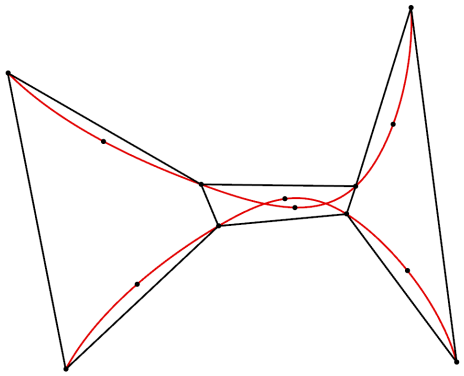

Figure 17.4: Illustration of a problematic input for the PQ strip subdivision scheme.

of $\mathbf{Q}_{L,l}$ to $\mathbf{Q}_{A,l}\mathbf{Q}'_{A,l}$. Depending on the input and design requirements, other heuristics for the locations of the points of $\mathcal{Q}_B$ might be more appropriate.

Although the constructed points $\mathbf{Q}_{B,im+j}$ do not generally lie on the the length-defining curve, the vertices of the original polyline will be a subset of $\mathcal{Q}_B$. Lastly, we construct the subdivided mesh as a loft between the two polylines $\mathcal{Q}_A$ and $\mathcal{Q}_B$.

Note that since the subdivided edges are obtained by scaling with respect to the intersection of adjacent interior input mesh edges, their extensions pass through the center of scaling of the corresponding face and are therefore pairwise coplanar:

Corollary 17.1. *The faces of the subdivided strip spanned by the polylines $\mathcal{Q}_A$ and $\mathcal{Q}_B$ are planar. Furthermore, the input strip and the subdivided strip have the same set of singularities.*

The preservation of the same set of singularities is especially advantageous. as it ensures that no new singularities are introduced during the subdivision process.

The overall computational complexity is $\Theta(nm)$: Cubic spline interpolation amounts in solving a tridiagonal system of linear equations, which can be solved in linear time ([72], Section 9.2.3) in the number of interpolated points. The remaining construction is linear in the number of sampled rulings.

17.2.1 Limitations

The success of the proposed construction heavily depends on the input. Specifically, when dealing with "thin" faces, the resulting subdivisions may not yield desirable outcomes, as depicted in Figure 17.4. However, in certain instances, this issue can be mitigated by making adjustments to the chosen knots or choosing a different trimming heuristic.

17.3 Regular PQ Mesh Subdivision

We experimented with propagating this method along the rows of a regular PQ mesh, resulting in a constructive subdivision approach for regular PQ meshes; see Figure 17.5.

Specifically, given a regular PQ mesh, we select one row of consecutive planar quads and subject this strip to the PQ strip subdivision discussed in Section 17.2; see Figure 17.5(b). Subsequently, we sequentially propagate this subdivision to adjacent rows, using the points on the common curve as the sampled points of the shape-defining curve; see Figure 17.5(c)-(d). Upon success, this

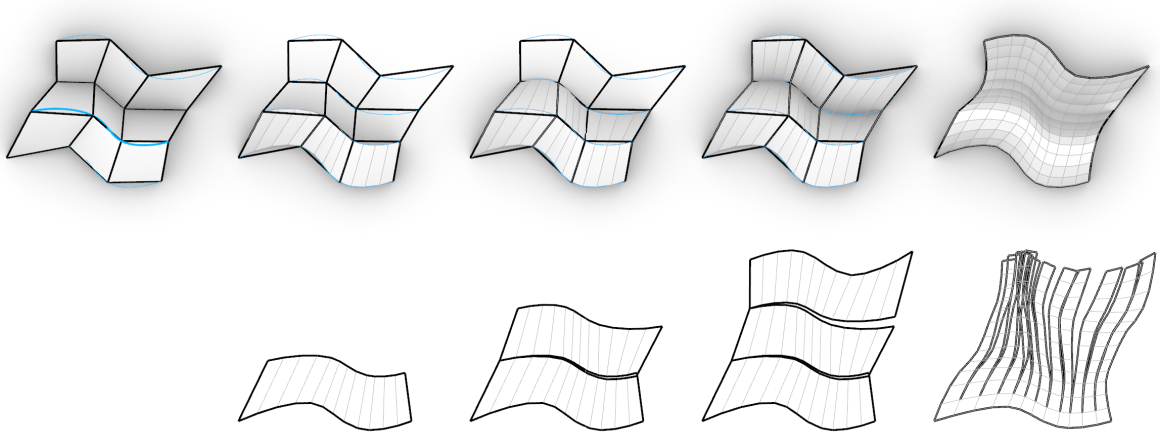

Figure 17.5: Illustration of the proposed regular PQ mesh subdivision construction. From left to right: Input mesh; Subdivision of first PQ strip with $m = 3$; Two propagations of the subdivision to neighboring strips; Subdivision of the resulting mesh in the other direction.

process yields a watertight, one-directional subdivision with planar faces; see Figure 17.5(d) and Figure 17.6a (top).

By performing these one-directional subdivision procedures in both directions with the same number of subdivisions, we obtain a subdivision scheme, wherein upon success each planar quad is replaced with $(m+1) \times (m+1)$ planar faces, as shown in Figure 17.5(e) and Figure 17.6a (bottom).

17.3.1 Limitations

In contrast to well-established subdivision schemes, our method lacks a guarantee for convexity and overall success. In particular, the possible issues discussed in the Section 17.2.1 can now occur at each sampled row. However, despite this limitation, the experimental results have been surprisingly promising, demonstrating a high level of well-behavedness; as illustrated in Figure 17.6a and Figure 17.6b.

17.4 Developable PQ Mesh Subdivision

Note, however, that the proposed subdivision scheme does not, in general, preserve the developability of vertices, even if the initial mesh corresponds to a developable coarse counterpart of a curved origami pattern; see Figure 17.5. In the following, we will discuss how to use the patch-to-patch approximation with ruling planes, as discussed in Section 12.7, to construct a subdivided mesh with developable vertices that approximates the input mesh.

Input. The input to our scheme is an almost developable regular PQ mesh, where one family of edges represents rulings, and the other family corresponds to discretized curves. It is essential to ensure that the mountain-valley assignment along the discretized curves is consistent.

Without loss of generality, we denote the vertices of the input mesh as $\mathbf{P}_{i,j}$ for $0 \leq i < r$ and $0 \leq j < n$, where the edges $\mathbf{P}_{i,j}\mathbf{P}_{i+1,j}$ represent rulings, and the polylines $\mathscr{P}_i = (\mathbf{P}_{i,0}, \ldots, \mathbf{P}_{i,n-1})$ correspond to the discretized curves.

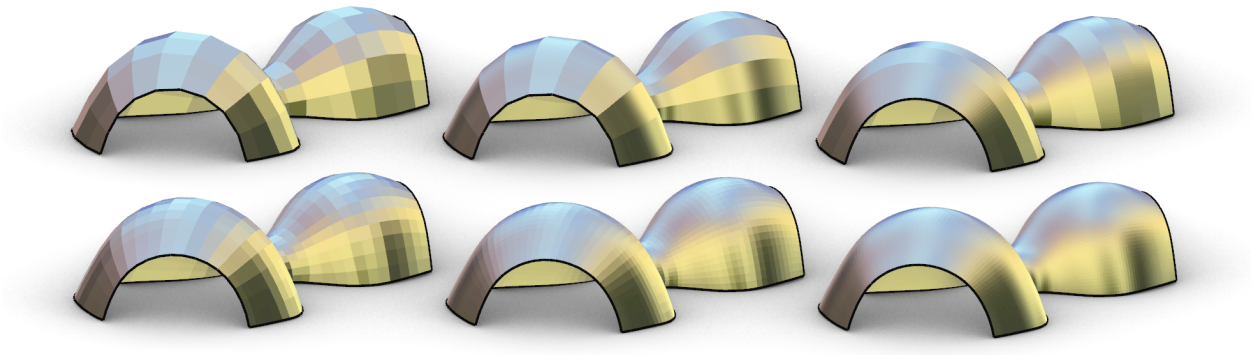

(a) First row: Input mesh and the proposed one-directional subdivisions.
Second row: Two-directional subdivision with $m \in \{2, 4, 8\}$.

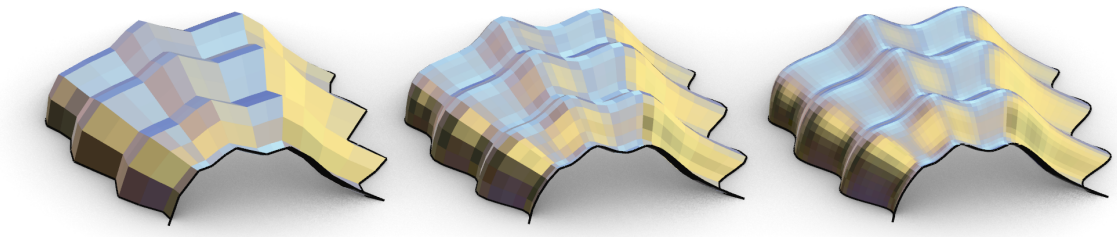

(b) Bidirectional subdivision with $m \in \{2, 4, 8\}$ of the freeform eggbox origami variation.

Figure 17.6: Examples of the proposed regular PQ mesh subdivision.

Subdiving the first PQ strip. Similarly to before, we begin by constructing a subdivision of the PQ strip that connects the polylines $\mathcal{P}_1$ with $\mathcal{P}_0$, where we select the subdivision of $\mathcal{P}_1$ to specify the shape-defining polyline. Let $\mathcal{Q}_1$ and $\mathcal{Q}_0$ denote the corresponding subdivided polylines.

Propagating the subdivision. We will now discuss how to connect a given subdivided PQ strip between $\mathcal{Q}_{i-1}$ and $\mathcal{Q}_i$ with the next row using a patch-to-patch approximation with ruling planes. This process will yield new locations for points of $\mathcal{Q}_i$ and incident rulings of the second surface, ensuring that the vertices of $\mathcal{Q}_i$ become developable; see Figure 17.7.

To achieve this, we define the ruling planes E_i as the planes spanned by $\mathbf{P}_{i+1,j}$ and the strip's rulings corresponding to the mesh edges $\mathbf{P}_{i-1,j}\mathbf{P}_{i,j}$. Additionally, we set $\mathbf{A}_0 = \mathbf{P}_{i,0}$ and $\mathbf{A}'_0 = \mathbf{P}_{i+1,0}$. Furthermore, we define the initial tangent direction as the projection of the tangent of the curve interpolating $\mathcal{P}_i$ at $\mathbf{A}_0$ to the first quad of the PQ strip connecting $\mathcal{Q}_{i-1}$ with $\mathcal{Q}_i$. Note that this uniquely defines the corresponding 2D inputs $\mathbf{a}_0$ and $\mathbf{a}'_0$, as discussed in Section 12.4.4.

Now, using the patch-to-patch approximation, we update the location of the points $\mathcal{Q}_i$ to the computed crease points. Additionally, we determine the ruling directions of the second patch and the points $\mathcal{Q}_{i+1}$ corresponding to the second boundary of the next strip.

It is important to note that the constructed rulings, in general, may not align with the ruling edges of the mesh. However, based on our experiments, we observed that for suitable, almost developable meshes, this deviation is not significant.

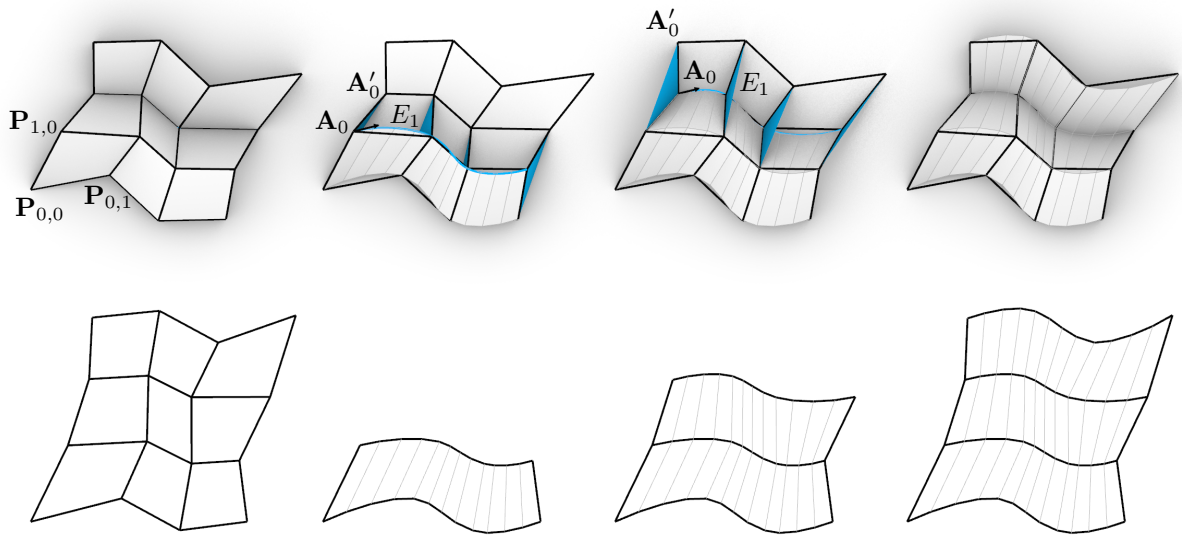

Figure 17.7: Illustration of the proposed developable regular PQ mesh subdivision construction. From left to right: Developable input mesh; Subdivision of the first PQ strip with $m = 3$; Patch-to-patch constructions using ruling planes; Subdivided developable PQ mesh.

Retrieving the mesh. By performing this construction sequentially for the $r - 2$ interior rows of the mesh, we obtain r subdivided polylines $\mathcal{Q}_i$. Finally, we construct the subdivided mesh by lofting between consecutive polylines. Due to this construction, the mesh possesses planar quad faces and developable vertices. Moreover, this entire process runs in linear time with respect to the number of sampled rulings, making it well-suited for interactive design.

Geodesic folds. Finally, note that a variation of this approach can be used to construct strips that compose a geodesic strip model; see Figure 17.9.

17.4.1 Results

We implemented our design system as a custom component for Grasshopper / Rhino [81, 57]. In combination with Crane [96] and Freeform Origami [99] software tools, we interactively design the coarse mesh while computing its smooth refinement.

Although the crease points have the possibility to move away from the initial mesh vertices, the singularities and vertices of the input and output mesh usually do not deviate too much (see e.g. Figure 17.1). We observed good results, which have numerically planar faces and numerically developable vertices.

17.4.2 Limitations and Future Work

We limit our input to a regular (degree-4) quadrangular mesh that is homeomorphic to a disk. Although adding singularities by inserting interior vertices with other valences can increase design possibilities, the application of our method is still restricted to symmetric cases (as shown in Figure 17.12).

Generic non-degree-4 meshes cause the sequential construction to loop back to the original position, and our current construction does not support closure constraints. However, we believe

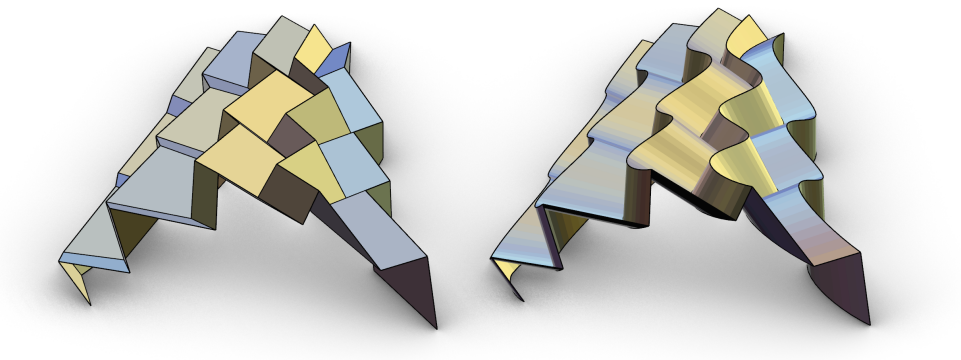

Figure 17.8: Left: A freeform variation of the Miura-ori origami pattern optimized for planarity of faces and developability of vertices. Right: One-directional developable refinement.

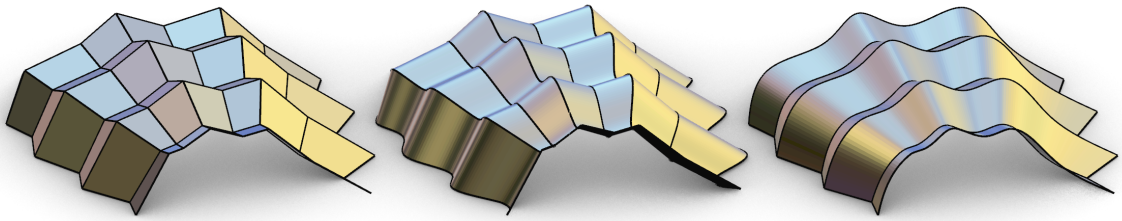

Figure 17.9: Left: A freeform variation of the flat-foldable eggbox origami pattern optimized for planarity of faces and bidirectional flat-foldability of vertices (BDFFPQ, [98]). Right: Refinement resulting in two one-directional flat-foldable PQ meshes, that is, discrete counterparts of geodesic strip models.

that some closure constraints can potentially be solved by optimization on the coarse mesh, thus preserving the overall efficiency of the constructive method. Nonetheless, characterizing reasonable closure constraints and implementing an interactive solver remain as future work.

Extending our method to algebraically defined smooth surfaces, possibly combining with [51], is also interesting future work. Because the ruling-length-based construction works for each sampled ruling, we may extract the positions of rulings for a parameter u whenever it is necessary. The only unsolved issue for the smooth representation is the need for computing the exact development, for which we currently rely on the PQ mesh.

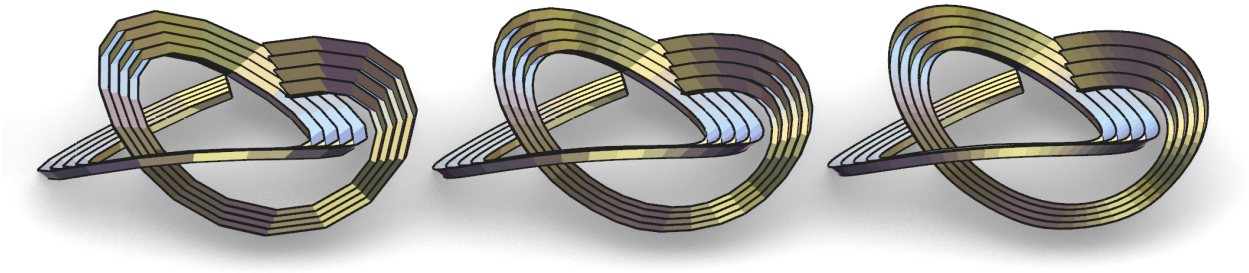

Figure 17.10: Application of the developable PQ mesh subdivision to a mesh approximating an open curve in shape of a trefoil knot with pleats.

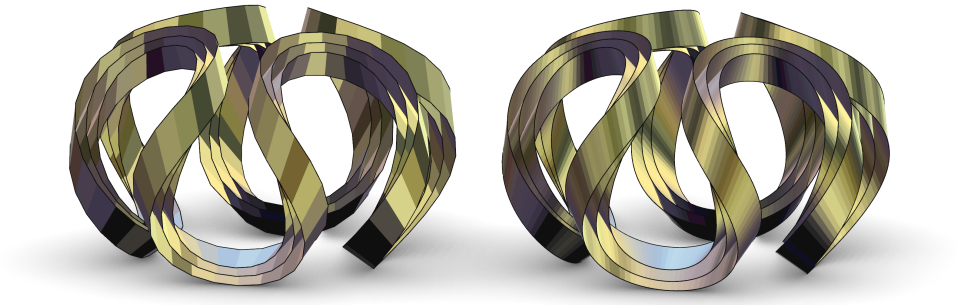

Figure 17.11: Application of the developable PQ mesh subdivision to a mesh approximating an open curve with pleats.

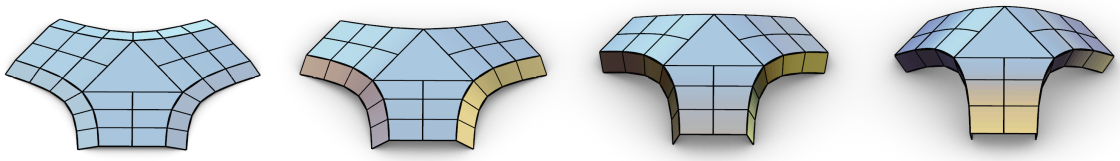

Figure 17.12: The motion of a subdivided tripod demonstrates a limitation of our method on a non-regular PQ mesh. Here, the method is applied to only one half of one arm and then mirrored using symmetry.

Epilogue

Chapter 18

Conclusion

18.1 Summary and Limitations

This dissertation examines shapes achieved by gluing or creasing flat sheets of material, like paper, along curves. The research advances existing theory for their computation, considers specific example shapes, and introduces novel tools for their computational design.

18.1.1 Theory of Gluing and Creasing Developable Patches

Summary of contributions

- We generalize the statement that C^2 ruled surfaces are developable if and only if their rulings are torsal to surfaces that are only C^1.
- For developable surfaces with C^2 directrices, we adapt the description of developable ruled surfaces and introduce patch developables.
- We generalize the approach of creasing along a curved crease with specified rulings to gluing two developed patches with specified rulings.
- We show how to join three patches with only partial ruling information.
- We show that gluing patches along tangent-parallel curves with parallel rulings of every second-to-next patch results in rigidly foldable structures.
- We formulate the join-and-fan method, a simplified computation for the case of gluing two smooth or discrete patches that are either cylinders or cones. We provide necessary and sufficient conditions for the existence of a rigid folding motion in the case of discrete creases.
- We discover two rigidly foldable discretizations of conic crease patterns and classify when they are flat-foldable.
- We formulate the patch-to-cylinder and patch-to-cone constructions that determine the crease between a smooth or discrete developable patch and a cylinder or a cone. By combining multiple constructions, we obtain a construction of a crease where the second surface consists of a sequence of cylinders and cones.

Limitations

Limited connectivity. The presented computations are applicable only sequentially. As such, they are limited to shapes with a tree-like connectivity of patches. Patches that form closed loops and glue or crease points incident to multiple glue or crease curves require special considerations.

Limited by algebraic complexity. The curvature-based approach for joining general developable patches leads to systems of differential equations that may become increasingly challenging to solve as the glue or crease pattern becomes more complex. In many cases, numerical differential solvers may accumulate numerical errors.

Computational limitation of partial ruling information. The presented method for joining three patches with only partial ruling information is restricted to combinations of curves where the relationship between the arc-length parametrization and curvature of one pair of joined curves is explicitly known. This limitation arises from the practical difficulty of solving for the input function of a numeric function.

Limited information on folding motion. While we have identified some valid combinations of glue or crease curves that result in rigidly-foldable crease or glue patterns, determining how the folding motion progresses is generally challenging. Real-life experiments can sometimes be misleading, as actual paper is forgiving and permits imperfections during folding.

18.1.2 Parametric Construction of Shapes Obtained by Gluing or Creasing Patches

Summary of contributions

- We determine a closed-form expression for the parametrization of some variations of the gluing of a polygon and a circle, and identify unique convex gluings.
- Up to elliptic integrals, we determine the parametrization of the Vesica Piscis and conic creases of constant fold angle.
- Up to numeric integrals and the integration of the Frenet-Serret equations, we compute approximations of numerous shapes, including families of elliptic Anti D-forms, pleated creases of closed curves, some variations of the gluing of a square and a circle, Klammer's kinetic sculpture, and David Huffman's hexagonal column.

Limitations

Need good guess for rulings. Currently, for the reconstruction of shapes achieved through gluing or creasing paper, we depend on the availability of appropriate initial guesses for ruling directions for at least some parts of the shape.

Challenges with spiraling rulings. When investigating shapes like D-forms or general spirals, none of the previously mentioned techniques were successful. We conjecture the existence of a category of shapes with rule segments exhibiting spiraling behavior, which cannot be effectively addressed using the methods developed in this thesis.

Numerical existence. Concerning the most general approach, which involves the integration of the Frenet-Serret equations, we currently lack the necessary tools to estimate numerical error and deduce (numerical) existence for certain shapes.

18.1.3 Computational Design Tools for Shapes Obtained by Gluing or Creasing Patches

Summary of contributions

- We implement the presented variations of the patch-to-cylinder and patch-to-cone constructions as an interactive design tool for constructing shapes with multiple curved creases.
- We implement a design tool for creating origami spirals from cones with planar creases.
- We propose two algorithmic design strategies to approximate a polyhedral shape with curved crease designs. The first method replaces polyhedron edges with right circular cylinders and vertices with cones connected to adjacent cylinders via smooth curved creases. The second method fills non-planar quad faces of a polyhedron with curved-crease molecules.
- We introduce a linear-time subdivision scheme for regular, developable planar quad meshes by replacing the faces of the mesh with discretized cylinders or cones.

Limitations

Limited connectivity. The additive constructions work only for tree-like connectivity of patches. Consequently, closing a circular array of patches relies on a careful setup or symmetry of the target shape.

Geometry limited to cylinders and cones. Our algorithmic design tools exploit the simplicity of cylinders and cones. General tangent developables are approximated by a series of cylinders and cones.

Software tools support only zero-thickness surfaces. In many applications, material thickness significantly impacts the behavior of the shape. The presented tools consider only zero-thickness surfaces, and are thus, in some cases, misleading when it comes to real-world behavior.

Limited support for fabrication. Some of the implemented tools could use more work on the workflow of actually obtaining a manufacturable cut and crease file or latches for connections of patches.

Not universal. The proposed design tools are limited to specific families of shapes and do not support the desirable feature of starting from a planar pattern and computing a valid ruling layout and corresponding 3D shape.

18.2 Open Problems and Future Work

We believe that shapes obtained by gluing or creasing planar sheets hold significant potential in the fabrication of versatile, functional, and material-efficient structures. One of our primary objectives

is to bridge the gap between theory and practical applications by providing easy access to the design and knowledge required for the computation and creation of such shapes.

In addition to encouraging further interdisciplinary research on the materialization and properties of these shapes, we have identified the following list of potential theoretical research directions that build upon the contents of this thesis.

18.2.1 Theoretical Background

Further analysis of C^1 developable patches. In Section 2.2.1, we demonstrate that ruled surfaces are developable surfaces if and only if their rulings are torsal. However, in the general, non-cylindrical, and non-conical cases, the singular curve might be only continuous and not continuously differentiable. In future work, we aim to investigate this special case in more detail and develop an approach to visualize examples of such surfaces.

Gluing without patch characteristics. In Section 2.2.1, we illustrate how to compute the development of C^1 developable ruled surfaces. Based on our discoveries, we intend to explore how gluing and creasing along directrices of general developables can be formulated without the need for the curvature-based approach presented in Part I of the thesis.

18.2.2 Part I: Curvature-Based Computation of Configurations

Special cases of gluing two patches with specified rulings. In Section 3.3, we extend the concept of creasing two patches to gluing. While two known special cases exist for creasing along a single curve, namely planar creases and creases with a constant fold angle, we leave the exploration of special cases for when two patches are glued along non-congruent curves as a subject for future work.

Rigid-ruling folding of planar and constant-angle creases. In Section 3.5.2, we demonstrate that tangent-parallel creases enable rigid-ruling folding motions. In generic discrete scenarios, tangent-parallel curves are the only curves compatible with planar creases, resulting in rigidly foldable crease-rule patterns. Interpreting smooth patches as the limit of a fine sampling of the discrete case, it is plausible that this property remains true in the smooth case. However, when dealing with constant-angle creases, there may be configurations that are not tangent-parallel, as illustrated in Section 6.3 by the logarithmic spiral example or Chapter 10 by compatible conic crease combinations with reciprocal eccentricity. Further exploration of compatible curves and an explanation of the difference between planar creases and creases with a constant fold angle are subjects for future research.

Closure constraints and spiraling rulings. As pointed out in Section 7.3, we conjecture that certain closed shapes, such as some spirals or D-forms derived from ellipses, have rulings that exhibit spiraling behavior, making the tools presented in this thesis inapplicable. Furthermore, the presented tools are limited to patches with tree-like connectivity, and closure of a circular array of patches currently relies on the symmetry of the shape. In future work, we aim to investigate tools for the parametric reconstruction of such shapes.

Numerical tools for existence proofs. As it is probably very unlikely to obtain closed-form solutions for some of the studied shapes, it would be desirable to seek alternative forms for math-

ematical existence claims. In future work, we aim to develop tools to rigorously establish the numerical existence of shapes.

Ruling solver. The ultimate goal in the study of shapes made from developable patches is to develop a strategy to determine a valid ruling layout for any given glue or crease pattern.

Exploring gluing and creasing of other surface types. We would be interested in exploring the concept of gluing and creasing of other families of surfaces, such as ruled surfaces or surfaces with constant Gaussian curvature.

18.2.3 Part II: Ruling-Length-Based Computation of Configurations of Joined Cylinders and Cones

Rigidly foldable combinations of projective cones with collinear apices. In Chapter 8, we address the special case of computing rigidly foldable configurations of glued or folded cylinders and cones using the join-and-fan method. Building upon Chapter 10, we aim in future work to classify combinations of triples of projective cones with collinear apices that result in rigidly foldable structures.

Design tool for rigidly foldable patterns from conics. Similar to Section 17.4, we aim to explore how a user-specified crease pattern can be approximated using a series of compatible conic crease combinations, not necessarily with collinear apices, to create flat and rigidly foldable crease patterns.

18.2.4 Part III: Ruling-Length-Based Computation of Creases

Generalization of patch-to-cylinder and patch-to-cone constructions to gluing. In Chapter 12, we discussed how to use a ruling-based approach to compute the crease between a cylinder and a cone with a specified cylinder base plane or cone apex. We wonder whether similar considerations can be applied to computing the glue curve between a patch and a cylinder or cone with a given ruling length.

Differently constraining curve in patch-to-patch construction. Additionally, we would like to explore variations of the patch-to-projective-cone construction by constraining the crease curve differently, such as by constraining it to lie on a Monge patch.

Variations of conic spirals. In Chapter 14, we demonstrate the construction of conic spirals using a circular array of an even number of curves. We would also like to explore alternative construction methods, including the possibility of creating rigidly foldable spirals. Additionally, inspired by Huffman, we aim to investigate spirals in which the creases are formed by an array of pairs of appropriate curves. Furthermore, drawing inspiration from Lukascheva's tessellation, we leave the exploration of methods for tessellating the spirals to future work.

Other pattern design tools. In Chapter 16, we discussed how to fill non-planar quads with curved-crease elements. In future work, we plan to explore other tessellations to approximate a given 3D shape using curved-crease elements.

Generalize regular PQ mesh subdivision. As of now, the subdivision method presented in Chapter 17 is limited to regular planar quad meshes. We aspire to investigate high-level optimization approaches to extend the method's applicability to meshes with more general connectivity.

Algorithmically streamlined production. In the future, we plan to further develop our implementation to facilitate the fabrication and design of computed shapes, including considerations for thickness, surface development, and the labeling of corresponding patches.

Bibliography

[1] Zachary Abel, Jason Cantarella, Erik D. Demaine, David Eppstein, Thomas C. Hull, Jason S. Ku, Robert J. Lang, and Tomohiro Tachi. Rigid origami vertices: Conditions and forcing sets. *Journal of Computational Geometry*, 7(1):171–184, 2016.

[2] Esther Dora Adler. *"A new unity!": The art and pedagogy of Josef Albers*. University of Maryland, College Park, 2004.

[3] Leonardo Alese. Propagation of curved folding: the folded annulus with multiple creases exists. *Beiträge zur Algebra und Geometrie/Contributions to Algebra and Geometry*, 63(1):19–43, 2022.

[4] Alexander D. Alexandrov. *Convex Polyhedra*. Springer, Berlin, 2005.

[5] Carlos Martinez Architekten. Knies Zauberhut, 2018–2020. https://carlosmartinez.ch/arbeiten/knies-kinderzoo/.

[6] Manan Arya, David Webb, Samuel C. Bradford, Louis Adams, Velibor Cormarkovic, Gary Wang, Mehran Mobrem, Kenzo Neff, Neal Beidleman, John D. Stienmier, Gregg Freebury, Kamron A. Medina, David Hepper, Dana E. Turse, George Antoun, Cory Rupp, and Laura Hoffman. Origami-inspired Optical Shield for a Starshade Inner Disk Testbed: Design, fabrication, and analysis. In *AIAA Scitech 2021 Forum*, 2021.

[7] Julia A. Bennell and Jose F. Oliveira. The geometry of nesting problems: A tutorial. *European Journal of Operational Research*, 184(2):397–415, 2008.

[8] Marcel Berger and Bernard Gostiaux. *Differential Geometry: Manifolds, Curves, and Surfaces*, volume 115. Springer Science & Business Media, 2012.

[9] Alexandre Binninger, Floor Verhoeven, Philipp Herholz, and Olga Sorkine-Hornung. Developable approximation via Gauss image thinning. *Computer Graphics Forum*, pages 289–300, 2021.

[10] Sergey Bochkanov. ALGLIB, 1999–2020. https://www.alglib.net/.

[11] Vincent Borrelli, Saïd Jabrane, Francis Lazarus, and Boris Thibert. Flat tori in three-dimensional space and convex integration. *Proceedings of the National Academy of Sciences*, 109(19):7218–7223, 2012.

[12] H. Brauner. *Differentialgeometrie, Vorlesung im WS 1966/1967*. Technische Hochschule Stuttgart, Mathematisches Institut B, 1966/67.

[13] Julie Steele Chalfant. *Analysis and design of developable surfaces for shipbuilding*. PhD thesis, Massachusetts Institute of Technology, 1997.

[14] Suryansh Chandra, Shajay Bhooshan, and Mustafa El-Sayed. Curve-folding polyhedra skeletons through smoothing. In *Origami^6: Proceedings of the 6th International Meeting on Origami in Science, Mathematics and Education (OSME 2014)*, pages 231–240, 2015.

[15] Erik D. Demaine, Martin Demaine, Duks Koschitz, and Tomohiro Tachi. A review on curved creases in art, design and mathematics. *Symmetry: Culture and Science*, 26(2):145–161, 2015.

[16] Erik D. Demaine, Martin L. Demaine, Vi Hart, Gregory N. Price, and Tomohiro Tachi. (Non)existence of pleated folds: how paper folds between creases. *Graphs and Combinatorics*, 27(3):377–397, 2011.

[17] Erik D. Demaine, Martin L. Demaine, David A. Huffman, Duks Koschitz, and Tomohiro Tachi. Characterization of curved creases and rulings: Design and analysis of lens tessellations. In *Origami^6: Proceedings of the 6th International Meeting on Origami in Science, Mathematics and Education (OSME 2015)*, pages 209–230, 2015.

[18] Erik D. Demaine, Martin L. Demaine, David A. Huffman, Duks Koschitz, and Tomohiro Tachi. Conic crease patterns with reflecting rule lines. In *Origami^7: Proceedings of the 7th International Meeting on Origami in Science, Mathematics and Education (OSME 2018)*, pages 573–590, 2018.

[19] Erik D. Demaine, Martin L. Demaine, and Duks Koschitz. Reconstructing David Huffman's legacy in curved-crease folding. In *Origami^5: Proceedings of the 5th International Meeting on Origami in Science, Mathematics and Education (OSME 2011)*, pages 39–52. 2011.

[20] Erik D. Demaine, Klara Mundilova, and Tomohiro Tachi. Locally flat and rigidly foldable discretizations of conic crease patterns with reflecting rule lines. In *ICGG 2022-Proceedings of the 20th International Conference on Geometry and Graphics*, pages 185–196. Springer, 2022.

[21] Erik D. Demaine and Gregory N. Price. Generalized D-Forms have no spurious creases. *Discrete & Computational Geometry*, 43(1):179, 2010.

[22] Erik D. Demaine and Tomohiro Tachi. Origamizer: A practical algorithm for folding any polyhedron. In *33rd International Symposium on Computational Geometry (SoCG 2017)*, 2017.

[23] Hans Dirnböck and Hellmuth Stachel. The development of the Oloid. *J. Geom. Graph*, 1:105–118, 1997.

[24] Thomas A. Evans, Robert J. Lang, Spencer P. Magleby, and Larry L. Howell. Rigidly foldable origami twists. *Origami^6: Proceedings of the 6th International Meeting on Origami in Science, Mathematics and Education (OSME 2015)*, 6(1):119–130, 2015.

[25] Riccardo Foschi, Robby Kraft, Rupert Maleczek, Klara Mundilova, and Tomohiro Tachi. How to use parametric curved folding design methods – a case study and comparison. *Proceedings of IASS Annual Symposia*, 2020(23):1–11, 2020.

[26] Dmitry Fuchs and Serge Tabachnikov. More on paperfolding. *The American Mathematical Monthly*, 106(1):27–35, 1999.

[27] Flux Furniture. Flux Chair. https://www.fluxfurniture.com/items/chair/.

[28] J.M. Gattas and Z. You. The behaviour of curved-crease foldcores under low-velocity impact loads. *International Journal of Solids and Structures*, 53:80–91, 2015.

[29] Karl F. Gauss and Peter Pesic. *General investigations of curved surfaces*. Courier Corporation, 2005.

[30] Frank Gehry Architects. Fondation Louis Vuitton. https://www.fondationlouisvuitton.fr/en/fondation/the-building.

[31] Georg Glaeser and Franz Gruber. Developable surfaces in contemporary architecture. *Journal of Mathematics and the Arts*, 1(1):59–71, 2007.

[32] Zaha Hadid. Arum (Venice Biennale 2012), 2012. https://www.robofold.com/make/consultancy/projects/arum-for-zaha-hadid-architects0.

[33] Philip Hartman and Aurel Wintner. On the fundamental equations of differential geometry. *American Journal of Mathematics*, 72(4):757–774, 1950.

[34] David A. Huffman. Curvature and creases: A primer on paper. *IEEE Transactions on computers*, 25(10):1010–1019, 1976.

[35] Victor C. Inza, Florian Rist, Johannes Wallner, and Helmut Pottmann. Developable quad meshes. *ACM Trans. Graph.*, (6), December 2022.

[36] Alexandra Ion, Michael Rabinovich, Philipp Herholz, and Olga Sorkine-Hornung. Shape approximation by developable wrapping. *ACM Trans. Graph.*, 39(6), November 2020.

[37] Ivan Izmestiev, Arvin Rasoulzadeh, and Jonas Tervooren. Isometric deformations of discrete and smooth T-surfaces. *arXiv preprint arXiv:2302.08925*, 2023.

[38] Caigui Jiang, Klara Mundilova, Florian Rist, Johannes Wallner, and Helmut Pottmann. Curve-pleated structures. *ACM Trans. Graph.*, 38(6):169:1–169:13, November 2019.

[39] Caigui Jiang, Cheng Wang, Florian Rist, Johannes Wallner, and Helmut Pottmann. Quad-mesh based isometric mappings and developable surfaces. *ACM Trans. Graph.*, 39(4), August 2020.

[40] Daniel Kane, Gregory N. Price, and Erik D. Demaine. A pseudopolynomial algorithm for Alexandrov's Theorem. In *Algorithms and Data Structures: 11th International Symposium, WADS 2009, Banff, Canada, August 21-23, 2009. Proceedings 11*, pages 435–446. Springer, 2009.

[41] Martin Kilian, Simon Flöry, Zhonggui Chen, Niloy J. Mitra, Alla Sheffer, and Helmut Pottmann. Developable surfaces with curved creases. *Advances in Architectural Geometry 2008*, pages 33–36, 2008.

[42] Maximilan Klammer. Polyannular cyclide: Challenging static architectures, an exploration on cyclic processes, shapes and movements. Master's thesis, Academy of Fine Arts Vienna, 2019.

[43] Duks Koschitz. *Computational design with curved creases: David Huffman's approach to paperfolding*. PhD thesis, MIT, 2014.

[44] Duks Koschitz. Curved-crease paperfolding shell. In *Proceedings of IASS Annual Symposia*, number 13, pages 1–8, 2019.

[45] Leon Kotin. Solutions of systems of periodic differential equations. *Journal of Mathematical Analysis and Applications*, 8(1):52–56, 1964.

[46] Robby Kraft, Rupert Maleczek, Klara Mundilova, and Tomohiro Tachi. From quad filling to wrinkled surfaces. *Advances in Architectural Geometry 2023*, 6:327, 2023.

[47] Robert J. Lang, Spencer Magleby, and Larry Howell. Single degree-of-freedom rigidly foldable cut origami flashers. *Journal of Mechanisms and Robotics*, 8(3):031005, 2016.

[48] Robert J. Lang, Todd Nelson, Spencer Magleby, and Larry Howell. Kinematics and discretization of curved-fold mechanisms. In *International Design Engineering Technical Conferences and Computers and Information in Engineering Conference*, volume 5B. American Society of Mechanical Engineers, 2017.

[49] Susan Latham. https://susanlatham.net/.

[50] Ting-Uei Lee, Yan Chen, Michael T. Heitzmann, and Joseph M. Gattas. Compliant curved-crease origami-inspired metamaterials with a programmable force-displacement response. *Materials & Design*, 207:109859, 2021.

[51] Stefan Leopoldseder and Helmut Pottmann. Approximation of developable surfaces with cone spline surfaces. *Computer-Aided Design*, 30(7):571–582, 1998.

[52] Ligang Liu, Lei Zhang, Yin Xu, Craig Gotsman, and Steven J. Gortler. A local/global approach to mesh parameterization. In *Computer Graphics Forum*, volume 27:5, pages 1495–1504, 2008.

[53] Ekaterina Lukasheva. *Curved Origami*. New Origami Publishing, 2021.

[54] Rupert Maleczek. https://maleczek.info/.

[55] Rupert Maleczek, Klara Mundilova, and Tomohiro Tachi. Curved crease edge rounding of polyhedral surfaces. In *Advances in Architectural Geometry 2020*, pages 130–153, 2020.

[56] Peter Mayrhofer. 3D-Modelling of special D-Forms made from elliptic shaped developments. In *ICGG 2010: Proceedings of the 8th International Conference on Geometry and Graphics*, 2010.

[57] McNeel. Rhinoceros3D. https://www.rhino3d.com/.

[58] Jun Mitani. Column-shaped origami design based on mirror reflections. *Journal for Geometry and Graphics*, 16(2):185–194, 2012.

[59] Jun Mitani. *Curved-Folding Origami Design*. CRC Press, 2019.

[60] Jun Mitani and Takeo Igarashi. Interactive design of planar curved folding by reflection. In *Pacific Graphics Short Papers*, 2011.

[61] Jeannine Mosely. The validity of the Orb, an Origami Model. In *Third International Meeting of Origami Science, Mathematics, and Education, AK Peters, Ltd*, pages 75–82, 2002.

[62] Fabian Muhs, Simon Thissen, and Peter Middendorf. Virtual process chain for optimization of sandwich foldcores under flatwise compression. *Thin-Walled Structures*, 157:107121, 2020.

[63] Klara Mundilova. Curved crease folds of spherical polyhedra with regular faces. In *Proceedings of Bridges 2019: Mathematics, Art, Music, Architecture, Education, Culture*, pages 423–426, 2019.

[64] Klara Mundilova. On mathematical folding of curved crease origami: Sliding developables and parametrizations of folds into cylinders and cones. *Computer-Aided Design*, 115:34–41, 2019.

[65] Klara Mundilova, Erik D. Demaine, Riccardo Foschi, Robby Kraft, Rupert Maleczek, and Tomohiro Tachi. Lotus: A curved folding design tool for Grasshopper. In *Proceedings of the 41st Annual Conference of the Association of Computer Aided Design in Architecture (ACADIA)*, pages 194–203, 2021.

[66] Klara Mundilova, Erik D. Demaine, Robert Lang, and Tomohiro Tachi. Curved-crease origami spirals constructed from reflected cones. In *Proceedings of Bridges 2023: Mathematics, Art, Music, Architecture, Education, Culture*, 2023.

[67] Klara Mundilova and Tony Wills. Folding the Vesica Piscis. In *Proceedings of Bridges 2018: Mathematics, Art, Music, Architecture, Education, Culture*, pages 535–538, 2018.

[68] John Nash. c^1 isometric imbeddings. *Annals of mathematics*, pages 383–396, 1954.

[69] Alfonso Parra Rubio, Camron Blackburn, Eyal Perry, Jan Tiepelt, Jurgis Ruza, Klara Mundilova, Quentin Bolsée, Rebecca Lin, Vera ven de Seyp, and Vlasta Kubusova. RnKolektive. https://www.rnkol.art/.

[70] Francisco Pérez and José Antonio Suárez. Quasi-developable B-spline surfaces in ship hull design. *Computer-Aided Design*, 39(10):853–862, 2007.

[71] Martin Peternell. Developable surface fitting to point clouds. *Computer Aided Geometric Design*, 21(8):785–803, 2004.

[72] Les Piegl and Wayne Tiller. *The NURBS book*. Springer Science & Business Media, 1996.

[73] Daniel Piker and Will Pearson. Plankton, 2013. https://github.com/meshmash/Plankton.

[74] Helmut Pottmann, Alexander Schiftner, Pengbo Bo, Heinz Schmiedhofer, Wenping Wang, Niccolo Baldassini, and Johannes Wallner. Freeform surfaces from single curved panels. *ACM Trans. Graph.*, 27(3):1–10, August 2008.

[75] Helmut Pottmann and Johannes Wallner. *Computational Line Geometry*. Mathematics and Visualization. Springer Berlin Heidelberg, 2010.

[76] Michael Rabinovich, Tim Hoffmann, and Olga Sorkine-Hornung. Discrete geodesic nets for modeling developable surfaces. *ACM Transactions on Graphics (TOG)*, 37(2):1–17, 2018.

[77] Michael Rabinovich, Tim Hoffmann, and Olga Sorkine-Hornung. The shape space of discrete orthogonal geodesic nets. *ACM Transactions on Graphics (TOG)*, 37(6):1–17, 2018.

[78] Michael Rabinovich, Tim Hoffmann, and Olga Sorkine-Hornung. Modeling curved folding with freeform deformations. *ACM Transactions on Graphics (TOG)*, 38(6):1–12, 2019.

[79] Rechenraum. Goat. https://www.rechenraum.com/en/goat.html.

[80] Ron Resch. http://www.ronresch.org/.

[81] David Rutten. Grasshopper. https://www.grasshopper3d.com/.

[82] Robert Sauer. *Differenzengeometrie*. Springer, 1970.

[83] Silvia Sellán, Noam Aigerman, and Alec Jacobson. Developability of heightfields via rank minimization. *ACM Trans. Graph.*, 39(4), August 2020.

[84] Kiumars Sharifmoghaddam, Rupert Maleczek, and Georg Nawratil. Generalizing rigid-foldable tubular structures of T-hedral type. *Mechanics Research Communications*, page 104151, 2023.

[85] Kiumars Sharifmoghaddam, Georg Nawratil, Arvin Rasoulzadeh, and Jonas Tervooren. Using flexible trapezoidal quad-surfaces for transformable design. In *Proceedings of IASS Annual Symposia*, number 28, pages 1–13, 2020.

[86] John Sharp. D-forms and developable surfaces. In *Renaissance Banff: mathematics, music, art, culture*, pages 121–128, 2005.

[87] John Sharp. *D-forms: Surprising new 3-D forms from flat curved shapes*. Tarquin Publications St. Albans, 2009.

[88] Justin Solomon, Etienne Vouga, Max Wardetzky, and Eitan Grinspun. Flexible developable surfaces. *Computer Graphics Forum*, 31(5):1567–1576, 2012.

[89] Olga Sorkine and Marc Alexa. As-rigid-as-possible surface modeling. In *Symposium on Geometry processing*, volume 4, pages 109–116, 2007.

[90] Michael D. Spivak. *A comprehensive introduction to differential geometry*, volume 3. 1999.

[91] Hellmuth Stachel. Two examples of solids constructed from given developments. *J. Geom. Graph*, 20:225–241, 2016.

[92] Oded Stein, Eitan Grinspun, and Keenan Crane. Developability of triangle meshes. *ACM Trans. Graph.*, 37(4), July 2018.

[93] Jacob Steiner. Die Theorie der Kegelschnitte in elementarer Darstellung Theil 1. *Jacob Steiner's Vorlesungen über synthetische Geometrie*, 1875.

[94] Gabriel Stern and Rupert Maleczek. Lens tesselation inspired surface approximation. In *Origami^7: Proceedings of the 7th International Meeting on Origami in Science, Mathematics and Education (OSME 2018)*, pages 865–876, 2018.

[95] Saadya Sternberg. *Sculptural Origami: Innovative Models, Plus a Gallery of the Artist's Work*. Dover Publications, 2011.

[96] Kai Suto, Yuta Noma, Kotaro Tanimichi, Koya Narumi, and Tomohiro Tachi. Crane: An integrated computational design platformfor functional, foldable, and fabricable origami products. *ACM Transactions on Computer-Human Interaction*, 2022.

[97] Richard Sweeney. https://richardsweeney.co.uk/.

[98] Tomohiro Tachi. Freeform rigid-foldable structure using bidirectionally flat-foldable planar quadrilateral mesh. In *Advances in Architectural Geometry 2010*, pages 87–102, Vienna, 2010. Springer Vienna.

[99] Tomohiro Tachi. Freeform variations of origami. *Journal for Geometry and Graphics*, 14(2):203–215, 2010.

[100] Tomohiro Tachi. One-DOF rigid foldable structures from space curves. In *Proceedings of the IABSE-IASS Symposium*, pages 20–23, 2011.

[101] Tomohiro Tachi. Composite rigid-foldable curved origami structure. *Proceedings of Transformables*, pages 18–20, 2013.

[102] Tomohiro Tachi and Thomas C. Hull. Self-foldability of rigid origami. *Journal of Mechanisms and Robotics*, 9(2), 2017.

[103] Chengcheng Tang, Pengbo Bo, Johannes Wallner, and Helmut Pottmann. Interactive design of developable surfaces. *ACM Trans. Graph.*, 35(2), jan 2016.

[104] Russell E. Todres. Translation of W. Wunderlich's "On a developable Möbius band". *Journal of Elasticity*, 119:23–34, 2015.

[105] Godfried Toussaint. Simple proofs of a geometric property of four-bar linkages. *The American mathematical monthly*, 110(6):482–494, 2003.

[106] William T. Tutte. How to draw a graph. *Proceedings of the London Mathematical Society*, pages 743–767, 1963.

[107] Floor Verhoeven, Amir Vaxman, Tim Hoffmann, and Olga Sorkine-Hornung. Dev2PQ: Planar quadrilateral strip remeshing of developable surfaces. *ACM Trans. Graph.*, 41(3), March 2022.

[108] Tony Wills. D-Forms: 3D forms from two 2D sheets. In *Proceedings of Bridges 206: Mathematics, Art, Music, Architecture, Education, Culture*, pages 503–510, 2006.

[109] Hans M. Wingler. *The Bauhaus: Weimar, Dessau, Berlin, Chicago.* MIT Press, Cambridge, Massachusetts, 1969.

[110] Steven Woodruff. *How Curved Creases Enhance the Stiffness and Enable Shape Morphing of Thin-Sheet Structures.* PhD thesis, University of Michigan, 2022.

[111] Walter Wunderlich. Über ein abwickelbares Möbiusband. *Monatshefte für Mathematik*, 66(3):276–289, 1962.

[112] Chao Yuan, Nan Cao, and Yang Shi. A survey of developable surfaces: From shape modeling to manufacturing. *arXiv preprint arXiv:2304.09587*, 2023.